

Hackers' new assault on
scholarly journals p. 903

On the history of
plate tectonics p. 915

Patrolling monocytes
protect the lungs p. 955

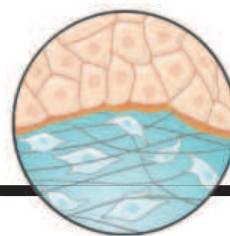
Science

\$10
20 NOVEMBER 2015
science.org

AAAS

Eyes in the armor

Double duty for biominerals
in a mollusk's shell pp. 899 & 952



NEWS

IN BRIEF

892 Roundup of the week's news

IN DEPTH

894 LISA PATHFINDER TESTS SPACETIME SENSOR

A European space probe is set to pave the way for measurements of gravitational waves *By D. Clery*

895 A FASTER, BRIGHTER PICTURE OF BRAIN CELLS IN ACTION

New voltage-sensor achieves submillisecond precision *By E. Underwood*

► REPORT BY Y. GONG ET AL.

10.1126/science.aab0810

896 NIH PROGRAM FAILS TO LAUNCH BLACKS IN BIOTECH

Small Business Innovation Research program makes almost no grants to African-Americans *By J. Mervis*

897 EUROPE'S RESEARCH CHIEF WANTS SCIENTISTS TO SPEAK UP

Commissioner Carlos Moedas is confident that science and innovation will bring growth to a divided continent *By T. Rabesandratana*

898 HUMANS MAY HAVE REACHED CHILE BY 18,500 YEARS AGO

Monte Verde stone tools may be the oldest in the Americas *By A. Gibbons*

899 CRYSTALLINE EYES OF CHITONS INSPIRE MATERIALS SCIENTISTS

Mollusk makes hundreds of eyes from shell mineral *By E. Pennisi*

► REPORT P. 952

FEATURES

900 WHAT DOES A DISEASE DESERVE?

A move to end NIH's AIDS earmark fuels debate over whether funding should reflect disease burden *By J. Kaiser*

903 HOW TO HIJACK A JOURNAL

A patient hacker can take over a journal's official Web domain with relative ease—as I found out by doing so myself *By J. Bohannon*

INSIGHTS

BOOKS ET AL.

906 THINGS TO DO IN A RETIREMENT HOME TRAILER PARK

By A. Wright,

MY DEGENERATION

By P. Dunlap-Shohl, reviewed by A. W. Frank

PERSPECTIVES

908 RESTORING VOICE

Engineered vocal cords could soon replace damaged tissue

By J. L. Long and D. K. Chhetri

► SCIENCE TRANSLATIONAL MEDICINE

RESEARCH ARTICLE BY C. LING ET AL.; PODCAST

909 MAPPING THE BIRTH OF THE SLEEP CONNECTOME

Hindbrain neurons flip the switch between REM sleep, non-REM sleep, and wakefulness *By V. V. Vyazovskiy*

► REPORT P. 957

911 TRANSPORT: A ROADBLOCK TO CLIMATE CHANGE MITIGATION?

Urban mobility solutions foster climate mitigation *By F. Creutzig et al.*

913 PUTTING THE BREAKS ON MEIOSIS

Yeast and birds reveal remarkable evolutionary stability in recombination patterns *By M. Lichten*

► RESEARCH ARTICLES PP. 928 & 932

914 MAGNETIC FIELDS MAKE WAVES IN CUPRATES

High magnetic fields reveal underlying electronic states in high-temperature superconductors

By M.-H. Julien

► REPORT P. 949

915 100 YEARS OF CONTINENTAL DRIFT

One hundred years ago, Alfred Wegener laid the foundations for the theory of plate tectonics *By M. Romano and R. L. Cifelli*

917 PEROVSKITE SOLAR CELLS JOIN THE MAJOR LEAGUE

Highly efficient perovskite solar cells show promise for future low-cost electricity generation *By M. Sessolo and H. J. Bolink*

► REPORT P. 944

918 OPENING THE WINDOW FOR AQUEOUS ELECTROLYTES

Lithium batteries can operate with a safer "water-in-salt" electrolyte *By L. Smith and B. Dunn*

► RESEARCH ARTICLE P. 938



CONTENTS



913, 928, & 932

Genetic recombination in birds

20 NOVEMBER 2015 • VOLUME 350 • ISSUE 6263

LETTERS

920 WILDFIRES: WEIGH POLICY EFFECTIVENESS

By M. M. Boer et al.

920 WILDFIRES: SYSTEMIC CHANGES REQUIRED

By M. Thompson et al.

920 RESPONSE

By M. North et al.

921 ERRATA

RESEARCH

IN BRIEF

923 From *Science* and other journals

REVIEW

926 NEURODEVELOPMENT

Genes, circuits, and precision therapies for autism and related neurodevelopmental disorders M. Sahin and M. Sur

REVIEW SUMMARY; FOR FULL TEXT:
dx.doi.org/10.1126/science.aab3897

RESEARCH ARTICLES

927 STEM CELL REGULATION

Bidirectional Notch signaling regulates *Drosophila* intestinal stem cell multipotency Z. Guo and B. Ohlstein

RESEARCH ARTICLE SUMMARY; FOR FULL TEXT:
dx.doi.org/10.1126/science.aab0988

NONHUMAN GENETICS

928 Stable recombination hotspots in birds S. Singhal et al.

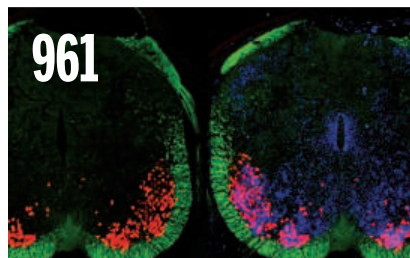
932 Nonparadoxical evolutionary stability of the recombination initiation landscape in yeast I. Lam and S. Keeney

► PERSPECTIVE P. 913

938 BATTERIES

“Water-in-salt” electrolyte enables high-voltage aqueous lithium-ion chemistries L. Suo et al.

► PERSPECTIVE P. 918



REPORTS

944 SOLAR CELLS

Efficient and stable large-area perovskite solar cells with inorganic charge extraction layers W. Chen et al.

► PERSPECTIVE P. 917

949 SUPERCONDUCTIVITY

Three-dimensional charge density wave order in $\text{YBa}_2\text{Cu}_3\text{O}_{6.67}$ at high magnetic fields S. Gerber et al.

► PERSPECTIVE P. 914

952 BIOLOGICAL MATERIALS

Multifunctionality of chiton biomineralized armor with an integrated visual system L. Li et al.

► NEWS STORY P. 899; VIDEO

957 SLEEP RESEARCH

Cells of a common developmental origin regulate REM/non-REM sleep and wakefulness in mice Y. Hayashi et al.

► PERSPECTIVE P. 909

961 AXON GUIDANCE

Operational redundancy in axon guidance through the multifunctional receptor Robo3 and its ligand NELL2 A. Jaworski et al.

965 CAMOUFLAGE

Open-ocean fish reveal an omnidirectional solution to camouflage in polarized environments P. C. Brady et al.

970 PARASITOLOGY

Helminth infection, fecundity, and age of first pregnancy in women A. D. Blackwell et al.

972 CANCER IMMUNOLOGY

Chemotherapy-induced antitumor immunity requires formyl peptide receptor 1 E. Vacchelli et al.

978 GENE REGULATION

Transcription factor trapping by RNA in gene regulatory elements A. A. Sigova et al.

981 IMMUNOLOGY

Tissue residency of innate lymphoid cells in lymphoid and nonlymphoid organs G. Gasteiger et al.

985 CANCER IMMUNOLOGY

Patrolling monocytes control tumor metastasis to the lung R. N. Hanna et al.

DEPARTMENTS

891 EDITORIAL

America's science legacy
By Neil deGrasse Tyson

► VIDEO

998 WORKING LIFE

A doctor's dilemma
By Elisabeth Pain

ON THE COVER



Superimposed optical and scanning electron micrographs of the mineralized protective armor plates of the chiton *Acanthopleura granulata*. Coincident with the dark pigments are image-forming

lenses primarily composed of aragonite, in marked contrast to the protein-based eyes of most animals. In addition to providing mechanical protection, such design simultaneously allows the organism to monitor potential predatory attacks through optical vision. See pages 899 and 952. Image: Ling Li

SCIENCE (ISSN 0036-8075) is published weekly on Friday, except the last week in December, by the American Association for the Advancement of Science, 1200 New York Avenue, NW, Washington, DC 20005. Periodicals mail postage (publication No. 484460) paid at Washington, DC, and additional mailing offices. Copyright © 2015 by the American Association for the Advancement of Science. The title SCIENCE is a registered trademark of the AAAS. Domestic individual membership and subscription (51 issues): \$153 (\$74 allocated to subscription). Foreign postage extra: Mexico, Caribbean (surface mail) \$55; other countries (air assist delivery) \$85. First class, airmail, student, and emeritus rates on request. Canadian rates with GST available upon request. GST #R1254 88122. Publications Mail Agreement Number 1069624. Printed in the U.S.A. Change of address: Allow 4 weeks, giving old and new addresses and 8-digit account number. Postmaster: Send change of address to AAAS, P.O. Box 96178, Washington, DC 20090-6178. Single-copy sales: \$10.00 current issue, \$15.00 back issue prepaid includes surface postage; bulk rates on request. Authorization to photocopy material for internal or personal use under circumstances not falling within the fair use provisions of the Copyright Act is granted by AAAS to libraries and other users registered with the Copyright Clearance Center (CCC) Transactional Reporting Service, provided that \$30.00 per article is paid directly to CCC, 222 Rosewood Drive, Danvers, MA 01923. The identification code for Science is 0036-8075. Science is indexed in the Reader's Guide to Periodical Literature and in several specialized indexes.

Editor-in-Chief Marcia McNutt

Executive Editor Monica M. Bradford **News Editor** Tim Appenzeller

Managing Editor, Research Journals Katrina L. Kelner

Deputy Editors Barbara R. Jasny, Andrew M. Sugden(UK), Valda J. Vinson, Jake S. Yeston

Research and Insights

SR. EDITORS Caroline Ash(UK), Gilbert J. Chin, Lisa D. Chong, Julia Fahrenkamp-Uppenbrink(UK), Pamela J. Hines, Stella M. Hurlty(UK), Paula A. Kiberstis, Marc S. Lavine(Canada), Kristen L. Mueller, Ian S. Osborne(UK), Beverly A. Purnell, L. Bryan Ray, Guy Riddihough, H. Jesse Smith, Jelena Stajic, Peter Stern(UK), Phillip D. Szurmi, Brad Wible, Nicholas S. Wigginton, Laura M. Zahn **ASSOCIATE EDITORS** Brent Grocholski, Keith T. Smith, Sacha Vignieri **ASSOCIATE BOOK REVIEW EDITOR** Valerie B. Thompson **ASSOCIATE LETTERS EDITOR** Jennifer Sills **CHIEF CONTENT PRODUCTION EDITOR** Cara Tate **SR. CONTENT PRODUCTION EDITOR** Harry Jack, Lauren Kmec **CONTENT PRODUCTION EDITORS** Jeffrey E. Cook, Chris Filiatreau, Cynthia Howe, Barbara P. Ordway, Catherine Wolner **SR. EDITORIAL COORDINATORS** Carolyn Kyle, Beverly Shields **EDITORIAL COORDINATORS** Ramatoulaye Diop, Joi S. Granger, Lisa Johnson, Anita Wynn **PUBLICATIONS ASSISTANTS** Aneera Dobbins, Jeffrey Hearn, Dona Mathieu, Le-Toya Mayne Flood, Shannon McMahon, Scott Miller, Jerry Richardson, Rachel Roberts(UK), Alice Whaley(UK), Brian White **EXECUTIVE ASSISTANT** Anna Bashkurova **ADMINISTRATIVE SUPPORT** Janet Clements(UK), Lizanne Newton(UK), Maryrose Madrid, Laura-Nadine Schuhmacher (UK, Intern), Alix Welch (Intern), John Wood(UK)

News

NEWS MANAGING EDITOR John Travis **INTERNATIONAL EDITOR** Richard Stone **DEPUTY NEWS EDITORS** Daniel Clery(UK), Robert Coontz, Elizabeth Culotta, David Grimm, David Malakoff, Leslie Roberts **CONTRIBUTING EDITOR** Martin Enserink(Europe) **SR. CORRESPONDENTS** Jeffrey Mervis, Elizabeth Pennisi **NEWS WRITERS** Adrian Cho, Jon Cohen, Jennifer Couzin-Frankel, Carolyn Gramling, Eric Hand, Jocelyn Kaiser, Catherine Maticic, Kelly Servick, Robert F. Service, Erik Stokstad(Cambridge, UK), Emily Underwood **INTERNS** Hanae Armitage, Emily DeMarco, Annick Laurent, Laura Olivieri, Juan David Romero **CONTRIBUTING CORRESPONDENTS** Michael Balter(Paris), John Bohannon, Ann Gibbons, Mara Hvistendahl, Sam Kean, Eli Kirsch, Kai Kupferschmidt(Berlin), Andrew Lawler, Christina Larson(Beijing), Mitch Leslie, Charles C. Mann, Eliot Marshall, Virginia Morell, Dennis Normile(Tokyo), Heather Pringle, Tania Rabesandratana(London), Gretchen Vogel(Berlin), Lizzie Wade(Mexico City) **CAREERS** Donisha Adams, Rachel Bernstein **COPY EDITORS** Julia Cole, Jennifer Levin (Chief) **ADMINISTRATIVE SUPPORT** Jessica Williams

Executive Publisher Rush D. Holt

Publisher Kent R. Anderson **Chief Digital Media Officer** Rob Covey

BUSINESS OPERATIONS AND PORTFOLIO MANAGEMENT DIRECTOR Sarah Whalen **BUSINESS SYSTEMS AND FINANCIAL ANALYSIS DIRECTOR** Randy Yi **MANAGER OF FULFILLMENT SYSTEMS** Neal Hawkins **SYSTEMS ANALYST** Nicole Mehmedovic **ASSISTANT DIRECTOR, BUSINESS OPERATIONS** Eric Knott **MANAGER, BUSINESS OPERATIONS** Jessica Tierney **BUSINESS ANALYSTS** Cory Lipman, Cooper Tilton, Celeste Troxler **FINANCIAL ANALYST** Robert Clark **RIGHTS AND PERMISSIONS ASSISTANT DIRECTOR** Emilie David **PERMISSIONS ASSOCIATE** Elizabeth Sandler **RIGHTS, CONTRACTS, AND LICENSING ASSOCIATE** Lili Kiser

MARKETING DIRECTOR Elise Swinehart **ASSOCIATE DIRECTOR OF ACQUISITION AND RETENTION** Julianne Wielga **MARKETING ASSOCIATE** Elizabeth Sattler **SR. MARKETING EXECUTIVE** Jennifer Reeves **ASSOCIATE DIRECTOR, CREATIVE SERVICES** Tzeitel Sorrosa **ART ASSOCIATE** Seil Lee **JR. ART ASSOCIATE** Kim Huynh **ASSISTANT COMMERCIAL EDITOR** Selby Frame **MARKETING PROJECT MANAGER** Angelissa McArthur **PROGRAM DIRECTOR, AAAS MEMBER CENTRAL** Peggy Mihelich **FULFILLMENT SYSTEMS AND OPERATIONS** membership@aaas.org **MANAGER, MEMBER SERVICES** Pat Butler **SPECIALISTS** LaToya Casteel, Terrance Morrison, Latasha Russell **MANAGER, DATA ENTRY** Mickie Napoleoni **DATA ENTRY SPECIALISTS** JJ Regan, Brenden Aquilino, Fiona Giblin

DIRECTOR, SITE LICENSING Tom Ryan **DIRECTOR, CORPORATE RELATIONS** Eileen Bernadette Moran **SR. PUBLISHER RELATIONS SPECIALIST** Kiki Forsythe **PUBLISHER RELATIONS MANAGER** Catherine Holland **PUBLISHER RELATIONS, EASTERN REGION** Keith Layson **PUBLISHER RELATIONS, WESTERN REGION** Ryan Rexroth **SALES RESEARCH COORDINATOR** Aiesha Marshall **MANAGER, SITE LICENSE OPERATIONS** Iqo Edim **SENIOR PRODUCTION SPECIALIST** Robert Koepke **SENIOR OPERATIONS ANALYST** Lana Guz **FULFILLMENT ANALYST** Judy Lillibridge **ASSOCIATE DIRECTOR, MARKETING** Christina Schlecht **MARKETING ASSOCIATES** Thomas Landreth, Isa Sesay-Bah

WEB TECHNOLOGIES SR. DEVELOPER Chris Coleman **DEVELOPERS** Dan Berger, Jimmy Marks, Ryan Jensen **SR. PROJECT MANAGER** Trista Smith

CREATIVE DIRECTOR, MULTIMEDIA Martyn Green **DIRECTOR OF ANALYTICS** Enrique Gonzales **SR. WEB PRODUCER** Sarah Crespi **WEB PRODUCER** Alison Crawford **VIDEO PRODUCER** Nguyen Nguyen **SOCIAL MEDIA PRODUCER** Meghna Sachdev

DIRECTOR OF OPERATIONS PRINT AND ONLINE Lizabeth Harman **DESIGN/PRINT STRATEGY MANAGER** Jason Hillman **QUALITY TECHNICAL MANAGER** Marcus Spiegel **PROJECT ACCOUNT MANAGER** Tara Kelly **DIGITAL PRODUCTION MANAGER** Lisa Stanford **ASSISTANT MANAGER DIGITAL/PRINT** Rebecca Doshi **SENIOR CONTENT SPECIALISTS** Steve Forrester, Antoinette Hodal, Lori Murphy, Anthony Rosen **CONTENT SPECIALISTS** Jacob Hedrick, Kimberley Oster

DESIGN DIRECTOR Beth Rakouskas **DESIGN EDITOR** Marcy Atarod **SENIOR DESIGNER** Garvin Grullón **DESIGNER** Chrystal Smith **GRAPHICS MANAGING EDITOR** Alberto Cuadra **SENIOR SCIENTIFIC ILLUSTRATORS** Chris Bickel, Katharine Sutliff **SCIENTIFIC ILLUSTRATOR** Valerie Altounian **SENIOR ART ASSOCIATES** Holly Bishop, Nathalie Cary, Preston Huey **SENIOR PHOTO EDITOR** William Douthitt **PHOTO EDITORS** Leslie Blizard, Christy Steele

DIRECTOR, GLOBAL COLLABORATION, CUSTOM PUBLICATIONS, ADVERTISING Bill Moran **EDITOR, CUSTOM PUBLISHING** Sean Sanders: 202-326-6430 **ASSISTANT EDITOR, CUSTOM PUBLISHING** Tianna Hicklin: 202-326-6463 **ADVERTISING MARKETING MANAGER** Justin Sawyers: 202-326-7061 **science_advertising@aaas.org** **ADVERTISING MARKETING ASSOCIATE** Javia Flemmings **ADVERTISING SUPPORT MANAGER** Karen Foote: 202-326-6740 **ADVERTISING PRODUCTION OPERATIONS MANAGER** Deborah Tompkins **SR. PRODUCTION SPECIALIST/GRAPHIC DESIGNER** Amy Hardcastle **PRODUCTION SPECIALIST** Yuse Lajimimuh **SR. TRAFFIC ASSOCIATE** Christine Hall **SALES COORDINATOR** Shirley Young **ASSOCIATE DIRECTOR, COLLABORATION, CUSTOM PUBLICATIONS/CHINA/TAIWAN/KOREA/SINGAPORE** Ruolei Wu: +86-186 0082 9345, rwu@aaas.org **COLLABORATION/ CUSTOM PUBLICATIONS/JAPAN** Adarsh Sandhu + 81532-81-5142 asandhu@aaas.org **EAST COAST/E. CANADA** Laurie Faraday: 508-747-9395, FAX 617-507-8189 **WEST COAST/W. CANADA** Lynne Stickrod: 415-931-9782, FAX 415-520-6940 **MIDWEST** Jeffrey Dembski: 847-498-4520 x3005, Steven Loerch: 847-498-4520 x3006 **UK EUROPE/ASIA** Roger Gonçalves: TEL/FAX +41 43 243 1358 **JAPAN** Katsuyoshi Fukamizu(Tokyo): +81-3-3219-5777 kfukamizu@aaas.org **CHINA/TAIWAN** Ruolei Wu: +86-186 0082 9345, rwu@aaas.org

WORLDWIDE ASSOCIATE DIRECTOR OF SCIENCE CAREERS Tracy Holmes: +44 (0) 1223 326525, FAX +44 (0) 1223 326532 tholmes@science-int.co.uk **CLASSIFIED advertise@sciencereaders.org** **U.S. SALES** Tina Burks: 202-326-6577 **Nancy Toema:** 202-326-6578 **SALES ADMINISTRATOR** Marci Gallun **EUROPE/ROW SALES** Axel Gesatzki, Sarah Lelange **Stickrod:** 415-931-9782, FAX 415-520-6940 **MIDWEST** Jeffrey Dembski: 847-498-4520 x3005, Steven Loerch: 847-498-4520 x3006 **UK EUROPE/ASIA** Roger Gonçalves: TEL/FAX +41 43 243 1358 **JAPAN** Katsuyoshi Fukamizu(Tokyo): +81-3-3219-5777 kfukamizu@aaas.org **CHINA/TAIWAN** Ruolei Wu: +86-186 0082 9345, rwu@aaas.org **MARKETING MANAGER** Allison Pritchard **MARKETING ASSOCIATE** Aimee Aponte

AAAS BOARD OF DIRECTORS RETIRING PRESIDENT, CHAIR Gerald R. Fink **PRESIDENT** Geraldine (Geri) Richmond **PRESIDENT-ELECT** Barbara A. Schaaf **TREASURER** David Evans **SHAW CHIEF EXECUTIVE OFFICER** Rush D. Holt **BOARD** Bonnie L. Bassler, May R. Berenbaum, Carlos J. Bustamante, Stephen P. A. Fodor, Claire M. Fraser, Michael S. Gazzaniga, Laura H. Greene, Elizabeth Loftus, Mercedes Pascual

SUBSCRIPTION SERVICES For change of address, missing issues, new orders and renewals, and payment questions: 866-434-AAAS (2227) or 202-326-6417, FAX 202-842-1065. Mailing addresses: AAAS, P.O. Box 96178, Washington, DC 20090-6178 or AAAS Member Services, 1200 New York Avenue, NW, Washington, DC 20005

INSTITUTIONAL SITE LICENSES 202-326-6730 **REPRINTS:** Author Inquiries 800-635-7181 **COMMERCIAL INQUIRIES** 803-359-4578 **PERMISSIONS** 202-326-6765, permissions@aaas.org **AAAS Member Services** 202-326-6417 or http://membercentral.aaas.org/discouints

Science serves as a forum for discussion of important issues related to the advancement of science by publishing material on which a consensus has been reached as well as including the presentation of minority of conflicting points of view. Accordingly, all articles published in Science—including editorials, news and comment, and books reviews—are signed and reflect the individual views of the authors and not official points of view adopted by AAAS or the institutions with which the authors are affiliated.

INFORMATION FOR AUTHORS See pages 678 and 679 of the 6 February 2015 issue or access www.sciencemag.org/about/authors

SENIOR EDITORIAL BOARD

Robert H. Grubbs, *California Institute of Technology*, Gary King, *Harvard University*
Susan M. Rosenberg, *Baylor College of Medicine*, Ali Shalithard, *Northwestern University*
Feinberg School of Medicine, Michael S. Turner, *U. of Chicago*

BOARD OF REVIEWING EDITORS (Statistics board members indicated with \$)

Adriano Aguzzi, *U. Hospital Zurich*
Takuzo Aida, *U. of Tokyo*
Leslie Aiello, *Wenner-Gren Foundation*
Judith Allen, *U. of Edinburgh*
Sonia Altizer, *U. of Georgia*
Sebastian Amigorena, *Institut Curie*
Kathryn Anderson, *Memorial Sloan-Kettering Cancer Center*
Meinrat O. Andrae, *Max-Planck Inst. Mainz*
Paola Arlotta, *Harvard U.*
Johan Auwerx, *EPFL*
David Awechselom, *U. of Chicago*
Clare Baker, *University of Cambridge*
Jordi Bascompte, *University of Zurich*
Jacundo Batista, *London Research Inst.*
Ray H. Baughman, *U. of Texas, Dallas*
David Baum, *U. of Wisconsin*
Carlo Beenakker, *Leiden U.*
Kamran Behnia, *ESPCI-ParisTech*
Yasmine Belkaid, *NIH, NIH*
Philip Benfey, *Duke U.*
Stephen J. Benkovic, *Penn State U.*
May Berenbaum, *U. of Illinois*
Gabriele Bergers, *U. of California, San Francisco*
Bradley Bernstein, *Massachusetts General Hospital*
Peer Bork, *EMBL*
Bernard Bourdon, *Ecole Normale Supérieure de Lyon*
Chris Bowler, *Ecole Normale Supérieure*
Ian Boyd, *U. of St. Andrews*
Emily Brodsky, *U. of California, Santa Cruz*
Ron Brookmeyer, *U. of California Los Angeles (\$)*
Christian Büchel, *U. Hamburg-Eppendorf*
Joseph A. Burns, *Cornell U.*
Carter Tribble Butts, *U. of California, Irvine*
Gyorgy Buzsaki, *New York U. School of Medicine*
Blanche Capel, *Duke U.*
Mats Carlsson, *U. of Oslo*
Ib Chorkendorff, *U. of Denmark*
David Clapham, *Children's Hospital Boston*
David Clary, *U. of Oxford*
Joel Cohen, *Rockefeller U., Columbia U.*
James J. Collins, *MIT*
Robert Cook-Deegan, *Duke U.*
Alan Cowman, *Walter & Eliza Hall Inst.*
Robert H. Crabtree, *Yale U.*
Roberta Croce, *Vrije Universiteit*
Janet Currie, *Princeton U.*
Jeff L. Dangi, *U. of North Carolina*
Tom Daniel, *U. of Washington*
Frans de Waal, *Emory U.*
Stanislas Dehaene, *Collège de France*
Robert Desimone, *MIT*
Claude Desplan, *New York U.*
Ap Dijksterhuis, *Radboud U. of Nijmegen*
Dennis Discher, *U. of Pennsylvania*
Gerald W. Dorn II, *Washington U. School of Medicine*
Jennifer A. Doudna, *U. of California, Berkeley*
Bruce Dunn, *U. of California, Los Angeles*
William Dunphy, *Caltch*
Christopher Dye, *WHO*
Todd Ehlers, *U. of Tübingen*
David Ehrhardt, *Carnegie Inst. of Washington*
Tim Elston, *U. of North Carolina at Chapel Hill*
Gerhard Ertl, *Fritz-Haber-Institut, Berlin*
Barry Everitt, *U. of Cambridge*
Ernst Fehr, *U. of Zurich*
Anne C. Ferguson-Smith, *U. of Cambridge*
Michael Feuer, *The George Washington U.*
Toren Finkel, *NHLBI, NIH*
Kate Fitzgerald, *U. of Massachusetts*
Peter Fratzl, *Max-Planck Inst.*
Elaine Fuchs, *Rockefeller U.*
Daniel Geschwind, *UCLA*
Karl-Heinz Glassmeier, *TU Braunschweig*
Ramón Gonzalez, *Rice U.*
Julia R. Greer, *Caltch*
Elizabeth Grove, *U. of Chicago*
Nicolas Gruber, *ETH Zurich*
Kip Guy, *St. Jude's Children's Research Hospital*
Taekjip Ha, *U. of Illinois at Urbana-Champaign*
Christian Hassel, *Ludwig Maximilians U.*
Michael Hasselmo, *Boston U.*
Martin Heimann, *Max-Planck Inst. Jena*
Yka Helariutta, *U. of Cambridge*
James A. Hendler, *Rensselaer Polytechnic Inst.*
Janet G. Hering, *Swiss Fed. Inst. of Aquatic Science & Technology*
Kai-Uwe Hinrichs, *U. of Bremen*
Kei Hirose, *Tokyo Inst. of Technology*
David Hodell, *U. of Cambridge*
David Holden, *Imperial College*
Lora Hooper, *UT Southwestern Medical Ctr. at Dallas*
Raymond Huey, *U. of Washington*
Auke Ijspeert, *EPFL Lausanne*
Steven Jacobsen, *U. of California, Los Angeles*
Kai Jonsson, *EPFL Lausanne*
Peter Jonas, *Inst. of Science & Technology (IST) Austria*
Matt Kaebberlein, *U. of Washington*
William Kaelin Jr., *Dana-Farber Cancer Inst.*
Daniel Kahne, *Harvard U.*
Daniel Kammen, *U. of California, Berkeley*
Masashi Kawasaki, *U. of Tokyo*
Y. Narry Kim, *Seoul National U.*
Joel Kingsolver, *U. of North Carolina at Chapel Hill*
Robert Kingston, *Harvard Medical School*
Etienne Kochlin, *Ecole Normale Supérieure*
Alexander Koldkin, *Johns Hopkins U.*
Leonid Kruglyak, *UCLA*
Thomas Langer, *U. of Cologne*
Mitchell A. Lazar, *U. of Pennsylvania*
David Lazer, *Harvard U.*
Thomas Lecuit, *IBDM*
Virginia Lee, *U. of Pennsylvania*
Stanley Lemon, *U. of North Carolina at Chapel Hill*
Ottoline Leyser, *Cambridge U.*
Wendell Lim, *U.C. San Francisco*
Marcia C. Linn, *U. of California, Berkeley*
Jianguo Liu, *Michigan State U.*
Luis Liz-Marzan, *CIC bioGUNE*
Jonathan Losos, *Harvard U.*
Kei Lu, *Chinese Acad. of Sciences*
Christian Lüscher, *U. of Geneva*
Laura Machesky, *CRUK Beatson Inst. for Cancer Research*
Anne Magurran, *U. of St. Andrews*
Oscar Marin, *CSIC & U. Miguel Hernández*
Charles Marshall, *U. of California, Berkeley*
C. Robertson McClung, *Dartmouth College*
Graham Medley, *U. of Warwick*
Tom Misteli, *NCI*
Yasushi Miyashita, *U. of Tokyo*
Mary Ann Moran, *U. of Georgia*
Richard Morris, *U. of Edinburgh*
Alison Mutsaers-Reif, *NC State U. (\$)*
Thomas Murray, *The Hastings Center*
James Neuman, *Stanford U. School of Med.*
Daniel Neukam, *U. of California, Berkeley*
Kitty Niemeijer, *U. of Twente*
Pär Nordlund, *Karolinska Inst.*
Helga Nowotny, *European Research Advisory Board*
Ben Olken, *MIT*
Joe Orenstein, *U. of California Berkeley & Lawrence Berkeley National Lab*
Harry Orr, *U. of Minnesota*
Andrew Oswald, *U. of Warwick*
Steve Palumbi, *Stanford U.*
Jane Parker, *Max-Planck Inst. of Plant Breeding Research*
Giovanni Parmigiani, *Dana-Farber Cancer Inst. (\$)*
Donald R. Paul, *U. of Texas, Austin*
John H. J. Petrini, *Memorial Sloan-Kettering Cancer Center*
Samuel Pfaff, *Salk Institute for Biological Studies*
Joshua Plotkin, *U. of Pennsylvania*
Albert Polman, *FOM Institute AMOLF*
Philippe Pouchin, *CNRS*
Jonathan Pritchard, *Stanford U.*
David Randall, *Colorado State U.*
Colin Renfrew, *U. of Cambridge*
Felix Rey, *Institut Pasteur*
Trevor Robbins, *U. of Cambridge*
Jim Roberts, *Fred Hutchinson Cancer Research Ctr.*
Barbara A. Romanowicz, *U. of California, Berkeley*
Amy Rosenzweig, *Northwestern University*
Jens Rostrup-Nielsen, *Haldor Topsøe*
Mike Ryan, *U. of Texas, Austin*
Mitsunori Saitou, *Kyoto U.*
Shimon Sakaguchi, *Kyoto U.*
Miguel Salmeron, *Lawrence Berkeley National Lab*
Jürgen Sandkühler, *University of Vienna*
Alexander Schier, *Harvard U.*
Randy Seeley, *U. of Cincinnati*
Vladimir Shalae, *Purdue U.*
Robert Siliciano, *Johns Hopkins School of Medicine*
Deni Simon, *Arizona State U.*
Uri Simonsohn, *U. of Pennsylvania*
Alison Smith, *John Innes Centre*
Richard Smith, *U. of North Carolina (\$)*
John Speakman, *U. of Aberdeen*
Allan C. Spradling, *Carnegie Institution of Washington*
Jonathan Sprent, *Gavran Inst. of Medical Research*
Eric Steig, *U. of Washington*
Paula Stephan, *George State U. and National Bureau of Economic Research*
Molly Stevens, *Imperial College London*
V. S. Subrahmanian, *U. of Maryland*
Ira Tabas, *Columbia U.*
Sarah Teichmann, *Cambridge U.*
John Thomas, *North Carolina State U.*
Shubha Tole, *Tata Institute of Fundamental Research*
Christopher Tyler-Smith, *The Wellcome Trust Sanger Inst.*
Herbert Virgin, *Washington U.*
Beth Vogelstein, *Johns Hopkins U.*
Cynthia Volkert, *U. of Göttingen*
Douglas Wallace, *Dalhousie U.*
David Wallace, *Weizmann Inst. of Science*
Ian Walmsey, *U. of Oxford*
Jane-Ling Wang, *U. of California, Davis*
David A. Wardle, *Swedish U. of Agric. Sciences*
David Waxman, *Fudan U.*
Jonathan Weissman, *U. of California, San Francisco*
Chris Wikle, *U. of Missouri (\$)*
Ian A. Wilson, *The Scripps Res. Inst. (\$)*
Timothy D. Wilson, *U. of Virginia*
Rosemary Wyse, *Johns Hopkins U.*
Jan Zaenen, *Leiden U.*
Kenneth Zaret, *U. of Pennsylvania School of Medicine*
Jonathan Zehr, *U. of California, Santa Cruz*
Len Zon, *Children's Hospital Boston*
Maria Zuber, *MIT*

BOOK REVIEW BOARD

David Bloom, *Harvard U.*, Samuel Bowring, *MIT*, Angela Creager, *Princeton U.*, Richard Sweder, *U. of Chicago*, Ed Wasserman, *DuPont*

America's science legacy

In 1863, U.S. President Abraham Lincoln delivered his now famous Gettysburg Address on the open field of that bloody Civil War battle. Not many speeches by political leaders get remembered beyond the moment. Even fewer ever get cut into stone. In this case, of course, both are true. We know the words. We recite passages from it. And, in its entirety, the speech graces a wall of the Lincoln Memorial in Washington, DC.

The gravity of the Civil War, and its importance to what America would become as a nation, understandably eclipse the memories of other milestones in the Lincoln presidency. The year before the war, for example, Lincoln created the system of land grant colleges that would indelibly influence how Americans would be educated. Known also as the people's colleges, they were conceived with the idea that they would provide practical knowledge and science in a developing democratic republic.

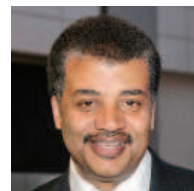
In 2013, I was asked by the Abraham Lincoln Presidential Library Foundation to write a 272-word speech, inspired in any way—directly or peripherally, emotionally

or historically—by Lincoln's 272-word Gettysburg Address, which would see its 150th anniversary that November. I claim no particular expertise on the American Civil War, on Lincoln's presidency, or on American history in general, a point I made quite clear to the foundation. But this unique opportunity forced me to think more deeply about the power of a president to shape the country's mission statement. Then I remembered that in 1863, Lincoln also had something seminal to say about the future of science in America, a topic I think about often.

My "speech" now appears alongside dozens of others, solicited from selected Americans such as former U.S. presidents, social and political leaders, business leaders, and thinkers. The collection, published earlier this year, is titled *Gettysburg Replies: The World Responds to Abraham Lincoln's Gettysburg Address*.

Titled "The Seedbed,"* I offer the speech as a reminder of America's science legacy; and as an appeal to advance all that this legacy can do for the nation's future.

– Neil deGrasse Tyson



Neil deGrasse Tyson is an astrophysicist and the Frederick P. Rose Director of the Hayden Planetarium at the American Museum of Natural History, New York, NY.

VIDEO

Watch the video "Neil's Gettysburg Reply" <http://scim.ag/sciencelegacy>

The Seedbed

One and a half centuries ago, Civil War divided these United States of America. Yet in its wake, we would anneal as one nation, indivisible.

During the bloody year of his Gettysburg Address, President Lincoln chartered the National Academy of Sciences—comprised of fifty distinguished American researchers whose task was then, as now, to advise Congress and the Executive Branch of all ways the frontier of science may contribute to the health, wealth, and security of its residents.

As a young nation, just four score and seven years old, we had plucked the engineering fruits of the Industrial Revolution that transformed Europe, but Americans had yet to embrace the meaning of science to society.

Now with more than two thousand members, the National Academy encompasses dozens of fields undreamt of at the time of Lincoln's charter. Quantum Physics, discovered in the

1920s, now drives nearly one third of the world's wealth, forming the basis for our computer revolution in the creation, storage, and retrieval of information. And as we continue to warm our planet, Climatology may be our only hope to save us from ourselves.

During the centennial of its charter, President Kennedy addressed the Academy membership, noting, "The range and depth of scientific achievement in this room constitutes the seedbed of our nation's future."

In this, the twenty-first century, innovations in science and technology form the primary engines of economic growth. While most remember honest Abe for war and peace, and slavery and freedom, the time has come to remember him for setting our Nation on a course of scientifically enlightened governance, without which we all may perish from this Earth.

*From *Gettysburg Replies*. Copyright © 2015 by Abraham Lincoln Presidential Library Foundation. Used by arrangement with the publisher. All rights reserved. No part of this excerpt may be reproduced or printed without permission in writing from Rowman & Littlefield.

IN BRIEF

Brazil mud could wreak years of havoc



Deadly slow-motion mudslide destroys town and poisons water supplies.

As a result of two mining dams that collapsed on 12 November, an enormous wake of toxic mud has engulfed and destroyed the Brazilian town of Bento Rodrigues, and the damage continues to spread down the Doce River. The mudslide has forced 500 people to relocate and has already claimed nine lives; 19 others are listed as missing. The mud has also contaminated the river with metals such as zinc, arsenic, mercury, and copper, poisoning its potential as a water source. Toxic conditions have wiped out aquatic life hundreds of kilometers downriver, and experts say that biodiversity will take an irreparable hit. By early next week, the mud is expected to reach the Atlantic. Samarco Mineração SA manages and operates the mines and dams; on 12 November, the Brazilian government fined the company \$66 million, but that number could increase. As the deadly sludge continues to creep along, towns up to 330 kilometers away are preparing for potential disaster, shipping in extra water supplies for schools and hospitals.

AROUND THE WORLD

Russian scientists form nonprofit

MOSCOW | Hoping to fill a void left by the closure in July of Dynasty, Russia's only private research funder, a group of scientists is planning to launch a new foundation. Dynasty spent \$30 million from 2002 to 2015 on seed money for young Russian scientists and on competitions for science teachers, science festivals, and public lectures by world-class researchers. However, because it received funds from outside of Russia, it ran afoul of Russia's "foreign agents" law and was forced to wind up its activities in July. The new nonprofit, called Evolution, has only managed to raise tens of thousands of dollars so far—and has accordingly set modest ambitions. Initially it will focus on science popularization, including publishing Russian science authors and translating science books into Russian. <http://scim.ag/EvolutionRussia>

Expo 2015 site to host research

MILAN, ITALY | The site of Expo 2015, this year's science-themed Universal Exhibition in Milan, Italy, may get a second life as an international hot spot for science and technology. The Universal Exhibition, whose motto was "Feeding the Planet, Energy for Life," closed on 31 October after drawing more than 21 million visitors over 6 months. The Italian government plans to shell out €150 million annually for 10 years to redevelop the 100-hectare area as a research campus for as many as 1600 researchers. The new science hub, dubbed the Human Technopole, would focus on genomics, big data, aging, and nutrition. http://scim.ag/_EXPO2015

Report: no herbicide-cancer link

PARMA, ITALY | The common herbicide glyphosate is unlikely to increase the risk of cancer, at least in its pure form, according to a 12 November assessment from the European Food Safety Authority (EFSA). A report earlier this year by the World Health Organization's International Agency for Research on Cancer (IARC) classified glyphosate as "probably carcinogenic to humans." But the IARC report included epidemiological studies of commercially

available herbicides, such as Roundup, that have multiple ingredients. The EFSA report focused on studies that involved pure glyphosate. It also included several unpublished studies that IARC did not use. EFSA says more studies are needed to evaluate whether commercially available formulations of glyphosate are safe. The EFSA evaluation did set a recommended maximum short-term limit for glyphosate intake: 0.5 milligrams per kilogram of body weight. The new report will influence the European Union's decision on whether to keep the compound on its list of approved chemical substances; that approval expires at the end of 2015. http://scim.ag/_glyphosate

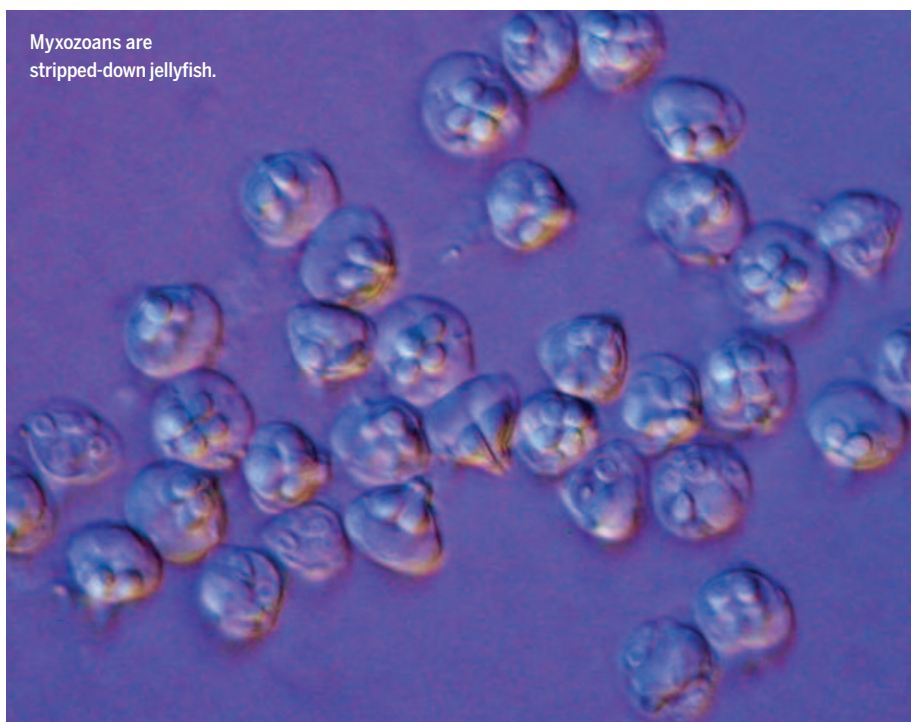
Scientists protest work conditions

SANTIAGO | Frustrated scientists took to the streets in Chile last week to protest low research spending, frail science institutions, poor career prospects, and what they see as the government's overall disregard for science. On 12 November, 2500 researchers, technicians, and students marched to La Moneda, the presidential palace in Santiago, to deliver an open letter that expressed their "desolation" with government decisions that "will plunge the country into ignorance and poverty." The signatories demanded that the government set up a science ministry and promote science as a part of the "national culture." The protest came on the heels of the resignation on 29 October of Francisco Brieva as head of Chile's research funding agency, the National Commission for Scientific and Technological Research; Brieva told Chile's *El Mercurio* newspaper on 1 November that the country's bureaucracy stifled his plans to kick-start public investment in science, and that he hadn't received a paycheck in 6 months. http://scim.ag/_ChileProtest

Last known Ebola case released

CONAKRY | A newborn baby who recovered from Ebola was released from a treatment center here on 16 November. The infant, whose mother died of the disease, is the country's last known case of Ebola. The last people under quarantine after possible exposure to the virus were released 2 days earlier. Guinea now starts a 42-day countdown—twice the incubation period for the virus—before it can be officially declared Ebola-free. Sierra Leone was declared free of the virus on 7 November and Liberia has been officially Ebola-free since September. The world's largest outbreak of Ebola, which sickened more than 28,000 and killed more than 11,000, started in Guinea in December 2013.

Myxozoans are stripped-down jellyfish.



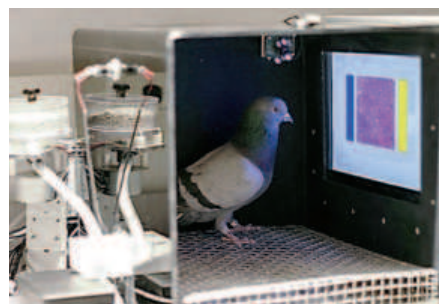
Fish parasite once a jellyfish

Tiny fish parasites called myxozoans were once considered protists, a group including amoebae and slime mold. But Paulyn Cartwright, an evolutionary biologist at the University of Kansas, Lawrence, and other scientists suspected these parasites might instead be kin to jellyfish. Myxozoan cells contain a capsule with a barbed filament that they use to latch onto the host—it looks suspiciously like the stinging cells of a jellyfish. This week, in the *Proceedings of the National Academy of Sciences*, Cartwright and her team report a comparative survey of the genomes of two myxozoans, true jellyfish and *Polypodium hydriforme*, a parasite with a jellyfishlike life stage. The study confirms that myxozoans are cnidarians, the genus that includes jellyfish, which lost both cells and DNA. Their genomes, one-fortieth the size of their jellyfish kin, lack genes for multicellular development and differentiation, as well as those for cell-to-cell communication. The next step, Cartwright says, is to figure out how a complex, multicellular jellyfish could evolve into a few-celled parasite.

FINDINGS

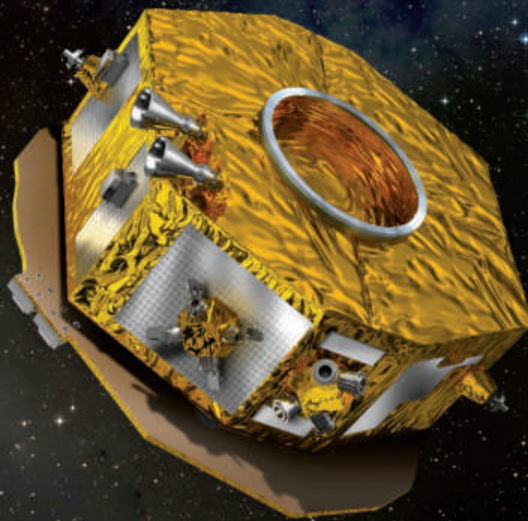
Trained pigeons ID cancer

Can birds spot cancer? Like humans, they have excellent visual systems—and they are cheaper to train than medical students. A study this week in *PLOS ONE* put pigeons



Pigeons peck to identify cancerous tissue.

to the test. Researchers trained the birds to examine microscope images of breast tissue on a computer touchscreen; the birds pecked colored buttons to distinguish cancerous from healthy tissue. If the birds correctly identified cancer, they got a food pellet. In a matter of days, the pigeons' performance improved to better than random; by the end of a month, their accuracy rose to as high as 80%. But the real power came from the flock: By combining identifications from different birds, the accuracy rose to 99%—on par with trained human experts, and better than a computer doing automatic image analysis. So are trained pigeons the future of cancer diagnosis? "I doubt it," says lead author Richard Levenson, a pathologist and technologist at the University of California, Davis. "I suspect that computers will get there first." http://scim.ag/_pigeons



SPACE PHYSICS

LISA Pathfinder tests spacetime sensor

A European space probe is set to pave the way for measurements of gravitational waves

By Daniel Clery

In early December, the European Space Agency (ESA) will launch a spacecraft with a deceptively modest goal. It will not observe Earth or search space for quasars or exoplanets. Instead, it will set two cubes of gold-platinum alloy—each slightly larger than a golf ball—floating freely in weightlessness and attempt to measure their distance apart to the nearest trillionth of a meter. But if it succeeds, the €430 million Laser Interferometer Space Antenna (LISA) Pathfinder mission will open the way for major ambitions.

By making such precise measurements in space, the mission will prove the concept of the roughly €1 billion Evolved LISA (eLISA). To be launched in roughly 20 years if all goes well, eLISA aims to detect the gravitational waves emitted by some of the universe's most titanic processes, such as the death spiral of the super-massive black holes at the heart of galaxies. Detecting gravitational waves—a feat that detectors on Earth are also vying to achieve—"will be like going to a black-and-white movie and suddenly someone turns on the color," says physicist Mike Cruise, whose group at the University of Birmingham in the United Kingdom built part of the laser metrology equipment for LISA Pathfinder.

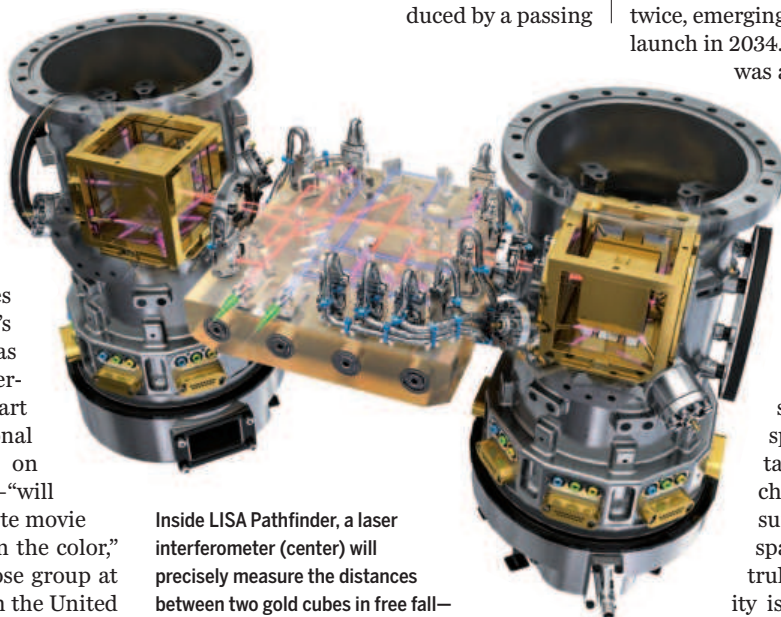
Physicists have been on the hunt for gravitational waves—one of the more striking predictions of Einstein's general relativity—since the 1960s. The biggest current effort, the \$620 million Laser Interferometer Gravitational-Wave Observatory (LIGO) in Louisiana and Washington states, recently started up again after a major upgrade (*Science*, 6 March, p. 1084). In LIGO, physicists bounce laser beams along two 4-kilometer vacuum tubes, producing an interference pattern sensitive to the minuscule squeeze and stretch of space produced by a passing

gravitational wave. The trouble is that a multitude of other vibrations can mimic that signal: everything from surf crashing on beaches to the churning of Earth's core.

In space, the problem of vibrations disappears and real estate is cheap, allowing the arms to be far longer, monitored by free-flying spacecraft. A space-based detector was first proposed in the 1980s and coalesced into ESA's LISA. NASA joined the project, but it hasn't had an easy ride. In 2011 NASA pulled out because of budget problems and the mission was redesigned twice, emerging as eLISA and penciled in for launch in 2034. "In every review, the science was always rated as outstanding,"

says Paul McNamara, ESA project scientist for LISA Pathfinder. But when it came to selection, "it was always everyone's second favorite mission," he says.

eLISA's arms will be 5 million kilometers long. Three spacecraft will fly in formation around the sun, beaming lasers through space to measure their distances from one another. The challenge for eLISA is to ensure that the mirrors in each spacecraft are shielded and truly free-floating, so that gravity is the only force acting. "We have to make sure there are no interfering forces," Cruise says. Solar



Inside LISA Pathfinder, a laser interferometer (center) will precisely measure the distances between two gold cubes in free fall—a technique that future spacecraft will use to detect gravitational waves.

The 2.9-meter-wide LISA Pathfinder will test technologies for a planned fleet of spacecraft that would orbit the sun 5 million kilometers apart.

wind and radiation or gravitational and magnetic forces from the spacecraft could all skew the results.

LISA Pathfinder replicates one arm of eLISA, but with 5 million kilometers shrunk down to 35 centimeters. The two alloy cubes are the mirrors; they will float inside the spacecraft while a laser interferometer measures the distance between them. “Almost all the technologies you need for eLISA are in LISA Pathfinder. Only the long arms are missing,” says Karsten Danzmann of the Albert Einstein Institute in Hannover, Germany, co-principal investigator for LISA Pathfinder.

Even if the prototype succeeds, astronomers will have to wait decades to look through their gravitational-wave telescope. It’s likely that LIGO or another instrument will be the first to detect spacetime ripples—perhaps in the next few years. But each detection technique is sensitive to waves with different frequencies and hence different astrophysical sources.

LIGO and similar detectors in Europe and Japan are sensitive to high-frequency waves from events such as the merger of binary neutron stars or black holes of a few times the mass of the sun. eLISA would pick up lower frequencies—about one beat every 1000 seconds—produced by much more massive, slower moving objects such as supermassive black holes. “When galaxies merge, their central black holes sink to the center and eventually merge [as they shed energy] by gravitational wave emission,” says theorist Jonathan Gair of the University of Edinburgh. “We’ll see the whole process.”

Other targets include small black holes falling into supermassive ones, and run-of-the-mill stars, such as white dwarfs, orbiting in binary pairs. eLISA will be able to take a census of such pairs across the Milky Way. And each measurement will be a test of general relativity itself, to see whether—after a century of stress testing—it still holds true in all circumstances. “If things deviate, even by a small amount, we can detect that,” Gair says.

The first step will be LISA Pathfinder’s launch from the ESA spaceport in Kourou, French Guiana. A couple months later, when the spacecraft has reached its destination 1.5 million kilometers from Earth, the team will be on the edge of their seats, says principal investigator Stefano Vitale of the University of Trento in Italy. “The moment we release the test masses in free flight, [that will be] a first in space science.” ■

NEUROSCIENCE

A faster, brighter picture of brain cells in action

New voltage-sensor achieves submillisecond precision

By Emily Underwood

At the heart of all brain activity—thoughts, perceptions, emotions, and memories—are rapid surges of electrical activity, called action potentials, that zip through neurons and transmit information throughout the brain. Capturing this play of activity across large numbers of neurons is essential to understanding cognition, but existing techniques for monitoring neurons are too slow, or their scope too limited, for scientists to really see the brain at work.

This week online in *Science*, a research team led by a physicist at Stanford University in Palo Alto, California, reports a new technique that renders spikes of electrical activity visible under a microscope as flashes of light with a temporal resolution of about 0.2 milliseconds. At that speed, scientists will be able to observe not just when cells fire a full-blown action potential, but more subtle electrical activity within individual neurons’ branches, says neuroscientist Van Wedeen of Harvard Medical School in Boston. “The field has been waiting for this for years.” Timing is everything in the brain, he notes, and witnessing such rapid dynamics “could reveal aspects of neural code we’ve never had experimental access to before.”

At present, scientists can record the aggregate electrical activity of large groups of cells with electrodes placed on the scalp or inserted into brain tissue. They can also record directly from individual neurons in a dish or animal using microelectrodes. But none of these techniques is well suited to recording details of a live brain’s electrical activity within individual neurons of a chosen genetic type, says Mark Schnitzer, the principal investigator of the new study.

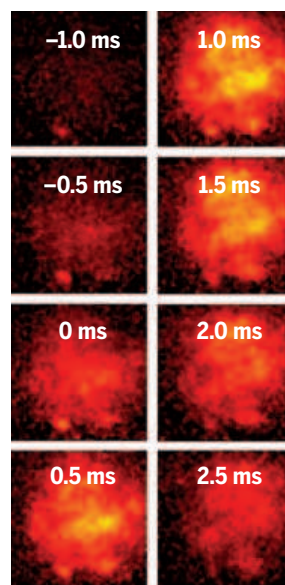
So-called calcium imaging, in which neurons are coaxed to fluoresce in response to

the surges of calcium ions that accompany action potentials, can track many individual neurons at once. But it is too slow to capture much of their electrical chatter, which unfolds within milliseconds or even fractions of a millisecond, Schnitzer says. In search of faster methods, his group and others have endowed neurons with genes for fluorescent proteins that brighten or dim when they sense changes in voltage in the cell membranes. But most voltage indicators fluoresce weakly, forcing researchers to use such powerful beams of light to reveal the sensors’ faint glow that it “barbecues anything living,” Wedeen says.

Yiyang Gong, formerly a postdoc in Schnitzer’s lab and now a professor at Duke University in Durham, North Carolina, has worked with the Stanford team to create a much brighter voltage sensor than those developed by other groups, while maintaining light levels that can be used in living animals. The group combined a fluorescent protein engineered by Nathan Shaner and colleagues at the Scintillon Institute with another, fungus-derived protein that responds five to six times

more quickly to changes in voltage than the one used in their previous model. The new work is “the first demonstration that one can image action potentials optically in an awake mammalian brain,” Schnitzer says.

The new voltage sensors can also be expressed in just specific types of neurons, adding to the method’s usefulness. They can’t be used for extended periods, however, because the proteins lose their sensitivity to light after about 10 minutes of continuous exposure. But by using multiple short exposures, investigators should be able to observe neural activity for much longer periods, Schnitzer notes. “This should be the next big thing as the methods get refined and extended,” says Bruce Rosen, director of the Center for Biomedical Imaging at Harvard University, “I think this is pretty cool.” ■



Voltage spreading through a fly neuron over several milliseconds.

FUNDING

NIH program fails to launch blacks in biotech

Small Business Innovation Research program makes almost no grants to African-Americans

By Jeffrey Mervis

The National Institutes of Health (NIH) gave out three-quarters of a billion dollars this year as part of a long-running federal research program to encourage innovation among small businesses. But for African-American scientists, the Small Business Innovation Research (SBIR) program may as well not exist.

A new study by the U.S. National Academies of Sciences, Engineering, and Medicine documents their near-invisibility in the NIH program, which each year gives out hundreds of awards to help small businesses translate biomedical discoveries into products. In a survey of principal investigators (PIs) who received a late-stage SBIR award between 2001 and 2010, just two of the 604 respondents were African-American. Hispanics did only slightly better, earning 2% of these phase II awards, and there was one Native American PI (see graphic, right). “Levels of participation by underserved groups are low and declining,” the new report concludes.

The low minority participation in NIH’s SBIR program mirrors that of other NIH programs. A 2011 NIH study of its core R01 science grants reported that just 1.4% of applicants were African-American and 3.2% were Hispanic (*Science*, 19 August 2011, p. 925). The so-called Ginther report also found that black applicants were less likely than whites to win NIH funding; the gap was 10 percentage points. Similarly, the new academies report finds that minority-owned businesses have a lower success rate in winning initial SBIR grants than majority-owned businesses (10% versus 18% in 2014, for example).

The numbers are symptomatic of the vanishingly small presence of black scientists in the biotech sector, note those who follow the issue. “SBIR is the end of the pipeline for a successful scientist who plans to commercialize a discovery,” says Chad Womack, who runs a science scholarship program for minorities sponsored by the United Negro

College Fund and the Merck Foundation. “And there just aren’t enough African-American scientists in that space, at that level, to take advantage of the opportunity.”

Womack, an African-American biomedical researcher, has firsthand knowledge of the problem: NIH rejected his 2007 SBIR application for a company he co-founded after doing a postdoc at the agency, and the tiny vaccine development startup fell victim to the 2008 financial meltdown. But he doesn’t fault NIH. “I think SBIR is a great program; in fact, I’d love to see it expanded.”

Offered by 11 federal agencies, SBIR awards, typically up to \$150,000 in phase I and \$1 million in phase II, are funded

according to the academies panel, chaired by Jacques Gansler, a former top Pentagon official now at the University of Maryland, College Park.

“The objective of fostering the participation of women and underserved minorities has not been met” by the NIH program, the new report concludes. The earlier report reached a similar conclusion for DOD.

Matthew Portnoy, who oversees NIH’s SBIR and STTR programs, says the report reaffirms a 2009 academies study that concluded “we are meeting the [innovation] goals but we are having a problem with outreach.” NIH initially tried to broaden participation by improving the geographic distribution of its grants, he says. Now, it plans to focus more explicitly on outreach to minorities and women. “It’s not an easy problem,” he adds, “and we’re definitely interested in any good ideas.”

One approach the panel explicitly rejected was using quotas to boost minority participation. “You lower your standards by doing that,” Gansler says. “It’s not a charity; a lot of agencies already object to SBIR because they see it as a drain on their research programs.”

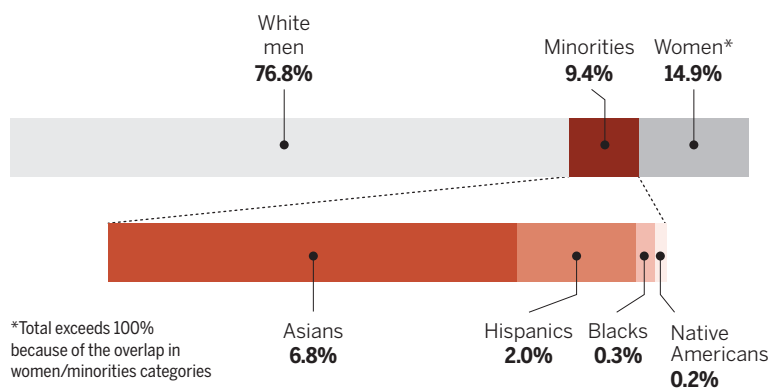
Womack believes part of the answer is more support for minority scientists. “If you really want to pump up the numbers,

then you have to help people with the nuts and bolts of what it takes” to prepare a strong application, he says. A more comprehensive strategy would start by connecting with undergraduate and graduate students, says Womack, who hopes that the next phase of his scholarship program will focus on “bioentrepreneurship.”

Talitha Hampton, a program manager for AstraZeneca in Gaithersburg, Maryland, and president of the National Organization of Black Chemists and Chemical Engineers, is looking even farther upstream to elementary schools. She said a recent hands-on science workshop for minority students in Maryland, called The Crayon CEO, helped install more positive attitudes toward entrepreneurship. “That’s where it has to start.” ■

Nearly invisible

A new study finds that African-Americans make up a tiny slice (bottom bar) of the small percentage of minorities who are principal investigators on NIH SBIR grants.



through a small tax on the extramural research budgets of each agency. That tax has been rising slowly, and will reach 3.2% in 2017. An additional 0.45% goes to a sister program, called Small Business Technology Transfer (STTR), which funds university-based startups. In 2015, the government spent \$2.3 billion on SBIR/STTR, with nearly half funneled through the Department of Defense (DOD); NIH is the second largest player in the SBIR program.

NIH and DOD are generally doing well in meeting SBIR’s overall goal of backing innovation by small businesses, according to the new NIH report and one done earlier this year on DOD’s program. But SBIR also has an explicit mandate from Congress to enhance opportunities for women and minorities. And that’s not happening,



Moedas says he can talk to European Commission President Jean-Claude Juncker any time he wants.

Q&A

Europe's research chief wants scientists to speak up

Commissioner Carlos Moedas is confident that science and innovation will bring growth to a divided continent

By Tania Rabesandratana, in Brussels

Last week, European research commissioner Carlos Moedas revealed the names of seven scientists who will serve as the commission's main science advisers. The announcement of the prestigious group—which includes Fields medal-winning mathematician Cédric Villani, CERN Director Rolf-Dieter Heuer, and the United Kingdom's chief climatologist, Julia Slingo—was generally welcomed by scientists. It brought an end to a year of suspense since the awkward exit of Scottish biologist Anne Glover, the first and only chief scientific adviser in the commission's history (*Science*, 21 November 2014, p. 904).

How to replace Glover's position was one of the first challenges awaiting Moedas when he took office in November 2014. It took his team months to come up with a new advice system, of which the high-level panel is a key component. "It's better to do it right than to do it quick," he says. (For more on the panel, see <http://scim.ag/ECsciadvisers>.)

One of 28 E.U. commissioners led by President Jean-Claude Juncker—one per member state—Moedas is a smiling, mild-mannered polyglot with experience in engineering, real estate, and investment banking. Before becoming commissioner, he served as secretary of state to the prime minister of his home country, Portugal, but he had no experience in research policy.

His maneuvering space is small; Europe's flagship research program, the 7-year, €80 billion Horizon 2020, was launched before Moedas arrived. Still, he plans to leave his mark; in a big speech in June, he announced plans to help innovation flourish, boost science data sharing, and develop science ties with other continents.

Science met with Moedas in his office on the ninth floor of the commission's iconic Berlaymont building in Brussels. This interview has been edited for brevity and clarity.

Q: The European Union has been rattled by growing euroskepticism and deep, divisive crises, from the economic crunch to the refugees' plight. How does this affect

science? Are member states still willing to work together on research policy?

A: I think the core of science ministers around Europe is very strong. They believe that if you want to get more jobs, if you want to get more growth, you need an innovation-driven system and economy. The countries that invested more in science and innovation actually weathered the economic crisis better. Of course it has been a difficult year, but I felt that because of that, my colleagues from the member states around the table had stronger voices to tell their government how important it is for all of us that we keep investing in science.

Q: What's the evidence that science is good for growth?

A: Let me show you. [On his iPad, Moedas displays a graph produced by the Organisation for Economic Co-operation and Development.] On this chart, you see that more than 60% of [gross domestic product] growth between 1995 and 2007 was due to innovation. In the concept of productivity you have three parts: getting more productive through labor, through capital, or through new technologies and methods. That [third part] is called multifactorial productivity and that is actually a proxy for innovation.

One of the things where I can add value in this portfolio is that I have a background as an engineer, then dedicated part of my life to economics. It's a problem sometimes when scientists talk to politicians that there are no bridges [between their two languages]. I consider it a big part of my job. If I'm able to do that, then politicians will understand and will put resources and money into science and innovation.

Q: Critics say your research portfolio is "invisible" in the commission. Has science been overshadowed by bigger issues?

A: I don't think that's true. I talk to President Juncker any time I want; he has given me more and more responsibilities and gives me freedom to work. I always felt the support of the president, I feel that I'm quite close to him.

Q: One of President Juncker's first moves last year was setting up the European Fund for Strategic Investments [EFSI], a stimulus package to boost the European Union's economy. Scientists were angry that the fund took money from Horizon 2020.

A: The president was the first one to say that the EFSI should be about the knowledge economy, innovation and science. Now, we have another tool [in addition to

Horizon 2020] for innovation in Europe, and I think that's good. At the end of the day you will have more money for those projects because the leverage is higher—you have money from member states, from the European Investment Bank, and private money. It will be interesting for you to get the numbers when I leave office.

Q: In June you introduced the idea of a European Innovation Council, modeled after the European Research Council [ERC], which was launched in 2007 to fund basic research. What is happening with this plan?

A: There are lots of [funding tools] for innovation but most innovators don't know where they are, so the first stage is putting a bunch of instruments that exist into one place so people know where to go. The second stage is how can you get a vision for innovation instruments that are more bottom-up, like the ERC. You don't tell people what to do, they tell you what they want to do. People will be able to develop their ideas without going through a call for proposals, without us telling them "do this, find me the next iPad," for example. It took several commissioners' terms to create the ERC, so I don't know where I'll get in 5 years—but at least I want to have a base, something that people understand as their tool for innovation.

Q: Last month, governments in 19 out of 28 E.U. countries made use of a new possibility to reject the cultivation of genetically modified (GM) crops on their land. Some researchers say this is a loss for science. What do you think?

A: Of course you have to respect that some member states now have that possibility to opt out. I'm a big believer in saying we need more and more research to actually get more scientific evidence into subjects like GM organisms. Then politicians can make the right decisions.

Q: You had no research policy experience when you took the job last year. What's been the most striking thing you've come across?

A: That's an interesting question. [He pauses to think.] I'll tell you what strikes me. Scientists underestimate their power and their voice, and that's a pity. You have all these interest groups in society fighting for different things, but scientists are a kind of low-profile group. They don't raise their voice together when they need to, but they should; it would help me. They could influence the policies of a country much more. When a scientist talks, people listen. ■

ARCHAEOLOGY

Humans may have reached Chile by 18,500 years ago

Monte Verde stone tools may be the oldest in the Americas

By Ann Gibbons

Archaeologist Tom Dillehay didn't want to return to Monte Verde. Decades ago, his discoveries at the famous site in southern Chile showed that humans occupied South America by 14,500 years ago, thousands of years earlier than thought, stirring a long and exhausting controversy. Now, Dillehay, of Vanderbilt University in Nashville, has been lured back—and he is preparing for renewed debate. He reports in *PLOS ONE* this week that people at Monte Verde built fires, cooked plants and meat, and used tools 18,500 years ago, which would push back the peopling of the Americas by another 4000 years.

If his team is correct, the discovery will "shake up both the archaeology and genomics of the peopling of the Americas," says archaeologist Jon Erlandson of the University of Oregon in Eugene. Genetic studies suggest that the ancestors of Paleoindians first left Siberia no earlier than 23,000 years ago (*Science*, 21 August, p. 841), so Dillehay's new dates suggest they wasted

little time in reaching the southern tip of the Americas. And the find raises questions about the North American record, where no one has found widely accepted evidence of occupation before 14,300 years ago. "Where the hell were the people in North America at that hour?" wonders archaeologist David Meltzer of Southern Methodist University in Dallas, Texas.

When Dillehay began his work at Monte Verde in the 1970s, most researchers thought the Clovis people, who hunted big game in North America starting about 13,000 years ago (using calibrated radiocarbon dates), were the first Americans. When Dillehay reported traces of huts, hearths, human footprints, and artifacts that were thousands of years older, he was forced to defend every detail of his dig to skeptical colleagues. By now, though, most archaeologists accept the older occupation at Monte Verde and a few other sites.

When the Chilean government invited

Dillehay to survey the full extent of Monte Verde, he at first refused. "I was tired of it," he says. But in 2013, fearing another team's survey might damage the site, he returned, hoping to spend a few weeks collecting new evidence of ancient plants and climate by digging 50 small test trenches across a 20,000-square-meter area. But the dig turned up 39 stone artifacts, including flakes, a "chopper," and cores, embedded near plants or animal bones that had been burned in small fires at 12 areas. This suggests a "spotty, ephemeral presence," he says.

His team radiocarbon dated the plants and animal bone to between 14,500 and 18,500 years ago, and perhaps as early as 19,000 years ago. The last ice age was only just starting to wane at that time, leaving a cool temperate rain forest at Monte Verde,

about 60 kilometers from the Pacific Ocean. Dillehay speculates that early Paleoindians moved along deglaciated corridors between the coast and the Andes, hunting paleo llamas and elephantlike gomphotheres.

Not everyone is convinced. Archaeologist

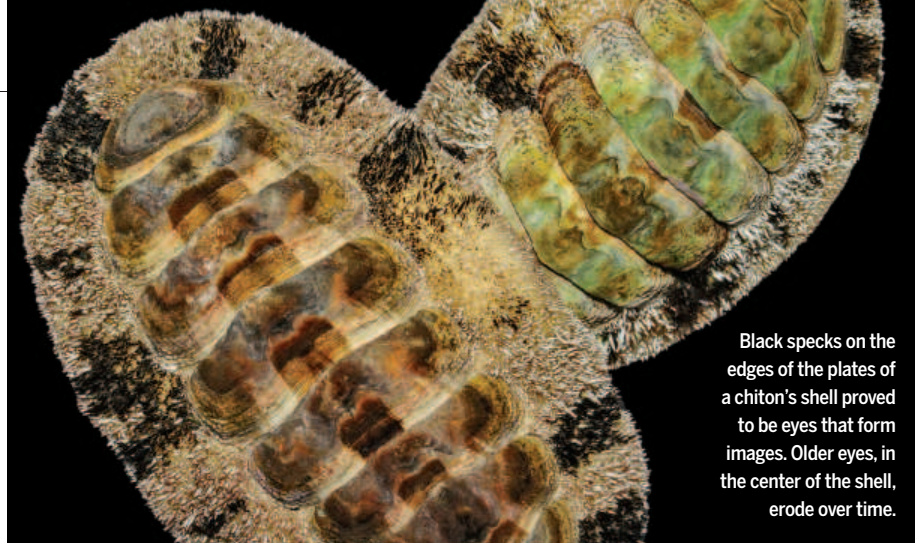
Michael Waters of Texas A&M University in College Station questions whether the stone artifacts were actually humanmade, and says that the team hasn't eliminated the possibility that the fires were natural.

Dillehay concedes that his team found few unequivocal stone tools, which are the strongest evidence of a human presence. But he notes that about one-third of the tools were made from exotic materials such as limestone and white quartz from outside the area, suggesting that people transported the stone. Meltzer finds this compelling. "The specimens don't scream out 'made by human hands,'" he agrees, "but Dillehay's group has made a careful assessment of their form and raw material ... It's evidence we cannot ignore."

Much is at stake, which suggests that the onus is on Dillehay once again to prove his case. "I guess that part of my destiny is that this damn site simply will not let go of us," he says. ■

"Part of my destiny is that this damn site simply will not let go of us."

Tom Dillehay, Vanderbilt University



BIOMATERIALS

Crystalline eyes of chitons inspire materials scientists

Mollusk makes hundreds of eyes from shell mineral

By Elizabeth Pennisi

Slow-moving and shaped like pebbles, most chitons are far from showy. But a close look at some of these marine mollusks reveals something remarkable: up to 1000 tiny eyes, each a bit smaller than the period at the end of this sentence, studding their plated shells. Now, on page 952, a team of materials scientists, engineers, and biologists describes how chitons build the lenses of their eyes from the same hard mineral that armors their shells. The work offers a striking example of how a single material can perform two jobs—seeing and protecting—at once. And it may offer insight to materials scientists seeking to design their own dual-use materials.

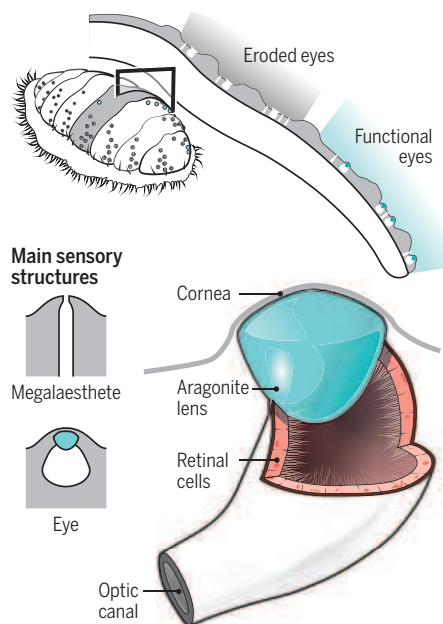
It's a "great paper," says materials scientist Peter Fratzl of the Max Planck Institute of Colloids and Interfaces in Potsdam, Germany. "What nature has perfected is to use comparatively simple, cheap starting materials and turn them into an exquisite, multifunctional material," he says. "We want to copy that approach."

Chitons move sluggishly up and down rocks or reefs in the intertidal zone, clamping tightly to the surface when threatened by fish, birds, or other predators. Yet they are quite successful, with a 500-million-year-long fossil record and a thousand species thriving today along wave-swept shores worldwide. "They are clearly doing something right," says Julia Sigwart, an evolutionary biologist at Queen's University Belfast in Ireland.

Only about 100 species have eyes, and until 10 years ago, researchers thought the eyes too small to be of much use, especially because all chitons have other light sensitive structures called megalasthetes. But a few years ago, after hearing about the eyes from molecular systematist Douglas Eernisse of California State University, Fullerton, Daniel Speiser decided to give captive chitons a vi-

A chiton's many eyes

A slice through a chiton's shell reveals an upper layer pitted with light-sensing megalasthetes and eyes.



sion test. When he blocked light with black circles, the animals clamped down, suggesting they were detecting images. "The eyes ... let the chiton distinguish an actual object, say a predator, from a passing shadow," says Speiser, now a visual ecologist at the University of South Carolina, Columbia.

Speiser, Eernisse, and others described chitons' visual system, reporting in 2011 that in contrast with the protein lenses found in most animals, including humans, chiton lenses are made of aragonite, the same calcium carbonate mineral that makes up their shells. Working in the lab of materials scientist Christine Ortiz at the Massachusetts Institute of Technology in Cambridge, graduate students Matthew Connors and Ling Li then explored how the eyes are made and how well they work.

Using high-resolution microscopy and x-ray techniques, as well as computer modeling, Li and Connors found that the oblong lens is made of large crystals, aligned to allow light through relatively unimpeded. Up to 100 photo-sensitive cells form a retina (see graphic, below). When the team suspended isolated lenses in water, they found that they could project recognizable images of a fish. "It actually forms a shockingly clear image," says sensory ecologist Sönke Johnsen of Duke University in Durham, North Carolina.

But chiton vision has a cost. Mechanical tests verified that the lenses create weak spots in the armor. "In order to see, they had to back off on mechanical protection," says Sheila Patek, a Duke evolutionary biomechanist. Protrusions in the shell partly compensate, so that the eyes nestle in protective grooves. But dual use does constrain how well the shell performs any single function.

For example, chitons could see better if their lenses were bigger or formed from just a single crystal. But that might compromise the shell's integrity too much. "Sometimes we assume nature is perfect," says biologist Andrew Parker from the Natural History Museum in London. "But more often than not it is a perfect compromise."

Co-author Joanna Aizenberg from Harvard University and others would like to come up with their own perfect compromises to create new dual-function materials that combine light-sensing and strength. The work on chitons hints at how that might be done—for example, by changing the shape or sizes of crystals. Johnsen also wonders whether the chiton visual system might inspire a network of multiple eyes in the skin of robots. "Nature has reached some very clever material solutions that we can harness," Fratzl says. "It allows you to dream about implementing similar kinds of ideas into technical systems." ■

FEATURES



Pressure from AIDS groups such as ACT UP, protesting at the White House in 1987, propelled Congress to begin earmarking research funding for HIV/AIDS.

WHAT DOES A DISEASE DESERVE?

A move to end NIH's AIDS earmark fuels debate over whether funding should reflect disease burden

By Jocelyn Kaiser

In the early 1990s, as the deadly HIV/AIDS epidemic marched across the United States and the world, lawmakers in Congress and top officials at the National Institutes of Health (NIH) reached an unusual understanding: Roughly 10% of the NIH budget would be dedicated to fighting the devastating disease. Since then, the steady flow of research cash—some \$3 billion this year—has helped transform HIV infection from a death sentence to a manageable disease for many people, and some researchers believe they are getting closer to developing a vaccine that could halt new infections.

That special arrangement is now under fire. Health policy experts, lawmakers, and even NIH officials have wondered why, 2 decades after AIDS death rates began dropping dramatically in the United States, the disease still gets a lion's share of NIH resources. As questions have arisen about how HIV/AIDS funds are spent, NIH has also resolved to refocus AIDS money on ending the epidemic. Some voice a broader critique: that NIH's spending on a disease often doesn't align with how much suffering it causes. They note that diseases imposing a relatively small burden on U.S. society, such as AIDS, can get a larger share of NIH

funding than those that cause greater harm, such as heart disease (see graph, p. 901). NIH's spending priorities can be "out of whack" says Senator Bill Cassidy (R-LA), a physician who serves on a panel that helps set NIH's budget.

Recently, while responding to pointed questions from Cassidy about the issue, NIH Director Francis Collins said the agency is ready to abandon the 10% set-aside. If Congress follows through on proposals to give NIH a hefty funding boost for 2016, its HIV/AIDS portfolio need not necessarily grow in "lock-step" with the increase as it has in the past, Collins said at a 7 October hearing.

At the same time, NIH is taking a broader look at disease spending. Next month officials are expected to release an agency-wide strategic plan that they say will address how disease burden should influence the allocation of research dollars.

The ferment worries AIDS research advocates. “HIV/AIDS research could shrink as a percentage of the total [NIH budget] for the first time” in more than 2 decades, laments Kimberly Miller of the HIV Medicine Association in Arlington, Virginia, which represents health workers who treat HIV-infected patients. Long-time NIH observers also wonder whether the developments signal a re-emergence of the sometimes fierce disease funding wars of the past, when advocates for breast cancer research and other diseases battled for a bigger share of the NIH pie. Already, Cassidy has proposed shifting some AIDS spending to neurodegenerative diseases such as Alzheimer’s.

Some in the biomedical research community, however, welcome these developments. “I’m glad the questioning is happening no matter how annoying it may be to some people,” says Claiborne Johnston, a stroke researcher at the University of Texas, Austin, who has studied disease funding trends. “I hope ultimately that we figure out a way to truly address, through our research and our care, some of these conditions that definitely are neglected.”

FROM ALMOST THE VERY beginning, NIH’s AIDS earmark has created tensions. After activists helped persuade Congress to ramp up HIV/AIDS funding in the 1980s, lawmakers agreed to cap it at 10% of NIH’s budget, but keep that proportion year after year. NIH officials argued that AIDS deserved a special allocation because it was a new disease, was still spreading, and had become the leading cause of death for U.S. adults between 25 and 44 years old. Key lawmakers were convinced, and since then AIDS research, which NIH has treated as its own distinct pool of funding, has essentially expanded in sync with the agency’s overall budget.

It wasn’t long before the deal inspired advocates for breast cancer and several other diseases to publicly argue that those fields, too, deserved large budget increases. Those 1990s campaigns ultimately met with mixed success in Congress. But the so-called disease wars did stir tensions within the large coalition of university, patient, and science

groups that advocate for greater biomedical research spending. Those allies traditionally try to present a united front, for fear that internal divisions could fragment and endanger political support for overall NIH spending increases.

Now, that uneasy alliance has again come under pressure as the threat of AIDS has faded domestically. As new drugs made the disease more manageable, the number

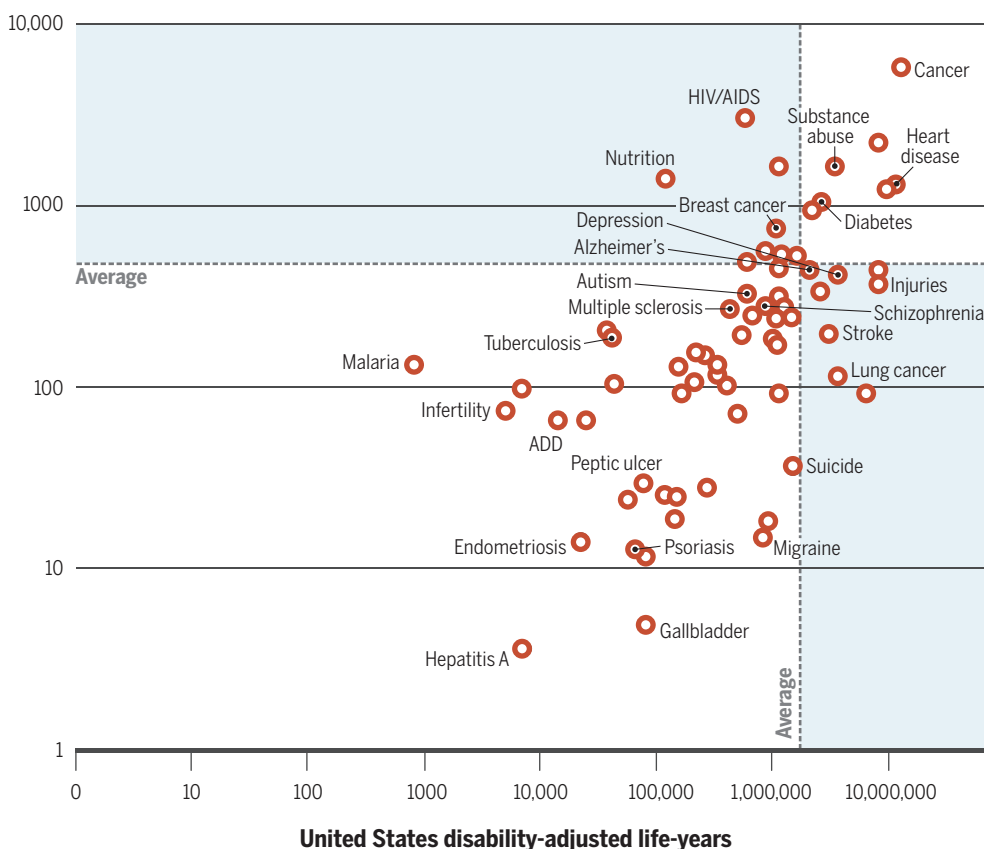
to be justified,” he said.

Many AIDS research advocates and NIH officials continue to defend the earmark, arguing that the global AIDS death rate remains high, and that researchers are making strides toward a vaccine. “I’m looking forward to a time when ... we have ended the AIDS epidemic and there won’t be any argument about what you want to do with the money, because you won’t need the

A matter of proportion

Alzheimer’s, lung cancer, and some other diseases that impose a relatively high health burden (years lost to early death or disability) get less NIH funding than lower burden diseases such as HIV/AIDS.

Research spending, 2010 (millions of dollars)



of deaths directly attributed to HIV plummeted in the United States from 45,000 per year in 1995 to 7000 in 2013. At the same time, some patient groups have recently helped persuade some lawmakers that they should be concerned about the much higher toll of other diseases, such as stroke and diabetes, and the staggering projected costs of caring for Alzheimer’s patients. Representative Andy Harris (R-MD), another physician who has taken an interest in NIH policy, noted at a hearing last March that NIH spends 100 times less per U.S. heart disease death than it does per AIDS death. The “stunning” discrepancy “needs

money,” said Anthony Fauci, the head of the National Institute of Allergy and Infectious Diseases (NIAID), which oversees about half of NIH’s AIDS spending, during a hearing this past April. Robert Eisinger, acting director of the NIH Office of AIDS Research, also notes that the billions spent on AIDS research have produced “numerous cross-over benefits” for other diseases—new drugs that treat hepatitis B infection came out of AIDS research, for example.

Yet congressional support for the AIDS set-aside has begun to crack. In a report accompanying the 2015 spending bill for NIH, House of Representatives and Senate appro-

priators omitted some oft-repeated instructions telling NIH to keep AIDS at 10% of its budget. The omission signaled their desire for NIH to abandon the earmark, says Chris Meekins, a staffer for Harris.

WITHIN NIH, top officials are also scrutinizing AIDS spending, about half of which is doled out by institutes and centers that don't focus primarily on infectious disease. Last year, Collins ordered a sweeping review of the AIDS portfolio. One pilot analysis by NIH staff found a surprise: 15% of grants did not have HIV/AIDS in the title or abstract, suggesting they were only remotely connected to AIDS. That finding added to existing concerns, both within and outside of NIH, that requiring institute directors to spend their dedicated AIDS money can encourage them to look far afield for projects to fund, or force them to lower their standards. At NIH's National Heart, Lung, and Blood Institute, for example, 42% of AIDS grant proposals received funding in 2012, compared with just 18% for non-AIDS projects, Cassidy noted at the October Senate hearing. "They're getting too much money for HIV/AIDS," Cassidy said. "Can we move money out of that area?"

This past August, in a bid to tighten controls on AIDS spending, Collins announced a revised set of research priorities (see box, right). Vaccines and potential cures are at the top; at the bottom are studies of diseases that sometimes co-occur with AIDS, such as malaria, and basic virology and immunology work that doesn't necessarily include HIV. Also at risk of losing new AIDS funding, the memo suggests, is behavioral research that doesn't focus specifically on AIDS, such as studies of risky sexual behaviors and drug abuse. Although exactly how the new priorities will influence NIH's funding decisions is uncertain, many behavioral researchers are "very nervous," says epidemiologist David Celentano of Johns Hopkins University in Baltimore, Maryland.

At some NIH institutes, directors have found that disbursing the AIDS money is a distraction from their main mission. Thomas Insel, who stepped down last month as director of the National Institute of Mental Health (NIMH), says he was surprised to realize 3 years ago that the \$180 million his institute was spending on AIDS research (12% of NIMH's budget) nearly matched its spending on disorders such as anxiety and

schizophrenia. Insel shifted some of the AIDS grants and his HIV/AIDS program staff to NIAID, to ensure better coordination with that institute's bigger AIDS program.

In Congress, some lawmakers are taking direct aim at the earmark. This past summer, during a Senate spending panel debate on NIH's 2016 appropriation, Cassidy proposed taking \$235 million out of NIAID's AIDS budget and giving it to other institutes studying neurodegenerative diseases.

The proposal dovetailed with a major push by patient groups to increase NIH funding for Alzheimer's disease, which has helped produce a 30% funding leap for Alzheimer's over the past 4 years. But Robert Egge, chief public policy officer for the Alzheimer's Association, and George Vradenburg, chair of the influential group UsAgainstAlzheimer's, say their organizations did not ask Cassidy to offer his Alzheimer's proposal.

In the end, Cassidy's measure failed. Still, the move shook the AIDS research community. "To find more money for Alzheimer's you have to cut HIV/AIDS, [that] makes no sense," says Miller, who is part of a coalition of AIDS groups now lobbying to preserve AIDS funding.

THE DEBATE over how much NIH's spending priorities should reflect disease burden goes back to at least the late 1990s, when *The New England Journal of Medicine*

published an analysis suggesting that NIH wasn't spending enough on certain high-burden conditions, such as peptic ulcers and pneumonia. In a 2011 study revisiting the issue in *PLOS ONE*, Johnston and co-authors found that diseases with strong advocates (breast cancer, for example) enjoy relatively robust funding, whereas spending lags on those that carry a stigma, such as depression, alcoholism, and lung cancer, despite the higher burden they impose on society. Although "you can't expect a perfect correlation" with funding, says Johnston, "the clearest take-home message is: Some conditions below the line are those where we blame the victim."

This past summer, for the first time, NIH published its own comparison of health burden and spending. It confirmed that AIDS and cancer receive relatively generous funding, whereas others, such as migraine and chronic obstructive pulmonary disease, receive disproportionately little. An agency official commented on a blog that "we're

looking forward to using these analyses as a jumping off point for a larger conversation about priority setting." And Collins has said in hearings that a new NIH-wide strategic plan due out in December will address disease burden.

Some observers are skeptical that the new plan will have much influence, given the many factors that influence spending, from tight budgets to the power of certain disease groups. And NIH officials caution that, in the end, disease burden data, which have limitations, can't alone be the basis for funding allocations. Institutes must consider the scientific quality of proposals, as well as the need to balance basic and clinical research. They note that it makes sense to spend relatively more on rare diseases that otherwise would be neglected, because they can shed light on common diseases. And infectious diseases can't be funded strictly based on the number of U.S. cases, because it's not possible to predict when viruses such as Ebola and severe acute respiratory syndrome—which have had little impact in the United States—might flare up and cross borders. At the same time, pouring new money into a disease just because it imposes a high social cost can be misguided, NIH insiders say. If the field lacks a critical mass of researchers, or promising research avenues, the money could be wasted.

Johnston and others who call for more attention to disease burden don't buy that. "It's a circular argument," he says. "Scientific promise happens when you have investments in an area. ... If you fund the science, there will be more promise in that area."

Insel agrees, to a point. He says that when he did a disease burden analysis of NIMH and NIH spending on mental illnesses compared with other diseases, he was struck by how every mental illness was "under the line," or appeared to get short shrift. This year he shored up funding for the two areas that lagged the most—suicide prevention and eating disorders—in order to stimulate fresh approaches. A decision NIMH made a few years ago to ramp up autism research—amid a push from activists—had convinced him that doing so wouldn't be a waste of dollars where there is "scientific traction." After the infusion of new funding into autism, he says, "we saw better proposals."

Whether that kind of redistribution catches on across NIH remains to be seen. But some AIDS researchers are already resigned to losing their special status, whether the initiative comes from Congress or NIH itself. "For a long time we were the golden child. ... We had a 30-year run," Celentano says. But now, "I think we need to justify better why we should be at the table." ■

NIH's new AIDS research priorities

High priority

Vaccines, new therapies, cure strategies, HIV-associated diseases, related basic research

Medium priority

Basic research and projects on health and social issues that "meaningfully" include HIV/AIDS and "will advance HIV treatment or prevention"

Low priority

Epidemiology of diseases that occur with HIV/AIDS and basic studies on copathogens that are not in the context of HIV infection, behavioral studies where HIV/AIDS is only one outcome



HOW TO HIJACK A JOURNAL

A patient hacker can take over a journal's official Web domain with relative ease—as I found out by doing so myself

By John Bohannon

Even by the standards of Internet scams, the scheme is brazen. According to a tip sent to *Science*, fraudsters are snatching entire Web addresses, known as Internet domains, right out from under academic publishers, erecting fake versions of their sites, and hijacking their journals, along with their Web traffic.

Website spoofing has been around since the rise of Internet search engines, but it's only in the past few years that scholarly journals have been targeted. The usual method

is to build a convincing version of a website at a similar address—www.sciencemag.org rather than www.sciencemag.org—and then drive Web traffic to the fake site. But snatching the official domain is an insidious twist: Unsuspecting visitors who log into the hijacked journal sites might give away passwords or money as they try to pay subscriptions or article processing fees. And because the co-opted site retains the official Web address of the real journal, how can you tell it's fake?

After the tip came in from Mehdi Dadkhah, an information technology scientist based in Isfahan, Iran, *Science* put me on the case. Not only did my investigation confirm that this scam is real, identifying 24 recently snatched journal domains, I discovered how the hijackers are likely doing it.

The only hard part is identifying vulnerable journals. Once the targets are identified, snatching their domains is easy. To test my theory, I snatched one myself. For a day, visitors to the official Web domain

ONLINE

Find a list of snatched journals at <http://scim.ag/hijackdata>

of an academic contemporary art journal based in Croatia were redirected to Rick Astley's 1987 classic music video, "Never Gonna Give You Up." (The editors there weren't upset when they learned of the switch because the journal was already moving to a new domain.)

This new style of journal hijacking can flourish only when journals are careless about website administration and security. But the few cases so far should sound an alarm, publishing experts say. "Other busi-

Another may be the money changing hands. Most of this \$10 billion industry is still tied up with subscriptions, paid primarily by libraries, but a growing slice comes from gold open-access publishing, the business model in which authors of accepted papers pay up front for their publication. This part of the market took in about \$250 million last year and is on course to double in a few years. That cash flow and the amateurish website administration of many scholarly publishers make for juicy targets.

Serial Numbers (ISSNs), titles, and Web and postal addresses of more than 12,000 publications. If the Web address of an online journal matches its official record on Web of Science, then you could be confident that it's the real deal. No longer: There is no simple way to identify a journal that has lost control of its own Web domain.

Dadkhan has been investigating journal fraudsters ever since he himself was duped in 2013. Ironically, it happened as he sought to publish his master's thesis research on Internet security. Like countless researchers, he received a spam email inviting him to present his research at a scientific conference for a fee of \$600. It was a large sum for him, but the organizers promised to publish his work as part of the conference proceedings in a journal that was indexed by Thomson Reuters. So he paid up.

Then things took a strange turn. The conference was “virtual,” with no real-world gathering—in fact no conference happened at all. And the publication? It turned out to be a cloned version of the real journal on a different website. Dadkhah made a stink and eventually got his money back—a rare escape.

Since then, he has become one of the go-to experts on journal fraud. Recently, disgruntled authors began approaching him about a new scam. Euromed Communications, a publisher of biomedical journals and books based in the United Kingdom, may have been the first target. The trouble began a few years ago when the company's founding director died of cancer. During the management reshuffle, a \$10 bill went unpaid: It was the annual registration fee for the company's Web domain. "We tried to reregister it but it was too late," says Peter Hall, the company's new director. "Someone had already snapped it up."

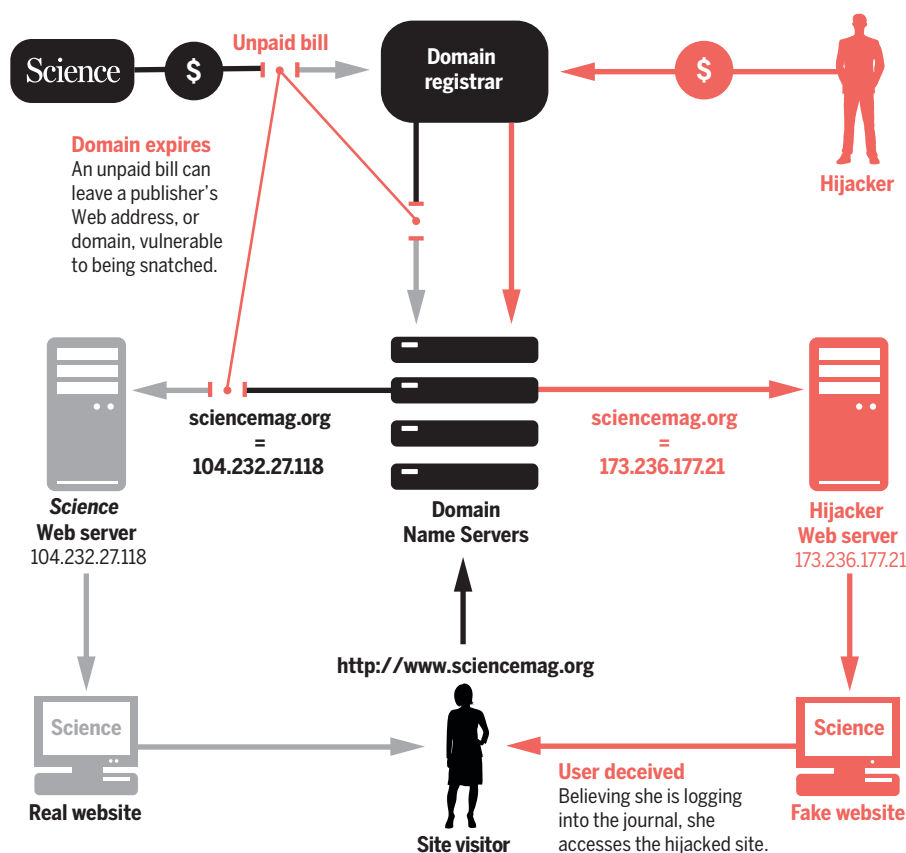
Since then, Euromed Communications has transitioned its publications to a new domain. Things went smoothly until June of this year. “We started getting emails from angry researchers,” Hall says. The researchers claimed to have paid the subscription fee for one of the company’s publications, a pharmaceutical industry trade journal called *GMP Review*, through the official website but received nothing in return.

Sure enough, *GMP Review* had been hijacked. Even today, the top hit in a Google search for “*GMP Review*” points to the old Web domain, where visitors find an imitation of the journal’s website. One difference that few notice is the lack of any email or telephone contacts for the editor. Instead, a “contact” button brings visitors to a Web form that sends communication directly to the hijackers.

"It's a real nuisance," Hall laments, but there is little he can do about it. Anyone

Don't forget to pay your bills

Publishers have to periodically pay to register their journals' Web domains, and failure to do so can allow a waiting hacker to swoop in and snatch a domain for their own purposes, such as erecting a fake journal site.



nesses invest heavily in cybersecurity, and scholarly journals will necessarily need to follow,” warns Phil Davis, a former university librarian who is now a consultant in the scholarly publishing industry. “There is a lot more than just money at stake. Reputations and trust are on the line.”

LONG IGNORED BY THE CRIMINAL underworld, academic journal websites are finally getting noticed. One reason is the sheer scale of today's online publishing—more than 2 million digital articles were published by more than 20,000 journals last year.

Jeffrey Beall, a librarian at the University of Colorado, Denver, who tracks abuse in scholarly publishing, has so far identified 88 journals that are facing competition from fake imitators on different websites. “The list keeps growing,” he says. But snatching a journal’s actual Internet domain is a new twist—one Beall wasn’t aware of until *Science* alerted him to the practice.

Until domain-snatching came along, journal hijacking was easy to spot. You just turned to a trusted list of reputable journals, such as Web of Science. Curated by Thomson Reuters, it lists the International Standard

can buy a Web domain from private registration companies who neither vet nor care whether the purchaser has a “right” to it. In this case, the journal’s was purchased through a private firm in Australia—the hijackers themselves could be anywhere. At least now, after the publisher contacted Thomson Reuters to explain the situation, Web of Science lists the correct Web address for Hall’s company.

A similar fate befell *Ludus Vitalis*, a respected philosophy of science journal published by the Centro Lombardo Toledano in Mexico City, except those hijackers went one step further. Not only did they snatch the journal’s official domain and clone the journal site, they are accepting submissions. You can publish your research in the fake *Ludus Vitalis* for \$150. The fake journal now has a steady stream of papers from a range of disciplines, boldly declaring on its website that it is indexed by Thomson Reuters. The real publishers declined to comment, although in an online forum with researchers they acknowledged that the site was not under their control.

HOW MANY OTHER ACADEMIC JOURNAL domains have been snatched? Thomson Reuters declined to comment on journal hijacking or to help me probe its extent. But Dadkhah suggested two ways to spot a hijacking. First, check the domain registration data online by performing a WHOIS query. (It’s not an acronym, but rather a computer protocol to look up “who is” behind a particular domain.) If the registration date is recent but the journal has been around for years, that’s the first clue. Also suspicious is if the domain’s country of registration is different from the journal’s publisher, or if the publisher’s name and contact information are kept anonymous by private domain registrars.

I wrote a program to automate Dadkhah’s search method. I started by scraping the publicly accessible records from Web of Science. That generated a list of more than 12,000 journal Web domains. I ran WHOIS queries on all of them. Filtering the records by the registration creation date gave me a list of the journals with Web domains that changed hands within the past year.

After examining those websites, searching the Internet for signs of the real publishers, and trying to contact them when things looked fishy, I identified 24 journals indexed by Thomson Reuters whose web domains appear to have been recently snatched. (That list, along with all of the code and data from this investigation are at <http://scim.ag/hijackdata>.)

So far, *GMP Review* and *Ludus Vitalis* are the only ones with fake journals open

for business. Several sites are being used for unrelated commercial enterprises—apparently simply hoping to benefit from any traffic. For example, the official Web of Science domains for the *Journal of Plant Biotechnology*, published by a Korean scholarly society, and *Graphis Scripta*, a botany journal published by the Nordic Lichen Society, now promote balding cures and payday loans, respectively.

In some cases, the motivation of the hijacker is difficult to discern. For example,

“There is a lot more than just money at stake. Reputations and trust are on the line.”

Phil Davis, publishing consultant

Web of Science listings for seven journals published by the University of Liverpool Press all point to liverpool-unipress.co.uk, which now hosts a half-built website that encourages visitors to submit proposals for manuscripts but only offers a generic “contact” button that seems to send communication to the hijackers. An amateurish hijack in progress? “It seems that they are using our name,” officials at the real publisher told *Science*. “This is something we are looking into.”

About a third of the snatched domains are under construction or preparing to be sold. For example, jardinbotanicolankester.org, the domain officially listed by Thomson Reuters for *Lankesteriana*, a plant science journal published by the University of Costa Rica, now hosts nothing but a link to a private auction to buy the domain. According to Adam Karremans, the managing editor, that domain was never registered by the journal. “I can only assume [Thomson Reuters] took that link from another source by mistake,” he says.

That hints at a possible alternative route for hijacking: Fool Thomson Reuters by posing as the publisher and asking them to list your own domain instead of the real one. That is what happened to *Acta Physico-Chimica Sinica*, a journal published by Peking University in China, according to the editor, Ouyang Jianhua. “It is not the original website of the journal, in fact we do not have any relation with this URL. I do not know why Thomson Reuters links to it.” (Thomson Reuters declined to comment.) The site listed by Web of Science is under construction.

BUSTLING MARKETS ALREADY EXIST for buying expired domains with obvious commercial potential—those that are very short

or consist of a common English word. But academic journal domains are often long and esoteric, so the hijackers must have their own strategy for finding their victims. With my journal domain-tracking code up and running, I realized that this might just be the trick. The only tweak needed was to filter the data by the domain’s expiration date. That yields a list of potential targets to stalk, and when to strike.

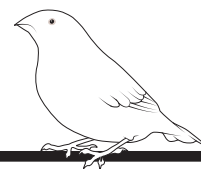
That’s when I became a hijacker myself. Why not buy one of the expired domains immediately, if only to save it? Web of Science listed art.hr as the domain for *Život Umjetnosti* (*Journal of Contemporary Art*), published for the past 50 years by the Institute of Art History in Zagreb. To purchase a .hr domain, I had to hire a European company to serve as my proxy, and I beat the hijackers to it.

My prank is very unlikely to have inconvenienced readers. The publisher moved the journal to a new Web domain in June and notified Thomson Reuters, says the editor, Sandra Križić Roban. “They got the information about the new URL,” she says, but as *Science* went to press, Web of Science still points to the domain that I now control. (I took down the music video, and the site now shows a relevant *skcd* cartoon and a prominent link to the real journal and this story.)

It won’t be the last journal domain to get snatched. “Many publishers still rooted in the print world have never completely gotten used to the details of running a website,” says Stewart Wills, the former Web editor of *Science*. “It’s not surprising that a bill comes in and falls through the cracks. [But] you need to practice due diligence, hire adequate staff, or use an external website vendor,” he says. “The penalty for not professionalizing your online operation is now far too high.”

And it’s not just small journal publishers that are vulnerable. The entire publishing industry relies on digital object identifiers (DOIs) to map Web addresses to scholarly papers. That system stopped working briefly in January because the registration of the doi.org domain expired. “For all the redundancy built into our systems—multiple servers, multiple hosting sites, Raid drives, redundant power—we were undone by a simple administrative task,” reads a mea culpa statement on the blog of CrossRef, the organization that maintains the DOI system. “Truly, we are humbled.”

If a site like CrossRef were hijacked, the consequences for academia would be enormous, Davis says. “We’d have to pay a ransom or create an entirely new system,” he says. “Going back to print publishing is simply not an option for science journals.” ■



BOOKS *et al.*

MEDICINE

The picture of health

A new series of graphic novels features intimate portraits of illness

By Arthur W. Frank

That a major university press would publish a series of graphic novels may come as a surprise to those who think of these works as comic books on steroids, offering plots about superheroes to younger readers. This image of the graphic novel became definitely outdated in 1986 with the publication of Art Spiegelman's second-generation Holocaust memoir, *Maus: A Survivor's Tale*. *Maus* won a Pulitzer Prize, was the subject of a show at New York's Museum of Modern Art, and has been translated into 50 languages. The next most acclaimed graphic novel might be Alison Bechdel's *Fun Home*, published in 2006, which inspired a musical currently enjoying an extended run on Broadway. Bechdel was a 2014 winner of a MacArthur "Genius" Award.

Within the graphic-novel genre, first-person accounts of both illness and clinical practice are an established subgenre. The new "Graphic Medicine" series, launched this spring by Pennsylvania State University Press, not only provides another publication outlet for such works but also lends them greater legitimacy. That counts when, for example, clinicians recommend books to patients or when assigned readings are being selected for health humanities courses. All of which brings us to the two books under review: What are they about, for whom are they written, and how



A strained relationship takes on new depth when a son moves in with his ailing father in *Things to Do in a Retirement Home Trailer Park*.

The reviewer is professor emeritus in the Department of Sociology, University of Calgary, Calgary, AB T2N 1N4, Canada. E-mail: arthurwfrank@gmail.com

might such books change the ways that health care research is practiced?

Aneurin Wright grew up in the American west, where *Things to Do* is set. Like *Maus* and *Fun Home*, *Things to Do* is a family drama. The story begins when Wright's father, who has emphysema, breaks the news that he has been certified by his physician for hospice care. Wright is not sure what "hospice" means but soon gets the message: His father is expected to live for less than six months. Wright decides to move in with his father, caring for him until he dies. Father and son have a troubled history together. The story is about their reconciliation, the progress of a terminal disease, issues of home care, and, ultimately, death itself. Writers from Simone de Beauvoir to Philip Roth have written about their parents' deaths; a research literature on palliative care abounds. What can graphic novels do, distinctively, with this material?

Reading *Things to Do*, I felt I was going through an experience with a real person, not a clinical or social-scientific typification of a person. That person reacted differently than I think I would, but I was brought close enough to the experience to feel how I might react and measure that against what Wright does. That does not, in itself, distinguish *Things to Do* from first-person prose accounts. The graphic-novel medium allows the reader to experience flashbacks, fantasies (such as stamping out a neighbor who has a particular talent for saying the wrong things), dreams, and distortions of reality that make the narrator's point of view compelling. We see both Wright—or his drawn avatar—and what Wright sees and imagines. The reader is both spectator and participant in Wright's frustrations and in his eventual sense of having done something of great value.

We readers care for Wright, the avatar narrator, because we care with him, and we care with him because the images in his head become our images. We share his struggles to care for a father who in the past has been at least threatening and perhaps abusive and who remains difficult to care for in the present. Eventually, we share Wright's sense of loss that manifests as both a feeling of liberation from the work of caring and a void that leaves Wright in need of care himself.

In the end, a serious joy pervades *Things to Do*. In my decades of reading the hospice and palliative care literature, I cannot think of a single book that would be a better companion for family members beginning on this particular work of caring. The book is equally valuable for home-care health workers, whom Wright depicts

Things to Do in a Retirement Home Trailer Park

... When You're 29 and Unemployed

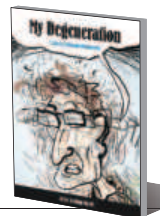
Aneurin Wright

Pennsylvania State University Press, 2015. 320 pp.

My Degeneration A Journey Through Parkinson's

Peter Dunlap-Shohl

Pennsylvania State University Press, 2015. 106 pp.



as vivid characters, each doing his or her work with dedication and expertise.

Peter Dunlap-Shohl's *My Degeneration* is a shorter book, less ambitious in its existential themes than *Things to Do*, but a model of how to fill a particular niche. The book is an extended and more engaging version of the patient-information booklets given out in clinics and support groups. We learn some elementary neural chemistry, how the drug Sinemet works, and when it fails. We learn about deep brain stimulation, what it achieves, and its limits. But unlike educational booklets, such information is contextualized within a highly personal story. Dunlap-Shohl was an editorial cartoonist with the *Anchorage Daily News*,

a position he apparently had to give up because of his illness, diagnosed when he was 43. He has now been living with Parkinson's for more than a decade.

Like *Things to Do*, *My Degeneration* is written for both patients and clinicians. In one of the funniest segments, Dunlap-Shohl presents a series of drawings of bad doctors: "the gimlet-eyed skeptic" who accuses her patient of making up his symptoms, the "cheery prophet" who forecasts inevitable physical decline, "the blithe know-it-all," and several more. For patients, these irreverent archetypes validate their experiences. Clinicians, too, stand to gain a better appreciation of how they might appear to their patients.

The narrative line in these books is often fragmented, incomplete, alternating between surreal fantasy and reality. That is how life is experienced. The books under review reconfirm my belief that personal accounts of illness—both prose and graphic—should provide the starting point and benchmark for what academic health research aspires to say about the experience of illness. More immediately to those who are ill and who work to care for the ill, these books are companions that will both validate and challenge ways of acting and reacting. I hope copies of both will become fixtures in clinical settings and in health care education.

10.1126/science.aad5288



Parkinson's disease gets personal in Peter Dunlap-Shohl's *My Degeneration*.

PERSPECTIVES

TISSUE ENGINEERING

Restoring voice

Engineered vocal cords could soon replace damaged tissue

By Jennifer L. Long^{1,2} and Dinesh K. Chhetri¹

In most mammals, a vocal sound begins with the vibration of paired vocal cords within the larynx. These delicate structures—more accurately called vocal folds because they resemble folded layers of fabric—can stiffen after traumatic injury, cancer treatment, or unknown environmental or genetic insults. Current voice medicine has limited options to repair or replace damaged vocal folds when the voice disturbance is disabling (1). A recent study by Ling *et al.* (2) reports a tissue engineering approach that could lead to implants that replace the unique vocal fold mucosa and restore vocalization.

Vocal folds are made of specialized and complex layers of extracellular matrix constituents and cells, with a microstructure that promotes pliability and resilience (see the figure). Human vocal folds undulate with wavelike regularity in response to airflow

from the lungs and collide with each other hundreds of times per second during speech. Sound waves result from the rapidly repeating airflow interruptions. When stiffened, their functional extracellular matrix and epithelium are replaced by scar tissue that does not easily vibrate during voicing.

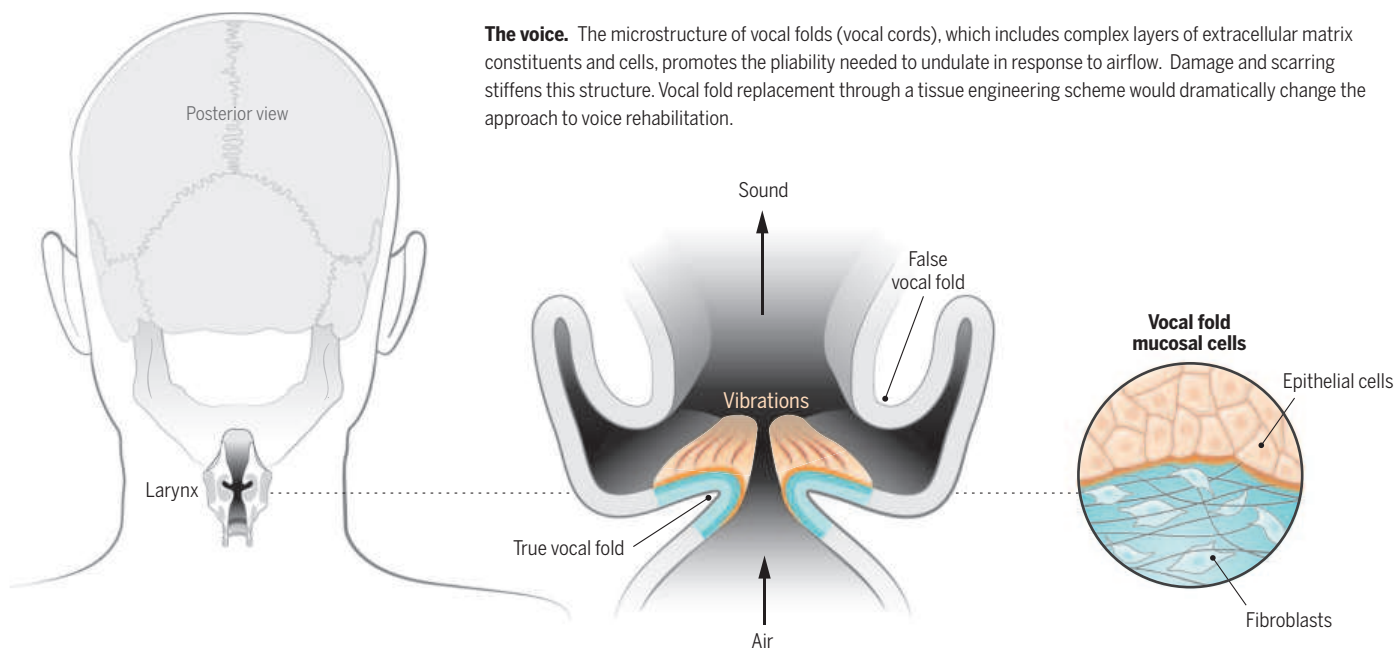
Ling *et al.* introduce an engineered tissue structure that they hope can replace the vocal fold mucosa as treatment for scarring. Primary human vocal fold cells are not widely available because of the irreparable voice injury caused by their excision. The authors isolated fibroblasts and epithelial cells from normal human vocal folds that were surgically removed for unrelated reasons. They expanded these cells and then assembled them into a three-dimensional collagen gel culture to mimic the vocal fold mucosa, which consists of epithelium overlying a “lamina propria” layer of fibroblasts in extracellular matrix. As the tissue-engineered construct developed in vitro, its profile of protein expression (proteome) took on new features relevant to tissue assembly and was different from either cell type cultured alone in collagen. Notably, the proteome contained numerous extracellular matrix proteins that are found in the vocal fold. Thus, the coculture approach with primary human vocal fold cells may provide a pathway to develop the sophisticated extracellular matrix organization that underpins vocal fold vibration. Although that degree of maturity was not yet achieved in vitro, the material’s rheologic behavior was similar to that of excised native vocal fold mucosa.

The key specialized function of the vocal fold mucosa is periodic vibration powered by the aerodynamic energy of a translaryngeal pressure gradient. That vibration is due to

the vocal folds’ unique pliability and is not satisfactorily achieved with other tissues such as skin or oral mucosa. Ling *et al.* demonstrated this function in vitro by applying their engineered tissue to excised canine larynges subjected to airflow (3). Quantitative analysis of digital images showed excellent tissue vibration similar to that of native vocal folds, at least for a short duration. Vibration occurred even though the immature extracellular matrix in the engineered tissue differed greatly from vocal folds. This supports the notion that the epithelium itself is critical for phonation, in addition to the underlying microstructure (4). The promising results should prompt longer-term vibration studies that better simulate actual voice use patterns.

A major issue that will face any non-autologous cell-based vocal fold implant is rejection by the immune system. Most solid organ transplants are performed for life-threatening diseases, for which the risk-benefit ratio of immunosuppressive medication is acceptable. Vocal fold mucosal disorders instead affect quality, not quantity, of life. Partly for that reason, only two whole-larynx transplants have been performed, and one of the patients was already immunosuppressed (5, 6). For widespread clinical application, a vocal fold graft cannot require host immune modulation. To assess immunogenicity, Ling *et al.* implanted their tissue grafts under the kidney capsules of mutant mice that were genetically engineered to replicate the human immune system. The grafts were not rejected, even when the immune cells and vocal fold cells came from different donors. This fortunate result may be attributed to the purity of the implanted cell populations, which are free of the antigen-presenting leukocytes present in whole-organ transplants.

¹Department of Head and Neck Surgery, University of California, Los Angeles, CA 90095, USA. ²Greater Los Angeles Veterans Affairs Medical Center, Research Service, Los Angeles, CA 90073, USA. E-mail: jlong@mednet.ucla.edu; dchhetri@mednet.ucla.edu



The voice. The microstructure of vocal folds (vocal cords), which includes complex layers of extracellular matrix constituents and cells, promotes the pliability needed to undulate in response to airflow. Damage and scarring stiffens this structure. Vocal fold replacement through a tissue engineering scheme would dramatically change the approach to voice rehabilitation.

Ling *et al.*'s work lends hope that vocal fold cell transplants might be feasible without immunosuppression.

A hurdle yet to be addressed is the healing after implantation. Ling *et al.* placed their construct in the mouse kidney solely to assess immune response, not function after healing. The vocal folds are subject to unique stresses that may affect wound healing, including drying from constant airflow, exposure to bacterial flora and pathogens, and phonatory trauma. Scar formation within the construct would again impair the voice, and the implant would be futile. In that light, precisely replicating the vocal fold microstructure in vitro may be less important than controlling the environment for in vivo wound healing. Previous studies of vocal fold mucosa implantation in rabbits revealed some extracellular matrix alteration, although vibration was preserved (7). Identifying those features of an implant that minimize scarring during wound healing is critical for clinical application of this emerging technology.

The complete vocal fold mucosa replacement as proposed by Ling *et al.* is a radical approach for severe vocal fold scarring (see the figure). A failed implant could worsen a person's voice, so it would initially be limited to the most refractory cases. For less severe scarring, a less risky approach such as cell injections is appropriate and is further along the clinical pipeline. Autologous fibroblasts and mesenchymal stem cells both have shown promise for improving function after injection into scarred vocal fold lamina propria (8, 9). But even if cell injections prove successful in clinical trials, there will undoubtedly still be patients whose extensive scarring cannot be reversed and who would benefit from complete mucosal replacement. Furthermore, if function and nontumorigenicity are demonstrated, a mucosal replacement such as that of Ling *et al.* could be considered at the time of laryngeal cancer resection. This single-surgery scheme would dramatically change the approach to vocal fold cancer treatment and voice rehabilitation. ■

REFERENCES AND NOTES

1. N.V. Welham *et al.*, *Laryngoscope* **121**, 1252 (2011).
2. X.X. Ling *et al.*, *Sci. Transl. Med.* **7**, 314ra187 (2015).
3. J. Long *et al.*, *Otolaryngol. Head Neck Surg.* **142**, 438 (2010).
4. J.R. Tse, Z. Zhang, J. Long, *J. Acoust. Soc. Am.* **138**, EL60 (2015).
5. D.G. Farwell *et al.*, *Laryngoscope* **123**, 2502 (2013).
6. R.R. Lorenz, M. Strome, *Otolaryngol. Head Neck Surg.* **150**, 509 (2014).
7. J. Long *et al.*, *Laryngoscope* **125**, 406 (2015).
8. D. Chhetri, G. Berke, *Laryngoscope* **121**, 785 (2011).
9. B. Svensson *et al.*, *Laryngoscope* **121**, 2185 (2011).

ACKNOWLEDGMENTS

Supported by VA Career Development Award IK2BX001944 (J.L.L.) and NIH grant R01 DC011300 (D.K.C.).

NEUROSCIENCE

Mapping the birth of the sleep connectome

Hindbrain neurons flip the switch between REM sleep, non-REM sleep, and wakefulness

By Vladyslav V. Vyazovskiy

We generally fall asleep and then wake up at least 25,000 to 30,000 times throughout our lifetime. Transitions between sleep and waking appear to occur seamlessly, but the underlying mechanisms are extraordinarily complex. There is much interest in characterizing the brain's neuronal circuitry that control these shifts in state, and recent research has pointed to specific populations of neurons in the brainstem, hypothalamus, basal forebrain, and thalamus. On page 957 of this issue, Hayashi *et al.* (1) report that a specific population of neurons in the early developing hindbrain gives rise to subpopulations that contribute to the sleep-wake circuitry.

As the body transitions from wakefulness to sleep, the brain state descends into non-rapid eye movement (non-REM) sleep. Heart rate and body temperature steadily decrease until "deep sleep" is achieved. Electroencephalogram (EEG) is dominated by slow waves of electrical activity (frequencies of 1 to 4 Hz). At regular intervals, while remaining asleep, we make spontaneous excursions into a distinctly different state called rapid eye movement (REM) sleep. Heart rate and breathing increase, EEG slow waves disappear, and the brain becomes more active—hence the name "paradoxical sleep." How and why we transition between these three states of vigilance—wakefulness, non-REM sleep, and REM sleep—is unclear (see the figure).

Although studies of the neuronal systems regulating sleep usually target adult animals, Hayashi *et al.* examined the very moment when some essential elements of sleep circuitry are just starting to unfold. This occurs during the early embryonic stage when sleep and wakefulness, as they are traditionally viewed, are not yet manifested. The authors identified a population of neurons in the mouse embryonic brain that originates from the cerebellar rhombic lip, part of the developing hindbrain. These neurons transiently express the transcription factor Atoh1, and

the authors used this property to genetically label this cell population at a specific stage of development for subsequent targeting. These neurons migrate to the pontine tegmentum—one of the key areas in sleep circuitry—and then divide into two subpopulations, defined on the basis of their distribution relative to the superior cerebellar peduncle. To selectively stimulate these neurons selectively, a chemogenetic approach was used. In this case, the technique—designer receptors exclusively activated by designer drugs (DREADDs)—involved expressing a gene encoding a mutated M3 muscarinic receptor (hM3Dq) in the neurons of interest. The receptor does not have an endogenous ligand but binds to an externally administered drug (clozapine-*N*-oxide). The drug triggers receptor signaling and activation of the neuron.

"A key question...is whether artificially induced vigilance states...make a difference with respect to ongoing and future states."

Thus, only those neurons expressing hM3Dq can be activated by the drug. Hayashi *et al.* found that the selective activation in adult animals of those medial cells that expressed Atoh1 at embryonic day 10.5 (Atoh1-E10.5-medial cells) led to a pronounced suppression of EEG-defined REM sleep. The authors propose that this population of neurons is essential for switching between non-REM and REM sleep.

Interestingly, qualitatively similar effects, both during the light and dark phases of the day, also have been observed after activation of deep mesencephalic nucleus (dDpMe) inhibitory neurons, which represent one of the targets of Atoh1-E10.5-medial cells. At the same time, stimulating the other subpopulation of Atoh1-expressing neurons (Atoh1-E10.5-lateral cells) produced wakefulness, whereas sleep was largely suppressed. It is still unknown whether the role of Atoh1-E10.5-expressing cells in the regulation of

Department of Physiology, Anatomy and Genetics, University of Oxford, Oxford, UK. E-mail: vladyslav.vyazovskiy@dpag.ox.ac.uk

10.1126/science.aad7695

sleep-wake states is preprogrammed from the very earliest stages of embryogenesis or whether they assume this role after they reach their final destination in the pontine tegmentum. Nevertheless, the remarkable finding remains that two groups of cells, while sharing a common developmental lineage, appear to assume distinctly different roles with respect to REM–non-REM and sleep-wake transitions in adulthood.

Evidence suggests that REM sleep is homeostatically regulated, and the “pressure” or “need” for REM sleep accumulates either exclusively during non-REM sleep or simply in the absence of REM sleep, such as during wakefulness or non-REM sleep (2–4). On the other hand, non-REM sleep is also homeostatically regulated (5), and may “compete” with REM sleep for expression (6). Therefore, the results of Hayashi *et al.* should not only stimulate new thinking about the development of sleep circuits in ontogeny, but the study also appeals for a critical consideration of how and whether artificially induced states of vigilance are regulated. Although specific circuits appear to be implicated in the induction or a suppression of a specific state of vigilance, such as waking, non-REM or REM sleep (7–9), it is important to bear in mind that vigilance states are not independent. That is, a decrease of any vigilance state is invariably compensated by another state of vigilance. The reduction in REM sleep after stimulation of Atoh1-E10.5-medial cells or dDpMe inhibitory cells suggests that these subpopulations are implicated in non-REM–REM sleep switching. However, an alternative possibility is that homeostatic sleep regulatory mechanisms are primarily affected. To address this possibility, Hayashi *et al.* performed selective REM sleep deprivation by arousing the animals every time they attempted to enter REM sleep, prior to suppressing REM sleep chemogenetically. Interestingly, even though REM sleep deprivation increased REM sleep pressure, activation of the dDpMe neurons effectively prevented REM sleep from occurring. This suggests that Atoh1-E10.5-medial cells do not merely participate in REM sleep generation but might target the mechanisms responsible for homeostatic regulation of REM sleep.

Throughout sleep, episodes of non-REM and REM sleep do not occur at random, and their alternation and properties are influenced by preceding states; for example, longer REM sleep episodes are usually followed by a longer non-REM sleep episode (3). Con-

sistent with earlier reports (4), Hayashi *et al.* found that non-REM sleep during selective REM sleep deprivation was reduced. The possibility remains, therefore, that increased pressure for non-REM sleep, together with the non-REM sleep-promoting effect of dDpMe inhibitory neuron activation, prevented subsequent compensatory increase of REM sleep. Moreover, it cannot be excluded that even when EEG-defined REM sleep is eliminated, covert REM sleep continues undetected, such as in ultrabrief episodes, in the form of non-REM sleep with muscle at-



Are you sleeping? The neuronal circuitry that controls spontaneous transitions between the different states of vigilance—wakefulness, non-REM, and REM sleep—is still not clear.

nia or in some type of a mixed state. This possibility is suggested by the finding that when REM sleep was reduced by activation of either Atoh1-E10.5 medial cells or DpMe inhibitory neurons, EEG slow-wave activity in non-REM sleep was also lower. Consistently, in depressed human patients, treatment with the monoamine oxidase inhibitor phenelzine not only suppressed REM sleep, but also resulted in lower frontal slow-wave activity during non-REM sleep (10). EEG slow-wave activity in non-REM sleep is an important variable, as it not only indicates that the animal is in non-REM sleep, but also appears to be a sensitive marker of sleep depth and preceding sleep-wake history (11). Thus, the study by Hayashi *et al.* suggests that REM sleep may be a key player in non-REM sleep homeostasis.

A number of factors collectively determine whether an animal will be awake or asleep at any given moment. Among those are the light-dark cycle and internal circadian time, homeostatic needs such as hunger or thirst,

and preceding sleep-wake history. Importantly, spontaneous wakefulness and sleep also affect subsequent sleep states and waking behaviors. For example, the need for sleep dissipates during deep restorative sleep, and we wake up fresh and rested, but then sleep need again increases progressively with time spent awake and active. A key question, therefore, is whether artificially induced vigilance states are also regulated, and whether they also make a difference with respect to ongoing and future states. For example, although stimulating Atoh1-E10.5-lateral cells

in the adult mouse brain increased the amount of time that mice spent awake, the quality of wakefulness also might have been affected. It is unclear if homeostatic sleep pressure increases during such artificially induced wakefulness at a rate similar to that observed during spontaneous wakefulness. Whether the animal can learn and respond to the environment and “feel” awake, or if it merely is in a wake-like state, is also unclear. Finally, it remains to be determined whether sleep need dissipates in the absence of REM sleep after stimulation of Atoh1-E10.5-medial cells, and whether such artificially induced sleep provides the benefits of sleep occurring spontaneously.

The ultimate test for the sleep circuit will be to establish whether turning it on or off leads to an occurrence of brain states that are not merely similar in appearance to spontaneous sleep and wakefulness but are functionally indistinguishable from them. Spontaneous and artificially induced states may look the same to the researcher, but unless the animal subject fails to “tell” the difference between them, the test is not passed. ■

REFERENCES AND NOTES

1. Y. Hayashi *et al.*, *Science* **350**, 957 (2015).
2. P. Franken, *J. Sleep Res.* **11**, 17 (2002).
3. J. H. Benington, H. C. Heller, *Am. J. Physiol.* **266**, R1992 (1994).
4. T. Endo *et al.*, *Psychiatry Res.* **66**, 97 (1997).
5. S. Daan, D. G. Beersma, A. A. Borbély, *Am. J. Physiol.* **246**, R161 (1984).
6. D. G. Beersma *et al.*, *Electroencephalogr. Clin. Neurophysiol.* **76**, 114 (1990).
7. P. Fort *et al.*, *Eur. J. Neurosci.* **29**, 1741 (2009).
8. C. B. Saper *et al.*, *Neuron* **68**, 1023 (2010).
9. S. H. Lee, Y. Dan, *Neuron* **76**, 209 (2012).
10. H. P. Landolt, J. C. Gillin, *Neuropsychopharmacology* **27**, 462 (2002).
11. P. Achermann *et al.*, *Brain Res. Bull.* **31**, 97 (1993).

ACKNOWLEDGMENTS

Supported by Wellcome Trust Strategic Award (98461/Z/12/Z).

10.1126/science.aad6489

Transport: A roadblock to climate change mitigation?

Urban mobility solutions foster climate mitigation

By Felix Creutzig,^{1,2*} Patrick Jochem,³
Oreane Y. Edelenbosch,⁴ Linus
Mattauch,^{1,2} Detlef P. van Vuuren,^{4,5}
David McCollum,⁶ Jan Minx^{1,7}

Global emissions scenarios studies, such as those informing the Intergovernmental Panel on Climate Change (IPCC) 5th Assessment Report (AR5), highlight the importance of the transport sector for climate change mitigation—along with the difficulties of achieving deep reductions therein (1) [supplementary materials (SM)]. Transport is responsible for about 23% of total energy-related CO₂ emissions worldwide (2). The sector is growing

POLICY more rapidly than most others, with emissions projected to double by 2050. Global scenario studies, specifically those produced by integrated assessment models (IAMs), communicate aggregate mitigation potentials by sectors in IPCC reports. Yet recent evidence indicates that emissions may be reduced further than these global scenario studies suggest—if policy-makers use the full suite of policies at their disposal.

If current trends continue, the global number of light-duty vehicles will roughly double by midcentury, driven by rising affluence especially in China, India, and South East Asia (3). Demand for freight transport (road, rail, shipping, and air) and passenger aviation is projected to surge as well.

In recent years, CO₂ emissions from transport have stabilized in the European Union and the United States as fuel economy and emission standards were tightened. Municipalities worldwide have implemented local measures to reduce emissions of urban transport systems. However, these efforts have not been able to slow sectoral emission growth on the global level; there needs to be a broader suite of complementary, and enforced, policies in order to succeed.

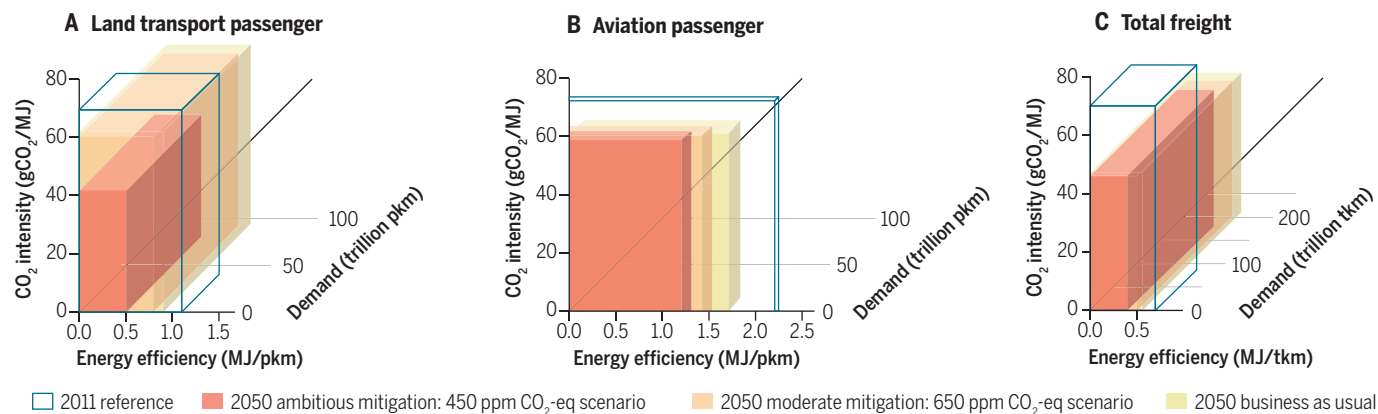
The IPCC AR5 indicates that stabilization of CO₂ emissions in the transport sector by 2050 at roughly 2010 levels would be consistent with the 2°C global mean temperature increase target [i.e., 430 to 480 parts per million (ppm) CO₂-equivalent (CO₂-eq)]. But this transport mitigation burden is conditional on emission reductions in other sectors. The 2050 target for the transport sector is relatively modest because, in these global emissions scenarios, the power sector often compensates for residual emissions in the transport sector by removing CO₂ from the atmosphere via bioenergy and carbon capture and storage (SM). If non-transport reductions turn out to be more difficult to achieve, then transport would need to halve its emissions by midcentury.

CAN AMBITIOUS CO₂ REDUCTIONS BE ACHIEVED? Transport mitigation options can, in principle, lower emissions by reducing (i) overall transport demand growth (reducing distance traveled; shifting to more

efficient modes), (ii) the amount of energy needed for propelling a vehicle over a given distance (increase fuel efficiency), or (iii) the carbon intensity of transport fuels [gCO₂/MJ] (fuel shift). In global scenarios, options (ii) and (iii) form the main mitigation options (1). In contrast, many urban transport experts highlight the potential of option (i), such as compact urban development, bus rapid transit, bicycle highways, and telecommuting. As the last-mentioned options often lead to nonclimate benefits at the local level, they are increasingly becoming part of municipal agendas worldwide. But current-generation global IAMs lack necessary spatial and/or jurisdictional resolution to represent local, often idiosyncratic, solutions of this type. Whereas IAMs remain crucial for the big picture, transport-specific models with higher resolution in space and technological data complement IAMs and show that more ambitious mitigation appears plausible.

“...transport could...nearly halve its CO₂ emissions by midcentury...”

We illustrate the main challenges using results of three representative scenario runs by the IAM IMAGE (see the figure, A to C) (SM) (4) in order to then contextualize the relevance of additional mitigation options. In the most ambitious case, total emissions in the transport sector will be 4.2 Gt CO₂ in 2050, within the range of the 430 to 480 ppm CO₂-eq scenarios. But which transport sector developments substantiate mitigation scenarios? We sketch key elements of the solution space, following the IPCC (1, 2) and, drawing on other literature, point to two options in land passen-



Modeled transport CO₂ emissions, in 2011 and in 2050, based on data from 2005. (See SM). (A) Land passenger (passenger-kilometer, pkm); (B) aviation; and (C) freight transport (metric ton-kilometer, tkm), as modeled by the IAM IMAGE (14) (See SM). Emissions, calculated as the product of the three axes (CO₂ intensity, energy efficiency, and demand), can be visualized by the volume of the boxes.

ger transport that complement the solution space: electric cars and urban transport demand management.

The scenarios show that passenger road transport continues to be responsible for the highest emissions share within the transport sector (part A); but aviation displays the highest growth in emissions (part B), consistent with historical trends of shifting to faster modes. Aviation requires considerable fuel per passenger-km traveled (part B), whereas maritime transport, a major component of freight demand, is highly fuel-efficient (part C).

Road transport could contribute a major mitigation share by (i) continuing to aggressively increase efficiency; (ii) shifting from fossil fuels to electric-drive vehicles;

“Infrastructure investments and behavioral options can produce cost savings that are not typically included in global estimates of mitigation costs.”

and (iii) slowing demand growth, especially in urban settings. First, continuously improved technical standards in road transport in all major auto markets worldwide have resulted in efficiency gains for new light-duty vehicles of about 2 to 4% per year (5). Although this rate can be extrapolated for another decade, future efficiency gains are likely to become more costly without sacrificing vehicle size, safety, equipment, or comfort. But a shift in societal preferences toward smaller cars would allow for reduced incremental costs.

Second, deeply decarbonizing road transport would involve a large-scale shift from gasoline and diesel to biofuels, electricity, and/or hydrogen, either in dedicated battery-electric or fuel-cell vehicles or in mixed configurations, such as plug-in hybrid-electric vehicles. Our scenario, similar to those assessed by AR5, indicates only partial decarbonization until 2050 (Fig. 1A), mostly because production of

advanced vehicle technologies and low-carbon fuels with high-energy density are expected to remain costly for several decades (relative to gasoline and diesel used in efficient conventional vehicles). There is no agreement on which of the three alternative energy carriers will replace for fossil liquid fuels in the long term, but it appears likely that one or several of these will come to dominate in the second half of this century if deep cuts in emissions are to be achieved (6). Battery-electric mobility, for instance, might take off faster than expected owing to substantial declines in battery prices (7), which would make battery-electric travel less expensive than conventional fossil fuel-based mobility [(8) see also SM]. Hence, battery-electric cars are likely to reduce emissions further until 2050 [even though indirect emissions from electricity generation are not negligible (9)], on top of the emission reduction shown in IMAGE.

Third, infrastructure development, land-use policies and behavioral interventions can catalyze further emission reductions; these, however, are hard to assess quantitatively in current-generation global IAMs that lack the fine-scale resolution of local infrastructure and behavioral issues (10). In general, those strategies are not modeled explicitly. Options include shifting to modes with low carbon intensities, parking management and congestion charges, smart growth policies, and behavioral measures. Such options also carry potentially large social benefits, e.g., reduced noise, air pollution; traffic congestion; and risk of obesity-related diseases, depression, and dementia, which often create strong incentives for local action. In sum, the combined mitigation potential in urban transport via spatial planning, transport pricing, and behavioral options amounts to 20 to 50% between 2010 and 2050, compared with baseline (11) (fig. S1).

Infrastructure investments and behavioral options can produce cost savings that are not typically included in global estimates of mitigation costs. Although low-carbon infrastructure options may include expensive up-front construction (e.g., high-speed rail tracks), such investments could lead to enormous savings from building and maintaining fewer roads and parking spaces over coming decades. One study puts these infrastructure investment cost savings for low-carbon transport at around \$20 trillion by 2050 globally (12). Rededicating existing urban infrastructure to non-motorized transport (e.g., pedestrian zones and bicycle lanes) can be achieved at little cost. Behavioral interventions have mostly zero or low monetary costs (SM),

but unlocking their considerable mitigation potential requires policies that explicitly take nonstandard preferences, beliefs, and decision-making processes into account, as well as normative considerations of policy-makers (13).

If both urban transport mitigation options and increasingly cost-effective battery-electric cars are fully utilized, there are reasons to believe global transport could be on track to nearly halve its CO₂ emissions by midcentury, which would bring the sector in line with the 2°C target (SM). Higher fuel taxes would foster long-term development toward compact urban form and low-carbon urban transport (14) and, at the same time, incentivize faster market penetration of battery-electric vehicles (7). In fact, avoiding rebound effects—associated with the substantially greater efficiency of electric vehicles—necessitates high prices on fossil fuels. So far, however, we see little global appetite among policy-makers for seriously discussing thorny transport issues in public debates and international climate negotiations. Unless this changes swiftly, transport may remain a roadblock to the world's efforts to mitigate climate change. ■

REFERENCES AND NOTES

1. O. Edenhofer et al., in *Climate Change 2014: Mitigation of Climate Change. Contribution of Working Group III to the Fifth Assessment Report of the Intergovernmental Panel on Climate Change*, O. Edenhofer et al., Eds. (Cambridge Univ. Press, New York, 2014), pp. 33–108.
2. R. Sims et al., in *Climate Change 2014: Mitigation of Climate Change. Contribution of Working Group III to the Fifth Assessment Report of the Intergovernmental Panel on Climate Change*, O. Edenhofer et al., Eds. (Cambridge Univ. Press, New York, 2014), pp. 599–670.
3. D. Sperling, D. Gordon, *Two Billion Cars* (Oxford Univ. Press, New York, 2009).
4. B. Girod, D. P. van Vuuren, S. Deetman, *Energy Policy* **45**, 152 (2012).
5. S. L. Winkler, T. J. Wallington, H. Maas, H. Hass, *Environ. Sci. Technol.* **48**, 6453 (2014).
6. R. Pietzcker et al., *Energy* **64**, 95 (2014).
7. B. Nykvist, M. Nilsson, *Nat. Clim. Change* **5**, 329 (2015).
8. National Research Council, *Transitions to Alternative Fuels and Vehicles* (National Academies Press, Washington, DC, 2013).
9. P. Jochem, S. Babrowski, W. Fichtner, *Transp. Res. A: Policy Pract.* **78**, 68 (2015).
10. T. Schwanen, D. Banister, J. Anable, *Transp. Res. A Policy Pract.* **45**, 993 (2011).
11. F. Creutzig, *Transp. Rev.* 10.1080/01441647.2015.1079277 (2015).
12. J. Dulac, “Global land transport infrastructure requirements” (International Energy Agency, Paris, 2013).
13. L. Mattauch, M. Ridgway, F. Creutzig, *Transp. Res. Part D Transp. Environ.* 10.1016/j.trd.2015.08.006 (2015).
14. F. Creutzig, *Urban Clim.* **10**, 63 (2014).

ACKNOWLEDGMENTS

We thank B. Girod and J. Römer for support in modeling and R. Pietzcker, W. Rothengatter, and Y. Hayashi for helpful discussions. We acknowledge funding by EU Framework Programme 7 (FP 7) 2007–2013 no. 308329 (ADVANCE).

SUPPLEMENTARY MATERIALS

www.sciencemag.org/content/350/6263/911/suppl/DC1

¹Mercator Research Institute on Global Commons and Climate Change (MCC), 10829 Berlin, Germany. ²Technical University Berlin, 10623 Berlin, Germany. ³Karlsruhe Institute of Technology (KIT), 76131 Karlsruhe, Germany. ⁴PBL Netherlands Environmental Assessment Agency, 3720AH Bilthoven, Netherlands. ⁵Copernicus Institute of Sustainable Development of Geosciences, Utrecht University, 3584CS Utrecht, Netherlands. ⁶International Institute for Applied Systems Analysis (IIASA), 2361 Laxenburg, Austria. ⁷Hertie School of Governance, 10117 Berlin, Germany. *Corresponding author. E-mail: creutzig@mcc-berlin.net

Putting the breaks on meiosis

Yeast and birds reveal remarkable evolutionary stability in recombination patterns

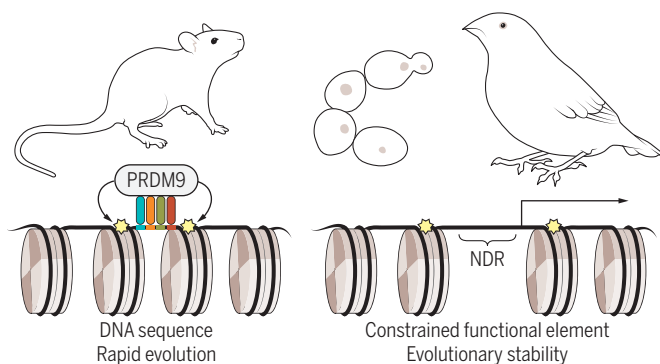
By Michael Lichten

Sexual reproduction involves the production of haploid gametes from diploid cells through a series of genome divisions, called meiosis. Accurate meiotic chromosome segregation requires homologous recombination, initiated by programmed DNA double-strand breaks (DSBs). DSBs are focused at sites, called hotspots, where recombination preferentially occurs (1). Because DSB repair by recombination involves copying information from an unbroken chromosome, one prevailing view is that, over time, DSB hotspots should be replaced by “cold” sequence variants that reduce DSBs at the same site (2). Consistent with this paradigm, hotspot patterns in mice and primates display high divergence between species and even individuals (3). This view is now challenged by two research articles in this issue, by Lam and Keeney (page 932) and Singhal *et al.* (page 928), that characterize recombination hotspot patterns in species of budding yeast (4) and birds (5), respectively. Both papers document remarkable hotspot pattern stability over evolutionary time, suggesting that the picture in mammals may be the exception rather than the rule.

Lam and Keeney compared genome-wide meiotic DSB maps in *Saccharomyces cerevisiae* strains with roughly the same sequence divergence—a measure of separation in evolutionary time—as humans and chimpanzees, and in four *Saccharomyces* species, including a pair (*S. cerevisiae* and *S. kudriavzevii*) with roughly the same sequence divergence as mammals and birds. Hotspot patterns among *S. cerevisiae* strains showed almost complete overlap, and even the distantly related *S. cerevisiae* and *S. kudriavzevii* showed a greater than 80% overlap in hotspot locations. Even more remarkably, Lam and Keeney found that different species often displayed similar fine-structure break distributions and DSB frequencies at individual hotspots. Thus,

in contrast to the rapid divergence seen in mammals, hotspot patterns in budding yeast show a high degree of conservation.

Singhal, Leffler, and colleagues derived meiotic recombination maps from single-nucleotide polymorphism distributions in small populations of two Australian birds, the zebra finch and long-tailed finch, again with sequence divergence similar to that between humans and chimpanzees. As with



Different mechanisms, different outcomes. In mammals, meiotic recombination hotspots contain sequences where PRDM9 binds and forms chromatin marks (stars) that promote double-strand breaks. Both PRDM9 and its target sequences evolve rapidly. In yeast, birds, and other eukaryotes, breaks form at preexisting genomic elements with recombination-independent functions that ensure evolutionary stability—in this example, a nucleosome-depleted region (NDR) with a gene promoter that already contains break-promoting chromatin marks.

yeast, a large fraction of hotspots in the two finches (>70%) colocalized. Using elevated GC content, a hallmark of GC-biased gene conversion (6), as a signal for hotspots, the authors examined the ensemble of hotspots shared between the two finches in three other species: the Australian double-barred finch, the medium ground finch from the Galapagos, and the Old World collared flycatcher. Despite their broad geographical and evolutionary separation, all five species showed elevated GC content at these loci, consistent with the retention of a substantial subset of hotspots. Thus, in birds as in yeast, but unlike in mammals, meiotic recombination patterns appear to be highly conserved over broad swaths of evolutionary time.

The cause of this difference may be found in the different ways that yeast and mammals designate DSB hotspots (1). Yeast hotspots do not share specific sequences, but instead are located in the nucleosome-depleted regions (NDRs) already present in

mitotic cells. NDRs contain gene promoters and are flanked by nucleosomes that contain histone H3 methylated at lysine 4 (H3K4me). H3K4me is implicated primarily in promoter function but is also used to recruit DSB-forming proteins during meiosis. In contrast, in most mammals, hotspots show no particular correlation with preexisting chromatin elements. Instead, they contain binding sites for positive-regulatory domain zinc finger protein 9 (PRDM9), a meiotic protein with a highly variable zinc finger array that recognizes specific sequences and that catalyzes the formation of H3K4me in its vicinity. Thus, yeast hotspots are likely maintained because their constituent elements perform other important functions. PRDM9-designated hotspots in mammals are under no such constraints, and thus can undergo rapid

evolution in which hotspot evaporation is balanced by the rapid evolution of new binding specificity in PRDM9 (7). The finding that bird hotspots are also conserved suggests that birds, like yeast, designate hotspots using genomic elements that are under functional selection.

The existence of at least two different modes of hotspot designation, with accompanying differences in evolutionary stability, raises a question: If birds and yeast do it one way, and most mammals do it another way, what about other eukaryotes? In this regard, it is worth noting that hotspots also appear to be sequence-independent, and are associated with functional genomic elements, in plants (8); in dogs,

which naturally lack a functional PRDM9 (9); and even in *Prdm9*^{-/-} mutant mice (10). These observations, together with the exciting findings of Lam and Keeney and of Singhal *et al.*, raise the intriguing possibility that the yeast and bird paradigm for hotspot designation may be the primordial one, and that the mammalian mechanism of sequence-based designation may be a relative latecomer to the game. ■

REFERENCES

1. B. de Massy, *Annu. Rev. Genet.* **47**, 563 (2013).
2. A. Nicolas *et al.*, *Nature* **338**, 35 (1989).
3. F. Baudat, Y. Imai, B. de Massy, *Nat. Rev. Genet.* **14**, 794 (2013).
4. I. Lam, S. Keeney, *Science* **350**, 932 (2015).
5. S. Singhal *et al.*, *Science* **350**, 928 (2015).
6. M. T. Webster, L. D. Hurst, *Trends Genet.* **28**, 101 (2012).
7. Y. Leseqque *et al.*, *PLoS Genet.* **10**, e1004790 (2014).
8. K. Choi *et al.*, *Nat. Genet.* **45**, 1327 (2013).
9. A. Auton *et al.*, *PLoS Genet.* **9**, e1003984 (2013).
10. K. Brick *et al.*, *Nature* **485**, 642 (2012).

National Cancer Institute, Bethesda, MD 20892, USA.
E-mail: mlichten@helix.nih.gov

ILLUSTRATION: P. HUEY/SCIENCE

PHYSICS

Magnetic fields make waves in cuprates

High magnetic fields reveal underlying electronic states in high-temperature superconductors

By Marc-Henri Julien

Physicists have been struggling for nearly 30 years to pinpoint the unusual electronic states of the copper oxides (or cuprates) that make these materials superconducting at high critical temperatures (T_c). Recently, it appears that consensus may be finally emerging on the presence of periodic modulations in the electronic density, a phenomenon called charge density wave (CDW) or, more broadly, charge order—and now considered to be a crucial piece of the cuprate puzzle. But how this piece exactly fits into the puzzle remains unclear. On page 949 of this issue, Gerber *et al.* (1) report the observation that the CDW becomes coherent in the three dimensions of space when subjected to high magnetic fields. These latest results provide invaluable information for elucidating why charge order occurs and why superconductivity cares about it.

A chronological recap is useful to understand how it is that, in 2015, we can still learn from x-ray diffraction about $\text{YBa}_2\text{Cu}_3\text{O}_y$ (YBCO), arguably the most famous super-

conductor of the cuprate family. The first direct evidence of charge order in a cuprate dates back to the discovery of “stripes” in $\text{La}_{1.48}\text{Nd}_{0.4}\text{Sr}_{0.12}\text{CuO}_4$ (2). Below a sharp temperature onset, a CDW, intertwined with a magnetic modulation, propagates coherently over relatively long distances in one direction of each conducting (CuO_2) plane. While other hints of charge order have fueled the debate, the long-range order of the stripe materials has long remained an epiphenomenon and, to many of those obsessed with finding the mechanism of superconductivity, a purported red herring. In the absence of new experimental facts, especially in a clean cuprate such as YBCO, exchanges between “pro-stripes” and “stripe-skeptics” were, to say the least, contentious.

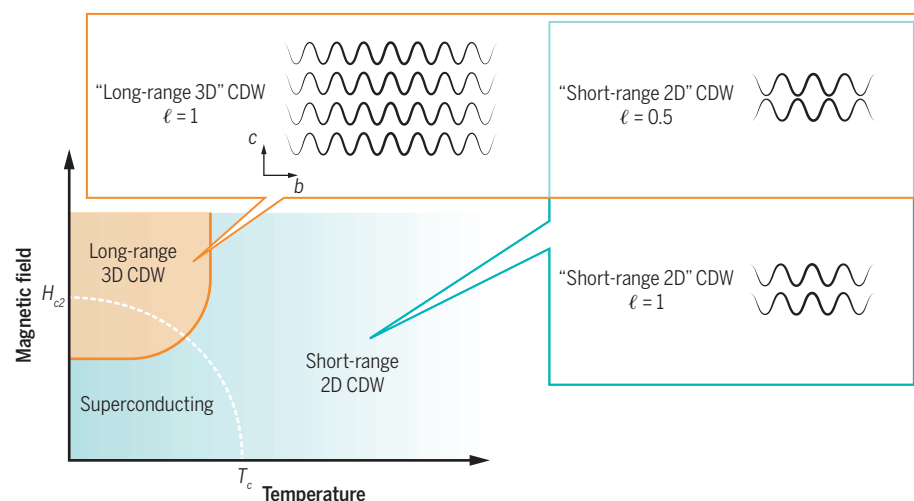
In 2007, however, a series of transport measurements in high magnetic fields found the first indications that electronic order actually occurs, in some form, in YBCO (3). In 2011, nuclear magnetic resonance (NMR) experiments (4) demonstrated that the order in question is a CDW that had been hidden for 25 years because it develops in the CuO_2 planes only after an intense field has sufficiently weakened superconductivity. Sharp signatures of this phase (3–5) suggested that it is the second case of long-range charge order in cuprates. However, because it was ob-

served only in high fields, this CDW was soon overshadowed by the next wave of discoveries: X-ray (6, 7) and NMR (8) experiments in YBCO found that static, but (relatively) short-range, charge order forms at higher temperatures and already in zero field (see the figure). Similar x-ray observations soon followed in various cuprate families (9), thereby confirming early scanning tunneling microscopy observations of modulations resembling a plaid pattern of perpendicular sets of stripes (10, 11).

Charge density waves have been known to occur in many low-dimensional metals since the 1970s. But how electronic and structural degrees-of-freedom precisely conspire to trigger the wave is still the subject of active research, especially in two-dimensional (2D) systems. Cuprates are not only 2D metals; they are particularly complex ones, with chemical disorder, strong repulsion between electrons, and ubiquitous short-lived magnetism. It may thus not be surprising that the hundred or so theory papers in the last 4 years have not been enough to build a consensus on the origin of the CDW. Even less clear is the connection to superconductivity. All experiments point to an evident competition between superconductivity and CDW order. But it is tempting to hypothesize a more intricate (though not necessarily causal) relationship given that the high-field CDW is apparently bounded below in temperature by the zero-field T_c (4) and as a function of doping (the y in $\text{YBa}_2\text{Cu}_3\text{O}_y$) by the optimal doping for superconductivity (12).

Our knowledge of the CDW may well be incomplete as it relies largely on the short-range state, which, in principle, may not be as reliable as long-range order. However, Gerber *et al.* now put the high-field CDW of YBCO back under the spotlight. They combined millisecond-long pulses of intense magnetic fields with femtosecond pulses from a free-electron laser, the newest generation of x-ray radiation sources whose unmatched peak brightness promises breakthroughs in physics, chemistry, biology, and earth sciences. In addition to opening new avenues for research in high magnetic fields, this experimental tour-de-force provides a much awaited, direct, and quantitative observation of the long-range CDW order in high magnetic fields.

Specifically, Gerber *et al.* find a coherence length of (at least) four lattice constants in



Mapping out the cuprates. Magnetic field versus temperature phase diagram of $\text{YBa}_2\text{Cu}_3\text{O}_y$ with $T_c \approx 60$ K, from x-ray (1, 6, 7), NMR (4, 8), and ultrasound (5) experiments. Continuous and dotted lines represent proven phase transitions. The insets represent charge density modulations along the crystallographic b -axis (no information concerning the a -axis is yet known in high fields) and their correlation in the c -axis direction (perpendicular to the CuO_2 planes). $\ell = 1$ (0.5) refers to the stacking period of one (two) lattice constant(s) along the c -axis (1). The 3D ($\ell = 1$) and 2D ($\ell = 0.5$) modulations coexist at high fields and low temperatures.

the direction perpendicular to the CuO_2 planes and thus term the long-range CDW order “three-dimensional” (3D), in contrast with the essentially 2D nature of its short-range partner. By comparison, the coherence length parallel to the planes exceeds 40 lattice constants. But the most unexpected result is that the two types of modulations stack differently from one CuO_2 bilayer to the next one: The 3D order simply stacks in-phase, whereas the 2D modulations are in-phase only every other bilayer (1, 7). Furthermore, the results corroborate previous findings (8) that the long-range and short-range CDWs do not simply convert into one another when the temperature is varied, as one would expect at a standard phase transition. Instead, the short-range modulations persist underneath the long-range CDW. Yet, with identical wave vectors in the crystallographic b direction, the two phases are unlikely to constitute different orders.

No doubt, this puzzling phenomenology will motivate much theoretical work. For example, among the scenarios to be examined are antiphase charge oscillations induced in two consecutive CuO_2 bilayers by oxygen defects located in the intervening layer. Such modulations pinned by disorder would indeed be short-ranged, quasi-2D, and likely present both above and below the high-field transition (8). Were such a scenario to explain the short-range modulations, the only genuine, intrinsically static CDW order would be the high-field state. In any event, whatever the final explanation is, because locating the boundary between CDW order and CDW fluctuations is crucial for understanding the interplay with superconductivity, the questions raised by the high-magnetic field results have far-reaching implications.

The findings of Gerber *et al.* raise more immediate questions that mark out the path for the next experiments: Is there a single, sharp transition at some field value? Is there a similar CDW modulation propagating along the a -axis of the planes? What happens at even higher fields? The answer to any of these questions will certainly move the field forward; a new chapter of the cuprate saga begins. ■

REFERENCES

1. S. Gerber *et al.*, *Science* **350**, 949 (2015).
2. J. M. Tranquada *et al.*, *Nature* **375**, 561 (1995).
3. N. Doiron-Leyraud *et al.*, *Nature* **447**, 565 (2007).
4. T. Wu *et al.*, *Nature* **477**, 191 (2011).
5. D. LeBoeuf *et al.*, *Nat. Phys.* **9**, 79 (2013).
6. G. Ghiringhelli *et al.*, *Science* **337**, 821 (2012).
7. J. Chang *et al.*, *Nat. Phys.* **8**, 871 (2012).
8. T. Wu *et al.*, *Nat. Commun.* **6**, 6438 (2015).
9. R. Comin, A. Damascelli, <http://arxiv.org/abs/1509.03313> (2015).
10. J. E. Hoffman *et al.*, *Science* **295**, 466 (2002).
11. C. Howald *et al.*, *Phys. Rev. B* **67**, 014533 (2003).
12. B. Ramshaw *et al.*, *Science* **348**, 317 (2015).

10.1126/science.aad3279

GEOLOGY

100 years of continental drift

One hundred years ago, Alfred Wegener laid the foundations for the theory of plate tectonics

By Marco Romano¹ and Richard L. Cifelli²

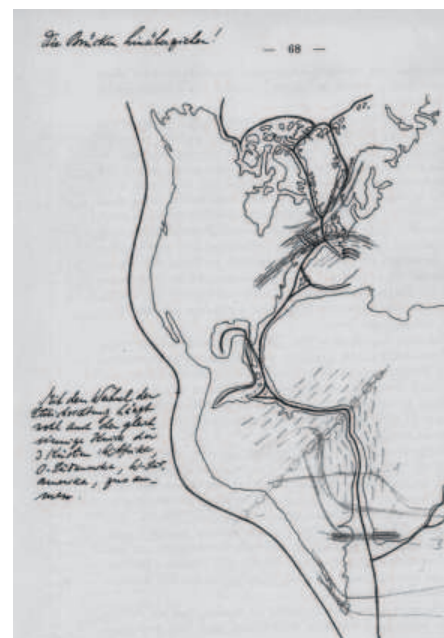
Alfred Wegener (1880–1930) was a leading explorer, geophysicist, and meteorologist from Germany, and pioneer in the exploration of Greenland (1). His seminal volume of meteorology (2) is universally considered a fundamental manual for this discipline and was long a reference text for students and specialists. Wegener's preeminent scientific legacy, however, is the continental drift hypothesis. He first presented his thesis to the scientific community on 6 January 1912 at the Geological Society of Frankfurt am Main, but his famous monograph on the subject dates to 1915 (3).

Wegener argued that, in the distant past, Earth's major landmasses were assembled in a single supercontinent that began to break up about the beginning of the Jurassic (see the first figure). Subsequent fragmentation and motion led to the current configuration. Now universally accepted as the theory of plate tectonics, Wegener's thesis synthesizes and explains an extraordinary range of facts about Earth's history and processes. It is to the earth sciences what Darwin's theory of evolution is to the life sciences.

Earlier scholars such as Francis Bacon, Alexander von Humboldt, and Eduard Suess had recognized the matching Atlantic coastlines of South America and Africa (4). It remained for Wegener, however, to fully explore the idea of shifting continents and assemble a diverse array of supporting geological, paleontological, and geophysical evidence. Juxtaposing continents like so many pieces of a jigsaw puzzle, Wegener demonstrated striking similarities between the geological structures, fossils, and rock sequences on opposite sides of the Atlantic. He commented that once reassembled, these structures lined up like rows of print on a torn newspaper [p. 87 in the first English translation; see (3)]. Using then-new geophysical concepts such as isostasy (that is, the dynamic equilibrium between Earth layers of differing densities) and radiogenic heat, Wegener envisioned continents as huge plates made up of mainly light rock floating in denser, solid, but much more

plastic oceanic rock. This proposal contradicted the orthodox interpretation of Earth in contraction, which had been introduced by Descartes and Leibnitz and expanded by James Dwight Dana and Eduard Suess.

Wegener's 1915 publication unleashed a firestorm of debate. Among the few eminent supporters were Émile Argand, an expert on Alpine geology, and the South African geologist Alexander du Toit. The drift hypothesis was so iconoclastic that it earned vitriol, ridicule, and scorn from specialists, whose own published records were premised on a horizontally immobile Earth crust. Paleontol-



Ancient supercontinent. Alfred Wegener postulated the past existence of a supercontinent in which the continents were merged. The page shown is from a reproduction of Wegener's own copy of the 1915 monograph, containing his handwritten notes, sketches, and marginalia. At the top, Wegener writes “pull over the bridges!”—a reference to earlier suggestions of sunken intercontinental bridges.

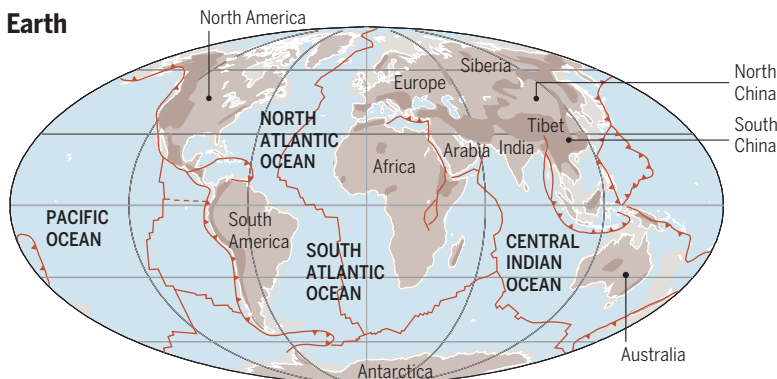
ogists were quick to point to their own expertise, some invoking the existence of sunken intercontinental bridges (5). The strongest attacks came from geophysicists, who could not imagine what forces could move rigid crust. Among the most hostile and bitter opponents were Sir Harold Jeffreys and Rollin T. Chamberlain (6). As a consequence, the theory was

¹Dipartimento di Scienze della Terra, Sapienza, Università di Roma, P.le A. Moro 5, 00185 Roma, Italy. ²Sam Noble Museum, 2401 Chautauqua Avenue, Norman, OK 73072, USA. E-mail: marco.romano@uniroma1.it; rlc@ou.edu

Early Triassic



Modern Earth



Future Earth



- Continental margin
- Modern landmass
- Mountains
- Spreading zones
- ▲ Subduction zones

Merge, break up, merge again. According to modern reconstructions, Pangaea formed about 300 million years ago and began to break apart about 175 million years ago. About 250 million years from now, the continents will come together in a new supercontinent, Pangaea Proxima.

soon shelved and forgotten.

Beginning in the late 1950s, however, studies of paleomagnetism, oceanic ridges, and the relatively young age of oceanic sediments provided indisputable proof for the phenomenon of seafloor spreading. A revised synthetic theory emerged, based on studies in many disciplines. Numerical analysis, for example, upheld Wegener's suggested fit of Atlantic-facing landmasses (7). Reversal patterns of the Earth's magnetic field, recorded in mirror-image sequences on opposing sides of oceanic ridges, convincingly identify those ridges as spreading zones. In the terrestrial realm, the apparent polar wander paths recorded in rock sequences document crustal

movement through geologic time (4, 8). This sweeping combination of evidence from disparate sources, the "plate tectonics revolution," is comparable to the Galilean or Copernican revolution in astronomy (9).

Wegener's early critics had identified critical flaws in his theory—most importantly, the lack of a plausible mechanism (6, 8). Wegener had envisioned continental crust as moving through the underlying oceanic crust, much like an iceberg drifts through water. As possible mechanisms, he suggested centrifugal force related to Earth's rotation, and (perhaps) astronomical forces related to precession of Earth's axis. Skeptics legitimately noted that oceanic crust is rigid and

that Earth's rotation is an inadequate source for the colossal force needed to move plates. The current view is that radiogenic heat causes convection cells to develop in the asthenosphere (a ductile, upper part of the mantle). This convection moves the overlying crust and uppermost mantle, which together behave as a set of rigid plates. Viewed in this way, continents are merely floating passengers in a larger dynamic system (8).

Understanding is sufficiently refined that the future organization of continents can be predicted. In about 250 million years the continents will be reunited in a single mass, a "Pangaea Proxima" (10) analogous to the Pangaea first envisioned by Wegener (see the second figure). The application of plate tectonics theory extends well beyond Earth itself, to include the possibility of active plate tectonics on recently discovered extrasolar super-Earths, potentially habitable planets up to 10 times the mass of Earth (11–13).

The changing fortunes of Wegener's hypothesis provide an incisive and instructive example of paradigm shift. Continental drift was initially criticized and rejected, mainly on geophysical grounds. Paradoxically, advances in that realm later vindicated Wegener and led to the plate tectonics synthesis. Major initiatives such as the Joint Oceanographic Institutes Deep Earth Sampling program and its successors have led to profound advances in understanding the mechanisms that were so baffling to earlier generations of Earth scientists. A century of hindsight brings new focus to Wegener's vision and allows us to appreciate his pioneering arguments. As T. S. Eliot noted in his 1942 poem *Little Gidding*, "We shall not cease from exploration, and the end of all our exploring will be to arrive where we started and know the place for the first time." ■

REFERENCES

1. M. T. Greene, *Alfred Wegener: Science, Exploration, and the Theory of Continental Drift* (Johns Hopkins Univ. Press, Baltimore, 2015).
2. A. Wegener, *Thermodynamik der Atmosphäre* (J. A. Barth, 1911).
3. A. Wegener, *Die Entstehung der Kontinente und Ozeane* (F. Vieweg, Braunschweig, 1915).
4. A. Bosellini, *Tettonica delle Placche e Geologia* (Bovolenta Editore, Ferrara, Italy, 1978).
5. G. G. Simpson, *Am. J. Sci.* **241**, 1 (1943).
6. W. van der Gracht et al., *Theory of Continental Drift* (American Association of Petroleum Geologists, Tulsa, OK, 1928).
7. E. Bullard et al., *Philos. Trans. R. Soc. London* **A258**, 6 (1965).
8. H. R. Frankel, *The Continental Drift Controversy* (Columbia Univ. Press, New York, 2012).
9. R. S. Dietz, J. C. Holden, *Sci. Am.* **223**, 30 (October 1970).
10. C. R. Scotese, *Atlas of Earth History*, vol. 1, *Paleogeography* (PALEOMAP Project, Arlington, TX, 2001). Copies of the Atlas can be downloaded at: www.researchgate.net/publication/264741875_Atlas_of_Earth_History.
11. V. Stamenković et al., *Astrophys. J.* **748**, 1 (2013).
12. P. J. Tackley et al., *Icarus* **225**, 50 (2013).
13. C. Stein et al., *Earth Planet. Sci. Lett.* **361**, 448 (2013).

10.1126/science.aad6230

Perovskite solar cells join the major league

Highly efficient perovskite solar cells show promise for future low-cost electricity generation

By Michele Sessolo and Henk J. Bolink*

Just six years after their discovery, organolead halide perovskite solar cells have taken the lead among emergent photovoltaic (PV) technologies, thanks to the demonstration of power conversion efficiencies (PCEs) of up to 20% (1, 2). The perovskite precursor compounds are abundant and inexpensive and can easily be converted into thin films. Perovskite photovoltaics can therefore, in principle, generate electricity at a very low cost. However, high efficiencies have been limited to very small devices. On page 944 of this issue, Chen *et al.* (3) report perovskite solar cells of 1 cm² with a certified efficiency of 15%.

The highest perovskite solar cell efficiencies, certified by independent accredited institutes, were all obtained on devices with areas below 0.1 cm². To enable comparison with other photovoltaic technologies and appear in the solar cell efficiency tables compiled by public test centers, areas of at least 1 cm² for cells illuminated under one-sun conditions (corresponding to standard illumination with irradiance of 1 kW/m²) are required (4). Several studies have shown progress toward the fabrication of large-area devices and modules (5–9). One very recent report mentions a PCE above 15% for perovskite solar cells with cell area larger than 1 cm², but this value has not been certified (10). Chen *et al.* now describe perovskite solar cells with doped inorganic charge extraction contacts that lead to PCEs above 15% on a 1-cm² cell, certified by an accredited test institute. This value is among the highest certified efficiencies to date among thin-film solar cells (see the table) (4).

Perovskite solar cells are multilayer devices built on a transparent electrode and capped with a reflective metal electrode. The highest certified efficiencies have been obtained on n-i-p type cells, which consist of an n-type TiO₂ bottom layer, a perovskite absorber (the i layer), and a p-type organic semiconductor top layer. Chen *et al.* use an inverted architecture, with a planar p-type NiO thin film as the bottom layer of the device and a bilayer con-

sisting of a fullerene derivative covered with a TiO₂ thin film as the top electron-selective contact. They show that the solar cell's efficiency is limited by the conductivity of the metal oxide layers, which can be increased by doping. Doping was achieved by incorporating Li⁺ and Mg²⁺ into the NiO.

The top, n-type TiO₂ layer was prepared by depositing a precursor from solution with subsequent heating at 70°C to prevent damage to the underlying fullerene and perovskite films. However, at this low processing temperature, mainly amorphous, low-conductivity TiO₂ is formed. Chen *et al.* show that doping this layer with Nb⁵⁺ ions increases its conductivity and hence also the performance of the solar cells. The increase in conductivity

1-cm² cells; for the latter, the accredited certification laboratory of the National Institute of Advanced Industrial Science and Technology in Japan obtained a value of 15.0%. The difference between smaller and larger devices is primarily due to a reduction in the fill factor, which the authors attribute to the high sheet resistance of the fluorine-doped tin oxide used as the transparent conductor. Much more conductive transparent electrodes have been identified, the use of which would lead to a smaller reduction in the fill factor and PCEs when increasing the device area (12).

Besides efficiency, device stability is a critical factor when comparing different PV technologies. Organolead halide perovskites are not stable in ambient conditions, but the stability of the corresponding solar cells can be considerably enhanced when the perovskite absorber is sandwiched between metal oxide films (13). In the device layout used by Chen *et al.*, the perovskite layer is also protected by metal oxide layers on both sides. The hydrophobic fullerene derivative between the perovskite and the top metal oxide further hinders water diffusion to the perovskite layer. For the resulting devices, encapsulated with a glass cover slide using an ultraviolet curable adhesive, the device performance goes down over 1000 hours by only 5% if stored in the dark, and by 10% when continuously illuminated.

The advances demonstrated by Chen *et al.* are substantial, but further improvements are needed before perovskite solar cells become ready for production. For this to be achieved, the fabrication of larger area cells and modules with even lower losses compared to the small cell performances are needed, combined with a further increase in stability. ■

REFERENCES

1. A. Kojima *et al.*, *J. Am. Chem. Soc.* **131**, 6050 (2009).
2. W. S. Yang *et al.*, *Science* **348**, 1234 (2015).
3. W. Chen *et al.*, *Science* **350**, 944 (2015).
4. M. A. Green *et al.*, *Prog. Photovoltaics: Res. Appl.* **23**, 805 (2015).
5. J. Seo *et al.*, *Energy Environ. Sci.* **7**, 2642 (2014).
6. O. Malinkiewicz *et al.*, *Adv. Energy Mater.* **4**, 1400345 (2014).
7. S. Razza *et al.*, *J. Power Sources* **277**, 286 (2015).
8. D. Vak *et al.*, *Adv. Energy Mater.* **5**, 1500328 (2015).
9. J. H. Heo *et al.*, *Energy Environ. Sci.* **8**, 1602 (2015).
10. M. Yang *et al.*, *Adv. Mater.* **27**, 6363 (2015).
11. H. J. Snaith *et al.*, *J. Phys. Chem. Lett.* **5**, 1511 (2014).
12. K. Ellmer, *Nat. Photon.* **6**, 809 (2012).
13. J. You *et al.*, *Nat. Nano* **10**, 1038/nnano.2015.230 (2015).

10.1126/science.aad5891

Efficiency ranking of thin-film solar cells*

THIN-FILM ABSORBER	EFFICIENCY (%)	AREA (cm ²)	CREDITS
GaAs	28.8 ± 0.9	0.9927	Alta devices
CIGS	21.0 ± 0.6	0.9927	Solibro
CdTe	21.0 ± 0.4	1.0623	First solar
Hybrid perovskite†	15.0 ± 0.6	1.017	NIMS
Si (amorphous)	10.2 ± 0.3	1.001	AIST
Dye-sensitized	11.9 ± 0.4	1.005	Sharp
Organic	11.0 ± 0.3	0.993	Toshiba

*Data from (4); †Chen *et al.* (3)

of the metal oxide layers is only about one order of magnitude. Thus, very thin metal oxide layers (10 to 20 nm) must be used to limit resistive losses. The defect-free preparation of such thin doped metal oxides on a 1-cm² area is quite an achievement. Further improvements in the conductivities of the charge extraction layers would allow the use of thicker films, making large-scale production much easier.

Perovskite solar cells, particularly those based on metal oxides, often suffer from a dependence of the current-voltage (I-V) curve on the voltage scan direction (11). The resulting hysteresis in the I-V curve complicates device characterization and makes it difficult to accurately determine device efficiency. The doped p-i-n solar cells described by Chen *et al.* are virtually hysteresis-free at low scan speeds, allowing precise determination of the efficiency. The authors measured PCEs of 18.3% for small-area cells and of 16.2% for the

BATTERIES

Opening the window for aqueous electrolytes

Lithium batteries can operate with a safer “water-in-salt” electrolyte

By Leland Smith and Bruce Dunn

By facilitating ion motion between electrodes, electrolytes help to harness the chemical energy in a battery to produce a current and supply usable electric power. Among liquid electrolytes, there are traditional solutions of salt dissolved in solvents (aqueous or organic) and ionic liquids. Lithium-ion batteries, whether for consumer electronics or electric vehicles, have used nonaqueous liquid electrolytes because of their higher voltage stability. Although aqueous electrolytes would be safer and more environmentally benign, the electrochemical voltage window (1.23 V) precludes the use of high-voltage electrode couples that enable the high energy density of lithium-ion batteries. On page 938 of this issue, Suo *et al.* (1) change this perception by demonstrating an operating window of 3 V created by increasing the salt concentration to form “water-in-salt” electrolytes.

The voltage and charge stored in an electrochemical cell are determined by the chemistry of the electrodes. However, for a given pair of electrodes, it is only possible to build a viable electrochemical cell if there is an electrolyte that can remain stable against the electrode components over the voltage range. For aqueous systems, the thermodynamic voltage limit is 1.23 V, although there are kinetic considerations that may cause the measured voltage for water breakdown to deviate from the theoretical value (2). Indeed, important work in electrocatalysis is devoted to decreasing those kinetic limitations (3). Nonetheless, as the cell voltage increases beyond 1.23 V, water electrolysis will begin to dominate the cell chemistry.

The electrolysis of water produces gaseous products (H_2 and O_2) that depart the electrode-electrolyte interface, freeing up the electrode surface so that more electroly-

sis can occur. For other electrolyte-electrode combinations, electrolyte breakdown can result in the formation of insoluble solid materials at the electrode surface (4). These decomposition products can widen the effective voltage stability range of the electrolyte above the thermodynamic value.

The electrolyte solvent, salt, and electrode may all contribute to the formation of solid materials at the electrode-electrolyte interface. Such interfacial layers play a central role in many of today's commercially important batteries. For example, a

ceeding what is typically obtained from aqueous electrolytes. The high stability is attributed to the electrochemical reduction of bis(trifluoromethane sulfonyl)imide at the anode surface, which forms an SEI layer consisting primarily of LiF, and is accompanied by a shift in the oxygen evolution reaction to higher voltages (1).

The most obvious benefit of the water-in-salt electrolyte is an increased variety of available lithium electrode materials as compared to traditional water-based electrolytes, as seen in the figure. Although organic

electrolytes provide a wider voltage window, Suo *et al.* suggest that with a window of 3 V, energy densities of 100 Wh/kg are attainable. The development of batteries offering such high energy density plus the safety advantages of an aqueous electrolyte is certain to have an impact, especially in the area of consumer electronics. Moreover, the use of a water-tolerant electrolyte is likely to improve recycling and reclamation efforts as well as offer the opportunity to fabricate lithium-ion batteries without the need for expensive dry rooms. There is also the likelihood that such water-in-salt electrolytes can be applied to salts that are less expensive than

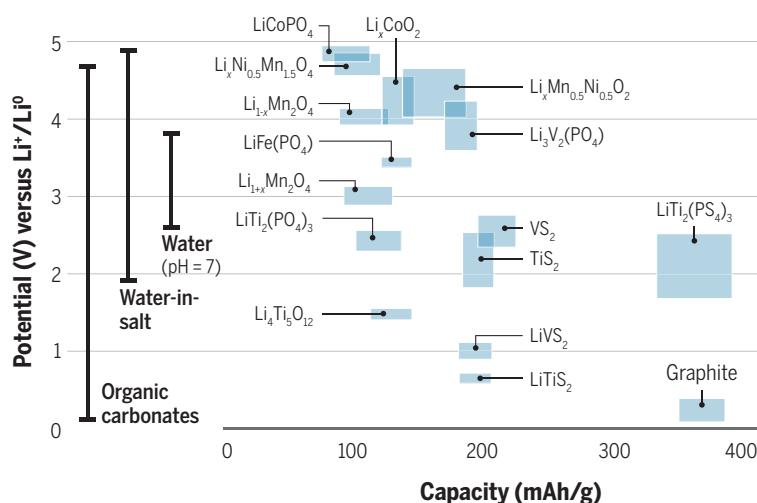
lithium bis(trifluoromethane sulfonyl)imide, as well as to other battery chemistries. The latter may be especially important for the rapidly emerging field of sodium-ion batteries, which potentially offer a lower cost per watt-hour than lithium-ion batteries (6). ■

REFERENCES AND NOTES

1. L. Suo *et al.*, *Science* **350**, 938 (2015).
2. K. Zeng, D. Zhang, *Prog. Energ. Combust.* **36**, 307 (2010).
3. J. Suntivich *et al.*, *Science* **334**, 1383 (2011).
4. P. Verma *et al.*, *Electrochim. Acta* **55**, 6332 (2010).
5. P. Ruetschi, *J. Electrochem. Soc.* **120**, 331 (1973).
6. M. D. Slater *et al.*, *Adv. Funct. Mater.* **23**, 947 (2013).
7. J. B. Goodenough, Y. Kim, *Chem. Mater.* **22**, 587 (2010).

ACKNOWLEDGMENTS

Supported as part of the Nanostructures for Electrical Energy Storage (NEES), an Energy Frontier Research Center funded by the U.S. Department of Energy, Office of Science.



A new type of solid-electrolyte interphase (SEI) layer. The voltage stability limits of organic, water-in-salt, and aqueous (pH = 7) electrolytes are compared to the chemical potential of various lithium intercalation materials. The discovery of SEI formation in water-based electrolytes is an exciting development for aqueous lithium and beyond-lithium battery chemistries.

$PbSO_4$ film at the electrode surface allows lead-acid batteries to operate at ~2.0 V, well beyond the thermodynamic limit of water electrolysis (5). In lithium-ion batteries, the decomposition of organic liquid electrolytes at the anode results in the formation of an interfacial layer containing species such as Li_2CO_3 and LiF, in addition to organic materials (3). This solid-electrolyte interphase (SEI) allows organic electrolytes in lithium-ion batteries to operate at potentials below their thermodynamic stability limit of ~0.8 V versus Li/Li^+ (3).

The work of Suo *et al.* presents an exciting new development in the area of solid interfacial layers. Highly concentrated (>20 mol/kg) aqueous mixtures of lithium bis(trifluoromethane sulfonyl)imide yielded a voltage stability window of 3.0 V, far ex-

LETTERS

Edited by Jennifer Sills

Wildfires: Weigh policy effectiveness

IN THEIR POLICY Forum “Reform forest fire management” (18 September, p. 1280), M. P. North *et al.* commendably advocate a more rational strategy for managing fire in U.S. forests. However, their prediction that the extent and severity of wildfires can be substantially reduced by introducing managed fires is not well supported by the evidence.

Wildfires are rare events in many forested regions of the world, with annual area burned typically being less than 5% (1–3). An area treated to reduce fuels is unlikely to encounter wildfire before fuels recover to hazardous levels (3, 4). On average, each hectare reduction in wildfire area requires many hectares of treatment (2–4), which can be expressed as the ratio of the reduction in wildfire area to the area of treatment. Wide variations in this ratio exist, ranging from zero [e.g., Californian forests and chaparral and Australian grasslands, where treatment has led to no reduction in wildfire extent (3, 5)] to one [e.g., Australian savannas, where the reduction in wildfire area is equal to the area of treatment (3)]. In many cases (such as Australian forests), this ratio is less than 0.3 (2, 6), implying that high rates of treatment (i.e., more than 10% of the landscape per year) are required to produce major reductions in wildfire area. The rates of treatment required to be effective are often unaffordable across large areas (7).

Studies in Australia and the United States show that weather is a stronger determinant of fire severity than is fuel (8, 9). Fuel treatment, whether by managed fires or other means, may be most cost-effective when strategically targeted in close proximity to assets at risk (such as homes or vulnerable habitat locations), where any reduction in wildfire severity will have a greater likelihood of immediate protective effects compared with more broadly dispersed treatments (1, 10).

**Matthias M. Boer,^{1*} Owen F. Price,²
Ross A. Bradstock²**

¹Hawkesbury Institute for the Environment, Western Sydney University, Richmond, NSW 2753, Australia.

²Centre for Environmental Risk Management of Bushfire, University of Wollongong, Wollongong, NSW 2522, Australia.

*Corresponding author.

E-mail: m.boer@westernsydney.edu.au



REFERENCES

1. M.A. Moritz *et al.*, *Nature* **515**, 58 (2014).
2. M.M. Boer, R.J. Sadler, R. Wittkuhn, L. McCaw, P.F. Grierson, *For. Ecol. Manag.* **259**, 132 (2009).
3. O.F. Price *et al.*, *Int. J. Wildland Fire* **24**, 297 (2015).
4. P.A. M. Fernandes, *Curr. For. Rep.* **1**, 118 (2015).
5. O.F. Price, R. Bradstock, J.E. Keeley, A.D. Syphard, *J. Environ. Manag.* **113**, 301 (2012).
6. O.F. Price, T.D. Penman, R.A. Bradstock, M. Boer, H. Clarke, *J. Biogeogr.* **42**, 2234 (2015).
7. R.A. Bradstock *et al.*, *J. Environ. Manag.* **105**, 66 (2012).
8. R.A. Bradstock, K.A. Hammill, L. Collins, O. Price, *Landsc. Ecol.* **25**, 607 (2010).
9. J.M. Lydersen, M.P. North, B.M. Collins, *For. Ecol. Manag.* **328**, 326 (2014).
10. D.E. Calkin, J.D. Cohen, M.A. Finney, M.P. Thompson, *Proc. Natl. Acad. Sci. U.S.A.* **111**, 746 (2014).

Wildfires: Systemic changes required

IN THEIR POLICY Forum “Reform forest fire management” (18 September, p. 1280), M. P. North *et al.* highlight public support and improved spatial planning as key leverage points to deemphasize fire exclusion and expand beneficial fire. Although these steps are necessary, we caution that they are insufficient to overcome barriers to change.

There needs to be a deeper, systems-level understanding of the fire management system. The behavior of fire managers is a direct and logical result of the structure of the system in which they operate, influenced by factors such as incentives, culture, and capacity. If managers are judged by fire exclusion, that will become the dominant paradigm. Managers within this system may operate at cross-purposes, as shown by the widely divergent fire management policies and objectives across jurisdictional boundaries (1, 2). The joint influences of complexity, conflict, and uncertainty lead to a risk-averse decision structure constrained by perceptions and pressures, and susceptible to suboptimal decision biases and solutions to problems. The emphasis on aggressive suppression over less tangible ecological

benefits and hazard mitigation disconnects fire management objectives from underlying resource management objectives.

Infusing risk management principles into fire management decisions would directly address these systemic issues. We propose that efforts targeting transformation focus on four areas: (i) Engage in multiparty risk communication and prioritization of investments based on who can most efficiently mitigate risks. (ii) Track how, why, and with what information decisions are made, and ensure that decision processes are relevant and responsive to organizational and stakeholder needs. (iii) Invest in research to improve knowledge of fire management effectiveness, and consistently integrate new information. (iv) Cultivate a workforce well versed in risk management and the means to integrate this knowledge into decision-making.

Transforming fire management is not an inevitable consequence of enhanced support or planning alone; it requires meaningful organizational change in how and why fire response is determined. Adopting systems and risk analysis principles to better understand and improve fire management decisions is a critical step toward effecting comprehensive change.

Matthew Thompson,^{1*}

Christopher Dunn,² Dave Calkin¹

¹Rocky Mountain Research Station, Missoula, MT 59807, USA. ²Oregon State University, Corvallis, OR 97331, USA.

*Corresponding author.

E-mail: mpthompson02@fs.fed.us

REFERENCES

1. D. Calkin, M.P. Thompson, A.A. Ager, M. Finney, *For. Pol. Econ.* **13**, 378 (2011).
2. National Cohesive Wildland Fire Management Strategy (www.forestsandrangelands.gov/strategy/index.shtml).

Response

WE AGREE WITH Boer *et al.* that vigorous fire suppression is needed near valued assets

such as homes, but fire management is also urgently needed in more remote areas to ecologically restore western U.S. forests and increase their resilience to future fire and climate change. Owing to past and present suppression efforts, many forests remain in an ecologically degraded state until they burn (1), often more severely than they would have in the absence of degradation, leaving large areas void of trees for several decades. These contemporary fire patterns need to be mitigated, and treatments that include fire are most effective (2). Weather is a strong influence on wildfire severity, but much of the current pattern is due to heavy fuel loads and aggressive suppression, which ensures that most fires only occur during extreme weather conditions when they escape early containment (3). Restoring the environment would realign fire severity and change patterns to which forests have adapted (4, 5).

Under current conditions, wildfires rarely burn fuel-reduced forests, yet in many areas, these low probabilities result from aggressive suppression efforts. The point of using more managed fire is to increase the area of fuels reduction and substantially change the current ratio of treated to wildfire

burned area. Furthermore, climate change and fire projection models indicate that fire frequency and extent will be increasing (6). Finally, cost estimates for proactive managed fire use, even if currently only 10% of treated areas are intersected by wildfire, are much lower than suppression and structure loss costs (7, 8).

Managed fire is a vital tool for ecological restoration and for strengthening the resilience of dry forests and the biodiversity they support, particularly under warming climate conditions. The widespread use of managed fire has substantial ecological benefits for restoring dry forests, which go beyond the social concerns that wildfires raise for the wildland-urban interface.

Thompson *et al.* raise additional issues we could not cover in our Policy Forum. We support their suggestions for within-agency reforms as essential for coping with risks inherent in forest fire management.

**Malcolm North,^{1,2} Scott Stephens,²
Brandon Collins,^{1,3} James Agee,⁴
Greg Aplet,⁵ Jerry Franklin,⁴ Pete Fulé⁶**

¹USFS Pacific Southwest Research Station, Davis, CA 95618, USA. ²University of California, Davis, CA 95616, USA. ³University of California, Berkeley, CA

94720, USA. ⁴University of Washington, Seattle, WA 98195, USA. ⁵The Wilderness Society, Denver, CO 80202, USA. ⁶Northern Arizona University, Flagstaff, AZ 86011, USA.

*Corresponding author. E-mail: mpnorth@ucdavis.edu

REFERENCES

1. W.J. Bond, J.E. Keeley, *Trends Ecol. Evol.* **20**, 387 (2005).
2. S.L. Stephens *et al.*, *Ecol. Appl.* **19**, 305 (2009).
3. J.D. Miller *et al.*, *Ecosystems* **12**, 16 (2009).
4. S.A. Parks *et al.*, *Ecosystems* **17**, 29 (2014).
5. B. Collins *et al.*, *Ecosystems* **12**, 114 (2009).
6. H.K. Preisler *et al.*, *Int. J. Wildland. Fire* **20**, 508 (2011).
7. G. Snider, P.J. Daugherty, D. Wood, *J. For.* **104**, 431 (2006).
8. M. North, B. Collins, S. Stephens, *J. For.* **110**, 392 (2012).

ERRATA

Erratum for the Report “Recruitment of RNA polymerase II by the pioneer transcription factor PHA-4” by H.-T. Hsu *et al.*, *Science* **350, aad5928 (2015).** Published online 16 October 2015; 10.1126/science.aad5928

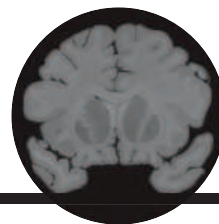
Erratum for the Report “Spreading depression triggers headache by activating neuronal Panx1 channels” by H. Karatas *et al.*, *Science* **350, aad5166 (2015).** Published online 2 October 2015; 10.1126/science.aad5166

Erratum for the Report “A neoplastic gene fusion mimics trans-splicing of RNAs in normal human cells” by H. Li *et al.*, *Science* **350, aad3463 (2015).** Published online 2 October 2015; 10.1126/science.aad3463

RESEARCH

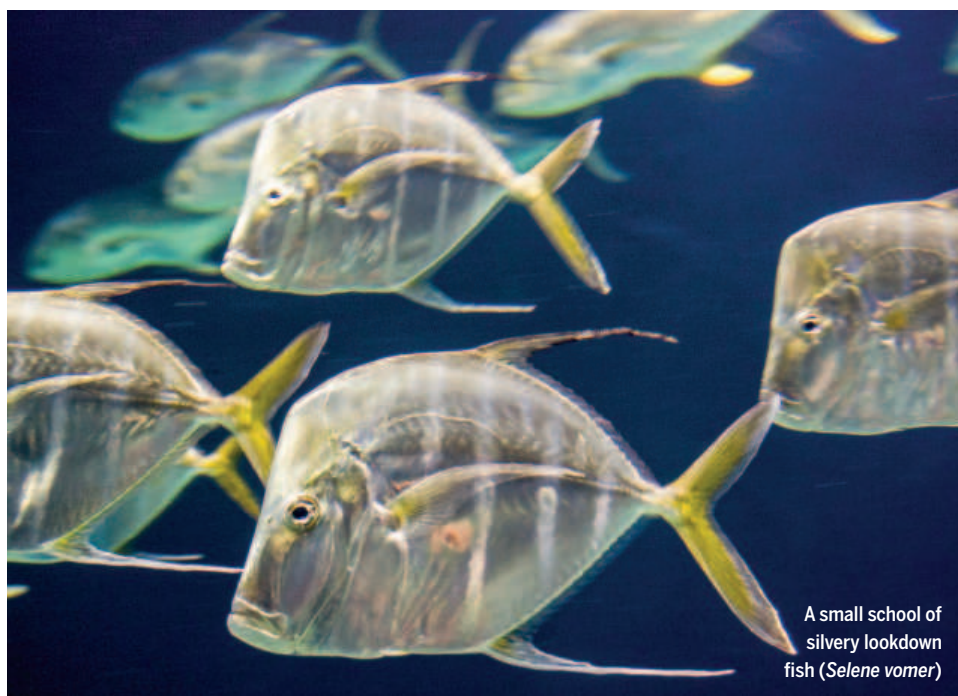
Shedding light on neurodevelopmental disorders

Sahin and Sur, p. 926



IN SCIENCE JOURNALS

Edited by Stella Hurtley



A small school of silvery lookdown fish (*Selene vomer*)

CAMOUFLAGE

Disappearing act

Unlike coastal regions and reefs, the open ocean is mostly empty. Many fish species, nonetheless, spend most of their lives there. Such emptiness makes camouflage exceedingly difficult, so how does an organism hide in water filled with bouncing and reflected light? Brady *et al.* show that some families of fish have evolved skin that reflects and polarizes light, allowing them to blend into their mirrorlike conditions more easily. These results help to explain the silvery coloration found in sea-living fish across the world's oceans. — SNV

Science, this issue p. 965

CANCER

Blocking transcription in tumors, STAT

STAT3 is a transcription factor known to contribute to many cancers, but it is very difficult to target with conventional drugs. Taking an alternative approach, Hong *et al.* used antisense molecules that bind to messenger RNA to prevent STAT3 protein from being made. The potent antisense molecules penetrated cells without being dissolved in lipid. One new antisense drug, AZD9150, successfully inhibited cancer in a variety of preclinical models, as well as in cancer patients for whom one or more previous treatments had failed. These findings pave the way for additional clinical testing. — YN

Sci. Transl. Med. 7, 314ra185 (2015).

PARASITOLOGY

Parasitic worms influence human fecundity

Parasitic worms infect 2 billion people globally. Mostly, such infections are symptomless and individual worm burdens are low. Blackwell *et al.* monitored the fecundity of Tsimane women in Bolivia. These women have on



Bolivian women surrounded by their children

average of 10 children in their lifetimes. However, if they had successive hookworm infections, lifetime births dropped to 7. Surprisingly, if the women were chronically infested with roundworm, they had as many as 12 children. These effects may relate to the balance of immune responses that the different worms induce, rather than to the physiological costs of parasitism. — CA

Science, this issue p. 970

SOLAR CELLS

Perovskites go large

Solar cells made of planar organic-inorganic perovskites now have reported efficiencies exceeding 20%. However, these values have been determined from small illuminated areas.

Chen *et al.* used highly doped inorganic charge extraction layers to make solar cells on the 1 cm² scale (see the Perspective by Sessolo and Bolink). The layers helped to protect the active layer from degradation by air. The cells achieved government-lab-certified efficiencies of >15%. Furthermore, 90% of the efficiency was maintained after 1000 hours of operation. — PDS

Science, this issue p. 944;
see also p. 917

SUPERCONDUCTIVITY

Discerning charge patterns in a cuprate

Copper oxides are well known to be able to achieve the order required for superconductivity. They can also achieve another order—one that produces

patterns in their charge density. Experiments using nuclear magnetic resonance and resonant x-ray scattering have both detected this so-called charge density wave (CDW) in yttrium-based cuprates. However, the nature of the CDW appeared to be different in the two types of measurement. Gerber *et al.* used pulsed magnetic fields of up to 28 T, combined with scattering, to bridge the gap (see the Perspective by Julien). As the magnetic field increased, a two-dimensional CDW gave way to a three-dimensional one. — JSt

Science, this issue p. 949;
see also p. 914

BIOLOGICAL MATERIALS

A set of strong eyes

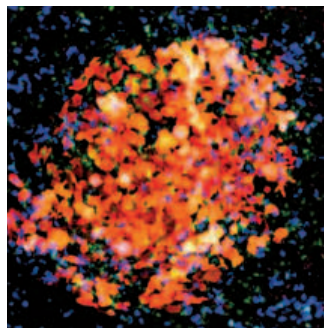
Although many biological tissues serve more than one purpose, rarely are they optimized to do multiple tasks well. When you try to optimize for one functionality, it comes at the expense of another. Li *et al.* investigated the biomineralized armor of the small mollusc chiton *Acanthopleura granulata*. The armor appears to be optimized for both mechanical strength and for image capture by hundreds of integral aragonite-based lenses. — MSL

Science, this issue p. 952

CANCER IMMUNOLOGY

Monocytes block tumor access to the lung

Metastatic cancer is especially hard to treat. In order to find potential new therapeutic targets, scientists are trying to understand the cellular events



Tumor cells (red) in mouse lungs recruit patrolling monocytes (green)

that promote or prevent metastasis. Hanna *et al.* now report a role for patrolling monocytes in blocking tumor metastasis to the lungs in mice. Tumors in mice engineered to lack patrolling monocytes showed increased metastasis to the lung but not to other tissues. Patrolling monocytes resided in the microvasculature of the lung, where they engulfed tumor material, which may explain how these cells prevent tumors from colonizing the lung. — KLM

Science, this issue p. 985

SLEEP RESEARCH

Neurons that regulate sleep stages

Just what sleep is for remains a bit of a mystery. During sleep, we switch several times between so-called rapid eye movement (REM) and non-REM sleep. Hayashi *et al.* used sophisticated developmental cell fate mapping to look at the neurons involved in the two types of sleep in mice (see the Perspective by Vyazovinskiy). They identified a genetically marked population of neurons that promote non-REM sleep at the expense of REM sleep. — PRS

Science, this issue p. 957;
see also p. 909

PLANT BIOTECHNOLOGY

Would an electrical rose still smell as sweet?

Can electricity and plants be mixed? Stavrinidou *et al.* built key electronic components using conducting polymers inside roses. They based their approach on the similarity between roots, stems, leaves, and vascular circuitry in plants; and contacts, interconnections, devices, and wires in electronic circuits. This technology may lead to new ways of monitoring and regulating plant physiology, of harvesting energy from photosynthesis, and of achieving genetic modification for plant optimization. Thus, the term “power plant” may soon have a new meaning! — ZHK

Sci. Adv. 10.1126/sciadv.01136 (2015).

IN OTHER JOURNALS

Edited by **Sacha Vignieri**
and **Jesse Smith**

ANIMAL BEHAVIOR

Just called to say “I love you”

Grooming among social species is thought to build and maintain social bonds. Vocal communication can similarly bond groups and has been thought to increase the number of individuals that can bond, because it is easier to call than to cleanse. Kulahci *et al.* looked at patterns of grooming and contact calling in ring-tailed lemurs and found just the opposite, however. Specifically, the animals that responded to each other's specific contact calls were those with the tightest bond, as measured by the amount of time spent grooming. Thus, their calls and responses seem to act as “grooming at a distance,” by reinforcing the tighter bonds between just a few animals, rather than expanding the number of animals that are able to bond. — SNV

Anim. Behav. 10.1016/j.anbehav.2015.09.016 (2015).



Ring-tailed lemurs call to their closest companions to reinforce their bond

PHOTOS: (FROM LEFT) RICHARD N. HANNA, LA JOLLA INSTITUTE FOR ALLERGY AND IMMUNOLOGY; © GERRY ELLIS/MINDEN PICTURES/CORBIS

ALSO IN SCIENCE JOURNALS

Edited by Stella Hurtley

NEURODEVELOPMENT

Help for neurodevelopmental disorders

When the brain does not develop normally, the disabilities that ensue can affect a person for life. Sahin and Sur review how emerging knowledge of the molecular biology behind a suite of neurodevelopmental disorders is shedding light on the group as a whole. The new knowledge offers tantalizing leads toward more effective therapies. — PJH

Science, this issue p. 926

STEM CELL REGULATION

Notch role in multipotency or cell fate

Multipotent *Drosophila* intestinal stem cells (ISCs) generate either nutrient-absorbing enterocytes (ECs) or secretory enteroendocrine cells (EECs). Guo and Ohlstein investigated the role of Notch signaling in this process. They tracked ISC asymmetric divisions and found that EEC daughter cells, which have a low level of Notch, signal back to the ISC in order to keep it multipotent. However, during EC production, ISCs activate strong Notch signaling in daughters. Thus, Notch signaling functions in two directions to achieve stem cell multipotency. — BAP

Science, this issue p. 927

NONHUMAN GENETICS

Recombination: The birds and the yeast

Apes and mice have a specific gene, *PRDM9*, that is associated with genomic regions with

high rates of recombination, called hotspots. In species with *PRDM9*, hotspots move rapidly within the genome, varying among populations and closely related species (see the Perspective by Lichten). To investigate recombination hotspots in species lacking *PRDM9*, Singhal *et al.* examined bird genomes, which lack a *PRDM9* gene. They looked closely at the genomes of finch species and found that recombination was localized to the promoter regions of genes and highly conserved over millions of years. Similarly, Lam and Keeney examined recombination localization within yeast, which also lacks *PRDM9*. They found a similar more-or-less fixed pattern of hotspots. Thus, recombination in species lacking a *PRDM9* gene shows similar patterns of hotspot localization and evolution. — LMZ

Science, this issue p. 913, p. 928; see also p. 932

BATTERIES

A concentrated effort for battery safety

Aqueous electrolytes are limited to run below 1.23 V to avoid degradation. Suo *et al.* smash through this limit with an aqueous salt solution containing lithium (Li) bis(trifluoromethane sulfonyl)imide to create an electrolyte that has an electrochemical window of 3 V (see the Perspective by Smith and Dunn). They used extremely high-concentration solutions, which suppressed hydrogen evolution and electrode oxidation. At these concentrations, the Li solvation shell changes because there simply is not enough water to neutralize the Li⁺ charge. Thus,

flammable organic electrolytes could potentially be replaced with a safer aqueous alternative. — MSL

Science, this issue p. 938; see also p. 918

AXON GUIDANCE

No going back

The mammalian spinal cord coordinates neuronal systems across the body. Axons that cross the spinal cord midline during development first need permission to cross and then instruction not to keep crossing back and forth. Jaworski *et al.* studied the axonal guidance receptor ROBO3 and found a ligand NELL2 in mice that appears to help in this process. — PJH

Science, this issue p. 961

GENE REGULATION

Noncoding RNA helps protein binding

Besides reading the coding regions of genes, RNA polymerase generates RNA at promoter-proximal and -distal DNA elements, but the function of these molecules is largely unknown. Sigova *et al.* show that these RNAs facilitate interactions between gene regulators and the regulatory elements they occupy. Nascent RNA associates with the transcription factor YY1 and increases its ability to bind DNA. Thus, transcription at active regulatory elements may provide a positive feedback loop that reinforces regulatory elements contributing to the stability of gene expression programs. — BAP

Science, this issue p. 978

IMMUNOLOGY

Establishing a longtime residency

Innate lymphoid cells (ILCs) are a subset of immune cells that promote barrier immunity in tissues such as the gut and lungs and help to maintain immune homeostasis. Gasteiger *et al.* investigated how the body maintains its pools of ILCs in such peripheral tissues, as well as in immune tissues such as the lymph nodes and the spleen. In mice surgically joined to share their bloodstreams, unlike lymphocytes, most ILCs did not circulate through the blood. Instead, ILCs resided long term in tissues, even in the face of inflammation or infection. — KLM

Science, this issue p. 981

CANCER IMMUNOLOGY

How dying tumor cells get noticed

Besides killing tumor cells directly, some chemotherapies, such as anthracyclines, also activate the immune system to kill tumors. Vacchelli *et al.* discovered that in mice, anthracycline-induced antitumor immunity requires immune cells to express the protein formyl peptide receptor 1 (FPR1). Dendritic cells (DCs) near tumors expressed especially high amounts of FPR1. DCs normally capture fragments of dying tumor cells and use them to activate nearby T cells to kill tumors, but DCs lacking FPR1 failed to do this effectively. Individuals with breast or colon cancer expressing a variant of FPR1 and treated with anthracyclines showed poor metastasis-free and overall survival. Thus, FPR1 may affect anti-tumor immunity in people, too. — KLM

Science, this issue p. 972

GEOLOGY

Pioneer of plate tectonics

Why do the contours of Earth's continents fit together like a puzzle? 100 years ago, Alfred Wegener argued in his famous monograph on "continental drift" that all continents were once part of one supercontinent. In a Perspective, Romano and Cifelli chart the history of this theory, which is now called plate tectonics. At first derided by most scientists, plate tectonics became widely accepted in the 1960s as supporting evidence accumulated. Today, the theory is universally accepted. Scientists are even looking for signs of plate tectonics on other planets beyond the solar system. — JFU

Science, this issue p. 915

CANCER

Targeting drug-resistant prostate tumors

The activity of the mTOR pathway is often increased in various cancers. Hsieh *et al.* found that the levels of 4EBP1, an mTOR target that inhibits protein synthesis, determined whether different cell types in prostate tumors were resistant to an mTOR inhibitor. Compared to basal cells, luminal prostate epithelial cells expressed more 4EBP1, synthesized protein at lower rates, and were less sensitive to the mTOR inhibitor. Decreasing 4EBP1 levels suppressed resistance to the mTOR inhibitor, so co-targeting 4EBP1 may improve therapeutic outcomes for prostate cancer patients. — LKF

Sci. Signal. **8**, ra116 (2015).

patterns in their charge density. Experiments using nuclear magnetic resonance and resonant x-ray scattering have both detected this so-called charge density wave (CDW) in yttrium-based cuprates. However, the nature of the CDW appeared to be different in the two types of measurement. Gerber *et al.* used pulsed magnetic fields of up to 28 T, combined with scattering, to bridge the gap (see the Perspective by Julien). As the magnetic field increased, a two-dimensional CDW gave way to a three-dimensional one. — JSt

Science, this issue p. 949;
see also p. 914

BIOLOGICAL MATERIALS

A set of strong eyes

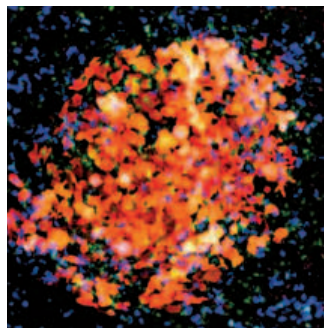
Although many biological tissues serve more than one purpose, rarely are they optimized to do multiple tasks well. When you try to optimize for one functionality, it comes at the expense of another. Li *et al.* investigated the biomineralized armor of the small mollusc chiton *Acanthopleura granulata*. The armor appears to be optimized for both mechanical strength and for image capture by hundreds of integral aragonite-based lenses. — MSL

Science, this issue p. 952

CANCER IMMUNOLOGY

Monocytes block tumor access to the lung

Metastatic cancer is especially hard to treat. In order to find potential new therapeutic targets, scientists are trying to understand the cellular events



Tumor cells (red) in mouse lungs recruit patrolling monocytes (green)

that promote or prevent metastasis. Hanna *et al.* now report a role for patrolling monocytes in blocking tumor metastasis to the lungs in mice. Tumors in mice engineered to lack patrolling monocytes showed increased metastasis to the lung but not to other tissues. Patrolling monocytes resided in the microvasculature of the lung, where they engulfed tumor material, which may explain how these cells prevent tumors from colonizing the lung. — KLM

Science, this issue p. 985

SLEEP RESEARCH

Neurons that regulate sleep stages

Just what sleep is for remains a bit of a mystery. During sleep, we switch several times between so-called rapid eye movement (REM) and non-REM sleep. Hayashi *et al.* used sophisticated developmental cell fate mapping to look at the neurons involved in the two types of sleep in mice (see the Perspective by Vyazovinskiy). They identified a genetically marked population of neurons that promote non-REM sleep at the expense of REM sleep. — PRS

Science, this issue p. 957;
see also p. 909

PLANT BIOTECHNOLOGY

Would an electrical rose still smell as sweet?

Can electricity and plants be mixed? Stavrinidou *et al.* built key electronic components using conducting polymers inside roses. They based their approach on the similarity between roots, stems, leaves, and vascular circuitry in plants; and contacts, interconnections, devices, and wires in electronic circuits. This technology may lead to new ways of monitoring and regulating plant physiology, of harvesting energy from photosynthesis, and of achieving genetic modification for plant optimization. Thus, the term “power plant” may soon have a new meaning! — ZHK

Sci. Adv. 10.1126/sciadv.01136 (2015).

IN OTHER JOURNALS

Edited by **Sacha Vignieri**
and **Jesse Smith**

ANIMAL BEHAVIOR

Just called to say “I love you”

Grooming among social species is thought to build and maintain social bonds. Vocal communication can similarly bond groups and has been thought to increase the number of individuals that can bond, because it is easier to call than to cleanse. Kulahci *et al.* looked at patterns of grooming and contact calling in ring-tailed lemurs and found just the opposite, however. Specifically, the animals that responded to each other's specific contact calls were those with the tightest bond, as measured by the amount of time spent grooming. Thus, their calls and responses seem to act as “grooming at a distance,” by reinforcing the tighter bonds between just a few animals, rather than expanding the number of animals that are able to bond. — SNV

Anim. Behav. 10.1016/j.anbehav.2015.09.016 (2015).



Ring-tailed lemurs call to their closest companions to reinforce their bond

PHOTOS: (FROM LEFT) RICHARD N. HANNA, LA JOLLA INSTITUTE FOR ALLERGY AND IMMUNOLOGY; © GERRY ELLIS/MINDEN PICTURES/CORBIS

ENVIRONMENT

Pesticides in wild plants

Are honey bees harmed by agricultural neonicotinoid pesticide use? Field studies attempting to address this question have often found neonicotinoid contamination in control colonies. Botias *et al.* now show, from a field study conducted in Sussex, UK, that neonicotinoid concentrations in the pollen and nectar of wildflowers growing at the margins of treated oilseed rape fields were higher overall than in pollen from the treated plants. Most neonicotinoids brought back to hives came from these contaminated wildflowers. Such wild plant contamination may be one reason for the contaminated controls in previous studies. Other invertebrates will also be affected by chronic exposure to neonicotinoids from wild plants and soils near treated fields. — JFU

Environ. Sci. Technol. 10.1021/acs.est.5b03459 (2015).

PSYCHOLOGY

Mixed reviews boost competence perception

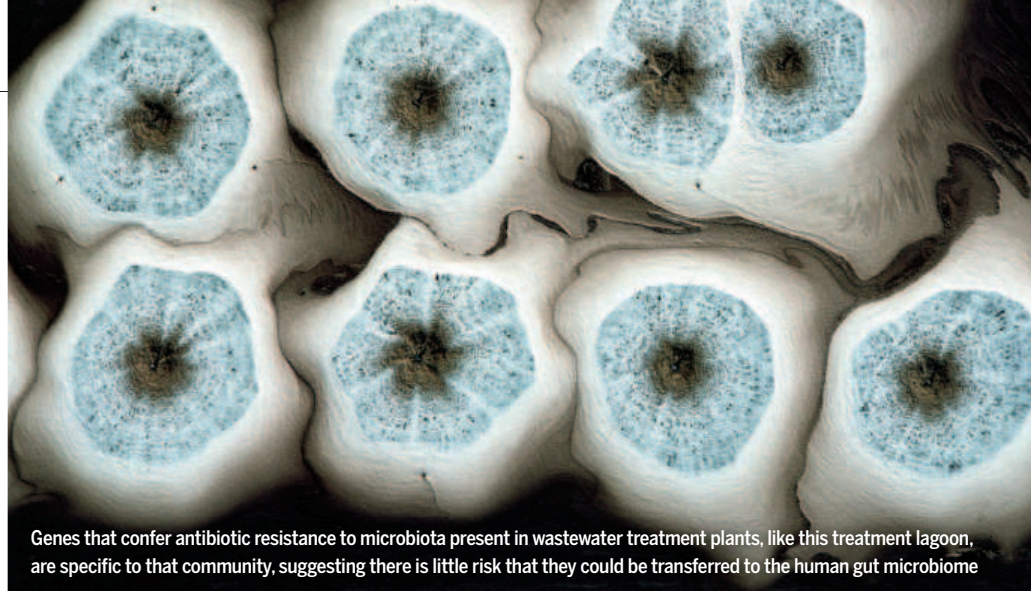
Writers of letters of reference often refrain from mentioning an applicant's negative traits, but this can backfire because describing a person only with positive adjectives relating to his competence can induce the prospective employer to draw negative inferences about his warmth: the so-called innuendo effect. Kervyn *et al.* extend this research to show that adding a mixed evaluation of a candidate's warmth or good nature boosts the perception of her competence in comparison to a uniformly positive characterization of her warmth: the compensation effect. — GJC

J. Exp. Soc. Psychol. **62**, 17 (2016).

SPINTRONICS

Make way for liquid spintronics

In addition to charge, electrons have another degree of freedom: spin, a type of



Genes that confer antibiotic resistance to microbiota present in wastewater treatment plants, like this treatment lagoon, are specific to that community, suggesting there is little risk that they could be transferred to the human gut microbiome

ANTIBIOTIC RESISTANCE

Unique wastewater antibiotic resistome

Antibiotic resistance is currently high on the list of alarms. Wastewater treatment plants essentially use microbiological bioremediation to clean up water. As such, they are an obvious potential source of mobile antibiotic resistance genes from human pathogens. Munck *et al.* have been investigating the risks wastewater plants pose for antibiotic resistance. They identified resistance genes in samples from 7 different years by screening with 15 antibiotics. Deep metagenomic sequencing revealed a stably maintained core set of novel genes that conferred resistance to all the antibiotics tested. This "resistome" was specific to this microbiological community, indicating that there is in fact little scope for transfer into the human gut microbiota. Although this is a reason to be cheerful, it is sobering to note that the unique wastewater genescape persists because of high levels of ambient antibiotics. — CA

Nat. Commun. 10.1038/ncomms9452 (2015)

quantum-mechanical angular momentum. In the same way that conventional electronics requires a power source, spin-based electronics ("spintronics") needs a source of spin current. To achieve this, researchers typically use magnets. Takahashi *et al.* now show that all you need is a flowing liquid metal in which mechanical motion is coupled with spin. For this demonstration, they used mercury flowing through a cylindrical quartz pipe. The vorticity of the liquid flow acted as a source of spin current, which was detected as electrical voltage. The discovery may enable fluid spintronic devices. — JS

Nat. Phys. 10.1038/nphys3526 (2015).

HEART DEVELOPMENT

Coronary artery smooth muscle origin

Cardiovascular diseases, such as atherosclerosis, heart failure,

and heart valve problems, are a major cause of death worldwide. Defining mechanisms of normal heart development may reveal ways to manipulate cells and guide treatment. Volz *et al.* now identify pericytes as the progenitors to the smooth muscle of coronary arteries, the vessels supplying blood to ventricular heart muscle. Coronary artery smooth muscle cells (caSMCs) are found deep in the myocardium; however, they originate from the mesothelial covering of the heart, or epicardium. Clonal analysis and lineage tracing studies reveal that in embryos, Notch-responsive pericytes lining the coronary vascular plexus and located near arteries develop into caSMCs. Such progenitor cells are also present in the adult heart, suggesting possible relevance to heart regeneration therapies. — BAP

eLife 10.7554/eLife.10036 (2015).

SOLAR PHYSICS

Searching for the Sun's magnetic poles

Earth's magnetic axis and rotational axis don't line up, leading to magnetic north and south poles located some distance from the "true" rotational poles. In contrast, successful models of the Sun's magnetic field have assumed that the two axes are aligned, although it is difficult to see the Sun's poles from Earth. Yabar *et al.* analyzed 5 years of data from NASA's Solar Dynamics Observatory, and after removing interfering active regions (around sunspots), they discovered a periodic magnetic signal that matches the Sun's rotation. They interpret this as a magnetic axis offset from the rotation axis, as seen in some other stars, and suggest that it may explain some aspects of Earth's space weather. — KTS

Mon. Not. R. Astron. Soc. **453**, L69 (2015).

REVIEW SUMMARY

NEURODEVELOPMENT

Genes, circuits, and precision therapies for autism and related neurodevelopmental disorders

Mustafa Sahin* and Mriganka Sur*

BACKGROUND: Neurodevelopmental disorders are caused by abnormalities in the developing brain. Such abnormalities can occur as a result of germline or somatic mutations or because of epigenetic or environmental factors. These disorders affect a large number of children in the developed world, as well as the developing world. The societal cost of neurodevelopmental disorders is immense, making the pursuit of treatments for individuals with neurodevelopmental disorders a top unmet medical need.

ADVANCES: Research in the genetics of neurodevelopmental disorders such as autism suggests that several hundred genes are likely involved as risk factors for these disorders. This heterogeneity presents both a challenge and an opportunity for researchers. Although the exact identity of many of the genes remains to be discovered, functional analysis of genes underlying several single-gene disorders has yielded considerable progress. Most genes identified to date appear to encode proteins that serve certain

conserved pathways: protein synthesis, transcriptional or epigenetic regulation, and synaptic signaling. Genetic syndromes such as fragile X syndrome, Rett syndrome, and tuberous sclerosis complex provide insights into the molecular pathways commonly affected in autism spectrum disorder (ASD). Understanding the basic biology of these diseases has led to mechanism-based treatment designs.

These genetic disorders, once thought to be irreversible, are now the subject of trailblazing new clinical trials for neurodevelopmental disorders. On the basis of research in genetic mouse models, it is hypothesized that different genetic disorders will respond to different therapies, such as mammalian target of rapamycin inhibitors (tuberous sclerosis and PTEN hamartoma tumor syndrome), metabotropic glutamate receptor 5 antagonists (fragile X and 16p11.2 deletion), and insulin-like growth factor 1 (Rett and Phelan-McDermid syndromes). It is not yet clear whether such trials will result in approval of the drugs for these specific conditions. Subsets of non-syndromic autism patients may also benefit from

one of these therapies, but further investigation will be required to provide the tools and methods to stratify the individuals with non-syndromic autism into treatment groups.

A remaining hurdle is the lack of precise understanding about the brain regions and neuronal circuits underlying autism. Studies in mouse models of autism suggest abnormalities in specific brain regions, as well as in certain cell types. Excitatory and inhibitory neurons in the neocortex, as well as subcortical structures such as basal ganglia and cerebellum, have been implicated. Astrocytes and microglia also play roles in ASD. Further studies will be required to provide definitive evidence that similar brain regions, cell types, and circuits are relevant to autism symptoms in the human brain.

OUTLOOK: The next generation of research in neurodevelopmental disorders must address the neural circuitry underlying behavioral symptoms and comorbidities, the cell types in these circuits, and common signaling pathways that link diverse genes. Early attempts at treating neurodevelopmental disorders have yielded mixed

ON OUR WEB SITE

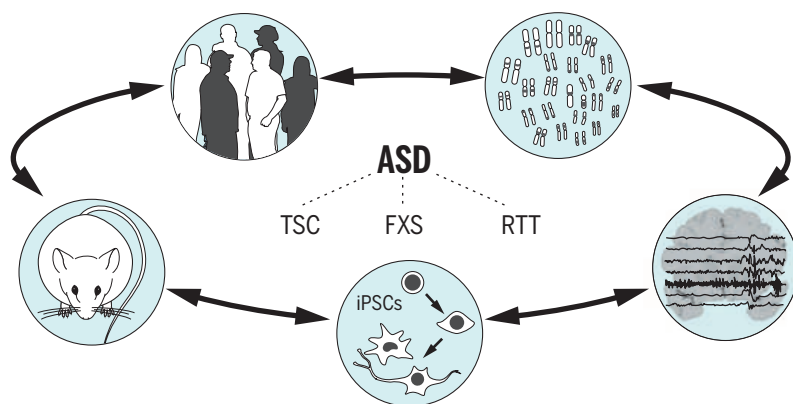
Read the full article at <http://dx.doi.org/10.1126/science.aab3897>

results, underscoring the necessity of choosing the right cohort of patients to treat, developing more sensitive and dynamic outcome measures, using cogent biomarkers, and utilizing technologies such as stem cell-derived neurons to predict response to treatment.

Biomarkers can be helpful in predicting subjects most likely to respond, confirm target engagement, and detect early signals of efficacy. Given that ASD represents circuit dysfunction, biomarkers that allow us to analyze autism-related circuit function are likely to be most relevant. Especially, translatable biomarkers that can be used in both mouse models and human subjects, such as electroencephalography, magnetic resonance imaging, visual or auditory evoked potentials, and eye-blink conditioning, can be particularly powerful.

One potential new tool to identify those who are likely to respond is induced pluripotent stem cell (iPSC)-derived neurons. This technology allows the possibility of testing the effects of a compound on a patient's neurons before it is given to the patient. Modeling the effects of mutations in iPSC-derived neurons can be informative about the molecular and cellular defects underlying autism.

Only when we can leverage the heterogeneity of neurodevelopmental disorders into precision medicine will the mechanism-based therapeutics for these disorders start to unlock success. ■



Translational research and clinical trials in ASD. Translational studies in ASD have gained momentum from genetically defined causes such as fragile X syndrome (FXS), Rett syndrome (RTT), and tuberous sclerosis complex (TSC). The patients with these disorders are phenotyped in detail by means of advanced imaging and electrophysiology studies, with the aim of identifying potential biomarkers. There are cell-based models (both rodent and human) as well as mouse models of these syndromes, enabling preclinical trials. Together, these efforts have led to clinical trials in some of these disorders. It is important to remember that the discovery cycle will likely take more than one round to achieve safe and effective therapies for these disorders.

The list of author affiliations is available in the full article online.

*Corresponding author. E-mail: mustafa.sahin@childrens.harvard.edu; msur@mit.edu

Cite this article as M. Sahin and M. Sur, *Science* 350, aab3897 (2015). DOI: 10.1126/science.aab3897

REVIEW

NEURODEVELOPMENT

Genes, circuits, and precision therapies for autism and related neurodevelopmental disorders

Mustafa Sahin^{1*} and Mriganka Sur^{2*}

Research in the genetics of neurodevelopmental disorders such as autism suggests that several hundred genes are likely risk factors for these disorders. This heterogeneity presents a challenge and an opportunity at the same time. Although the exact identity of many of the genes remains to be discovered, genes identified to date encode proteins that play roles in certain conserved pathways: protein synthesis, transcriptional and epigenetic regulation, and synaptic signaling. The next generation of research in neurodevelopmental disorders must address the neural circuitry underlying the behavioral symptoms and comorbidities, the cell types playing critical roles in these circuits, and common intercellular signaling pathways that link diverse genes. Results from clinical trials have been mixed so far. Only when we can leverage the heterogeneity of neurodevelopmental disorders into precision medicine will the mechanism-based therapeutics for these disorders start to unlock success.

Neurodevelopmental disorders include a wide range of conditions such as epilepsy, intellectual disability, and autism spectrum disorder (ASD). Patients with ASD exhibit early-childhood onset of symptoms, first described over 60 years ago (1), that persist throughout life and produce notable impairments in social, communicative, cognitive, and behavioral functioning (2). According to the U.S. Centers for Disease Control, ASD affects 1 in 68 children and 1 in 42 boys. ASD is a major public health problem that leads to considerable disability and disrupts families, resulting in a total annual societal cost of ~\$35 billion in the United States alone (3).

ASD diagnosis comprises a constellation of behavioral symptoms, as defined by a group of experts (DSM-5), and requires persistent deficits in social communication and interaction across multiple contexts, as well as restricted, repetitive patterns of behavior, interests, and activities. A key characteristic in ASD is its heterogeneity. Patients with ASD present with wide variation and levels of impairment with different comorbidities, and the expression of these symptoms can change over time. Heterogeneity has been a huge obstacle in ASD research, but in recent years, researchers have started to take advantage of the heterogeneity of ASD. Rather than focusing on “pure autism” (autism not confounded by

intellectual disability) (4, 5), research has now opened up to examining genetic disorders with high penetrance of ASD, such as fragile X syndrome (FXS), Rett syndrome (RIT), and tuberous sclerosis complex (TSC), which have now come to the forefront of translational efforts to find treatments for subsets of mechanism-based classification of ASD (6). Complementary to this effort is the National Institute of Mental Health (NIMH) initiative to define psychiatric disorders according to mechanistic descriptions of symptom clusters rather than symptom inventories, also known as research domain criteria (7, 8). In ASD, the etiology seems to vary according to the individual's genome and interaction with his or her environment. Genetic heterogeneity and overlap with other neuropsychiatric disorders make it difficult to find a unique risk factor for ASD. Improved understanding and classification of ASD-based domains and levels of analysis could improve precision and treatment efficacy.

Here, we review research on neurodevelopmental disorders that spans genes, molecules, cells, and circuits, as well as the whole individual and environment. We discuss current efforts and obstacles in clinical trials and offer recommendations for the future that lead toward precision medicine.

Genes

The genetic component of ASD susceptibility is evidenced by twin studies that demonstrated higher concordance of ASD among monozygotic than dizygotic twins and has benefited from modern genome scanning initiatives to yield many new genes worthy of further study. Genome analysis revealed the association of copy-number variants (such as 15q11-13, 16p11.2, and 22q11.2) and

single-nucleotide variants with ASD. Some of these variants are de novo (not found in either parent) and thus easier to deem as causal. Variants that are not de novo or sequencing variants that are not obviously deleterious are harder to evaluate. Several studies have used whole-exome sequencing to reveal a number of ASD susceptibility genes, such as *CHD8*, *GRIN2B*, and *SCN2A*. These studies estimate that 400 to 1000 genes are involved in ASD susceptibility (9). The vast majority of ASD susceptibility genes have not yet been identified and will require much larger cohorts for adequate statistical power, as was necessary for schizophrenia (10). Germline mutations are not the only contributor to brain disorders; somatic mutations that affect a subset of brain neurons can cause epilepsy, brain malformations, and quite possibly ASD (11). Somatic mosaicism affecting the brain will confound the genetic analysis of cohorts, which are almost always based on bulk DNA derived from the blood and intended to represent the inherited genome.

Along with larger cohort sizes, identifying many of the remaining hundreds of ASD susceptibility genes will require thoughtful and innovative study designs. One approach is to study families with consanguinity to reduce inherited variation and help identify rare recessive variants (12, 13). Another approach is to study groups that are relatively protected from ASD. Because ASD is much more common among males than females, focusing on families with a history of severe autism among women appears to enrich for highly penetrant rare variants (14).

The estimated heritability of ASD is 0.7 to 0.8, which, while relatively high, leaves room for non-inherited factors, including de novo mutations and epigenetic and environmental factors, leading to a complex risk architecture. Environmental influences such as perinatal injury and maternal infection could play an important role in the context of a susceptible genetic background and contribute to the development of ASD. For instance, premature infants with isolated cerebellar hemorrhage have a 30-fold higher incidence of ASDs compared to the general population (15, 16). Other epidemiological studies have implicated activation of the maternal immune system during gestation as a contributor to the development of various neuropsychiatric disorders (17–19) and more specifically in the development of autism (19–21). Maternal immune activation leads to region-specific changes in brain cytokines (22) and neuropathological changes that can be detected even in nonhuman primates (23). Interestingly, maternal immune activation is implicated in the exacerbation of syndromic forms of ASD. For example, maternal immune activation has been shown to intensify social behavior deficits observed in *Tsc2*^{+/-} mutant mice (24). Finally, the relationship between the gut microbiome and neurodevelopmental symptoms has attracted attention (25). Autism and accompanying gastrointestinal symptoms are associated with distinct gut microbial compositions (26). Furthermore, probiotic treatment can improve both the metabolic abnormalities and the behavioral deficits in

¹F. M. Kirby Center for Neurobiology, Translational Neuroscience Center, Department of Neurology, Boston Children's Hospital, Boston, MA 02115, USA. ²Simons Center for the Social Brain, Picower Institute for Learning and Memory, Department of Brain and Cognitive Sciences, Massachusetts Institute of Technology, Cambridge, MA 02139, USA.

*Corresponding author. E-mail: mustafa.sahin@childrens.harvard.edu; msur@mit.edu

a maternal immune activation mouse model, supporting a connection between gut microbiome and autism (27). Further studies are needed to test how robust these initial observations are and what cellular mechanisms mediate them.

Molecular and cellular pathways

Every identified ASD susceptibility gene sheds new light on the cellular mechanisms underlying ASD. Many of the genes implicated in ASD converge onto a few major signaling pathways: transcriptional control and chromatin remodeling, protein synthesis and cellular metabolism, and synapse development and function (6, 28–30). Although many of these cellular processes are shared between neurons and nonneuronal cells, they appear to play roles particularly relevant to ASD in the brain (Fig. 1).

Transcriptional control and chromatin remodeling

Several ASD genes influence transcription (31, 32), including those that are highly penetrant such as

Rett syndrome. MeCP2 (methyl CpG binding protein 2), which underlies Rett syndrome, is a molecular multitasker that regulates gene expression by interacting with chromatin remodeling, transcription, and splicing (33). Initial findings suggested that MeCP2 binds to methylated CpG sites in the promoters of genes and associates with chromatin silencing complexes to repress gene expression (34–36). However, subsequent studies have demonstrated that MeCP2 also interacts with chromatin and transcriptional activators to activate gene expression (37, 38). MeCP2 also mediates microRNA-mediated posttranscriptional control of gene expression (39, 40), as does FMRP (fragile X mental retardation protein) (41).

Signaling pathways and protein synthesis

One cellular process that has been implicated in multiple studies is that of mRNA synthesis and protein translation (28). Two key pathways that contribute to synaptic function are the PI3K/mTOR (phosphatidylinositol 3-kinase/mammalian target of rapamycin) pathway

and the Ras-MAPK (mitogen-activated protein kinase) pathway. These pathways have been linked to neurodevelopmental disorders and to synaptic dysfunction. Owing to the availability of specific and Food and Drug Administration (FDA)-approved inhibitors, the mTOR pathway has been well characterized. TSC and PTEN (phosphatase and tensin homolog) hamartoma tumor syndrome (PHTS) are two paradigmatic “mTORopathies” such that loss of TSC1, TSC2, or PTEN function leads to activation of mTOR kinase activity and high incidence of intellectual disability, seizures, and ASD (42). Other mutations in this pathway that present with ASD include the *neurofibromin 1* (*NF1*) gene that results in neurofibromatosis type I. *NF1* encodes a guanosine triphosphatase-activating protein that suppresses the activity of the proto-oncogene *Ras* and also alters mTOR activity.

Dysregulation of protein synthesis is a prominent feature of several other neurodevelopmental disorders, such as FXS (43). FMRP is an mRNA binding protein that regulates the translation of mRNAs and is silenced in FXS, resulting in

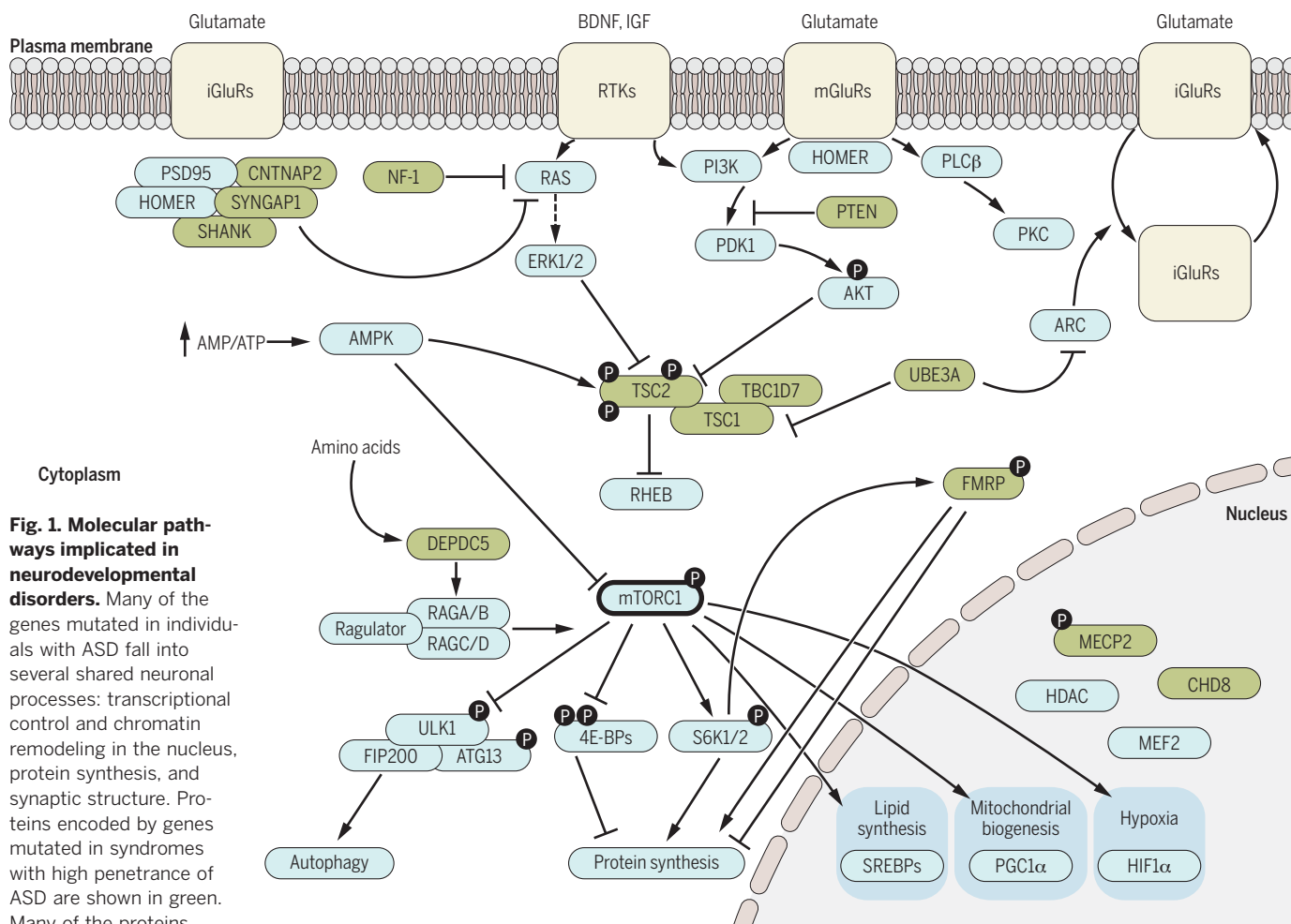


Fig. 1. Molecular pathways implicated in neurodevelopmental disorders. Many of the genes mutated in individuals with ASD fall into several shared neuronal processes: transcriptional control and chromatin remodeling in the nucleus, protein synthesis, and synaptic structure. Proteins encoded by genes mutated in syndromes with high penetrance of ASD are shown in green. Many of the proteins (such as MECP2 and FMRP) have multiple functions and interactions in the cell but are represented with the dominant functional role for the sake of clarity. Abbreviations not found in text include the following: RTKs, receptor tyrosine kinases; iGluRs, metabotropic glutamate receptors; PGC1- α , peroxisome proliferator-activated receptor gamma coactivator 1-alpha; SREBP, sterol regulatory element-binding proteins; HIF1 α , hypoxia-inducible factor 1 alpha; ULK1, unc-51-like kinase 1; ARC, activity-regulated cytoskeleton-associated protein; UBE3A, ubiquitin protein ligase E3A.

and the Ras-MAPK (mitogen-activated protein kinase) pathway. These pathways have been linked to neurodevelopmental disorders and to synaptic dysfunction. Owing to the availability of specific and Food and Drug Administration (FDA)-approved inhibitors, the mTOR pathway has been well characterized. TSC and PTEN (phosphatase and tensin homolog) hamartoma tumor syndrome (PHTS) are two paradigmatic “mTORopathies” such that loss of TSC1, TSC2, or PTEN function leads to activation of mTOR kinase activity and high incidence of intellectual disability, seizures, and ASD (42). Other mutations in this pathway that present with ASD include the *neurofibromin 1* (*NF1*) gene that results in neurofibromatosis type I. *NF1* encodes a guanosine triphosphatase-activating protein that suppresses the activity of the proto-oncogene *Ras* and also alters mTOR activity.

aberrant protein synthesis from key transcripts implicated in synaptic plasticity (44). Likewise, while MeCP2 influences expression of several hundred genes (37), levels of BDNF (brain-derived neurotrophic factor) and IGF1 (insulin-like growth factor 1) are reduced in *Mecp2* mutant mice, along with other molecules that cause both the PI3K/mTOR and ERK/MAPK pathways to be down-regulated (37, 45–49). Treatment with recombinant human IGF1 up-regulates these pathways in mice and induced pluripotent stem cell (iPSC)-derived human neurons (50, 51) and ameliorates symptoms in mice (48). Preliminary results in human trials also appear promising (52). It is important to remember that PI3K/mTOR and ERK/MAPK pathways regulate a large number of cellular processes, including transcription, autophagy, metabolism, and organelle biogenesis and maintenance. The role of each of these cellular processes in the pathogenesis and therapeutics of ASD remains to be determined.

Disruptions of signaling pathways can change scaffolding of proteins at synapses. Such changes may cause neurodevelopmental disorders. PSD95 (postsynaptic density protein 95) anchors *N*-methyl-D-aspartate (NMDA) and AMPA receptors at glutamatergic synapses. PSD95 expression is influenced by PI3K signaling; its levels, as well as excitatory synaptic transmission, are reduced in *Mecp2* mutant mice (48) and rescued by IGF1 application. Similarly, *SHANK3*, which lies in the 22q13.3 deletion region associated with Phelan-McDermid syndrome (PMS), encodes a synaptic protein that regulates other protein partners, such as PSD95; up-regulation of the PI3K pathway by IGF1 rescues synaptic deficits in iPSC-derived human patient neurons (53) and *Shank3* mutant mice (54), at least partly by up-regulating PSD95.

Molecular convergence of pathways implicated by human genetics of ASD is apparent in studies of the *Fmr1* knockout mouse. First, among the

mRNA binding partners of FMRP are postsynaptic proteins such as SHANK3 and signaling proteins such as TSC2 and PTEN. Second, a number of studies in *Fmr1* knockout mice indicate that interfering with protein synthesis in different ways can normalize the phenotype of the knockout mice. Knockout of S6 kinase (55), Cebp (56), and PI3K (57, 58) is sufficient to ameliorate aspects of the *Fmr1* knockout pathogenesis, raising the possibility of having multiple potential targets for intervening with loss of FMRP. Dysregulation of metabotropic glutamate receptor (mGluR) and aberrant mGluR-dependent long-term depression (LTD) have been reported first in FXS mouse models (59, 60) and in several other ASD animal models, including *Nlgn3* (*neuroligin 3*) knockout and 16p11.2 knockout (61, 62). Although we do not yet know if murine hippocampal LTD models the human ASD brain function, these findings raise the possibility that convergent cellular and molecular pathway targets exist in subsets of ASDs.

Brain regions and neural circuits

Molecular pathways in brain cells affect the function of neurons and synapses, and hence neuronal connectivity and circuits, to modify brain function. However, we lack insight about the brain regions and neuronal circuits underlying ASD. We do not yet know whether one cell type or circuit is crucial for the behavioral deficits observed in ASD patients. It is likely that different gene mutations perturb the neural circuitry underlying social interactions and repetitive behaviors at different nodes, resulting in a complicated matrix of genes, brain regions, and behavioral correlates (Fig. 2).

Histopathological and imaging-based evidence that implicates specific brain regions and circuits underlying ASD is limited. The pathological studies are hampered by small sample size, and thus there is an urgent need for systematic and wide-

spread collection of pathological specimens from those affected with a wide range of ASD. Imaging studies have been performed mostly on those with high-functioning ASD because patients must be able to tolerate and comply with magnetic resonance imaging (MRI) protocols. Thus, although the functional MRI studies performed to date implicate certain areas of the brain in the “high functioning” ASD group, it is not clear whether the same circuits are involved in those who have more severe cognitive deficits. It is also possible that differences between ASD and control groups identified in such studies do not represent the aberrant circuits that are causally related to the behavioral abnormalities, but instead represent the activation of other brain regions that compensate for the neural circuitry abnormalities. Clinical protocols that enable MRI studies in ASD patients with intellectual disability and those who are younger will enhance our understanding of ASD and its associated neural circuitry. Such studies performed in individuals with genetically identified subsets of ASD may also shed light on genotype-phenotype correlations (63, 64).

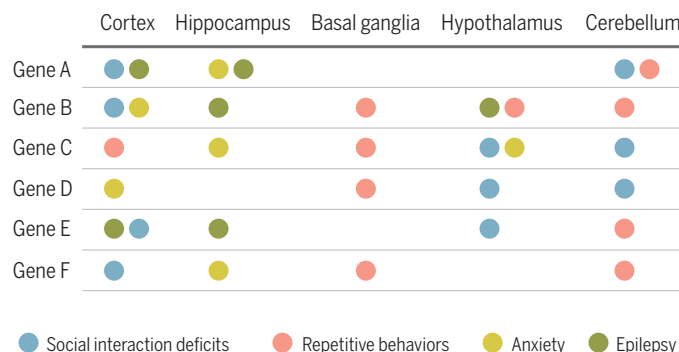
In addition to functional MRI, complementary techniques to investigate neuronal connectivity such as structural MRI, diffusion tensor imaging tractography, near-infrared spectroscopy, magnetoencephalography, and EEG can contribute to our understanding of brain connectivity at different time scales and with different spatial resolutions. It is likely that we will need to corroborate the findings from one modality with that from others to determine the most robust connectivity abnormalities in ASD. Some of these techniques may be more amenable for individuals at different ages and at different functional levels.

Studies in genetic mouse models of ASD suggest abnormalities in specific brain regions, as well as in certain cell types. Two studies analyzed the coexpression patterns of a number of ASD genes in the human brain (65, 66). One study found enrichment in mid-gestation layer 5/6 cortical projection neurons, and the other found enrichment in superficial cortical layers and glutamatergic projection neurons. Although the exact layers of the cortex involved were different in the two analyses, the fact that cortical projection neurons were indicated in both studies is potentially important.

In addition to cortical projection neurons, there is increasing evidence for the role of other neuronal subtypes in the pathogenesis of ASD. Multiple mouse models of ASD display reduction in parvalbumin (PV)-cell density in the neocortex (67). PV knockout mice display behavioral phenotypes with relevance to the core symptoms present in human ASD patients (68). In contrast, other groups have reported a selective increase in PV-immunopositive interneurons in the CA1 and CA3 subfields and calretinin-immunopositive neurons in CA1 in patients with ASD (69). Loss of PTEN in mice results in a preferential loss of a different subtype of GABAergic (γ -aminobutyric acid-releasing) neurons, somatostatin (SST) interneurons (70). Interneuron-specific deletions of ASD-related genes result in neurodevelopmental deficits in

Fig. 2. Hypothetical matrix of genetic mutations and brain regions mapping onto behavioral profiles.

The approach to focus on mechanistic descriptions of symptom clusters rather than symptom inventories requires an understanding of the neural circuit(s) underlying these behavioral symptoms. One way to examine the neural circuits in animal models is to probe the relationship between a gene's function in a certain brain region and the behavioral deficits in the animal. Use of conditional knockout mice has started to provide such information in certain genetic diseases such as TSC and RTT (93, 118). This matrix represents a hypothetical framework, which needs to be populated by future experimentation. One concrete example of this approach is currently in effect in epilepsy. Absence seizures are thought to arise from voltage-gated calcium channel dysfunction in the thalamus and respond best to ethosuximide treatment. In contrast, complex partial seizures occur as a result of increased excitation or decreased inhibition and thus respond to glutamate antagonists or GABAergic agonists. Such delineation of genetic, cellular, and circuit defects also may prove helpful in treating behavioral deficits associated with ASD with better precision.



mice. For example, loss of MeCP2 from GABAergic interneurons leads to autistic-like repetitive movements, seizures, and deficits in auditory event-related potentials (71, 72). Deficits in inhibitory neurotransmission, along with altered balance of excitation and inhibition (73), have been consistently observed in cortical and hippocampal neurons and circuits in diverse mouse models (74–77). In addition, the reversal potential of GABA may not mature fully when specific ASD genes are mutated, causing GABA to be depolarizing rather than hyperpolarizing (78). Consistent with these findings, a propensity for seizures is a major phenotype of ASDs. Taken together, these findings make a compelling case for dysregulation of inhibition as having a major role in neurodevelopmental disorders. More generally, cell type-specific and brain region-specific deletion of ASD genes is crucial for dissecting the circuit pathophysiology of ASD and in tying it to distinct symptom domains.

Connections between basal ganglia and cortex may underlie certain aspects of ASD. *Neurologin1* knockout mice exhibit ASD-like repetitive behaviors and abnormal corticostriatal synapses (79). *Neurologin3* mutants have similar abnormalities, but the defect appears to be due to a selective synaptic impairment in the nucleus accumbens/ventral striatum (80). SHANK3 is expressed in the basal ganglia, and *Shank3* knockout mice exhibit repetitive grooming behavior, abnormal social interactions, and changes at corticostriatal synapses (81). The cerebellum is implicated in the pathogenesis of ASD via histopathology, imaging, and

epidemiological studies of injury. First, neuropathological studies demonstrate loss of cerebellar Purkinje cells in individuals diagnosed with ASD versus typically developing controls (82–85). Second, imaging studies of patients diagnosed with ASD indicate gray and white matter abnormalities in the cerebellum, dating to early childhood (86–90). Premature infants with isolated cerebellar hemorrhage have a higher incidence of ASDs, suggesting that cerebellar dysfunction early in life contributes to the pathogenesis of autism (15, 16). The developmental vulnerability of this circuit is further illustrated by study of genetic syndromes associated with ASD. Positron emission tomography studies in pediatric TSC patients with ASD demonstrate hypermetabolism in the cerebellar nuclei—the output of the cerebellar cortex—in TSC patients with ASD but not in TSC patients without ASD (91). The selective loss of *Tsc1* or *Tsc2* genes in the output cells of the cerebellum, the Purkinje neurons, appears to be sufficient to lead to an autistic-like phenotype in the two mouse models of TSC (92, 93). These findings suggest that abnormal cerebellar function contributes to ASD. Non-neuronal cells in the brain such as astrocytes and microglia have also been implicated in the pathogenesis of neurodevelopmental disorders (94). Astrocyte processes extend into excitatory synapses, and they influence synaptic development (95) and synaptic transmission via uptake of glutamate (96), as well as by calcium-mediated alterations in synaptic function and plasticity (97, 98). ASD genes such as *Fmr1* and *Mecp2* are now known to influence astrocyte function (99).

Astrocytes express mGluRs, providing a pathway for mGluR signaling to influence fragile X pathophysiology (100). Astrocyte-specific restoration of MeCP2 in *Mecp2* mutant mice restores function (101). Microglia also shape neuronal development and plasticity, and modulate synaptic transmission in the adult brain, via cytokine and chemokine release, as well as phagocytosis (102, 103). Transplantation of wild-type microglia has been reported as reversing symptoms in a mouse model of Rett syndrome, though the interpretation of these findings remains controversial (104, 105).

Treatments

Despite the many discoveries in basic neuroscience and human genetics, FDA-approved drugs for ASD patients are limited to risperidone (a dopamine antagonist) and aripiprazole (a dopamine agonist), which are both aimed at treating irritability and not the core features of ASD. Given the large number of genes that potentially confer ASD risk, the genetic heterogeneity of ASD presents a substantial obstacle to development of one-size-fits-all therapies. One can imagine several scenarios. It would be ideal to have one treatment for all causes of ASD. This seems rather unlikely; ASD is not one disease, and some genetic causes of ASD appear to have diametrically opposite manifestations at the synaptic level (106). It is also equally unlikely that different interventions can be developed for every genetic cause of ASD. So, the most realistic (and hopeful) scenario is that there will be a convergence upon a few molecular and circuit pathways that can be targeted by a limited number of interventions. The current

Table 1. Clinical trials for genetically defined neurodevelopmental disorders. The table lists the trials listed for genetic syndromes highly associated with ASD according to a search on the clinicaltrials.gov website on 30 July 2015. Only actively recruiting or recently completed trials are included. The final column lists primary or secondary end points with relevance to neurodevelopment.		
Disorder	Study drug	ASD/neurocognitive outcomes
Tuberous sclerosis	Everolimus (RAD001)	ASD, memory, language skills, cognition, general executive function outcomes, behavioral changes, frequency or reduction of epileptiform events, reduced mTOR signaling
	rhIGF-1	Behavior, cognition, cortical function, motor function
Rett syndrome	Fingolimod (FTY720)	Slow regression of motor or language skills
	Dextromethorphan	Seizures, behavioral problems, cognition
	Glatiramer acetate	Epileptic activity, general behavior
	NNZ-2566	EEG, behavior, autonomic function
Fragile X syndrome	Acamprosate	Inattention or hyperactivity, social impairment, behavior, cognition
	NNZ-2566	Behavior, global and functional outcome measures
	Ganaxolone	Behavior, anxiety, attention, cognition
	Metadoxine (MG01CI)	Attention-deficit hyperactivity disorder
	Epigallocatechin-3-gallate (EGCG)	Improve intellectual disability, learning, memory, language
Angelman syndrome	Minocycline	Motor development, behavior, cognition, language
	RG1662	Cognition, behavior
Down syndrome	Low-dose nicotine	Cognitive improvement
	Donepezil (E2020)	Activities of daily living
Phelan-McDermid syndrome	Thyroid hormone and folinic acid	Psychomotor development
	rhIGF-1	Behavior, language, motor skills

focus is on the genetic syndromes with high penetrance of ASD symptoms, often caused by single-gene mutations (Table 1). That mouse models of many of the syndromes associated with ASD respond positively to treatment, even in adulthood (107–109), has further bolstered optimism about the utility of pharmacological treatments in these disorders.

One of the first attempts at testing mechanism-based therapies in ASD was performed in FXS. The mGluR theory of fragile X predicted that many symptoms of FXS are due to exaggerated responses to activation of mGluRs. This was demonstrated to be true in many animal models of FXS (110). Nonetheless, two mGluR antagonists (one made by Roche and another by Novartis) failed to show efficacy in phase 2 trials (111). These negative results highlight the difficulties associated with clinical trials in neurodevelopmental disorders: Did the drugs engage their targets in the central nervous system? Were the end points chosen dynamic within the duration of the trial? Was the placebo effect too large? Was the right group of patients (e.g., patients at an appropriate stage of symptoms, or a subset with a particular genotype) chosen for enrollment?

Another important issue raised by these studies is how to best utilize animal models for developing therapies. Physiological and behavioral analyses in mice have been crucial for advancing our understanding of circuitry underlying social interactions and repetitive behaviors. However, a “good” mouse model needs to have both construct and face validity (112). More important, the circuit that is being analyzed needs to have some direct relevance to outcome measures in humans. Only then can the pharmacological interventions that modulate that circuit be translated effectively from mice to humans.

It is surprising that relatively few pharmacokinetic and pharmacodynamic (PK/PD) relationships are tested in preclinical studies in mouse models of neurodevelopmental disorders. Although the pharmacokinetics will not be the same for a compound in mice and humans, understanding how much of the target needs to be engaged and over what period of time it must be engaged to achieve efficacy is crucial to interpret the preclinical data correctly and translate the findings to clinical studies. To identify the correct target, more detailed preclinical studies will be necessary going forward. In terms of early-stage clinical

trials, many interventions look promising in open-label studies but fail to show efficacy when compared to placebo. Thus, more placebo-controlled phase 2 trials will be needed.

Biomarkers can be crucial for predicting subjects most likely to respond to a test drug, confirming target engagement, and detecting early signals of efficacy. Finding biomarkers that will segregate similarly diagnosed ASD patients into subsets of biologically more homogeneous populations is a critical feature of good clinical trial design. A “stratification biomarker” can be a biochemical measure from patient samples, a structural feature of a human imaging study, or a functional feature of an imaging or electrophysiological study. Aside from stratification, biomarkers can also be helpful in early diagnosis and assessing phenotype and severity, as well as measuring PK/PD in drug studies. Given that ASD represents circuit dysfunction, biomarkers that allow us to examine ASD-related circuits are likely to be most relevant. Especially, translatable biomarkers that can be used in both mouse models and human subjects can be particularly powerful [e.g., EEG, MRI, visual or auditory evoked potentials, or eye-blink conditioning (64, 113–115)]. Similarly,

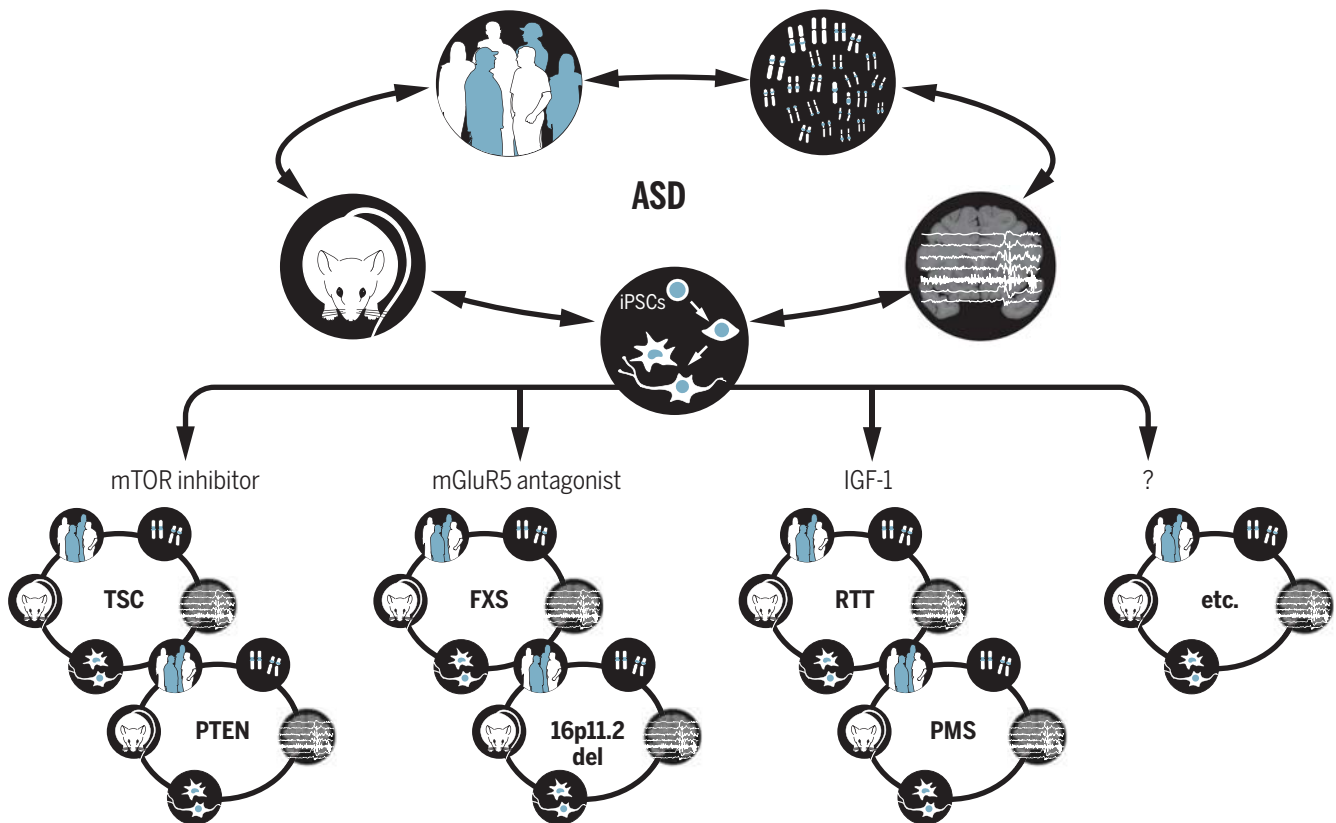


Fig. 3. Translational research and clinical trials in ASD. Translational studies in ASD have gained momentum from genetically defined causes such as FXS, TSC, and RTT. The patients with these disorders are phenotyped in detail by means of advanced imaging and electrophysiology studies, with the aim of identifying potential biomarkers. There are cell-based models (both rodent and human) as well as mouse models of these syndromes, enabling preclinical trials. Together, these efforts have led to clinical trials in some of these disorders. Based on the preclinical trials, the hypothesis is that different etiologies

of ASD will respond to different therapies, such as mTOR inhibitors (TSC and PTEN), mGluR5 antagonists (FXS and 16p11.2 deletion), and IGF-1 (RTT and PMS). Subsets of nonsyndromic ASD patients may also benefit from one of these therapies, but further studies will be required to provide the tools and methods to stratify the individuals with nonsyndromic ASD into treatment groups. It is important to remember that the discovery cycle will likely take more than one round to achieve safe and effective therapies for these disorders.

outcome measures that are circuit-based may be more fruitful in detecting efficacy rather than measuring global functioning. A panel of relevant biomarkers, which together provide a unique profile of a patient, may be a crucial component of precision trial design in the future.

One of the most important questions about treatments is when mechanism-based treatments need to be initiated. Since the behavioral manifestations of ASD occur quite early in development, one may have to intervene before symptoms arise. Animal models of syndromic ASD indicate that restoring function well into adulthood can rescue some of the symptoms of the disease (107–109). It is not yet clear if the same is true in humans and what exactly the critical windows for treatment are. However, regardless of age at treatment onset, relevant biomarkers and efficacy measures would be important for establishing the effectiveness of treatment.

One potential new tool to identify subjects who are likely to respond to a test drug is iPSC-derived neurons. This technology allows the possibility of testing the effects of a compound on a patient's neurons first before giving it to the patient. Modeling the effects of mutations in iPSC-derived neurons can be informative about the molecular and cellular defects but is unlikely with the current technology to provide insights on the emergent dysfunctions at the level of neuronal circuits. Nonetheless, a preliminary testing of efficacy in a patient's iPSC-derived neurons should be a vital component of trial design for precision medicine.

Since many of the diseases being targeted in these initial trials are genetic, they may be amenable to gene therapy in theory. Gene therapy using viral vectors is undergoing a renaissance and may be particularly applicable to diseases that arise from loss of function of a particular gene such as *MECP2* or *CDKL5* (*cyclin-dependent kinase-like 5*). Aside from the delivery issues, one must pay close attention to the dosage effects, because many of the genes that result in an ASD-related phenotype also have deleterious effects when they are expressed at high dosage. Thus, expression of the exogenous genes may have to be regulated tightly in spatial and temporal terms, as well as levels of expression.

If we reach success in single genetically defined syndromes, there will be two new roadblocks in generalizing these findings to the larger ASD population. First, such an extension will require a comparative analysis of the different genetically defined causes of ASD to determine whether effective treatments in one may also be effective in another (Fig. 3). Such comparative understanding of the genetic etiologies underlying ASD is in its infancy (106). A second and more difficult hurdle will be applying these findings to the "idiopathic" genetically unknown or undefined ASD population. Currently, we do not have an analytical tool to determine if an individual with ASD would benefit from a treatment that is effective, for example, in TSC or in FXS. A marker to classify patients according to genetic, biochemical, or circuit abnormalities does not

yet exist. However, even single-gene conditions involve multiple potential targets, and combination therapies are likely to be more effective than single drugs for single targets (47). The success of targeted pharmacological interventions would require integration of multiple kinds of data: knowledge of the genetic mutation and its signaling pathways and synaptic molecules, effectiveness of the therapy on neuronal and synaptic phenotypes in patient-derived neurons and non-neuronal cells in culture, and even analysis of transplanted human neurons in mice.

Although pharmacological treatments may normalize neuronal and synaptic abnormalities, cognitive function is still dependent on complex circuits and interaction of the individual with his or her environment. Thus, pharmacological treatments alone may not be sufficient to reach the optimal outcome without behavioral treatments. Behavioral interventions appear promising in mouse models (116, 117) and could be combined with pharmacological interventions in future clinical trials. While simply correcting the synaptic abnormality with a pharmacological agent may not be sufficient to affect behavioral changes, it could accelerate the rate of learning and sociability in the setting of behavioral interventions. Although combining treatments adds complexity to the trial design, a few such trials are in the planning stages. Trials based on a mechanistic understanding of the disease, performed on a well-defined group of subjects, with evidence of target engagement and supportive biomarkers, are the most likely to succeed. Once such trials prove effective in the highly penetrant genetic syndromes, the next challenge will be to identify patients with idiopathic autism who may benefit from the same treatment. Such an approach will finally realize the notion of precision medicine for autism and related neurodevelopmental disorders.

REFERENCES AND NOTES

1. L. Kanner, Autistic disturbances of affective contact. *Nerv. Child* **2**, 217–250 (1943).
2. C. Lord, in *Understanding Autism: From Basic Neuroscience to Treatment*, S. O. Moldin, J. L. R. Rubenstein, Ed. (Taylor & Francis, Boca Raton, FL, 2006), pp. 1–23.
3. M. Ganz, in *Understanding Autism: From Basic Neuroscience to Treatment*, S. O. Moldin, J. L. R. Rubenstein, Ed. (Taylor & Francis, Boca Raton, FL, 2006), pp. 475–502.
4. G. Vivanti, J. Barbaro, K. Hudry, C. Dissanayake, M. Prior, Intellectual development in autism spectrum disorders: New insights from longitudinal studies. *Front. Hum. Neurosci.* **7**, 354 (2013). doi: [10.3389/fnhum.2013.00354](https://doi.org/10.3389/fnhum.2013.00354); pmid: [23847518](https://pubmed.ncbi.nlm.nih.gov/23847518/)
5. C. Gillberg, E. Fernell, Autism plus versus autism pure. *J. Autism Dev. Disord.* **44**, 3274–3276 (2014). doi: [10.1007/s10803-014-2163-1](https://doi.org/10.1007/s10803-014-2163-1); pmid: [24958434](https://pubmed.ncbi.nlm.nih.gov/24958434/)
6. D. Ebrahimi-Fakhari, M. Sahin, Autism and the synapse: Emerging mechanisms and mechanism-based therapies. *Curr. Opin. Neurol.* **28**, 91–102 (2015). doi: [10.1097/WCO.0000000000000186](https://doi.org/10.1097/WCO.0000000000000186); pmid: [25695134](https://pubmed.ncbi.nlm.nih.gov/25695134/)
7. B. J. Casey, M. E. Oliveri, T. Insel, A neurodevelopmental perspective on the research domain criteria (RDoC) framework. *Biol. Psychiatry* **76**, 350–353 (2014). doi: [10.1016/j.biopsych.2014.01.006](https://doi.org/10.1016/j.biopsych.2014.01.006); pmid: [25103538](https://pubmed.ncbi.nlm.nih.gov/25103538/)
8. T. Insel et al., Research domain criteria (RDoC): Toward a new classification framework for research on mental disorders. *Am. J. Psychiatry* **167**, 748–751 (2010). doi: [10.1176/appi.ajp.2010.09091379](https://doi.org/10.1176/appi.ajp.2010.09091379); pmid: [20595427](https://pubmed.ncbi.nlm.nih.gov/20595427/)
9. D. H. Geschwind, M. W. State, Gene hunting in autism spectrum disorder: On the path to precision medicine. *Lancet Neurol.* (2015). doi: [10.1016/S1474-4422\(15\)00044-7](https://doi.org/10.1016/S1474-4422(15)00044-7); pmid: [25891009](https://pubmed.ncbi.nlm.nih.gov/25891009/)
10. S. Ripke et al., Biological insights from 108 schizophrenia-associated genetic loci. *Nature* **511**, 421–427 (2014). doi: [10.1038/nature13595](https://doi.org/10.1038/nature13595); pmid: [25056061](https://pubmed.ncbi.nlm.nih.gov/25056061/)
11. A. Poduri, G. D. Evrony, X. Cai, C. A. Walsh, Somatic mutation, genomic variation, and neurological disease. *Science* **341**, 1237758 (2013). doi: [10.1126/science.1237758](https://doi.org/10.1126/science.1237758); pmid: [23828942](https://pubmed.ncbi.nlm.nih.gov/23828942/)
12. T. W. Yu et al., Using whole-exome sequencing to identify inherited causes of autism. *Neuron* **77**, 259–273 (2013). pmid: [23352163](https://pubmed.ncbi.nlm.nih.gov/23352163/)
13. E. M. Morrow et al., Identifying autism loci and genes by tracing recent shared ancestry. *Science* **321**, 218–223 (2008). doi: [10.1126/science.1157657](https://doi.org/10.1126/science.1157657); pmid: [18621663](https://pubmed.ncbi.nlm.nih.gov/18621663/)
14. T. N. Turner et al., Loss of δ -catenin function in severe autism. *Nature* **520**, 51–56 (2015). doi: [10.1038/nature14186](https://doi.org/10.1038/nature14186); pmid: [25807484](https://pubmed.ncbi.nlm.nih.gov/25807484/)
15. C. Limperopoulos et al., Does cerebellar injury in premature infants contribute to the high prevalence of long-term cognitive, learning, and behavioral disability in survivors? *Pediatrics* **120**, 584–593 (2007). doi: [10.1542/peds.2007-1041](https://doi.org/10.1542/peds.2007-1041); pmid: [17766532](https://pubmed.ncbi.nlm.nih.gov/17766532/)
16. C. Limperopoulos, G. Chilingaryan, N. Guizard, R. L. Robertson, A. J. Du Plessis, Cerebellar injury in the premature infant is associated with impaired growth of specific cerebral regions. *Pediatr. Res.* **68**, 145–150 (2010). doi: [10.1203/PDR.0b013e3181e1d032](https://doi.org/10.1203/PDR.0b013e3181e1d032); pmid: [20389260](https://pubmed.ncbi.nlm.nih.gov/20389260/)
17. L. Shi, S. H. Fatemi, R. W. Sidwell, P. H. Patterson, Maternal influenza infection causes marked behavioral and pharmacological changes in the offspring. *J. Neurosci.* **23**, 297–302 (2003). pmid: [12514227](https://pubmed.ncbi.nlm.nih.gov/12514227/)
18. P. H. Patterson, Immune involvement in schizophrenia and autism: Etiology, pathology and animal models. *Behav. Brain Res.* **204**, 313–321 (2009). doi: [10.1016/j.bbr.2008.12.016](https://doi.org/10.1016/j.bbr.2008.12.016); pmid: [19136031](https://pubmed.ncbi.nlm.nih.gov/19136031/)
19. P. A. Garay, A. K. McAllister, Novel roles for immune molecules in neural development: Implications for neurodevelopmental disorders. *Front. Synaptic Neurosci.* **2**, 136 (2010). doi: [10.3389/fnsyn.2010.00136](https://doi.org/10.3389/fnsyn.2010.00136); pmid: [21423522](https://pubmed.ncbi.nlm.nih.gov/21423522/)
20. K. Garbett et al., Immune transcriptome alterations in the temporal cortex of subjects with autism. *Neurobiol. Dis.* **30**, 303–311 (2008). doi: [10.1016/j.nbd.2008.01.012](https://doi.org/10.1016/j.nbd.2008.01.012); pmid: [18378158](https://pubmed.ncbi.nlm.nih.gov/18378158/)
21. D. L. Vargas, C. Nascimbene, C. Krishnan, A. W. Zimmerman, C. A. Pardo, Neuroglial activation and neuroinflammation in the brain of patients with autism. *Ann. Neurol.* **57**, 67–81 (2005). doi: [10.1002/ana.20315](https://doi.org/10.1002/ana.20315); pmid: [15546155](https://pubmed.ncbi.nlm.nih.gov/15546155/)
22. P. A. Garay, E. Y. Hsiao, P. H. Patterson, A. K. McAllister, Maternal immune activation causes age- and region-specific changes in brain cytokines in offspring throughout development. *Brain Behav. Immun.* **31**, 54–68 (2013). doi: [10.1016/j.bbi.2012.07.008](https://doi.org/10.1016/j.bbi.2012.07.008); pmid: [22841693](https://pubmed.ncbi.nlm.nih.gov/22841693/)
23. R. K. Weir et al., Preliminary evidence of neuropathology in nonhuman primates prenatally exposed to maternal immune activation. *Brain Behav. Immun.* **48**, 139–146 (2015). doi: [10.1016/j.bbi.2015.03.009](https://doi.org/10.1016/j.bbi.2015.03.009); pmid: [25816799](https://pubmed.ncbi.nlm.nih.gov/25816799/)
24. D. Ehninger et al., Gestational immune activation and Tsc2 haploinsufficiency cooperate to disrupt fetal survival and may perturb social behavior in adult mice. *Mol. Psychiatry* **17**, 62–70 (2012). doi: [10.1038/mp.2010.115](https://doi.org/10.1038/mp.2010.115); pmid: [21079609](https://pubmed.ncbi.nlm.nih.gov/21079609/)
25. J. G. Mülle, W. G. Sharp, J. F. Cubells, The gut microbiome: A new frontier in autism research. *Curr. Psychiatry Rep.* **15**, 337 (2013). doi: [10.1007/s11920-012-0337-0](https://doi.org/10.1007/s11920-012-0337-0); pmid: [23307560](https://pubmed.ncbi.nlm.nih.gov/23307560/)
26. D. W. Kang et al., Reduced incidence of Prevotella and other fermenters in intestinal microflora of autistic children. *PLOS ONE* **8**, e68322 (2013). pmid: [23844187](https://pubmed.ncbi.nlm.nih.gov/23844187/)
27. E. Y. Hsiao et al., Microbiota modulate behavioral and physiological abnormalities associated with neurodevelopmental disorders. *Cell* **155**, 1451–1463 (2013). doi: [10.1016/j.cell.2013.11.024](https://doi.org/10.1016/j.cell.2013.11.024); pmid: [24315484](https://pubmed.ncbi.nlm.nih.gov/24315484/)
28. R. J. Kelleher 3rd, M. F. Bear, The autistic neuron: Troubled translation? *Cell* **135**, 401–406 (2008). doi: [10.1016/j.cell.2008.10.017](https://doi.org/10.1016/j.cell.2008.10.017); pmid: [18984149](https://pubmed.ncbi.nlm.nih.gov/18984149/)
29. H. Y. Zoghbi, M. F. Bear, Synaptic dysfunction in neurodevelopmental disorders associated with autism and intellectual disabilities. *Cold Spring Harb. Perspect. Biol.* **4**, a009886 (2012). doi: [10.1101/cshperspect.a009886](https://doi.org/10.1101/cshperspect.a009886); pmid: [22258914](https://pubmed.ncbi.nlm.nih.gov/22258914/)
30. T. C. Südhof, Neurotrogins and neurexins link synaptic function to cognitive disease. *Nature* **455**, 903–911 (2008). doi: [10.1038/nature07456](https://doi.org/10.1038/nature07456); pmid: [18923512](https://pubmed.ncbi.nlm.nih.gov/18923512/)
31. I. Iossifov et al., De novo gene disruptions in children on the autistic spectrum. *Neuron* **74**, 285–299 (2012). doi: [10.1016/j.neuron.2012.04.009](https://doi.org/10.1016/j.neuron.2012.04.009); pmid: [22542183](https://pubmed.ncbi.nlm.nih.gov/22542183/)

32. R. Bernier *et al.*, Disruptive CHD8 mutations define a subtype of autism early in development. *Cell* **158**, 263–276 (2014). doi: [10.1016/j.cell.2014.06.017](#); pmid: [24998929](#)
33. J. Castro, N. Mellios, M. Sur, Mechanisms and therapeutic challenges in autism spectrum disorders: Insights from Rett syndrome. *Curr. Opin. Neurol.* **26**, 154–159 (2013). doi: [10.1097/WCO.0b013e32835f19a7](#); pmid: [23449173](#)
34. X. Nan, F. J. Campoy, A. Bird, MeCP2 is a transcriptional repressor with abundant binding sites in genomic chromatin. *Cell* **88**, 471–481 (1997). doi: [10.1016/S0092-8674\(00\)81887-5](#); pmid: [9038338](#)
35. R. R. Meehan, J. D. Lewis, A. P. Bird, Characterization of MeCP2, a vertebrate DNA binding protein with affinity for methylated DNA. *Nucleic Acids Res.* **20**, 5085–5092 (1992). doi: [10.1093/nar/20.19.5085](#); pmid: [1408825](#)
36. P. L. Jones *et al.*, Methylated DNA and MeCP2 recruit histone deacetylase to repress transcription. *Nat. Genet.* **19**, 187–191 (1998). doi: [10.1038/561](#); pmid: [9620779](#)
37. M. Chahrouh *et al.*, MeCP2, a key contributor to neurological disease, activates and represses transcription. *Science* **320**, 1224–1229 (2008). doi: [10.1126/science.1153252](#); pmid: [18511691](#)
38. S. Ben-Shachar, M. Chahrouh, C. Thaller, C. A. Shaw, H. Y. Zoghbi, Mouse models of MeCP2 disorders share gene expression changes in the cerebellum and hypothalamus. *Hum. Mol. Genet.* **18**, 2431–2442 (2009). doi: [10.1093/hmg/ddp181](#); pmid: [19369296](#)
39. R. G. Urdinguio *et al.*, Disrupted microRNA expression caused by Mecp2 loss in a mouse model of Rett syndrome. *Epigenetics* **5**, 656–663 (2010). doi: [10.4161/epi.5.7.13055](#); pmid: [20716963](#)
40. H. Wu *et al.*, Genome-wide analysis reveals methyl-CpG-binding protein 2-dependent regulation of microRNAs in a mouse model of Rett syndrome. *Proc. Natl. Acad. Sci. U.S.A.* **107**, 18161–18166 (2010). doi: [10.1073/pnas.1005595107](#); pmid: [20921386](#)
41. P. Jin *et al.*, Biochemical and genetic interaction between the fragile X mental retardation protein and the microRNA pathway. *Nat. Neurosci.* **7**, 113–117 (2004). doi: [10.1038/nrn1174](#); pmid: [14703574](#)
42. J. O. Lipton, M. Sahin, The neurology of mTOR. *Neuron* **84**, 275–291 (2014). doi: [10.1016/j.neuron.2014.09.034](#); pmid: [25374355](#)
43. M. Qin *et al.*, Altered cerebral protein synthesis in fragile X syndrome: Studies in human subjects and knockout mice. *J. Cereb. Blood Flow Metab.* **33**, 499–507 (2013). doi: [10.1038/jcbfm.2012.205](#); pmid: [23299245](#)
44. J. C. Darnell *et al.*, FMRP stalls ribosomal translocation on mRNAs linked to synaptic function and autism. *Cell* **146**, 247–261 (2011). doi: [10.1016/j.cell.2011.06.013](#); pmid: [21784246](#)
45. Q. Chang, G. Khare, V. Dani, S. Nelson, R. Jaenisch, The disease progression of Mecp2 mutant mice is affected by the level of BDNF expression. *Neuron* **49**, 341–348 (2006). doi: [10.1016/j.neuron.2005.12.027](#); pmid: [16446138](#)
46. D. Tropea *et al.*, Partial reversal of Rett Syndrome-like symptoms in MeCP2 mutant mice. *Proc. Natl. Acad. Sci. U.S.A.* **106**, 2029–2034 (2009). doi: [10.1073/pnas.0812394106](#); pmid: [19208815](#)
47. N. Mellios *et al.*, β 2-Adrenergic receptor agonist ameliorates phenotypes and corrects microRNA-mediated IGF1 deficits in a mouse model of Rett syndrome. *Proc. Natl. Acad. Sci. U.S.A.* **111**, 9947–9952 (2014). doi: [10.1073/pnas.1309426111](#); pmid: [24958851](#)
48. J. Castro *et al.*, Functional recovery with recombinant human IGF1 treatment in a mouse model of Rett Syndrome. *Proc. Natl. Acad. Sci. U.S.A.* **111**, 9941–9946 (2014). doi: [10.1073/pnas.1311685111](#); pmid: [24958891](#)
49. S. Ricciardi *et al.*, Reduced AKT/mTOR signaling and protein synthesis dysregulation in a Rett syndrome animal model. *Hum. Mol. Genet.* **20**, 1182–1196 (2011). doi: [10.1093/hmg/ddq563](#); pmid: [21212100](#)
50. M. C. Marchetto *et al.*, A model for neural development and treatment of Rett syndrome using human induced pluripotent stem cells. *Cell* **143**, 527–539 (2010). doi: [10.1016/j.cell.2010.10.016](#); pmid: [21074045](#)
51. Y. Li *et al.*, Global transcriptional and translational repression in human-embryonic-stem-cell-derived Rett syndrome neurons. *Cell Stem Cell* **13**, 446–458 (2013). doi: [10.1016/j.stem.2013.09.001](#); pmid: [24094325](#)
52. O. S. Khwaja *et al.*, Safety, pharmacokinetics, and preliminary assessment of efficacy of mecamsermin (recombinant human IGF-1) for the treatment of Rett syndrome. *Proc. Natl. Acad. Sci. U.S.A.* **111**, 4596–4601 (2014). doi: [10.1073/pnas.1311411111](#); pmid: [24623853](#)
53. A. Shcheglovitov *et al.*, SHANK3 and IGF1 restore synaptic deficits in neurons from 22q13 deletion syndrome patients. *Nature* **503**, 267–271 (2013). pmid: [24132240](#)
54. O. Bozdagi, T. Tavassoli, J. D. Buxbaum, Insulin-like growth factor-1 rescues synaptic and motor deficits in a mouse model of autism and developmental delay. *Mol. Autism* **4**, 9 (2013). doi: [10.1186/2040-2392-4-9](#); pmid: [23621888](#)
55. A. Bhattacharya *et al.*, Genetic removal of p70 S6 kinase 1 corrects molecular, synaptic, and behavioral phenotypes in fragile X syndrome mice. *Neuron* **76**, 325–337 (2012). doi: [10.1016/j.neuron.2012.07.022](#); pmid: [23083736](#)
56. T. Udagawa *et al.*, Genetic and acute CPEB1 depletion ameliorate fragile X pathophysiology. *Nat. Med.* **19**, 1473–1477 (2013). doi: [10.1038/nm.3353](#); pmid: [24141422](#)
57. C. Gross *et al.*, Selective role of the catalytic PI3K subunit p110 β in impaired higher order cognition in fragile X syndrome. *Cell Rep.* **11**, 681–688 (2015). doi: [10.1016/j.celrep.2015.03.065](#); pmid: [25921527](#)
58. C. Gross *et al.*, Increased expression of the PI3K enhancer PIKE mediates deficits in synaptic plasticity and behavior in fragile X syndrome. *Cell Rep.* **11**, 727–736 (2015). doi: [10.1016/j.celrep.2015.03.060](#); pmid: [25921541](#)
59. K. M. Huber, M. S. Kayser, M. F. Bear, Role for rapid dendritic protein synthesis in hippocampal mGluR-dependent long-term depression. *Science* **288**, 1254–1256 (2000). doi: [10.1126/science.288.5469.1254](#); pmid: [10818003](#)
60. K. M. Huber, S. M. Gallagher, S. T. Warren, M. F. Bear, Altered synaptic plasticity in a mouse model of fragile X mental retardation. *Proc. Natl. Acad. Sci. U.S.A.* **99**, 7746–7750 (2002). doi: [10.1073/pnas.122205699](#); pmid: [12032354](#)
61. D. Tian *et al.*, Contribution of mGluR5 to pathophysiology in a mouse model of human chromosome 16p11.2 microdeletion. *Nat. Neurosci.* **18**, 182–184 (2015). doi: [10.1038/nn.3911](#); pmid: [25581360](#)
62. S. J. Baudouin *et al.*, Shared synaptic pathophysiology in syndromic and nonsyndromic rodent models of autism. *Science* **338**, 128–132 (2012). doi: [10.1126/science.1224159](#); pmid: [22983708](#)
63. A. A. Scott-Van Zeeland *et al.*, Altered functional connectivity in frontal lobe circuits is associated with variation in the autism risk gene CNTNAP2. *Sci. Transl. Med.* **2**, 56ra80 (2010). doi: [10.1126/scitranslmed.3001344](#); pmid: [21048216](#)
64. J. M. Peters *et al.*, Loss of white matter microstructural integrity is associated with adverse neurological outcome in tuberous sclerosis complex. *Acad. Radiol.* **19**, 17–25 (2012). doi: [10.1016/j.acra.2011.08.016](#); pmid: [22142677](#)
65. A. J. Willsey *et al.*, Coexpression networks implicate human midfetal deep cortical projection neurons in the pathogenesis of autism. *Cell* **155**, 997–1007 (2013). doi: [10.1016/j.cell.2013.10.020](#); pmid: [24267886](#)
66. N. N. Parikshak *et al.*, Integrative functional genomic analyses implicate specific molecular pathways and circuits in autism. *Cell* **155**, 1008–1021 (2013). doi: [10.1016/j.cell.2013.10.031](#); pmid: [24267887](#)
67. N. Gogolla *et al.*, Common circuit defect of excitatory-inhibitory balance in mouse models of autism. *J. Neurodev. Disord.* **1**, 172–181 (2009). doi: [10.1007/s11689-009-9023-x](#); pmid: [20664807](#)
68. M. Wöhr *et al.*, Lack of parvalbumin in mice leads to behavioral deficits relevant to all human autism core symptoms and related neural morphofunctional abnormalities. *Transl. Psychiatry* **5**, e525 (2015). doi: [10.1038/tp.2015.19](#); pmid: [25756808](#)
69. Y. A. Lawrence, T. L. Kemper, M. L. Bauman, G. J. Blatt, Parvalbumin-, calbindin-, and calretinin-immunoreactive hippocampal interneuron density in autism. *Acta Neurol. Scand.* **121**, 99–108 (2010). doi: [10.1111/j.1600-0404.2009.01234.x](#); pmid: [19719810](#)
70. D. Vogt, K. K. Cho, A. T. Lee, V. S. Sohal, J. L. Rubenstein, The parvalbumin/somatostatin ratio is increased in Pten mutant mice and by human PTEN ASD alleles. *Cell Rep.* **11**, 944–956 (2015). doi: [10.1016/j.celrep.2015.04.019](#); pmid: [25937288](#)
71. D. Goffin, E. S. Brodtkin, J. A. Blendy, S. J. Siegel, Z. Zhou, Cellular origins of auditory event-related potential deficits in Rett syndrome. *Nat. Neurosci.* **17**, 804–806 (2014). doi: [10.1038/nn.3710](#); pmid: [24777420](#)
72. H. T. Chao *et al.*, Dysfunction in GABA signalling mediates autism-like stereotypies and Rett syndrome phenotypes. *Nature* **468**, 263–269 (2010). doi: [10.1038/nature09582](#); pmid: [21068835](#)
73. J. L. Rubenstein, M. M. Merzenich, Model of autism: Increased ratio of excitation/inhibition in key neural systems. *Genes Brain Behav.* **2**, 255–267 (2003). doi: [10.1034/j.1601-183X.2003.00037.x](#); pmid: [14606691](#)
74. G. Calfa, W. Li, J. M. Rutherford, L. Pozzo-Miller, Excitation/inhibition imbalance and impaired synaptic inhibition in hippocampal area CA3 of Mecp2 knockout mice. *Hippocampus* **25**, 159–168 (2015). doi: [10.1002/hipo.22360](#); pmid: [25209930](#)
75. V. S. Dani *et al.*, Reduced cortical activity due to a shift in the balance between excitation and inhibition in a mouse model of Rett syndrome. *Proc. Natl. Acad. Sci. U.S.A.* **102**, 12560–12565 (2005). doi: [10.1073/pnas.0506071102](#); pmid: [16116096](#)
76. H. T. Chao, H. Y. Zoghbi, C. Rosenmund, MeCP2 controls excitatory synaptic strength by regulating glutamatergic synapse number. *Neuron* **56**, 58–65 (2007). doi: [10.1016/j.neuron.2007.08.018](#); pmid: [17920015](#)
77. L. Wood, N. W. Gray, Z. Zhou, M. E. Greenberg, G. M. Shepherd, Synaptic circuit abnormalities of motor-frontal layer 2/3 pyramidal neurons in an RNA interference model of methyl-CpG-binding protein 2 deficiency. *J. Neurosci.* **29**, 12440–12448 (2009). doi: [10.1523/JNEUROSCI.3321-09.2009](#); pmid: [19812320](#)
78. Y. Ben-Ari, J. L. Gaiares, R. Tyzio, R. Khazipov, GABA: A pioneer transmitter that excites immature neurons and generates primitive oscillations. *Physiol. Rev.* **87**, 1215–1284 (2007). doi: [10.1152/physrev.00017.2006](#); pmid: [17928584](#)
79. J. Blundell *et al.*, Neuroligin-1 deletion results in impaired spatial memory and increased repetitive behavior. *J. Neurosci.* **30**, 2115–2129 (2010). doi: [10.1523/JNEUROSCI.4517-09.2010](#); pmid: [20147539](#)
80. P. E. Rothwell *et al.*, Autism-associated neuroligin-3 mutations commonly impair striatal circuits to boost repetitive behaviors. *Cell* **158**, 198–212 (2014). doi: [10.1016/j.cell.2014.04.045](#); pmid: [24995986](#)
81. J. Peça *et al.*, Shank3 mutant mice display autistic-like behaviours and striatal dysfunction. *Nature* **472**, 437–442 (2011). doi: [10.1038/nature09965](#); pmid: [21423165](#)
82. M. L. Bauman, T. L. Kemper, Neuroanatomic observations of the brain in autism: A review and future directions. *Int. J. Dev. Neurosci.* **23**, 183–187 (2005). doi: [10.1016/j.jdeveu.2004.09.006](#); pmid: [15749244](#)
83. M. F. Casanova, The neuropathology of autism. *Brain Pathol.* **17**, 422–433 (2007). doi: [10.1111/j.1750-3639.2007.00100.x](#); pmid: [17919128](#)
84. S. H. Fatemi *et al.*, Consensus paper: Pathological role of the cerebellum in autism. *Cerebellum* **11**, 777–807 (2012). pmid: [22370873](#)
85. E. R. Whitney, T. L. Kemper, M. L. Bauman, D. L. Rosene, G. J. Blatt, Cerebellar Purkinje cells are reduced in a subpopulation of autistic brains: A stereological experiment using calbindin-D28k. *Cerebellum* **7**, 406–416 (2008). doi: [10.1007/s12311-008-0043-y](#); pmid: [18587625](#)
86. E. Courchesne, R. Yeung-Courchesne, G. A. Press, J. R. Hesselink, T. L. Jernigan, Hypoplasia of cerebellar vermal lobules VI and VII in autism. *N. Engl. J. Med.* **318**, 1349–1354 (1988). doi: [10.1056/NEJM198805263182102](#); pmid: [3367935](#)
87. D. G. Amaral, C. M. Schumann, C. W. Nordahl, Neuroanatomy of autism. *Trends Neurosci.* **31**, 137–145 (2008). doi: [10.1016/j.tins.2007.12.005](#); pmid: [18258309](#)
88. W. R. Kates *et al.*, Neuroanatomic variation in monozygotic twin pairs discordant for the narrow phenotype for autism. *Am. J. Psychiatry* **161**, 539–546 (2004). doi: [10.1176/appi.app.161.3.539](#); pmid: [14992981](#)
89. N. Akshoomoff *et al.*, Outcome classification of preschool children with autism spectrum disorders using MRI brain measures. *J. Am. Acad. Child Adolesc. Psychiatry* **43**, 349–357 (2004). doi: [10.1097/00004583-200403000-00018](#); pmid: [15076269](#)
90. G. Allen, E. Courchesne, Differential effects of developmental cerebellar abnormality on cognitive and motor functions in the cerebellum: An fMRI study of autism. *Am. J. Psychiatry* **160**, 262–273 (2003). doi: [10.1176/appi.app.160.2.262](#); pmid: [12562572](#)
91. E. Asano *et al.*, Autism in tuberous sclerosis complex is related to both cortical and subcortical dysfunction. *Neurology* **57**, 1269–1277 (2001). doi: [10.1212/WNL.57.7.1269](#); pmid: [11591847](#)
92. R. M. Reith *et al.*, Loss of Tsc2 in Purkinje cells is associated with autistic-like behavior in a mouse model of tuberous sclerosis complex. *Neurobiol. Dis.* **51**, 93–103 (2013). doi: [10.1016/j.nbd.2012.10.014](#); pmid: [23123587](#)

93. P. T. Tsai *et al.*, Autistic-like behaviour and cerebellar dysfunction in Purkinje cell Tsc1 mutant mice. *Nature* **488**, 647–651 (2012). doi: [10.1038/nature11310](https://doi.org/10.1038/nature11310); pmid: [22763451](https://pubmed.ncbi.nlm.nih.gov/22763451/)
94. A. V. Molofsky *et al.*, Astrocytes and disease: A neurodevelopmental perspective. *Genes Dev.* **26**, 891–907 (2012). doi: [10.1101/gad.188326.112](https://doi.org/10.1101/gad.188326.112); pmid: [22549954](https://pubmed.ncbi.nlm.nih.gov/22549954/)
95. C. Eroglu, B. A. Barres, Regulation of synaptic connectivity by glia. *Nature* **468**, 223–231 (2010). doi: [10.1038/nature09612](https://doi.org/10.1038/nature09612); pmid: [21068831](https://pubmed.ncbi.nlm.nih.gov/21068831/)
96. J. Schummers, H. Yu, M. Sur, Tuned responses of astrocytes and their influence on hemodynamic signals in the visual cortex. *Science* **320**, 1638–1643 (2008). doi: [10.1126/science.1156120](https://doi.org/10.1126/science.1156120); pmid: [18566287](https://pubmed.ncbi.nlm.nih.gov/18566287/)
97. N. Chen *et al.*, Nucleus basalis-enabled stimulus-specific plasticity in the visual cortex is mediated by astrocytes. *Proc. Natl. Acad. Sci. U.S.A.* **109**, E2832–E2841 (2012). doi: [10.1073/pnas.1206557109](https://doi.org/10.1073/pnas.1206557109); pmid: [23012414](https://pubmed.ncbi.nlm.nih.gov/23012414/)
98. P. G. Haydon, M. Nedergaard, How do astrocytes participate in neural plasticity? *Cold Spring Harb. Perspect. Biol.* **7**, a020438 (2015). doi: [10.1101/cshperspect.a020438](https://doi.org/10.1101/cshperspect.a020438); pmid: [25502516](https://pubmed.ncbi.nlm.nih.gov/25502516/)
99. D. H. Yasui *et al.*, MeCP2 modulates gene expression pathways in astrocytes. *Mol. Autism* **4**, 3 (2013). doi: [10.1186/2040-2392-4-3](https://doi.org/10.1186/2040-2392-4-3); pmid: [23351786](https://pubmed.ncbi.nlm.nih.gov/23351786/)
100. H. Higashimori *et al.*, Astroglial FMRP-dependent translational down-regulation of mGluR5 underlies glutamate transporter GLT1 dysregulation in the fragile X mouse. *Hum. Mol. Genet.* **22**, 2041–2054 (2013). doi: [10.1093/hmg/ddt055](https://doi.org/10.1093/hmg/ddt055); pmid: [23396537](https://pubmed.ncbi.nlm.nih.gov/23396537/)
101. D. T. Lioy *et al.*, A role for glia in the progression of Rett's syndrome. *Nature* **475**, 497–500 (2011). doi: [10.1038/nature10214](https://doi.org/10.1038/nature10214); pmid: [21716289](https://pubmed.ncbi.nlm.nih.gov/21716289/)
102. A. L. Xavier, J. R. Menezes, S. A. Goldman, M. Nedergaard, Fine-tuning the central nervous system: Microglial modelling of cells and synapses. *Philos. Trans. R. Soc. London B Biol. Sci.* **369**, 20130593 (2014). doi: [10.1098/rstb.2013.0593](https://doi.org/10.1098/rstb.2013.0593); pmid: [25225087](https://pubmed.ncbi.nlm.nih.gov/25225087/)
103. D. P. Schafer, E. K. Lehrman, B. Stevens, The “quad-partite” synapse: Microglia-synapse interactions in the developing and mature CNS. *Glia* **61**, 24–36 (2013). doi: [10.1002/glia.22389](https://doi.org/10.1002/glia.22389); pmid: [22829357](https://pubmed.ncbi.nlm.nih.gov/22829357/)
104. N. C. Derecki *et al.*, Wild-type microglia arrest pathology in a mouse model of Rett syndrome. *Nature* **484**, 105–109 (2012). doi: [10.1038/nature10907](https://doi.org/10.1038/nature10907); pmid: [22425995](https://pubmed.ncbi.nlm.nih.gov/22425995/)
105. J. Wang *et al.*, Wild-type microglia do not reverse pathology in mouse models of Rett syndrome. *Nature* **521**, E1–E4 (2015). doi: [10.1038/nature14444](https://doi.org/10.1038/nature14444); pmid: [25993969](https://pubmed.ncbi.nlm.nih.gov/25993969/)
106. B. D. Auerbach, E. K. Osterweil, M. F. Bear, Mutations causing syndromic autism define an axis of synaptic pathophysiology. *Nature* **480**, 63–68 (2011). doi: [10.1038/nature10658](https://doi.org/10.1038/nature10658); pmid: [22113615](https://pubmed.ncbi.nlm.nih.gov/22113615/)
107. J. Guy, J. Gan, J. Selfridge, S. Cobb, A. Bird, Reversal of neurological defects in a mouse model of Rett syndrome. *Science* **315**, 1143–1147 (2007). doi: [10.1126/science.11728994](https://doi.org/10.1126/science.11728994); pmid: [17289941](https://pubmed.ncbi.nlm.nih.gov/17289941/)
108. A. Michalon *et al.*, Chronic pharmacological mGlu5 inhibition corrects fragile X in adult mice. *Neuron* **74**, 49–56 (2012). doi: [10.1016/j.neuron.2012.03.009](https://doi.org/10.1016/j.neuron.2012.03.009); pmid: [22500629](https://pubmed.ncbi.nlm.nih.gov/22500629/)
109. D. Ehninger *et al.*, Reversal of learning deficits in a Tsc2+/- mouse model of tuberous sclerosis. *Nat. Med.* **14**, 843–848 (2008). doi: [10.1038/nm1788](https://doi.org/10.1038/nm1788); pmid: [18568033](https://pubmed.ncbi.nlm.nih.gov/18568033/)
110. D. D. Krueger, M. F. Bear, Toward fulfilling the promise of molecular medicine in fragile X syndrome. *Annu. Rev. Med.* **62**, 411–429 (2011). doi: [10.1146/annurev-med-061109-134644](https://doi.org/10.1146/annurev-med-061109-134644); pmid: [21090964](https://pubmed.ncbi.nlm.nih.gov/21090964/)
111. S. H. Scharf, G. Jaeschke, J. G. Wettstein, L. Lindemann, Metabotropic glutamate receptor 5 as drug target for Fragile X syndrome. *Curr. Opin. Pharmacol.* **20**, 124–134 (2015). doi: [10.1016/j.coph.2014.11.004](https://doi.org/10.1016/j.coph.2014.11.004); pmid: [25488569](https://pubmed.ncbi.nlm.nih.gov/25488569/)
112. J. L. Silverman, M. Yang, C. Lord, J. N. Crawley, Behavioural phenotyping assays for mouse models of autism. *Nat. Rev. Neurosci.* **11**, 490–502 (2010). doi: [10.1038/nrn2851](https://doi.org/10.1038/nrn2851); pmid: [20559336](https://pubmed.ncbi.nlm.nih.gov/20559336/)
113. B. C. Reeb-Sutherland, N. A. Fox, Eyeblink conditioning: A non-invasive biomarker for neurodevelopmental disorders. *J. Autism Dev. Disord.* **45**, 376–394 (2015). doi: [10.1007/s10803-013-1905-9](https://doi.org/10.1007/s10803-013-1905-9); pmid: [23942847](https://pubmed.ncbi.nlm.nih.gov/23942847/)
114. M. J. Gandal *et al.*, Validating γ oscillations and delayed auditory responses as translational biomarkers of autism. *Biol. Psychiatry* **68**, 1100–1106 (2010). doi: [10.1016/j.biopsych.2010.09.031](https://doi.org/10.1016/j.biopsych.2010.09.031); pmid: [21130222](https://pubmed.ncbi.nlm.nih.gov/21130222/)
115. S. Durand *et al.*, NMDA receptor regulation prevents regression of visual cortical function in the absence of MeCP2. *Neuron* **76**, 1078–1090 (2012). doi: [10.1016/j.neuron.2012.12.004](https://doi.org/10.1016/j.neuron.2012.12.004); pmid: [23259945](https://pubmed.ncbi.nlm.nih.gov/23259945/)
116. M. Kondo *et al.*, Environmental enrichment ameliorates a motor coordination deficit in a mouse model of Rett syndrome—MeCP2 gene dosage effects and BDNF expression. *Eur. J. Neurosci.* **27**, 3342–3350 (2008). doi: [10.1111/j.1460-9568.2008.06305.x](https://doi.org/10.1111/j.1460-9568.2008.06305.x); pmid: [18557922](https://pubmed.ncbi.nlm.nih.gov/18557922/)
117. L. Restivo *et al.*, Enriched environment promotes behavioral and morphological recovery in a mouse model for the fragile X syndrome. *Proc. Natl. Acad. Sci. U.S.A.* **102**, 11557–11562 (2005). doi: [10.1073/pnas.0504984102](https://doi.org/10.1073/pnas.0504984102); pmid: [16076950](https://pubmed.ncbi.nlm.nih.gov/16076950/)
118. S. L. Fyffe *et al.*, Deletion of MeCP2 in Sim1-expressing neurons reveals a critical role for MeCP2 in feeding behavior, aggression, and the response to stress. *Neuron* **59**, 947–958 (2008). doi: [10.1016/j.neuron.2008.07.030](https://doi.org/10.1016/j.neuron.2008.07.030); pmid: [18817733](https://pubmed.ncbi.nlm.nih.gov/18817733/)

ACKNOWLEDGMENTS

We thank R. Kleiman, A. Poduri, and K. Dies for critically reviewing the manuscript. Due to limited space, we have not quoted all literature in the field, and we apologize to those whose articles are not referenced. Research in M. Sur's laboratory is supported by NIH grants MH085802, NS090473, and EY007023; NSF grant EF1451125; and the Simons Foundation Autism Research Initiative. Research in M. Sahin's laboratory is supported by the NIH (U01 NS082320, P20 NS080199, and P30 HD018655), Department of Defense (W81XWH-13-1-0040), Tuberous Sclerosis Alliance, Autism Speaks, Nancy Lurie Marks Family Foundation, Simons Foundation, Boston Children's Hospital Translational Research Program, and Novartis and Shire. The Developmental Synaptopathies Consortium (U54NS092090) is a part of the National Center for Advancing Translational Sciences (NCATS) Rare Diseases Clinical Research Network (RDCRN). RDCRN is an initiative of the Office of Rare Diseases Research (ORDR), NCATS, funded through collaboration between NCATS, NIMH, the National Institute of Neurological Disorders and Stroke, and the Eunice Kennedy Shriver National Institute of Child Health and Human Development.

10.1126/science.aab3897

RESEARCH ARTICLE SUMMARY

STEM CELL REGULATION

Bidirectional Notch signaling regulates *Drosophila* intestinal stem cell multipotency

Zheng Guo and Benjamin Ohlstein*

INTRODUCTION: In the *Drosophila* adult midgut, multipotent intestinal stem cells (ISCs) produce two types of daughter cells: nutrient-absorbing enterocytes (ECs) and secretory enteroendocrine (ee) cells. Notch signaling between ISCs and their daughters directs the proper specification of both of these cell types. Previous work suggests that ISCs expressing high levels of the Notch ligand Delta (DI) strongly activate the Notch signaling pathway in their daughters and result in their differentiation into ECs. By contrast, ISCs that express low levels of DI direct their daughters to become ee cells. However, in this unidirectional Notch signaling model, the mechanisms regulating differential DI expression in ISCs are poorly understood.

RATIONALE: During *Drosophila* pupal midgut development, pupal ISCs only make ee cells. Therefore, we examined how ee cells are made and evaluated the role of Notch signaling function during this developmental time window. On the basis of insights obtained from pupal development, we also asked whether similar mechanisms were used by ISCs in the adult midgut to generate ee cells.

RESULTS: The ee cell fate marker Prospero (Pros) appeared in pupal ISCs at 44 hours after pupal formation (APF). From 44 to 96 hours APF, ISCs first divided asymmetrically, generating one ISC and one ee cell, followed by symmetric division of both ISCs and ee cells, resulting in a pair of ISCs and a pair of ee cells. During ISC asymmetric divisions, Pros was asymmetrically segregated to the basal daughter cell, a process that depended on the function of the Par complex. After ISC asymmetric division, the ee daughter cell expressed the Notch ligand DI and activated the Notch signaling pathway in ISCs. Loss of Notch signaling in pupal ISCs induced all stem cells to differentiate into ee cells, whereas low-level activation of Notch signaling in pupal ISCs blocked ee cell formation. During ee symmetric divisions, Pros distribution was symmetric; however, cell polarity and Notch signaling remained asymmetric. Loss of Notch signaling between progeny of ee symmetric divisions disrupted expression of peptide hormones in ee cells, indicating a role for Notch signaling in proper ee specification. We also investigated the Notch pathway in adult ISCs and confirmed that postmitotic Notch signaling from ee daughter cells also regulates ISC multipotency.

CONCLUSION: Consistent with previous work, high levels of DI in ISCs activate high levels of Notch in the daughter cell, promoting EC differentiation. In contrast, after asymmetric localization of Pros, ISCs require a low Notch signal from their immediate ee cell

ON OUR WEB SITE

Read the full article at <http://dx.doi.org/10.1126/science.aab0988>

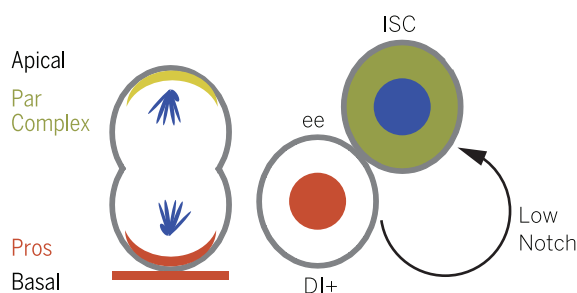
daughters to maintain multipotency. Thus, Notch signaling is both bidirectional and context-dependent. Previous work also has suggested that ISCs remain basal during EC formation

and that basal ISCs activate the Notch pathway in daughter cells. Our data show that ISCs are apically located during ee cell formation and that basal ee cells activate the Notch pathway in ISCs. Therefore, Notch signaling is always unidirectional in terms of polarity: Basal daughter cells express the Notch ligand DI in order to activate the Notch signaling pathway in daughters after asymmetric ISC divisions.

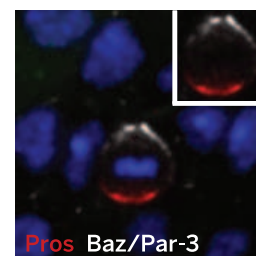
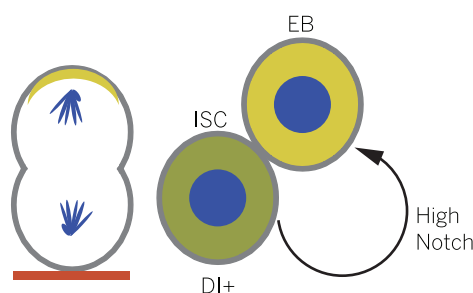
Our work provides further evidence that mechanisms regulating tissue homeostasis are more conserved between the *Drosophila* and mammalian intestine than previously thought. Inhibition of Notch signaling in the mouse intestine induces crypt base columnar stem cell loss and secretory cell hyperplasia, and ectopic Notch signaling promotes EC differentiation. Loss of Notch signaling in *Drosophila* ISCs also leads to stem cell loss and premature ee cell formation, whereas high Notch signaling promotes stem cell differentiation into ECs. Because Notch signaling also plays important roles in common lymphoid progenitors making B cells and T cells, and in airway basal cells making secretory cells and ciliated cells, it is tempting to speculate that bidirectional Notch signaling may regulate multipotency in these and other progenitors and stem cells. ■

The list of author affiliations is available in the full article online.
*Corresponding author. E-mail: bo2160@columbia.edu
Cite this article as Z. Guo, B. Ohlstein, *Science* 350, aab0988 (2015). DOI: 10.1126/science.aab0988

ee cell formation:



EC formation:



Bidirectional Notch signaling and unidirectional polarity. Left: During enteroendocrine cell (ee) formation, the Par complex induces asymmetric segregation of Prospero (Pros), and the Notch signaling ligand Delta (DI) is expressed in a basal Pros⁺ ee. Low Notch signaling from a basal ee to an intestinal stem cell (ISC) maintains ISC identity. Right: During enterocyte (EC) production, strong Notch signaling from a basal ISC to an enteroblast (EB) promotes EC differentiation.

RESEARCH ARTICLE

STEM CELL REGULATION

Bidirectional Notch signaling regulates *Drosophila* intestinal stem cell multipotency

Zheng Guo and Benjamin Ohlstein*

Drosophila intestinal stem cells (ISCs) generate enterocytes (ECs) and enteroendocrine (ee) cells. Previous work suggests that different levels of the Notch ligand Delta (DI) in ISCs unidirectionally activate Notch in daughters to control multipotency. However, the mechanisms driving different outcomes remain unknown. We found that during ee cell formation, the ee cell marker Prospero localizes to the basal side of dividing ISCs. After asymmetric division, the ee daughter cell acts as a source of DI that induces low Notch activity in the ISC to maintain identity. Alternatively, ISCs expressing DI induce high Notch activity in daughter cells to promote EC formation. Our data reveal a conserved role for Notch in *Drosophila* and mammalian ISC maintenance and suggest that bidirectional Notch signaling may regulate multipotency in other systems.

The *Drosophila* midgut is maintained by multipotent intestinal stem cells (ISCs) that give rise to either absorptive enterocytes (ECs) or hormone-producing enteroendocrine (ee) cells (1, 2). ISCs orchestrate the proper developmental and regenerative ratios of differentiated cell types. However, the mechanisms that control multipotency of ISCs remain an enigma. Previous work (3) suggested that high levels of the contact-dependent Notch signaling pathway ligand Delta (DI) in ISCs drive high levels of Notch activity in the daughter cell, resulting in EC formation, whereas low levels of DI in ISCs drive low levels of Notch activity in the daughter cell, resulting in ee cell formation (fig. S1A). How the ISC achieves differential DI expression remains unknown.

ISC asymmetric divisions specify ee cells

During pupation, ISCs only give rise to ee cells, providing a unique platform to explore Notch signaling in multipotency decision (4, 5). To identify the time during which Notch signaling may be required, we first characterized the generation of pupal ISCs and ee cells. The progenitor driver *esg-Gal4* (1), driving *UAS-GFP* [green fluorescent protein (*esg>GFP*)], and the ee cell marker Prospero [Pros (1, 2)] were used to quantify wild-type ISC and ee cell numbers between 24 and 96 hours after pupal formation (APF) (Fig. 1A). Punctate Pros staining was first detectable in the anterior midgut at 44 hours APF (Fig. 1, B and B'); by 54 hours APF, Pros was present in the entire intestine (fig. S1B). At 44 hours APF, ISC number was almost 600. From 44 to 54 hours APF, ISC number (GFP⁺, Pros⁺) dipped to ~270,

followed by an increase to ~1200 (green line, Fig. 1A) by 96 hours APF. From 44 to 96 hours APF, Pros⁺ cell number increased from 0 to ~1200 (red line, Fig. 1A), resulting in a total of 2400 cells by the end of pupation at 96 hours APF (blue line, Fig. 1A).

To determine how ~600 ISCs amplify by a factor of 4 to give rise to an equal ratio of ISCs and ee cells during this time, we induced wild-type MARCM (mosaic analysis with repressible cell marker) clones (6) at different time points during pupal development and quantified the cellular composition of clones at 96 hours APF (Fig. 1, C and E). Using the MARCM system, homozygous clones become positively labeled with GFP after flippase-catalyzed recombination. When clones were induced at 36 hours APF, 61.2% of them (*n* = 96) were four-cell clones containing two ISCs and two Pros⁺ ee cells (Fig. 1, D and D', and fig. S1C). When clones were induced at 48 hours APF, 67.1% of clones (*n* = 137) contained two cells (fig. S1D), with 43% containing two ISCs (Fig. 1, F and F') and 57% containing two ee cells (Fig. 1, G and G'). These data suggest that from 44 to 96 hours APF, ISCs first divide asymmetrically, generating one ISC and one ee cell, followed by symmetric division of both ISCs and ee cells, resulting in a pair of ISCs and a pair of ee cells (Fig. 1C).

To further investigate pupal ISC and ee cell division order and outcomes, we induced wild-type MARCM clones at 30 hours APF and examined the cellular composition of clones at 56 hours APF (fig. S1F). We found that 63.5% of clones (*n* = 52) were two-cell clones containing one ISC and one Pros⁺ ee cell (fig. S1, E to H). An additional 13.5% of clones were three-cell clones containing one ISC and two Pros⁺ ee cells (fig. S1, E, F, I, and J). These data confirmed that the first ISC division was asymmetric and suggested that ee cells symmetrically divide prior to the initiation of ISC symmetric divisions.

After identifying the time period during which ee cells are generated, we next sought to determine the mechanism by which an asymmetric outcome of the initial ISC division is achieved to give rise to an ee daughter. From 44 to 56 hours APF, Pros asymmetrically localized to the basal side of dividing ISCs (Fig. 1, H to N, and fig. S1, L to P). Asymmetric Pros distribution began at prometaphase (Fig. 1H) (*n* = 50), generated a basal crescent pattern during metaphase and anaphase (Fig. 1, I to K) (*n* = 200), and localized into the basal cell nucleus during cytokinesis (Fig. 1N) (*n* = 100). During anaphase and telophase, the original apical daughter cell extended a basal protrusion whose presence correlated with its movement toward a basal position (Fig. 1, J to N, and fig. S1K) (*n* = 50). At the end of the asymmetric division, both daughter cells were basally located (Fig. 1N) (*n* = 100).

In *Drosophila* neuroblasts (NBs), the Par complex supplies an apical cue establishing apical-basal (A-B) polarity to ensure asymmetric segregation of Miranda (Mira) into the basal cell (7–9). Mira functions as an adaptor protein that binds Pros and forms a crescent that is basally localized in mitotic cells (10–14). After asymmetric division, Mira is degraded, releasing Pros from the basal cell membrane and allowing Pros to translocate into the nucleus (10, 11, 15–18). By using antibodies to Mira and Bazooka (Baz; the homolog of Par-3 and a core component of the Par complex), we found that Mira colocalized with Pros during ISC asymmetric divisions (Fig. 2, A and B, and fig. S2, A and B). By contrast, Baz localized to an apical crescent, which was mutually exclusive with Pros staining during ISC asymmetric divisions (Fig. 2, C and D, and fig. S2, C to E). To disrupt A-B polarity, we used the temperature-inducible progenitor cell driver *esg-Gal4 tub-Gal80^{ts}* (*esg^{ts}*) (1) to drive RNA interference (RNAi) against *baz*, and transferred animals to the permissive temperature (30°C) from 24 to 48 hours APF (see supplementary materials for experimental details of how developmental milestones at 18°C and 30°C were normalized to pupal development at 25°C). Whereas we observed asymmetric localization of Pros in wild-type ISCs, knockdown of Baz resulted in the even distribution of Pros on cell membranes during mitosis (Fig. 2, E and F). In addition to its role in segregating proteins to the basal membrane during NB divisions, Baz controls mitotic spindle orientation (7, 8, 19). We quantified wild-type (*esg>GFP*) and *esg^{ts}>baz* RNAi ISC metaphase spindle orientation by measuring the angle formed between the basal cell membrane and dividing spindles (Fig. 2, G and H, and fig. S2, F to J). Whereas wild-type ISC metaphase division angles concentrated around 80° (Fig. 2I), *esg^{ts}>baz* RNAi ISC division angles were randomly spread (Fig. 2J). At 64 hours APF, as a consequence of disrupting Pros asymmetric segregation relative to the wild-type control (Fig. 2K), *esg^{ts}>baz* RNAi intestine contained a cluster of four GFP⁺ cells that were all Pros⁺ (Fig. 2L). To confirm *baz* RNAi results, we generated *baz^Δ* MARCM clones at 24 hours APF and examined them at 92 hours APF. Every

Department of Genetics and Development, Columbia University Medical Center, New York, NY 10032, USA.

*Corresponding author. E-mail: bo2160@columbia.edu

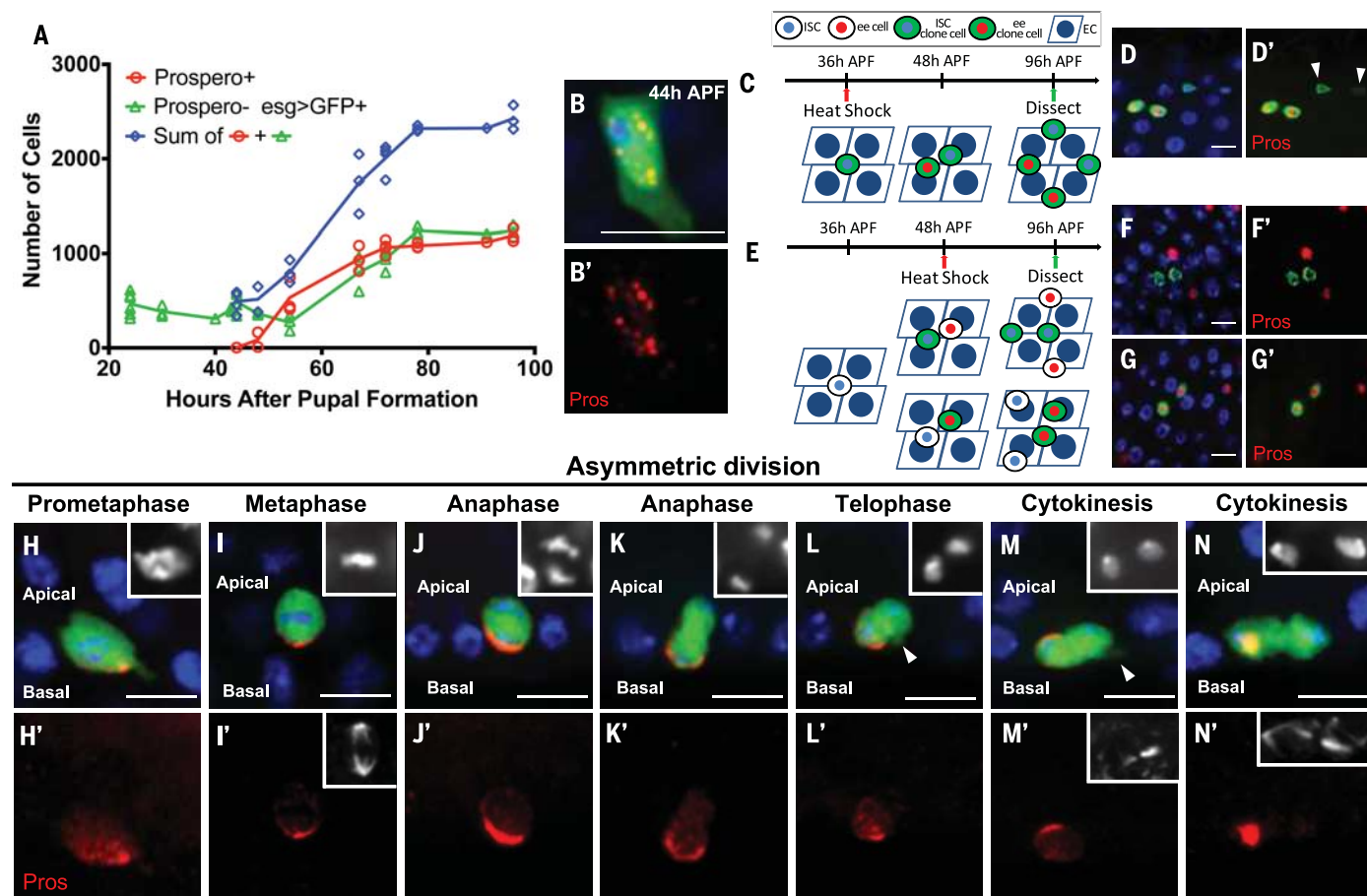


Fig. 1. ee cells are specified by ISCs asymmetric divisions. (A) Numbers of ISCs (Prospero- *esg>GFP*⁺) and ee cells (Prospero⁺) during pupal development. Each data point represents one pupal midgut. Curves were generated by connecting adjacent average value positions. (B) Pros staining at 44 hours APF. Here and in all images, blue indicates 4',6-diamidino-2-phenylindole (DAPI) and red indicates Pros; green indicates *esg>GFP* except where otherwise specified. (C and E) Schematic representation of wild-type MARCM clones and their outcomes induced at 36 hours APF (C) or 48 hours APF (E) and examined

at 96 hours APF. (D) A four-cell clone (green) induced at 36 hours APF contains two Pros⁺ cells and two ISCs [arrowhead in (D')]. (F and G) Two-cell clones induced at 48 hours APF contain either two ISCs (Pros⁻) (F) or two ee cells (Pros⁺) (G). (H to N) Pros asymmetrically localizes to the basal side during ISC mitosis. The apical daughter gradually moves toward the basal side during anaphase [(J) and (K)] and telophase [(L) to (N)]. The apical daughter extends a projection toward the basal side during telophase [arrowhead in (L) and (M)]. Insets in (H) to (N), DAPI; insets in (I'), (M'), and (N'), α -tubulin. Scale bars, 10 μ m.

control wild-type MARCM clone had Pros⁻ ISCs ($n = 128$; Fig. 2M), whereas 45% of *baz*⁴ clones contained only Pros⁺ ee cells ($n = 71$; Fig. 2N). Therefore, asymmetric distribution of Pros by the Par complex is critical for proper ee cell specification and ISC maintenance.

ee cells activate Notch in ISCs

To determine the role of Notch signaling during ISC asymmetric divisions, we stained for expression of D1 and the Notch response element LacZ (*NRE-lacZ*) from 40 to 51 hours APF. At 40 hours APF, D1 was not detectable in ISCs (fig. S3A). However, by 44 hours APF, D1, but not *NRE-lacZ*, was present in ISCs (fig. S3, B and C). At 48 to 51 hours APF, after asymmetric division of ISCs, D1 became localized to Pros⁺ ee daughter cells (Fig. 3A), whereas *NRE-lacZ* staining was present in pupal ISCs (Fig. 3B and fig. S3D). Together, our data demonstrate that ee cells induce Notch activity in pupal ISCs after asymmetric divisions.

To knock down Notch signaling during pupation, we used *esg*^{ts} to drive *UAS-D1* RNAi and transferred animals to the permissive temperature (30°C) from 24 to 92 hours APF (Fig. 3C). Relative to control intestine (Fig. 3D), knockdown of Notch signaling in pupal ISCs led to all *esg*^{ts}>*D1* RNAi; *GFP*⁺ cells expressing Pros at the end of pupation (Fig. 3E and fig. S3E), which suggests that knockdown of Notch signaling during pupal development results in loss of pupal ISCs. We next followed the fate of pupal GFP⁺ cells into adulthood (Fig. 3C). In control *esg*^{ts} intestine, all intestinal progenitors were GFP⁺ (Fig. 3F and fig. S3G) at 3 days after eclosion (AE). By contrast, *esg*^{ts}>*D1* RNAi intestine contained either no GFP⁺ cells (Fig. 3G) or only rare ones (fig. S3F) at 3 days AE. Similar results were obtained using *UAS-Notch* RNAi and *UAS-Notch*^{DN} (a Notch receptor that can bind the ligand D1 but lacks the transcription regulation domain Cdc10) (20) (fig. S3, H and I), which suggests that knockdown of Notch signaling

during pupal development results in loss of ISCs.

In addition, to identify the precise time window in which Notch is required for maintaining stem cell identity, we cultured *esg*^{ts}>*D1* RNAi and *esg*^{ts}>*Notch* RNAi flies at 18°C for various times corresponding to 42, 53, 64, 76, and 87 hours APF at 25°C. Pupae were then transferred to 30°C to permit *esg-Gal4* expression. Intestines were examined before eclosion, as assessed by the appearance of black wings and mature bristles (21) (fig. S4A). At or before 53 hours APF, knockdown of Notch signaling in ISCs resulted in ISC loss (fig. S4, B and C). After 64 hours APF, knockdown of Notch signaling had no effect on ISC maintenance (fig. S4D). Therefore, Notch signaling is required to maintain ISC fate for only a brief period after asymmetric division.

To corroborate the RNAi knockdown results, we generated *Notch*^{55ell} null MARCM clones at 24 hours APF and examined them at 92 hours APF (Fig. 3C). In wild-type MARCM clones, about

Insets, Pros; white, α -tubulin. **(I and J)** Radial histogram quantification of division angles in control (*esg>GFP*) (I) and *esg^{ts>baz} RNAi* (J) metaphase ISCs. **(K)** After 64 hours of APF control (*esg^{ts>baz}>GFP*), the four GFP⁺ cells are two Pros⁺, two Pros⁻. **(L)** Segment of *esg^{ts>baz} RNAi* intestine contains four GFP⁺ cells, all Pros⁺. Hours in (K) and (L) correspond to developmental times at 25°C. **(M and N)** Wild-type MARCM clones (M) and *baz⁴* MARCM clones (N), both shown in green, were induced at 24 hours APF and examined at 92 hours APF. Wild-type MARCM clones contain two Pros⁺ cells (arrowheads) and two Pros⁻ cells (asterisks); all *baz⁴* MARCM clone cells are Pros⁺ (arrowheads). Scale bars, 10 μ m.

Because Notch signaling is asymmetric during specification of EMCs, we next asked whether Notch signaling is also asymmetric during EMC divisions. At 71 hours APF, after EMC division, one daughter in each pair of Pros⁺ cells was Dl⁺ (Fig. 4F and fig. S5E) and one daughter was *NRE-lacZ*⁺ (Fig. 4G and fig. S5, F to H), demonstrating that Notch signaling is asymmetric. To determine

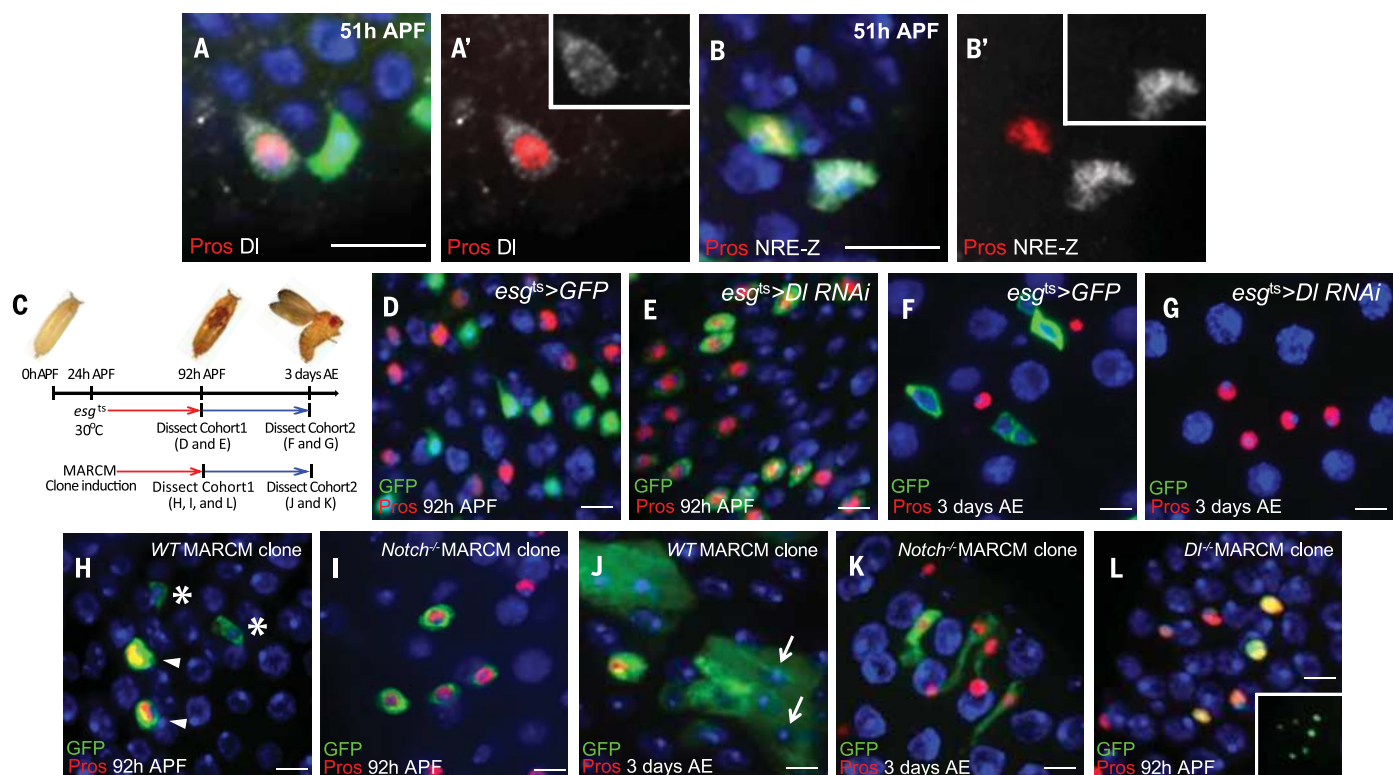


Fig. 3. ee cells induce Notch activity in ISCs to prevent ISCs from differentiating into ee cells during pupal development. Hours correspond to developmental times at 25°C (see supplementary materials for experiment details). (A) DI [inset in (A')] is present in a Pros⁺ cell at 51 hours APF. (B) The Notch signaling reporter *NRE-lacZ* [inset in (B')] is present in a pupal ISC (Pros⁺) at 51 hours APF. (C) Schematic of the genetic manipulations carried out during pupal development. (D and E) Cohort 1: Midguts were examined at 92 hours APF. In control animals (D), strong *esg^{ts}>GFP*⁺ cells are Pros⁺; in *esg^{ts}>DI RNAi* animals (E), all GFP⁺ cells are Pros⁺. (F and G) Cohort 2: Midguts were examined at 3 days AE. In

control animals (F), progenitor cells (ISCs and enteroblasts) are *esg^{ts}>GFP*⁺. (G) In *esg^{ts}>DI RNAi* animals, GFP⁺ cells are absent and all diploid cells are Pros⁺ ee cells. (H and I) Cohort 1: MARCM clones (green) were examined at 92 hours APF. Wild-type clone (H) contains two Pros⁺ cells (arrowheads) and two Pros⁺ cells (asterisks); all Notch mutant clone cells (I) are Pros⁺. (J and K) Cohort 2: MARCM clones were examined at 3 days AE. Wild-type clone (J) contains multiple ECs (arrows); Notch mutant clone (K) contains four Pros⁺ cells (sagittal view). (L) DI mutant MARCM clones were examined at 92 hours APF. All mutant cells are Pros⁺. Inset, clonal marker. Scale bars, 10 μm.

whether asymmetric Notch signaling is functionally relevant, we induced *Notch^{55e11}* clones at 24 hours APF and found that mutant cells at 92 hours APF did not express the hormone DH31 or the neuropeptide motif FMRamide (Fig. 4, H to M). Consistent with this result, culturing *esg^{ts}>DI RNAi* or *esg^{ts}>Notch RNAi* pupae at 30°C before 64 hours APF blocked DH31 expression in ee cells (fig. S4, A to D). Hence, Notch signaling is required by EMC daughters to properly specify ee cell fate.

Two thresholds of Notch signaling

Expression of an activated form of Notch in adult stem cells promotes their differentiation into ECs (1, 3). Consistent with a previous report (5), we found that expression of an activated form of the Notch receptor (*Notch^{intra1790}*; see Fig. 5J) by *esg^{ts}* at 30°C was sufficient to promote differentiation of all pupal ISCs into Pdm1⁺ ECs (Fig. 5, G and H, and fig. S6, H and I) (22). Given that pupal ISCs are *NRE-lacZ*⁺ after asymmetric divisions, we wondered why they did not differentiate into ECs. We noticed after ISC asymmetric division that *NRE-lacZ* staining in ISCs decreased or be-

came absent as pupal development proceeded (fig. S5, F to H), which suggests that (i) endogenous Notch signaling in pupal ISCs is weaker than 30°C misexpression of *Notch^{intra1790}*, and (ii) weak Notch signaling is sufficient to block ee cell differentiation in pupal ISCs but not to induce EC differentiation. Because the level of *Notch^{intra1790}* expression by *esg^{ts}* depends on temperature (23), we created a Notch signaling gradient in pupal ISCs by culturing *esg^{ts}>Notch^{intra1790}* flies at 30°, 27°, 25°, and 18°C (fig. S6, A to G) and examined their intestines before eclosion. Whereas *esg^{ts}>GFP* control intestine contained both ISCs and ee cells, expression of *Notch^{intra1790}* at 30° and 27°C completely blocked ee cell formation (Fig. 5, A, B, C, and F). Pros⁺ cells were also drastically decreased in *esg^{ts}>Notch^{intra1790}* intestine reared at 25°C (Fig. 5, D and F), whereas *esg^{ts}>Notch^{intra1790}* had no effect on ee cell number in animals raised at 18°C (Fig. 5, E and F). Although GFP⁺ ISCs in *esg^{ts}>Notch^{intra1790}* intestine reared at 27°C had enough Notch signaling to block ee cell formation, ISCs did not differentiate into Pdm1⁺ ECs (Fig. 5I). In addition, we ectopically expressed two additional isoforms of the Notch intra-

cellular domain (Fig. 5J) at 30°C. In descending order of transcriptional activation activity, the three *Notch^{intra}* isoforms are *Notch^{intra1790}* > *Notch¹⁷⁹²⁻²¹⁵⁶* > *Notch¹⁸⁹⁵⁻²¹¹⁶* (24). Whereas *Notch¹⁷⁹²⁻²¹⁵⁶* driven by *esg^{ts}* induced all ISCs to differentiate into Pdm1⁺ ECs (Fig. 5K), *esg^{ts}>Notch¹⁸⁹⁵⁻²¹¹⁶* blocked ee cell formation (Fig. 5L) but failed to drive ISC differentiation into ECs (Fig. 5M). These experiments reveal two thresholds of Notch signaling: High Notch signaling promotes EC differentiation, whereas low Notch signaling in ISCs maintains ISCs by preventing their differentiation into ee cells.

Adult ee formation is conserved

To determine whether a similar mechanism is used by adult ISCs to generate ee cells, we counted all Pros⁺ cells that were also positive for the mitotic marker PH3 in *esg>GFP* adult intestine. Similar to previous reports (25–27), 7.9% (44/558) of PH3⁺ cells were Pros⁺. In 27.3% of these cells (12/44), Pros was asymmetrically localized to the basal side of dividing ISCs (Fig. 6, A and A', and fig. S7, A to C, G, and H). In the remaining 72.7% (32/44), Pros was symmetrically

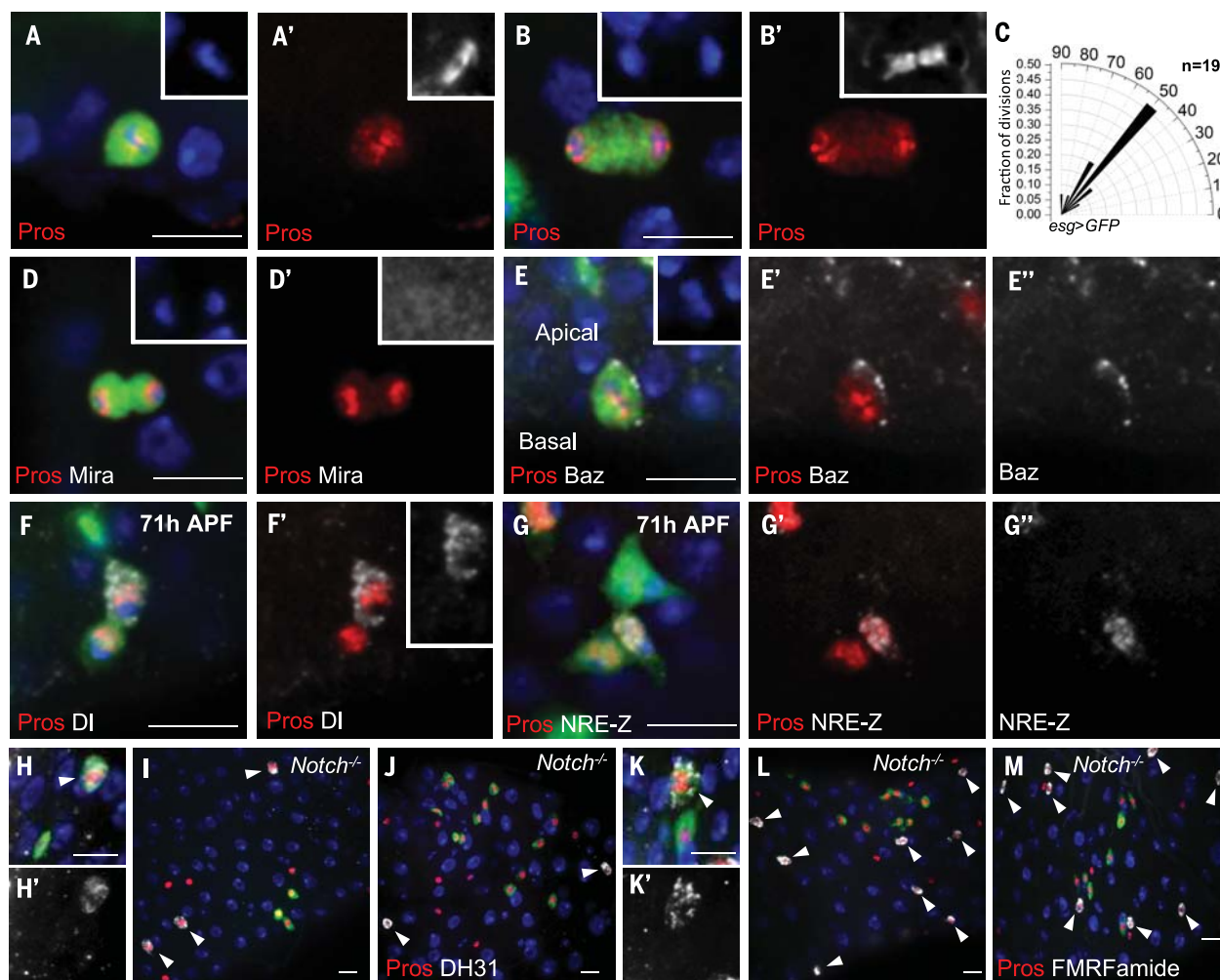


Fig. 4. EMC divisions are symmetric for Prospero distribution but asymmetric for cell polarity and Notch signaling. (A and B) Pros symmetrically localizes to both daughters during EMC metaphase (A) and telophase (B). Insets in (A) and (B), DAPI; insets in (A') and (B'), α -tubulin. (C) Radial histogram quantification of division angles in metaphase of *esg>GFP* EMC mitosis. (D) Mira staining is absent during EMC division. Inset in (D), DAPI; inset in (D'), Mira (enhanced levels). (E) Baz staining (E') localizes as a crescent on the apical cell membrane during EMC metaphase. Inset in (E), DAPI. (F) After EMC division (71 hours APF), strong DI staining [inset in (F')] is present in one of the Pros⁺ pair of cells. (G) After EMC division (71 hours APF), one of the two Pros⁺ cells is *NRE-lacZ*⁺

(G'). (H to M) Wild-type [(H), (H'), (K), and (K')] and Notch mutant [(I), (J), (L), and (M)] MARCM clones were induced at 24 hours APF, and midguts were dissected at 92 hours APF. In (H) and (H'), the peptide hormone DH31 (arrowhead) is present in a wild-type MARCM ee clone cell (green). Red, Pros; white, DH31. In (I) and (J), Notch mutant MARCM clones (green) are Pros⁺ but fail to stain for DH31. Arrowheads denote all DH31⁺ cells (white). [(K) and (K')] The neuropeptide motif FMRamide is present in a wild-type MARCM ee clone cell (green). Red, Pros; white, FMRamide. [(L) and (M)] Notch mutant MARCM clones (green) are Pros⁺ but fail to stain for FMRamide. Arrowheads denote all FMRamide⁺ cells (white). Scale bars, 10 μm.

localized to both daughters (fig. S8), similar to what we observed during pupation (Fig. 4, A and B). We next generated two-cell wild-type MARCM clones containing one ISC and one Pros⁺ ee cell and examined the pattern of DI and *NRE-lacZ* expression. As was the case during pupal development, DI was present in the ee cell but not the ISC (Fig. 6, B and B'). Furthermore, the ISC, but not the ee cell, was *NRE-lacZ*⁺ (Fig. 6, C and C').

In the *Drosophila* adult midgut, the proneural gene *asense* is necessary and sufficient for ee differentiation (27–29). Occasionally, adult ISCs express *Asense* and make ee cells (27–29). To force all adult ISCs to express Pros and generate ee cells, we ectopically expressed *Asense* in adult ISCs. Pros asymmetrically localized in every dividing

ISC within 36 hours after the onset of overexpression (Fig. 6, D and D', and fig. S7, D to F). After asymmetric divisions, DI was present in ee cells (fig. S9A) and ISCs were positive for *NRE-lacZ* (fig. S9B).

To gain further evidence that Notch signaling functions the same way in adult and pupal ISCs during the ee cell-making process, we overexpressed *UAS-asense* and an RNAi against Notch together in adult ISCs by using *esg⁶⁶*. After 8 days, most ISCs were lost (Fig. 6, G and H, and fig. S9, C and D). To demonstrate that lost ISCs differentiated into ee cells, we made *UAS-asense* MARCM clones and *UAS-asense; Df^{ReoF10}* MARCM clones in adults. *UAS-asense* clones always contained one Pros⁺ *NRE-lacZ*⁺ cell, which corresponded to the

ISC (Fig. 6, E and E', and fig. S9, E to G). In *UAS-asense; Df^{ReoF10}* clones, all cells were Pros⁺ (Fig. 6, F and F', and fig. S9, H and I). Moreover, relative to 5 days after clone induction (ACI), *UAS-asense; Df^{ReoF10}* clone number in the posterior midgut was markedly decreased by 10 days ACI (fig. S9, J to L), indicating that ISCs were lost after differentiating into ee cells. Overall, our results demonstrate Notch signaling is required in adult ISCs to maintain stem cell identity during ee cell production.

Discussion

Our findings provide insight into the molecular mechanisms regulating ISC multipotency. Consistent with previous work, high levels of DI in ISCs activate high levels of Notch in the daughter

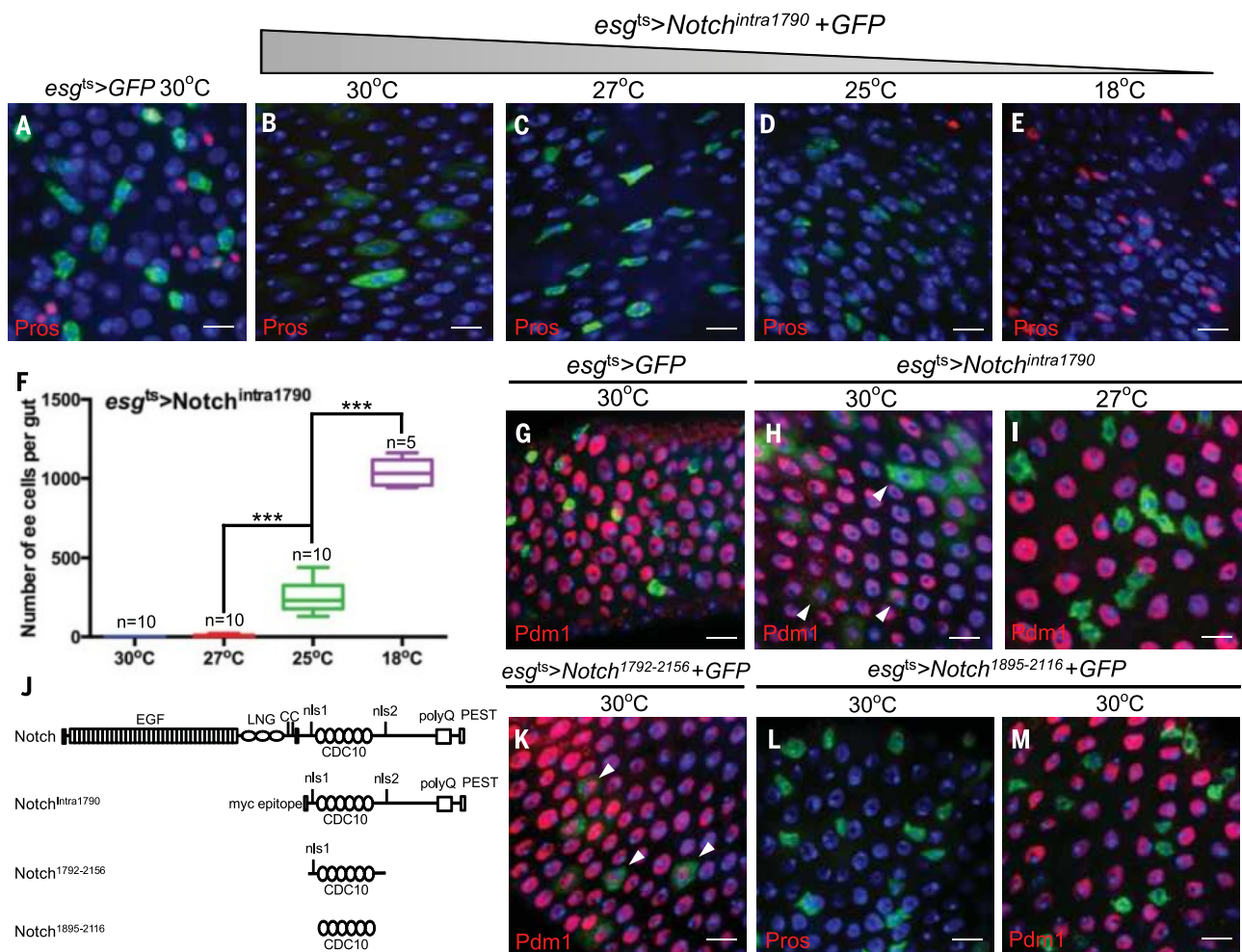


Fig. 5. High Notch signaling promotes EC differentiation, whereas low Notch signaling inhibits ee differentiation. (A to E) Flies were cultured at 18°C until 48 hours APF. Pupae were then moved to various temperatures, and their intestines were analyzed immediately before eclosion. (A) Pros⁺ cells are present in *esg^{ts}>GFP* control intestine. [(B) to (E)] Pros⁺ cells are absent in *esg^{ts}>Notch^{intra1790}* midguts from animals reared at 30°C (B) and 27°C (C). Rare Pros⁺ cells are present at 25°C (D). Pros⁺ cells are readily apparent at 18°C (E). (F) Quantification of Pros⁺ cell numbers in *esg^{ts}>Notch^{intra1790}*

intestine for each of the tested temperatures. ****P* < 0.0001. (G) *esg^{ts}>GFP* cells are negative for the EC maker Pdm1. (H) *esg^{ts}>Notch^{intra1790}* ISCs differentiate into Pdm1⁺ cells (arrowheads) at 30°C. (I) *esg^{ts}>Notch^{intra1790}* ISCs (GFP⁺) are Pdm1[−] at 27°C. (J) Diagram of different Notch protein isoforms used. (K) *esg^{ts}>Notch^{intra1792-2156}* ISCs differentiate into Pdm1⁺ cells (arrowheads) at 30°C. (L) *esg^{ts}>Notch^{intra1895-2116}* guts lack Pros⁺ cells at 30°C. (M) *esg^{ts}>Notch^{intra1895-2116}* ISCs (GFP⁺) do not differentiate into ECs (Pdm1⁺) at 30°C. Scale bars, 10 μm.

cell, promoting EC differentiation (3, 27, 30). By contrast, after asymmetric localization of Pros, ISCs require a low Notch signal from their immediate ee cell daughters to remain multipotent. Thus, Notch signaling is both bidirectional and context-dependent (Fig. 6I and fig. S10). Previous work also has suggested that ISCs remain basal during EC formation and that basal ISCs activate the Notch pathway in apical daughter cells (3, 30). However, our data show that ISCs are apically located during ee cell formation and that basal ee cells activate the Notch pathway in apical ISCs. Therefore, Notch signaling is always unidirectional in terms of polarity: Basal daughter cells express Dl, the Notch ligand, in order to activate the Notch signaling pathway in apical daughters during asymmetric ISC divisions.

How might asymmetric Notch signaling between ISCs and ee cells be established and main-

tained? A recent adult ISC study described the asymmetric segregation of Sara endosomes into the enteroblast, where Notch signaling is activated by Dl and Notch receptor in Sara endosomes (31). Therefore, asymmetric segregation of Sara may also play a role in Notch activation similar to that played by ISCs during ee cell production. In addition, other intracellular trafficking processes, such as asymmetric activation of Dl recycling endosome Rab11 (32) and Arp3 actin polymerization-dependent Dl transportation (33), may also be involved. After mitotic divisions, the basal cell always expresses higher levels of Dl. Although it is unknown why this is the case, the high levels of Dl could inhibit the Notch receptor in the basal cell through a process known as cis inhibition, thereby biasing the direction of Notch signaling toward the apical cell.

After activation of Notch signaling, ISCs toggle from making ee cells to making ECs (fig. S10). Yet although the ISC transiently experiences Notch signaling, it will continue to make only ECs for many divisions afterward. Why might that be? One intriguing possibility is that ISCs would retain an epigenetic memory of Notch signaling, which could act to continuously inhibit Asense expression (27, 29) and repress ee cell formation. That memory might then be reversed by expression of an ee cell-promoting signal, currently unidentified, and/or diluted after a set number of ISC divisions. In addition, loss of the Slit-Robo signaling pathway has recently been shown to result in a modest increase in ee cell production by ISCs (25, 34), raising the possibility that Slit-Robo signaling may prolong the effect of the Notch signaling pathway once ee cells and ISCs are no longer in contact.

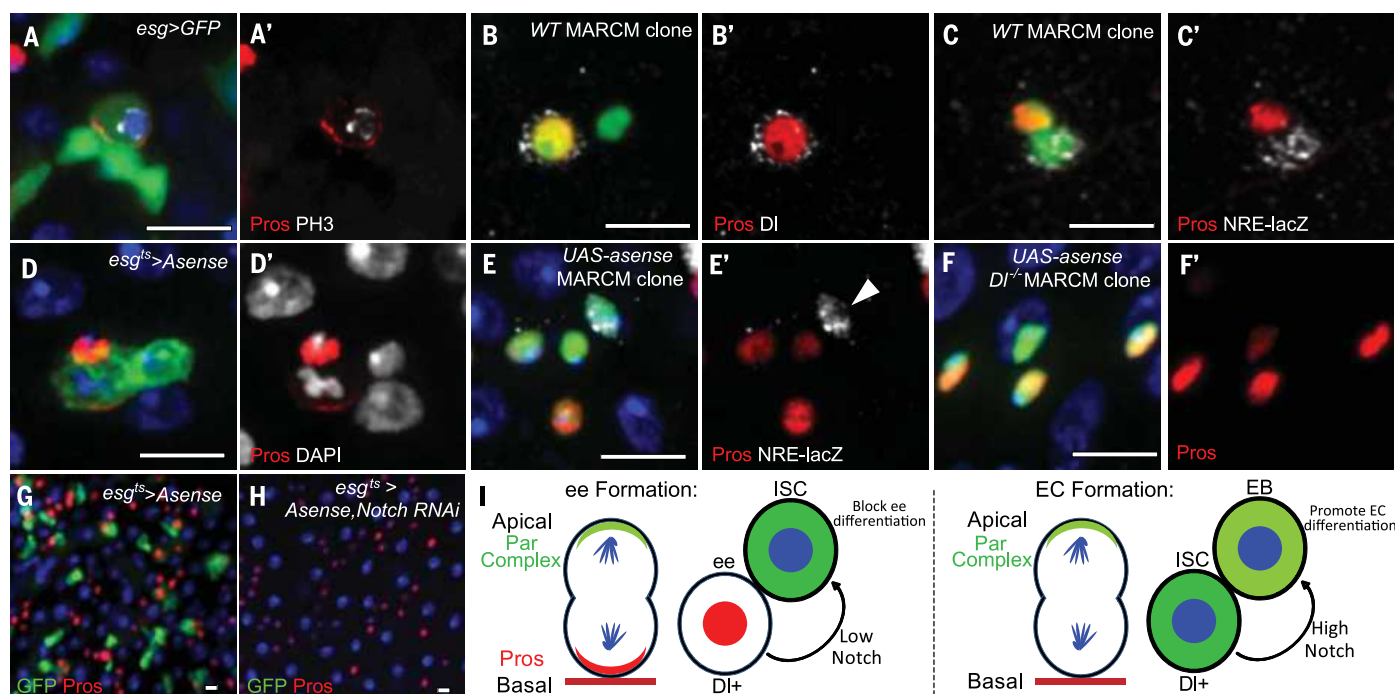


Fig. 6. Postmitotic Notch signaling from ee daughters regulates ISC identity. (A) Pros localizes to a crescent in an adult dividing *esg>GFP*⁺ cell. (B) A two-cell wild-type MARCM clone contains an ee cell (nuclear Pros⁺) positive for DI. (C) A two-cell MARCM clone contains one ee (nuclear Pros⁺) and an ISC positive for *NRE-lacZ*. (D) Asymmetric localization of Pros in an *esg>Asense* cell undergoing mitosis. (E) A MARCM clone driving *Asense* overexpression contains three ee cells (Pros⁺) and a *NRE-lacZ*⁺ ISC [arrowhead in (E')]. Green, clone marker. (F) A *DI* mutant MARCM clone driving *Asense* mis-

expression. All clone cells are Pros⁺. Green, clone marker. (G) *Asense* overexpression by *esg*^{ts} for 8 days in the adult midgut. ISCs are GFP⁺ Pros⁺ cells. (H) Overexpression of *Asense* and Notch RNAi by *esg*^{ts} for 8 days during the adult period. *esg*^{ts}>*GFP*⁺ cells are absent; all remaining diploid cells are Pros⁺. (I) Model of how bidirectional Notch regulates ISC multipotency. Left: Notch signaling from a basal ee cell to an apical ISC blocks ee differentiation and maintains ISC identity. Right: Notch signaling from a basal ISC to an apical enteroblast (EB) promotes EC differentiation. Scale bars, 10 μ m.

Drosophila NBs are derived from ectoderm, whereas ISCs originate from endodermal tissue (35). Despite their distinct germ layer origins, pupal ISC asymmetric divisions share many similarities with embryo and larval type I NBs. Both ISCs and NBs express DI relative to their neighbors before asymmetric divisions (36). During mitosis, both ISCs and NBs use Baz/Par-3 to define apical-basal polarity, and they both segregate Mira and Pros to the basal daughter cell to direct cell type specification (37). After asymmetric division, ganglion mother cells (GMCs) and EMCs are Notch signaling pathway-negative, whereas NBs and ISCs are Notch signaling pathway-positive (38, 39). Moreover, both GMCs and EMCs divide once more using asymmetric Notch signaling to establish different cell fates between their daughters (19).

Pupal ISCs are, however, different from NBs in a number of ways. Throughout mitosis, the NB remains in an apical position, whereas the location of the ISC depends on the phase of the cell cycle and the type of progenitor produced. NBs give rise to two daughters of unequal size (19)—a larger NB and a smaller GMC—whereas the two daughters generated by ISC divisions are similar in cell size. Furthermore, NBs give rise to only one type of progenitor, the GMC. ISCs, on the other hand, are capable of producing two types of progenitors: an enteroblast or an EMC (fig. S10).

Our data provide evidence that mechanisms regulating tissue homeostasis are more conserved between the *Drosophila* and mammalian intestine than previously thought. Inhibition of Notch signaling in the mouse intestine induces crypt base columnar stem cell loss and secretory cell hyperplasia, and ectopic Notch signaling promotes EC differentiation (40–43). We have shown that loss of Notch signaling in *Drosophila* ISCs also leads to stem cell loss and premature ee cell formation, whereas high Notch signaling promotes stem cell differentiation into ECs. Because Notch signaling also plays important roles in common lymphoid progenitors making B cells and T cells (44) and in airway basal cells making secretory cells and ciliated cells (45), it is tempting to speculate that bidirectional Notch signaling may regulate multipotency in these and other progenitors and stem cells.

REFERENCES AND NOTES

1. C. A. Micchelli, N. Perrimon, Evidence that stem cells reside in the adult *Drosophila* midgut epithelium. *Nature* **439**, 475–479 (2006). doi: [10.1038/nature04371](https://doi.org/10.1038/nature04371); pmid: [16340959](https://pubmed.ncbi.nlm.nih.gov/16340959/)
2. B. Ohlstein, A. Spradling, The adult *Drosophila* posterior midgut is maintained by pluripotent stem cells. *Nature* **439**, 470–474 (2006). doi: [10.1038/nature04333](https://doi.org/10.1038/nature04333); pmid: [16340960](https://pubmed.ncbi.nlm.nih.gov/16340960/)
3. B. Ohlstein, A. Spradling, Multipotent *Drosophila* intestinal stem cells specify daughter cell fates by differential notch signaling. *Science* **315**, 988–992 (2007). doi: [10.1126/science.1136606](https://doi.org/10.1126/science.1136606); pmid: [17303754](https://pubmed.ncbi.nlm.nih.gov/17303754/)

4. C. A. Micchelli, L. Sudmeier, N. Perrimon, S. Tang, R. Beehler-Evans, Identification of adult midgut precursors in *Drosophila*. *Gene Expr. Patterns* **11**, 12–21 (2011). doi: [10.1016/j.gexp.2010.08.005](https://doi.org/10.1016/j.gexp.2010.08.005); pmid: [20804858](https://pubmed.ncbi.nlm.nih.gov/20804858/)
5. S. Takashima et al., Development of the *Drosophila* entero-endocrine lineage and its specification by the Notch signaling pathway. *Dev. Biol.* **353**, 161–172 (2011). doi: [10.1016/j.ydbio.2011.01.039](https://doi.org/10.1016/j.ydbio.2011.01.039); pmid: [21382366](https://pubmed.ncbi.nlm.nih.gov/21382366/)
6. T. Lee, L. Luo, Mosaic analysis with a repressible cell marker (MARCM) for *Drosophila* neural development. *Trends Neurosci.* **24**, 251–254 (2001). doi: [10.1016/S0166-2236\(00\)01791-4](https://doi.org/10.1016/S0166-2236(00)01791-4); pmid: [11311363](https://pubmed.ncbi.nlm.nih.gov/11311363/)
7. M. Schober, M. Schaefer, J. A. Knoblich, Bazooka recruits Inscuteable to orient asymmetric cell divisions in *Drosophila* neuroblasts. *Nature* **402**, 548–551 (1999). doi: [10.1038/990135](https://doi.org/10.1038/990135); pmid: [10591217](https://pubmed.ncbi.nlm.nih.gov/10591217/)
8. A. Wodarz, A. Ramrath, U. Kuchinke, E. Knust, Bazooka provides an apical cue for Inscuteable localization in *Drosophila* neuroblasts. *Nature* **402**, 544–547 (1999). doi: [10.1038/990128](https://doi.org/10.1038/990128); pmid: [10591216](https://pubmed.ncbi.nlm.nih.gov/10591216/)
9. Y. Izumi, N. Ohta, A. Itoh-Furuya, N. Fuse, F. Matsuzaki, Differential functions of G protein and Baz-aPKC signaling pathways in *Drosophila* neuroblast asymmetric division. *J. Cell Biol.* **164**, 729–738 (2004). doi: [10.1083/jcb.200309162](https://doi.org/10.1083/jcb.200309162); pmid: [14981094](https://pubmed.ncbi.nlm.nih.gov/14981094/)
10. H. Ikeshima-Kataoka, J. B. Skeath, Y. Nabeshima, C. Q. Doe, F. Matsuzaki, Miranda directs Prospero to a daughter cell during *Drosophila* asymmetric divisions. *Nature* **390**, 625–629 (1997). doi: [10.1038/37641](https://doi.org/10.1038/37641); pmid: [9403694](https://pubmed.ncbi.nlm.nih.gov/9403694/)
11. C. P. Shen, L. Y. Jan, Y. N. Jan, N. Jan, Miranda is required for the asymmetric localization of Prospero during mitosis in *Drosophila*. *Cell* **90**, 449–458 (1997). doi: [10.1016/S0092-8674\(00\)80505-X](https://doi.org/10.1016/S0092-8674(00)80505-X); pmid: [9267025](https://pubmed.ncbi.nlm.nih.gov/9267025/)
12. J. Hirata, H. Nakagoshi, Y. Nabeshima, F. Matsuzaki, Asymmetric segregation of the homeodomain protein Prospero during *Drosophila* development. *Nature* **377**, 627–630 (1995). doi: [10.1038/377627a0](https://doi.org/10.1038/377627a0); pmid: [7566173](https://pubmed.ncbi.nlm.nih.gov/7566173/)

13. J. A. Knoblich, L. Y. Jan, Y. N. Jan, Asymmetric segregation of Numb and Prospero during cell division. *Nature* **377**, 624–627 (1995). doi: [10.1038/377624a0](#); pmid: [7566172](#)
14. E. P. Spana, C. Q. Doe, The prospero transcription factor is asymmetrically localized to the cell cortex during neuroblast mitosis in *Drosophila*. *Development* **121**, 3187–3195 (1995). pmid: [7588053](#)
15. S. Fuerstenberg, C. Y. Peng, P. Alvarez-Ortiz, T. Hor, C. Q. Doe, Identification of Miranda protein domains regulating asymmetric cortical localization, cargo binding, and cortical release. *Mol. Cell. Neurosci.* **12**, 325–339 (1998). doi: [10.1006/mcne.1998.0724](#); pmid: [9888987](#)
16. F. Matsuzaki, T. Ohshiro, H. Ikeshima-Kataoka, H. Izumi, miranda localizes staufer and prospero asymmetrically in mitotic neuroblasts and epithelial cells in early *Drosophila* embryogenesis. *Development* **125**, 4089–4098 (1998). pmid: [9735369](#)
17. A. J. Schudt *et al.*, Miranda mediates asymmetric protein and RNA localization in the developing nervous system. *Genes Dev.* **12**, 1847–1857 (1998). doi: [10.1101/gad.12.12.1847](#); pmid: [9637686](#)
18. C. P. Shen *et al.*, Miranda as a multidomain adapter linking apically localized Inscuteable and basally localized Staufer and Prospero during asymmetric cell division in *Drosophila*. *Genes Dev.* **12**, 1837–1846 (1998). doi: [10.1101/gad.12.12.1837](#); pmid: [9637685](#)
19. F. Roegiers, Y. N. Jan, Asymmetric cell division. *Curr. Opin. Cell Biol.* **16**, 195–205 (2004). doi: [10.1016/j.ccb.2004.02.010](#); pmid: [15196564](#)
20. V. Zecchini, K. Brennan, A. Martinez-Arias, An activity of Notch regulates JNK signalling and affects dorsal closure in *Drosophila*. *Curr. Biol.* **9**, 460 (1999). doi: [10.1016/j.ccb.2004.02.010](#); pmid: [15196564](#)
21. S. P. Bainbridge, M. Bownes, Staging the metamorphosis of *Drosophila melanogaster*. *J. Embryol. Exp. Morphol.* **66**, 57–80 (1981). pmid: [6802923](#)
22. W. C. Lee, K. Beebe, L. Sudmeier, C. A. Micchelli, Adenomatous polyposis coli regulates *Drosophila* intestinal stem cell proliferation. *Development* **136**, 2255–2264 (2009). doi: [10.1242/dev.035196](#); pmid: [19502486](#)
23. M. P. Zeidler *et al.*, Temperature-sensitive control of protein activity by conditionally splicing inteins. *Nat. Biotechnol.* **22**, 871–876 (2004). doi: [10.1038/nbt979](#); pmid: [15184905](#)
24. S. Kidd, T. Lieber, M. W. Young, Ligand-induced cleavage and regulation of nuclear entry of Notch in *Drosophila melanogaster* embryos. *Genes Dev.* **12**, 3728–3740 (1998). doi: [10.1101/gad.12.23.3728](#); pmid: [9851979](#)
25. B. Biteau, H. Jasper, Slit/Robo signaling regulates cell fate decisions in the intestinal stem cell lineage of *Drosophila*. *Cell Rep.* **7**, 1867–1875 (2014). doi: [10.1016/j.celrep.2014.05.024](#); pmid: [24931602](#)
26. N. Zielke *et al.*, Fly-FUCCI: A versatile tool for studying cell proliferation in complex tissues. *Cell Rep.* **7**, 588–598 (2014). doi: [10.1016/j.celrep.2014.03.020](#); pmid: [24726363](#)
27. X. Zeng, S. X. Hou, Enterendocrine cells are generated from stem cells through a distinct progenitor in the adult *Drosophila* posterior midgut. *Development* **142**, 644–653 (2015). doi: [10.1242/dev.113357](#); pmid: [25670791](#)
28. A. J. Bardin, C. N. Perdigoto, T. D. Southall, A. H. Brand, F. Schweisguth, Transcriptional control of stem cell maintenance in the *Drosophila* intestine. *Development* **137**, 705–714 (2010). doi: [10.1242/dev.039404](#); pmid: [20147375](#)
29. X. Zeng, X. Lin, S. X. Hou, The Osa-containing SWI/SNF chromatin-remodeling complex regulates stem cell commitment in the adult *Drosophila* intestine. *Development* **140**, 3532–3540 (2013). doi: [10.1242/dev.096891](#); pmid: [23942514](#)
30. S. Goulas, R. Conder, J. A. Knoblich, The Par complex and integrins direct asymmetric cell division in adult intestinal stem cells. *Cell Stem Cell* **11**, 529–540 (2012). doi: [10.1016/j.stem.2012.06.017](#); pmid: [23040479](#)
31. C. Montagne, M. Gonzalez-Gaitan, Sara endosomes and the asymmetric division of intestinal stem cells. *Development* **141**, 2014–2023 (2014). doi: [10.1242/dev.104240](#); pmid: [24803650](#)
32. G. Emery *et al.*, Asymmetric Rab 11 endosomes regulate delta recycling and specify cell fate in the *Drosophila* nervous system. *Cell* **122**, 763–773 (2005). doi: [10.1016/j.cell.2005.08.017](#); pmid: [16137758](#)
33. A. Rajan, A. C. Tien, C. M. Haueter, K. L. Schulze, H. J. Bellen, The Arp2/3 complex and WASp are required for apical trafficking of Delta into microvilli during cell fate specification of sensory organ precursors. *Nat. Cell Biol.* **11**, 815–824 (2009). doi: [10.1038/ncb1888](#); pmid: [19543274](#)
34. X. Zeng *et al.*, Genome-wide RNAi screen identifies networks involved in intestinal stem cell regulation in *Drosophila*. *Cell Rep.* **10**, 1226–1238 (2015). doi: [10.1016/j.celrep.2015.01.051](#); pmid: [25704823](#)
35. H. Nakagoshi, Functional specification in the *Drosophila* endoderm. *Dev. Growth Differ.* **47**, 383–392 (2005). doi: [10.1111/j.1440-169X.2005.00811.x](#); pmid: [16109036](#)
36. S. Artavanis-Tsakonas, C. Delidakis, R. G. Fehon, The Notch locus and the cell biology of neuroblast segregation. *Annu. Rev. Cell Biol.* **7**, 427–452 (1991). doi: [10.1146/annurev.cb.07.110191.002235](#); pmid: [1809352](#)
37. C. C. Homem, J. A. Knoblich, *Drosophila* neuroblasts: A model for stem cell biology. *Development* **139**, 4297–4310 (2012). doi: [10.1242/dev.080515](#); pmid: [23132240](#)
38. H. Wang *et al.*, Aurora-A acts as a tumor suppressor and regulates self-renewal of *Drosophila* neuroblasts. *Genes Dev.* **20**, 3453–3463 (2006). doi: [10.1101/gad.1487506](#); pmid: [17182870](#)
39. U. Koch, R. Lehal, F. Radtke, Stem cells living with a Notch. *Development* **140**, 689–704 (2013). doi: [10.1242/dev.080614](#); pmid: [23362343](#)
40. S. Fre *et al.*, Notch signals control the fate of immature progenitor cells in the intestine. *Nature* **435**, 964–968 (2005). doi: [10.1038/nature03589](#); pmid: [15959516](#)
41. B. Z. Stanger, R. Datar, L. C. Murtaugh, D. A. Melton, Direct regulation of intestinal fate by Notch. *Proc. Natl. Acad. Sci. U.S.A.* **102**, 12443–12448 (2005). doi: [10.1073/pnas.0505690102](#); pmid: [16107537](#)
42. J. H. van Es *et al.*, Notch/gamma-secretase inhibition turns proliferative cells in intestinal crypts and adenomas into goblet cells. *Nature* **435**, 959–963 (2005). doi: [10.1038/nature03659](#); pmid: [15959515](#)
43. K. L. VanDussen *et al.*, Notch signaling modulates proliferation and differentiation of intestinal crypt base columnar stem cells. *Development* **139**, 488–497 (2012). doi: [10.1242/dev.070763](#); pmid: [22190634](#)
44. F. Radtke, H. R. MacDonald, F. Tacchini-Cottier, Regulation of innate and adaptive immunity by Notch. *Nat. Rev. Immunol.* **13**, 427–437 (2013). doi: [10.1038/nri3445](#); pmid: [23665520](#)
45. M. Mori *et al.*, Notch3-Jagged signaling controls the pool of undifferentiated airway progenitors. *Development* **142**, 258–267 (2015). doi: [10.1242/dev.116855](#); pmid: [25564622](#)

ACKNOWLEDGMENTS

We thank S. Feng, R. Mann, S. Kidd, T. Lieber, M. Zecca, G. Struhl, H. Bellen, G. Veenstra, C. Doe, Y. Jan, T. Nystul, and M. Muskavitch for their generous gifts of fly stocks and reagents; I. Driver for production of the Pdm1 antibody; and E. Lucchetta, N. Rafel, C. Montagne, S. Kidd, and T. Lieber for helpful discussions. Supported by NIH grant R01 DK082456-05 (B.O.).

SUPPLEMENTARY MATERIALS

www.sciencemag.org/content/350/6263/aab0988/suppl/DC1
Materials and Methods
Figs. S1 to S10
References (46–48)

16 March 2015; accepted 29 September 2015
10.1126/science.aab0988

RESEARCH ARTICLES

NONHUMAN GENETICS

Stable recombination hotspots in birds

Sonal Singhal,^{1,2,*†} Ellen M. Leffler,^{3,4,*} Keerthi Sannareddy,³ Isaac Turner,⁴ Oliver Venn,⁴ Daniel M. Hooper,⁵ Alva I. Strand,¹ Qiye Li,⁶ Brian Raney,⁷ Christopher N. Balakrishnan,⁸ Simon C. Griffith,⁹ Gil McVean,⁴ Molly Przeworski^{1,2,†}

The DNA-binding protein PRDM9 has a critical role in specifying meiotic recombination hotspots in mice and apes, but it appears to be absent from other vertebrate species, including birds. To study the evolution and determinants of recombination in species lacking the gene that encodes PRDM9, we inferred fine-scale genetic maps from population resequencing data for two bird species: the zebra finch, *Taeniopygia guttata*, and the long-tailed finch, *Poephila acuticauda*. We found that both species have recombination hotspots, which are enriched near functional genomic elements. Unlike in mice and apes, most hotspots are shared between the two species, and their conservation seems to extend over tens of millions of years. These observations suggest that in the absence of PRDM9, recombination targets functional features that both enable access to the genome and constrain its evolution.

Meiotic recombination is a ubiquitous and fundamental genetic process that shapes variation in populations, yet our understanding of its underlying mechanisms is based on a handful of model organisms, scattered throughout the tree of life. One pattern shared among most sexually reproducing species is that meiotic recombination tends to occur in short segments of hundreds to thousands of base pairs, termed “recombination hotspots” (1). In apes and mice, the location of hotspots is largely determined by PRDM9, a zinc-finger protein that binds to specific motifs in the genome during meiotic prophase and generates histone H3 lysine 4 trimethylation (H3K4me3) marks, eventually leading to double-strand breaks (DSBs) and both crossover and noncrossover resolutions (2–5). In mammals, the zinc-finger domain of the gene *PRDM9* evolves quickly, with evidence of positive selection on residues in contact with DNA (2, 6); as a result, there is rapid turnover of hotspot locations across populations, subspecies, and species (7–10).

Although PRDM9 plays a pivotal role in controlling recombination localization in mice and apes, many species lacking *PRDM9* nonetheless have hotspots (6). An artificial example is provided by *Prdm9* knockout mice. Despite being sterile, they make similar numbers of DSBs as wild-type mice make, and their recombination

hotspots appear to default to residual H3K4me3 mark locations, notably at promoters (10). A natural but puzzling example is provided by canids, which carry premature stop codons in *PRDM9* yet are able to recombine and remain fertile (11, 12). As with *Prdm9* knockout mice, in dogs and in other species without *PRDM9*—such as the yeast *Saccharomyces cerevisiae* and the plant *Arabidopsis thaliana*—hotspots tend to occur at promoters or other regions with promoter-like features (11, 13, 14). In yet other taxa without *PRDM9*, including *Drosophila* species (15), honeybees (16), and *Caenorhabditis elegans* (17), short intense recombination hotspots appear to be absent altogether.

To further explore how the absence of *PRDM9* shapes the fine-scale recombination landscape and influences its evolution, we turned to birds, because an analysis of the chicken genome suggested that it may not have *PRDM9* (6). We first confirmed the absence of *PRDM9* across reptiles by querying the genomes of 48 species of birds, three species of crocodilians, two species of turtles, and one species of lizard for *PRDM9* (18), finding that only the turtle genomes contain putative orthologs with all three *PRDM9* domains (fig. S1). We also found no expression of any *PRDM9*-like transcripts in RNA sequencing data from testis tissue of the zebra finch (*Taeniopygia guttata*) (18). Given the likely absence of *PRDM9* in birds, we asked: Is recombination nonetheless concentrated in hotspots in these species? If so, how quickly do the hotspots evolve? Where does recombination tend to occur in the genome? To address these questions, we generated whole-genome resequencing data for wild populations

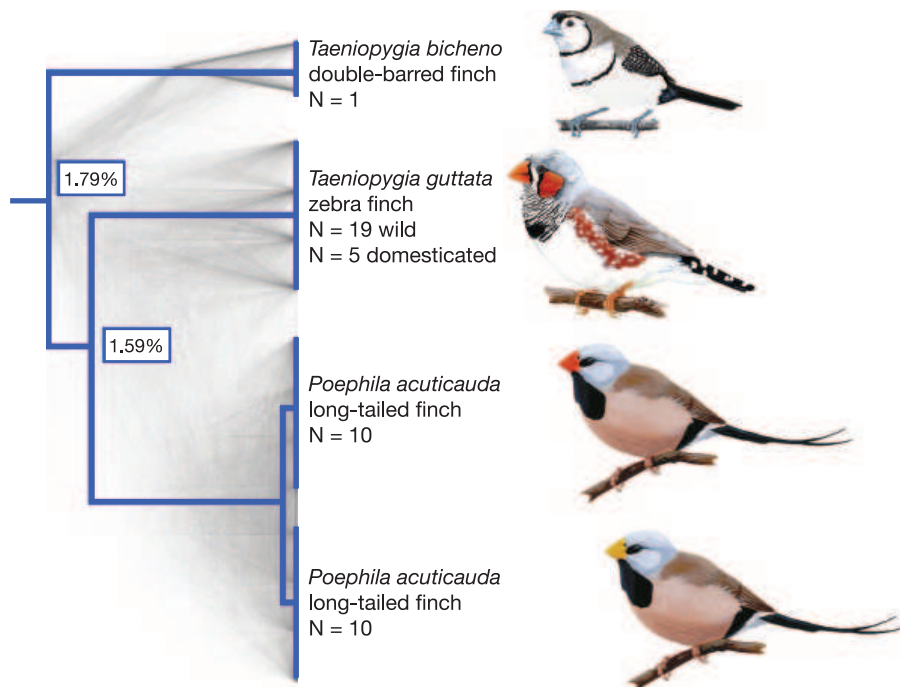


Fig. 1. Species tree for the finch species in this study. Species sampled were double-barred finch, zebra finch, and the two long-tailed finch subspecies. The tree was rooted with the medium ground finch and collared flycatcher (full phylogeny is shown in Fig. 4). Shown in gray are 1000 gene trees, which were used to infer the species tree (18). The pairwise divergence between species is indicated at nodes, as measured by the genome-wide average across autosomes.

¹Department of Biological Sciences, Columbia University, New York, NY 10027, USA. ²Department of Systems Biology, Columbia University, New York, NY 10032, USA. ³Department of Human Genetics, University of Chicago, Chicago, IL 60637, USA. ⁴Wellcome Trust Centre for Human Genetics, University of Oxford, Oxford OX3 7BN, UK. ⁵Committee on Evolutionary Biology, University of Chicago, Chicago, IL 60637, USA. ⁶China National Genebank, BGI-Shenzhen, Shenzhen 518083, China. ⁷Center for Biomolecular Science and Engineering, University of California–Santa Cruz, Santa Cruz, CA 95064, USA. ⁸Department of Biology, East Carolina University, Greenville, NC 27858, USA. ⁹Department of Biological Sciences, Macquarie University, Sydney, NSW 2109, Australia.

*These authors contributed equally to this work. †Corresponding author. E-mail: sonal.singhal@gmail.com (S.S.); molly.przew@gmail.com (M.P.)

of two bird species and inferred fine-scale genetic maps from patterns of linkage disequilibrium.

Inferring fine-scale recombination maps

We sampled three species of finch in the family Estrildidae: zebra finch (*Taeniopygia guttata*; $n = 19$ wild unrelated birds and $n = 5$ birds from a domesticated nuclear family); long-tailed finch (*Poephila acuticauda*; $n = 20$, including 10 of each of two similar subspecies with average autosomal $F_{ST} = 0.039$); and, for use as an outgroup, double-barred finch (*Taeniopygia bichenovii*; $n = 1$) [Fig. 1 and table S1 (18)]. Despite extensive incomplete lineage sorting between the species, they do not appear to have diverged with gene flow (fig. S2). Moreover, nucleotide divergence among the three finch species is similar to that among humans, chimpanzees, and gorillas, providing a well-matched comparison to apes (Fig. 1) (8, 9).

We mapped reads from all individuals to the zebra finch reference genome [1 Gb assembled across 34 chromosomes (19)] and generated de novo single-nucleotide polymorphism (SNP) calls for all three species. After filtering for quality, we identified 44.6 million SNPs in the zebra finch, 26.2 million SNPs in the long-tailed finch, and 3.0 million SNPs in the double-barred finch (table S2). These SNP numbers correspond to autosomal nucleotide diversities of $\pi = 0.82\%$ and $\theta_w = 1.37\%$ in the zebra finch and $\pi = 0.55\%$ and $\theta_w = 0.73\%$ in the long-tailed finch, about 10 times higher than estimates in apes (20). Assuming a mutation rate per base pair per generation of 7×10^{-10} (18), these diversity levels suggest a long-term effective population size (N_e) of 4.8×10^6 and 2.5×10^6 for the zebra finch and long-tailed finch, respectively. Thus, these two species have much larger N_e than most other species for which there exist fine-scale recombination maps, with N_e being more reflective of biodiversity at large (fig. S3).

Next, we inferred haplotypes for the zebra finch and long-tailed finch, using a linkage-disequilibrium approach that incorporated phase-informative reads and family phasing. From the haplotypes, we estimated fine-scale recombination maps using the program LDhelmet, which works well for species with higher nucleotide diversity (15). The resulting maps estimated median recombination rates in the zebra finch and long-tailed finch genomes as $\hat{\rho} = 26.2/\text{kb}$ and $14.0/\text{kb}$, respectively, which corresponds to a median rate of 0.14 centimorgans (cM)/Mb in both species (18). Simulations indicated that we had limited power to identify hotspots in regions with high recombination rates (fig. S4), so we restricted our analyses to the 18 largest chromosomes in the reference genome (930 Mb; 91% of the assembled genome). For these 18 chromosomes, our results accord well with recombination maps inferred from a more limited pedigree-based study of zebra finch (21), with a correlation of 0.90 for rates estimated at the 5-Mb scale (fig. S5), providing confidence in our rate inferences.

Hotspots and their evolution

To identify hotspots in the genome, we operationally defined them as regions that are at least

2 kb in length; have at least five times the background recombination rate as estimated across the 80 kb of sequence surrounding the region; and are statistically supported as hotspots by a likelihood ratio test (18). This approach yielded 3949 hotspots in the zebra finch genome and 4933 hotspots in the long-tailed finch genome (Fig. 2 and figs. S6 and S7), with one hotspot detected on average every 215 and 179 kb in the two species, respectively. Both the lower density of hotspots in the zebra finch relative to the long-tailed finch and the lower density of hotspots in the finches relative to humans are consistent with simulations that indicate decreased power to detect hotspots when the background population recombination rate is higher [figs. S4 and S8 (18)]. The hotspots were detected after aggressively filtering our SNP data sets and show no evidence of having higher phasing error rates than the rest of the genome (fig. S9 and tables S3 and S4).

Considering hotspots to be shared if their midpoints occur within 3 kb of each other, 73% of

zebra finch hotspots (2874 of 3949 hotspots) were detected as shared between the two species (fig. S10) when only 4.4% were expected to overlap by chance (figs. S10 and S11); similar results were obtained under different criteria for hotspot sharing (table S5). The true fraction of shared hotspots between the zebra finch and long-tailed finch is probably higher than observed, because we do not have complete statistical power (fig. S4) and because simulations suggest that we are unlikely to detect spurious cases of hotspot sharing (18). On the other hand, the observed levels of sharing are somewhat lower than expected, compared with a model in which all hotspots are identical in the two species (fig. S12).

This conservation of hotspots contrasts sharply with comparative analyses in apes and mice, where, even across populations with modest levels of genetic differentiation, there is no hotspot sharing (8–10). In fact, if we apply the same criterion for hotspot sharing to humans and chimpanzees, only 10.5% of chimpanzee hotspots overlap

Fig. 2. Recombination rates across hotspots in zebra finch and long-tailed finch genomes. Average relative recombination rate ($\hat{\rho}$ /bp divided by the background $\hat{\rho}$ of 20 kb on either side of the hotspot) across (A) hotspots detected only in the zebra finch genome ($n = 1075$), (B) those detected only in the long-tailed finch genome ($n = 2059$), and (C) those inferred as shared in the two species ($n = 2874$). Shared hotspots are those whose midpoints occur within 3 kb of each other. Recombination rates in the zebra finch are shown in blue, and those in the long-tailed finch are shown in red. The orientation of hotspots is with respect to the genomic sequence.

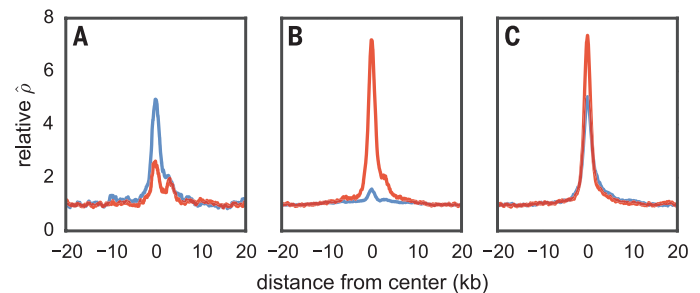
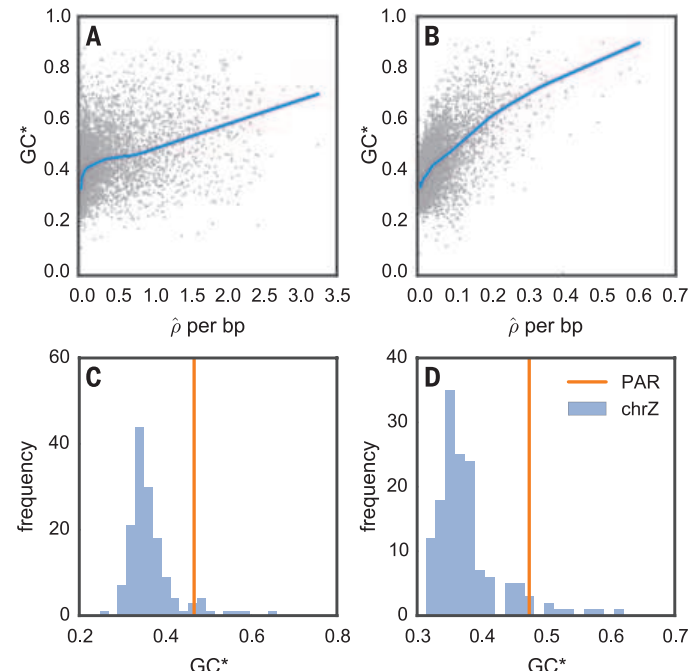


Fig. 3. Equilibrium GC content (GC*) and broad-scale recombination rates in zebra finch and long-tailed finch genomes. (A and B) Relationship between GC* (18) and $\hat{\rho}$ /bp for the zebra finch (A) and long-tailed finch (B) across all autosomal chromosomes. Both GC* and $\hat{\rho}$ were calculated across 50-kb windows with local regression curves shown for a span of 0.2. (C and D) GC* and PAR for the zebra finch (C) and long-tailed finch (D). The histogram shows GC* for chromosome Z across 500-kb windows; GC* for the 450-kb PAR is shown by the vertical line.



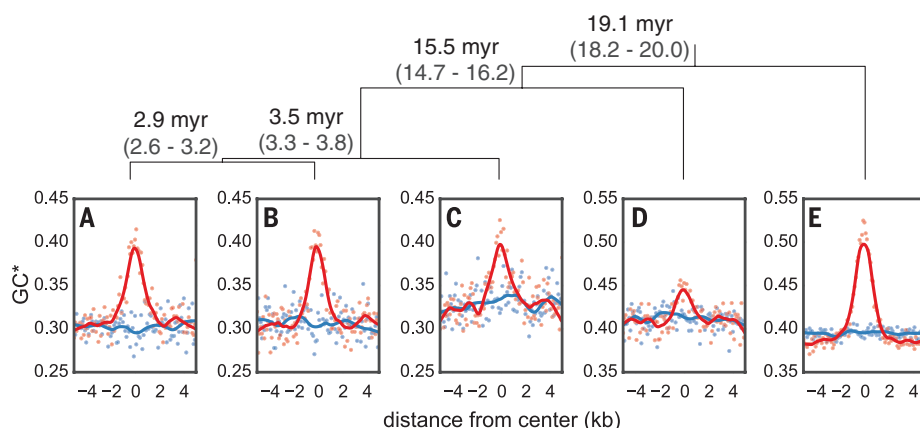


Fig. 4. Expected GC* around hotspots and matched coldspots for five bird species. Points (hotspots in red and coldspots in blue) represent GC* estimated from the lineage-specific substitutions aggregated in 100-bp bins from the center of all hotspots in (A) zebra finch and (B) long-tailed finch. GC* for (C) the double-barred finch, (D) the medium ground finch, and (E) the collared flycatcher was calculated around hotspots identified as shared between the zebra finch and long-tailed finch. Local regression curves are shown for a span of 0.2. The orientation of hotspots is with respect to the genomic sequence. The species tree (18) above the panels is shown with estimated divergence times in millions of years (myr) and its 95% highest posterior density in gray.

with human hotspots when a 7.2% overlap is expected by chance (fig. S11).

To provide further support for the validity of the inferred hotspots, we tested whether they show evidence for GC-biased gene conversion (gBGC), measured as higher expected equilibrium levels of GC content (GC*) (18). Because evidence for gBGC in birds is somewhat indirect (22), we first looked for support for gBGC at broad genomic scales, finding a positive relationship between recombination rate and GC* (Fig. 3, A and B). Narrowing our focus to the regions surrounding hotspots, we observed that hotspots exhibit peaked GC* relative to both flanking sequences and “coldspots” (regions without peaks in recombination) matched for the same overall GC and CpG content (Fig. 4, A and B). A similar phenomenon is evident in intraspecies variation data: At hotspots but not at matched coldspots, derived alleles segregate at a higher frequency at AT-to-GC polymorphisms than at GC-to-AT polymorphisms (fig. S13). Thus, two independent signatures of recombination—namely, patterns of linkage disequilibrium and of base composition—converge in demonstrating that finches have recombination hotspots and that these are conserved over much longer time scales than in apes and mice (8–10).

After observing the pattern of gBGC at hotspots in the zebra finch and long-tailed finch genomes, we tested how far the conservation of hotspot locations extends across the avian phylogeny by additionally considering the genomes of the double-barred finch [an estimated ~3.5 million years diverged from the zebra finch (18)], medium ground finch *Geospiza fortis* [~15.5 million years diverged from the zebra finch (23)], and collared flycatcher *Ficedula albicollis* [~19.1 million years diverged from the zebra finch (24)]. Because we only had a single diploid genome from these species, we tested for hotspot conservation indirectly by determining whether these species

had peaks in GC* at the hotspot locations that we had inferred to be shared between the zebra finch and long-tailed finch. We found localized GC* peaks at hotspots in all three species (Fig. 4, C to E), suggesting that the conservation of hotspots extends across tens of millions of years of evolution. These findings mirror those obtained from four species of *Saccharomyces* yeast, which show nearly complete conservation of hotspot locations and intensities across species that are 15 million years diverged (25). Almost all hotspots in *Saccharomyces* yeast occur at promoters, which are evolutionarily stable, suggesting that how hotspot locations are specified influences how they evolve (12, 26).

The localization of hotspots in the genome

Hotspots in the zebra finch and long-tailed finch genomes are enriched near transcription start sites (TSSs), transcription stop sites (TESs), and CpG islands (CGIs), with close to half of all hotspots occurring within 3 kb of one of these features (~17% occur within 3 kb of both an annotated TSS and a CGI, 3% within 3 kb of both a TES and a CGI, and ~26% within 3 kb of a CGI only; fig. S14). In particular, the hotspots near CGIs are more likely to be shared between species and exhibit stronger evidence for gBGC, compared with hotspots distant from CGIs (fig. S15), providing further support for the importance of these elements in the targeting of recombination. Consistent with the findings about hotspots, recombination rates are nearly two times higher near annotated TSSs and TESs (Fig. 5, A and B). This pattern appears to be driven mainly by their colocalization with CGIs (Fig. 5, A and B, and fig. S16): Rates near CGIs are more than three times higher, with only a small further increase if they are near a TSS or a TES (Fig. 5, C and D, and fig. S17).

A positive association between proximity to the TSS and recombination rate has been pre-

viously reported in a number of species without *PRDM9*, including *S. cerevisiae*, the monkey flower *Mimulus guttatus*, dogs, and *A. thaliana* (11, 13, 14, 27), and an association between TES and recombination rate has been shown in *A. thaliana* (14). In turn, the link between CGIs and recombination rates has been found both in species without *PRDM9*, including dogs (11), and, albeit more weakly, in species with *PRDM9*, including humans and chimpanzees (9). Moreover, the relationship between distance to CGIs and recombination rate remains significant after controlling for expression levels in zebra finch testes (Spearman's $r = -0.1$; $P = 4.32 \times 10^{-27}$; fig. S18). This increase in recombination rates near TSSs, TESs, and CGIs supports a model in which, particularly in the absence of *PRDM9*-binding specificity, recombination is concentrated at functional elements that are accessible to the recombination machinery. TSSs, TESs, and CGIs all coincide with destabilization of nearby nucleosome occupancy (28, 29), and both TSSs and CGIs serve as sites of transcription initiation (30). One implication is that the structure of linkage disequilibrium may differ systematically between species with and without *PRDM9*, with tighter coupling between regulatory and exonic variants in species with *PRDM9*.

Under a model in which the recombination machinery tends to target accessible genomic elements, we would not necessarily expect to see enrichment of specific binding motifs associated with hotspot activity. Accordingly, when we tested for motifs enriched in hotspots relative to coldspots, the top motifs in both species were strings of adenines that are also enriched in *A. thaliana* and yeast hotspots and that may be nucleosome-depleted or facilitate nucleosome removal (fig. S19) (13, 31). We also found a number of additional motifs that are GC-rich and perhaps indicative of CGIs.

At even finer resolution, recombination rates are higher in exonic than in intronic regions, as is observed in *A. thaliana* (14), dogs (11), and *M. guttatus* (27), and higher toward the ends of the gene than in the middle (Fig. 5, E and F). One possibility for these patterns is that DSBs preferentially initiate in exons near the TSS and TES, and their resolution occurs in intervening exons and introns. The specific mechanism by which DSBs would preferentially initiate in exons is unknown, but the pattern is consistent with an important role for chromatin marks that distinguish exons from introns (28).

Contrasting tempos of broad- and fine-scale recombination rate evolution

Median recombination rates across and within chromosomes vary over nearly six orders of magnitude (figs. S8 and S20), creating a heterogeneous landscape of broad-scale recombination rates across the genome, with regions of elevated recombination near telomeres and large intervening deserts [as inferred from zebra finch pedigree data (21)]. Most of the recombination events in the zebra finch and long-tailed finch occur in a narrow portion of the genome, with 82 and 70%

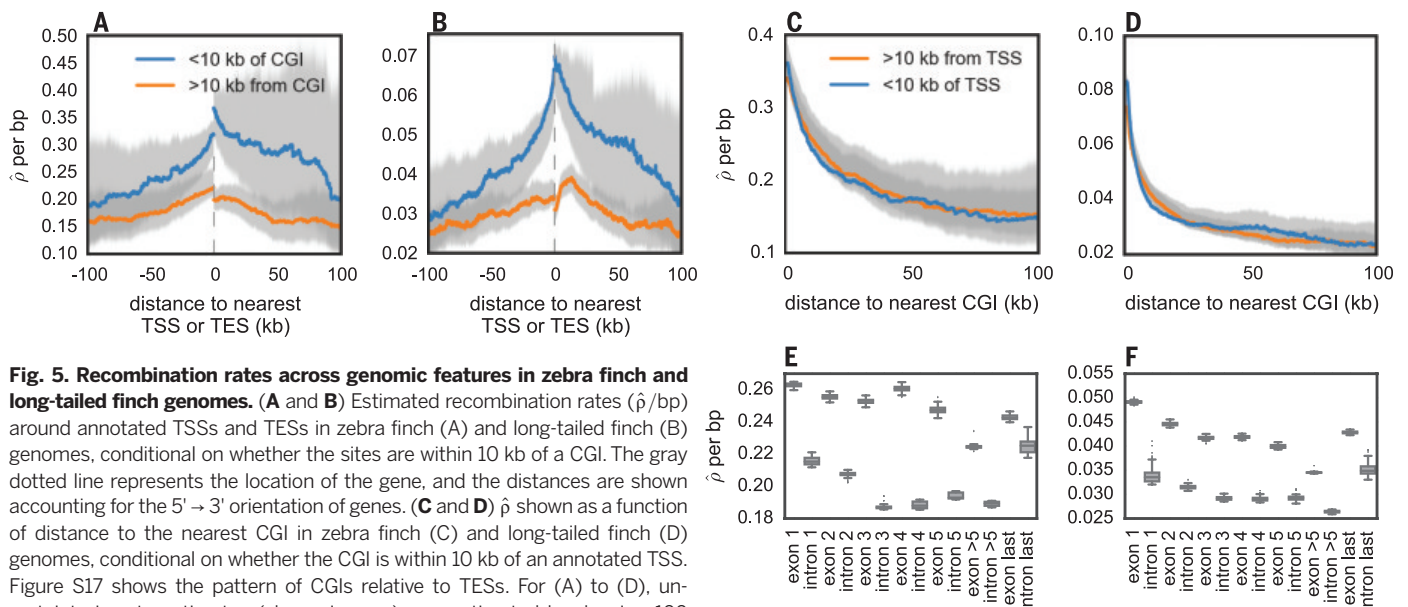


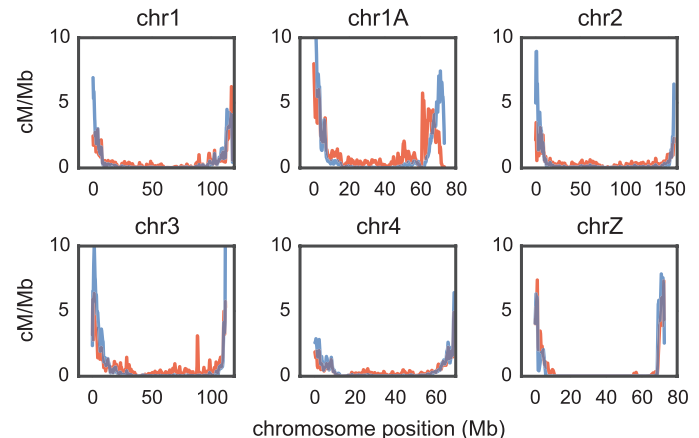
Fig. 5. Recombination rates across genomic features in zebra finch and long-tailed finch genomes. (A and B) Estimated recombination rates ($\hat{\rho}$ /bp) around annotated TSSs and TESs in zebra finch (A) and long-tailed finch (B) genomes, conditional on whether the sites are within 10 kb of a CGI. The gray dotted line represents the location of the gene, and the distances are shown accounting for the 5' to 3' orientation of genes. (C and D) $\hat{\rho}$ shown as a function of distance to the nearest CGI in zebra finch (C) and long-tailed finch (D) genomes, conditional on whether the CGI is within 10 kb of an annotated TSS. Figure S17 shows the pattern of CGIs relative to TESs. For (A) to (D), uncertainty in rate estimates (shown in gray) was estimated by drawing 100 bootstrap samples and recalculating means. (E and F) $\hat{\rho}$ within exons and introns for genes that have ≥ 5 exons ($n = 7131$) in zebra finch (E) and long-tailed finch (F) genomes. Figure S28 shows simulation results that suggest that the inference of higher background $\hat{\rho}$ in exons does not reflect differences in diversity levels between exons and introns.

of events localized to 20% of the genome in the zebra finch and long-tailed finch, respectively (fig. S21). In particular, recombination rates for the Z sex chromosome are two orders of magnitude lower than those for the most similarly sized autosome, chromosome 1A, even after accounting for the lack of recombination in females (fig. S8) (27). Although cytological data indicate that both zebra finches and long-tailed finches harbor a pericentric inversion polymorphism over much of chromosome Z (32, 33), such an inversion is unlikely to explain this extreme difference (18).

Between the zebra finch and long-tailed finch, broad-scale rates are highly similar, with genome-wide correlations of 0.82 and 0.86 at the 10-kb and 1-Mb scales, respectively (Fig. 6 and fig. S20). Despite this broad-scale concordance, we infer that some genomic regions between the two species have very different rates of recombination (fig. S22), and we found tentative support for some of these changes in the derived allele frequency spectra (fig. S23). Moreover, at a greater evolutionary distance, broad-scale patterns differ markedly; the collared flycatcher (~19 million years diverged) has a relatively homogeneous recombination landscape compared with the zebra finch and long-tailed finch (24). This evolution of broad-scale rates is particularly notable because, in many species, shifts in broad-scale recombination patterns can be explained almost entirely by chromosomal rearrangements, shifts in karyotypes, and changes in chromosome lengths (9, 34, 35). However, there is no obvious pattern by which chromosomal rearrangements drive differences in recombination rates between the zebra finch and long-tailed finch (fig. S22), and, despite harboring a number of small inversions between them, the collared flycatcher and zebra

Fig. 6. Comparative recombination rates in zebra finch and long-tailed finch genomes. Zebra finch rates are shown in red; long-tailed finch rates are shown in blue.

Estimated rates [cM/Mb; obtained from $\hat{\rho}$ /bp (18)] are shown as rolling means calculated across 100-kb windows. We show here the five largest autosomal chromosomes and chromosome Z (fig. S20 shows all chromosomes). Rate estimates for chromosome Z should be taken with caution for both biological and technical reasons [more information is given in (18)].



finch have similar karyotypes and syntenic genomes (24). The evidence that broad-scale recombination patterns have changed across the same phylogenetic breadth for which we see hotspot conservation suggests two nonexclusive possibilities that merit further investigation: The heats or locations of some hotspots have evolved, or rates have changed in regions that fall outside of our operational definition of hotspots.

The impact of recombination on the genome

Given the marked variation in recombination rates across the genome, we consider the consequences for genome evolution. Increased recombination rates drive increasing GC content in the genome, presumably via gBGC, and we see this phenomenon both at the genome-wide scale (Fig. 3, A and

B) and at the scale of hotspots (Fig. 4). An extreme example is provided by the pseudoautosomal region (PAR), which we identified on an unassembled scaffold from chromosome Z, using estimates of coverage in males and females. We confirmed the PAR by inferring homology to PARs identified in the medium ground finch and collared flycatcher (fig. S24). The PAR is short, estimated to be just 450 kb, and subject to an obligate crossover in every female meiosis (36); as such, it has very high recombination rates. The consequence is visible in the high GC* for the PAR, which exceeds estimates of GC* across most of the rest of chromosome Z in both species (Fig. 3, C and D).

Further, as has been reported for many other organisms, including chickens (37–39), our results suggest that recombination is positively correlated with levels of nucleotide diversity, particularly on the Z chromosome (figs. S25 to S27). This

observation is consistent with widespread effects of linked selection in these species (40).

Conclusion

Finches lack *PRDM9*, yet they nonetheless harbor hotspots, with recombination concentrated at functional elements (TESs, TSSs, and CGIs) that likely denote greater accessibility to the cellular recombination machinery. In sharp contrast to apes and mice, the hotspot locations are conserved among species several millions of years diverged and probably over tens of millions of years. These results suggest that the genetic architecture of recombination influences the rate at which hotspots evolve. Whereas the binding specificity of *PRDM9* drives rapid turnover, the reliance on accessible functional genomic features leads to stasis. This hypothesis dovetails with recent results in yeast, in which recombination is concentrated at promoters and hotspots are stable in intensity and location over tens of millions of years (25). To further investigate how deeply this stasis extends and to explore the taxonomic generality of these findings, the approaches illustrated here can be applied to other sequenced bird species (41) and beyond. In doing so, we will begin to better understand why species differ so drastically in their specification of hotspots and, in particular, why a subset relies on *PRDM9*.

REFERENCES AND NOTES

- B. de Massy, *Annu. Rev. Genet.* **47**, 563–599 (2013).
- S. Myers *et al.*, *Science* **327**, 876–879 (2010).
- I. L. Berg *et al.*, *Nat. Genet.* **42**, 859–863 (2010).
- F. Baudat *et al.*, *Science* **327**, 836–840 (2010).
- A. L. Williams *et al.*, *eLife* **4**, e04637 (2015).
- P. L. Oliver *et al.*, *PLOS Genet.* **5**, e1000753 (2009).
- A. G. Hinch *et al.*, *Nature* **476**, 170–175 (2011).
- L. S. Tevison *et al.*, <http://biorxiv.org/search/013755> (2015).
- A. Auton *et al.*, *Science* **336**, 193–198 (2012).
- K. Brick, F. Smagulova, P. Khil, R. D. Camerini-Otero, G. V. Petukhova, *Nature* **485**, 642–645 (2012).
- A. Auton *et al.*, *PLOS Genet.* **9**, e1003984 (2013).
- E. Axelsson *et al.*, *Genome Res.* **22**, 51–63 (2012).
- J. Pan *et al.*, *Cell* **144**, 719–731 (2011).
- K. Choi *et al.*, *Nat. Genet.* **45**, 1327–1336 (2013).
- A. H. Chan, P. A. Jenkins, Y. S. Song, *PLOS Genet.* **8**, e1003090 (2012).
- A. Wallberg, S. Glémin, M. T. Webster, *PLOS Genet.* **11**, e1005189 (2015).
- T. Kaur, M. V. Rockman, *Genetics* **196**, 137–148 (2014).
- Materials and methods are available as supplementary materials on Science Online.
- W. C. Warren *et al.*, *Nature* **464**, 757–762 (2010).
- E. M. Leffler *et al.*, *PLOS Biol.* **10**, e1001388 (2012).
- N. Backström *et al.*, *Genome Res.* **20**, 485–495 (2010).
- C. C. Weber, B. Boussau, J. Romiguier, E. D. Jarvis, H. Ellegren, *Genome Biol.* **15**, 549 (2014).
- G. Zhang, P. Parker, B. Li, J. Wang, *GigaScience* 10.5524/100040 (2012).
- T. Kawakami *et al.*, *Mol. Ecol.* **23**, 4035–4058 (2014).
- I. Lam, S. Keeney, *Science* **350**, 932–937 (2015).
- A. Nicolas, D. Treco, N. P. Schultes, J. W. Szostak, *Nature* **338**, 35–39 (1989).
- U. Hellsten *et al.*, *Proc. Natl. Acad. Sci. U.S.A.* **110**, 19478–19482 (2013).
- P. A. Jones, *Nat. Rev. Genet.* **13**, 484–492 (2012).
- N. Kaplan *et al.*, *Nature* **458**, 362–366 (2009).
- A. M. Deaton, A. Bird, *Genes Dev.* **25**, 1010–1022 (2011).
- E. Wijner *et al.*, *eLife* **2**, e01426 (2013).
- L. Christidis, *Genetica* **71**, 81–97 (1986).
- Y. Itoh, K. Kamp, C. N. Balakrishnan, A. P. Arnold, *Chromosoma* **120**, 255–264 (2011).
- B. L. Dumont, B. A. Payseur, *Evolution* **62**, 276–294 (2008).
- M. I. Jensen-Seaman *et al.*, *Genome Res.* **14**, 528–538 (2004).
- S. P. Otto *et al.*, *Trends Genet.* **27**, 358–367 (2011).
- M. W. Nachman, *Trends Genet.* **17**, 481–485 (2001).
- D. J. Begun, C. F. Aquadro, *Nature* **356**, 519–520 (1992).
- C. F. Mugal, P. F. Arndt, H. Ellegren, *Mol. Biol. Evol.* **30**, 1700–1712 (2013).
- B. Charlesworth, M. T. Morgan, D. Charlesworth, *Genetics* **134**, 1289–1303 (1993).
- G. Zhang *et al.*, *Science* **346**, 1311–1320 (2014).

ACKNOWLEDGMENTS

This project was started when M.P. was a Howard Hughes Medical Institute Early Career Scientist and was funded, in part, by Wellcome Trust grants 086786/Z/08/Z to O.V. and 090532/Z/09/Z to the Wellcome Trust Centre for Human Genetics. We thank B. de Massy, C. Grey, S. Myers, T. Price, M. Schumer, J. Wall, A. Williams, and J. Willis for helpful discussions and/or comments on the manuscript; K. Argoud and P. Piazza at the Genomics Core at the Wellcome Trust Centre for Human Genetics for assistance with laboratory work; and M. T. Gilbert for sharing the zebra finch gene annotations in advance of publication. We thank I. Lam and S. Keeney for sharing their unpublished manuscript with us, S. Keeney for many helpful discussions, and A. Johnson for the illustrations used in Fig. 1.

Binary Alignment Map files for genomic data and filtered variant call files for the zebra finch, long-tailed finch, and double-barred finch are available at www.ebi.ac.uk/ena/data/view/PRJEB10586. Sequence reads for zebra finch RNA sequencing experiments are available at www.ncbi.nlm.nih.gov/bioproject/?term=PRJNA295077. Masked genome files, the reconstructed ancestral genome, and recombination maps for both species are available at DataDryad (doi: 10.5061/dryad.f24j). All scripts and an electronic laboratory notebook for this work are available at <https://github.com/singhal/postdoc> and <https://github.com/singhal/labnotebook>, respectively.

SUPPLEMENTARY MATERIALS

www.sciencemag.org/content/350/6263/928/suppl/DC1
Materials and Methods
Figs. S1 to S35
Tables S1 to S6
References (42–94)

23 July 2015; accepted 5 October 2015
10.1126/science.1250843

NONHUMAN GENETICS

Nonparadoxical evolutionary stability of the recombination initiation landscape in yeast

Isabel Lam^{1,2} and Scott Keeney^{1,2,3*}

The nonrandom distribution of meiotic recombination shapes heredity and genetic diversification. Theoretically, hotspots—favored sites of recombination initiation—either evolve rapidly toward extinction or are conserved, especially if they are chromosomal features under selective constraint, such as promoters. We tested these theories by comparing genome-wide recombination initiation maps from widely divergent *Saccharomyces* species. We find that hotspots frequently overlap with promoters in the species tested, and consequently, hotspot positions are well conserved. Remarkably, the relative strength of individual hotspots is also highly conserved, as are larger-scale features of the distribution of recombination initiation. This stability, not predicted by prior models, suggests that the particular shape of the yeast recombination landscape is adaptive and helps in understanding evolutionary dynamics of recombination in other species.

DNA double-strand breaks (DSBs) generated by the SpoII protein initiate meiotic recombination, which alters genetic linkage and promotes pairing and accurate chromosome segregation (1). DSBs are distributed nonrandomly across genomes, occurring often within narrow regions called hotspots (2). Theoretical work exploring evolutionary dynamics of recombination has led to a prevailing hypothesis, the “hotspot paradox,” that predicts rapid hotspot extinction (3–7). This view rests on biased gene conversion, in which the broken chromosome copies genetic information from its uncult homolog and may generate an extra copy of a genetic variant (Fig. 1A). Consequently, hotspot alleles with different DSB activity deviate from a Mendelian segregation ratio, with recombinationally less active alleles overrepresented among the offspring.

This type of meiotic drive is observed in yeast (8) and humans (9) and predicts that mutations that reduce or eliminate hotspot activity will be rapidly fixed in populations, whereas hotspot-activating mutations are rapidly extinguished (3, 5, 10). The paradox is that hotspots exist at all despite this drive against them.

One answer to this paradox comes from *PRDM9*, a mammalian histone methyltransferase with an array of Zn-finger modules that rapidly evolve new DNA binding specificity (11). *PRDM9* targets DSB formation near its binding sites and thus dictates hotspot positions. *PRDM9* recognition motifs, which have no known intrinsic function, are lost quickly from genomes of humans and mice because of meiotic drive from biased gene conversion (12–14), but the appearance of new *PRDM9* alleles with different sequence specificity creates new hotspots and redraws the recombination landscape (11). This hotspot-targeting mechanism confirms the rapid extinction predicted by the hotspot paradox and explains how hotspots can, nonetheless, exist. However, most taxa (including yeast and some mammals) lack such a system, so it has remained unclear how generalizable this solution is.

¹Louis V. Gerstner, Jr., Graduate School of Biomedical Sciences, Memorial Sloan Kettering Cancer Center, New York, NY 10065, USA. ²Molecular Biology Program, Memorial Sloan Kettering Cancer Center, New York, NY 10065, USA.

³Howard Hughes Medical Institute, Memorial Sloan Kettering Cancer Center, New York, NY 10065, USA.

*Corresponding author. E-mail: s-keeney@ski.mskcc.org (S.K.).

An alternative view predicts that hotspot positions can be evolutionarily stable if Spo11 targets genomic features that are under selective constraint for functions unrelated to their roles as hotspots (8, 15). This hypothesis derives from the correspondence of most hotspots in *S. cerevisiae* to promoter-containing intergenic regions (IGRs) (15). However, theoretical studies have considered this implausible as a mechanism to preserve hotspots (3, 10). Instead, many studies start from the assumption that the hotspot life span must always be short and that the fine-scale recombination initiation landscape will always be highly dynamic over evolutionary scales (4, 6, 7, 16). This assumption is appropriate for primates and mice because they use PRDM9 but has not been evaluated for other taxa.

High-resolution DSB maps in *Saccharomyces*

To distinguish between these models, we asked whether the DSB landscape is conserved in yeast. Previously, population genetic data were used to deduce a recombination map in *S. paradoxus* and compare it with *S. cerevisiae* (17). Partial conservation was inferred, but the data had insufficient resolution to detect individual hotspots (15). We overcame these limitations by comparing high-resolution, whole-genome DSB maps between wide-

ly diverged *Saccharomyces* species and between *S. cerevisiae* strains (the laboratory strain SK1 and wild-derived strains YPS128 and UWOPS03-461.4) (18) (Fig. 1B and table S1). DSB maps were generated by deep-sequencing DNA oligonucleotides (oligos) covalently bound to Spo11 as a byproduct of DSB formation (15, 19) (Fig. 1A and table S2).

The *Saccharomyces sensu stricto* clade last shared a common ancestor ~20 million years ago (20). We examined species ranging from *S. paradoxus*, with coding sequence divergence from *S. cerevisiae* comparable to that between humans and mice (~100 million years divergence), to *S. kudriavzevii*, roughly as distant as mammals from birds (~300 million years divergence) (21) (Fig. 1B). The *S. cerevisiae* strains chosen display 0.5 to 0.7% sequence divergence, comparable to the polymorphism density between humans and chimpanzees. Most differences are simple sequence polymorphisms (single-nucleotide polymorphisms and small indels), with few large-scale structural differences aside from one discussed below (18, 22).

All yeasts examined underwent synchronous and efficient meiosis (fig. S1A); hence, the strain SK1 is not anomalous in this regard. As in *S. cerevisiae*, two major size classes of Spo11-oligo complexes were observed (Fig. 1C and fig. S1B), which reflect oligos of similar length distributions (Fig. 1D). Each oligo is a tag that records where Spo11

generated a DSB, and maps based on deep sequencing (23) agree spatially and quantitatively with direct detection of DSBs by Southern blot (15). Biological replicate maps were highly reproducible (Fig. 1E and fig. S2), and most sequenced reads (>98%) were mapped uniquely (table S2).

Targeting of breaks to promoters is conserved

We asked whether targeting of promoters is conserved among yeast. We mapped nucleosomes by sequencing micrococcal nuclease-resistant DNA (MNase-seq) from meiotic cultures (23). In *S. cerevisiae*, DSBs form preferentially in promoter-associated nucleosome-depleted regions (NDRs) (15, 24), and promoter chromatin structure during mitotic growth is conserved among other *Saccharomyces* species (25). Spo11 oligos were highly enriched in promoter NDRs in all species tested, whether examined at individual locations (Fig. 2A and fig. S3A) or averaged across annotated genes (Fig. 2B and fig. S3B). Many Spo11 oligos mapped to promoter-containing IGRs (i.e., IGRs flanked by divergent or tandemly oriented genes), whereas few mapped to convergent IGRs (i.e., lacking promoters) or within genes (Fig. 2D and fig. S3D). We conclude that the Spo11 preference for promoters is a stable feature of the *Saccharomyces* DSB landscape.

Similar numbers of Spo11-oligo hotspots (~4000) were identified in all species (table S3). When

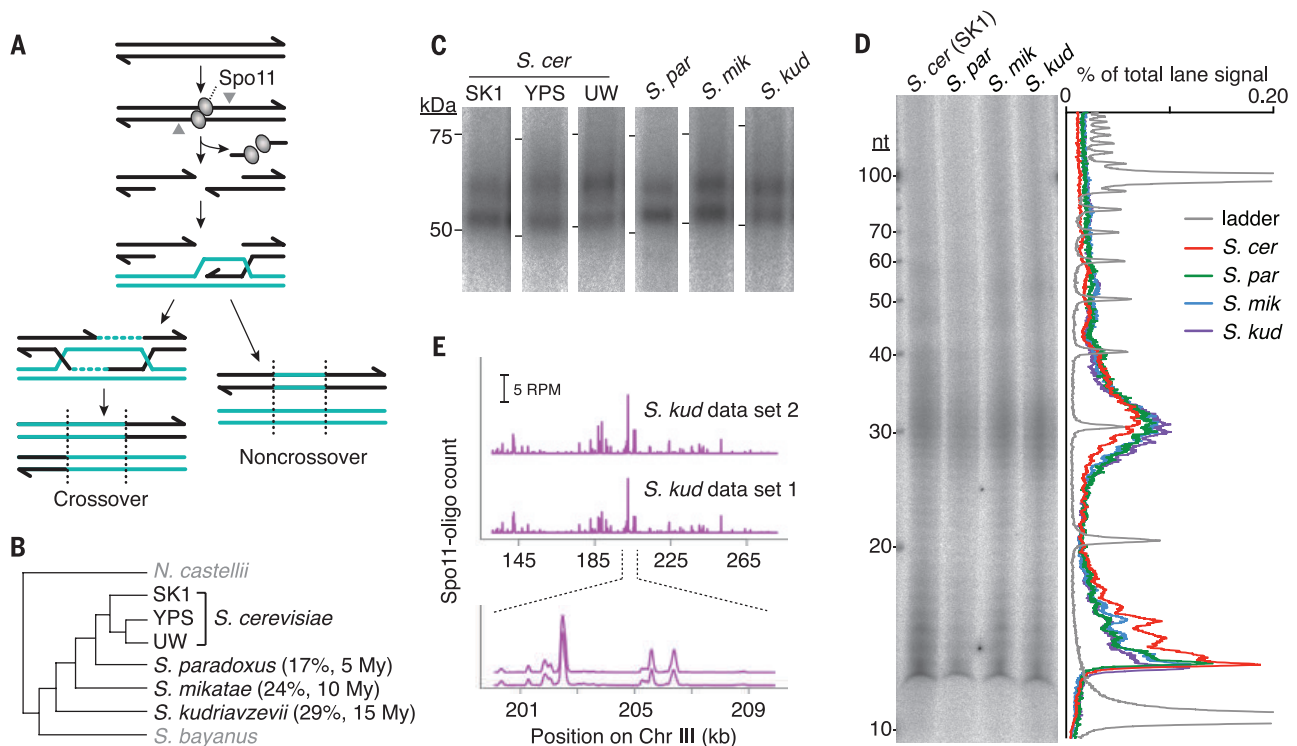


Fig. 1. Generation of Spo11-oligo maps. (A) Meiotic recombination. Spo11 generates covalent protein-linked DSBs; endonucleolytic cleavage (gray arrowheads) liberates Spo11 bound to short oligos. DSB ends are resected and repaired to yield crossover or noncrossover products. The broken chromosome (black) copies information from the uncut allele (teal). (B) Schematic of *Saccharomyces* phylogeny (18, 20). Black, species and/or strains in this study; genic sequence divergence from *S. cerevisiae* (42) and estimated time since last common ancestor (20) are shown. YPS, YPS128; UW, UWOPS03-461.4. (C and D) Conserved sizes of Spo11 oligos. Immunoprecipitated, radiolabeled Spo11-oligo complexes were separated by SDS–polyacrylamide gel electrophoresis (C) or were digested with proteinase K and resolved on a denaturing polyacrylamide gel (D). Autoradiographs [with lane traces in (D)] are shown. (E) Reproducibility of *S. kudriavzevii* Spo11-oligo maps. RPM, reads per million mapped; profiles were smoothed with a 201-bp Hann window.

ceator (20) are shown. YPS, YPS128; UW, UWOPS03-461.4. (C and D) Conserved sizes of Spo11 oligos. Immunoprecipitated, radiolabeled Spo11-oligo complexes were separated by SDS–polyacrylamide gel electrophoresis (C) or were digested with proteinase K and resolved on a denaturing polyacrylamide gel (D). Autoradiographs [with lane traces in (D)] are shown. (E) Reproducibility of *S. kudriavzevii* Spo11-oligo maps. RPM, reads per million mapped; profiles were smoothed with a 201-bp Hann window.

ranked by Spo11-oligo count, hotspots formed a smooth continuum over a wide range, with nearly superimposable cumulative curves in all species (Fig. 2E and fig. S3E). Hence, the distribution of DSBs among hotspots is the same. Hotspots had low average nucleosome occupancy (Fig. 2C and fig. S3C), consistent with open chromatin structure, which provides a window of opportunity for Spo11 (26). The distribution of hotspot width was also nearly identical, with wider hotspots tending to have more Spo11 oligos (Fig. 2F and fig. S3F). Conserved hotspot width agrees with conservation of NDR width observed previously (25). Most hotspots overlapped the same promoter-containing IGRs in all species examined (Fig. 2G and fig. S3G). The low frequency of sex and outcrossing in yeasts could slow hotspot extinction compared with obligately outcrossed species (17), but the yeasts examined here have had ample sexual generations to allow biased gene conversion to erode hotspots. For example, there have been an estimated >200,000 outcrossed sexual generations since divergence of *S. cerevisiae* from *S. kudriavzevii*, comparable with the number of human sexual generations since divergence from chimpanzees (23). Thus, as predicted (8), DSB hotspot locations

can be preserved when the targeted chromosome architecture is conserved.

Conservation of DSB frequency in hotspots

The hotspot paradox predicts that hotspot strength should vary widely even if their locations are conserved. Furthermore, the rate of hotspot extinction should scale with hotspot heat, because alleles that experience frequent DSBs provide more chances for loss (3–5, 10, 13). The selective constraint model is agnostic in this regard: If cis-acting sequence polymorphisms can quantitatively modulate DSB formation without ablating Spo11 targeting (which has been experimentally shown [e.g., (27)]), then hotspot heats will change rapidly. On the other hand, if DSB frequency (not just position) is tied to selectively constrained features or if DSB frequency is itself constrained, then hotspot heats will tend to be conserved.

To address this question, we summed Spo11 oligos within 3426 promoter-containing IGRs that could be stringently and unambiguously matched between species on the basis of conservation of flanking coding sequences (Fig. 3A and table S4). This group contains 81% of divergent and tandem IGRs and accounts for 83% of promoter-

proximal hotspots in *S. cerevisiae*; thus, most of the relevant Spo11-targeted genomic space is included. An IGR-centric approach is preferable to relying on more arbitrary hotspot definitions (23). Within-IGR Spo11-oligo counts were highly similar between *S. cerevisiae* strains: We observed correlation coefficients (0.89 to 0.92) that were nearly as high as for comparisons between biological replicates (0.97 to 1.00) (Fig. 3, B to D; fig. S4A; and table S4). Thus, intraspecies variation of DSB heat within these IGRs is low, despite ~0.7 to 1% median sequence divergence.

Strong correlations were also found between species, with little change in correlation strength over large evolutionary distances (Fig. 3, B to D, and fig. S4A). Moreover, the hottest 1% of promoter IGRs in *S. cerevisiae* SK1 were enriched among the hottest IGRs in other species, with a median percentile ranking within the top 5%, even in *S. kudriavzevii* (Fig. 3, E and F). This was only modestly greater than the extent of conservation of the coldest IGRs (Fig. 3E). Theoretical modeling of biased gene conversion predicts that strong hotspots are less likely to be shared between species than weak ones (5). We found specific examples where strong hotspots in one species were substantially weaker in other species (Fig. 3G), so there is no

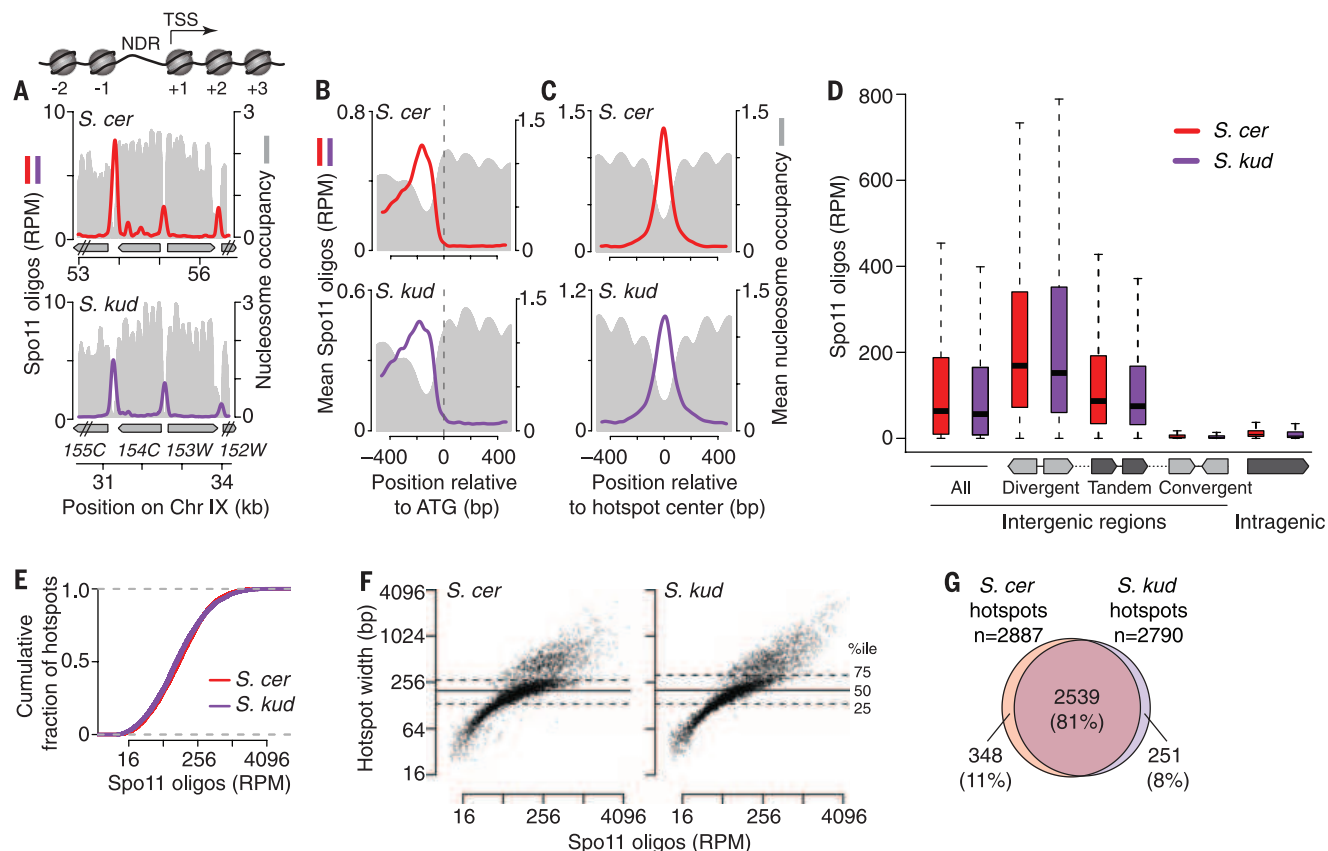


Fig. 2. Conserved targeting of DSBs to promoters. (A) Overlap of DSB hotspots with promoter NDRs is evolutionarily conserved. The cartoon depicts typical yeast promoter chromatin structure, with an NDR upstream of the transcription start site (TSS). Sample region (around *YIL154C*) compares Spo11 oligos with the nucleosome map (MNase-seq read depth relative to genome average). (B) Average Spo11-oligo and nucleosome profiles around start codons (*S. cer* SK1, $n = 5766$; *S. kud*, $n = 5578$). (C) Average Spo11-oligo and nucleosome profiles at hotspots (*S. cer* SK1, $n = 4099$; *S. kud*, $n = 3976$). Spo11-oligo profiles were smoothed with

201-bp (A) or 75-bp [(B) and (C)] Hann window. (D) Spo11 oligos map preferentially to IGRs containing promoters. In box plots, thick horizontal lines indicate medians, box edges show the 25th and 75th percentiles, and whiskers indicate lowest and highest values within 1.5-fold of the interquartile range; outliers are not shown. (E) Hotspot intensity varies over similar smooth continua in *S. cerevisiae* (SK1) and *S. kudriavzevii*. (F) Similar distributions of widths versus Spo11-oligo counts in hotspots. (G) Conserved hotspot positions. Most promoter-containing IGRs hosting Spo11-oligo hotspots in *S. cerevisiae* (SK1) also had hotspots in *S. kudriavzevii*.

absolute barrier to evolutionary changes. But the behavior of most IGRs leads us to conclude that the hottest hotspots present in the last common ancestor of *Saccharomyces* tended to retain high Spo11 target activity and that it has been rare for ancestrally cold promoters to acquire strong hotspot activity.

This high degree of yeast hotspot conservation differs markedly from that in humans: DSB hotspot heat between men sharing the same or similar *PRDM9* alleles (28) was less conserved than between *S. cerevisiae* strains despite much greater sequence identity (Fig. 3, C and D, and fig. S4B). This difference is consistent with *PRDM9* motif erosion contributing to variation in hotspot strength between individuals (28).

Conservation of the DSB landscape over larger size scales

Hotspots are only one level of nonrandomness in the DSB landscape in that they reside within larger domains of greater or lesser DSB potential (2, 15). In several taxa, conservation has been noted for the distribution of crossover recombination over broad genomic regions (16), but conserva-

tion of DSB distributions has not been evaluated. We therefore investigated if large-scale features of the DSB landscape are also conserved in yeast. Spo11-oligo maps demonstrated that DSB suppression observed near telomeres and centromeres (15, 26) is preserved (Fig. 4, A and B, and fig. S5, A and B). This result is not surprising, as recombination in these subchromosomal regions can interfere with genome integrity: Subtelomeric regions are rife with repetitive DNA elements that can undergo nonallelic homologous recombination (29), and crossing over that occurs close to centromeres can cause segregation errors (30).

More remarkably, however, Spo11-oligo counts were also well correlated between species when we compared ~20-kb segments in syntenic regions across interstitial (i.e., nontelomeric and noncentromeric) portions of the chromosomes (Fig. 4, C and D; fig. S5, C to F; and table S5). This scale is comparable to the average length of the chromatin loops of meiotic chromosomes, and DNA segments of this size typically encompass multiple hotspots (1, 15). These findings indicate that the larger-scale domain structure of the DSB

landscape is also evolutionarily stable. Spo11-oligo counts were correlated with G + C content of DNA in each species tested, with weaker correlation over short distances (~1 kb) and stronger correlations over large distances (Fig. 4E). This scale-dependent pattern is consistent with the hypothesis that large-scale DSB domains, like hotspots, reflect selective constraint on the underlying chromosomal architecture (15). Furthermore, such large-scale domains presumably reflect factors—such as attachment of chromatin loops to chromosome axes—that work in cis but at a distance from DSB hotspots. Because such factors are too far away to be frequently included in gene conversion tracts and are thus not subject to loss through biased gene conversion, they are not expected to evolve as rapidly as hotspots (3, 5, 16, 31).

Chromosome length affects DSB frequency

In *S. cerevisiae*, DSB density is anticorrelated with chromosome size, i.e., smaller chromosomes on average incur more DSBs per kilobase than larger ones (15). This relation is conserved in other

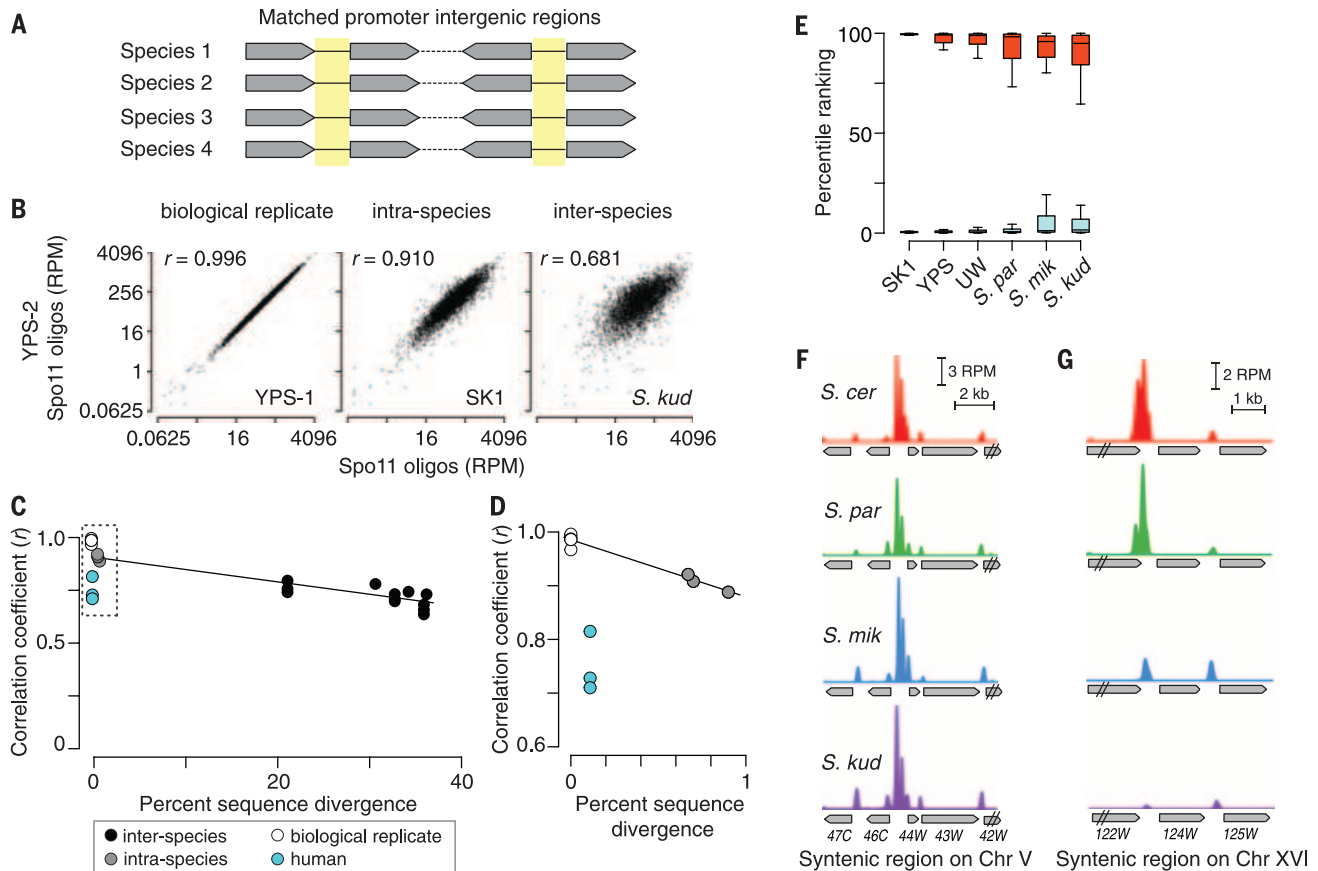


Fig. 3. Conservation of hotspot strength. (A) Promoter-containing IGRs were matched between species using conservation of flanking genes. (B) Comparison of Spo11-oligo counts (\log_2 scale) within 3426 IGRs that were matched in all four species. Correlation coefficients for the \log_2 -transformed data are shown (Pearson's r). (C and D) Spo11-oligo counts in promoter IGRs remain highly correlated despite wide sequence divergence. Correlation coefficients [as in (B)] are plotted against the median sequence divergence within IGRs, which is substantially greater than the coding sequence divergence in Fig. 1B (22). (D) is a closer view of the boxed region in (C). Black lines highlight the

yeast comparisons; they are not regression lines. Human data [from ref. (28)] are for three men with identical or similar *PRDM9* alleles (37,345 hotspots) (see fig. S4B); each had ~0.1% sequence difference from the reference genome (28)]. (E) The hottest hotspots have stayed hot, and the coldest have stayed cold. Percentile rankings in other strains and species are shown for the matched promoter IGRs with the most (red) and least (cyan) Spo11 oligos in SK1 (top and bottom 1%). Box plots are as in fig. S3D. (F and G) Examples of a strong Spo11-oligo hotspot from SK1 whose heat is conserved (F), *YEL046C*, and one whose heat is not (G), *YPR124W*.

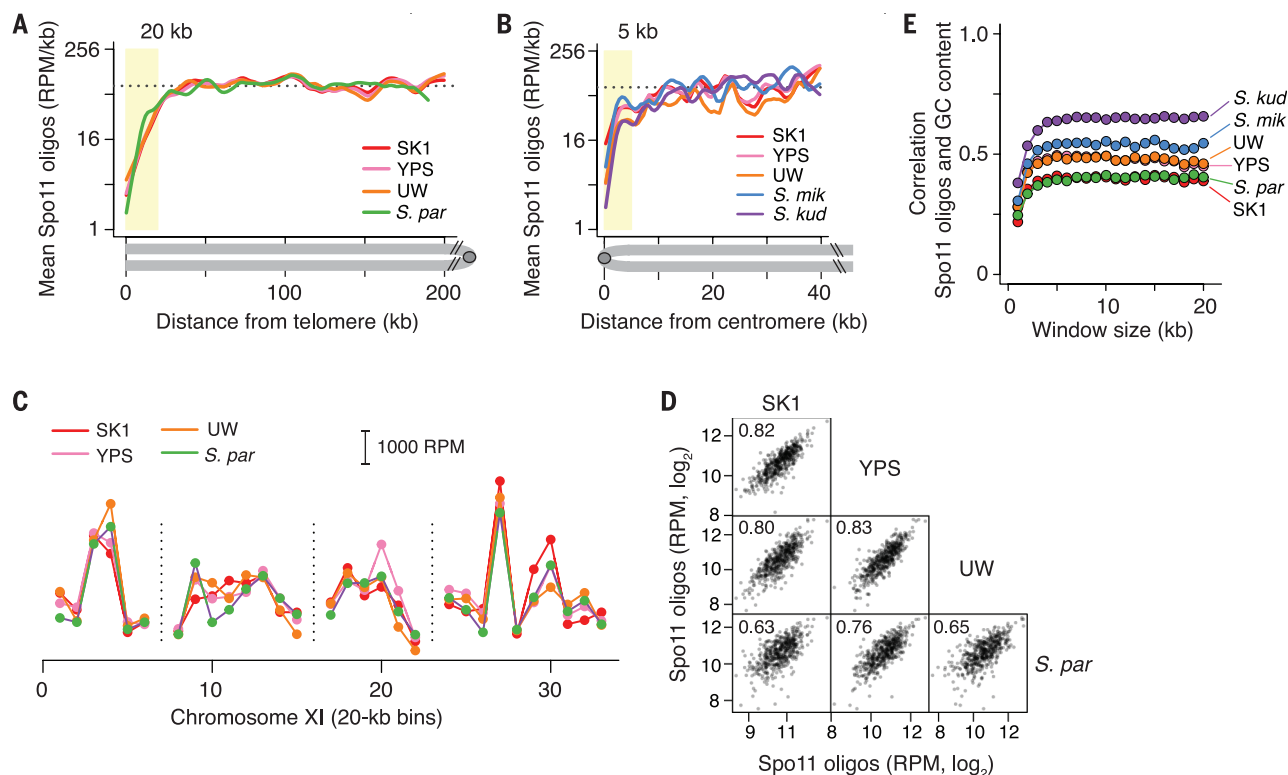


Fig. 4. Conservation of large-scale features of the DSB landscape. (A and B) Telomere-proximal and pericentric DSB suppression. Lines are smoothed fit (Lowess) of Spo11-oligo densities in 500-bp bins averaged across 32 chromosome arms. Dashed line, genome average in SK1; yellow shading, DSB suppression zones. Genome assemblies are not complete enough to evaluate telomeres of *S. mikatae* or *S. kudriavzevii*. **(C and D)** Large-scale hot and cold interstitial domains are conserved. Interstitial segments (excluding subtelomeres and pericentromeres)

were defined as syntenic between *S. cerevisiae* and *S. paradoxus* if orthologous genes were in the same order in both species. Spo11-oligo counts were summed in these syntenic segments divided into 20-kb bins (table S5). A representative example is shown in (C) (vertical dashed lines denote synteny breaks, mostly from unresolved annotation discrepancies), and genome-wide scatter plots and correlation coefficients are in (D). **(E)** Correlation (Pearson's r) between mean Spo11-oligo counts and GC content binned in windows of varying size.

Saccharomycetes (Fig. 5A and fig. S6). This whole-chromosome control of DSB density is in large part a patterning effect of a negative-feedback circuit in which homologous chromosomes that have successfully engaged one another stop making additional DSBs (32). Perhaps smaller chromosomes tend to take more time to engage their homologs and thus enjoy a longer window of opportunity to make DSBs. It has been argued (15) that this form of DSB regulation can account for the earlier finding that smaller chromosomes undergo more crossing over per kilobase than larger chromosomes (33). However, whereas chromosome bisection and fusion experiments have demonstrated that difference in chromosome length is the cause of variation in crossover density (33), this has not been formally tested for DSBs.

S. mikatae provides a natural experiment, as reciprocal translocations have placed parts of ancestral chromosome VI onto longer chromosomes in that species (23) (Fig. 5B). DNA segments syntenic with the left and right arms of ancestral chromosome VI had a Spo11-oligo density predicted by their chromosome length: Density was higher when the segments resided on the short chromosome VI in *S. cerevisiae* but lower when on longer chromosomes in *S. mikatae* (Fig. 5B). Syntenic segments on similar-length chromosomes exhibited matched Spo11-oligo densities (Fig. 5C).

These findings indicate that whole-chromosome variation in DSB density is a direct consequence of chromosome size per se and is thus in large part extrinsic to the DNA sequence.

Conclusions

Our observations fit the hypothesis that hotspots tend to be stable if Spo11 targets functional genomic elements that are evolutionarily constrained (8). Conversely, evolutionary stability of DSB hotspots may indicate constrained function(s), even if that function is presently unknown. Note that DSB hotspots are well conserved between the *Schizosaccharomyces* species *S. pombe* and *S. kambucha* (~0.5% sequence divergence) (34), despite mapping to sites without known function (35). In contrast, in *Drosophila*, which lacks a PRDM9-like system but also does not preferentially target recombination to promoters or known functional elements, the fine-scale distribution of recombination appears to evolve rapidly (36).

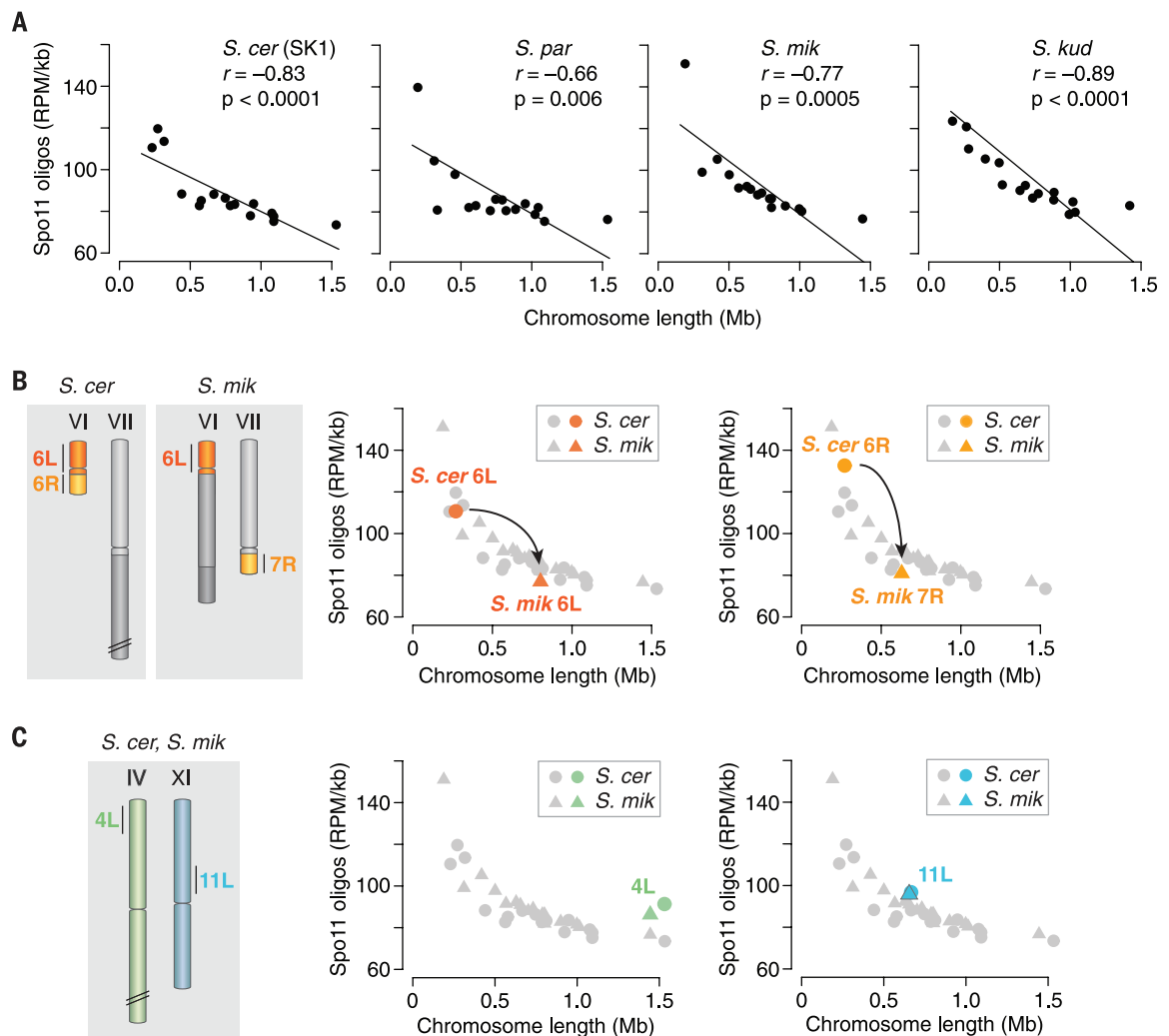
Strong conservation in Saccharomycetes of DSB frequencies within hotspots, across subchromosomal domains, and even across whole chromosomes supports the hypothesis that this conservation traces back to shaping of the DSB landscape by selectively constrained chromosomal features that work combinatorially, hierarchically, and over multiple size scales (15). For example, transcription,

function of telomeres and centromeres, as well as sister chromatid cohesion, rely on and shape chromosome structures over scales ranging from tens to millions of base pairs (bp). Because these structures in turn mold the DSB landscape, selective pressure to maintain them for gene expression, cell division, and other processes imposes a tendency to conserve the DSB landscape. However, the remarkable strength of conservation across millions of years of evolution leads us to speculate that the specific shape of the yeast DSB landscape may confer fitness benefits. The recombination distribution is a heritable trait subject to selection (16, 37), so we speculate that selective pressures may operate more directly on the DSB landscape genome-wide, perhaps related to accurate meiotic chromosome segregation and/or beneficial effects of disrupting or maintaining linkage groups at various size scales (37, 38).

Finally, we note that available evidence in plants, birds, and canids—all apparently lacking a PRDM9-like hotspot targeting mechanism—points to preferential action of Spo11 at promoters, CpG islands, and/or other genomic elements that are under selective constraint to maintain functions separate from being Spo11 targets (39–41). In finches, high-resolution recombination maps inferred from population genetic data reveal evolutionary stability of recombination hotspots, analogous to *Saccharomyces* but

Fig. 5. DSB density is influenced by chromosome length. (A) The anticorrelation between chromosome length and DSB density is conserved. Each point is one chromosome.

(B) A natural experiment demonstrating chromosome length-dependent DSB control. The schematic illustrates syntenic segments on chromosomes of different size in *S. cerevisiae* and *S. mikatae*. The plots show that Spo11-oligo density is higher on these segments in *S. cerevisiae* (when on a short chromosome) than in *S. mikatae* (longer chromosomes). Gray symbols are whole-chromosome values from A for comparison. Note that the segments from ancestral chromosome VI display a Spo11-oligo density closely matched to that of the whole-chromosome value appropriate for the size of the chromosome on which they reside. (C) Control syntenic regions on similarly sized chromosomes have equivalent Spo11-oligo densities in both species.



wholly unlike PRDM9-reliant apes or mice (41). Thus, not only is it untrue that recombination initiation landscapes inevitably evolve rapidly, conservation is likely to be a common pattern for many sexual species.

REFERENCES AND NOTES

1. B. de Massy, *Annu. Rev. Genet.* **47**, 563–599 (2013).
2. L. Kauppi, A. J. Jeffreys, S. Keeney, *Nat. Rev. Genet.* **5**, 413–424 (2004).
3. A. Boulton, R. S. Myers, R. J. Redfield, *Proc. Natl. Acad. Sci. U.S.A.* **94**, 8058–8063 (1997).
4. P. Calabrese, *Proc. Natl. Acad. Sci. U.S.A.* **104**, 4748–4752 (2007).
5. G. Coop, S. R. Myers, *PLoS Genet.* **3**, e35 (2007).
6. U. Friberg, W. R. Rice, *Genetics* **179**, 2229–2238 (2008).
7. F. Ubeda, J. F. Wilkins, *J. Evol. Biol.* **24**, 541–553 (2011).
8. A. Nicolas, D. Treco, N. P. Schultes, J. W. Szostak, *Nature* **338**, 35–39 (1989).
9. A. J. Jeffreys, R. Neumann, *Nat. Genet.* **31**, 267–271 (2002).
10. M. Pineda-Krch, R. J. Redfield, *Genetics* **169**, 2319–2333 (2005).
11. F. Baudat, Y. Imai, B. de Massy, *Nat. Rev. Genet.* **14**, 794–806 (2013).
12. C. L. Baker et al., *PLoS Genet.* **11**, e1004916 (2015).
13. F. Cole et al., *Nat. Genet.* **46**, 1072–1080 (2014).
14. S. Myers et al., *Science* **327**, 876–879 (2010).
15. J. Pan et al., *Cell* **144**, 719–731 (2011).
16. C. S. Smukowski, M. A. Noor, *Heredity* **107**, 496–508 (2011).
17. I. J. Tsai, A. Burt, V. Koufopanou, *Proc. Natl. Acad. Sci. U.S.A.* **107**, 7847–7852 (2010).
18. G. Liti et al., *Nature* **458**, 337–341 (2009).
19. M. J. Neale, J. Pan, S. Keeney, *Nature* **436**, 1053–1057 (2005).
20. T. Replinsky, V. Koufopanou, D. Greig, G. Bell, *Trends Ecol. Evol.* **23**, 494–501 (2008).
21. B. Dujon, *Trends Genet.* **22**, 375–387 (2006).
22. M. Kellis, N. Patterson, M. Endrizzi, B. Birren, E. S. Lander, *Nature* **423**, 241–254 (2003).
23. Materials and methods are available as supporting material on Science Online.
24. L. E. Berchowitz, S. E. Hanlon, J. D. Lieb, G. P. Copenhaver, *Genome Res.* **19**, 2245–2257 (2009).
25. A. M. Tsankov, D. A. Thompson, A. Socha, A. Regev, O. J. Rando, *PLoS Biol.* **8**, e1000414 (2010).
26. M. Lichten, in *Recombination and Meiosis*, R. Egel, D. H. Lankenau, Eds. (Springer-Verlag, Heidelberg, 2008), vol. 3, pp. 165–193.
27. M. A. White, M. Dominska, T. D. Petes, *Proc. Natl. Acad. Sci. U.S.A.* **90**, 6621–6625 (1993).
28. F. Pratto et al., *Science* **346**, 1256442 (2014).
29. E. J. Louis, *Yeast* **11**, 1553–1573 (1995).
30. B. Rockmill, K. Voelkel-Meiman, G. S. Roeder, *Genetics* **174**, 1745–1754 (2006).
31. A. D. Peters, *Genetics* **178**, 1579–1593 (2008).
32. D. Thacker, N. Mohibullah, X. Zhu, S. Keeney, *Nature* **510**, 241–246 (2014).
33. D. B. Kaback, V. Guacci, D. Barber, J. W. Mahon, *Science* **256**, 228–232 (1992).
34. S. E. Zanders et al., *eLife* **3**, e02630 (2014).
35. K. R. Fowler, M. Sasaki, N. Milman, S. Keeney, G. R. Smith, *Genome Res.* **24**, 1650–1664 (2014).
36. C. S. Smukowski Heil, C. Ellison, M. Dubin, M. A. Noor, *Genome Biol. Evol.* **7**, 2829–2842 (2015).
37. G. Coop, M. Przeworski, *Nat. Rev. Genet.* **8**, 23–34 (2007).
38. P. J. Keller, M. Knop, *PLoS Genet.* **5**, e1000533 (2009).
39. A. Auton et al., *PLoS Genet.* **9**, e1003984 (2013).
40. K. Choi, I. R. Henderson, *Plant J.* **83**, 52–61 (2015).
41. S. Singhal et al., *Science* **350**, 928–932 (2015).
42. G. Liti et al., *BMC Genomics* **14**, 69 (2013).

ACKNOWLEDGMENTS

Sequencing data were deposited at the Gene Expression Omnibus (GEO) under accession number GSE71930. We are grateful to D. Greig, C. Hittinger, G. Liti, E. Louis, C. Müller, and J. Roop for providing strains and advice on culturing *Saccharomyces* species; A. Viale and the Integrated Genomics Operation, Memorial Sloan Kettering Cancer Center (MSKCC), for sequencing; N. Socci (Bioinformatics Core Facility, MSKCC) for mapping Spo11-oligo and MNase-seq reads; S. Shuman for gifts of T4 RNA ligase; and S. Kim, J. Lange, N. Mohibullah, S. Tischfield, and X. Zhu for discussions. We thank M. Przeworski for discussions, communicating data before publication, and comments on the manuscript. This work was supported by NIH grant R01 GM058673. I.L. was supported in part by NIH fellowship F31 GM097861.

SUPPLEMENTARY MATERIALS

www.sciencemag.org/content/350/6263/932/suppl/DC1
Materials and Methods
Figs. S1 to S6
Tables S1 to S5
References (43–56)

23 July 2015; accepted 5 October 2015
10.1126/science.aad0814

BATTERIES

“Water-in-salt” electrolyte enables high-voltage aqueous lithium-ion chemistries

Liumin Suo,¹ Oleg Borodin,² Tao Gao,¹ Marco Olguin,² Janet Ho,² Xiulin Fan,¹ Chao Luo,¹ Chunsheng Wang,^{1*} Kang Xu^{2*}

Lithium-ion batteries raise safety, environmental, and cost concerns, which mostly arise from their nonaqueous electrolytes. The use of aqueous alternatives is limited by their narrow electrochemical stability window (1.23 volts), which sets an intrinsic limit on the practical voltage and energy output. We report a highly concentrated aqueous electrolyte whose window was expanded to ~3.0 volts with the formation of an electrode-electrolyte interphase. A full lithium-ion battery of 2.3 volts using such an aqueous electrolyte was demonstrated to cycle up to 1000 times, with nearly 100% coulombic efficiency at both low (0.15 coulomb) and high (4.5 coulombs) discharge and charge rates.

Lithium-ion (Li-ion) batteries power much of our digital and mobile lifestyle (1, 2). However, their adoption in more strategically important applications such as vehicle electrification and grid storage has been slower, mainly because of concerns raised over their safety, cost, and environmental impact (3). Most of these concerns come from the nonaqueous electrolytes needed to withstand the high voltages (>3.0 V) of the chemistries (4), because the ester-based solvents are highly flammable and reactive with the charged electrodes (5), and the lithium salt (LiPF₆) is thermally unstable and extremely toxic (6). Substantial costs are incurred not only directly by these electrolyte components but also to a larger degree by the stringent moisture-free process and safety management required for the dangerous combination of flammable electrolytes and energy-intensive electrodes (4, 7, 8).

Aqueous electrolytes could resolve these concerns (9–11), but their electrochemical stability window (1.23 V) is too narrow to support most of the electrochemical couples used in Li-ion batteries. Hydrogen evolution at the anode presents the most severe challenge, as it occurs at a potential (2.21 to 3.04 V versus Li, depending on pH value) far above where most Li-ion battery anode materials operate. Even in trace amounts, hydrogen severely deteriorates the electrode structure during cycling. A common practice to suppress hydrogen evolution in aqueous electrochemistry is to adjust the alkalinity (12, 13), so that the water reduction potential shifts downward to allow the use of anode materials otherwise prohibited under neutral or acidic conditions. However, as

the overall electrochemical stability window of aqueous electrolytes remains constant, anodic stability against oxygen evolution suffers a corresponding compromise, as illustrated by a Pourbaix diagram (9). A maximum voltage of 1.5 V was achieved in aqueous Li-ion batteries, where the residual currents for H₂ or O₂ evolution still brought high self-discharge rates despite the moderate cell voltage (9–11).

In contrast to nonaqueous electrolyte systems, where cathode and anode materials often operate far beyond the thermodynamic stability limits of electrolyte components (4, 14), kinetic protection from a solid-electrolyte interphase (SEI) in aqueous media has never been considered possible. Such interphases, situating between electrode surfaces and electrolyte, are formed by sacrificial electrolyte decomposition during the initial charging, and they constitute a barrier allowing ionic conduction but forbidding electronic conduction. Their presence substantially expands the usable electrochemical stability window of electrolytes. In conventional aqueous electrolytes, a protective interphase is absent because none of the decomposition products from water (H₂, O₂, or OH[−]) can deposit in a dense solid state. In the absence of interphases, aqueous Li-ion batteries are typically limited to low voltage (<1.5 V) and low energy density (<70 Wh/kg), often with rapid fading of capacity and low coulombic efficiency. The latter is especially pronounced at low C rates, where C refers to nominal capacity of the cell, and a rate of *n*C represents the discharge current that can drain this capacity in 1/*n* hours. (For most batteries, a rate of 1 C means that the discharge current will discharge the entire battery in 1 hour.)

We report the formation of such interphases in an aqueous electrolyte by manipulating the source of electrolyte decomposition during the initial charging processes. A “water-in-salt” electrolyte is obtained by dissolving lithium bis(trifluoromethane sulfonyl)imide (LiTFSI) at extremely high concentrations (molality >20 m)

in water. This leads to an anion-containing Li⁺ solvation sheath, which results in the formation of a dense interphase on the anode surface mainly arising from anion reduction. Combined with the substantially reduced electrochemical activity of water at such a high concentration, this highly concentrated water-in-salt electrolyte provides an expanded electrochemical stability window of ~3.0 V. A full aqueous Li-ion battery constructed with a model electrochemical couple (LiMn₂O₄ and Mo₆S₈) demonstrated an open circuit voltage (OCV) of 2.3 V and was cycled at nearly 100% coulombic efficiency for up to 1000 cycles at both low (0.15 C) and high (4.5 C) rates.

Water-in-salt electrolytes

LiTFSI was chosen as the salt because of its high solubility in water (>20 m at 25°C) and high stability against hydrolysis (15). When the LiTFSI concentration is above 5 m, the water-in-salt definition applies, as the salt outnumbers the solvent in this binary system by both weight and volume (fig. S1). In these solutions, the average number of water molecules available to solvate each ion is far below the “solvation numbers” that are well established in conventional electrolytes (~1.0 m). Instead, interionic attractions become more pronounced relative to solvent-ion interactions, incurring unusual physicochemical properties (16–20). More important, the interphasial chemistry on electrode surfaces could be altered as a direct consequence of the different cation solvation sheath structure (14, 21–24). This “cation solvation–interphase chemistry” correlation has been leveraged to manipulate the electrochemical behavior of nonaqueous electrolytes on both graphitic anode and metal oxide cathodes (17, 23, 25, 26), but its effect on aqueous electrolytes had remained unexplored. Figures S2 to S4 summarize the physical and transport properties of LiTFSI in water at varying concentrations. According to the thermal analysis of the highly concentrated solutions, solutions at both 20 and 21 m are “true” liquids at room temperature (25°C) that can be supercooled down to ~−90°C with negligible crystallinity (27). The room-temperature conductivity of 21 m solution remains ~10 mS/cm, comparable to that of nonaqueous electrolytes (9.0 mS/cm) used in commercial Li-ion batteries (figs. S3 and S4).

The electrochemical stability window for these aqueous electrolytes was evaluated with cyclic voltammetry (CV) on stainless steel electrodes, whose first cathodic and anodic scans are shown in Fig. 1. The overall stability window expands as the LiTFSI concentration increases, with both oxygen and hydrogen evolution potentials pushed well beyond the thermodynamic stability limits of water. Closer examination of Fig. 1A shows that the onset of reduction at all concentrations occurs at ~2.80 V, before rapidly accelerating at 2.63 V and then reaching a plateau. Quantum chemistry calculations predict the onset of LiTFSI reduction at such high concentrations around 2.7 to 2.9 V, which is slightly higher than the hydrogen evolution process (2.63 V) corresponding to the exponential current increase. Thus, prior

¹Department of Chemical and Biomolecular Engineering, University of Maryland, College Park, MD 20740, USA.

²Electrochemistry Branch, Sensor and Electron Devices Directorate, Power and Energy Division, U.S. Army Research Laboratory, Adelphi, MD 20783, USA.

*Corresponding author. E-mail: cswang@umd.edu (C.W.); conrad.k.xu.civ@mail.mil (K.X.)

to hydrogen evolution, the reduction of TFSI seems to result in a passivation process that intensifies with salt concentration and reduces the plateau current by more than an order of magnitude, from 2.47 mA/cm² (1 m) to 0.18 mA/cm² (21 m). This passivation eventually suppresses hydrogen evolution, pushing its onset from 2.63 V to 1.90 V. On the cathode side (Fig. 1B), oxygen evolution also seems to be suppressed with increasing salt concentration but no clear passivation process is observed, probably as a result of the reduced water activity when coordinated to Li⁺ at high concentration as well as an inner Helmholtz layer increasingly populated by TFSI anions (28). Overall, a stability window of ~3.0 V is achieved because of the very high concentration of LiTFSI (Fig. 1C), with both cathodic (~1.9 V versus Li) and anodic (~4.9 V versus Li) limits beyond those defined by the Pourbaix diagram of water at pH 7 (cathodic ~2.63 V versus Li, anodic ~3.86 V versus Li).

The model cathode and anode materials LiMn₂O₄ and Mo₆S₈ (fig. S5) were chosen as active working electrodes in CV experiments to verify the expanded stability window. Figure 2A demonstrates two redox couples of LiMn₂O₄, which gradually shift from 4.09/4.17 V and 4.22/4.31 V in 5 m solution to 4.17/4.37 V and 4.31/4.49 V in 21 m solution, while the reaction kinetics become slower at high salt concentrations. For Mo₆S₈, a single lithiation/delithiation process was observed at ~2.5 V in dilute solutions, and only when salt concentrations reached 10 m or above did the second lithiation/delithiation at ~2.3 V appear. The modulation of redox processes

toward positive potentials, observed in all cases in Fig. 2A, is attributed to the Li⁺ activity change in the solution according to the Nernst equation (see supplementary materials). It is this modulation that moves the second redox process of Mo₆S₈ into the expanded electrochemical stability window of the water-in-salt electrolyte, allowing the full and reversible use of its Li storage sites otherwise inaccessible in diluted aqueous solutions (fig. S6). Hence, a 2.3 V aqueous LiMn₂O₄/Mo₆S₈ full Li-ion cell is enabled by the water-in-salt electrolyte (Fig. 2B). In control electrolytes using LiNO₃ and Li₂SO₄ (figs. S7 and S8), similar positive modulations of Mo₆S₈ were observed; however, their limited solubility prohibited the appearance of the second lithiation/delithiation process. Even at the highest possible LiNO₃ concentration (12.5 m), hydrogen evolution still overwhelms the second lithiation of Mo₆S₈ at ~2.5 V versus Li (fig. S7), without any sign of passivation. Thus, the high concentration of LiTFSI in water not only reduces water activity and modulates redox potentials, but also suppresses hydrogen evolution through the formation of an interphase.

A high-voltage aqueous Li-ion battery

A full Li-ion cell using a LiMn₂O₄ cathode and a Mo₆S₈ anode was assembled to evaluate the viability of the water-in-salt electrolyte at 21 m (Fig. 2, B to D, and figs. S9 to S12). The cathode/anode mass ratio was set to 2:1 in order to compensate for the irreversible capacity at the Mo₆S₈ anode due to formation of SEI during the initial cycles. At 0.15 C, the cell displayed

two voltage plateaus at 1.50 V and 2.00 V, respectively (fig. S9), delivering a discharge capacity of 47 mAh per gram of total electrode mass. A conservative estimate made on the basis of average voltage and capacity places the energy density in the vicinity of 84 Wh per kilogram of total electrode mass. To further explore the energy density achievable in the ideal scenario where Li⁺ consumption is minimized during the initial interphase formation, we matched a Mo₆S₈ anode recovered from a cycled full cell with a fresh LiMn₂O₄ cathode at 1:1 ratio. Such a full cell delivered an energy density of 100 Wh per kilogram of total electrode mass (fig. S11). A full aqueous Li-ion cell using Mo₆S₈ and LiNi_{0.8}Co_{0.15}Al_{0.05}O₂ cathode also cycled reversibly but yielded a lower capacity (fig. S13).

Figure 2, C and D, displays the cycling stability and coulombic efficiency of LiMn₂O₄/Mo₆S₈ full cells at low (0.15 C) and high (4.5 C) rates. Excellent stability with high capacity retention (68% with 1000 cycles at 4.5 C and 78% with 100 cycles at 0.15 C) and near 100% coulombic efficiency are observed at both rates (fig. S14). As shown by Dahn and colleagues, the most rigorous proof of stability does not come from the number of cycles, but rather from the time spent by a system at a fully charged state (29) as well as from high coulombic efficiency at low C rates. In previous studies, the cycling stability of aqueous Li-ion cells was often tactically evaluated at high instead of low rates, so that the effect of residual hydrogen and oxygen evolution on cycling stability would be less apparent. To reveal how much impact the trace parasitic

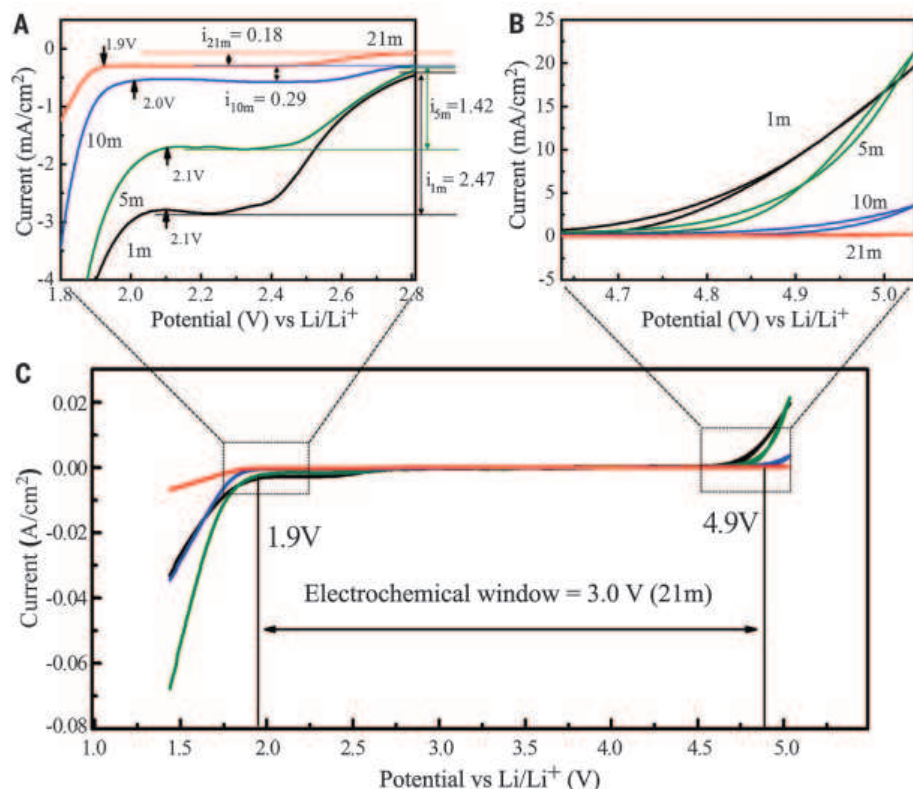


Fig. 1. The electrochemical stability window of LiTFSI-H₂O electrolytes on nonactive electrodes. Measurements were taken at different concentrations (molality) with cyclic voltammetry (CV) on stainless steel working electrodes between -1.8 V and 1.8 V versus Ag/AgCl at 10 mV/s, wherein the potential has been converted to Li/Li⁺ reference for convenience. (A) Overall electrochemical stability window. (B and C) Magnified view of the regions outlined near anodic and cathodic extremes in (A).

reactions in water-in-salt electrolyte exert on full Li-ion cell performance, we monitored the open-circuit voltage decay of fully charged cells upon storage and then immediately measured the recoverable capacity. The results (figs. S15 and S16) confirm the negligible effect of either hydrogen or oxygen evolution. Only in longer-term cycling tests would the effect of parasitic reactions become more apparent, as evidenced by the slow but steady fading of capacity shown in Fig. 2, C and D; this finding suggests that the interphasial chemistry needs to be tailored for more effective protection. Elevated temperature (45°C) did not induce accelerated capacity fading, which indicates that the SEI formed should be stable against dissolution (fig. S12).

Interphasial chemistry and its importance

High salt concentration deviates solution dynamics from an ideal state (30). To quantify such deviation, we calculated the relative Li^+ activity coefficients in electrolytes based on the peak potential shifts as measured from CV (Fig. 2A). The details are given in supplementary text and tables S1 and S2; fig. S17 summarizes the dependence of these coefficients on salt concentration, which experiences a steady rise from 5 m to 21 m. According to Bockris and Reddy, this

increase of activity coefficients at high concentration reflects the deprived population of water as a free solvent and the intensified cation-anion interaction (30).

The interplay among Li^+ , TFSI⁻, and water was also investigated with spectroscopies. Major Raman vibrational signals are summarized in fig. S18 and table S3; Fig. 3A compares the shift of the most intense peak at 744 cm^{-1} as the salt concentration increases, with crystalline LiTFSI as the reference (top trace). Evidently this vibration mode is rather sensitive to the change of the anion environment, drifting from 744.6 cm^{-1} at 5.0 m to 748.5 cm^{-1} at 21 m. The latter is essentially identical to that in a crystalline lattice. On the basis of the previous assignment of a 748 cm^{-1} peak in nonaqueous electrolytes (37), we attribute this band to the formation of a percolated TFSI⁻ anionic network in the highly concentrated solutions. In the ^{17}O nuclear magnetic resonance (NMR) spectra, the two sets of oxygen nuclei were assigned to water (~0 ppm) and TFSI⁻ (~154 ppm), respectively; Fig. 3B displays the change in ^{17}O chemical shifts for both nuclei with LiTFSI concentration. The water ^{17}O signal is rather sensitive to the presence of salt, because Li^+ directly interacts with the lone pair electrons of water oxygen. Its coordination with Li^+ results in the deshielding, as indicated

by the downshift displacement in its chemical shift, while the increasing salt concentration above 10 m intensifies this effect. On the other hand, the ^{17}O signal at 154 ppm seems to be rather insensitive to the presence of salt, although its successive downshift is still visible. This can be attributed to the fact that oxygen on TFSI⁻ does not directly coordinate with Li^+ for salt concentrations less than 10 m.

Both oxygen nuclei display obvious peak broadening at salt concentrations greater than 10 m, as if the anion environment gradually transitions into a semisolid state similar to a LiTFSI crystal. Such an intimate interaction between cation and anion, as revealed by Raman and NMR spectroscopy, bears close resemblance to an ionic liquid, where on average each Li^+ is surrounded by at least one anion. Naturally, when Li^+ in this coordination environment is brought into the vicinity of the anode surface, TFSI⁻ would be reasonably expected to display its own electrochemical features.

The relationship between solution structure and electrochemical properties is further revealed from molecular dynamics simulations. For dilute solutions (≤ 5 m), Li^+ remains well hydrated in its primary solvation sheath with sufficient free water available (Fig. 3C). In such electrolytes, attempts to lithiate an anode, whose

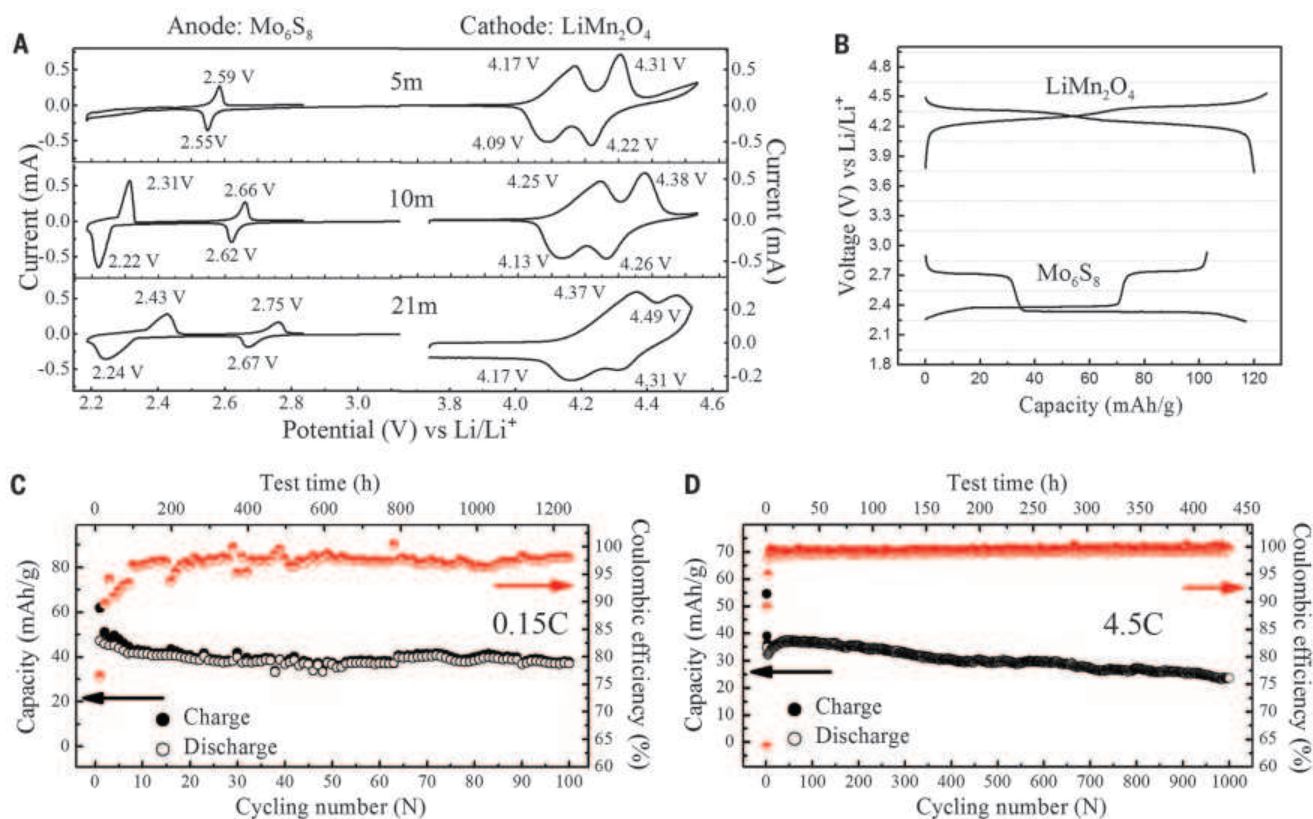


Fig. 2. Electrochemical performance on active electrodes. (A) Electrochemical stability window of electrolytes at various LiTFSI concentrations as measured with CV on active (LiMn₂O₄ and Mo₆S₈) electrode surfaces at 0.1 mV/s. (B) Typical voltage profile of LiMn₂O₄ and Mo₆S₈ electrodes in 21 m LiTFSI solution at constant current (0.2 C). Data in (A) and (B) were collected in a three-electrode device including Mo₆S₈ and LiMn₂O₄ as working electrodes and Ag/AgCl as reference electrode. (C and D) Cycling stability and coulombic efficiency of full aqueous Li-ion cells using Mo₆S₈ and LiMn₂O₄ as anode and cathode materials in 21 m LiTFSI solution, at low (0.15 C) and high (4.5 C) rates, respectively.

lithiation potential is below that of water reduction, would lead to preferential reduction of water and sustained hydrogen evolution, which would prevent not only any Li^+ intercalation but also any possible reduction of TFSI^- . However, with LiTFSI concentrations increased beyond 20 m, molecular dynamics simulation predicts that on average two TFSI^- anions would be observed in each Li^+ primary solvation sheath (Fig. 3D), and such a high probability of TFSI^- leads to an interphasial chemistry dominated by the reduction of TFSI^- .

The reduction potential of TFSI^- is also altered by its intimate interaction with Li^+ . According to density functional theory (DFT) calculations (Fig. 4A and fig. S19), aggregates such as $\text{Li}_2(\text{TFSI})(\text{H}_2\text{O})_x$ become reductively unstable below 2.9 V versus Li, which is substantially higher than the reduction potential for the isolated TFSI^- anion at 1.4 V (Fig. 4A) and hydrogen evolution at 2.63 V. Further corroborating the preferential reduction of TFSI^- over water, a density-of-states analysis obtained from DFT calculations indicates that both the TFSI^- conduction band minimum and the water valence band maximum shift to lower potentials with increasing salt concentration. At >20 m, this trend leads to a premature TFSI^- reduction and delayed water oxidation (Fig. 4B and supplementary materials). We therefore conclude that this reduction process generates sufficient LiF from TFSI^- to form an anode-

electrolyte interphase, which kinetically prevents sustained reduction of both water and TFSI^- in a similar manner as an SEI in nonaqueous electrolytes does. The earlier observation that TFSI^- was electrochemically reduced to LiF on an anode surface in nonaqueous electrolyte (32, 33) in conjunction with limited solubility of LiF in water make this speculation reasonable. In retrospect, an ideal lithium salt that could enable the formation of an aqueous SEI should be not only highly soluble and chemically stable in water but also susceptible to electrochemical reduction at a desired potential (i.e., a potential higher than that of H_2 evolution), producing a solid product insoluble in aqueous media. Lithium salts meeting these requirements include those based on fluoroalkyl sulfonamide anions, to which LiTFSI belongs, as well as fluoroalkyl sulfonate anions. Compared with the higher cost of imides, sulfonates might make more appropriate candidates. At least one such sulfonate salt (lithium trifluoromethane sulfone) has been found to yield nearly identical electrochemical stability to that of LiTFSI (fig. S20).

To demonstrate the existence of an interphase in our aqueous electrolytes, we conducted x-ray photoelectron spectroscopy (XPS) on an anode recovered after a complete lithiation cycle. Figure 4C shows the valence electrons' binding energies for a few detected elements. Included as comparisons are the spectra of the pristine Mo_6S_8 , whose

$\text{Mo } 3d$ and $\text{S } 2p$ signals serve as references, and $\text{F } 1s$ detected therein at 689.5 eV came from poly(tetrafluoroethylene) (PTFE) used as binder in the composite electrode. The most conspicuous change after being charged to 2.3 V (corresponding to full lithiation of Mo_6S_8) is the disappearance of both $\text{S } 2p$ and $\text{Mo } 3d$ signals, and the appearance of $\text{Li } 1s$ and $\text{F } 1s$ signals, the latter of which is identified to be a CF_3 species. Hence, lithiation left the anode surface completely covered with species originated from TFSI^- , while the CF_3 species could arise from either excess LiTFSI remaining on the anode surface, or its incomplete reduction products. Etching this surface by Ar^+ reveals an underlying interphase consisting overwhelmingly of LiF , which not only precedes the reappearance of the original $\text{S } 2p$ and $\text{Mo } 3d$ signals but remains even after prolonged (1920 s) sputtering. This resistance against sputtering is undoubtedly the consequence of a very dense surface interphase.

On the basis of earlier reports that TFSI^- is electrochemically reduced to LiF (32, 33), we believe that in the current water-in-salt electrolytes, this LiF -rich interphase serves as an electron barrier preventing the reduction of water while allowing Li^+ migration. Evidence also comes from transmission electron microscopy (TEM) images of the cycled Mo_6S_8 , whose surface, when compared with the pristine state, is found to be covered with a crystalline phase 10 to 15 nm

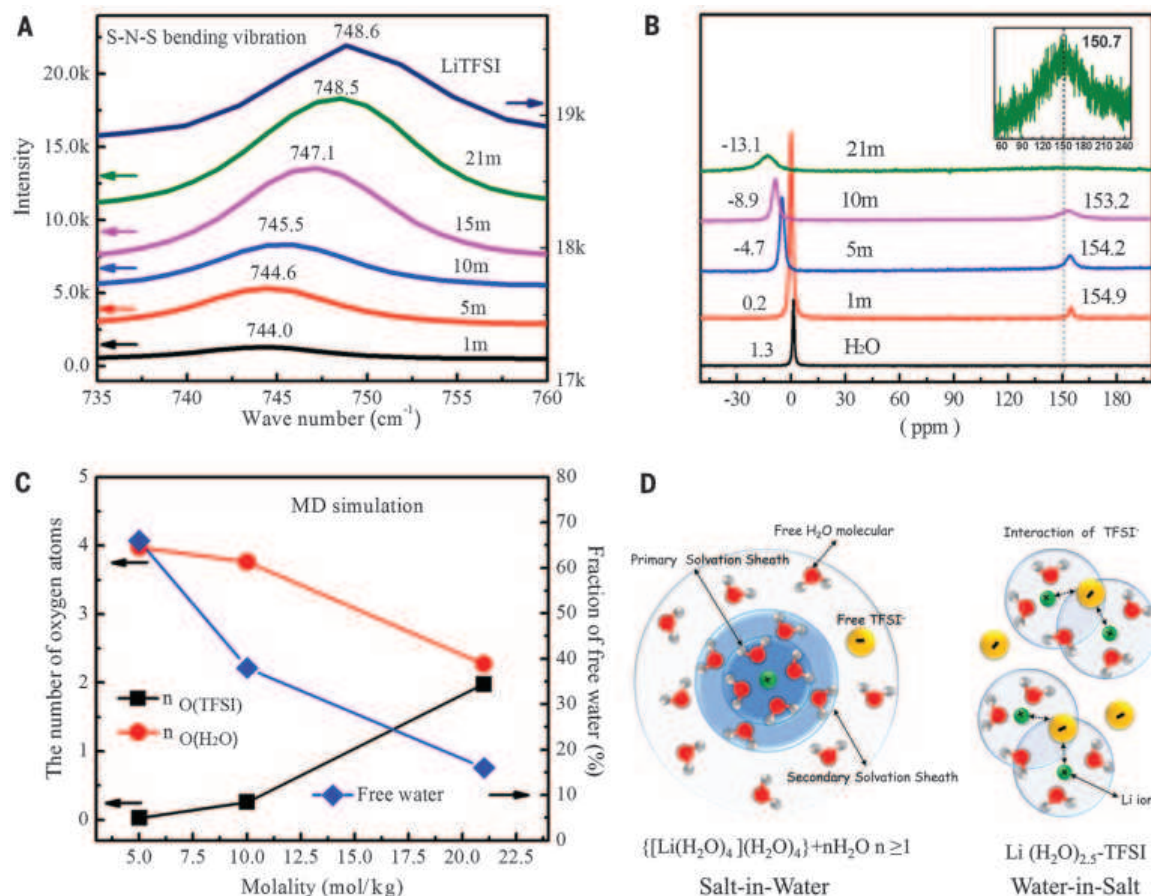


Fig. 3. The effect of LiTFSI concentration on ion-solvent and ion-ion interactions. (A) Progression of Raman vibration at $\sim 744 \text{ cm}^{-1}$ with salt concentration. (B) Change of chemical shifts for ^{17}O nuclei in solvent (water) and anion (TFSI^-). The inset shows the TFSI^- peak at 21 m. (C) Numbers of water and TFSI^- oxygen atoms within the Li^+ primary solvation sheath of 0.27 nm and the fraction of “free” water not bound to any Li^+ , all obtained from molecular dynamics simulations. (D) Illustration of the evolution of the Li^+ primary solvation sheath in diluted and water-in-salt solutions.

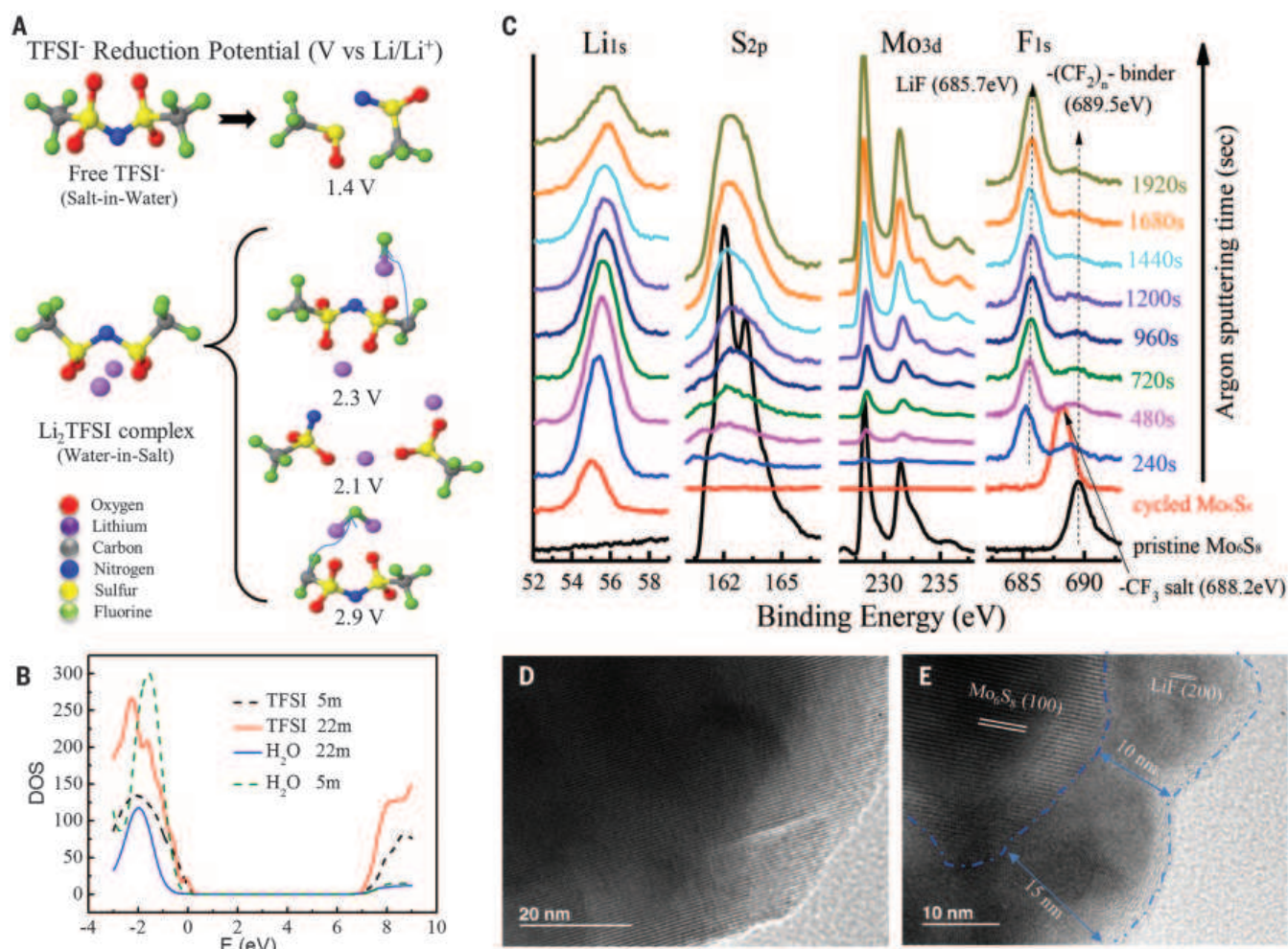


Fig. 4. SEI formation in aqueous electrolyte. (A) Predicted reduction potentials from G4MP2 quantum chemistry calculations. (B) Projected density of states (DOS) for H₂O-LiTFSI electrolyte from HSE06 DFT calculations. (C) X-ray photoelectron spectroscopy (XPS) spectrum of pristine (bottom) and cycled Mo₆S₈ at full lithiation state after various durations of Ar⁺ sputtering. (D and E) TEM images of pristine Mo₆S₈ (D) and cycled Mo₆S₈ (E).

thick (Fig. 4, D and E). The interplanar spacing of this crystalline phase identifies it as imperfect crystalline LiF. Further confirmation comes from TEM energy-dispersive x-ray spectroscopy (EDX) analysis (fig. S21), whose line scan reveals that F evenly distributes on the Mo₆S₈ particle surface. This aqueous LiF-based SEI, originating from TFSI⁻ reduction and crystalline in nature, seems to differ chemically from the composite interphases that have been well characterized in non-aqueous electrolytes (4, 14), where solvent reduction products contribute overwhelmingly as the chemical building blocks. On the cathode surface, however, no such LiF-based SEI was found even after extended cycling (figs. S22 and S23).

Summarizing all the spectra information, an overall picture of the Li⁺ solvation sheath and its role in interphasial chemistry emerges. In dilute solutions (< 5 m) (34, 35), the abundance of water can afford a conventional solvation sheath structure (i.e., four water molecules per Li⁺ in the primary and more in the loosely bound secondary sheath) (36), where Li⁺ and TFSI⁻ are well separated by water. When salt concentration increases to a certain level (>10 m), the

insufficient water population leads to a drastic change in Li⁺ solvation sheath structure. In particular, at 21 m, there are only 2.6 water molecules per Li⁺, which can no longer effectively neutralize the electrostatic field created by the formal charge on Li⁺; consequently, TFSI⁻ enters the Li⁺ solvation sheath, leading to intimate Li⁺-TFSI⁻ interactions as observed in Raman and ¹⁷O NMR spectroscopy. A direct result of this anion-containing solvation sheath is an interphasial chemistry on the anode consisting of mainly LiF from TFSI⁻ reduction, which is enabled not only by the high probability of TFSI⁻ in the Li⁺ solvation sheath, but also by its reduction potential, which is now higher than that of water. Simultaneously, the scarcity of free water molecules due to high salt concentration contributes to their inactivity that benefits both cathodic and anodic stability limits. These factors work in synergy to realize an expanded electrochemical stability window of 3.0 V (Fig. 1C).

Battery performance can be quantified with four parameters: cell voltage, capacity, coulombic efficiency, and cycling stability. The first two

determine the battery's energy density; the latter two dictate its lifetime and energy efficiency. For comparison, we plotted our water-in-salt battery in Fig. 5A against other aqueous systems previously investigated using these parameters. More than 1000 cycles were reported for electrochemical couples of LiMn₂O₄/acetylene black (37) and LiFePO₄/LiTi₂(PO₄)₃ (13). Their excellent stability, however, was achieved at the expense of voltage (<1.25 V) and energy density (<50 Wh/kg). On the other hand, efforts to increase cell voltage to ~1.50 V were accompanied by an appreciable compromise in cycling stability (10, 38–41). In all cases, energy densities were below 75 Wh/kg. The formation of an anode-electrolyte interphase in a water-in-salt electrolyte enables us to decouple voltage from cycling stability and achieve high values for both.

Note that the electrochemical couple used in our study (LiMn₂O₄ and Mo₆S₈) did not actually make full use of the expanded electrochemical stability window; thus, further advances in exploring more powerful and energetic battery chemistry for this electrolyte system are possible. From our perspective, perhaps more important

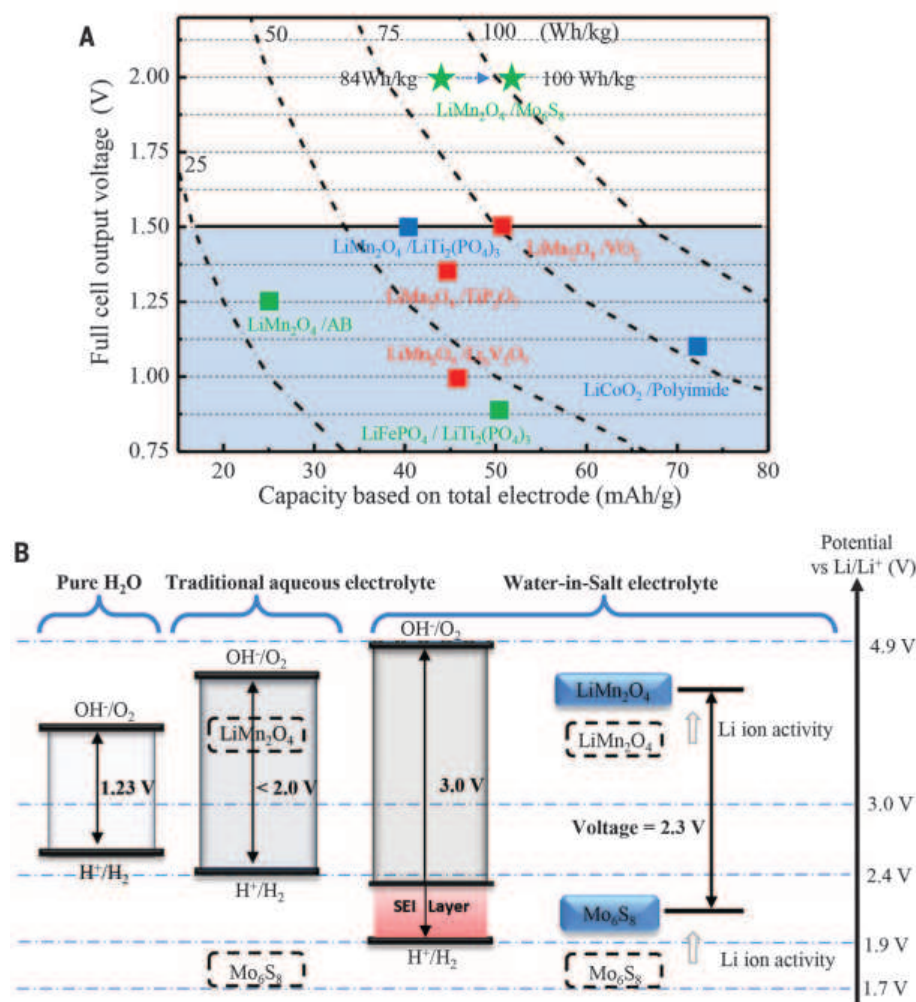


Fig. 5. The performance of aqueous Li-ion chemistries benefits from the expanded electrochemical stability window of aqueous electrolytes.

(A) Performance of aqueous Li-ion batteries based on various electrochemical couples. Color code for cycling stability: red, <100 cycles; blue, 100 to 200 cycles; green, >1000 cycles. (B) Illustration of expanded electrochemical stability window for water-in-salt electrolytes together with the modulated redox couples of LiMn_2O_4 cathode and Mo_6S_8 anode caused by high salt concentration.

than the electrochemical performance described in Fig. 2, C and D, is the fact that an interphase could form and function in aqueous electrolytes, which opens new avenues to aqueous electrochemistry (Fig. 5B).

REFERENCES AND NOTES

- M. Armand, J. M. Tarascon, *Nature* **451**, 652–657 (2008).
- M. S. Whittingham, *Chem. Rev.* **104**, 4271–4302 (2004).
- B. Dunn, H. Kamath, J. M. Tarascon, *Science* **334**, 928–935 (2011).
- K. Xu, *Chem. Rev.* **104**, 4303–4418 (2004).
- L. Hu, K. Xu, *Proc. Natl. Acad. Sci. U.S.A.* **111**, 3205–3206 (2014).
- A. Hammami, N. Raymond, M. Armand, *Nature* **424**, 635–636 (2003).
- J. B. Goodenough, Y. Kim, *Chem. Mater.* **22**, 587–603 (2010).
- J. M. Tarascon, M. Armand, *Nature* **414**, 359–367 (2001).
- H. Kim et al., *Chem. Rev.* **114**, 11788–11827 (2014).
- W. Li, J. R. Dahn, D. S. Wainwright, *Science* **264**, 1115–1118 (1994).
- Y. G. Wang, J. Yi, Y. Y. Xia, *Adv. Energy Mater.* **2**, 830–840 (2012).
- W. Li, W. R. McKinnon, J. R. Dahn, *J. Electrochem. Soc.* **141**, 2310–2316 (1994).
- J.-Y. Luo, W.-J. Cui, P. He, Y.-Y. Xia, *Nat. Chem.* **2**, 760–765 (2010).
- K. Xu, *Chem. Rev.* **114**, 11503–11618 (2014).
- S. F. Lux et al., *J. Electrochem. Soc.* **160**, A1694–A1700 (2013).
- C. A. Angell, C. Liu, E. Sanchez, *Nature* **362**, 137–139 (1993).
- K. Yoshida, M. Tsuchiya, N. Tachikawa, K. Dokko, M. Watanabe, *J. Phys. Chem. C* **115**, 18384–18394 (2011).
- L. Suo, Y.-S. Hu, H. Li, M. Armand, L. Chen, *Nat. Commun.* **4**, 1481 (2013).
- K. Ueno et al., *J. Phys. Chem. B* **116**, 11323–11331 (2012).
- J.-W. Park et al., *J. Phys. Chem. C* **117**, 4431–4440 (2013).
- K. Xu, Y. Lam, S. S. Zhang, T. R. Jow, T. B. Curtis, *J. Phys. Chem. C* **111**, 7411–7421 (2007).
- K. Xu, A. von Cresce, *J. Mater. Chem.* **21**, 9849–9864 (2011).
- M. Nie et al., *J. Phys. Chem. C* **117**, 25381–25389 (2013).
- S.-K. Jeong et al., *Electrochem. Commun.* **31**, 24–27 (2013).
- Y. Yamada et al., *J. Am. Chem. Soc.* **136**, 5039–5046 (2014).
- K. Yoshida et al., *J. Am. Chem. Soc.* **133**, 13121–13129 (2011).
- G. Perron, D. Brouillette, J. E. Desnoyers, *Can. J. Chem.* **75**, 1608–1614 (1997).
- D. W. McOwen et al., *Energy Environ. Sci.* **7**, 416–426 (2014).
- J. C. Burns et al., *J. Electrochem. Soc.* **158**, A255 (2011).
- J. O. M. Bockris, A. K. N. Reddy, *Modern Electrochemistry* (Kluwer Academic/Plenum, New York, ed. 2, 2000).
- D. M. Seo, O. Borodin, S.-D. Han, P. D. Boyle, W. A. Henderson, *J. Electrochem. Soc.* **159**, A1489–A1500 (2012).
- E. Krämer et al., *J. Electrochem. Soc.* **160**, A356–A360 (2013).
- A. v. Cresce, S. M. Russell, D. R. Baker, K. J. Gaskell, K. Xu, *Nano Lett.* **14**, 1405–1412 (2014).
- Y. Marcus, *Chem. Rev.* **109**, 1346–1370 (2009).
- H. Ohtaki, T. Radnai, *Chem. Rev.* **93**, 1157–1204 (1993).
- B. Gogle, R. Vazquez, S. Greenbaum, A. Cresce, K. Xu, *J. Phys. Chem. Lett.* **4**, 1664–1668 (2013).
- Y.-G. Wang, Y.-Y. Xia, *J. Electrochem. Soc.* **153**, A450–A454 (2006).
- J. Y. Luo, Y. Y. Xia, *Adv. Funct. Mater.* **17**, 3877–3884 (2007).
- H. Wang, Y. Zeng, K. Huang, S. Liu, L. Chen, *Electrochim. Acta* **52**, 5102–5107 (2007).
- H. Wang, K. Huang, Y. Zeng, S. Yang, L. Chen, *Electrochim. Acta* **52**, 3280–3285 (2007).
- H. Qin, Z. P. Song, H. Zhan, Y. H. Zhou, *J. Power Sources* **249**, 367–372 (2014).

ACKNOWLEDGMENTS

C.W. and K.X. gratefully acknowledge both funding and inspiration from P. Liu of DOE ARPA-E (DEAR0000389). We also acknowledge the support of the Maryland Nano Center and its Nisplab. The Nisplab is supported in part by the NSF as a MRSEC Shared Experimental Facility. We thank K. Gaskell, Y.-F. Lam, S.-C. Liou, A. Goyal, and S. R. Raghavan for technical support and helpful discussions. Modeling efforts were supported by ARL Enterprise for Multiscale Research of Materials. M.O. was supported by an Oak Ridge Associated Universities postdoctoral fellowship.

SUPPLEMENTARY MATERIALS

www.sciencemag.org/content/350/6263/938/suppl/DC1
Materials and Methods
Supplementary Text
Figs. S1 to S27
Tables S1 to S5
References (42–61)

19 March 2015; accepted 25 September 2015
10.1126/science.aab1595

REPORTS

SOLAR CELLS

Efficient and stable large-area perovskite solar cells with inorganic charge extraction layers

Wei Chen,^{1,2*} Yongzhen Wu,^{1*} Youfeng Yue,¹ Jian Liu,¹ Wenjun Zhang,² Xudong Yang,³ Han Chen,³ Enbing Bi,³ Islam Ashrafui,¹ Michael Grätzel,^{4,†} Liyuan Han^{1,3,†}

The recent dramatic rise in power conversion efficiencies (PCEs) of perovskite solar cells (PSCs) has triggered intense research worldwide. However, high PCE values have often been reached with poor stability at an illuminated area of typically less than 0.1 square centimeter. We used heavily doped inorganic charge extraction layers in planar PSCs to achieve very rapid carrier extraction, even with 10- to 20-nanometer-thick layers, avoiding pinholes and eliminating local structural defects over large areas. The robust inorganic nature of the layers allowed for the fabrication of PSCs with an aperture area >1 square centimeter that have a PCE >15%, as certified by an accredited photovoltaic calibration laboratory. Hysteresis in the current-voltage characteristics was eliminated; the PSCs were stable, with >90% of the initial PCE remaining after 1000 hours of light soaking.

Organic-inorganic metal halide perovskite solar cells (PSCs) have attracted attention as a result of the meteoric rise in their solar-to-electric power conversion efficiencies (PCEs) over the past few years (1). In particular, methylammonium ($\text{CH}_3\text{NH}_3\text{PbI}_3$, denoted as MAPbI_3) and formamidinium lead iodide [$\text{CH}(\text{NH}_2)_2\text{PbI}_3$] emerged as highly attractive solar light-harvesting materials because of their intense broadband absorption, high charge carrier mobility, low-cost precursor materials, and simple solution processing (2, 3). Their ambipolar semiconducting characteristics further enable variable device architectures, ranging from mesoscopic to planar structures with n-i-p or p-i-n layouts (4). Mesoporous TiO_2 -based PSCs have reached the highest performance levels thus far (5–7), with a certified PCE of 20.1% (8). However, there is growing interest in inverted (p-i-n) planar device architectures that typically use a MAPbI_3 -PCBM ([6,6]-phenyl- C_{61} -butyric acid methyl ester) bilayer junction, because of their simple fabrication and relatively small hysteresis (9–11). The true PCE and stability of planar PSCs remain open to debate, because these devices have not previously been

certified and their stability has been largely unexplored. Only hole-conductor-free mesoscopic PSCs using carbon as a back contact have hitherto shown promising stability under long-term light soaking and long-term heat exposure, but their certified PCE remains relatively low at 12.8% (12, 13).

Regardless of their architectures, all high-efficiency PSCs thus far have had small areas, with device sizes often <0.1 cm^2 (table S1) (14). Because such a small device size is likely to cause measurement errors, an obligatory minimum cell area of >1 cm^2 is required for certified PCEs to be recorded in the standard solar cell efficiency tables edited by public test centers, such as the National Renewable Energy Laboratory in the United States and the National Institute of Advanced Industrial Science and Technology (AIST) in Japan (15). It has been recommended that the efficiencies should be recorded with cell sizes of ideally 1 to 2 cm^2 or larger to allow comparison with competing technologies (16–19). Although a few studies have reported attempts to fabricate centimeter-scale PSCs—for example, by using a vacuum evaporation system (20) or modified two-step approach (21) to produce large-area MAPbI_3 films—the PCEs obtained for these devices reached only 10.9 to 12.6%. Apart from the small device areas, the widely recognized hysteresis and stability issues of PSCs have raised doubts about the reliability of previously claimed high efficiencies (22, 23).

The poor reproducibility and lack of uniformity of PSCs make it challenging to obtain high efficiencies with large devices. It is difficult to control the formation of cracks and pinholes in the selective carrier extraction layers over large areas. Because small-size PSCs typically show a wide

spread in their PCEs, previous work has focused on improving the uniformity of the perovskite layer by varying its deposition methods (3, 6, 10). However, fewer studies have aimed at identifying selective extraction layers for photogenerated charge carriers placed over the current collector to prevent their recombination at its surface (24–26), even though such selective contacts have turned out to be equally important to developing efficient solar-light harvesters (27). The dilemma with optimizing such charge carrier extraction layers in solar cells is that the film should be thin to minimize resistive losses, while at the same time, it should cover the entire collector area in a contiguous and uniform manner. Meeting these requirements becomes increasingly difficult as the device area increases.

Here we present a strategy that addresses simultaneously the scale-up and stability issues facing current PSC embodiments. We developed heavily p-doped (p^+) $\text{Ni}_x\text{Mg}_{1-x}\text{O}$ and n-doped (n^+) TiO_x contacts to extract selectively photogenerated charge carriers from an inverted planar MAPbI_3 -PCBM film architecture. We implemented the p- and n-doping by substituting $\text{Ni}(\text{Mg})^{2+}$ ions and Ti^{4+} ions on the $\text{Ni}_x\text{Mg}_{1-x}\text{O}$ lattice and TiO_x matrix with Li^+ and Nb^{5+} ions, respectively. The resulting dramatic increase in the electrical conductivity enabled 10- to 20-nm-thick oxide layers to be used for selective extraction of one type of charge carrier, while improving the electronic blocking effect for the other type by reducing the density of pinholes and cracks over large areas. Accordingly, the series resistance (R_s) of the oxides decreased and the shunt resistance (R_{sh}) greatly increased with respect to the undoped layers, leading to an excellent fill factor (FF), with values exceeding 0.8, and hysteresis-free behavior. With this strategy, we successfully fabricated large-size (>1 cm^2) PSCs with an efficiency of up to 16.2%. A PCE of 15% was certified by a public test center (Calibration, Standards and Measurement Team at the Research Center for Photovoltaics, AIST). This is listed as the first official efficiency entry for PSCs in the most recent edition of the solar cell efficiency tables (28). Moreover, the devices based on these stable p^+ and n^+ inorganic metal-oxide charge extraction layers show high stability, rendering them attractive for future practical deployment of PSCs.

We fabricated PSCs with an inverted planar device architecture (Fig. 1A); a cross-sectional scanning electron microscopy (SEM) image of this architecture is shown in Fig. 1B. We first deposited the NiO-based hole extraction layer onto fluorine-doped tin oxide (FTO) glass by means of spray pyrolysis. The precursor solution was composed of nickel (II) acetylacetonate, either alone or together with doping cations (Mg^{2+} from magnesium acetate tetrahydrate and Li^+ from lithium acetate) in a super-dehydrated acetonitrile and ethanol mixture. The MAPbI_3 perovskite layer, with a thickness of ~300 nm, was deposited using a reported method (6); this was followed by the deposition of a thin PCBM layer (80 nm), accomplished by spin-coating its chlorobenzol solution (20 mg ml^{-1}) at 1000 rpm for 30 s. An n^+ -type TiO_x -based electron

¹Photovoltaic Materials Unit, National Institute for Materials Science, Tsukuba, Ibaraki 305-0047, Japan. ²Michael Grätzel Centre for Mesoscopic Solar Cells, Wuhan National Laboratory for Optoelectronics, Huazhong University of Science and Technology, Wuhan, China. ³State Key Laboratory of Metal Matrix Composites, Shanghai Jiao Tong University, 800 Dong Chuan Road, Minhang District, Shanghai 200240, China. ⁴Laboratory of Photonics and Interfaces, Department of Chemistry and Chemical Engineering, Swiss Federal Institute of Technology, Station 6, CH-1015 Lausanne, Switzerland.

*These authors contributed equally to this work.

†Corresponding author. E-mail: michael.gratzel@epfl.ch (M.G.); han.liyuan@nims.go.jp (L.H.)

extraction layer with and without Nb^{5+} doping was further deposited on the PCBM by spin-coating a diluted methanol solution of titanium isopropoxide (alone or mixed with niobium ethoxide), followed by controlled hydrolysis and condensation (14). Finally, the device was completed by thermal evaporation of a 100-nm-thick Ag cathode. The band alignments of relevant functional layers are shown in Fig. 1C, based on the energy levels determined by ultraviolet (UV) photoelectron spectroscopy and UV-visible absorption spectroscopy measurements (fig. S1) (14). The uniformity of the perovskite and PCBM layers was examined by means of cross-sectional SEM (fig. S2) (14). The full x-ray photoelectron spectroscopy (XPS) spectra of the NiO- and TiO_x -based charge carrier extraction layers are shown in fig. S3 (14), revealing the designated compositions for the target materials. A close-up view of the morphology of the charge carrier extraction layers is shown in fig. S4 (14). Their pinhole densities were examined by electrical measurement, as discussed below.

The stoichiometric form of NiO is a wide-band-gap semiconductor with a very low intrinsic conductivity of $10^{-13} \text{ S cm}^{-1}$ (29). Self-doping by introducing Ni^{3+} acceptors into the NiO crystal lattice renders the crystals more conductive, depending on the film deposition techniques and conditions (11, 30–32). The room-temperature specific conductivity of our NiO films, derived from Hall effect measurements, was $1.66 \times 10^{-4} \text{ S cm}^{-1}$. This value is much lower than that of the typically used p-type contact layer of PEDOT:PSS [poly(3,4-ethylenedioxythiophene) polystyrene sulfonate], which has a conductivity of 1 to

1000 S cm^{-1} (33). The low conductivity of NiO leads to a high R_s , resulting in a low FF for the solar cells (34). Substitutional doping with Li^+ is an effective way to increase the p-conductivity of NiO (35). Values of heavily p-doped NiO films can reach 1 to 10 S cm^{-1} at room temperature under optimal conditions (36). For our Li^+ -doped $\text{Ni}_x\text{Mg}_{1-x}\text{O}$ films, the conductivity is $2.32 \times 10^{-3} \text{ S cm}^{-1}$, ~12 times greater than that of the undoped reference.

A Mg^{2+} content of 15 mole percent (mol %) was alloyed in the Li^+ -doped nickel oxide film, to compensate for the undesirable positive shift of its valence band energy (E_{VB}) caused by incorporation of Li^+ into the lattice (fig. S1) (14, 35, 37, 38). The Li^+ content was adjusted to 5 mol %, giving the doped oxide the formula of $\text{Li}_{0.05}\text{Mg}_{0.15}\text{Ni}_{0.8}\text{O}$, assuming that the molar ratio of the three different cations in the spray pyrolysis solution was maintained in the mixed oxide. This codoping strategy is feasible because the mismatch of the ionic radii of Li^+ (0.76 Å), Mg^{2+} (0.71 Å), and Ni^{2+} (0.69 Å) is small, conferring good lattice stability to the $\text{Li}_x\text{Mg}_y\text{Ni}_{1-x-y}\text{O}$ ternary oxides. We compared the conductivity of the NiO and $\text{Li}_{0.05}\text{Mg}_{0.15}\text{Ni}_{0.8}\text{O}$ films using the contact-current mode of a scanning probe microscope (SPM) (Fig. 2, A and B). At a bias potential of 1.0 V, the electric current increased by a factor of ~10 (from ~0.3 nA to ~3 nA) upon replacing undoped NiO with a $\text{Li}_{0.05}\text{Mg}_{0.15}\text{Ni}_{0.8}\text{O}$ film. The XPS spectra in fig. S6 (14) reveal that the doping increased the relative content of Ni^{3+} acceptors in the $\text{Li}_{0.05}\text{Mg}_{0.15}\text{Ni}_{0.8}\text{O}$ sample. These findings are consistent with findings for Li^+ -doped NiO

films reported in (32), and they explain the increase in carrier concentration from $2.66 \times 10^{17} \text{ cm}^{-3}$ in the undoped NiO film to $6.46 \times 10^{18} \text{ cm}^{-3}$ in the $\text{Li}_{0.05}\text{Mg}_{0.15}\text{Ni}_{0.8}\text{O}$ film, which we derived from Hall effect measurements.

The electron specific n-type TiO_x contact commonly used for organic photovoltaic devices is normally fabricated by hydrolysis and condensation of titanium alkoxides at temperatures below 150°C (39, 40), where the crystallization of TiO_2 is slow. In order to prevent heat-induced degradation of the perovskite layer and the adjacent interfaces, we kept the annealing temperature of TiO_x films below 70°C . Although such TiO_x films have been used extensively in organic photovoltaic devices, the details of their structure and mechanism of electric conduction so far have not been elucidated (41). One commonly recognized problem is that the amorphous nature of TiO_x leads to extremely low specific conductivities that are in the range of 10^{-8} to $10^{-6} \text{ S cm}^{-1}$ (42). Nb^{5+} doping has proved to be effective for enhancing the conductivity of crystalline anatase TiO_2 films to $\sim 10^4 \text{ S cm}^{-1}$, enabling its use as a transparent conducting oxide similar to conventional indium tin oxide (ITO) (43). By analogy, this dopant is expected to also improve the conductivity of the amorphous TiO_x via substitution of Ti^{4+} with Nb^{5+} , which is expected to create donor centers. From the current-voltage (I - V) curves obtained from SPM measurements (Fig. 2B), the conductivity of the TiO_x film was estimated to increase from about $10^{-6} \text{ S cm}^{-1}$ to $10^{-5} \text{ S cm}^{-1}$ upon adding 5 mol % Nb^{5+} to the precursor solution. By resolving the XPS spectra in fig. S6 (14), we

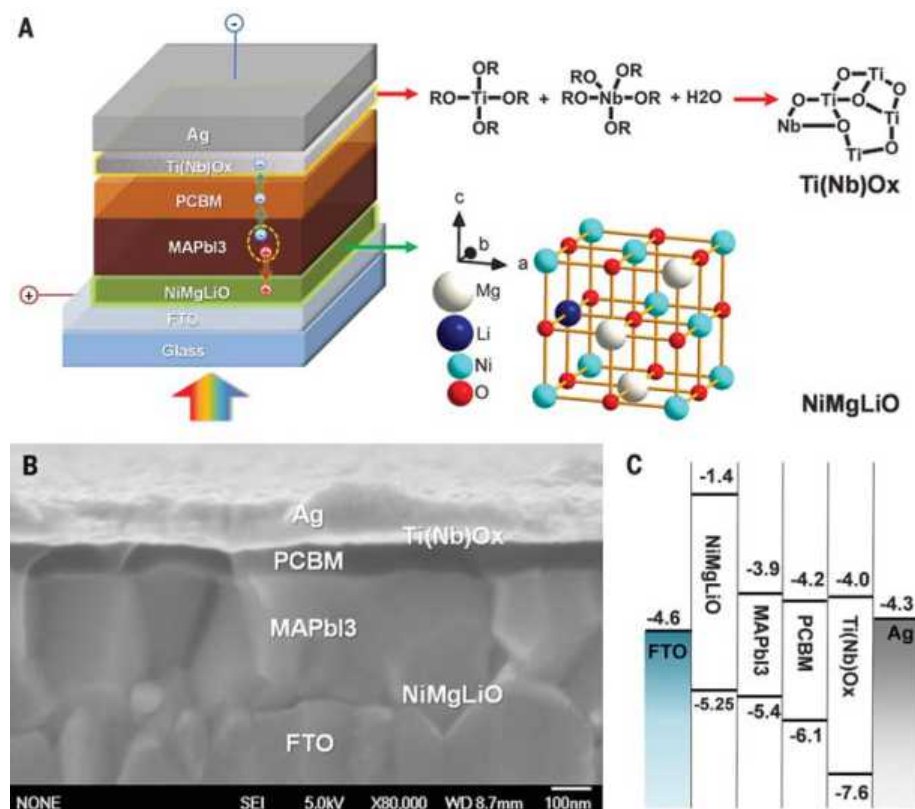


Fig. 1. Structure and band alignments of the PSC. (A) Diagram of the cell configuration highlighting the doped charge carrier extraction layers. The right panels show the composition of $\text{Ti}(\text{Nb})\text{O}_x$ and the crystal structure of Li^+ -doped $\text{Ni}_x\text{Mg}_{1-x}\text{O}$, denoted as $\text{NiMg}(\text{Li})\text{O}$. (B) A high-resolution cross-sectional SEM image of a complete solar cell [the corresponding energy-dispersive x-ray analysis results are shown in fig. S5 (14), demonstrating the presence of the p⁺ $\text{Ni}_x\text{Mg}_{1-x}\text{O}$ and n⁺ TiO_x charge extraction layers]. (C) Band alignments of the solar cell. The data for MAPbI_3 and PCBM are taken from (11).

observed that the relative content of Ti^{3+} in comparison with Ti^{4+} (i.e., the donor species in the TiO_x film, responsible for its n-type conductivity) increased as a result of Nb^{5+} doping.

We derived the optimal thickness of the NiO- and TiO_x -based charge extraction layers from the electrical measurements shown in fig. S7 (14). A complete NiO or TiO_x layer with no pinholes requires a thickness of at least 20 or 10 nm, respectively, regardless of the presence of dopants. These minimum thicknesses should depend on the surface chemistry and morphology of the underlayers (FTO for NiO or PCBM for TiO_x), as well as the fabrication methods used for the NiO and TiO_x films. We compared small solar cells with sizes of 0.09 cm^2 and varied the NiO layer thickness from 10 to 20 to 40 nm, keeping that of the $\text{Ti}_{0.95}\text{Nb}_{0.05}\text{O}_x$ fixed at 10 nm. We fixed the $\text{Li}_{0.05}\text{Mg}_{0.15}\text{Ni}_{0.8}\text{O}$ layer thickness at 20 nm and varied that of the TiO_x films from 5 to 30 nm. For each condition, 20 cells were made and measured to establish any underlying trends. As shown in fig. S8 (14), although high performances occasionally can be achieved from devices with very thin charge carrier extraction layers ($\sim 10 \text{ nm}$ for NiO or $\sim 5 \text{ nm}$ for TiO_x), most such devices had lower PCEs because of lower FFs and open-circuit voltages (V_{oc}) (fig. S9) (14), which can be attributed to the presence of substantial numbers of pinholes. The reproducibility of the device performance was greatly enhanced as the thickness of charge extraction layers increased, and the optimal performance was attained with 20-nm NiO and 10-nm TiO_x films, in agreement with the electrical measurement. Further increasing the film thickness of the two charge

extraction layers can lead to a large decline in efficiency caused by increased internal resistance, larger optical loss, or both (fig. S10) (14). Thus, we fixed the thickness of NiO and TiO_x at 20 and 10 nm, respectively, for the studies described below of doping effect on device performance.

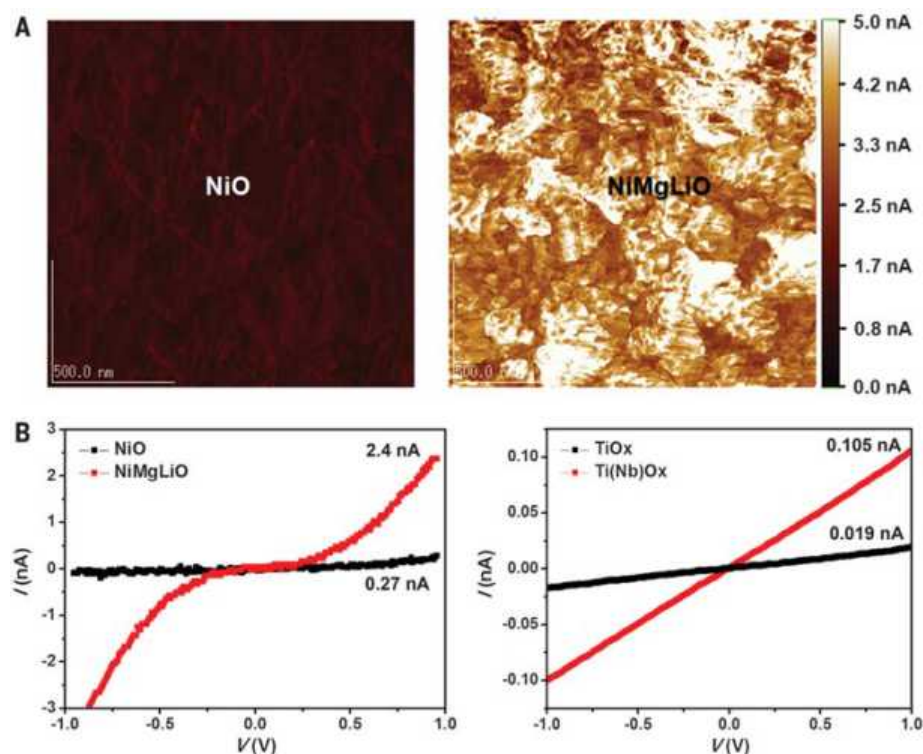
Figure 3A shows the effect of doping the NiO and TiO_x charge extraction layers on the photocurrent density–voltage (J - V) curves of PSCs, measured under simulated air mass (AM)–1.5 sunlight with a forward scanning direction. The short-circuit current (J_{sc}), V_{oc} , FF, and PCE data are listed in table S2 (14). Doping of NiO and TiO_x both reduced R_s and improved the FF and, to a lesser extent, J_{sc} and V_{oc} . The TiO_x electron extraction layers mainly affected the shape of J - V curves in the forward bias range from 0.7 to 1.0 V, where a Schottky barrier-type contact between PCBM and Ag strongly restricted efficient electron collection (fig. S9A) (14, 44). The Nb^{5+} doping of TiO_x reduced the interfacial electron transfer resistance and facilitated electron transport, increasing the photocurrent, especially in the 0.7- to 1.0-V forward bias region. The NiMg(Li)O-based hole extraction layer promoted ohmic contact formation at the FTO-MAPbI₃ interface by decreasing the barrier height through the staircase energy level alignment shown in Fig. 1C. Heavy p-doping of NiO increased the electrical conductivity, decreasing the charge transport resistance and hence enhancing hole extraction.

Doping of both NiO and TiO_x improved the cell performance by increasing the values of FF and V_{oc} to 0.827 and 1.083 V, respectively, leading to a PCE of 18.3% for this planar PSC with MAPbI₃. In comparison with PEDOT:PSS-based

PSCs, the V_{oc} was higher by $\sim 100 \text{ mV}$, indicating that with $\text{Li}_{0.05}\text{Mg}_{0.15}\text{Ni}_{0.8}\text{O}$, the holes can be extracted at a higher energy level (10). Furthermore, the FF of 0.827 is one of the highest values reported for PSCs (8, 9, 23), demonstrating the key role of the charge extraction layers in minimizing resistive losses and improving the photovoltaic performance.

To gain further insight into the reasons for the performance enhancement caused by the doping, we characterized the charge carrier extraction, transportation, and recombination by nanosecond time-resolved photoluminescence (PL) decay, using a picosecond laser flash as the excitation source, and by measuring transient photocurrent and photovoltage decays on the microsecond scale. The charge extraction in our cells includes the electron transfer from the MAPbI₃ absorber layer to the PCBM and TiO_x layers, the hole transfer to NiO, and the carrier transport in the TiO_x and NiO layers. The MAPbI₃/PCBM interface has been demonstrated to be very efficient for electron extraction (9–11). Doping of the TiO_x extraction layer is unlikely to have a direct impact on the electron injection rate, because of its physical separation from the MAPbI₃ by the 80-nm-thick PCBM layer. Nevertheless, it greatly accelerates the electron extraction by decreasing the electron transport time, as shown in Fig. 3C. Figure 3B shows the PL decays of the MAPbI₃ films on different substrates, including a glass slide and NiO and $\text{Li}_{0.05}\text{Mg}_{0.15}\text{Ni}_{0.8}\text{O}$ deposited on FTO glass. The MAPbI₃ itself showed a long PL lifetime of $>100 \text{ ns}$, indicating slow carrier recombination in the perovskite layer (10). When brought into contact with the p-type hole extraction layers, the PL

Fig. 2. Dopant-enhanced conductivity of NiO and TiO_x . (A) Comparison of the conductivity mapping results for NiO (left) and $\text{Li}_{0.05}\text{Mg}_{0.15}\text{Ni}_{0.8}\text{O}$ (right) films. (B) Comparison of the I - V curves of NiO and $\text{Li}_{0.05}\text{Mg}_{0.15}\text{Ni}_{0.8}\text{O}$ films deposited on FTO glass (left), and comparison of the I - V curves for TiO_x and $\text{Ti}_{0.95}\text{Nb}_{0.05}\text{O}_x$ films deposited on PCBM-ITO glass (right), obtained by SPM measurements. The thickness was 20 nm for both NiO- and TiO_x -based films.



lifetimes were shortened to a similar degree for both doped and undoped NiO-MAPbI₃ contacts. Thus, doping has a negligible influence on the hole injection.

We derived the charge transport and recombination time constants (τ_t and τ_r) from the transient photocurrent and photovoltage decays measured at the short and open circuit, respec-

tively (Fig. 3C). The τ_t decreased fivefold from 4.41 μ s for the undoped cell to 0.88 μ s for the doped cell, confirming the much faster charge transport through the doped charge carrier extraction layers, compared to the undoped ones. However, we found that the τ_r of the doped cell was substantially longer than that of the undoped one (84.8 versus 50.5 μ s; Fig. 3D), which we

attribute to slower interfacial charge recombination, because the very rapid carrier extraction prevents charge accumulation at the interface of the perovskite with the charge extraction layer. The doping-induced difference in charge transport and recombination kinetics should be the main factor responsible for the performance enhancement.

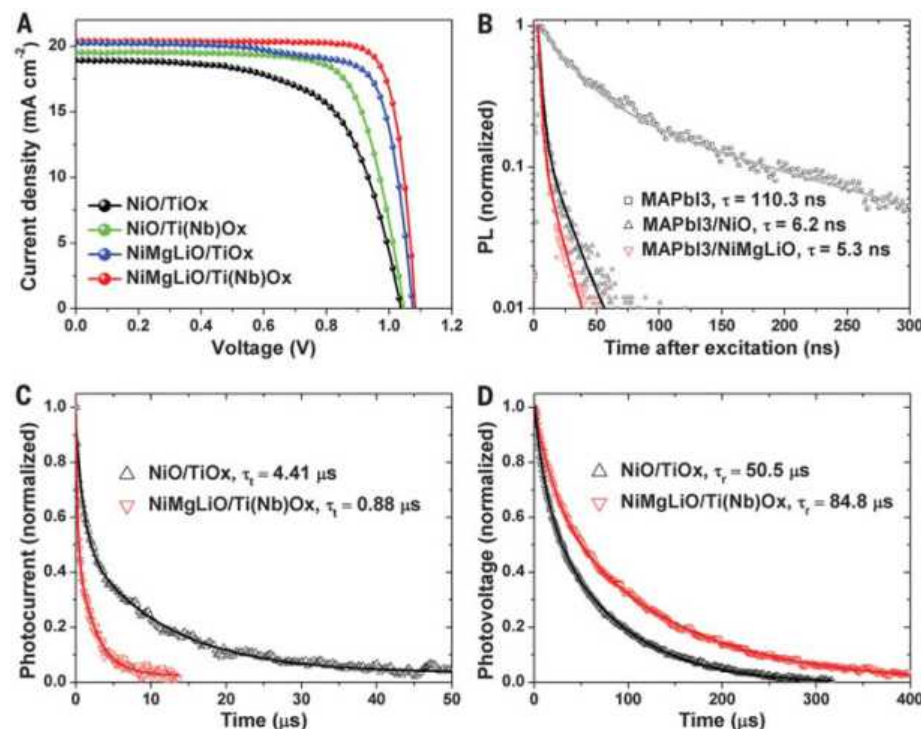


Fig. 3. Doping-enhanced photovoltaic performance.

(A) *J-V* curves of solar cells based on different combinations of charge extraction layers with standard thicknesses [NiO, NiMg(Li)O, 20 nm; TiO_x and Ti(Nb)O_x, 10 nm]. (B) Normalized PL transient decay curves of the MAPbI₃ layer on its own and MAPbI₃ at the controlled interfaces with NiO and NiMg(Li)O. Solid lines are fitted results with a double exponential decay. The time interval during which the PL decays to 1/e of the initial intensity is defined as the characteristic lifetime (τ) of free carriers after photoexcitation. (C) and (D) show normalized transient photocurrent and photovoltage decay curves, respectively, based on undoped and doped charge carrier extraction layers. The charge transport (τ_t) and recombination time (τ_r) are again defined as the time interval during which the photocurrent or photovoltage decays to 1/e of its initial value immediately after excitation.

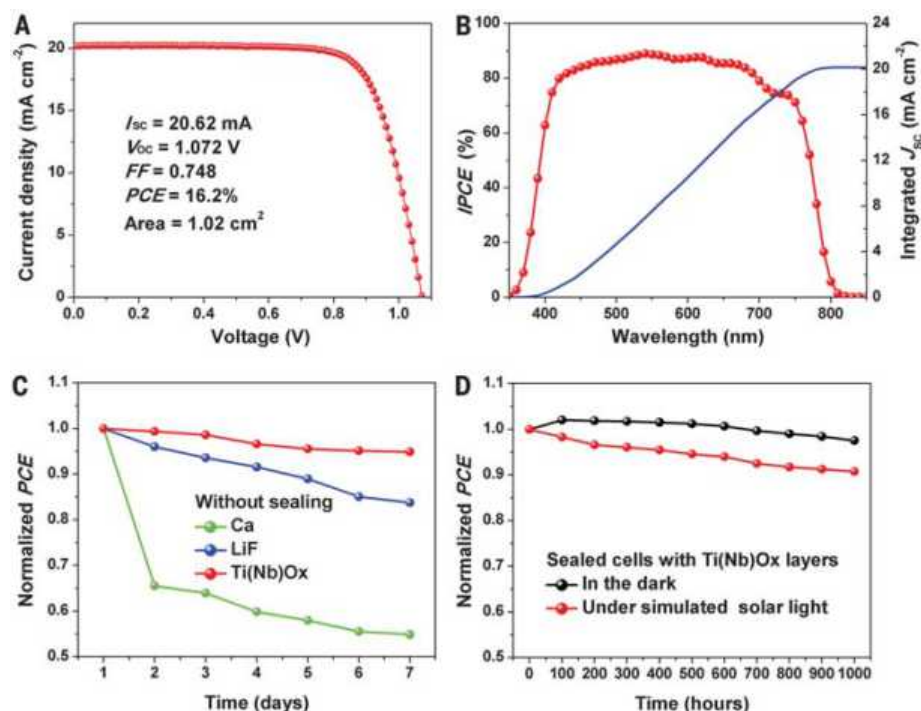


Fig. 4. Performance and stability of large-size cells.

(A) *J-V* curve of the best large cell endowed with antireflection film. (B) The corresponding IPCE spectrum (red) and integrated J_{sc} (blue). (C) The stability of the cells without sealing, based on different electron extraction layers of Ca (4 nm), LiF (1.5 nm), and Ti(Nb)O_x (10 nm) between PCBM and the Ag contact. The cells were kept in a dry cabinet (<20% humidity) in the dark and measured in ambient air. (D) Stability of sealed cells kept in the dark or under simulated solar light (AM 1.5; 100 mW cm⁻²; using a 420-nm UV light cut-off filter; surface temperature of the cell, 45° to 50°C; bias potential, 0 V).

We examined the hysteresis of our cells using different scan rates and directions. By decreasing the step width from 70 to 5 mV, the PCEs determined from the forward scan increased slightly from 18.14 to 18.35%. However, the reverse-scan PCEs decreased substantially from 22.35% at 70 mV/step (fig. S11A and table S3) (14) to 18.40% at 5 mV/step. The steady power outputs measurements (fig. S11D) (14) indicate that the PCEs obtained in forward scans and at small step widths (5 to 10 mV) are close to the real performance. The V_{oc} and PCE values obtained in a fast reverse scan (1.273 V and 22.35% at 70 mV/step) are largely overestimated. With the step widths of 5 to 10 mV, the PCE differences between forward and reverse scans are very small, within 0.3% in absolute PCE values, reflecting negligible hysteresis. A histogram comparing the difference in the PCEs obtained from scanning in the forward and reverse bias directions is shown in fig. S11C (14), supporting the absence of hysteresis for the optimized device architecture. In contrast, for undoped charge extraction layers, a pronounced hysteresis was observed even for slow scan rates (fig. S11E) (14), likely resulting from unbalanced charge accumulation at the two interfaces (45). Thus, the $\text{Li}_{0.05}\text{Mg}_{0.15}\text{Ni}_{0.8}\text{O}$ and $\text{Ti}_{0.95}\text{Nb}_{0.05}\text{O}_x$ charge extraction layers create robust low-impedance interfaces that can mitigate the J - V hysteresis under a routine scanning condition.

We fabricated cells with active areas $>1\text{ cm}^2$ as a first step toward the scale-up of the photovoltaic devices. Figure 4A shows the J - V curve of such a cell, with an aperture area of 1.02 cm^2 . The cell has excellent performance, with J_{sc} , V_{oc} , and FF reaching values of 20.21 mA cm^{-2} , 1.072 V , and 0.748 , respectively, corresponding to a PCE of 16.2%. Hysteresis for these large-area devices is also small (fig. S12) (14). The corresponding incident photon-to-current conversion efficiency (IPCE) (Fig. 4B) has a broad plateau with a maximum value of 90.1% over essentially the entire visible range. The integrated J_{sc} calculated from the IPCE matches well with the measured value. Compared with small-size cells (0.09 cm^2), a $\sim 10\%$ decrease in PCE was observed in large-size cells (1.02 cm^2), which is mainly caused by the large sheet resistance of the FTO. We sent one of our best large cells to a public test center (AIST) for certification. A PCE of 15.0% for a 1.017 cm^2 device was certified (fig. S13) (14).

To demonstrate the superiority of the solution-processable $\text{Ti}_{0.95}\text{Nb}_{0.05}\text{O}_x$ charge carrier extraction layer, two references, Ca (4 nm)/Ag and LiF (1.5 nm)/Ag, deposited by thermal evaporation, were compared with our best interfacial condition. As shown in Fig. 4C, without sealing, the $\text{Ti}(\text{Nb})\text{O}_x$ -based PSC has the best stability: Its PCE only decreased by $\sim 5\%$ of its initial value after 1 week. The Ca/Ag-based PSC degraded the fastest, decreasing from its initial PCE by $>30\%$ after 1 day and by $\sim 45\%$ within 1 week. This difference is attributed to the fast oxidation of the very reactive Ca, leading to dramatic losses in J_{sc} and FF. The LiF/Ag-based PSC lost 15% of its initial PCE within 1 week. The extremely thin LiF layer ($<2.5\text{ nm}$, as required for efficient tunneling)

(46) and the high sensitivity of LiF to moisture are likely to be responsible for the corresponding cell's inferior stability. It is possible that the stability of Ca- or LiF-based devices can be improved if they are thoroughly sealed. However, the requirement for sealing quality will be much more critical for Ca- and LiF-based devices than for the device based on the air-stable interface of $\text{Ti}_{0.95}\text{Nb}_{0.05}\text{O}_x$ (39).

The $\text{Ti}_{0.95}\text{Nb}_{0.05}\text{O}_x$ layer also shields the perovskite from the intrusion of humidity. It assumes a similar role in organic photovoltaic devices (39). We exposed bare MAPbI_3 , MAPbI_3 with PCBM, and MAPbI_3 with PCBM and $\text{Ti}(\text{Nb})\text{O}_x$ to ambient air under room light for 3 weeks. A difference in color degradation associated with perovskite decomposition became clearly visible (fig. S14) (14). Thus, it appears that the hydrophobic nature of PCBM may protect the perovskite from reaction with water, and the coating of $\text{Ti}(\text{Nb})\text{O}_x$ could further enhance the stability.

Figure 4D also shows the long-term stability of PSCs that use the optimized inorganic charge extraction layers. The silver back contact was protected by a covering glass, which was separated from the front FTO glass by a UV-activated glue used as a sealant. The cells maintained 97% of their initial PCE after being kept in the dark for 1000 hours. Exposing the cells for 1000 hours in short-circuit conditions to full sunlight from a solar simulator resulted in a PCE degradation of less than 10%. This degradation was generally consistent across 10 devices (fig. S15) (14), indicating good long-term stability. During this time, an electric charge of around $72,000\text{ C}$ (4.49×10^{23} electrons) passed through the device. Thus, the planar cell structure and the metal oxide extraction layers, as well as the organometal halide perovskite material, are robust enough to sustain continued current flow under light exposure for 1000 hours. A further increase in the PCE without sacrificing stability could be obtained by varying the composition of the perovskite, replacing, for example, part of the methylammonium cations in the MAPbI_3 perovskite with formamidinium (47) and a small fraction of the iodide anions with bromide.

REFERENCES AND NOTES

- G. Hodes, *Science* **342**, 317–318 (2013).
- G. Xing et al., *Science* **342**, 344–347 (2013).
- Q. Dong et al., *Science* **347**, 967–970 (2015).
- M. Liu, M. B. Johnston, H. J. Snaith, *Nature* **501**, 395–398 (2013).
- J. Burschka et al., *Nature* **499**, 316–319 (2013).
- N. J. Jeon et al., *Nat. Mater.* **13**, 897–903 (2014).
- N. J. Jeon et al., *Nature* **517**, 476–480 (2015).
- W. S. Yang et al., *Science* **348**, 1234–1237 (2015).
- J. H. Heo, H. J. Han, D. Kim, T. K. Ahn, S. H. Im, *Energy Environ. Sci.* **8**, 1602–1608 (2015).
- W. Nie et al., *Science* **347**, 522–525 (2015).
- J. H. Park et al., *Adv. Mater.* **27**, 4013–4019 (2015).
- A. Mei et al., *Science* **345**, 295–298 (2014).
- X. Li et al., *Energy Technol.* **3**, 551–555 (2015).
- Materials and methods are available as supplementary materials on Science Online.
- M. A. Green, K. Emery, Y. Hishikawa, W. Warta, E. D. Dunlop, *Prog. Photovolt. Res. Appl.* **23**, 1–9 (2015).
- M. C. Beard, J. M. Luther, A. J. Nozik, *Nat. Nanotechnol.* **9**, 951–954 (2014).
- E. Zimmermann et al., *Nat. Photonics* **8**, 669–672 (2014).

- K. D. G. I. Jayawardena, L. J. Rozanski, C. A. Mills, S. R. P. Silva, *Nat. Photonics* **9**, 207–208 (2015).
- Editorial, *Nat. Nanotechnol.* **9**, 657 (2014).
- O. Malinkiewicz et al., *Adv. Energy Mater.* **4**, 1400345 (2014).
- Z. Yang et al., *Nano Energy* **15**, 670–678 (2015).
- M. Grätzel, *Nat. Mater.* **13**, 838–842 (2014).
- M. Gunther, "Meteoritic rise of perovskite solar cells under scrutiny over efficiencies," *Chemistry World*, 2 March 2015; www.rsc.org/chemistryworld/2015/02/meteoritic-rise-perovskite-solar-cells-under-scrutiny-over-efficiencies.
- H. Zhou et al., *Science* **345**, 542–546 (2014).
- O. Malinkiewicz et al., *Nat. Photonics* **8**, 128–132 (2014).
- Q. Lin, A. Armin, R. C. R. Nagiri, P. L. Burn, P. Meredith, *Nat. Photonics* **9**, 106–112 (2015).
- A. G. Aberle, *Prog. Photovolt. Res. Appl.* **8**, 473–487 (2000).
- M. A. Green, K. Emery, Y. Hishikawa, W. Warta, E. D. Dunlop, *Prog. Photovolt. Res. Appl.* **23**, 805–812 (2015).
- M. A. Wittenauer, L. L. Van Zandt, *Philos. Mag. B* **46**, 659–667 (1982).
- J. H. Kim et al., *Adv. Mater.* **27**, 695–701 (2015).
- Z. Zhu et al., *Angew. Chem. Int. Ed.* **53**, 12571–12575 (2014).
- C. Wu, C. Yang, *Sol. Energy Mater. Sol. Cells* **132**, 492–498 (2015).
- Y. H. Kim et al., *Adv. Funct. Mater.* **21**, 1076–1081 (2011).
- X. F. Chen, H. M. Huang, X. L. Li, G. J. Liu, H. Zhang, *Int. J. Clin. Exp. Med.* **8**, 5044–5054 (2015).
- N. Alidoust, M. C. Toroker, J. A. Keith, E. A. Carter, *ChemSusChem* **7**, 195–201 (2014).
- U. S. Joshi, Y. Matsumoto, K. Itaka, M. Sumiya, H. Koinuma, *Appl. Surf. Sci.* **252**, 2524–2528 (2006).
- Z. Huang et al., *RSC Adv.* **4**, 60670–60674 (2014).
- J. Deng, M. Mortazavi, N. V. Medhekar, J. Zhe Liu, *J. Appl. Phys.* **112**, 123703 (2012).
- K. Lee et al., *Adv. Mater.* **19**, 2445–2449 (2007).
- T. Kuwabara, T. Nakayama, K. Uozumi, T. Yamaguchi, K. Takahashi, *Sol. Energy Mater. Sol. Cells* **92**, 1476–1482 (2008).
- T. Kuwabara, H. Sugiyama, T. Yamaguchi, K. Takahashi, *Thin Solid Films* **517**, 3766–3769 (2009).
- K. Wojciechowski, M. Saliba, T. Leijtens, A. Abate, H. J. Snaith, *Energy Environ. Sci.* **7**, 1142–1147 (2014).
- Y. Furubayashi et al., *Appl. Phys. Lett.* **86**, 252101–252103 (2005).
- S. Braun, W. R. Salaneck, M. Fahlman, *Adv. Mater.* **21**, 1450–1472 (2009).
- J. H. Heo et al., *Adv. Mater.* **27**, 3424–3430 (2015).
- X. Liu et al., *ACS Appl. Mater. Interfaces* **7**, 6230–6237 (2015).
- J. Liu et al., *Adv. Mater.* **27**, 4918–4923 (2015).

ACKNOWLEDGMENTS

This work was partially supported by the Core Research for Evolutional Science and Technology of the Japan Science and Technology Agency. The authors thank H. Kanai at the Materials Analysis Station of the National Institute for Materials Science, Japan, for high-resolution SEM image measurement and T. Shimizu and T. Ishikawa for technical support. L.H. thanks for H. Naito of Osaka Prefecture University and M. Shimizu of the Institute of Advanced Energy, Kyoto University for their useful discussions. M.G. acknowledges financial support of this work under the Swiss Nanotera and Swiss National Science Foundation PV2050 program and acknowledges his affiliation as a visiting faculty member with Nanyang Technological University, Singapore and the Advanced Institute for Nanotechnology at Sungkyunkwan University, Suwon, South Korea.

SUPPLEMENTARY MATERIALS

www.sciencemag.org/content/350/6263/944/suppl/DC1
Materials and Methods
Figs. S1 to S15
Tables S1 to S3
References (48–50)

27 July 2015; accepted 14 October 2015
Published online 29 October 2015
10.1126/science.121015

SUPERCONDUCTIVITY

Three-dimensional charge density wave order in $\text{YBa}_2\text{Cu}_3\text{O}_{6.67}$ at high magnetic fields

S. Gerber,^{1*} H. Jang,^{2*} H. Nojiri,³ S. Matsuzawa,³ H. Yasumura,³ D. A. Bonn,^{4,5} R. Liang,^{4,5} W. N. Hardy,^{4,5} Z. Islam,⁶ A. Mehta,² S. Song,⁷ M. Sikorski,⁷ D. Stefanescu,⁷ Y. Feng,⁷ S. A. Kivelson,⁸ T. P. Devereaux,¹ Z.-X. Shen,^{1,8} C.-C. Kao,⁹ W.-S. Lee,^{1†} D. Zhu,^{7†} J.-S. Lee^{2†}

Charge density wave (CDW) correlations have been shown to universally exist in cuprate superconductors. However, their nature at high fields inferred from nuclear magnetic resonance is distinct from that measured with x-ray scattering at zero and low fields. We combined a pulsed magnet with an x-ray free-electron laser to characterize the CDW in $\text{YBa}_2\text{Cu}_3\text{O}_{6.67}$ via x-ray scattering in fields of up to 28 tesla. While the zero-field CDW order, which develops at temperatures below ~150 kelvin, is essentially two dimensional, at lower temperature and beyond 15 tesla, another three-dimensionally ordered CDW emerges. The field-induced CDW appears around the zero-field superconducting transition temperature; in contrast, the incommensurate in-plane ordering vector is field-independent. This implies that the two forms of CDW and high-temperature superconductivity are intimately linked.

The universal existence of charge density wave (CDW) correlations in superconducting cuprates (1–12) raises profound questions regarding the role of charge order: Is it competing or more intimately intertwined with high-temperature superconductivity (HTSC) (13–16)? Uncovering the evolution of CDW order upon suppression of HTSC by an external magnetic field provides valuable insight into these issues. One of the most studied cuprate superconductors, $\text{YBa}_2\text{Cu}_3\text{O}_{6+\delta}$, has become a model material for the study of CDW phenomena in cuprates. Largely two-dimensional (2D), incommensurate CDW order with moderate correlation length has recently been found to coexist with HTSC by using x-ray scattering measurement (7, 8, 17, 18). The temperature and magnetic field dependencies of up to $\mu_0 H = 17$ T indicate a competition between CDW order and HTSC (8, 17). However, both nuclear magnetic resonance (NMR) (6, 19) and Hall coefficient measurements (20)

suggest that there is a distinct, more ordered CDW phase at higher fields and lower temperatures, with an NMR signature that is different than the NMR broadening (21) that correlates with the zero-field CDW. The existence of a phase transition or sharp crossover to a state with a distinct field-induced form of density wave order is also supported by ultrasonic measurements (22). However, there is a discrepancy between NMR (19) and ultrasonic measurements (22) regarding the onset field of this new state, and neither reveal the structure of the CDW at high fields. This calls for high-field x-ray scattering measurements of the CDW phenomenology in superconducting cuprates, which, however, is extremely challenging for existing techniques, especially because the scattering signal is so weak.

To gain insight into this critical question, one needs to introduce a different experimental approach. We performed x-ray scattering at an x-ray free electron laser (FEL) in the presence of pulsed high magnetic fields. The high brilliance of the x-ray FEL (23) enables the measurement of the weak CDW scattering signal with a single x-ray pulse (~50 fs) at the apex of a millisecond magnetic field pulse (24). This approach provides us with the opportunity to probe the CDW signal in $\text{YBa}_2\text{Cu}_3\text{O}_{6+\delta}$ at magnetic fields beyond 17 T, entering a field range comparable with that used in NMR (6, 19, 21), Hall coefficient (20), and ultrasonic measurements (22).

Shown in Fig. 1A is a schematic of how the two pulsed sources—the magnet and the x-ray FEL—were synchronized in order to study the CDW in detwinned, underdoped $\text{YBa}_2\text{Cu}_3\text{O}_{6.67}$ (YBCO) with ortho-VIII oxygen order (24). To monitor the field dependence of the CDW, an area detector was used to capture a cut of the kl plane in reciprocal space. The full view of the

zero-field diffraction pattern in the vicinity of the CDW position at the zero-field superconducting transition temperature, $T_c(H = 0) = 67$ K, is shown in Fig. 1B. In this geometry, we observed CDW features centered near $(0, 2-q, \pm\frac{1}{2})$ with an incommensuration $q \sim 0.318$ (7, 8, 17, 18). The detected diffraction pattern of the CDW shows that the correlation along the crystallographic c axis is very weak, resulting in a rodlike shape along the l direction. Moreover, we also measured the temperature dependence of the zero-field CDW (Fig. 1C) (24), reproducing earlier reports that the CDW signal is maximal at T_c and suppressed for $T < T_c$ (7, 8, 17, 18), which indicates a competition between CDW order and HTSC.

We first discuss the temperature dependence of the CDW at $\mu_0 H = 20$ T. The $(0, 2-q, l)$ CDW signal is shown in Fig. 2A at both 0 and 20 T. There is no field-induced change of the CDW at T_c , which is consistent with earlier results (8). With decreasing temperature ($T < T_c$), the CDW signal becomes sharper along the k direction and more intense than at zero field. This indicates that as the magnetic field suppresses superconductivity, the CDW order is enhanced (Fig. 2B). Surprisingly, as shown in the 2D difference map $I_{20T} - I_{0T}$ (Fig. 2A, bottom) the field-induced enhancement is most dramatic at $l \sim 1$, rather than at $l \sim \frac{1}{2}$ where the zero-field CDW signal is maximal (7, 8, 17, 18). This observation indicates that a different kind of CDW correlation emerges around $T_c(0)$ —well below the zero-field CDW onset temperature (Fig. 1C). As shown in Fig. 2C, the temperature dependence of the field-induced CDW is consistent with that of the CDW signatures inferred from NMR measurements (6), implying that both share the same origin.

Next, we explored the field-induced enhancement of CDW order at $T = 10$ K. The diffraction patterns at $\mu_0 H = 0 - 25$ T are shown in Fig. 3A, top. The projected intensities at both $l \sim \frac{1}{2}$ and $l \sim 1$ are depicted in Fig. 3A, bottom, integrated over the ranges of l indicated in Fig. 3A, right. Up to $\mu_0 H = 15$ T, the intensities of the CDW order at both $l \sim \frac{1}{2}$ and $l \sim 1$ are similar. Above 15 T, however, the intensity at $(0, 2-q, \sim 1)$ continues to grow strongly, whereas it saturates at $(0, 2-q, \sim \frac{1}{2})$ (Fig. 3B). This was confirmed in an equivalent CDW region $(0, 2+q, 1)$ (Fig. 4) (24), where we were able to follow the enhancement of CDW intensity at $l = 1$ up to our maximum field, $\mu_0 H = 28$ T. Furthermore, the in-plane correlation lengths ξ_k at $l \sim \frac{1}{2}$ and $l \sim 1$ start to diverge from each other at $\mu_0 H \sim 15$ T (Fig. 3C), which is suggestive of a transition; ξ_k at $l \sim 1$ increases for $\mu_0 H > 15$ T, whereas ξ_k at $l \sim \frac{1}{2}$ saturates or is slightly suppressed. As discussed in (24), the estimated correlation length at the highest magnetic fields may be limited by the instrument resolution. Nevertheless, the distinct field dependence of the CDW intensity and the correlation length confirm that the CDW order at $l \sim 1$ is different from that at $l \sim \frac{1}{2}$, and that both CDW orders coexist at high magnetic fields. In particular, the onset of the field-induced CDW ($l \sim 1$) above 15 T is consistent with NMR results in which the

¹Stanford Institute for Materials and Energy Science, SLAC National Accelerator Laboratory and Stanford University, Menlo Park, CA 94025, USA. ²Stanford Synchrotron Radiation Lightsource, SLAC National Accelerator Laboratory, Menlo Park, CA 94025, USA. ³Institute for Materials Research, Tohoku University, Katahira 2-1-1, Sendai, 980-8577, Japan. ⁴Department of Physics and Astronomy, University of British Columbia, Vancouver, British Columbia V6T 1Z1, Canada. ⁵Canadian Institute for Advanced Research, Toronto, Ontario M5G 1Z8, Canada. ⁶The Advanced Photon Source, Argonne National Laboratory, Argonne, IL 60439, USA. ⁷Linac Coherent Light Source, SLAC National Accelerator Laboratory, Menlo Park, CA 94025, USA. ⁸Geballe Laboratory for Advanced Materials, Departments of Physics and Applied Physics, Stanford University, Stanford, CA 94305, USA. ⁹SLAC National Accelerator Laboratory, Menlo Park, CA 94025, USA.

*These authors contributed equally to this work. †Corresponding author: dlzhu@slac.stanford.edu (D.Z.); leews@stanford.edu (W.-S.L.); jslee@slac.stanford.edu (J.-S.L.)

line-splitting signature of CDW order is absent at low fields (6, 19) and the ultrasonic measurements (22). Unfortunately, because of the relatively coarse field interval in Fig. 3, it is difficult to precisely determine the value of the onset field

(Fig. 3, B and C, shaded area) or to distinguish whether the field-induced CDW emerges in a phase-transition or a crossover.

Data shown in Fig. 3 motivate scrutiny of the field-induced CDW in the $l \sim 1$ region at the

highest accessible magnetic field of 28 T. Given our experimental configuration (24), a larger l range is accessible near $l = 1$ by monitoring the equivalent CDW reflection near $(0, 2+q, l)$, rather than near $(0, 2-q, \sim 1)$. As shown in Fig. 4, A and B,

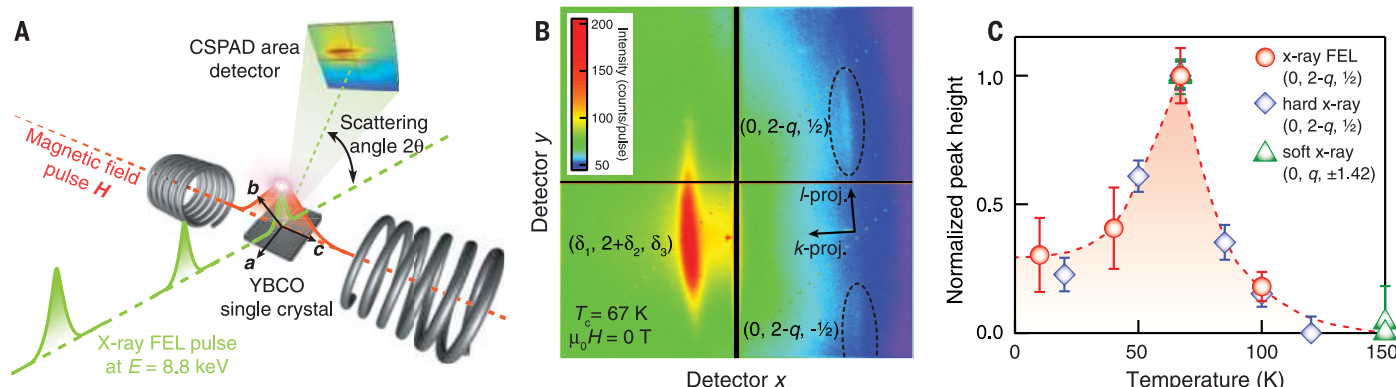
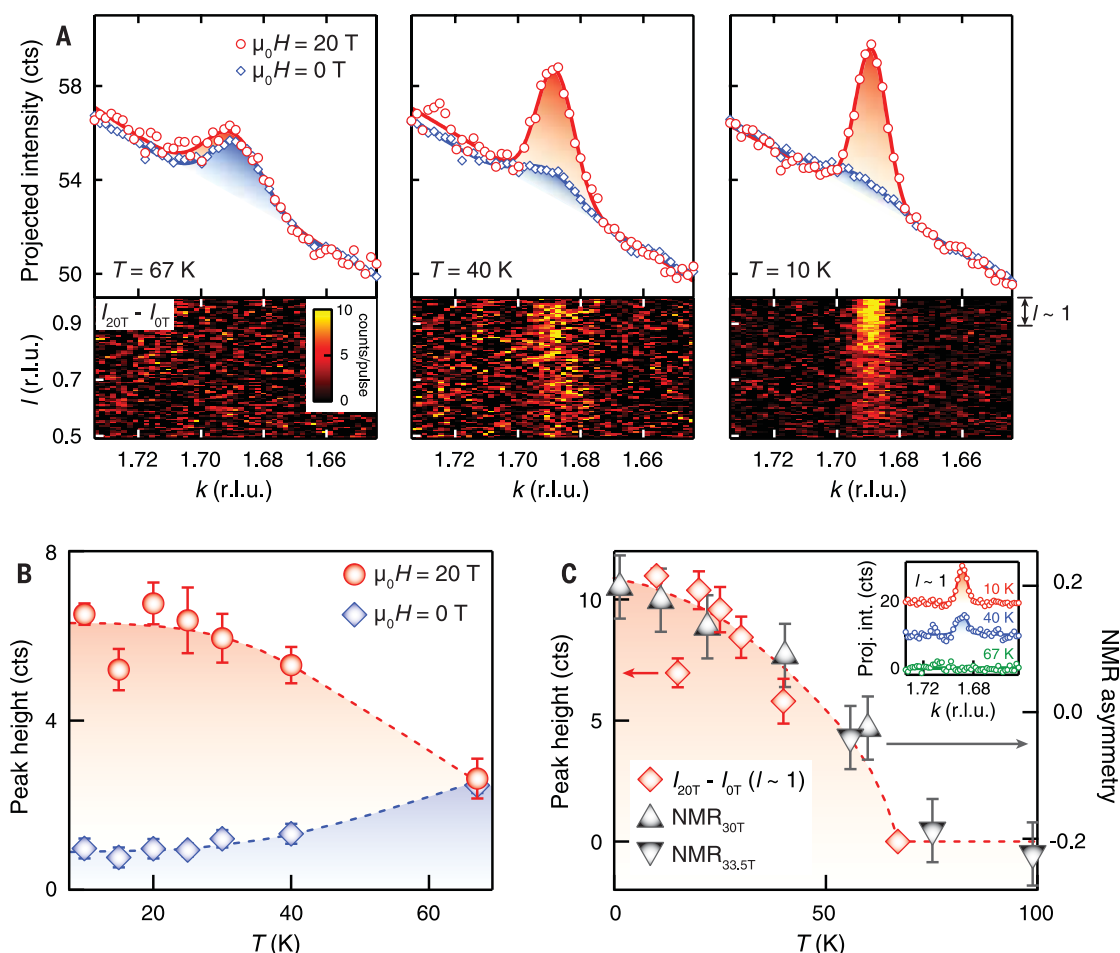


Fig. 1. Experimental setup and zero-field characterization. (A) The millisecond pulsed magnetic field and femtosecond x-ray FEL pulses are synchronized to obtain a diffraction pattern from the YBCO single crystal at the maximum magnetic field. The diffraction pattern was recorded by use of a 2D pixel array detector. (B) Zero-field diffraction pattern showing the $(0, 2-q, \pm\frac{1}{2})$ CDW peaks and the tail of the $(0, 2, 0)$ Bragg peak ($\delta_1 = -0.118$, $\delta_2 = 0.001$, $\delta_3 = 0.021$). The

sample rotation angle was optimized for the CDW position and not for the $(0, 2, 0)$ Bragg peak (24). (C) The temperature dependence of the CDW peak height near $(0, 2-q, \frac{1}{2})$ measured at the x-ray FEL is shown with red symbols. We have also taken data at synchrotron light sources using hard (blue symbols) and soft (green symbols) x-rays (24), which are shown for comparison. The dashed line is a guide to the eye, and the error bars denote 1 SD as obtained from the peak fitting.

Fig. 2. Temperature dependence of the CDW order at $\mu_0 H = 20$ T.

(A) Top and bottom show the evolution of the projected $(0, 2-q, \frac{1}{2})$ CDW peak profile along the k direction and the difference map of the diffraction pattern between $\mu_0 H = 0$ and 20 T, respectively, at representative temperatures of $T = 67, 40$, and 10 K. Positions are given in reciprocal lattice units (r.l.u.). Solid lines are Gaussian fits to the data with a second-order polynomial background. (B) Temperature dependence of the peak height from the projected CDW profiles at 0 and 20 T. (C) Peak height of the projected CDW profiles near $l \sim 1$ as a function of temperature. The projected CDW profiles [inset, traces offset by 10 counts (cts)] are obtained from the 2D difference map by integrating near $l \sim 1$, as indicated in (A). As a comparison, NMR data taken from (6) are superimposed. Dashed lines are guides to the eye. Error bars correspond to 1 SD.



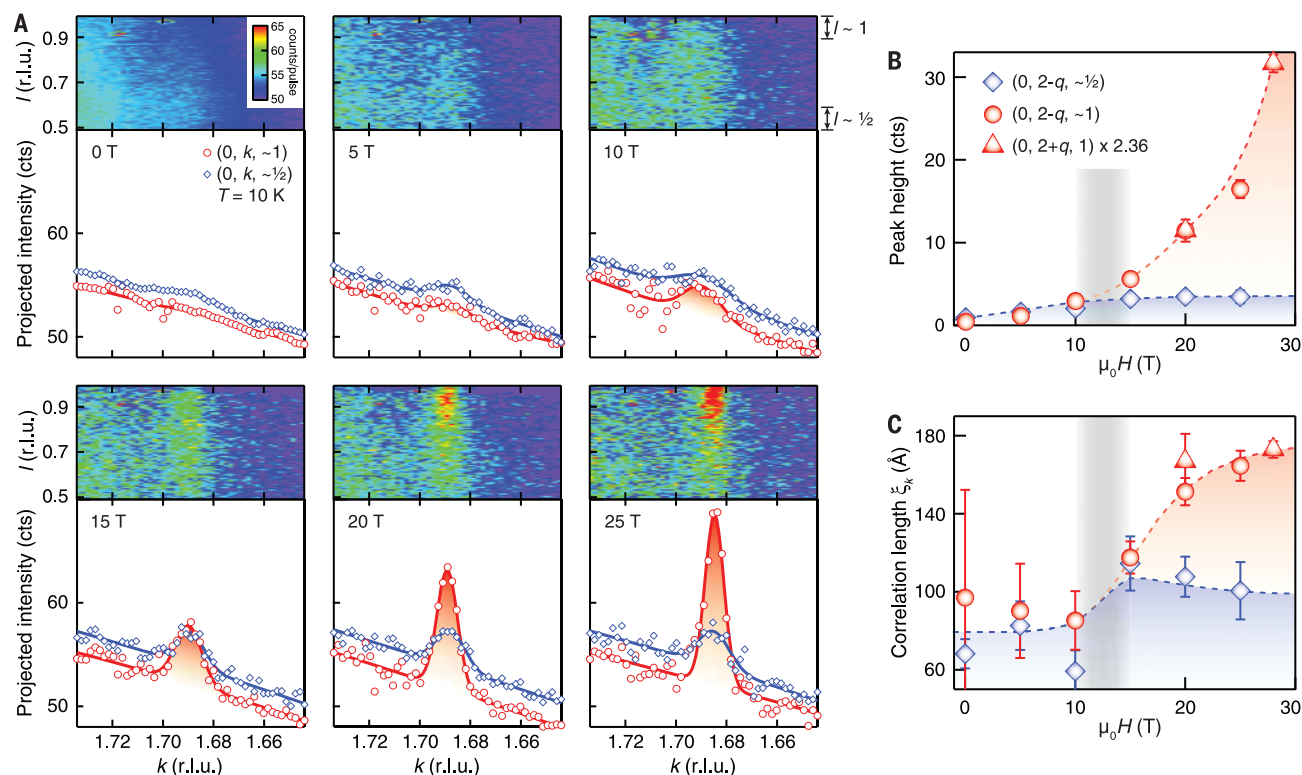


Fig. 3. Field dependence of the CDW order at $T = 10$ K. (A) CDW diffraction pattern (top) and projected CDW peak profiles (bottom) near $l \sim 1/2$ and $l \sim 1$, obtained through integration of the signal in the windows indicated on the image, in the field range $\mu_0 H = 0 - 25$ T. Features due to ice condensation on the sample surface that do not overlap with the CDW signal were subtracted from the diffraction patterns (24). Solid lines are Gaussian fits to the data with a second-order polynomial background. (B) Peak height of the projected CDW profile near $l \sim 1/2$

and $l \sim 1$ as a function of H . Data taken in an equivalent CDW region $(0, 2+q, 1)$, shown in Fig. 4, are superimposed by normalizing the values at 20 T. (C) H dependence of the in-plane correlation length $\xi_k = 1/\sigma_k$ deduced from Gaussian fits (σ_k is the Gaussian SD) to the projected CDW profile shown in (A) as well as Fig. 4C. Values of ξ_k have not been corrected for the instrument resolution and, therefore, represent lower bounds. The gray shaded area denotes the onset region of the $l \sim 1$ CDW component, and dashed lines are guides to the eye. Error bars correspond to 1 SD.

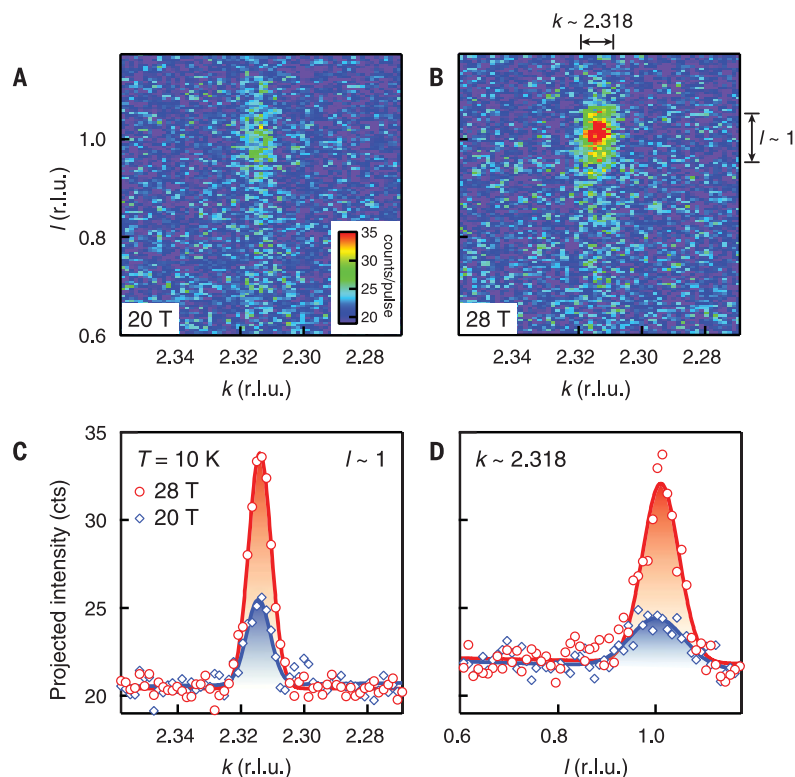


Fig. 4. Three-dimensional CDW order at $\mu_0 H > 20$ T. (A and B) CDW diffraction pattern near $(0, 2+q, l)$ at $\mu_0 H = 20$ and 28 T. (C and D) Projected CDW peak profiles along the k and l direction within the regions indicated in (B). Gaussian fits to the data with a linear background (solid lines) and taking into account the measurement accuracy, reveal that the field-induced CDW peak is centered at $k = 2.318(10)$ and $l = 1.00(2)$.

the CDW diffraction pattern at 28 T becomes sharper not only along the k direction (Fig. 3C) but also along the l direction (perpendicular to the CuO_2 planes). This indicates that CDW correlations along the c axis are enhanced— $\xi_l = 34(4)$ and $50(2)$ Å at 20 and 28 T, respectively, where the numbers in parentheses are the error bars—concomitant with roughly a threefold increase of the peak height. Even though these values of ξ_l are lower bounds, because they have not been corrected for the instrument resolution (24) they are considerably larger than that of the zero-field CDW ($\xi_l \sim 7$ Å) (8), indicating that the field-induced CDW at $l = 1$ is much more correlated in all three dimensions than is the zero-field CDW. Furthermore, as shown in Fig. 4, C and D, the CDW peak positions are identical at 20 and 28 T. There has been speculation that the in-plane component of the CDW Q vector may shift and lock in to a commensurate value at high magnetic fields (25). However, within our experimental resolution the field-induced in-plane components of the Q vector [$h = 0.00(1)$, $k = 0.318(10)$] are identical to that of the zero-field CDW.

A field-induced spin density wave (SDW) has been observed in $\text{La}_{2-x}\text{Sr}_x\text{CuO}_4$ at weaker fields ~ 6 T, which is also peaked at integer l owing to an alignment of SDW patches, associated with the vortex cores (26). However, the emergence of field-induced CDW order at $l = 1$ is unlikely to be caused by the alignment of CDW regions that are associated with vortices (2). This is because at magnetic fields beyond 20 T, the distance between vortices, if still present, would be less than ~ 100 Å in the CuO_2 plane (27), which is already smaller than the in-plane CDW correlation length at these field strengths (Fig. 3C).

There are implications of the observed field-induced 3D CDW at $l = 1$. First, its emergence at high fields and low temperatures implies a boundary that separates the phase diagram into different CDW regions, as also suggested by ultrasonic (22) and NMR measurements (19). Second, given that a field-dependence of the CDW order is only observed below $T_c(0)$ (Fig. 2), we infer that the enhancement is related to the suppression of superconductivity. Thus, the growth of the CDW peak intensity in fields up to 28 T suggests that superconducting correlations may exist beyond the upper critical field that was deduced from transport measurements (28, 29). Third, our observations shed light on quantum oscillation results, which have been interpreted as evidence for the existence of small electron pockets in the “nodal” region of the Brillouin zone (4, 5, 30). It is plausible that the Fermi surface is reconstructed by the stronger field-induced CDW at $l = 1$, rather than the shorter-range correlated one at $l \sim \frac{1}{2}$ (31). Last, the relation between the zero-field and field-induced CDW is puzzling. On the one hand, they seem unrelated because they exhibit distinct temperature and field dependences, as well as a different ordering perpendicular to the CuO_2 planes. On the other hand, they must be somehow related because they feature the same in-plane CDW incommensuration q . Thus, our results re-

veal a rich CDW phenomenology in cuprates, which is not a simple competition with HTSC.

REFERENCES AND NOTES

1. J. M. Tranquada, B. J. Sternlieb, J. D. Axe, Y. Nakamura, S. Uchida, *Nature* **375**, 561–563 (1995).
2. J. E. Hoffman *et al.*, *Science* **295**, 466–469 (2002).
3. C. Howald, H. Eisaki, N. Kaneko, A. Kapitulnik, *Proc. Natl. Acad. Sci. U.S.A.* **100**, 9705–9709 (2003).
4. N. Doiron-Leyraud *et al.*, *Nature* **447**, 565–568 (2007).
5. D. LeBoeuf *et al.*, *Nature* **450**, 533–536 (2007).
6. T. Wu *et al.*, *Nature* **477**, 191–194 (2011).
7. G. Ghiringhelli *et al.*, *Science* **337**, 821–825 (2012).
8. J. Chang *et al.*, *Nat. Phys.* **8**, 871–876 (2012).
9. R. Comin *et al.*, *Science* **343**, 390–392 (2014).
10. E. H. da Silva Neto *et al.*, *Science* **343**, 393–396 (2014).
11. W. Tabis *et al.*, *Nat. Commun.* **5**, 5875 (2014).
12. E. H. da Silva Neto *et al.*, *Science* **347**, 282–285 (2015).
13. E. Fradkin, S. A. Kivelson, *Nat. Phys.* **8**, 864–866 (2012).
14. H.-D. Chen, O. Vafeek, A. Yazdani, S.-C. Zhang, *Phys. Rev. Lett.* **93**, 187002 (2004).
15. P. A. Lee, *Phys. Rev. X* **4**, 031017 (2014).
16. D. F. Agterberg, J. Garaud, *Phys. Rev. B* **91**, 104512 (2015).
17. S. Blanco-Canosa *et al.*, *Phys. Rev. Lett.* **110**, 187001 (2013).
18. E. Blackburn *et al.*, *Phys. Rev. Lett.* **110**, 137004 (2013).
19. T. Wu *et al.*, *Nat. Commun.* **4**, 2113 (2013).
20. D. LeBoeuf *et al.*, *Phys. Rev. B* **83**, 054506 (2011).
21. T. Wu *et al.*, *Nat. Commun.* **6**, 6438 (2015).
22. D. LeBoeuf *et al.*, *Nat. Phys.* **9**, 79–83 (2013).
23. P. Emma *et al.*, *Nat. Photonics* **4**, 641–647 (2010).
24. Materials and methods are available as supplementary materials on Science Online.
25. E. M. Forgan *et al.*, <http://arxiv.org/abs/1504.01585> (2015).
26. B. Lake *et al.*, *Nat. Mater.* **4**, 658–662 (2005).
27. N. G. Leos *et al.*, *J. Phys. Soc. Jpn.* **84**, 044709 (2015).
28. G. Grissonnanché *et al.*, *Nat. Commun.* **5**, 3280 (2014).

29. G. Grissonnanché *et al.*, <http://arxiv.org/abs/1503.07572> (2015).
30. S. E. Sebastian, N. Harrison, G. G. Lonzarich, *Rep. Prog. Phys.* **75**, 102501 (2012).
31. S. E. Sebastian *et al.*, *Nature* **511**, 61–64 (2014).

ACKNOWLEDGMENTS

We thank J. Hastings, J. Defever, D. Damiani, G. Curie, and V. Borzenet for technical assistance in developing the scattering setup. Discussions with C. Mielke are acknowledged. This work was supported by the U.S. Department of Energy (DOE), Office of Science, Basic Energy Sciences, Materials Sciences and Engineering Division, under contract DE-AC02-76SF00515. X-ray FEL studies were carried out at the Linac Coherent Light Source, a Directorate of SLAC and an Office of Science User Facility operated for the DOE, Office of Science by Stanford University. Soft and hard x-ray scattering studies were carried out at the Stanford Synchrotron Radiation Lightsource, a Directorate of SLAC and an Office of Science User Facility operated for the DOE, Office of Science by Stanford University. Hard x-ray scattering studies were also conducted at the Advanced Photon Source, supported by the DOE, Office of Science, Office of Basic Energy Sciences under contract DE-AC02-06CH11357. S.G. acknowledges partial support by the Swiss National Science Foundation under fellowship P2EZP2_148737. H.N. acknowledges the support by Grants-in-Aid for Scientific Research (KAKENHI) 23224009, International Collaboration Center—Institute for Materials Research, and MD-program. Materials development was supported by the Natural Sciences and Engineering Research Council and by the Canadian Institute for Advanced Research.

SUPPLEMENTARY MATERIALS

www.sciencemag.org/content/350/6263/949/suppl/DC1
Materials and Methods
Figs. S1 to S5
References (32–35)

21 May 2015; accepted 30 September 2015
10.1126/science.aac6257

BIOLOGICAL MATERIALS

Multifunctionality of chiton biomineralized armor with an integrated visual system

Ling Li,^{1,2*} Matthew J. Connors,^{1*} Mathias Kolle,³ Grant T. England,² Daniel I. Speiser,⁴ Xianghui Xiao,⁵ Joanna Aizenberg,^{2,6,7} Christine Ortiz^{1†}

Nature provides a multitude of examples of multifunctional structural materials in which trade-offs are imposed by conflicting functional requirements. One such example is the biomineralized armor of the chiton *Acanthopleura granulata*, which incorporates an integrated sensory system that includes hundreds of eyes with aragonite-based lenses. We use optical experiments to demonstrate that these microscopic lenses are able to form images. Light scattering by the polycrystalline lenses is minimized by the use of relatively large, crystallographically aligned grains. Multiscale mechanical testing reveals that as the size, complexity, and functionality of the integrated sensory elements increase, the local mechanical performance of the armor decreases. However, *A. granulata* has evolved several strategies to compensate for its mechanical vulnerabilities to form a multipurpose system with co-optimized optical and structural functions.

The design of structural materials with additional integrated functionality, such as energy storage (1), sensing (2), and self-healing (3), is an emergent field that holds great potential for a diversity of engineering applications. Nature provides a multitude of multifunctional structural material systems, such as brittle stars (photosensation) (4), sponges (fiber-

optic feature) (5, 6), limpets (photonic coloration) (7), and bivalves (optical transparency) (8, 9). Understanding the materials-level trade-offs imposed by the conflicting functional requirements of these systems is key to extracting design principles for innovative material solutions (10, 11).

We investigate the multifunctional design and performance of the biomineralized armor of

the intertidal chiton *Acanthopleura granulata*, which contains an integrated visual system. Chitons are the only known group of extant mollusks to have living tissue integrated within the outermost layer of their shells (12). This tissue forms a complex network of channels that open dorsally as sensory organs known as aesthetes. A variety of functions have been proposed for the aesthetes (13), although observations of the phototactic behavior of a number of chitons (14, 15) suggest that photoreception may be a predominant role. In certain species, the aesthetes include hundreds of lens eyes (16, 17) that may be able to spatially resolve objects (18). In stark contrast to the protein-based lenses of most animal eyes, the lenses of chitons, like their shells, are principally composed of aragonite (18). Unlike the few other eyes known to contain lenses made of calcium carbonate, such as those of

trilobites (19, 20), the eyes of chitons are integrated within and dispersed across their entire dorsal shell surface instead of being localized to a particular region of the body. Although the calcitic lenses of brittle stars are also dispersed across their dorsal arm plates (4), it is unclear whether they enable spatial vision in a fashion similar to the lenses of chitons (18). Here, we show that the chiton *A. granulata* is able to tailor the local geometry, crystallography, and interfaces of aragonite to achieve a multifunctional armor.

The two main sensory structures in the shell of *A. granulata* (Fig. 1A and fig. S1) appear on the surface as small bumps ~ 50 μm in diameter (Fig. 1, B and C). The more numerous megal aesthetes, which are common to all chitons, maintain the same opacity as nonsensory regions and are capped with a pore, which appears as a black spot in scanning electron micrographs (SEMs) (Fig. 1C). The eyes are distinguished by their translucent lenses, which are encircled by dark areas containing the pigment pheomelanin (21) (outer diameter, 86 ± 4 μm ; $n = 10$) (Fig. 1B). Both sensory structures are located within the valleys formed by the large nonsensory protrusions (diameter, ~ 200 μm ; height, ~ 100 μm), as revealed by the three-dimensional (3D) stereographic reconstruction of the shell surface (Fig. 1, D and E). SEM imaging revealed that the surfaces of the lenses are much smoother than those covering the neighboring megal aesthetes and nonsensory protrusions (Fig. 1C, inset).

Synchrotron x-ray microcomputed tomography ($\mu\text{-CT}$) was used to investigate the 3D morphol-

ogy of the megal aesthetes and eyes (Fig. 1, F and G; fig. S2; and movies S1 and S2). In contrast to the cylindrical chamber of the megal aesthetes (width of chamber, ~ 40 μm), the specialized chamber underneath the lens is pear-shaped and has a depth and width of 56 ± 7 and 76 ± 5 μm , respectively ($n = 7$) (see fig. S3 for detailed morphometric measurements). This expansion results in an eye chamber whose volume is ~ 5 times as great as that of the megal aesthetes. Numerous small sensory pores, known as micraesthetes, were observed branching from the chambers of the megal aesthetes and eyes to the shell surface (fig. S2, bottom). Highly x-ray-absorbent structures, later determined to be intrachamber calcified material (ICCM), were discovered within both chambers (fig. S4). In the eye, the ICCM forms a C-shaped pocket that likely encircles the retina (Fig. 1G). The lens region of the eyes is 38 ± 2 μm ($n = 7$) thick and slightly elongated in the direction of the optic canal, which we denote as the longitudinal direction (Fig. 1H). Figure 1I illustrates the average cross-sectional shape of the lens in the longitudinal and transverse planes. The top and bottom surfaces of the lens were generally best fit with parabolic profiles in comparison with spherical ones (fig. S5).

Next, we compared the fine structure, composition, and crystallography of the lens region of the eyes to the bulk of the calcified portion of the outer shell layer. Polished cross sections of eyes viewed under cross-polarized light (Fig. 2A) showed that the lenses have a relatively uniform

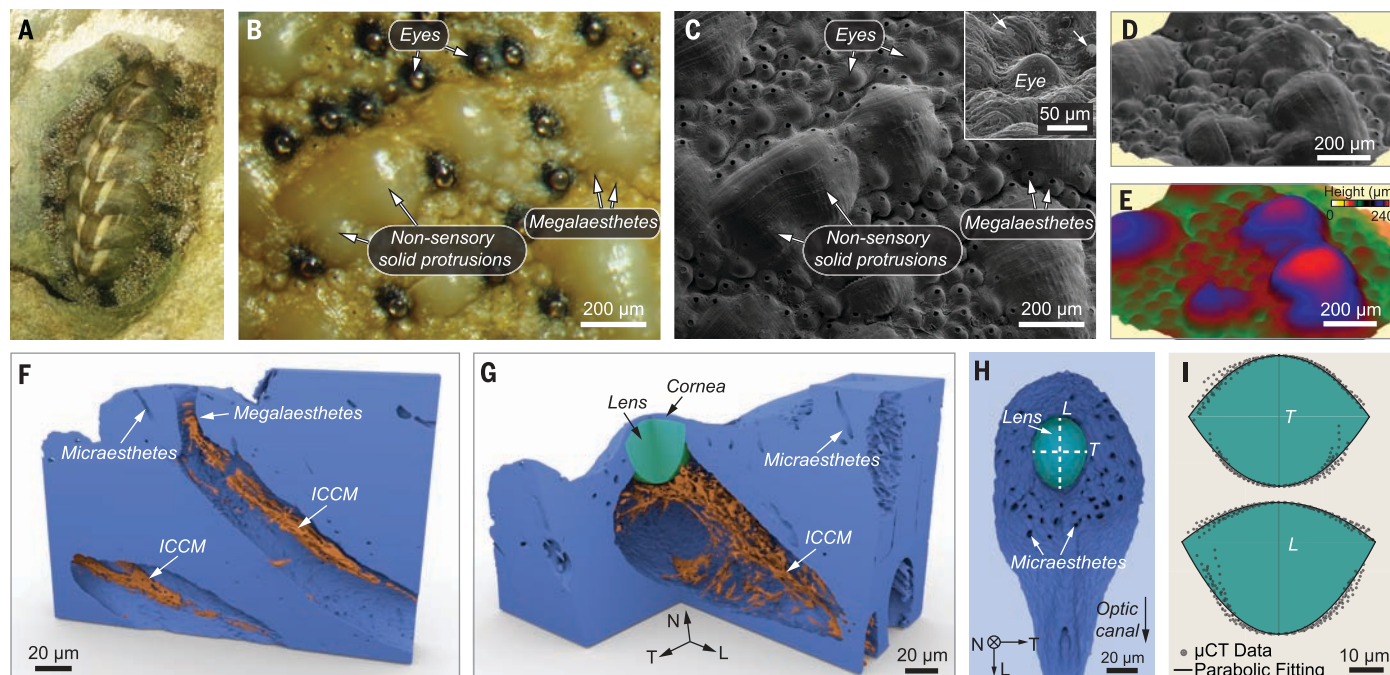


Fig. 1. Structure of the sensory elements integrated within the protective shell of the chiton *Acanthopleura granulata*. (A) Photograph of *A. granulata*, (B) light micrograph, and (C) corresponding SEM image of a region of the shell surface containing multiple eyes and megal aesthetes. The inset of (C) highlights the smooth and rough surfaces of the eyes and megal aesthetes (white arrows), respectively. (D and E) SEM-derived stereographic reconstruction of the shell surface: (D) surface morphology and (E) height. (F and G) 3D $\mu\text{-CT}$ reconstructions

of a megal aesthetes (F) and an eye (G), highlighting the calcified structures: outer shell layer and continuous cornea (blue), ICCM (orange), and lens (green). Numerous micraesthetes branch from the eyes and megal aesthetes. N, T, and L refer to normal, transverse, and longitudinal directions, respectively. (H) Bottom view of the lens region of (G), showing the elongated geometry along the optic canal direction (equivalent to longitudinal direction). (I) Curvature of the lenses in the T and L cross sections measured with $\mu\text{-CT}$ and fittings with parabolic curves.

grayscale level compared with the surrounding bulk granular microstructure, which is known to have weak preferred grain orientations in the chiton *Tonicella marmorea* (22). This suggested that the lens is either a single crystal or is polycrystalline with highly aligned grains. The clear boundaries between the lens and granular microstructure in Fig. 2A indicate a delicate control of crystallography in the lens region. A thin ($\sim 5\ \mu\text{m}$ thick) concavo-convex corneal layer covers the lens and is continuous with the surrounding granular microstructure. Sectioning an eye by focused ion beam (FIB) milling revealed the presence of two additional layers, L1 and L2, underlying the lens (Fig. 2B). Energy-dispersive x-ray spectroscopy (EDX) indicated that L1 is mainly composed of organic materials, whereas L2 contains calcium (Fig. 2C). Many struts branch dorsally from L2 to the chamber walls (Fig. S4). They correspond in size, shape, and location to the aforementioned ICCM observed in the chamber with μCT (Fig. 1G).

The crystallographic pole figures obtained with electron backscattered diffraction (EBSD) confirmed that the lens has a strong crystallographic texture, indicated by the regions of localized intensity, which is in stark contrast to the weak texture of the surrounding granular region (Fig. 2D). Integrating the c axis from the pole figure of the lens shows that the full width at half maximum is $\sim 4^\circ$, which indicates that the c axes of the grains are highly aligned (fig. S6). The high-resolution transmission electron microscopy (HRTEM) image and corresponding fast Fourier transformation (FFT) pattern from the lens (Fig. 2E) and the bright-field TEM image and corresponding selected-area electron diffraction (SAED) pattern of the granular microstructure (Fig. 2F) further highlight the small and large crystallographic mismatch between grains in the lens and granular microstructure, respectively. Because the effective refractive indices of aragonite are orientation-dependent,

the uniform crystallographic orientation of the grains in the lens likely minimizes light scattering. EBSD and SAED of multiple lenses found that the polar angle θ between the c axis and optical axis was about 45° , whereas the orientations of the a and b axes were inconsistent (fig. S7). Because aragonite is a pseudo-uniaxial crystal, the non-normal orientation of the c axes should generate double refraction, which is consistent with observations that the lenses are birefringent when viewed with polarized light (17, 18). In addition, EBSD showed that the lenses have an average grain size of roughly $10\ \mu\text{m}$, which is approximately an order of magnitude greater than that of the surrounding granular microstructure (fig. S8). High-resolution SEM images of polished cross sections display faint and clear grain boundaries in the lens and surrounding granular regions, respectively (fig. S9). The likely function of the large grains is to reduce the number and area of grain boundaries, which will minimize light scattering. Furthermore, HRTEM images suggest that the lens may possess less intracrystalline organic material than the surrounding granular microstructure (fig. S10), which may also serve to reduce light scattering (8). TEM imaging and corresponding electron diffraction suggest that layers L1 and L2 are amorphous, despite a fine conformal layered structure observed in L2 (Fig. 2, G and H).

The optical performance of individual eyes of *A. granulata* was investigated with both theoretical modeling and experimental measurements. First, key elements of the geometry, composition, and crystallography of the lens were combined in 2D ray-trace simulations to investigate the locations of rear focal points, F . For each possible external environment, air and seawater, F of the ordinary and extraordinary rays were calculated in two orthogonal extremes, the transverse and longitudinal cross sections (Fig. 3A; see fig. S11 for detailed simulation results). The ranges of F in air and seawater, 8 to 28 and 25 to $51\ \mu\text{m}$ below L2, respectively, lie within the geometrically per-

mitted axial range of photoreceptive tissue, ~ 4 to $52\ \mu\text{m}$, which is constrained above by ICCM and below by the bottom of the chamber. If θ were 0° or 90° instead of 45° , the maximum values of F in seawater would be 35 or $71\ \mu\text{m}$, which means the chamber would be unnecessarily large or small, respectively. Thus, the geometry of the chamber is highly consistent with $\theta \approx 45^\circ$.

The authors of a previous behavioral study of *A. granulata* hypothesized that the chiton may be required to use different polarizations of light to see in different tidal environments (18). In other words, only one of the two refractive indices of the birefringent lens could possibly focus light onto the photoreceptive region of the eye chamber in air, whereas the other does so in seawater. Although all of our simulated focal points fall within the eye chamber, we do not know the exact position and shape of the chiton retina, so we cannot conclude that birefringence is indeed functional. If this is not the case, it is puzzling why θ is not 0° , which would improve image quality by eliminating aberrations from double refraction as in trilobites (19) and brittle stars (4).

Because the small size (12) and perceived curvature (23) of the chiton lenses have cast doubt on their ability to form images, we decided to investigate experimentally their image formation capability by projecting objects through individual lenses in water (Fig. 3B, top). The middle image of Fig. 3B demonstrates that the lenses can form clear images of a predatory fish. These images are equivalent to those generated by a 20-cm-long fish that is 30 cm away. However, the bottom pixelated image of Fig. 3B represents what the eye is probably capable of resolving, because image quality is constrained by the spacing of the photoreceptors, $s \sim 7\ \mu\text{m}$ (18). This suggests that the maximum distance at which *A. granulata* can spatially resolve a 20-cm object is $\sim 2\ \text{m}$, because at this object distance the image will be approximately the size of a single photoreceptor. This resolution allows chitons to

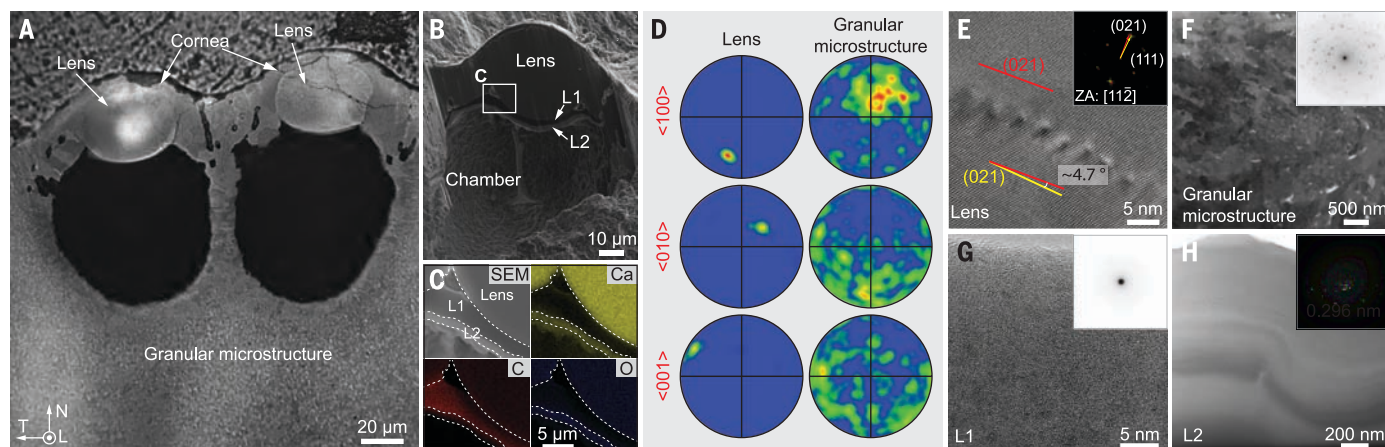


Fig. 2. Structural, compositional, and crystallographic features of the lens region of the eyes. (A) Polarized light micrograph of a polished cross section containing two eyes. (B) SEM image of a FIB-cut section of an eye. (C) Energy-dispersive spectroscopy (EDS) mapping of the bottom region of the eye shown in (B). (D) EBSD pole figures of the lens and surrounding granular microstructure in reference to the three principal orientations of aragonite. (E) HRTEM image of two adjacent aragonite grains in the lens with a small misorientation angle ($\sim 4.7^\circ$). (Inset) Corresponding FFT pattern with zone axis of $[11\bar{2}]$. (F to H) Bright-field TEM images and SAED patterns (insets) of the granular microstructure, L1, and L2, respectively.

quickly respond to approaching predators by clamping down to the substrate so that they are not easily dislodged (18).

The clear images produced by individual lenses allowed us to test the accuracy of our simulations. We determined the focal length, f , of individual eyes by measuring the dimensions of images produced from a known object at a number of object distances (Fig. 3C). The obtained $f = 72 \pm 17 \mu\text{m}$ is comparable to the maximum value of f , $65 \mu\text{m}$, determined from ray-trace simulations (Fig. 3A). This allowed us to quantify the resolution of an individual eye, $\Delta\phi$, using $\Delta\phi = \tan^{-1}(s/f)$ (24), which ranges from 8° to 13° in air and 6° to 9° in seawater, respectively. These results explain the outcome of previous behavioral experiments in which *A. granulata* was able to distinguish between dark targets with angular sizes of $\sim 9^\circ$ and equivalent, uniform decreases in illumination in both air and seawater (18).

Double refraction was observed during image-formation experiments (fig. S12), but not consistently, which may be because the optical axes of the lens and microscope were not aligned parallel in each trial. Similarly, the extent of astigmatism observed was variable, presumably because we did not know the orientation of the transverse and longitudinal directions of each lens relative to the horizontal and vertical lines of our test objects. However, the maximum astigmatism observed, $\Delta F = 19 \mu\text{m}$, is consistent with the maximum, $\Delta F = 17 \mu\text{m}$, predicted by our ray-trace simulations. Additional metrics of optical performance, including F number, sensitivity, and field of view, can be found in fig. S13.

Relative to the solid nonsensory regions of the outer shell layer, the integration of sensory struc-

tures introduces large, localized volumes of soft sensory tissue and modifies the aragonite-based microstructure at the intrinsic material level. We hypothesized that these changes might affect the mechanical robustness of the shell, which is surely critical to the survival of these animals. To test this hypothesis, we investigated the mechanical behavior of the outer shell layer with instrumented indentation at two length scales (Fig. 4). At the $\sim 5\text{-}\mu\text{m}$ scale (maximum load $\sim 5\text{ mN}$), both the lens and surrounding granular microstructure exhibit similar indentation modulus (E_{O-P} , $\sim 70\text{ GPa}$) and hardness (H_{O-P} , $\sim 5\text{ GPa}$) (Fig. 4A). However, nanoindentation with a sharp conospherical tip induces radial cracking in the lens region but not in the granular microstructure (Fig. 4B). This behavior of more brittle fracture in the lens region might be due to its pseudo-single crystalline nature. To probe the mechanical behavior on the scale of the entire sensory structures, we used a flat punch tip to perform “crush” experiments on the eyes, megalaeesthetes, and solid nonsensory regions (Fig. 4C). As illustrated by the load-depth curves in Fig. 4D, compression of eyes first induced gradual fracture of the protective corneal layer (Fig. 4D, inset) and eventually led to catastrophic failure by pushing the entire lens into the chamber, as shown in the post-test SEM image (Fig. 4E). The average load for the catastrophic fracture of a lens is slightly less than 1 N ($0.84 \pm 0.11\text{ N}$). With a maximum load of 1 N, the megalaeesthetes exhibited stepwise microfracture up to the maximum load without catastrophic failure (Fig. 4E). Similar indentation on the solid nonsensory protrusions induced a relatively small amount of permanent deformation, demonstrating its greater mechanical integrity (Fig. 4E).

The structure/property/performance relationships of the shell plates of *A. granulata* demonstrate that trade-offs are present at the materials level within a single protective armor system. The shells of chitons have evolved to satisfy two conflicting design requirements, protection and sensation. Three design aspects are fundamental to the functional integration of the sensory structures within the armor: (i) the incorporation of soft sensory tissue (creation of a porous network), (ii) modification of the local microscopic geometry of the armor material, and (iii) the material-level modification of the armor material.

Sensory integration necessitates the incorporation of living tissue, which creates porosity. This degrades the mechanical robustness of the armor, which can be seen by comparing the mechanical performance of megalaeesthetes to the solid nonsensory region. Depending on the species, megalaeesthetes may serve a variety of functions, including mechano-, chemo-, and/or photoreception (13–15). Increasing the integrated optical functionality from simple photoreception to spatial vision (in other words, advancing from light-sensitive megalaeesthetes to eyes) requires a much larger volume of soft tissue per sensory unit, as well as the modification of the local geometry of the armor material to form a lens. Although the eyes provide distinct advantages over megalaeesthetes—for example, the ability to distinguish the appearance of dark objects from uniform decreases in illumination—they further degrade the penetration resistance of the armor. This is demonstrated by the microindentation experiments, in which the megalaeesthetes exhibited stepwise microfractures while the eyes failed catastrophically at less than 1 N. Furthermore, at the

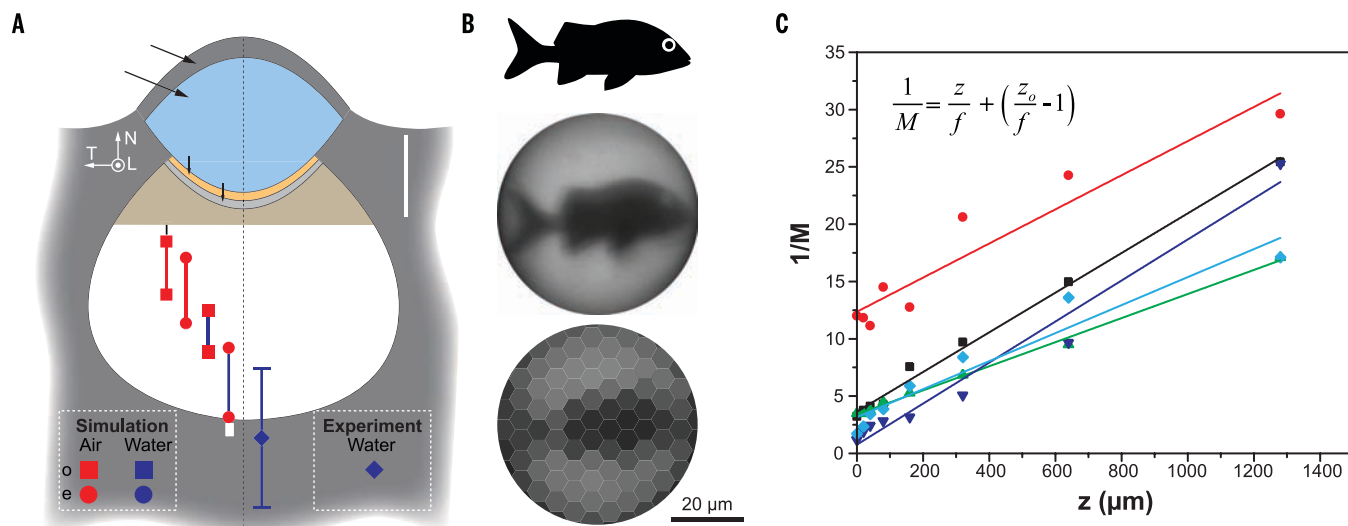


Fig. 3. Focal length and image formation capacity of individual eyes. (A) Positions of the rear focal points obtained from 2D ray-trace simulations (left) and experiments (right). The red or blue color signifies an external environment of air or water, respectively. T and L indicate the cross-sectional geometry simulated. The square and circle symbols correspond to the ordinary and extraordinary rays, respectively. The white region underneath

ICCM is the location of photoreceptive cells (17). **(B)** Image formation ability of an individual eye. (Top) The object, side profile of a predatory fish. (Middle) Image. (Bottom) Proposed physiological image resolution. Each hexagonal pixel is the size of a single photoreceptor. **(C)** Experimental measurements of the focal length f of five individual lenses derived from the slope of inverse magnification $1/M$ versus object distance z .

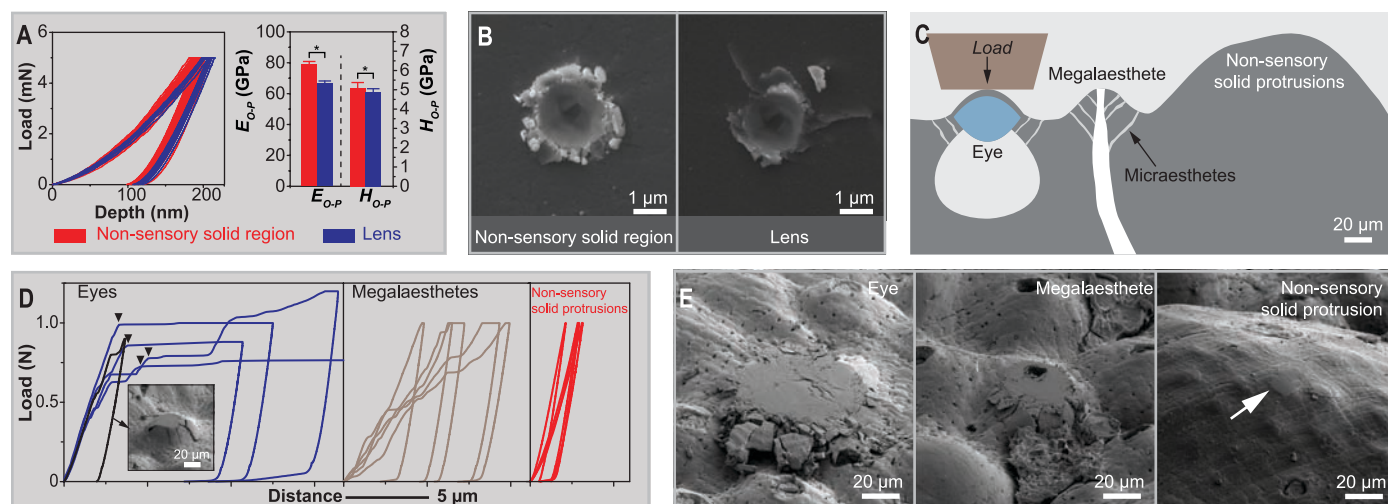


Fig. 4. Trade-offs between mechanical protection and sensory integration.

(A) Quantitative mechanical properties of the lens and nonsensory solid region determined through instrumented nanoindentation with a Berkovich tip. (Left) The nanoindentation load-depth curves. (Right) Indentation modulus and hardness. *, statistical significance at level of 0.05 via two-sample *t* test. The *n* numbers for lenses and nonsensory solid regions are 9 and 24, respectively. (B) SEM images of residual indents in the nonsensory region and lens, respectively, after nanoindentation with a conospherical tip (tip radius, ~1 μ m; semi-angle, 30°). (C) Schematic diagram of the microscopic com-

pression experiments on the three areas of the outer shell layer: nonsensory regions, megalaesthete, and eyes. (D) Microindentation force versus depth curves for the eyes, megalaesthete, and nonsensory regions (*n* = 5 for each of the three structural features). The relative size and geometry of the indenter is shown in (C). The SEM inset shows the onset of plastic deformation in the eye region, where the cornea fractures radially. (E) SEM images of residual indents in the eyes, megalaesthete, and nonsensory regions, respectively. The white arrow indicates the location of compression in the nonsensory region.

material level, increasing the grain size and alignment in the lens relative to the granular microstructure of nonsensory regions reduces scattering and improves the eye's ability to detect light (8). However, this causes the lens to fracture radially upon nanoindentation, which is in stark contrast to the relatively isotropic, localized damage observed in the nonsensory regions. These mechanical disadvantages may constrain the size of the eyes, which could improve in both resolution and sensitivity if larger (24).

Although functional integration decreases the local mechanical performance of the outer shell layer, *A. granulata* has developed strategies to compensate for its structural vulnerabilities. First, the mechanically weak sensory regions are strategically located in the valleys created by the protruding, robust nonsensory regions. This likely protects the delicate sensory structures from blunt impacts. These protrusions may also discourage fouling to make sure the sensory regions are not covered (25). Second, it's possible that chitons compensate for the mechanical weakness of the entire outer layer by having thick, hard underlying layers. This is consistent with observations of living chitons that had oyster-drill scars that penetrated the outer layer but did not pierce the inner layers (26). Last, the apparent redundancy of the eyes helps to reduce the impact of partial shell damage. Eyes in older parts of the shell are often damaged by erosion, and replacements are continually grown at the margins of the shell plates (16). Moreover, chitons face diverse types of predatory attacks that can harm the shell plates (22). From a visual performance perspective, redundancy also ensures that *A. granulata* can simultaneously monitor the entire hemi-

sphere for threats, which is important because the eyes are static structures and chitons can take several minutes to turn around. Additionally, redundancy may help improve sensitivity, signal-to-noise ratio, and the ability to distinguish false alarms from real threats (27).

REFERENCES AND NOTES

1. J. P. Thomas, M. A. Qidwai, *JOM* **57**, 18–24 (2005).
2. J. Liu et al., *Proc. Natl. Acad. Sci. U.S.A.* **110**, 6694–6699 (2013).
3. M. D. Hager, P. Greil, C. Leyens, S. van der Zwaag, U. S. Schubert, *Adv. Mater.* **22**, 5424–5430 (2010).
4. J. Aizenberg, A. Tkachenko, S. Weiner, L. Addadi, G. Hendler, *Nature* **412**, 819–822 (2001).
5. V. C. Sundar, A. D. Yablon, J. L. Grazul, M. Ilan, J. Aizenberg, *Nature* **424**, 899–900 (2003).
6. J. Aizenberg, V. C. Sundar, A. D. Yablon, J. C. Weaver, G. Chen, *Proc. Natl. Acad. Sci. U.S.A.* **101**, 3358–3363 (2004).
7. L. Li et al., *Nat. Commun.* **6**, 6322 (2015).
8. L. Li, C. Ortiz, *Adv. Mater.* **25**, 2344–2350 (2013).
9. L. Li, C. Ortiz, *Nat. Mater.* **13**, 501–507 (2014).
10. J. W. C. Dunlop, P. Fratzl, *Annu. Rev. Mater. Res.* **40**, 1–24 (2010).
11. P. Fratzl, J. W. C. Dunlop, R. Weinkamer, Eds., in *Materials Design Inspired by Nature: Function Through Inner Architecture* (Royal Society of Chemistry, Cambridge, UK, 2013).
12. J. M. Serb, D. J. Eernisse, *Evol. Educ. Outreach* **1**, 439–447 (2008).
13. S. Reindl, W. Salvenmoser, G. Haszprunar, *J. Submicrosc. Cytol. Pathol.* **29**, 135–151 (1997).
14. P. Omelich, *Veliger* **10**, 77–82 (1967).
15. P. R. Boyle, *Mar. Behav. Physiol.* **1**, 171–184 (1972).
16. H. N. Moseley, *Q. J. Microsc. Sci.* **25**, 37–60 (1885).
17. M. Nowikoff, *Z. Wiss. Zool.* **88**, 153–186 (1907).
18. D. I. Speiser, D. J. Eernisse, S. Johnsen, *Curr. Biol.* **21**, 665–670 (2011).
19. K. M. Towe, *Science* **179**, 1007–1009 (1973).
20. M. R. Lee, C. Torney, A. W. Owen, *Palaeontology* **50**, 1031–1037 (2007).
21. D. I. Speiser, D. G. DeMartini, T. H. Oakley, *J. Nat. Hist.* **48**, 2899–2911 (2014).
22. M. J. Connors et al., *J. Struct. Biol.* **177**, 314–328 (2012).
23. P. R. Boyle, Z. Zellforsch. Mikrosk. Anat. **102**, 313–332 (1969).
24. M. F. Land, D. E. Nilsson, *Animal Eyes* (Oxford Univ. Press, New York, 2012).
25. C. M. Kirschner, A. B. Brennan, *Annu. Rev. Mater. Res.* **42**, 211–229 (2012).

26. L. B. Arey, W. J. Grozier, *J. Exp. Zool.* **29**, 157–260 (1919).
27. D. E. Nilsson, *Philos. Trans. R. Soc. Lond. B Biol. Sci.* **346**, 195–212 (1994).

ACKNOWLEDGMENTS

We gratefully acknowledge support from the U.S. Army Research Office through the Massachusetts Institute of Technology (MIT) Institute for Soldier Nanotechnologies (contract W911NF-07-D-0004) and the National Security Science and Engineering Faculty Fellowship Program (N00244-09-1-0064). This work made use of the Materials Research Science and Engineering Center Shared Experimental Facilities at MIT, supported by the National Science Foundation under award number DMR-08-19762. Use of the Advanced Photon Source was supported by the U.S. Department of Energy, Office of Science, Office of Basic Energy Sciences, under contract no. DE-AC02-06CH11357. M.K. and J.A. gratefully acknowledge support by the NSF Designing Materials to Revolutionize and Engineer our Future program (DMR 1533985). M.K. thanks the Alexander von Humboldt Foundation for a Feodor Lynen Research Fellowship and gratefully acknowledges financial support from the MIT Department of Mechanical Engineering. D.I.S. gratefully acknowledges support by the NSF (DEB-1354831). We thank A. Schwartzman, Y. Zhang, and S. Chen for their technical assistance and E. Belmonte and B. Anseu for providing photographs of *A. granulata*. D.I.S. collected and identified chiton specimens. M.J.C. and X.X. performed synchrotron experiments. M.J.C. and L.L. processed and analyzed data from synchrotron experiments. L.L. performed electron microscopy studies and mechanical tests with data analysis. M.J.C., G.T.E., M.K., and L.L. performed optical measurements and data analysis. M.K. wrote the ray-tracing program. M.J.C. and M.K. performed ray-trace simulations. All authors interpreted results. L.L. and M.J.C. prepared figures, tables, and movies and wrote the draft manuscript. C.O. and J.A. supervised the project. All authors revised the manuscript for submission.

SUPPLEMENTARY MATERIALS

www.sciencemag.org/content/350/6263/952/suppl/DC1
Materials and Methods
Supplementary Text
Figs. S1 to S16
Movies S1 and S2
References (28–38)

29 July 2015; accepted 28 September 2015
10.1126/science.aad1246

SLEEP RESEARCH

Cells of a common developmental origin regulate REM/non-REM sleep and wakefulness in mice

Yu Hayashi,^{1,2*} Mitsuaki Kashiwagi,¹ Kosuke Yasuda,³ Reiko Ando,³ Mika Kanuka,¹ Kazuya Sakai,⁴ Shigeyoshi Itohara^{3*}

Mammalian sleep comprises rapid eye movement (REM) sleep and non-REM (NREM) sleep. To functionally isolate from the complex mixture of neurons populating the brainstem those involved in switching between REM and NREM sleep, we chemogenetically manipulated neurons of a specific embryonic cell lineage in mice. We identified excitatory glutamatergic neurons that inhibit REM sleep and promote NREM sleep. These neurons shared a common developmental origin with neurons promoting wakefulness; both derived from a pool of proneural hindbrain cells expressing *Atoh1* at embryonic day 10.5. We also identified inhibitory γ -aminobutyric acid-releasing neurons that act downstream to inhibit REM sleep. Artificial reduction or prolongation of REM sleep in turn affected slow-wave activity during subsequent NREM sleep, implicating REM sleep in the regulation of NREM sleep.

Lesion and pharmacologic studies to unveil the switching between rapid eye movement (REM) sleep and non-REM (NREM) sleep have implicated a key role for the pontine tegmentum (PT) (1–5). Within the PT, the peri-locus coeruleus (LC) α in cats and the equivalent sublaterodorsal nucleus (SLD) in rodents are critical for REM sleep induction (1, 3, 4). Neurons that negatively regulate REM sleep or promote the exit from REM sleep are far less understood, however, and whether such neurons locate within the PT is unclear. Various models have proposed the importance of interactions between cholinergic, monoaminergic, GABAergic (γ -aminobutyric acid-releasing), and glutamatergic neurons for sleep-stage switching (2, 4, 5). Except for the glutamatergic nature of REM sleep-promoting neurons in the SLD (6), the molecular identity and precise location of neurons participating in REM/NREM sleep switching remain elusive.

We focused on the embryonic cell lineage as a feature to isolate neurons with a specific function in sleep. The cerebellar rhombic lip (CRL), a neuroepithelial structure that emerges transiently in the vertebrate embryo, is the major source of cerebellar granule cells (7), but a subset of cells originating between embryonic day 10 to 12 (E10 to E12) migrate to the rostral hindbrain and contribute to a subpopulation of excitatory neurons in the PT (8–10). These cells transiently ex-

press the proneural transcription factor gene *Atoh1* (*Atonal homolog 1*, *Math1*) (8, 9) and can be precisely genetically labeled with the *Atoh1* enhancer (8, 11). We developed a transgenic mouse expressing the tamoxifen-inducible form of Cre (CreER^{T2}) under the *Atoh1* enhancer (*Atoh1-CreER^{T2}*). Crossing these mice with a Cre-dependent *Rosa26-loxP-stop-loxP(LSL)-NLS-lacZ* reporter strain (12) and administering tamoxifen at E10.5 resulted in reporter expression in cells migrating from the CRL at E13.5 (fig. S1A) that exhibited a dispersed distribution within the PT in adult mice (fig. S1, B to D) (8). These neurons (*Atoh1*-E10.5 cells) were either glutamatergic or cholinergic, based on the expression of *vesicular glutamate transporter 2* (*Vglut2*) or choline acetyltransferase (ChAT), respectively, but not GABAergic or noradrenergic, based on the expression of *glutamate decarboxylase 1* or tyrosine hydroxylase, respectively (fig. S1, E to H). These PT neurons did not derive from rhombic lip areas caudal to the CRL, as they were included in the midbrain-rhombomere1-derived domain, which can be labeled with *En1-Cre* (8, 13) (fig. S1I).

We first tested the effect of activating the *Atoh1*-E10.5 cells with DREADD (designer receptors exclusively activated by designer drugs) technology (14). *Atoh1-CreER^{T2}* mice were crossed with transgenic mice carrying a Cre-dependent tetracycline transactivator (tTA) transgene (*CAG-LSL-tTA*) (15) and administered tamoxifen at E10.5. Postnatally, we microinjected a recombinant adeno-associated virus (AAV) carrying a tTA-dependent hM3Dq transgene (AAV-TRE-hM3Dq-mCherry) (Fig. 1A) targeting two *Atoh1*-E10.5 subpopulations (Figs. 1 and 2): *Atoh1*-E10.5-medial cells, located ventromedial to the medial part of the superior cerebellar peduncle (scp) between the ventral part of the laterodorsal tegmentum (LDTgV) and the medial parabrachial nucleus (MPB) (fig. S1D and Fig. 1, A and B); and *Atoh1*-

E10.5-lateral cells, located dorsolateral to the scp within the lateral parabrachial nucleus (LPB) (fig. S1D and Fig. 2, A and B). hM3Dq is a DREADD receptor that evokes neural excitation upon binding of its ligand, clozapine-N-oxide (CNO). In both brain areas, CNO administration efficiently induced c-Fos expression, a marker of neural excitation (fig. S2).

We next evaluated the effect of exciting *Atoh1*-E10.5-medial cells (Fig. 1 and fig. S3). CNO was administered to three groups: mice double-transgenic for *CreER^{T2}* and *tTA* and transfected with hM3Dq-carrying AAV (dTg + hM3Dq) or with green fluorescent protein (GFP)-carrying AAV (dTg + GFP) to control for any nonspecific effects of CNO, and mice solely transgenic for *tTA* and transfected with hM3Dq-carrying AAV (sTg + hM3Dq) to control for any Cre nondependent expression of hM3Dq. When *Atoh1*-E10.5-medial cells were excited during the light phase [zeitgeber time (ZT) 5], REM sleep was drastically reduced and NREM sleep was increased in a Cre- and hM3Dq-dependent manner (Fig. 1C and fig. S3A). The large reduction in the REM sleep amount was due to a decrease in both the number and duration of REM sleep episodes, implying that these neurons regulate both entry into and exit from REM sleep (fig. S3, B and C). Unilateral injection of AAV was sufficient to produce these effects. Applying CNO during the dark phase produced similar effects (ZT 15) (fig. S3D). Awake periods appeared unaffected, suggesting that these neurons regulate REM/NREM sleep switching, but not sleep/wake switching.

Electroencephalography (EEG) properties during sleep vary among cortical areas (16). Simultaneously recording EEG from the frontal and parietal cortices showed that transitions from NREM sleep to REM sleep are asynchronous between the two cortical areas (fig. S4A) (16). This asynchronous state (termed “transitory state”) was reduced in the experimental group, indicating that the reduced REM sleep was not due to an extension of the transitory state (fig. S4, B to E).

Atoh1-E10.5 cells are either glutamatergic or cholinergic. To determine which subtype regulates REM and NREM sleep, we used the *Camk2a-LSL-tTA* strain (17). This largely reduced AAV transgene expression in cholinergic neurons (fig. S5), and yet CNO administration efficiently reduced REM sleep (fig. S3, E to G). We generated a transgenic mouse in which tTA expression was Cre dependent and under the control of the glutamatergic neuron-specific gene *Vglut2* promoter (*Vglut2-LSL-tTA*). This also reduced AAV transgene expression in cholinergic neurons (fig. S5), yet CNO administration efficiently reduced REM sleep (fig. S3, H to J). These findings strongly suggest that, of the *Atoh1*-E10.5-medial cells, glutamatergic neurons regulate REM and NREM sleep. These neurons locate near the REM sleep-promoting neurons in the SLD, but are more rostralolateral (4, 6).

We then tested the effect of activating *Atoh1*-E10.5-lateral cells (Fig. 2 and fig. S6). Animals spent more time awake at the expense of both REM and NREM sleep (Fig. 2C and fig. S6A).

¹International Institute for Integrative Sleep Medicine (WPI-IIS), University of Tsukuba, 1-1-1 Tennodai Tsukuba, Ibaraki 305-8575, Japan. ²Japan Science and Technology Agency (JST), PRESTO, 4-1-8 Honcho Kawaguchi, Saitama 332-0012, Japan. ³Laboratory for Behavioral Genetics, Brain Science Institute, RIKEN, 2-1 Hirosawa, Wako-city, Saitama 351-0198, Japan. ⁴Integrative Physiology of the Brain Arousal System, Lyon Neuroscience Research Center, INSERM U1028-CNRS UMR5292, School of Medicine, Claude Bernard University Lyon 1, F-69373 Lyon, France.

*Corresponding author. E-mail: hayashi.yu.f@u.tsukuba.ac.jp (Y.H.); sitohara@brain.riken.jp (S.I.)

Sleep was highly fragmented, resulting in increased numbers of both awake and NREM sleep episodes (fig. S6B). The *Atoh1*-E10.5-lateral cells that promote wakefulness are also likely glutamatergic, because the use of *Camk2a*-LSL-*tTA* had similar effects (fig. S6, D to F). These *Atoh1*-E10.5-lateral cells likely overlap with previously reported awake-promoting glutamatergic neurons in the lateral parabrachial nucleus (18). A correlation analysis of the AAV transfection range and effect on NREM sleep amount demonstrated distinct roles of *Atoh1*-E10.5-lateral cells and -medial cells in sleep regulation (Fig. 2D).

Atoh1-E10.5-medial cells are glutamatergic neurons that promote NREM sleep and inhibit REM sleep. We examined possible targets of these

neurons by expressing GFP and tracking their axons (Fig. 3A). Axons were detected in areas rostral to but not caudal to the soma. Axonal varicosities, reminiscent of presynaptic structures, were detected bilaterally within the mid-brain, in the dorsal area of the deep mesencephalic nucleus (dDpMe) (Fig. 3, B and C). The dDpMe and adjacent ventrolateral periaqueductal gray matter (vlPAG) contain neurons that negatively regulate REM sleep, although the type of neuron responsible is unknown (4, 19, 20). We examined the roles of inhibitory neurons, because they send axons to the SLD (21). AAVs carrying Cre-dependent transgenes were bilaterally micro-injected into this area in a knockin (KI) mouse strain expressing Cre under control of the *vesicular*

GABA transporter (Vgat) promoter (*Vgat*-Cre KI) (22) (Fig. 3D). Cre-derived transgene expression was detected almost exclusively in GABAergic neurons, as assessed by coexpression with *glutamate decarboxylase 1* (fig. S7A). Axonal varicosities of these GABAergic neurons were detected in the dorsocaudal area of the PT, which includes the SLD (Fig. 3E). CNO administration induced c-Fos expression in these neurons when hM3Dq was expressed (fig. S7, B to D). Similar to *Atoh1*-E10.5-medial cells, stimulating dDpMe inhibitory neurons at ZT 5 or ZT 15 reduced REM sleep and increased NREM sleep (Fig. 3F and fig. S8, A, C, E, and G). By contrast, hM4Di expression, a DREADD receptor that inhibits neural excitation upon binding of CNO, increased REM sleep,

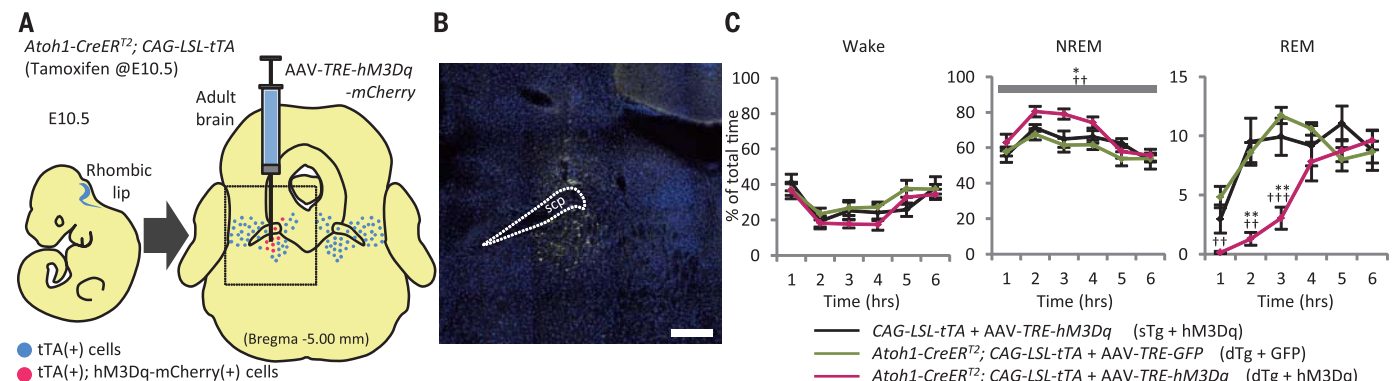


Fig. 1. *Atoh1*-E10.5-medial cells regulate REM/NREM sleep. (A) Labeling of *Atoh1*-E10.5 cells with tTA (left) and injection of AAV carrying tTA-dependent *hM3Dq*-mCherry into an area medioventral to the scp, between LDTgV and MPB (right). (B) hM3Dq-mCherry expression (yellow) in a region corresponding to the enclosed area in (A). Counterstain: DAPI (4',6-diamidino-2-phenylindole) (blue). Scale bar, 200 μ m. (C) Chemogenetic activation of

neurons in (B) increased NREM sleep and reduced REM sleep, but had no significant effect on wakefulness. Horizontal axes indicate time after CNO administration. Data represent mean \pm SEM. $n = 8$ animals per group. * $P < 0.05$; ** $P < 0.005$; *** $P < 0.001$ [post-hoc Tukey honest significant difference (HSD) test; *: dTg + hM3Dq VS sTg + hM3Dq; †: dTg + hM3Dq VS dTg + GFP].

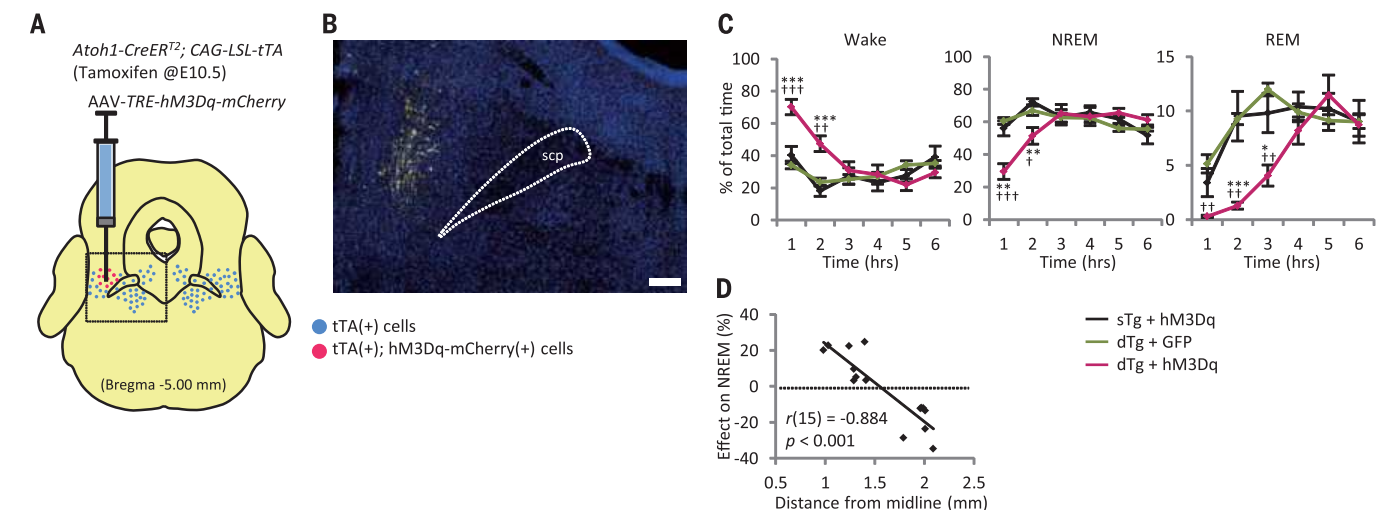


Fig. 2. *Atoh1*-E10.5-lateral cells regulate sleep/wake ratio. (A) Injection of AAV carrying tTA-dependent *hM3Dq*-mCherry dorsolateral to the scp, within the LPB. (B) hM3Dq-mCherry expression (yellow) in a region corresponding to the enclosed area in (A). Counterstain: DAPI (blue). Scale bar, 200 μ m. (C) Chemogenetic activation of neurons in (B) increased awake state and reduced NREM sleep and REM sleep. Horizontal axes indicate time after CNO administration. Data represent mean \pm SEM. $n = 7$ animals per group. *, † $P <$

0.05; ** $P < 0.005$; *** $P < 0.001$ (post-hoc Tukey HSD test; *: dTg + hM3Dq VS sTg + hM3Dq, †: dTg + hM3Dq VS dTg + GFP). (D) Correlation between location of hM3Dq-expressing cell medial boundary and effect on NREM sleep. Each symbol represents an individual mouse (dTg + hM3Dq), and the vertical axis indicates NREM sleep amount at 2 hours after CNO administration relative to that after saline administration. Pearson correlation coefficient r and level of significance p in two-tailed test are indicated.

mainly by increasing REM sleep episode numbers (Fig. 3G and fig. S8, H, J, and L). Similar results were observed in a transgenic mouse strain carrying *Vgat-Cre* (*Vgat-Cre* Tg) (23) (fig. S8, B, D, F, I, K, and M). Thus, dDpMe inhibitory neurons negatively regulate REM sleep, possibly by inhibiting REM-promoting neurons in the SLD. *Atoh1*-E10.5-medial cells might help to regulate REM/NREM sleep switching by activating these neurons. dDpMe neurons fire maximally during REM sleep, increasing their firing rate toward the end of REM sleep episodes (19). Thus, it might be that, during REM sleep, a gradual increase in dDpMe neuron firing promotes the exit from REM sleep, whereas basal activity during NREM sleep regulates entry into REM sleep, although further studies with cell-type specificity are required.

REM sleep is homeostatically regulated, and REM sleep deprivation (REMD) leads to a subsequent rebound (24). We examined the effect of 6-hours REMD from ZT 0 to ZT 6 on REM sleep inhibition caused by activating dDpMe inhibitory neurons (fig. S9). During REMD, REM sleep amount was reduced from ~6 to ~7% to less than 0.8% (fig. S9, B to D), and the number of entries into REM sleep gradually increased (fig. S9E), suggesting an increased REM sleep pressure. Even under increased REM sleep pressure following REMD, dDpMe inhibitory neurons strongly suppressed REM sleep (fig. S9, F and G). Thus, negative regulation of these neurons might underlie the homeostatic REM sleep rebound, or artificial activation of these neurons might erase (or override) the preceding history of REM sleep loss.

The function of REM sleep is poorly understood. Longer REM sleep episodes are associated with longer subsequent NREM sleep episodes, suggesting that REM sleep contributes to NREM sleep expression (25). We assessed this hypothesis using our transgenic systems to manipulate REM sleep. We first examined whether REM sleep enhances slow-wave activity (SWA) during subsequent NREM sleep, as higher SWA is associated with longer NREM sleep episodes. SWA, typically quantified as the spectral power of EEG in the delta range (0.5 to 4 Hz), reflects synchronized oscillations of cortical membrane potential and is most prominent during deep NREM sleep. Moreover, SWA contributes to synaptic plasticity and memory consolidation (26, 27). We analyzed the correlation between naturally occurring REM sleep episode duration and delta power in the subsequent NREM sleep. Absolute delta power was not compared because it is highly variable, even within the same individual (28). Therefore, the mean delta power of the subsequent NREM sleep episode (NREM_b) was calculated relative to the previous NREM sleep episode (NREM_a; fig. S10A; see supplementary methods for details), which revealed a significant positive correlation (fig. S10B). A previous study in humans did not reveal a significant correlation (29). This might be because absolute delta power was used for the previous analyses, which did not show a significant correlation in our study either, although a difference between the two animal species is also possible.

To determine whether REM sleep occurrence led to enhanced SWA during NREM sleep, we

manipulated REM sleep by chemogenetically activating or inhibiting the identified sleep regulatory circuit. First, REM sleep was transiently reduced by DREADD activation of either *Atoh1*-E10.5 medial cells or dDpMe inhibitory neurons. During reduced REM sleep, the NREM sleep delta power gradually decreased (Fig. 4, A and B). SWA seemed to recover immediately after REM sleep recovery (Fig. 4B and fig. S11). We defined three classes of REM sleep episodes: natural REM, shortened REM, and post-DREADD REM (fig. S12; see supplementary materials for details). We compared the EEG spectra of these episodes as well as the NREM, transitory, or awake episodes surrounding them (fig. S13). Shortened REM was associated with a slight increase in the delta range power (fig. S13A). By contrast, NREM sleep episodes around shortened REM initially appeared unaffected, whereas delta power was reduced after prolonged REM sleep inhibition (fig. S13C). The reduction in delta power recovered in the NREM episode immediately after post-DREADD REM (fig. S13C).

Next, in each class of REM sleep, we compared the mean normalized delta power between NREM_a and NREM_b. SWA in NREM_b after shortened REM was reduced compared to NREM_a, whereas SWA in NREM_b after post-DREADD REM was increased (Fig. 4, C to E). In addition, DREADD inhibition of dDpMe inhibitory neurons occasionally evoked long REM sleep episodes of at least 4 min, which were not observed under other conditions, although the mean REM sleep episode duration was not significantly changed (fig. S8, L and M). These REM sleep episodes, which we termed “prolonged REM,”

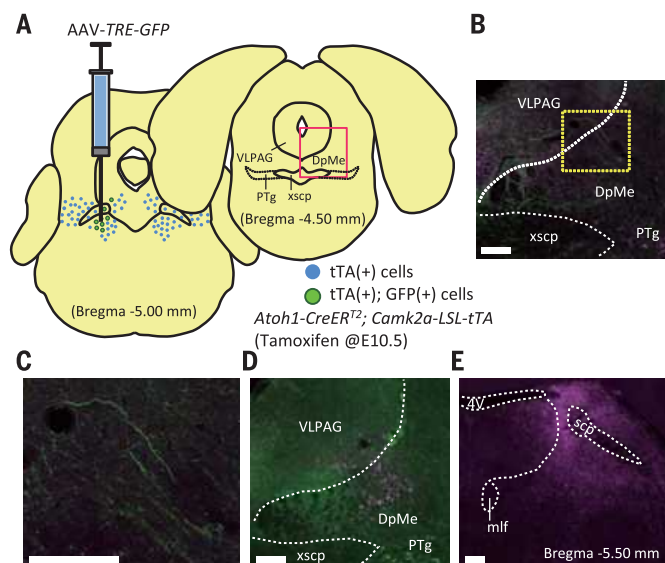
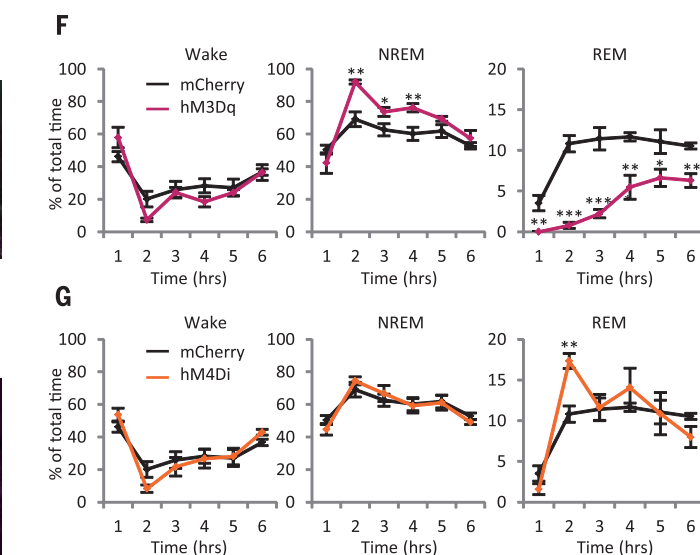


Fig. 3. Inhibitory neurons in dDpMe inhibit REM sleep. (A) Injection of AAV carrying tTA-dependent GFP into an area ventromedial to the scp (same area as in Fig. 1A). xscp, decussation of the superior cerebellar peduncle. (B) GFP (green)-positive axons were detected in a region rostral and contralateral to the AAV injection site, corresponding to the enclosed area in (A). Counterstain: ChAT (magenta). (C) Higher magnification of the area enclosed in (B). GFP-positive axon varicosities were detected. (D) AAV carrying Cre-dependent hM4Di-mCherry (magenta) was injected into dDpMe of *Vgat-Cre*



KL mice. Counterstain: ChAT (green). (E) hM4Di-mCherry (magenta)-positive axon varicosities were detected in a wide area in the dorso-caudal region of the pontine tegmentum. 4V, fourth ventricle. mlf, medial longitudinal fasciculus. (F and G) Chemogenetic activation (F) or inhibition (G) of dDpMe inhibitory neurons reduced or increased REM sleep, respectively. Horizontal axes indicate time after CNO administration. Data represent mean \pm SEM. $n = 6$ animals per group. * $P < 0.05$, ** $P < 0.005$, *** $P < 0.001$ [one-way analysis of variance (ANOVA)]. Scale bars, 200 μ m.

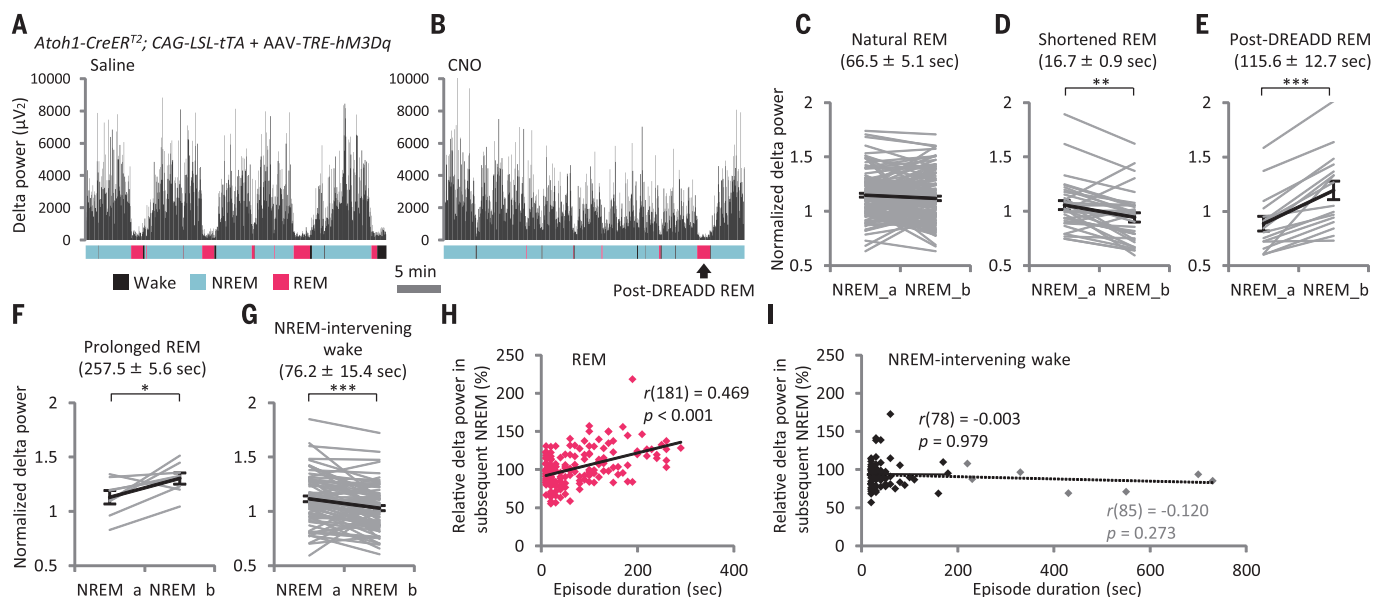


Fig. 4. REM sleep inhibition or extension affects SWA in subsequent NREM sleep. (A and B) Examples of delta power change after administering saline (A) or CNO (B) to a mouse expressing hm3Dq in REM sleep-inhibiting neurons. (C to G) Comparison of mean relative delta power in NREM sleep episodes before (NREM_a) and immediately after (NREM_b) the indicated REM sleep or awake episode. “Shortened REM” refers to REM sleep episodes less than 50% the mean duration that appeared after CNO administration. “Post-DREADD REM” refers to the first REM sleep episode after “shortened REM.” “Natural REM” refers to REM sleep episodes in mice transfected with

control AAV and administered CNO. See supplementary materials and fig. S12 for details. Numbers in parentheses indicate mean episode duration \pm SEM. Gray lines represent pairs of NREM sleep episodes. Black lines represent mean \pm SEM. * $P < 0.05$, ** $P < 0.005$, *** $P < 0.001$ (within-within-subjects ANOVA). (H and I) Correlation between NREM_b to NREM_a ratio and duration of intervening REM sleep (H) or intervening awake (I) episode. Pearson correlation coefficient r and level of significance p in two-tailed test are indicated. Statistical outliers and analyses including the outliers are indicated in gray.

were followed by NREM_b with increased SWA (Fig. 4F). Our results are somewhat consistent with a study in humans showing that SWA during NREM sleep is gradually reduced during selective REM sleep deprivation and returns to the initial level after REM sleep recovery (30), although we cannot completely exclude the involvement of a third factor evoked by the DREADD manipulation (e.g. hormone levels, neurotransmitters, etc.).

During the late light phase, when all SWA data were collected, NREM sleep episodes were occasionally interrupted by short awake episodes. These NREM-intervening awake episodes were followed by NREM_b with significantly reduced delta power (Fig. 4G). Thus, in contrast to the well-known SWA-enhancing effect of long awake periods lasting several hours (31), the NREM-intervening episodes observed here, which did not exceed ~13 min, did not increase SWA. We plotted the relative delta power of NREM_b against the episode duration of REM sleep episodes or NREM-intervening awake episodes (Fig. 4, H and I). Although delta power was significantly and positively correlated with REM sleep episode duration, no obvious correlation with NREM-intervening wakefulness was observed. Similar results were obtained when we separately plotted results from mice harboring *Atoh1-CreER^{T2}* or *Vgat-Cre* (fig. S14). A unique cortical activity or neuromodulator release mode during REM sleep might underlie the strong enhancement of SWA during ensuing NREM sleep. As

SWA is most intense in the first NREM sleep cycle in humans, and sleep deprivation also enhances subsequent SWA, homeostatic NREM sleep pressure accumulating during the awake state is likely the major factor responsible for SWA enhancement. Our findings therefore suggest another role for REM sleep. Finally, our transgenic system for REM sleep inhibition might also be effective for testing other proposed REM sleep functions, including brain development (32) and memory processing.

Our developmental cell fate mapping approach allowed us to identify a single genetically marked cell population that contributes to two distinct aspects of sleep regulation: neurons that promote NREM sleep at the expense of REM sleep, and neurons that promote wakefulness at the expense of sleep. The awake and NREM sleep states differ in terms of the level of consciousness, but share other features such as the presence of muscle tone and integrated thermoregulatory responses or respiration. Direct transitions from wakefulness to REM sleep do not occur in healthy states. Thus, REM sleep-promoting neurons are likely strongly inhibited during wakefulness. Both *Atoh1-E10.5*-medial and -lateral cells might share a common feature to inhibit the REM-promoting system, although cortical activating functions in lateral cells might be substituted for by a cortical synchronizing function in the medial cells. During evolution, REM and NREM sleep stages might have emerged from the modification of a subset of cells regulating sleep/wake cycles. The abundance

of REM sleep in neonates (32) and the confinement of increased SWA during NREM sleep in birds and mammals suggest that REM sleep closely resembles prototype sleep in ancestral animals. Further investigations into the function of *Atoh1-E10.5* cell equivalents in animals lacking obvious REM and NREM sleep, such as reptiles, might be meaningful toward understanding the evolution of mammalian sleep to its current complex state. In summary, our cell lineage-tracing approach, in combination with chemogenetic tools, will be useful for further investigation into the evolutionary origin and function of sleep, and other circuits controlling complex behaviors.

REFERENCES AND NOTES

- G. Vanni-Mercier, K. Sakai, J. S. Lin, M. Jouvet, *Arch. Ital. Biol.* **127**, 133–164 (1989).
- K. Sakai, S. Crochet, H. Onoe, *Arch. Ital. Biol.* **139**, 93–107 (2001).
- R. Boissard et al., *Eur. J. Neurosci.* **16**, 1959–1973 (2002).
- J. Lu, D. Sherman, M. Devor, C. B. Saper, *Nature* **441**, 589–594 (2006).
- P. H. Luppi et al., *Pflügers Arch.* **463**, 43–52 (2012).
- M. Krenzer et al., *PLOS ONE* **6**, e24998 (2011).
- J. Alder, N. K. Cho, M. E. Hatten, *Neuron* **17**, 389–399 (1996).
- R. Machold, G. Fishell, *Neuron* **48**, 17–24 (2005).
- V. Y. Wang, M. F. Rose, H. Y. Zoghbi, *Neuron* **48**, 31–43 (2005).
- M. J. Green et al., *Development* **141**, 389–398 (2014).
- A. W. Helms, A. L. Abney, N. Ben-Arie, H. Y. Zoghbi, J. E. Johnson, *Development* **127**, 1185–1196 (2000).
- Y. Kobayashi et al., *Front. Behav. Neurosci.* **7**, 17 (2013).

13. M. Zervas, S. Millet, S. Ahn, A. L. Joyner, *Neuron* **43**, 345–357 (2004).
14. B. N. Armbruster, X. Li, M. H. Pausch, S. Herlitze, B. L. Roth, *Proc. Natl. Acad. Sci. U.S.A.* **104**, 5163–5168 (2007).
15. K. Miyamichi et al., *Nature* **472**, 191–196 (2011).
16. V. V. Vyazovskiy, P. Achermann, A. A. Borbély, I. Tobler, *Arch. Ital. Biol.* **142**, 511–523 (2004).
17. T. Nakashiba, J. Z. Young, T. J. McHugh, D. L. Buhl, S. Tonegawa, *Science* **319**, 1260–1264 (2008).
18. S. Kaur et al., *J. Neurosci.* **33**, 7627–7640 (2013).
19. S. Crochet, H. Onoe, K. Sakai, *Eur. J. Neurosci.* **24**, 1404–1412 (2006).
20. E. Sapin et al., *PLOS ONE* **4**, e4272 (2009).
21. R. Boissard, P. Fort, D. Gervasoni, B. Barbagli, P. H. Luppi, *Eur. J. Neurosci.* **18**, 1627–1639 (2003).
22. L. Vong et al., *Neuron* **71**, 142–154 (2011).
23. I. Ogiwara et al., *Hum. Mol. Genet.* **22**, 4784–4804 (2013).
24. T. Endo, B. Schwierin, A. A. Borbély, I. Tobler, *Psychiatry Res.* **66**, 97–110 (1997).
25. J. H. Benington, H. C. Heller, *Prog. Neurobiol.* **44**, 433–449 (1994).
26. L. Marshall, H. Helgadóttir, M. Mölle, J. Born, *Nature* **444**, 610–613 (2006).
27. S. Chauvette, J. Seigneux, I. Timofeev, *Neuron* **75**, 1105–1113 (2012).
28. V. V. Vyazovskiy, B. A. Riedner, C. Cirelli, G. Tononi, *Sleep* **30**, 1631–1642 (2007).
29. O. Le Bon, P. Linkowski, *J. Neurophysiol.* **110**, 162–169 (2013).
30. D. G. Beersma, D. J. Dijk, C. G. Blok, I. Everhardus, *Electroencephalogr. Clin. Neurophysiol.* **76**, 114–122 (1990).
31. A. Suzuki, C. M. Sinton, R. W. Greene, M. Yanagisawa, *Proc. Natl. Acad. Sci. U.S.A.* **110**, 10288–10293 (2013).
32. H. P. Roffwarg, J. N. Muzio, W. C. Dement, *Science* **152**, 604–619 (1966).

ACKNOWLEDGMENTS

We thank M. Yanagisawa for support of experiments and critical reading of the manuscript; H. Hirase, Y. Koyama, and M. Matsumata for technical advice; C. Yokoyama and S. Tonegawa for comments on the manuscript; L. Luo, S. Tonegawa, T. Kaneko, B. Roth, C. Cepko, and K. Deisseroth for providing reagents; and all members of the Itohara laboratory and Hayashi laboratory for their support and discussion. CAG-LSL-tTA and Camk2-LSL-tTA mice were provided under a materials transfer agreement with Stanford University and the Massachusetts Institute of Technology, respectively. This work was supported by the Japan Science and Technology Agency PRESTO program; the Ministry of Education, Culture, Sports, Science, and Technology of Japan (MEXT) World Premier International Research Center Initiative (WPI); the MEXT KAKENHI for Scientific Research on Innovative Areas “Systems Molecular Ethology” (23115724) and “Memory Dynamism” (26115503); the Japan Society for the Promotion of Science KAKENHI grant nos. 23700403 and 21800090; the Mochida Memorial Foundation for Medical and Pharmaceutical Research; the Astellas Foundation for Research on Metabolic Disorders; the Sumitomo Foundation Grant for Basic Science Research Projects; the SENSHIN Medical Research Foundation; the Japan Foundation for Applied Enzymology (TMFC), and the RIKEN Special Postdoctoral Researcher Program (to Y.H.); and the Funding Program for World-Leading Innovative R&D on Science and Technology (FIRST Program) initiated by the Council for Science and Technology Policy (CSTP) and the RIKEN intramural fund (to S.I.). All data are stored in the International Institute for Integrative Sleep Medicine, University of Tsukuba and the Brain Science Institute, RIKEN.

SUPPLEMENTARY MATERIALS

www.sciencemag.org/content/350/6263/957/suppl/DC1
Materials and Methods
Supplementary Text
Figs. S1 to S14
Reference (33)
Data file S1

27 July 2015; accepted 7 October 2015
Published online 22 October 2015
10.1126/science.1251023

AXON GUIDANCE

Operational redundancy in axon guidance through the multifunctional receptor Robo3 and its ligand NELL2

Alexander Jaworski,^{1,2,3*} Irene Tom,⁴ Raymond K. Tong,⁴ Holly K. Gildea,³ Alexander W. Koch,^{4†} Lino C. Gonzalez,⁴ Marc Tessier-Lavigne^{1,2*}

Axon pathfinding is orchestrated by numerous guidance cues, including Slits and their Robo receptors, but it remains unclear how information from multiple cues is integrated or filtered. Robo3, a Robo family member, allows commissural axons to reach and cross the spinal cord midline by antagonizing Robo1/2–mediated repulsion from midline-expressed Slits and potentiating deleted in colorectal cancer (DCC)–mediated midline attraction to Netrin-1, but without binding either Slits or Netrins. We identified a secreted Robo3 ligand, neural epidermal growth factor-like-like 2 (NELL2), which repels mouse commissural axons through Robo3 and helps steer them to the midline. These findings identify NELL2 as an axon guidance cue and establish Robo3 as a multifunctional regulator of pathfinding that simultaneously mediates NELL2 repulsion, inhibits Slit repulsion, and facilitates Netrin attraction to achieve a common guidance purpose.

Nervous system development requires that axons of neurons navigate to their correct targets. Pathfinding is directed by molecular cues sensed by receptors in the axonal growth cone (1). We studied axon guidance in the mouse spinal cord. Commissural neurons in dorsal spinal cord send axons across the floor plate at the ventral midline in response to multiple cues (2). Netrin-1 and other signals expressed by floor plate attract these axons (3). After midline crossing, floor plate–derived repellants, including Slit proteins, expel them and prevent recrossing (4, 5). Commissural axons are insensitive to the repellants before crossing and insensitive to the attractants after crossing, indicating a switch in cue responsiveness (5, 6).

Slits signal through Robo family receptors. All three *Slit* genes are expressed by the floor plate, and commissural neurons express *Robo1*, *Robo2*, and *Robo3* (7). Slits bind Robo1 and Robo2 with high affinity to mediate midline repulsion in post-crossing axons (4, 5, 8, 9), but Robo3 does not bind Slit proteins (10–13). Robo3 exists in two splice isoforms with different intracellular domains: Robo3.1 is expressed on precrossing commissural axons and allows midline crossing by inhibiting Slit repulsion, whereas Robo3.2 is expressed postcrossing and prevents midline recrossing (12, 14). In mice lacking *Robo3*, all commissural axons fail to cross the midline and instead project through the ipsilateral ventral horn (12). Midline crossing is partially, but incompletely,

rescued in mice lacking *Robo1*, *Robo2*, and *Robo3* (8). Thus, Robo3 allows midline crossing partly by inhibiting Slit signaling through Robo1/2, but also through additional mechanisms. Indeed, Robo3 potentiates attraction by Netrin-1, mediated by the Netrin receptor DCC (13). However, Robo3 binds neither Netrin-1 nor Slits directly, suggesting that a Robo3 ligand might further contribute to midline guidance.

We screened an extracellular protein microarray (15, 16) with the Robo3 ectodomain fused to Fc (Robo3-ECD-Fc) and found that a fusion of NELL2 and Fc (NELL2-Fc) binds Robo3-ECD-Fc (fig. S1A). NELL2 is a secreted glycoprotein containing a laminin G-like domain, six epidermal growth factor (EGF)–like domains, and five von Willebrand factor (vWF) C domains (Fig. 1C) and is a human ortholog of chick Nel (neural EGF-like) (17, 18). Nel can inhibit retinal ganglion cell axon growth and induce growth cone collapse (19). We confirmed the interaction between NELL2 and Robo3 by means of surface plasmon resonance (SPR) (Fig. 1A). Robo3-ECD-Fc also binds human embryonic kidney (HEK) 293T cells expressing a NELL2-enhanced green fluorescent protein (EGFP) fusion construct tethered to cell surfaces by a glycosylphosphatidylinositol (GPI) anchor (NELL2-EGFP-GPI) in a flow cytometry assay (FACS) (fig. S1, F to J) with high affinity [median effective concentration (EC₅₀) of 10.9 ± 1.6 nM] (Fig. 1B). To determine whether NELL2 binds Robo3 expressed on cells, we transfected COS-7 cells with expression constructs for Robo3.1, Robo3.2, and as controls, DCC, Robo1, or Robo2 and tested for binding of alkaline phosphatase (AP) fusions of Netrin-1, Slit2 N-terminal fragment (Slit2-N), or NELL2. NELL2-AP binds cells that express Robo3.1 or Robo3.2 but not any of the other axon guidance receptors (Fig. 1E and fig. S1B); binding of Netrin-1-AP to DCC and of Slit2-N-AP to both Robo1 and Robo2 confirmed that

¹Division of Research, Genentech, South San Francisco, CA 94080, USA. ²Laboratory of Brain Development and Repair, The Rockefeller University, New York, NY 10065, USA.

³Department of Neuroscience, Brown University, Providence, RI 02912, USA. ⁴Department of Protein Chemistry, Genentech, South San Francisco, CA 94080, USA.

*Corresponding author. E-mail: alexander.jaworski@brown.edu (A.J.); marcl@rockefeller.edu (M.T.-L.) †Present address: Cardiovascular and Metabolic Diseases, Novartis Institutes for Biomedical Research, Cambridge, MA 02139, USA.

these receptors are expressed on the cell surface. Robo3.1 does not bind either Netrin-1 or Slit2-N (fig. S1, B and C) (10–13). Thus, Robo3 and NELL2 bind to each other specifically and with high affinity.

We next delineated which regions of Robo3 and NELL2 mediate their interaction. NELL2¹⁻⁶³⁸-AP, which lacks the C-terminal vWF domains, binds to Robo3.1-expressing cells, whereas NELL2¹⁻³⁹⁷-AP, which also lacks the six EGF-like domains, does not (Fig. 1, C and E). Furthermore, NELL2³⁹⁷⁻⁶³⁸-AP, which only contains the EGF-like domains, binds to Robo3.1-expressing cells (Fig. 1, C and E). We also found that NELL2-AP binds to COS-7 cells that express Robo3.1^{delta(73-535)}, which lacks its five N-terminal immunoglobulin (Ig)-like domains (Fig. 1, D and F), and that in an SPR assay, NELL2-Fc fails to bind Robo3-Ig-Fc, which only contains the Ig-like domains of Robo3 (fig. S1D) but does bind Robo3-FNIII-FLAG, which only contains the three fibronectin type III (FNIII) domains of Robo3 (fig. S1E). As shown with FACS, Robo3-FNIII-Fc binds NELL2-EGFP-GPI-expressing cells (fig. S1K). Thus, the NELL2 EGF-like domains mediate binding to the Robo3 FNIII domains.

Because Robo3 is expressed by commissural neurons (12), we studied NELL2-AP binding to

these neurons in vitro. NELL2-AP binds to commissural axons from Robo3 heterozygous embryos but less to axons from Robo3-null embryos (relative axonal binding, $100.0 \pm 8.4\%$ for Robo3^{+/+}, $26.4 \pm 4.0\%$ for Robo3^{-/-}; $P = 0.0044$, $n = 3$ embryos each) (Fig. 1G). Thus, Robo3 is a NELL2 receptor on commissural axons.

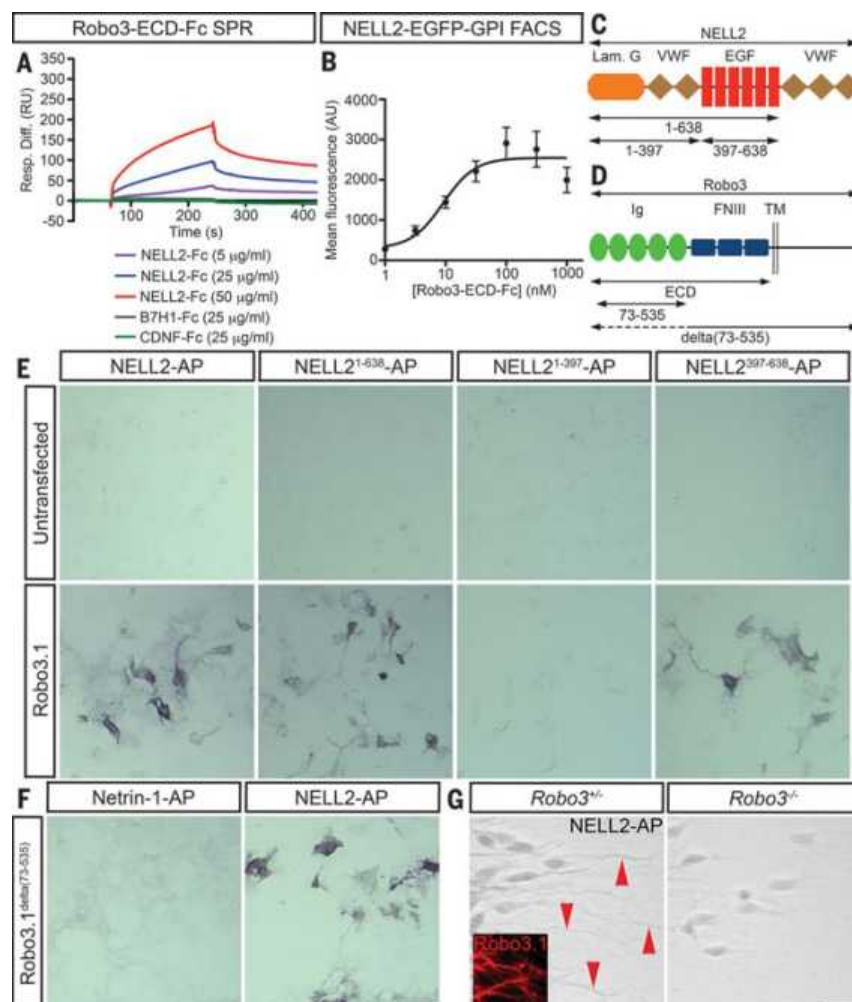
We also tested binding of the NELL2 relative NELL1 (18) to Robo3. NELL1-AP binds to COS-7 cells that express Robo3.1 (fig. S1L), and Robo3-FNIII-AP binds to cells that express either NELL1 or NELL2 (fig. S1M). Thus, Robo3 can bind both NELL1 and NELL2 through its FNIII domains.

We next examined NELL1 and NELL2 expression in spinal cord at the time of commissural axon growth to the midline [embryonic day (E) 9.5 to E12.5] by means of in situ hybridization. At E9.5, NELL2 is expressed in the presumptive motor column in the ventral horn (Fig. 2A). At E10.5, additional sites of expression include dorsal root ganglia, the dorsal mantle layer of the spinal cord, and a triangular population of cells close to the ventricle (Fig. 2B). We stained adjacent E10.5 spinal cord sections with antibodies against Robo3.1 and L1 to label pre- and postcrossing commissural axons, respectively (Fig. 2C). Pre-crossing axons project along the lateral edge of a

NELL2-free corridor between NELL2-expressing cells in the ventral horn and the ventricular zone (Fig. 2D). NELL2 expression in cells forming this ventral corridor persists at E11.5 (Fig. 2E) and E12.5 (Fig. 2F). We stained adjacent E12.5 sections with an antibody against HB9 to label motor neurons (Fig. 2G) and found that sites of highest NELL2 expression in the ventral horn represent motor neurons (Fig. 2H). In situ hybridization for NELL1 mRNA did not produce detectable signal in E9.5–E12.5 spinal cord sections (fig. S2). Thus, NELL2 is the predominant NELL family member expressed in mouse spinal cord during commissural axon guidance, and areas of NELL2 expression demarcate regions that these axons avoid en route to the midline.

The interaction of NELL2 with Robo3 and its expression during commissural axon growth to the midline suggest that NELL2 might regulate commissural axon guidance. We tested this idea by exposing commissural axons to NELL2 in vitro. Dorsal spinal cord explants from E11.5 mouse embryos were cultured with Netrin-1, which promotes radially symmetric growth of commissural axon fascicles (20). When confronted with aggregates of COS-7 cells that express either NELL2 and red fluorescent protein (RFP) or RFP

Fig. 1. NELL2 binds Robo3. (A) NELL2-Robo3 binding was studied by means of SPR. SPR sensorgrams show binding response of NELL2 or negative controls at indicated concentrations to immobilized Robo3-ECD-Fc. (B) NELL2-Robo3 binding was studied by means of FACS. The binding curve shows that EC₅₀ binding occurs at a Robo3-ECD concentration of 10.9 ± 1.6 nM. (C and D) Schematics of the (C) NELL2 and (D) Robo3 domain structures. (E) NELL2 domains mediating Robo3 binding were mapped by using a COS-7-based binding assay. NELL2¹⁻⁶³⁸-AP and NELL2³⁹⁷⁻⁶³⁸-AP specifically bind Robo3.1-expressing cells, but NELL2¹⁻³⁹⁷-AP does not. TM, transmembrane domain. (F) COS-7-based Robo3 domain mapping. Cells expressing Robo3.1^{delta(73-535)} specifically bind NELL2-AP, but not Netrin-1-AP. (G) NELL2-AP binding was studied on commissural neuron explants from E11.5 Robo3^{+/+} and Robo3^{-/-} embryos (grayscale). NELL2-AP binds cell bodies and axons (arrowheads) of Robo3^{+/+} commissural neurons [which express Robo3.1 (inset)], but not Robo3^{-/-} axons. Scale bars, (E) and (F) 100 μ m; (G) 20 μ m; inset, 40 μ m. Error bars indicate SEM.



alone (Fig. 3, A and B, and fig. S3, A, D, and E), commissural axons grow away from NELL2-expressing cells (Fig. 3B) but not control cells

(Fig. 3A), an effect that is statistically significant (Fig. 3E and fig. S3F). Overall axon growth is similar with NELL2-expressing and control cells (nor-

malized total axon length, $100 \pm 11.9\%$ for control, $103 \pm 13.8\%$ for NELL2; $P = 0.7022$, $n = 5$ experiments). Growing axons also turn away from

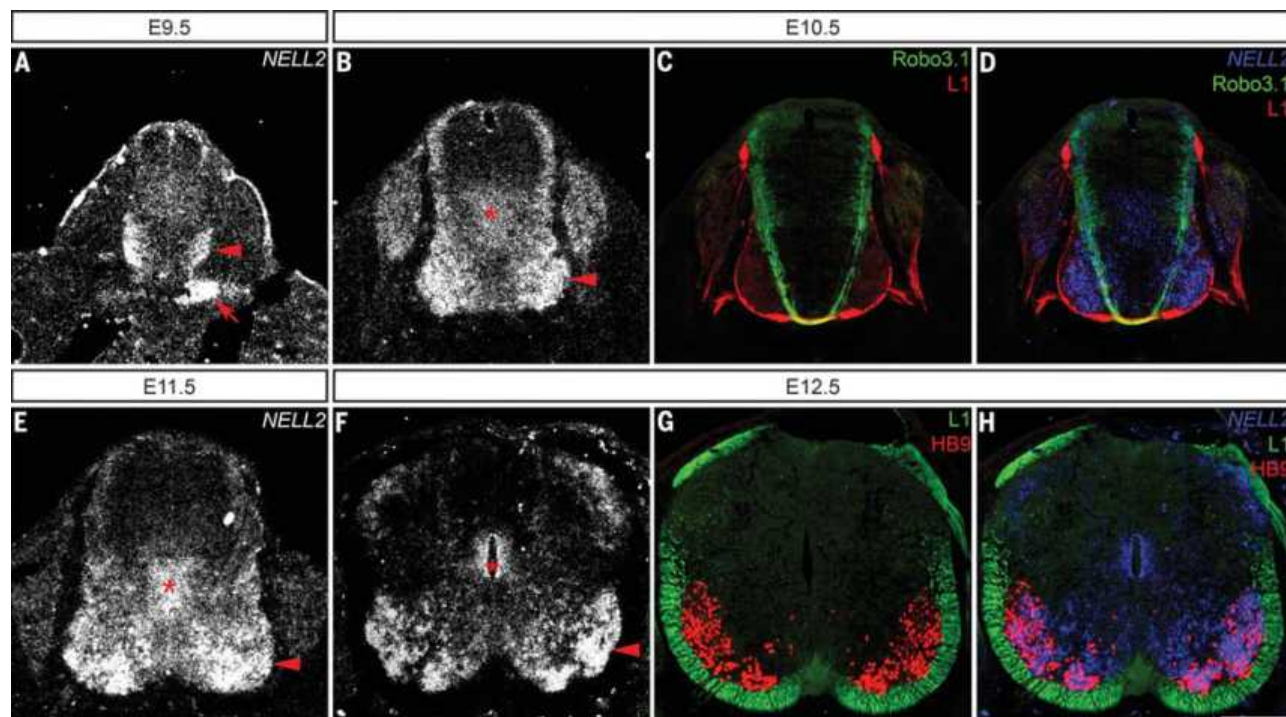


Fig. 2. NELL2 is expressed in the developing spinal cord. (A, B, E, and F) Transverse spinal cord sections from (A) E9.5, (B) E10.5, (E) E11.5, and (F) E12.5 mouse embryos were used for radioactive in situ hybridization to detect NELL2 mRNA. NELL2 exhibits strong expression in the developing motor column (arrowheads) at all ages examined [the arrow in (A) indicates a labeling artifact from folding of the tissue section]. From E10.5 through E12.5, NELL2 is also expressed in cells surrounding the central canal (asterisk). (C and D) Labeling

of E10.5 brachial spinal cord sections with (C) Robo3.1 and L1 antibodies was combined with (D) NELL2 in situ hybridization on adjacent sections. Robo3.1-positive commissural axons do not project through areas of high NELL2 expression. (G and H) Labeling of E12.5 brachial spinal cord sections with (G) L1 and HB9 antibodies was combined with (H) NELL2 in situ hybridization on adjacent sections. In the ventral horn, areas of high NELL2 expression correspond to the positions of HB9-positive motor neurons. Scale bar, 200 μ m.

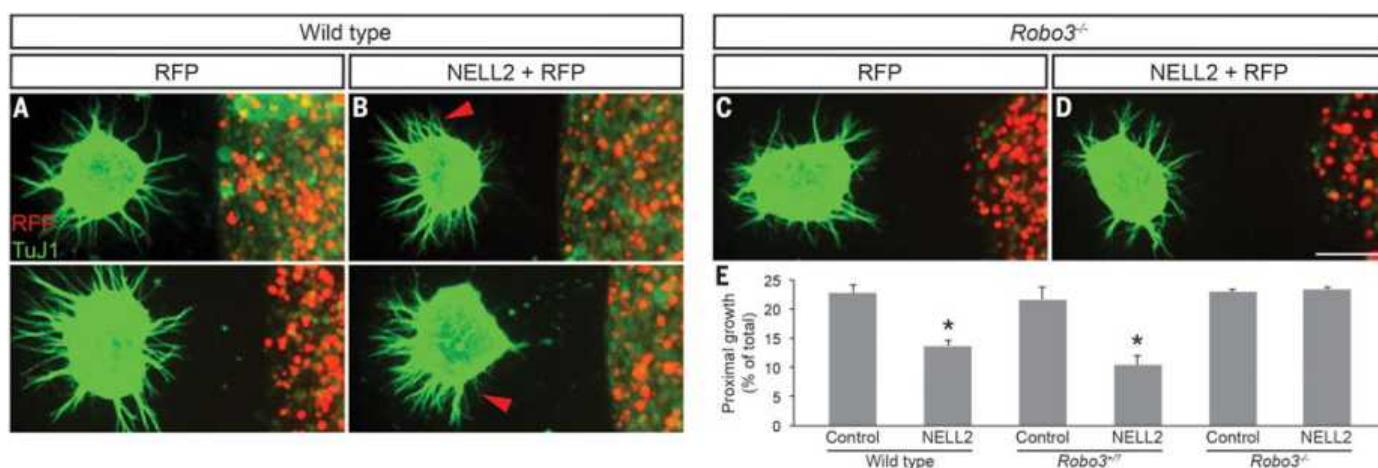


Fig. 3. NELL2 repels precrossing commissural axons through Robo3. (A and B) Wild-type E11.5 mouse dorsal spinal cord explants were cocultured with COS-7 cells that express (A) RFP or (B) RFP and NELL2 and stained for class III β -tubulin (TuJ1) to visualize axons (two examples each). NELL2 expression causes axon turning (arrowheads) away from cell aggregates. (E) Commissural axon growth in the proximal quadrant relative to COS-7 aggregates was quantified. Proximal growth is significantly lower with NELL2-expressing cells than with con-

trol cells ($P = 0.0009$). In (C) to (E), dorsal spinal cord explants from E11.5 Robo3 mutant embryos were cocultured with COS-7 cells that express (C) RFP or (D) RFP and NELL2 and labeled with an antibody to TuJ1, and (E) axon growth relative to COS-7 cells was quantified. Proximal growth relative to NELL2-expressing cells is significantly higher in Robo3^{-/-} explants ($n = 3$ independent experiments) than in explants from control (Robo3^{+/-} and wild-type) littermates ($P = 0.0123$, $n = 3$ independent experiments). Scale bar, 200 μ m. Error bars indicate SEM.

NELL2-expressing cells (ratio of axons turning toward versus away, 0.928 ± 0.046 for control, 0.505 ± 0.012 for *NELL2*; $P = 0.001$, $n = 5$ experiments; quantification method is provided in the supplementary materials) (Fig. 3C). With COS-7 cells that express *NELL1* (fig. S3, B and C), we found no statistically significant effect on commissural axon repulsion (fig. S3, G to I). Thus, *NELL2* repels commissural axons in vitro, but *NELL1* does not.

We next examined whether *Robo3* is required for *NELL2*-mediated repulsion. When dorsal spinal cord explants from *Robo3* heterozygous and wild-type embryos were cocultured with cells that express RFP or both *NELL2* and RFP, we observed repulsion of commissural axons from *NELL2*-expressing but not control cells (Fig. 3E). However, commissural axons from *Robo3* mutant explants are not significantly repelled by either control (Fig. 3, C and E) or *NELL2*-expressing cells (Fig. 3, D and E), indicating that *Robo3* is required for *NELL2*-mediated axon repulsion.

To determine whether *Robo1* and *Robo2* are recruited by *Robo3* to mediate *NELL2* repulsion, we studied the response of commissural axons from *Robo1*^{-/-}; *Robo2*^{-/-} embryos and wild-type littermates to *NELL2*. *Robo1* and *Robo2* are not required for *NELL2* repulsion (fig. S3J), arguing against cross-talk between *Robo3* and *Robo1/2* in this pathway.

The switch in *Robo3* isoforms upon midline crossing (14) might affect the response of commissural axons to *NELL2*. We used a postcrossing explant assay (5) to study the response of axons that have crossed the floor plate (fig. S3K). In

postcrossing explants cocultured with control cells (fig. S3L) or *NELL2*-expressing cells (fig. S3M), axonal growth is comparable (fig. S3N). Thus, precrossing commissural axons, which express *Robo3.1*, are repelled by *NELL2*, but postcrossing axons, which express *Robo3.2*, are not, even though both isoforms bind *NELL2*.

To assess the in vivo function of *NELL2*, we generated mice deficient in *NELL2* (fig. S4A). The abundance of *NELL2* mRNA is dramatically reduced in the mutant, as determined with quantitative reverse transcription polymerase chain reaction (RT-PCR) (fig. S4B) and in situ hybridization (fig. S4, C and D), suggesting that the mutant *NELL2* transcript is subject to nonsense-mediated mRNA decay and that the allele is null or near null.

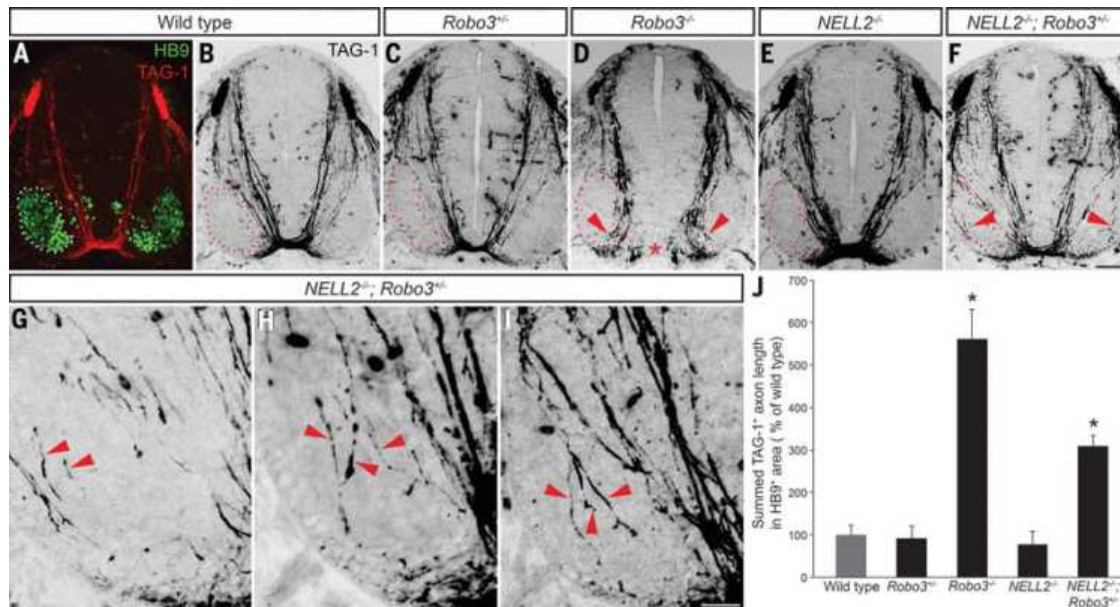
On the basis of the expression of *NELL2* by motor neurons and its *Robo3*-dependent repulsive activity for commissural axons, we reasoned that invasion of the motor column in *Robo3* mutant mice (12) might be caused not just by reduced midline Netrin attraction and increased midline Slit repulsion—the two known effects of loss of *Robo3*—but also at least partly by loss of *NELL2*-mediated repulsion. To compare the *Robo3*^{-/-} phenotype to a possible *NELL2*^{-/-} phenotype, we first quantified commissural axon invasion of the ventral horn in *Robo3* mutants. We stained spinal cord sections for transient axonal glycoprotein-1 (TAG-1) and HB9 to label precrossing commissural axons and motor neurons, respectively. In wild-type (Fig. 4, A and B) and *Robo3* heterozygous animals (Fig. 4C and fig. S4E), the majority of commissural axons avoid the region occupied by motor neurons, whereas in *Robo3*^{-/-} embryos, many more project

through the ventral-most portion of the motor column (Fig. 4D and fig. S4F). Invasion of the motor column in *Robo3* mutants was about sixfold greater than in wild-type or *Robo3*^{+/-} mice (Fig. 4J).

We did not observe an increase in axon growth through the motor column in *NELL2*^{-/-} (Fig. 4, E and J, and fig. S4G) or *NELL1*^{-/-}; *NELL2*^{-/-} mice (fig. S4, I to K). However, because *Robo3*-dependent mechanisms, including Slit silencing and Netrin potentiation, might be sufficient to promote guidance to the midline and avoidance of the motor column even in absence of *NELL2*, we generated mice that lacked not only both copies of *NELL2* but also one copy of *Robo3* and analyzed motor column invasion in this genetically sensitized background. In *NELL2*^{-/-}; *Robo3*^{+/-} embryos, there is a significant (approximately threefold) increase in commissural axon growth through the motor column (Fig. 4, F to J, and fig. S4H), an effect confirmed by using *Robo3* itself as marker for these axons (fig. S4, L and M). Thus, in collaboration with other cues, *NELL2* helps prevent commissural axons from entering the motor column, supporting a role for *NELL2* as a repulsive guidance cue in vivo. The function of the low level of *NELL2* expression in E10.5 dorsal spinal cord (Fig. 2B) remains to be determined.

Our results identify *NELL2* as a repulsive guidance cue that contributes to commissural axon guidance to the midline. *NELL2* acts directly through *Robo3*, which also serves indirectly as both a negative regulator of Slit signaling (12) and a positive regulator of Netrin signaling (13). Commissural axons invade the domain normally defined by *NELL2* expression only in mice that completely

Fig. 4. Commissural axons aberrantly enter the spinal cord ventral horn in *NELL2*^{-/-}; *Robo3*^{+/-} mice. (A to I) Transverse E11.5 mouse spinal cord sections were stained for TAG-1 and HB9. Shown are (A) double stainings and [(B) to (I)] inverted grayscale images of TAG-1 alone. (G) to (I) show high magnifications of the left ventral horn. In [(A) and (B)] wild-type and (C) *Robo3*^{+/-} embryos, commissural axons project to the midline and avoid the ventral horn occupied by motor neurons (dotted outline). In (D) *Robo3*^{-/-} embryos, axons fail to cross the midline (asterisk) and project through the ventral horn (arrowheads). In (E) *NELL2*^{-/-} embryos, axons cross the midline and avoid the ventral horn. In [(F) to (I)] *NELL2*^{-/-}; *Robo3*^{+/-} embryos, numerous axons (arrowheads) invade the ventral horn. (G) is a higher-magnification view of a region of (F). (J) Ventral horn invasion was quantified and is significantly higher in *Robo3*^{-/-} embryos ($n = 5$ embryos), than in wild-type ($P < 0.0001$, $n = 10$ embryos), *Robo3*^{+/-} ($P < 0.0001$, $n = 3$ embryos),



and project through the ventral horn (arrowheads). In (E) *NELL2*^{-/-} embryos, axons cross the midline and avoid the ventral horn. In [(F) to (I)] *NELL2*^{-/-}; *Robo3*^{+/-} embryos, numerous axons (arrowheads) invade the ventral horn. (G) is a higher-magnification view of a region of (F). (J) Ventral horn invasion was quantified and is significantly higher in *Robo3*^{-/-} embryos ($n = 5$ embryos), than in wild-type ($P < 0.0001$, $n = 10$ embryos), *Robo3*^{+/-} ($P < 0.0001$, $n = 3$ embryos),

NELL2^{-/-} ($P < 0.0001$, $n = 4$ embryos), and *NELL2*^{-/-}; *Robo3*^{+/-} embryos ($P < 0.0001$, $n = 7$ embryos). Axon growth in the ventral horn of *NELL2*^{-/-}; *Robo3*^{+/-} embryos is significantly higher than in wild-type ($P < 0.0001$), *Robo3*^{+/-} ($P = 0.001$), and *NELL2*^{-/-} embryos ($P = 0.0002$). *Robo3*^{+/-} and *NELL2*^{-/-} embryos are indistinguishable from wild type ($P = 0.8837$ and $P = 0.6645$, respectively). Scale bars, (A) to (F) 100 μ m; (G) to (I) 30 μ m. Error bars indicate SEM.

lack NELL2 and are also partially deficient in the receptor Robo3 (while remaining excluded in mice that either lack NELL2 or partially lack Robo3 in isolation), implying that the NELL2 signaling pathway collaborates with others to ensure avoidance of the motor column. Our results also show that Robo3.1 serves as an integrative hub: Its three diverse actions in response to three different cues—mediating NELL2 repulsion from the motor column, potentiating midline Netrin-1 attraction, and antagonizing midline Slit repulsion—act simultaneously, are mutually reinforcing, and serve the common purpose of steering commissural axons toward and across the midline. This multiplicity of mechanisms likely helps ensure high-fidelity steering of axons to their targets.

REFERENCES AND NOTES

1. A. L. Kolodkin, M. Tessier-Lavigne, *Cold Spring Harb. Perspect. Biol.* **3**, a001727 (2011).
2. B. J. Dickson, Y. Zou, *Cold Spring Harb. Perspect. Biol.* **2**, a002055 (2010).
3. T. E. Kennedy, T. Serafini, J. R. de la Torre, M. Tessier-Lavigne, *Cell* **78**, 425–435 (1994).
4. H. Long et al., *Neuron* **42**, 213–223 (2004).
5. Y. Zou, E. Stoeckli, H. Chen, M. Tessier-Lavigne, *Cell* **102**, 363–375 (2000).
6. R. Shirasaki, R. Katsumata, F. Murakami, *Science* **279**, 105–107 (1998).
7. B. J. Dickson, G. F. Gilestro, *Annu. Rev. Cell Dev. Biol.* **22**, 651–675 (2006).
8. A. Jaworski, H. Long, M. Tessier-Lavigne, *J. Neurosci.* **30**, 9445–9453 (2010).
9. K. Brose et al., *Cell* **96**, 795–806 (1999).
10. L. Camurri et al., *Mol. Cell. Neurosci.* **30**, 485–493 (2005).
11. E. T. Mambetisaeva, W. Andrews, L. Camurri, A. Annan, V. Sundaresan, *Dev. Dyn.* **233**, 41–51 (2005).
12. C. Sabatier et al., *Cell* **117**, 157–169 (2004).
13. P. Zelina et al., *Neuron* **84**, 1258–1272 (2014).
14. Z. Chen, B. B. Gore, H. Long, L. Ma, M. Tessier-Lavigne, *Neuron* **58**, 325–332 (2008).
15. S. R. Ramani et al., *Anal. Biochem.* **420**, 127–138 (2012).
16. P. C. G. Haddick et al., *PLOS ONE* **9**, e84823 (2014).
17. S. Matsushashi et al., *Dev. Dyn.* **203**, 212–222 (1995).
18. T. K. Watanabe et al., *Genomics* **38**, 273–276 (1996).
19. Y. Jiang et al., *Mol. Cell. Neurosci.* **41**, 113–119 (2009).
20. T. Serafini et al., *Cell* **78**, 409–424 (1994).

ACKNOWLEDGMENTS

We thank the members of the Tessier-Lavigne laboratory for discussion and suggestions. We are grateful to C. Cuiat for sharing NELL1 mutant mice, J. Ernst for help with purification of recombinant proteins, S. Warming for advice on the assembly of the NELL2 targeting vector by recombineering, M. Roose-Girma for help with generation of NELL2 mutant mice, and M. Yaylaoglu for providing probe templates for in situ hybridization. The NELL2 conditional and full knockout mice as well as cDNA constructs described here are available from A.J. under a material transfer agreement with Genentech. We also thank N. Velarde, D. Collado, K. Sono, and Y. Zhou for technical assistance. This work was supported by Genentech, The Rockefeller University, and Brown University. The supplementary materials contain additional data. Roche provided part of the support for the study but does not stand to benefit from it because no patents were filed.

SUPPLEMENTARY MATERIALS

www.sciencemag.org/content/350/6263/961/suppl/DC1
Materials and Methods
Figs. S1 to S4
Table S1
References (21–27)

17 August 2015; accepted 16 October 2015
10.1126/science.aad2615

CAMOUFLAGE

Open-ocean fish reveal an omnidirectional solution to camouflage in polarized environments

Parrish C. Brady,¹ Alexander A. Gilerson,² George W. Kattawar,³ James M. Sullivan,⁴ Michael S. Twardowski,⁴ Heidi M. Dierssen,⁵ Meng Gao,³ Kort Travis,¹ Robert Ian Etheredge,¹ Alberto Tonizzo,² Amir Ibrahim,² Carlos Carrizo,² Yalong Gu,² Brandon J. Russell,⁵ Kathryn Misilinski,¹ Shulei Zhao,¹ Molly E. Cummings¹

Despite appearing featureless to our eyes, the open ocean is a highly variable environment for polarization-sensitive viewers. Dynamic visual backgrounds coupled with predator encounters from all possible directions make this habitat one of the most challenging for camouflage. We tested open-ocean crypsis in nature by collecting more than 1500 videopolarimetry measurements from live fish from distinct habitats under a variety of viewing conditions. Open-ocean fish species exhibited camouflage that was superior to that of both nearshore fish and mirrorlike surfaces, with significantly higher crypsis at angles associated with predator detection and pursuit. Histological measurements revealed that specific arrangements of reflective guanine platelets in the fish's skin produce angle-dependent polarization modifications for polarocrypsis in the open ocean, suggesting a mechanism for natural selection to shape reflectance properties in this complex environment.

Perhaps more than any other environment on Earth, the nature of the open ocean greatly limits camouflage strategies. The absence of objects to hide behind or against requires cryptic animals to blend into a background that is in constant flux. Open-ocean visual backgrounds result from light scattering off of water molecules and microscopic particles, and early characterizations suggested that this background was temporally variable (due to changes in water composition) but spatially uniform [symmetrical in the horizontal plane with a predictable vertical intensity gradient (7)]. Early

theories proposed that the silvery sides of open-ocean fish evolved to mirror spatially homogeneous backgrounds (2–5) (figs. S1 and S2). This theory aligned with laboratory measurements showing more specular (mirrorlike) reflectance in open-ocean species and more diffuse (optically random) reflectance in their coastal counterparts (6). Recent research has unveiled an additional feature of light-scattering processes in open oceans that creates spatially heterogeneous backgrounds. Specifically, polarization (the directional vibration of light waves) generates changes in the light environment that vary with the Sun's position

in the sky (7–11). The angular variability of the polarized light field creates an environment where fish encounter different polarization fields in every direction. Under these conditions, mirrors are expected to be highly detectable to organisms with polarization-sensitive vision (12) (movies S1 and S2). Because the ability to detect polarized light is common across diverse fish families (13–15), natural selection is likely to influence the evolution of fish reflectance properties to address this dynamic heterogeneity.

Comparative measurements in the laboratory hint at adaptive differences in polarized reflectance between fish from distinct habitats. Measurements from an open-ocean fish (the lookdown, *Selene vomer*) reveal polarized reflectance properties that change based on incident polarization, whereas pinfish (*Lagodon rhomboides*) living in depolarized nearshore environments show no polarization-dependent reflectance (12). Lookdowns appear to alter their polarized reflection properties to match the change in background as the Sun changes position in the sky (12) (movie S3). Evidence for polarized reflectance modulation has been found in multiple open-ocean species (16, 17). Although these laboratory studies intriguingly suggest adaptations for camouflage, they cannot emulate the heterogeneity of natural light fields, and the ultimate test of crypsis must be conducted in the field.

¹Department of Integrative Biology, University of Texas, Austin, TX 78712, USA. ²Optical Remote Sensing Laboratory, the City College of New York–CUNY, New York, NY 10031, USA. ³Department of Physics and Astronomy and Institute for Quantum Science and Engineering, Texas A&M University, College Station, TX 77843-4242, USA. ⁴Harbor Branch Oceanographic Institute, Florida Atlantic University, Ft. Pierce, FL 34946, USA. ⁵Department of Marine Sciences, University of Connecticut Avery Point, 1080 Shennecossett Road, Groton, CT 06340-6048, USA.

*Corresponding author. E-mail: alexander.jaworski@brown.edu (A.J.); marci@rockefeller.edu (M.T.-L.) †Present address: Cardiovascular and Metabolic Diseases, Novartis Institutes for Biomedical Research, Cambridge, MA 02139, USA.

To empirically determine whether open-ocean fish have evolved a cryptic reflectance strategy for their heterogeneous polarized environment, we measured the contrasts of live open-ocean and coastal fish against the pelagic background in the Florida Keys and Curaçao. We tested whether open-ocean fish exhibit significantly lower contrast to their natural background [as measured by the Stokes contrast, S , which combines measures of polarization and intensity (fig. S3)] than fish that live in habitats with depolarized light. As a basis for comparison, we also tested whether open-ocean fish show lower contrast than previously proposed oceanic reflectance strategies (specular or diffuse mirror surfaces). Simultaneous videopolarimetry measurements from targets (fish and mirror surfaces) and water backgrounds were collected 2 to 4 m below the surface in deep open-ocean water (25 to 32 m depth) under a suite of solar elevation, predator (camera) viewing, and target positioning angles approximating an omnidirectional measurement (Fig. 1, movie S3, and supplementary materials and methods S1 and S2).

Field measurements verified the horizontal heterogeneity of the near-surface open-ocean polarized light environment (Fig. 1, D and E). A single 360° camera rotation around the horizon-

tal plane of the target (azimuthal rotation) revealed that background intensity and degree of polarization varied by a factor >2 , with the angle of polarization varying over 60° (Fig. 1E). Open-ocean species from the Carangidae fish family (lookdowns and bigeye scad, *Selar crumenophthalmus*) exhibited significantly lower contrast across viewing, solar, and target positioning angles than did carangid species inhabiting reef environments (bar jack, *Caranx ruber*; and almaco jack, *Seriola rivoliana*; Fig. 2 and table S1). Furthermore, open-ocean carangid fish revealed significantly lower contrasts than mirror surfaces, whereas reef-dwelling carangids showed significantly higher contrast than mirrors, and surface-skimming fish (ballyhoo, *Hemiramphus brasiliensis*) showed no difference (Fig. 2, A to E, figs. S4 to S6, and tables S2 to S9). The absence of fish polarocrypsis in reef environments is expected because of the depolarizing effects of the ocean floor (18), whereas a mirrorlike strategy may be sufficient for camouflage in the surface-skimming (<0.2 m) habitat of the ballyhoo, where the polarized field is chaotic (19).

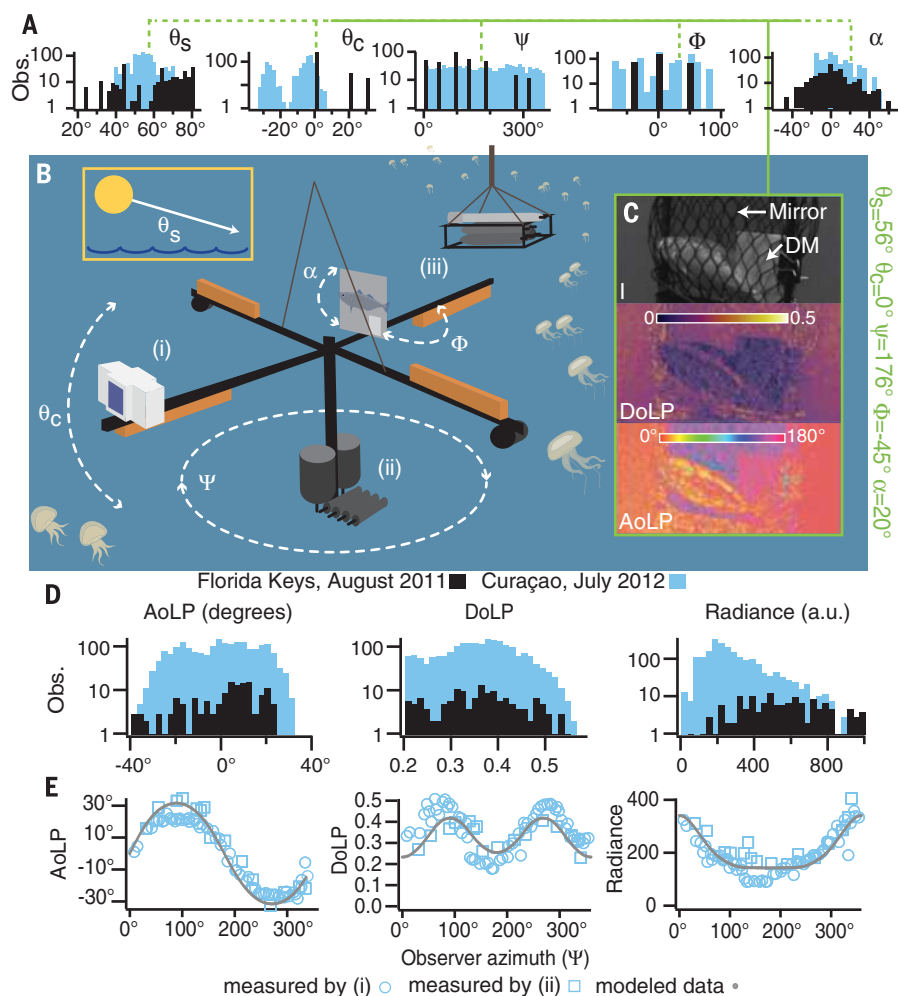
The lower omnidirectional contrast of carangids that occupy open-ocean habitats suggests that their surface properties are subject to selection for camouflage. If natural selection is shaping

fish reflectance, then we expect to find significant differences at viewing angles that are relevant for foraging and survival. Many carangid fish are piscivores (20, 21), requiring a stealthy approach to prey while minimizing detection from predators. Fish predation is biased around a $\sim 90^\circ$ cone centered on the prey's tail (22), and mirrors produce strong polarized reflections at these obtuse, predatory "chase angles" ($\pm 45^\circ$ from tail or head). Restricting our crypsis evaluation to chase angles only, we found that open-ocean carangid fish exhibit nearly twice the crypsis performance as nearshore carangids (table S1), and that these open-ocean species exhibited significantly lower contrasts than did mirror surfaces, whereas fish from other habitats did not (Figs. 2, F to J, and 3A and tables S2 and S6).

Although fish from open-ocean environments were more cryptic than our test surfaces (specular or diffuse mirrors) in nearly 75% of all chase-angle measurements from the field (Figs. 3A and 4A), we identified additional viewing angles in which these fish exhibit exceptional camouflage. Open-ocean carangids showed significantly lower contrast than mirrors or diffuse surfaces when viewed from above [camera inclination angle (θ_c) $< -10^\circ$; Figs. 3B and 4B, fig. S6, and tables S2 and S5] or positioned directly orthogonal to a

Fig. 1. Field measurement apparatus and angular configurations.

(A) More than 1500 measurements collected at different angular configurations of solar angle (θ_s), camera inclination angle (θ_c), camera azimuth angle (ψ), relative yaw angle (ϕ), and fish pitch angle (α) from the Florida Keys (black) and Curaçao (blue). (B) Measurements were obtained with a (i) videopolarimeter using a remotely operated underwater rotating platform (supplementary materials and methods S1 and S2 and movie S3) and validated by measurements with (ii) a hyperspectral radiometric polarimeter and (iii) inherent optical properties simultaneously recorded [e.g., volume-scattering function measurements with the Multi-Angle Scattering Optical Tool (MASCOT)]. In Curaçao, integrated digital compass and inertial sensors with the videopolarimeter provided nearly continuous azimuth (ψ) and pitch (θ_c) angle measurements. (C) Polarimetric image of a bigeye scad restrained against mirror and diffuse mirror (DM), shown in radiance (or intensity, I), degree of linear polarization (DoLP), and angle of linear polarization (AoLP). (D) Azimuthal (ψ) background measurements of the water column AoLP, DoLP, and radiance in Curaçao (blue) and Florida (black). (E) Measurements and simulations of the background light field for a single azimuthal rotation (3 min) on 7 July 2012 in Curaçao (measured 2.5 m below the surface in 26.5 m of ocean depth; supplementary materials and methods S2 and table S10).



predator viewer in the horizontal plane (detection angles, where the fish flank is perfectly perpendicular to the predator's view, fish yaw $\phi = 0^\circ \pm 10^\circ$; Figs. 3A and 4C and tables S2 and S5). Furthermore, open-ocean fish showed significant increases in crypsis when the Sun was moderately high in the sky (solar altitude $> 54\%$, Fig. 3C), as well as when potential predators were facing away from the Sun [camera azimuth angle (ψ) = 120° to 240° ; Fig. 3D].

In order to understand the structural mechanism underlying this superior polarocrypsis in open-ocean fish, we evaluated fish skin properties in the laboratory with scanning electron microscopy (SEM), light microscopy, and whole-body videopolarimetry measurements. We found that the specific orientation of the fish's guanine platelets allows these open-ocean carangids to blend into the consistent vertical intensity profile of the open ocean, while also providing them the ability to blend into variable polarized backgrounds. Specifically, SEM measurements revealed that the open-ocean carangids have guanine platelets that are well aligned in a vertical plane (e.g., θ_G guanine platelet roll angles exhibit a narrow angular distribution; Fig. 4D and fig. S1, C and D)

(16), which produces more specular reflection in the vertical direction and allows fish to match the predictable downward direction of light intensity in the open ocean. Meanwhile, the short axes of these guanine platelets have a very broad angular distribution (ϕ_G or yaw, Fig. 4D), which will result in greater diffuse intensity reflection along the horizontal axis [fig. S1M; similarly found in other silvery fish (23)]. This broad angular distribution in the horizontal plane may contribute to polarocrypsis by averaging the reflected light across a variable polarization background. Using both light microscopy and full-body videopolarimetry, we showed that the arrangement of guanine platelets produces two larger optical axes at the level of the whole fish (bulk reflectance; supplementary materials and methods S3 and Fig. 4E). These axes are roughly aligned with the anterior-posterior and dorsal-ventral axes of the fish (Fig. 4E). Full-body polarimetry measures of these fish in the lab confirm that these two axes have different polarization properties (see supplementary materials and methods S3 for in-depth results and discussion) that produce different polarization reflectance with different incident polarization light fields. Specifically, these two

optical axes are responsible for the incident-specific polarization reflectance that open-ocean carangids exhibit, because this surface will reflect fully preserved polarized light when the incident polarization angles align with one of these axes, and will reflect depolarized light when incident light is misaligned with either axis. This specific arrangement probably accounts for the improved crypsis ability relative to mirror surfaces at azimuth viewing angles such as (120° to 240° in Fig. 3D, where carangid fish surfaces will convert incident polarized light into lower-degree horizontally polarized light matching the background (fig. S7), whereas mirror surfaces, with angle-invariant reflection, will not.

Our in-field evaluation shows that polarocryptic open-ocean fish address crypsis with omnidirectional solutions. Polarocryptic fish not only reduce the conspicuous polarized reflections associated with mirrorlike surfaces but also exhibit angle-specific polarization reflective properties that are particularly honed for crypsis from viewing angles under natural selection (predatory chase and detection angles). Their context-dependent reflectance strategy surpasses both traditional devices [mirrors (24)] and modern

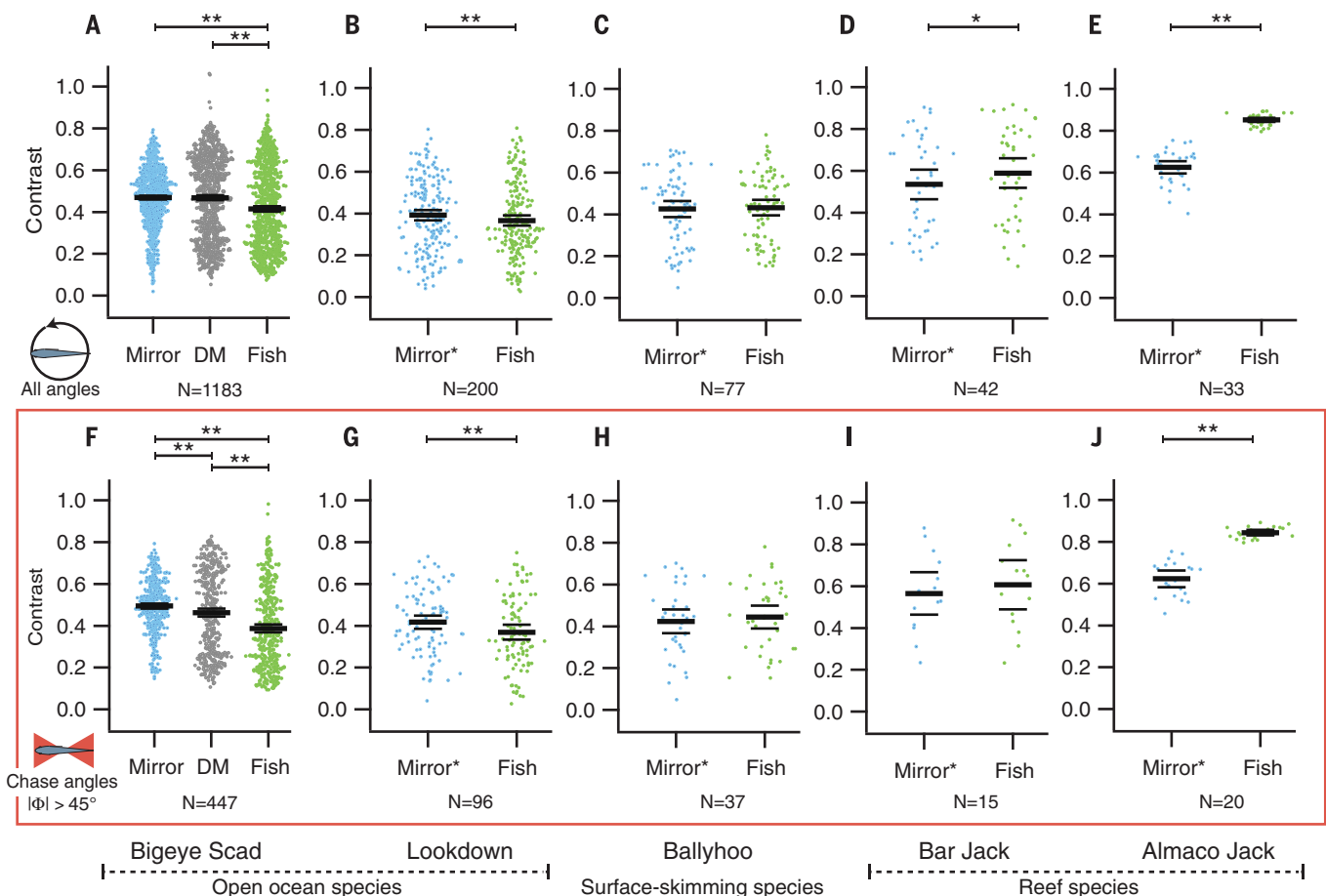


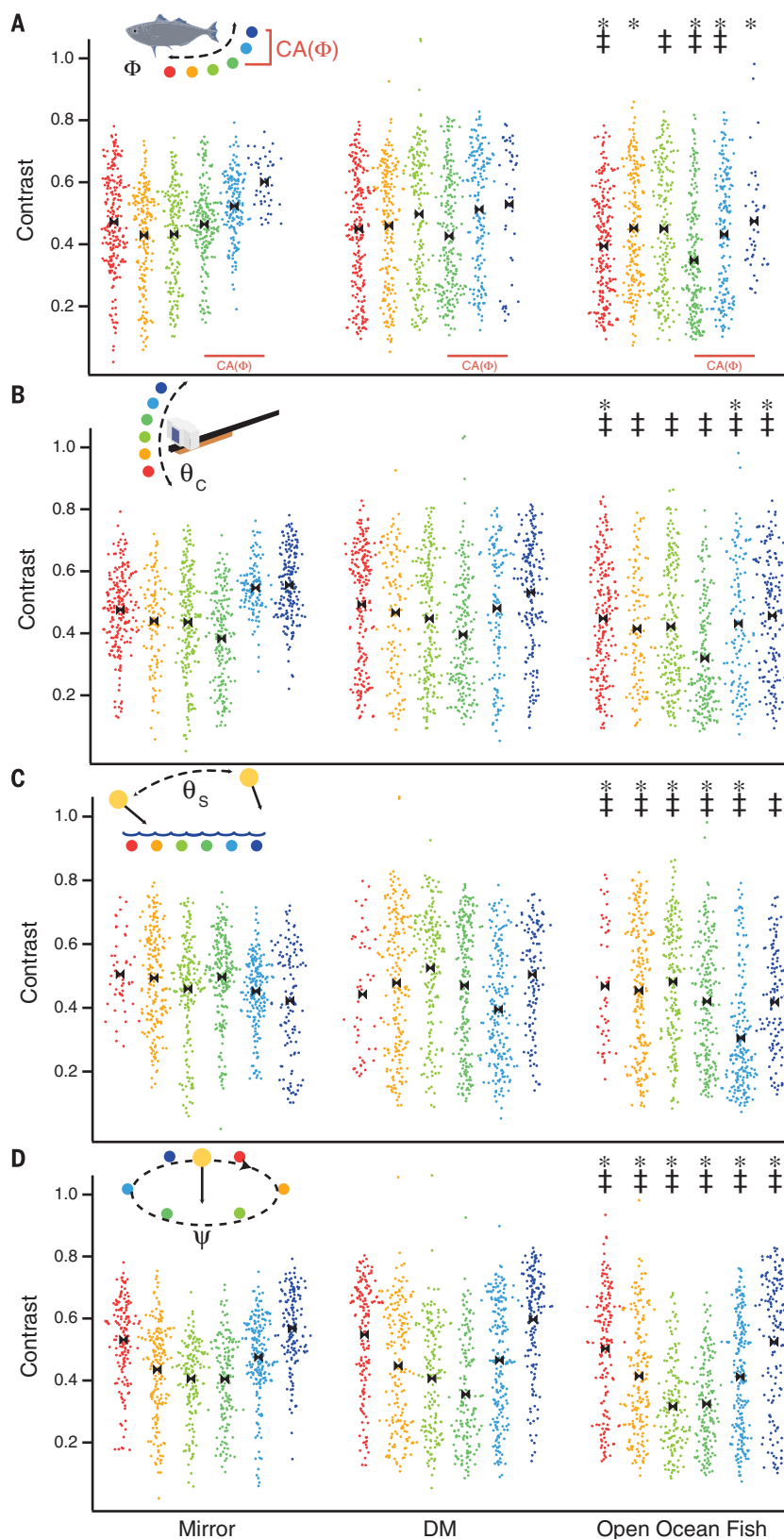
Fig. 2. Open-ocean fish species outperform nearshore fish and mirrored surfaces in epipelagic crypsis. (A to E) Videopolarimetric measurements of different species of silvery fish (green); specular mirror (mirror, blue), specular Mylar (mirror*, blue), and diffuse mirror (DM, gray) were evaluated in terms of S to the background environment (bigeye scad were measured in Curaçao; other fish were measured in Florida at 2 to 4 m below the surface in waters > 25 m deep) in blue wavelengths with a 470-nm peak. (F to J) Measurements collected within chase angles only ($|\phi| \geq 45^\circ$). Averages and standard errors are denoted by black bars; statistical significant differences are denoted by * ($P < 0.05$) and ** ($P < 0.01$) (tables S2 to S9 and figs. S4 to S6).

Fig. 3. Fine-scale evaluation of crypsis for the bigeye scad under different solar and viewing angles. Partitioning of the S distributions of Fig. 2A.

Each color corresponds to a particular angular interval bin, and the averages of each bin are marked on each distribution in black. Significant differences (found through t tests) between fish and specular mirror distributions are denoted by *, and significant differences between the fish and diffuse mirror distributions are denoted by †. **(A)** Contrast distributions by absolute value of the relative yaw angle, ϕ , with specific ϕ bins of red: $0^\circ < \phi \leq 15^\circ$, orange: $15^\circ < \phi \leq 30^\circ$, light green: $30^\circ < \phi \leq 45^\circ$, green: $45^\circ < \phi \leq 60^\circ$, light blue: $60^\circ < \phi \leq 75^\circ$, and blue: $75^\circ < \phi \leq 90^\circ$.

(B) Contrast distributions by camera/predator inclination, θ_C , with specific angular intervals of red: $-2.4^\circ < \theta_C \leq 10^\circ$, orange: $-3.4^\circ < \theta_C \leq -2.4^\circ$, light green: $-5.6^\circ < \theta_C \leq -3.4^\circ$, green: $-14.9^\circ < \theta_C \leq -5.6^\circ$, light blue: $-26.8^\circ < \theta_C \leq -14.9^\circ$, and blue: $-39.8^\circ < \theta_C \leq -26.8^\circ$.

(C) Contrast distributions by solar angle, θ_S , with specific bins representing red: $38^\circ < \theta_S \leq 44.4^\circ$, orange: $44.4^\circ < \theta_S \leq 50.8^\circ$, light green: $50.8^\circ < \theta_S \leq 54^\circ$, green: $54^\circ < \theta_S \leq 57.2^\circ$, light blue: $57.2^\circ < \theta_S \leq 63.6^\circ$, and blue: $63.6^\circ < \theta_S \leq 70^\circ$. **(D)** Contrast distributions by azimuth, ψ , the predator viewing angle relative to the Sun, with the specific intervals representing red: $0^\circ < \psi \leq 60^\circ$, orange: $60^\circ < \psi \leq 120^\circ$, light green: $120^\circ < \psi \leq 180^\circ$, green: $180^\circ < \psi \leq 240^\circ$, light blue: $240^\circ < \psi \leq 300^\circ$, and blue: $300^\circ < \psi \leq 360^\circ$.



devices [e.g., “invisibility cloaks” (25)] that camouflage well for specific tasks but suffer limitations in more complex natural environments. As sensor

technology extends beyond the relatively limited range of human sensory physiology and begins to fully capture nature’s complexity (e.g., polarization-

sensitive satellites), we should turn to natural systems for new materials and the means to use them effectively.

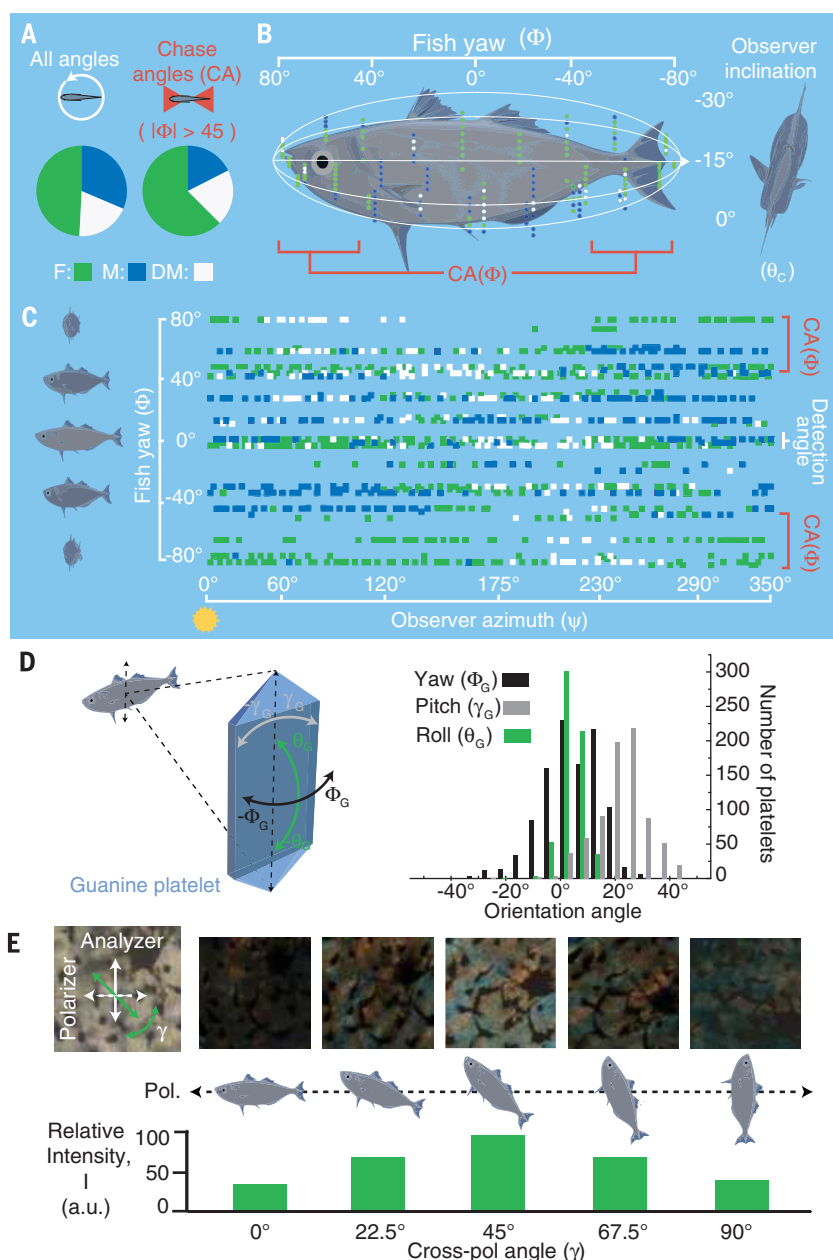


Fig. 4. Angular crypsis performance of bigeye scad in nature and in the laboratory. (A) Proportional crypsis performance (lowest S) for each surface reflector [F, bigeye scad (green); DM, diffuse mirror (white); and M, mirror (blue)] across all field measurement angles and chase angles only in the polarimeter's blue channel (a 470-nm peak). (B) and (C) The best-performing surface (lowest S) at measurements collected across (B) relative fish yaw and observer inclination angle [chase angles (CA) are noted] and (C) relative fish yaw and observer azimuth angles, with $\psi = 0^\circ$ representing the observer facing the Sun (for other contrast distributions, see fig. S3, and for model comparisons, see fig. S7). (D) Angular distributions of guanine platelet from three orientations (yaw, pitch, and roll) quantified from SEM measurements of bigeye scad skin, as in (16). (E) Cross-polarization light microscopy measurements of iridophore layers (collected from sagittal cross sections rotated in cross-polarization microscopy). The intensity of iridophore layers when rotated about the viewing axis between cross polarizers (linear polarizer and analyzer) produces angular (γ) dependent intensity with a maxima at 45° .

REFERENCES AND NOTES

1. A. Morel, K. J. Voss, B. Gentili, *J. Geophys. Res.* **C 100**, 13143–13150 (1995).
2. E. J. Denton, *Proc. R. Soc. London Ser. B* **258**, 285–313 (1970).
3. N. J. Marshall, S. Johnsen, in *Animal Camouflage: Mechanisms and Function*, M. Stevens, S. Merilaita, Eds. (Cambridge Univ. Press, Cambridge, 2011), pp. 186–211.
4. S. Johnsen, *Integr. Comp. Biol.* **43**, 580–590 (2003).
5. S. Johnsen, *Annu. Rev. Mar. Sci.* **6**, 369–392 (2014).
6. N. W. Pankhurst, J. N. Lythgoe, *J. Fish Biol.* **21**, 279–296 (1982).
7. T. W. Cronin, N. Shashar, *J. Exp. Biol.* **204**, 2461–2467 (2001).
8. S. Sabbah, A. Lerner, C. Erlick, N. Shashar, in *Recent Research Developments in Experimental & Theoretical Biology*, S. G. Pandalai, Ed. (Transworld Research Network, Trivandrum, Kerala, India, 2005), pp. 123–176.
9. T. H. Waterman, *Biol. Rev. Camb. Philos. Soc.* **81**, 111–115 (2006).
10. S. Sabbah, N. Shashar, *J. Opt. Soc. Am. A Opt. Image Sci. Vis.* **24**, 2049–2056 (2007).
11. Y. You et al., *Appl. Opt.* **50**, 4873–4893 (2011).
12. P. C. Brady, K. A. Travis, T. Maginnis, M. E. Cummings, *Proc. Natl. Acad. Sci. U.S.A.* **110**, 9764–9769 (2013).
13. N. W. Roberts, M. L. Porter, T. W. Cronin, *Proc. Phys. Soc. London. Sect. B* **366**, 627 (2011).
14. M. Kamermans, C. W. Hawryshyn, *Proc. Phys. Soc. Lond. Sect. B* **366**, 742 (2011).
15. G. M. Calabrese, P. C. Brady, V. Gruev, M. E. Cummings, *Proc. Natl. Acad. Sci. U.S.A.* **111**, 13397–13402 (2014).
16. S. Zhao, P. C. Brady, M. Gao, R. Etheredge, G. Kattawar, M. Cummings, *J. R. Soc. Interface* **12**, 10.1098/rsif.2014.1390 (2015).
17. T. Jordan, J. Partridge, N. Roberts, *Nat. Photon.* **6**, 759–763 (2012).
18. A. A. Gilerson et al., *Appl. Opt.* **52**, 8685–8705 (2013).
19. Y. You et al., *J. Geophys. Res. Oceans* **116**, C00H05 (2011).
20. J. K. Parrish, *Environ. Biol. Fishes* **34**, 257–263 (1992).
21. M. J. Cermak, *Biol. Bull.* **203**, 241–243 (2002).
22. N. O. Handegard et al., *Curr. Biol.* **22**, 1213–1217 (2012).
23. J. Haag, J. S. Jaffe, A. M. Sweeney, *Opt. Exp.* **21**, 3603–3616 (2013).
24. S. Johnsen, E. Gassmann, R. A. Reynolds, D. Stramski, C. Mobley, *Limnol. Oceanogr.* **59**, 1839–1852 (2014).
25. R. Schittny, M. Kadic, T. Bückmann, M. Wegener, *Science* **345**, 427–420 (2014).

ACKNOWLEDGMENTS

All experiments were approved by the University of Texas animal care committee (under Institutional Animal Care and Use Committee protocols AUP-2009-00022 and AUP-2015-00026). This research was supported by Office of Naval Research Multi-University Research Initiative grant N000140911054 to M.E.C., H.M.D., J.S., A.A.G., and G.W.K.; and NSF Division of Ocean Sciences grant 1130793 to M.E.C. and G.W.K. The data are deposited through the Dryad Digital Repository (10.5061/dryad.gt37j).

SUPPLEMENTARY MATERIALS

www.sciencemag.org/content/350/6263/965/suppl/DC1
Materials and Methods S1 to S5
Figs. S1 to S7
Tables S1 to S10
References (26–39)

26 September 2015; accepted 19 October 2015
10.1126/science.aad5284

PARASITOLOGY

Helminth infection, fecundity, and age of first pregnancy in women

Aaron D. Blackwell,^{1,2,3*} Marilyne A. Tamayo,⁴ Bret Beheim,^{2,5}
Benjamin C. Trumble,^{1,2,3,6,7} Jonathan Stieglitz,^{2,5,8} Paul L. Hooper,^{2,9}
Melanie Martin,^{1,2,3} Hillard Kaplan,^{2,5} Michael Gurven^{1,2,3}

Infection with intestinal helminths results in immunological changes that influence co-infections, and might influence fecundity by inducing immunological states affecting conception and pregnancy. We investigated associations between intestinal helminths and fertility in women, using 9 years of longitudinal data from 986 Bolivian forager-horticulturalists, experiencing natural fertility and 70% helminth prevalence. We found that different species of helminth are associated with contrasting effects on fecundity. Infection with roundworm (*Ascaris lumbricoides*) is associated with earlier first births and shortened interbirth intervals, whereas infection with hookworm is associated with delayed first pregnancy and extended interbirth intervals. Thus, helminths may have important effects on human fertility that reflect physiological and immunological consequences of infection.

Dysregulated immune function, and in particular autoimmune disease, has negative impacts on virtually every aspect of fecundity, including ovarian function, implantation, and pregnancy loss (1, 2). Healthy pregnancy is also associated with shifts in immune responses. During the luteal phase of the menstrual cycle, regulatory and type 2 (T_H2) T cell responses increase (3). If conception occurs, these shifts continue through pregnancy (4) and help to suppress type 1 (T_H1) T cell responses, increasing maternal tolerance of an immunologically distinct fetus (3). Because pregnancy is both affected by and alters immunity, parasites that result in systemic immunological changes might be expected to affect fecundity by altering the host's immune responses. Helminths, such as hookworm (*Ancylostoma duodenale* or *Necator americanus*) and giant roundworm (*Ascaris lumbricoides*), each infect 500 million to 800 million people (5) and are associated with immunological changes, such that host helper T cell populations generally shift from T_H1 toward T_H2 responses (6, 7) and the suppressive activity of regulatory T cells increases to modulate both T_H1 and T_H2 responses (8, 9). These shifts can alter susceptibility to other infectious diseases, such as malaria (10), giardiasis (11), and tuberculosis (12); are associated with reductions in many diseases that have inflammatory or auto-

immune etiology (13); and also resemble the T cell patterns that occur during pregnancy.

In humans, some helminth parasites can directly infect the reproductive organs or the fetus; for example, the filarial roundworm, *Wuchereria bancrofti*, can cause elephantiasis of the genitals (14). Animal studies have also examined life history changes associated with parasitism (15). Yet there are few data on the effects of intestinal helminth infections on human fecundity, fertility, or birth spacing. We prospectively examined the effect of helminth infection on the fecundity of women. We used 9 years of longitudinal data collected on 986 Tsimane forager-horticulturalist women living in the Amazonian lowlands of Bolivia (table S1). Tsimane are predominantly a natural fertility population, with infrequent (<5% prevalence) use of pharmaceutical contraceptives and a total fertility rate of nine births per woman (16). Helminths infect

70% of the population, the most common being hookworm (56%) and *A. lumbricoides* (15 to 20%) (11, 17).

In both animal and human studies, parasites have been shown to influence host reproduction via sexual behavior, brood or litter size, offspring size, incubation periods, conception rates, and pregnancy loss (18–22). In most cases, parasitism reduces host reproduction by compromising reproductive organs or reducing energy budgets (14, 23). However, among Tsimane adults, morbidity from intestinal helminth infections is low, particularly for *A. lumbricoides*. Controlling for age and co-infection in our sample, hookworm infection is associated with slightly lower body mass index (BMI) (generalized linear model, $\beta = -0.77 \text{ kg/m}^2$, $P < 0.001$) and hemoglobin ($\beta = -0.19 \text{ g/dl}$, $P = 0.005$), whereas *A. lumbricoides* is not ($\beta = -0.34 \text{ kg/m}^2$, $P = 0.180$; $\beta = -0.07 \text{ g/dl}$, $P = 0.413$). However, helminth infection is also associated with reductions in other infections, such as the intestinal protist *Giardia lamblia* (11). We hypothesized that intestinal helminths might increase fecundity because the associated immunological changes, resembling those occurring during pregnancy, modulate inflammatory responses that might otherwise impair fertility.

By using Cox proportional hazards models, we tested whether helminth infection was associated with changes in birth spacing for 561 multiparous women and the age of first pregnancy (AFP) for 425 nulliparous women (24). Consistent with our hypothesis, compared to being uninfected, *A. lumbricoides* infection was associated with an earlier AFP hazard ratio [(HR) = 3.06, confidence interval (CI) 1.91 to 4.91, $P < 0.001$ (Fig. 1 and Table 1)] and an increased hazard of pregnancy under age 32 years (at age 20: HR = 1.64, CI 1.16 to 2.33, $P = 0.005$). This association declines with age (interaction between *A. lumbricoides* and age: HR = 0.68 per decade, CI 0.51 to 0.89, $P = 0.006$) and becomes significantly negative by the age of 46 years (HR = 0.62, CI 0.38 to 1.00, $P = 0.05$). However, these late-life

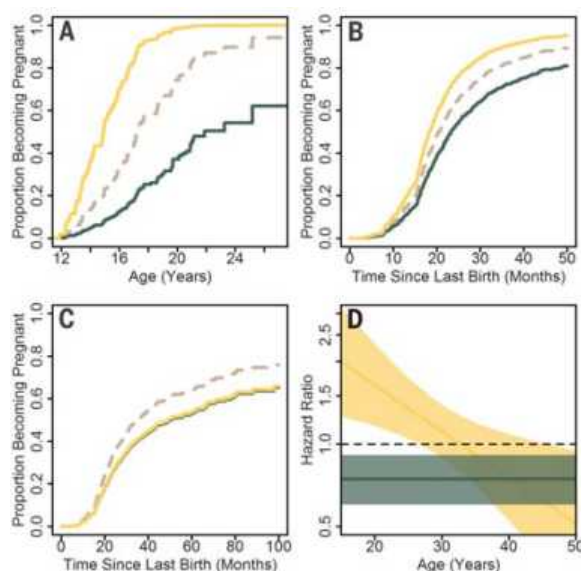


Fig. 1. Associations between infection and likelihood of becoming pregnant. (A to C) Kaplan-Meier curves from Cox proportional hazard models (table S2), representing the time to first pregnancy (A), and time to subsequent pregnancies at age 25 years (B) and age 40 years (C). Hazard ratios for conception associated with infection across ages are shown in (D). Colors indicate uninfected (dashed brown), infected with hookworm (solid dark green), or infected with *A. lumbricoides* (solid yellow).

¹Department of Anthropology, University of California Santa Barbara, CA 93106, USA. ²Tsimane Health and Life History Project, San Borja, Bolivia. ³Broom Center for Demography, University of California Santa Barbara, CA 93106, USA. ⁴Department of Anthropology, University of Missouri, Columbia, MO 65211, USA. ⁵Department of Anthropology, University of New Mexico, Albuquerque, NM 87131, USA. ⁶Center for Evolutionary Medicine, Arizona State University, Tempe, AZ 85287, USA. ⁷School of Human Evolution and Social Change, Arizona State University, Tempe, AZ, USA. ⁸Institute for Advanced Study in Toulouse, Toulouse, France. ⁹Department of Anthropology, Emory University, Atlanta, GA 30322, USA.

*Corresponding author. E-mail: blackwell@anth.ucsb.edu

negative associations are outweighed by positive associations during early life, such that a woman with *A. lumbricoides*, projected across her life span, would expect to have two more children than a woman who was never infected (Fig. 2).

In contrast, infection with hookworm was associated with a delayed age of first pregnancy (HR = 0.33, CI 0.20 to 0.54, $P < 0.001$) and a reduced hazard of subsequent pregnancies at all

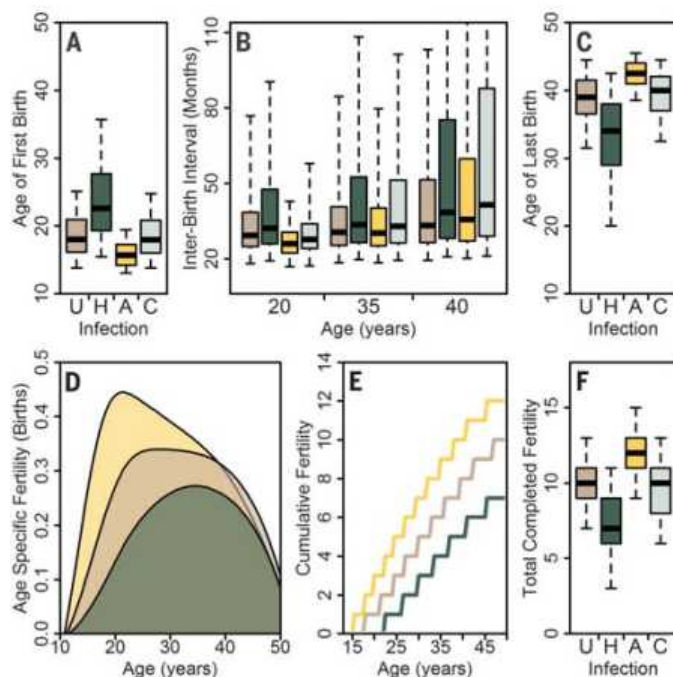
ages (HR = 0.71, CI 0.58 to 0.86, $P < 0.001$). A woman chronically infected with hookworm would be predicted to have three fewer children than an uninfected woman (Fig. 2). We found no interaction between infections, such that co-infection is associated with the additive effects of hookworm and *A. lumbricoides*.

These results are not altered by controlling for other likely confounds affecting fecundity or fecundity-altering behaviors, including phys-

ical condition, education (a proxy of acculturation), village location, season, and secular changes, even though these variables do affect fertility [tables S2 and S3, also see (25)]. The results are also not mediated by other comorbid infections or illnesses (table S4). Twenty percent of infected women were given antihelminthic drugs during medical visits. Receipt of antihelminthics was itself associated with a lower hazard of conceiving (HR = 0.75, CI 0.58 to 0.97, $P = 0.03$); however, neither controlling for treatment in models nor excluding these women appreciably altered hazard ratios from infection with either hookworm or *A. lumbricoides*. The results are also not driven by changing infection hazard during pregnancy. Although pregnancy is associated with an increased likelihood of hookworm infection, particularly in late pregnancy (table S6 and fig. S8), this relationship does not mediate the association between infection and conception hazards (24). Instead, it appears that hookworm-infected women occasionally clear their infections, during which time they become pregnant, followed quickly by subsequent reinfection with hookworm. Lastly, these associations are unlikely to be caused by consistent differences between individual women (e.g., genetic pleiotropies) that affect both fertility and risk of infection, because past parity is unrelated to likelihood of current infection [hookworm: odds ratio (OR) = 0.98 per birth, CI 0.90 to 1.08, $P = 0.65$; *A. lumbricoides*: OR 1.05 per birth, CI 0.93 to 1.18, $P = 0.46$].

Finding that hookworm and *A. lumbricoides* have contrasting associations with fecundity may seem unexpected. However, we suggest two reasons why we might observe such a pattern. First, although helminths are often discussed as if interchangeable, hookworm and *A. lumbricoides* do not have identical effects on the immune system. Whereas *A. lumbricoides* is

Fig. 2. Reproductive careers predicted from Cox proportional hazard models, showing the expected distributions of reproductive values for hypothetical women with persistent parasite status throughout life. Outcomes include age at first birth (A), interbirth intervals (B), age at last birth (C), age-specific fertility (births/woman per year) (D), median cumulative fertility over time (E), and total completed fertility by age 50 (F). Colors indicate uninfected (U, brown), infected with hookworm (H, dark green), infected with *A. lumbricoides* (A, yellow), or co-infected with hookworm and *A. lumbricoides* (C, light blue). Box plot whiskers display the 5th and 95th percentiles; bodies, the 25th, 50th, and 75th. Predictions are derived from the models in Fig. 1.



ages (HR = 0.71, CI 0.58 to 0.86, $P < 0.001$). A woman chronically infected with hookworm would be predicted to have three fewer children than an uninfected woman (Fig. 2). We found no interaction between infections, such that co-infection is associated with the additive effects of hookworm and *A. lumbricoides*.

Table 1. Cox proportional hazard models. Models also include generalized estimating equation cluster terms for individual and village. For each model, the number of individuals (n), number of medical observations (obs), and number of observed pregnancies (preg) are given. Dashes indicate variables not applicable for a given model or excluded by AIC. Details and additional excluded variables are given in tables S2 and S3.

Variable	Age of first pregnancy ($n = 425$, obs = 639, preg = 87)			Time to next pregnancy ($n = 561$, obs = 1623, preg = 405)		
	Exp(β)	95% CI	P	Exp(β)	95% CI	P
Age (decades)*	—	—	—	1.00	(0.80–1.25)	0.992
Age ⁴ (decades)*	—	—	—	0.95	(0.93–0.96)	<0.001
Hookworm	0.34	(0.20–0.58)	<0.001	0.74	(0.60–0.91)	0.004
<i>A. lumbricoides</i> †	3.06	(1.91–4.91)	<0.001	1.64	(1.16–2.33)	0.005
<i>A. lumbricoides</i> × age*	—	—	—	0.68	(0.51–0.89)	0.006
Treatment with antihelminthic	0.43	(0.19–0.97)	0.042	0.75	(0.58–0.97)	0.027
Education (years)	—	—	—	0.92	(0.86–0.99)	0.017
Speaks Spanish	—	—	—	0.74	(0.57–0.95)	0.018
Distance to town (10 km)	—	—	—	0.96	(0.91–1.00)	0.075
Season (P-spline)	—	—	<0.001	—	—	<0.001

*Age is centered at 20 years. Age was continuous to the nearest tenth of a year but is shown in decades to make the parameters more easily interpretable. Because age-related changes in fecundity are nonlinear, transformations ranging from age² to age⁵ were compared by AIC to select the age transformation (age⁴) that best fit the data (fig. S3). †For the time to next pregnancy model, the roundworm parameter represents the hazard ratio at age 20.

associated with a polarized T_H2 response (6), the response to hookworm has been reported as a mixed T_H1/T_H2 response (26, 27). Hookworm and *A. lumbricoides* also have differing effects on other diseases, such as malaria (10). Thus, the response to *A. lumbricoides* may be more favorable to conception and implantation, because it more closely resembles the immunological state in pregnancy and less closely resembles pro-inflammatory states that suppress fecundity. Second, hookworm infection may be more costly than *A. lumbricoides* infection, such that the costs imposed by infection, such as anemia and nutritional loss, outweigh any effect of immune modulation. Although we do not have direct measures of parasite load, hookworm is associated with both lower BMI and lower hemoglobin for women in our sample, whereas *A. lumbricoides* is not. Future studies will need to investigate the importance of parasite burden in these associations.

Although consistent with our hypothesis, it is still unexpected to see positive associations between fecundity and *A. lumbricoides* infection, given that most parasites decrease reproduction. However, this association might instead be understood not as de novo increases in fecundity, but as the suppression of responses that would otherwise decrease fecundity. For example, most organisms down-regulate reproductive effort during acute illness because inflammation suppresses reproductive function (28). If *A. lumbricoides* infection modulates inflammatory responses, then it might also limit inflammation-induced reproductive suppression, as well as sickness behavior and associated reductions in sexual activity (29, 30). If so, then the effects of *A. lumbricoides* might only be observed in the presence of other illnesses or conditions resulting in excess inflammation. An additional possibility is that the increase in fertility represents fecundity compensation, a host response in which reproductive effort is shifted toward earlier ages to compensate for increasing morbidity or mortality (15). However, our analysis cannot fully evaluate these kinds of lifetime or cumulative effects, because our longitudinal sample remains short relative to the human life span.

Regardless of mechanism, these results indicate that across populations, helminths may have unappreciated effects on demographic patterns, particularly given their high global prevalences (5).

REFERENCES AND NOTES

- H. J. A. Carp, C. Selmi, Y. Shoenfeld, *J. Autoimmun.* **38**, J266–J274 (2012).
- A. Sen, V. A. Kushnir, D. H. Barad, N. Gleicher, *Nat. Rev. Endocrinol.* **10**, 37–50 (2014).
- T. T. Jiang et al., *J. Immunol.* **192**, 4949–4956 (2014).
- A. L. Veenstra van Nieuwenhoven, M. J. Heineman, M. M. Faas, *Hum. Reprod. Update* **9**, 347–357 (2003).
- P. J. Hotez et al., *J. Clin. Invest.* **118**, 1311–1321 (2008).
- S. M. Geiger et al., *Parasite Immunol.* **24**, 499–509 (2002).
- R. M. Maizels, M. Yazdanbakhsh, *Nat. Rev. Immunol.* **3**, 733–744 (2003).
- L. J. Wammes et al., *Eur. J. Immunol.* **40**, 437–442 (2010).
- E. van Riet, F. C. Hartgers, M. Yazdanbakhsh, *Immunobiology* **212**, 475–490 (2007).
- J. A. Fernández-Niño et al., *Trans. R. Soc. Trop. Med. Hyg.* **106**, 701–708 (2012).
- A. D. Blackwell, M. Martin, H. Kaplan, M. Gurven, *Proc. Biol. Sci.* **280**, 20131671 (2013).
- V. O. Ezenwa, A. E. Jolles, *Science* **347**, 175–177 (2015).
- L. J. Wammes, H. Mpairwe, A. M. Elliott, M. Yazdanbakhsh, *Lancet Infect. Dis.* **14**, 1150–1162 (2014).
- J. McFall, A. Joseph, M. H. McFall, *Disease and Fertility* (Academic Press, Orlando, FL, 1984).
- M. Forbes, *Oikos* **67**, 444–450 (1993).
- L. McAllister, M. Gurven, H. Kaplan, J. Stieglitz, *Am. J. Hum. Biol.* **24**, 786–799 (2012).
- M. Martin, A. D. Blackwell, M. Gurven, H. Kaplan, in *Primates, Pathogens, and Evolution*, J. Brinkworth, K. Pechenkina, Eds. (Springer, New York, 2013), pp. 363–387.
- A. Möller, *J. Anim. Ecol.* **62**, 309–322 (1993).
- H. Hurd, *Trends Parasitol.* **17**, 363–368 (2001).
- P. Neuhaus, *Proc. Biol. Sci.* **270** (suppl. 2), S213–S215 (2003).
- L. Krishnan, L. J. Guilbert, T. G. Wegmann, M. Belosevic, T. R. Mosmann, *J. Immunol.* **156**, 653–662 (1996).
- R. Avitsur, R. Yirmiya, *Pharmacol. Biochem. Behav.* **64**, 787–796 (1999).
- M. Baudoin, *Evolution* **29**, 335–352 (1975).
- Materials and methods are available as supplementary materials on Science Online.
- H. Kaplan, P. L. Hooper, J. Stieglitz, M. Gurven, in *Population in the Human Sciences: Concepts, Models, Evidence*, Philip Kreager, B. Winne, S. Uljaszek, C. Capelli, Eds. (Oxford Univ. Press, Oxford, 2015), pp. 361–378.
- S. M. Geiger et al., *PLOS Negl. Trop. Dis.* **5**, e1280 (2011).
- H. J. McSorley, A. Loukas, *Parasite Immunol.* **32**, 549–559 (2010).
- K. B. H. Clancy et al., *Am. J. Hum. Biol.* **25**, 389–398 (2013).
- J. Stieglitz et al., *Brain Behav. Immun.* **49**, 130–139 (2015).
- E. C. Shattuck, M. P. Muehlenbein, *Am. J. Phys. Anthropol.* **157**, 1–18 (2015).

ACKNOWLEDGMENTS

We thank the Tsimane for their continued participation; our Bolivian project staff, including D. Eid, I. Maldonado, E. Cortez, N. Zabala, and many others; and four anonymous reviewers for their helpful comments. This work was supported by grants from the NIH/National Institute on Aging (R01AG024119, R56AG024119, P01AG022500) and the NSF (BCS-0422690). Data described in this paper are available as supplementary online materials. The study was reviewed and approved by the Gran Consejo Tsimane, the governing body overseeing Tsimane affairs, and by the institutional review boards of the University of California, Santa Barbara, and the University of New Mexico.

SUPPLEMENTARY MATERIALS

www.sciencemag.org/content/350/6263/970/suppl/DC1
Materials and Methods
Supplementary Text
Figs. S1 to S8
Tables S1 to S7
References (31–44)
Databases S1 and S2

12 June 2015; accepted 9 October 2015
10.1126/science.aac7902

CANCER IMMUNOLOGY

Chemotherapy-induced antitumor immunity requires formyl peptide receptor 1

Erika Vacchelli,^{1,2,3,4,5,*} Yuting Ma,^{1,2,3,4,5,6,7,*} Elisa E. Baracco,^{1,2,3,8} Antonella Sistigu,⁹ David P. Enot,^{1,2,3,10} Federico Pietrocola,^{1,2,3,8} Heng Yang,^{1,2,3,4,5,6,7} Sandy Adjemian,^{1,2,3} Kariman Chaba,^{1,2,3,4} Michaela Semeraro,^{1,11,12} Michele Signore,¹³ Adele De Ninno,¹⁴ Valeria Lucarini,¹³ Francesca Peschiaroli,¹³ Luca Businaro,¹⁴ Annamaria Gerardino,¹⁴ Gwennola Manic,⁹ Thomas Ulas,¹⁵ Patrick Günther,¹⁵ Joachim L. Schultze,¹⁵ Oliver Kepp,^{1,2,3,4,5} Gautier Stoll,^{1,2,3,4,5} Céline Lefebvre,^{1,16} Claire Mulot,^{17,18} Francesca Castoldi,^{1,2,3,8,19} Sylvie Rusakiewicz,^{1,11,12} Sylvain Ladoire,^{20,21,22} Lionel Apetoh,^{20,21,22} José Manuel Bravo-San Pedro,^{1,2,3,4,5} Monica Lucattelli,²³ Cécile Delarasse,²⁴ Valérie Boige,^{18,25} Michel Ducreux,^{8,25} Suzette Delaloge,^{16,26} Christophe Borg,²⁷ Fabrice André,^{1,16,28,29} Giovanna Schiavoni,¹³ Ilio Vitale,^{9,30} Pierre Laurent-Puig,^{17,18,31} Fabrizio Mattei,^{13,†} Laurence Zitvogel,^{1,8,11,12,††} Guido Kroemer,^{1,2,3,4,5,10,31,32,††}

Antitumor immunity driven by intratumoral dendritic cells contributes to the efficacy of anthracycline-based chemotherapy in cancer. We identified a loss-of-function allele of the gene coding for formyl peptide receptor 1 (FPR1) that was associated with poor metastasis-free and overall survival in breast and colorectal cancer patients receiving adjuvant chemotherapy. The therapeutic effects of anthracyclines were abrogated in tumor-bearing *Fpr1*^{−/−} mice due to impaired antitumor immunity. *Fpr1*-deficient dendritic cells failed to approach dying cancer cells and, as a result, could not elicit antitumor T cell immunity. Experiments performed in a microfluidic device confirmed that FPR1 and its ligand, annexin-1, promoted stable interactions between dying cancer cells and human or murine leukocytes. Altogether, these results highlight the importance of FPR1 in chemotherapy-induced anticancer immune responses.

The success of anticancer chemotherapy is linked to a durable tumor-targeting immune response (1). Accordingly, the presence of tumor-infiltrating dendritic cells (DCs) and CD8⁺ T lymphocytes at diagnosis increases

the likelihood of breast cancer patients responding to anthracyclines (2–6). One mechanism through which anthracyclines can stimulate an antitumor immunity is by inducing immunogenic cell death (ICD), and this mechanism implies

signaling through innate immune receptors including Toll-like receptors 3 (TLR3) and 4 (TLR4) (7–10).

We designed a screen for identifying candidate genetic defects that negatively affect chemotherapeutic responses. To this aim, we identified 328 nonsynonymous single-nucleotide polymorphisms (SNPs) affecting proteins involved in the recognition of dying cells by innate immune effectors (11) or influencing the incidence or prognosis of major human cancers and occurring in Caucasians with an allelic frequency >5% (table S1). DNA samples from breast cancer patients treated with adjuvant anthracycline-based chemotherapy (belonging to two independent cohorts) (table S2 and S3) were genotyped, and the effect of each SNP on overall survival (OS) was determined. When a dominant genetic model was applied, only one SNP was significantly (raw $P < 0.05$) associated with OS independent of major clinicopathological variables in both patient cohorts: rs867228 (fig. S1A, C to H). This SNP (1037A>C) affects exon 2 of the gene coding for formyl peptide receptor 1 (FPR1), which promotes the chemotactic interaction of neutrophils with necrotic hepatocytes (12, 13). rs867228 provokes an amino acid substitution (Glu³⁴⁶Ala) that suppresses FPR1 signaling (14, 15). Other SNPs with less drastic effects on FPR1

function (15, 16) had no effect on OS (fig. S1B and fig. S2, A to C). As opposed to patients bearing the most frequent *FPR1* allele (17) in homozygosis (*FPR1*^{CC}), women bearing the rs867228 loss-of-function allele of *FPR1* in homozygosis (*FPR1*^{AA}) or heterozygosis (*FPR1*^{CA}) exhibited reduced OS and metastasis-free survival (Fig. 1, A and B; fig. S2, D and E; and tables S4 and S5). Similarly, colorectal

cancer patients treated with oxaliplatin-based chemotherapy (table S6) and bearing the rs867228 loss-of-function allele of *FPR1* in homozygosis (*FPR1*^{AA}) exhibited reduced OS and progression-free survival (fig. S3, A to D, and tables S7 and S8). rs867228 had no effect on the OS of breast cancer patients bearing loss-of-function alleles of *TLR4* (rs4986790, Asp²⁹⁹Gly) (7, 18) (Fig. 1C and

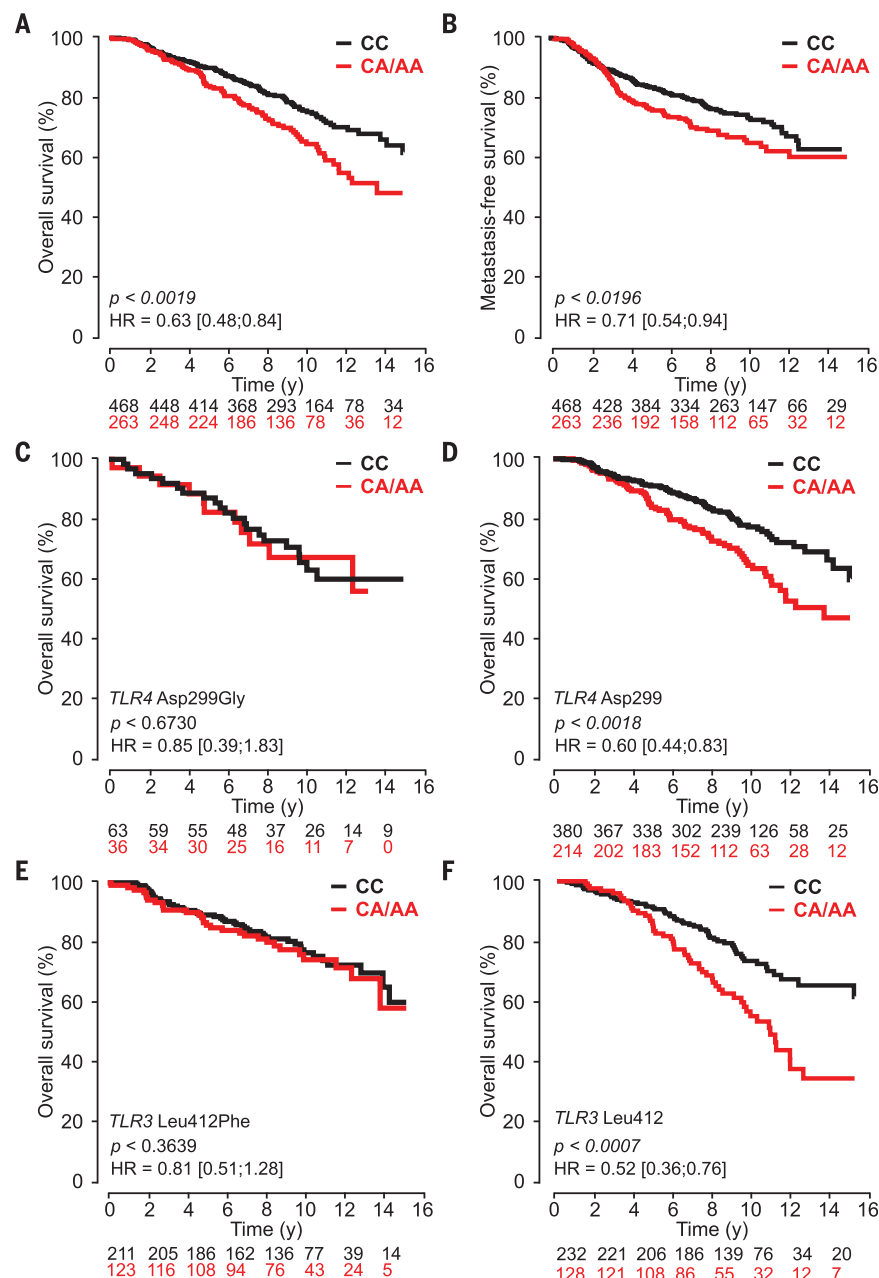


Fig. 1. Effects of *FPR1* deficiency on the survival of breast cancer patients. (A and B) Kaplan-Meier of the OS (A) or metastasis-free survival (MFS) (B) estimated in the combined cohort of patients ($n = 731$) treated with adjuvant anthracycline-based chemotherapy and bearing *FPR1* rs867228 with CC (wild type) or CA (heterozygous) + AA (mutated homozygous) genotypes. The analysis of the effect of *FPR1* rs867228 on OS yields a false discovery rate of 0.1090. (C and D) OS estimated in breast cancer patients bearing mutated (Asp²⁹⁹Gly) (C) or wild-type (Asp²⁹⁹Asp) (D) Toll-like receptor 4 (*TLR4*) (SNP rs4986790) genotypes according to the illustrated *FPR1* SNP rs867228 genotype. (E and F) Kaplan-Meier of the OS estimated in breast cancer patients bearing mutated (Leu⁴¹²Phe) (E) or wild-type (Leu⁴¹²Leu) (F) *TLR3* genotypes (SNP rs3775291) according to the *FPR1* SNP rs867228 genotype. Statistical significance was determined by likelihood ratio test (LRT). HR, hazard ratio.

¹Gustave Roussy Cancer Campus, Villejuif, France. ²INSERM, U1138, Paris, France. ³Équipe 11 Labellisée par la Ligue Nationale Contre le Cancer, Centre de Recherche des Cordeliers, Paris, France. ⁴Université Paris Descartes, Sorbonne Paris Cité, Paris, France. ⁵Université Pierre et Marie Curie, Paris, France. ⁶Suzhou Institute of Systems Medicine, Suzhou, Jiangsu, China. ⁷Chinese Academy of Medical Sciences and Peking Union Medical College, Beijing, China. ⁸Faculté de Médecine, Université Paris-Saclay, Kremlin-Bicêtre, France. ⁹Regina Elena National Cancer Institute, Rome, Italy. ¹⁰Metabolomics and Cell Biology Platforms, Gustave Roussy Cancer Campus, Villejuif, France. ¹¹INSERM, U1015, Villejuif, France. ¹²Center of Clinical Investigations in Biotherapies of Cancer (CICBT) 507, Villejuif, France. ¹³Department of Hematology, Oncology, and Molecular Medicine, Istituto Superiore di Sanità, Rome, Italy. ¹⁴Italian National Research Council, Institute for Photonics and Nanotechnology, Rome, Italy. ¹⁵Genomics and Immunoregulation, Life and Medical Science Center Institute, University of Bonn, Germany. ¹⁶INSERM, U981, Villejuif, France. ¹⁷Université Paris Sorbonne Cité, UMR5 775, INSERM, Paris, France. ¹⁸INSERM U1147, Centre de Ressources Biologiques (CRB) EPIGENETIC, Paris, France. ¹⁹Sotio, Prague, Czech Republic. ²⁰Department of Medical Oncology, Centre Georges-François Leclerc, Dijon, France. ²¹Université Bourgogne Franche-Comté, Dijon, France. ²²Centre Georges François Leclerc, Dijon, France. ²³Department of Life Sciences, University of Siena, Siena, Italy. ²⁴Institut du Cerveau et de la Moelle Épinrière, ICM CNRS UMR 7225 – INSERM U 1127 – UPMC-P6 UMR S 1127, Équipe Neurogénétique et Physiologie Hôpital de la Pitié-Salpêtrière, 47, Boulevard de l'Hôpital, 75013 Paris, France. ²⁵Department of Medical Oncology, Gustave Roussy Cancer Campus, Villejuif Cedex, France. ²⁶Department of Breast Oncology, Gustave Roussy Cancer Campus, Villejuif, France. ²⁷University of Franche-Comté, INSERM 1098, France. ²⁸Department of Biology and Pathology, Gustave Roussy Cancer Campus, Villejuif, France. ²⁹Department of Medical Oncology, Gustave Roussy Cancer Campus, Villejuif, France. ³⁰Department of Biology, University of Rome "Tor Vergata," Rome, Italy. ³¹Pôle de Biologie, Hôpital Européen Georges Pompidou, AP-HP, Paris, France. ³²Karolinska Institute, Department of Women's and Children's Health, Karolinska University Hospital, 17176 Stockholm, Sweden. *These authors contributed equally to this work. †These authors contributed equally to this work. ‡Corresponding author. E-mail: kroemer@orange.fr (G.K.); laurence.zitvogel@gustaveroussy.fr (L.Z.)

table S9) or *TLR3* (rs3775291, Leu⁴¹²Phe) (Fig. 1E and table S10). The negative effect of the *FPR1* polymorphism on OS was only evident in patients with normal *TLR3* and *TLR4* (Fig. 1, D and F, and tables S9 and S10), suggesting that *FPR1* participates in the same therapeutically relevant pathway as the one influenced by the two *TLRs*.

FPR1 is expressed by myeloid cells (www.proteinatlas.org; www.immgen.org), as well as by some carcinomas (19). Genetic inactivation of *Fpr1* (fig. S4A) did not affect the capacity of MCA205 fibrosarcoma cells treated with mitoxantrone or doxorubicin in vitro to vaccinate syngeneic, immunocompetent mice against a rechallenge with living cells of the same type (Fig. 2, A and B, and fig. S4A). Similar results

were obtained with wild-type (WT) and *Fpr1*^{-/-} TC-1 lung carcinoma cells (fig. S4A; fig. S6, A and B; and fig. S7, A and B). However, *Fpr1*^{-/-} mice failed to mount an immune response against anthracycline-treated MCA205 (Fig. 2, A and B, and fig. S5A) or TC-1 cells (fig. S6, A and B, and fig. S7, A and B) under conditions in which WT mice did so, suggesting that *Fpr1* must be expressed by host cells, not cancer cells, for anthracyclines to elicit antitumor immunity. Accordingly, *Fpr1*^{-/-} cancer cells responded to anthracycline-based chemotherapy in vivo as WT cancer cells did, whereas WT cancer cells growing in *Fpr1*^{-/-} hosts were resistant to anthracyclines (Fig. 2, C and D, and figs. S5B, S6C, S6D, S7C, and S7D).

Next, we investigated how *FPR1* may influence the immune response against dying cancer cells

by making bone marrow chimeras. WT mice receiving *Fpr1*^{-/-} bone marrow could not mount a protective immune response after vaccination with anthracycline-treated MCA205 cells (fig. S8A). Moreover, MCA205 cell-derived tumors became refractory to chemotherapy when they grew in WT mice that had received *Fpr1*^{-/-} bone marrow (fig. S8B). Conversely, tumors growing in *Fpr1*^{-/-} hosts reconstituted with WT bone marrow responded normally to anthracycline-based chemotherapy (fig. S8C). Thus, expression of *FPR1* by the host immune system contributes to the antineoplastic effects of chemotherapy.

Four ligands for *FPR1* have been described, namely: (i) cathepsin G (CTSG) (20); (ii) family with sequence similarity 19 [chemokine (C-C motif)-like], member A4 (FAM19A4) (21);

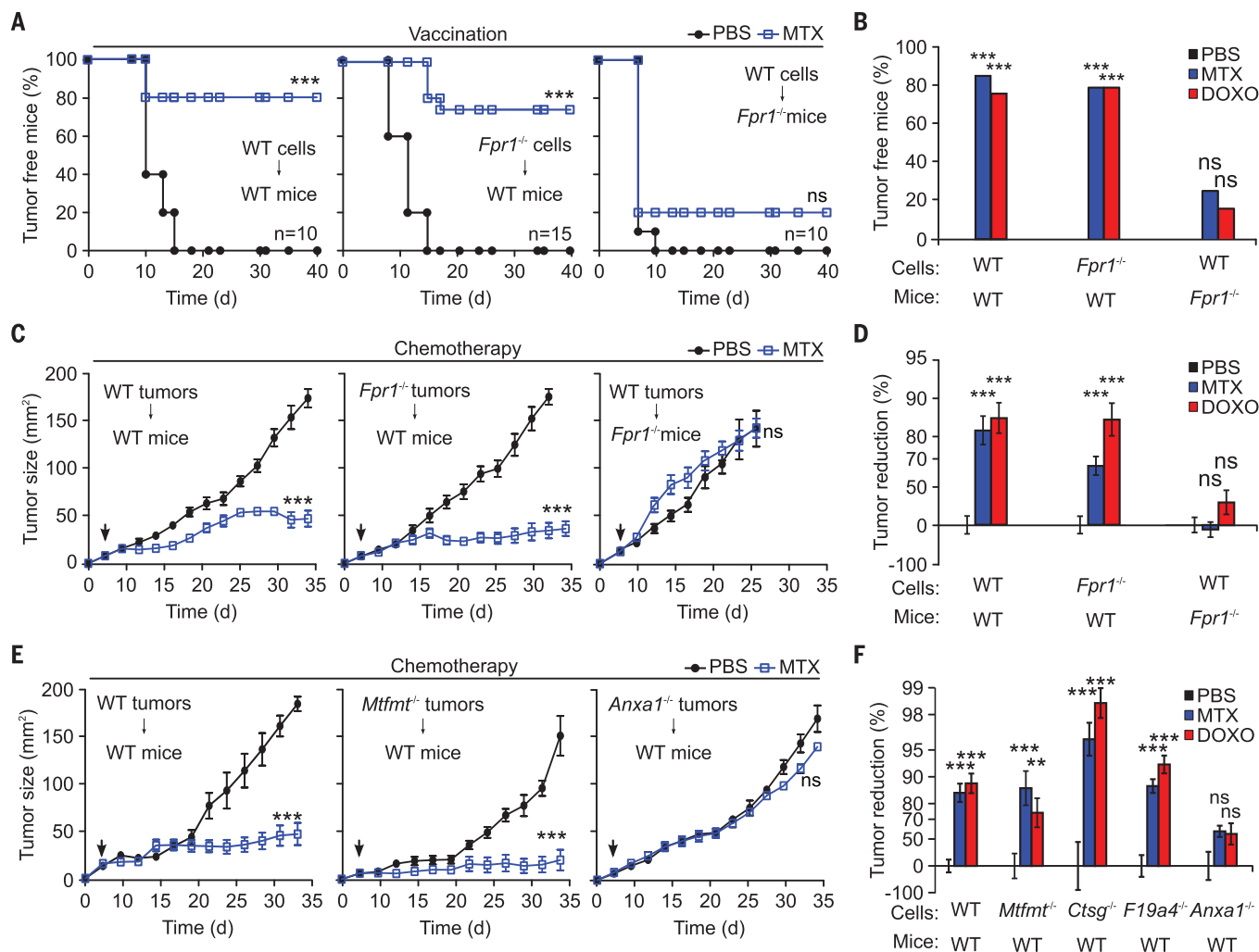


Fig. 2. Contribution of *Fpr1* and Annexin A1 to chemotherapy-induced tumor growth reduction. (A and B) WT or *Fpr1*^{-/-} MCA205 fibrosarcoma cells cultured overnight with mitoxantrone (MTX) or doxorubicin (DOXO) were inoculated subcutaneously into the flanks of WT C57BL/6 or *Fpr1*^{-/-} mice. Seven days later, animals were rechallenged into the opposite flank with live WT MCA205 cells. Representative experiment (A) and quantitative analysis of the data [from (A) and fig. S5A] in (B). (C and D) WT and *Fpr1*^{-/-} C57BL/6 mice bearing WT or *Fpr1*^{-/-} MCA205 fibrosarcomas were treated with MTX, DOXO, or phosphate-buffered saline (PBS) (as a vehicle control). Representative experiment in (C) and quantitative analysis of the

data [from (C) and fig. S5B]. (E and F) WT, *Mtfmt*^{-/-}, *Ctsg*^{-/-}, *F19a4*^{-/-}, or *Anxa1*^{-/-} MCA205 tumors were established in WT mice and treated with MTX, DOXO, or PBS (as a vehicle control). Results are representative for one experiment out of three involving at least five mice per group [(A), (C), and (E)] or are pooled from at least three independent experiments [(B), (D), and (F)]. Statistical significance was calculated by means of the likelihood ratio test (A), the chi-square test (B), the Wald test [(C) and (E)], and the contrast *t* test [(D) and (F)] when comparing to PBS controls. ns, not significant; *****P* < 0.001. Arrows in (C) and (E) indicate the initiation of chemotherapy.

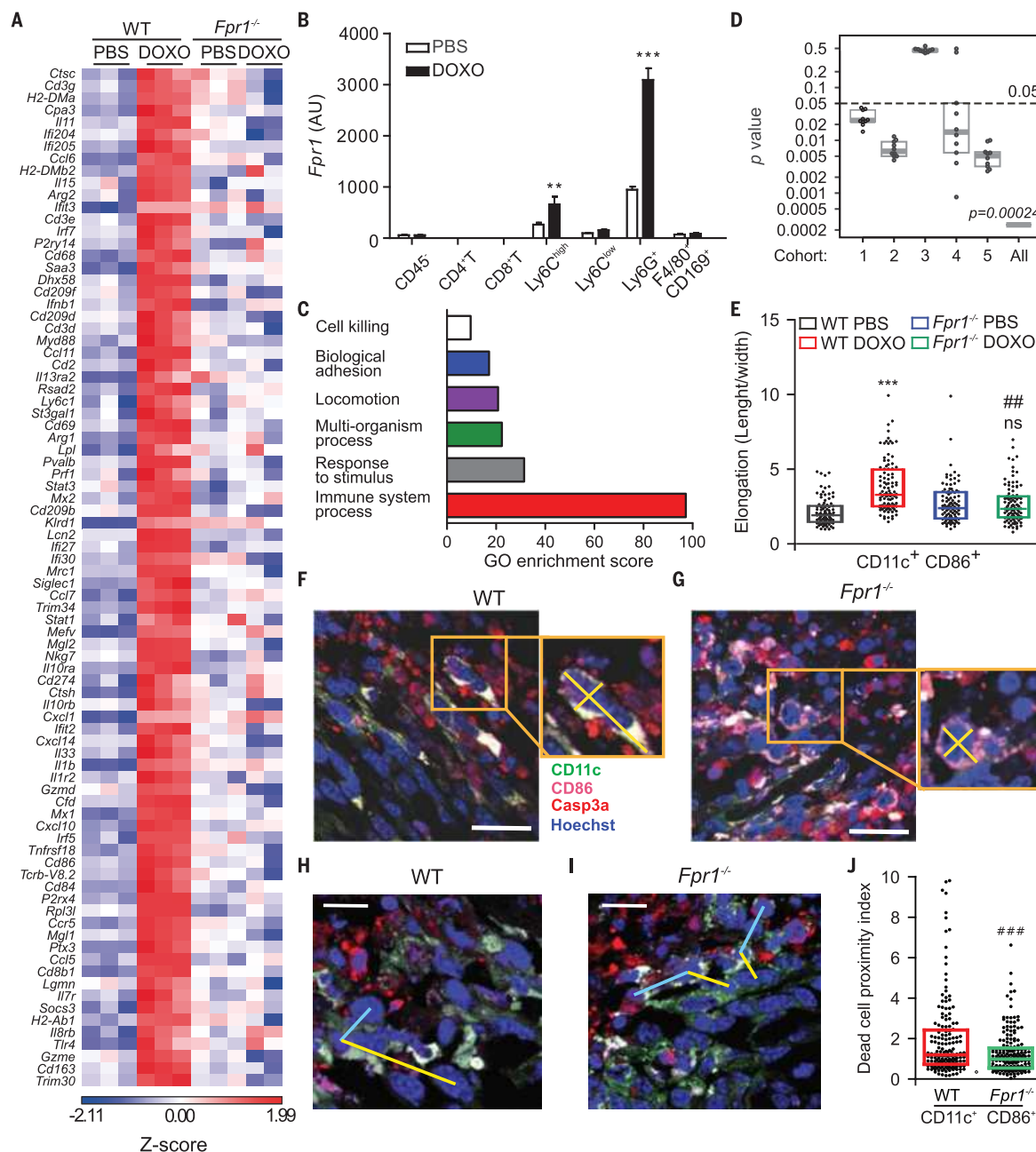


Fig. 3. Effect of FPR1 on the anticancer immune response and the intratumoral positioning of dendritic cells after chemotherapy. (A) WT or *Fpr1*^{-/-} mice bearing murine MCA205 fibrosarcomas were treated with doxorubicin (DOXO) or phosphate-buffered saline (PBS) (as a vehicle control), and tumors were harvested 48 hours later for microarray analysis. Immune-related genes up-regulated by DOXO administration in tumors from WT mice (but not from *Fpr1*^{-/-} mice) are listed. (B) Alternatively, tumors were recovered and tumor-infiltrating immune cells were sorted by fluorescence-activated cell sorting. *Fpr1* expression was assessed by quantitative real-time polymerase chain reaction. AU, arbitrary unit; ***P* < 0.01; ****P* < 0.001 (unpaired *t* test), as compared with PBS administration. (C) A total of 427 genes, identified as highly expressed specifically in DOXO-treated MCA205 tumors growing in WT mice (but not in *Fpr1*^{-/-} mice), were subjected to gene ontology analysis. (D) Analysis of the overexpression of the set of 84 immune-related genes identified in (A) on “responsive” as compared to “nonresponsive” tumors from five independent breast cancer patient cohorts by employing gene set analysis (GSA). The combined (All) *P* value was obtained using Fisher’s method. The vertical dotted line represents significance thresholds (*P* < 0.05). (E to G) Effect of chemotherapy with DOXO on the immune infiltrate of MCA205 fibrosarcomas.

Immunofluorescence stainings were performed on tumors recovered 2 days after chemotherapy. Quantitative analysis (E) of the immunostainings [(F) and (G)] are shown. In (E), the length/width ratio (elongation) was determined in 60 to 100 randomly chosen cells, using the morphometric methods illustrated in (F) and (G). Box plots report the lower and upper quartile plus the median value. ns, not significant; ****P* < 0.001, one-way analysis of variance (ANOVA), Bonferroni’s multiple comparison test, as compared with tumors harvested from mice with the same genetic background and receiving PBS; ###*P* < 0.01, as compared with tumors harvested from WT mice treated with DOXO. [(F) and (G)] Representative fluorescence micrographs of tumor-infiltrating DCs (CD11c⁺CD86⁺) in DOXO-treated, dead-cell (Casp3a⁺) enriched tumor sites are reported. Enlarged windows describe the method of length/width quantification. Scale bar, 10 μm. (H and I) Representative images showing the method employed to measure the intercellular distance between the same DC (CD11c⁺CD86⁺) and the closest Casp3a⁺ (blue line) or Casp3a⁺ (yellow line) DOXO-treated tumor cells. Scale bar, 20 μm. (J) Quantitative analysis of the dead-cell proximity index determined for tumor-infiltrating DCs. Data are represented as scatter dot plots. *****P* < 0.001 (*t* test), as compared with tumor cells from MTX-treated WT mice.

(iii) *N*-formylated peptides contained in bacteria and mitochondria (22); and (iv) annexin A1 (ANXA1), a ubiquitously expressed cytosolic protein (23). Knocking out the genes coding for *Ctsg* (fig. S4D), *Fam19a4* (fig. S4E), or mitochondrial

methionyl-tRNA formyltransferase (*Mtfmt*), an enzyme that catalyzes formylation reactions in mitochondria (24) (fig. S4B), had no effect on the capacity of MCA205 cells to elicit anticancer immune responses upon exposure to anthracyclines

in vitro and to respond to mitoxantrone and doxorubicin in vivo (Fig. 2, E and F; fig. S5, C and D; fig. S6, E to H; fig. S7, E to H; fig. S8, D and E; and fig. S9). Conversely, anthracycline-treated *Anxa1*^{-/-} MCA205 and TC-1 cells (fig. S4C) were

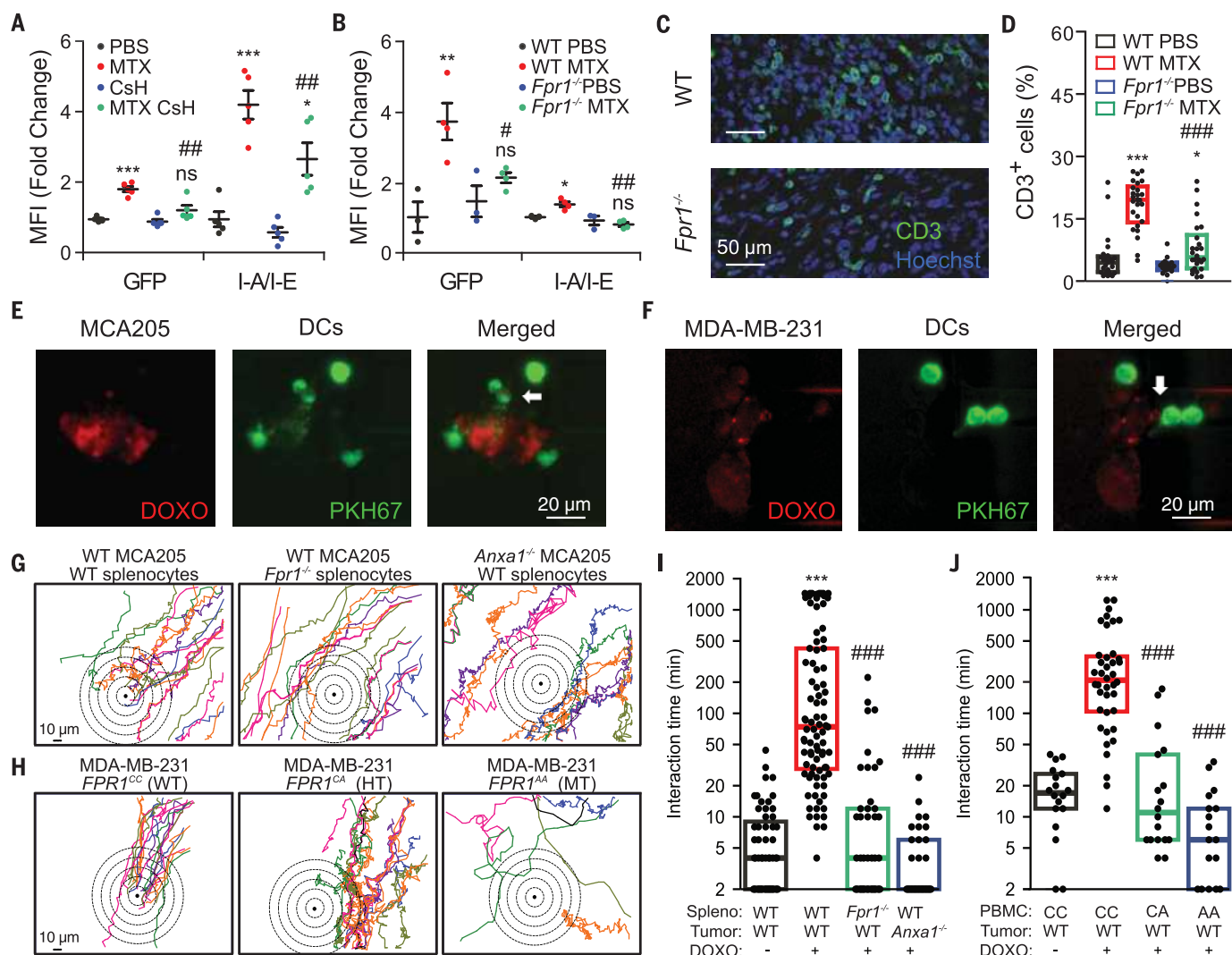


Fig. 4. Effect of FPR1 on dendritic cell function. (A and B) MyrPalm-GFP-expressing MCA205 fibrosarcoma tumors were implanted in WT (A) or *Fpr1*^{-/-} mice (B) and treated with mitoxantrone (MTX) or PBS as a vehicle control, alone or in combination with cyclosporin H (CsH) (A). Thirty-eight hours later, tumor-infiltrating CD11b⁺Ly6C^{high}Ly6G⁻ myeloid cells were isolated and assessed for tumor antigen uptake (indicated by GFP fluorescence intensity) or MHC class II (I-A/I-E) expression. Representative mean fluorescence intensities (MFIs) from three independent experiments are shown. ns, not significant; **P* < 0.05; ***P* < 0.01; ****P* < 0.001 (one-way ANOVA, Bonferroni's multiple comparison test), as compared with tumors recovered from WT mice subjected to the same treatment but not exposed to MTX (A) or from mice with the same genetic background receiving PBS (B). #*P* < 0.05; ##*P* < 0.01, as compared with tumors harvested from WT mice treated with MTX alone. (C and D) Immunofluorescence detection of CD3⁺ T cells in MCA205 tumors harvested from WT and *Fpr1*^{-/-} mice 7 days after MTX treatment. Representative fluorescence micrographs are shown in (C), and quantitative data are reported in (D). **P* < 0.05; ****P* < 0.001 (one-way ANOVA, Bonferroni's multiple comparison test), as compared with tumors harvested from mice with the same genetic background receiving PBS; ###*P* < 0.001, as compared with tumors harvested from WT mice treated with MTX. (E and F) Representative fluorescence

micrographs showing the interaction between MCA205-DOXO corpses (in red) and mouse DC (purified by means of CD11c microbeads and labeled with the PKH67 green fluorescent cell tracker) (E) or MDA-MB-231-DOXO corpses (in red) and human DC (PBMCs, labeled with PKH67) (F). White arrows indicate portions of DOXO corpses interacting with the DC. (G and H) Microfluidic time-lapse recordings of the interaction between DOXO-pretreated WT or *Anxa1*^{-/-} MCA205 cells and WT or *Fpr1*^{-/-} splenocytes (G) or, alternatively, between DOXO-pretreated human MDA-MB-231 breast cancer cells and PBMCs collected from healthy donors bearing *FPR1* CC (WT), CA (heterozygous, HT) or AA (mutated homozygous, MT) genotypes (H). Plots represent the trajectories of the individual splenocytes or PBMC (*n* = 6 to 30 cells per condition) toward target tumor cells (black spots) within 24 to 48 hours (splenocytes) or 48 to 72 hours (PBMC). (I and J) Quantification of the interaction times between WT or *Fpr1*^{-/-} splenocytes and WT or *Anxa1*^{-/-} MCA205 cells (I) or between *FPR1*^{CC}, *FPR1*^{CA}, or *FPR1*^{AA} PBMC and MDA-MB-231 cells (J) that had been exposed or not exposed to DOXO. Each dot represents a single spleen cell (*n* = 38 to 97 cells per condition) or a single PBMC (*n* = 20 to 40 cells per condition). ****P* < 0.001 (Mann Whitney test) referred to WT splenocytes (I) or *FPR1*^{CC} PBMC (J) challenged with untreated tumor cells. ###*P* < 0.001, compared with WT splenocytes (I) or *FPR1*^{CC} PBMC (J) challenged with DOXO-treated WT tumor cells.

unable to drive protective, tumor-targeting immune responses and formed tumors that were resistant to doxorubicin and mitoxantrone (Fig. 2, E and F; fig. S5, C and D; fig. S6, E to H; fig. S7, E to H; fig. S8, D and E). Both anthracyclines stimulated the secretion of Anxa1 by cancer cells (fig. S4F). Moreover, blockade of extracellular ANXA1 with a neutralizing antibody abrogated tumor growth reduction by anthracyclines in vivo (fig. S10), supporting the idea that ANXA1 is the functionally relevant FPR1 ligand.

Injection of the FPR1-specific antagonist cyclosporin H (CsH) (25) either concomitant with chemotherapy or 2 (but not 7) days after chemotherapy, abolished the anticancer effects of anthracyclines (fig. S11). Thus, FPR1 is likely to participate in the initial phase of the anticancer immune response. Microarray analyses of tumors collected from WT versus *Fpr1*^{-/-} mice 2 days after chemotherapy led to the identification of multiple genes that were induced by doxorubicin in WT (but not in *Fpr1*^{-/-}) hosts (Fig. 3, A to C, fig. S12, and table S11). These genes included several that are relevant for type I interferon responses, DC maturation and antigen processing/presentation, and cytotoxic T cell effector functions. *Fpr1* was expressed by intratumoral CD45⁺ leukocytes (not by CD45⁻ cells)—in particular, myeloid Ly6C^{high}Ly6G⁻ and Ly6G⁺ cells after chemotherapy in vivo (Fig. 3B and fig. S13, A to D). Moreover, *Fpr1* expression levels increased in bone marrow-derived DC confronted with dying (but not living) cancer cells in vitro (fig. S13, E to G). Ly6C^{high}Ly6G⁻ cells do (whereas Ly6G⁺ cells do not) contribute to the efficacy of anthracycline-based chemotherapy (26). Our results therefore suggest the importance of FPR1 expression in the Ly6C^{high}Ly6G⁻ myeloid cell population, which comprises DCs and their precursors (26). Elevated expression of the human orthologs of all immune-relevant genes influenced by *Fpr1* in mice (Fig. 3A) had a significant ($P < 0.05$) positive effect on the response of breast cancer patients to anthracyclines in four out of five cohorts studied (Fig. 3D), suggesting that these genes are clinically relevant. Moreover, the mutational status of *FPR1* influenced the expression level of several genes involved in antigen presentation within neoplastic lesions of breast cancer patients (fig. S14).

The presence or absence of *Anxa1* (in tumor cells) or that of *Fpr1* (in the host) did not affect the capacity of chemotherapy to elicit autophagy, apoptosis, and necrosis in cancer cells (fig. S15). Moreover, the absence of *Fpr1* in the host did not influence the density of tumor infiltration by CD11c⁺CD86⁺ DCs, macrophages, or granulocytes after chemotherapy (fig. S16A). Morphometric analyses of the ratio between the maximum length and the perpendicular width of tumor-infiltrating myeloid cells, reflecting cellular asymmetry related to migration (27), revealed a selective defect in the chemotherapy-induced elongation of intratumoral DCs (but not macrophages and granulocytes) in *Fpr1*^{-/-} hosts (Fig. 3, E to G, and figs. S16B and S17). Two days after chemotherapy, a sizeable fraction of cancer cells underwent apoptosis and hence contained immunofluorescence

microscopy-detectable active caspase 3 (Casp3a). In WT mice, CD11c⁺CD86⁺ DCs recruited to neoplastic lesions by chemotherapy were closer to the most proximal Casp3a⁺ (dying) cancer cell than to the nearest Casp3a⁻ (live) cancer cell. Indeed, their dead-cell proximity index (DCPI; i.e., the ratio between the distance of CD11c⁺CD86⁺ DCs from Casp3a⁺ cancer cells and the distance of CD11c⁺CD86⁺ DCs from Casp3a⁻ cancer cells) was consistently > 1. Conversely, the DCPI was close to 1 for CD11c⁺CD86⁺ DCs infiltrating tumors treated with anthracyclines in *Fpr1*^{-/-} hosts (Fig. 3, H to J). In accord with its expression pattern (Fig. 3B), *Fpr1* did not influence the DCPI of macrophages, yet affected that of neutrophils (fig. S17D). Thus, FPR1 determines the spatial positioning of DCs with respect to dying cancer cells. Accordingly, *Fpr1* blockade with CsH or *Fpr1* knockout reduced the capacity of intratumoral CD11b⁺Ly6C^{high}Ly6G⁻ cells (which include inflammatory DCs) (28) to acquire antigens from cancers engineered to express green fluorescent protein (GFP) tethered to the inner leaflet of the plasma membrane, in response to chemotherapy (Fig. 4, A and B, and fig. S18A). Moreover, *Fpr1* inhibition interfered with the capacity of tumor-infiltrating CD11b⁺Ly6C^{high}Ly6G⁻ cells to express increased levels of class II major histocompatibility complex (MHC) proteins (I-A/I-E) upon chemotherapy in vivo (Fig. 4, A and B, and fig. S18B). However, *Fpr1* knockout did not affect major DC functions in vitro and did not interfere with the presentation of soluble protein antigen by DC (figs. S19 and S20).

The failure of *Fpr1*^{-/-} DCs to encounter dying cancer cells and to take up tumor antigens should compromise T cell responses. Accordingly, the capacity of chemotherapy to stimulate the intratumoral proliferation of adoptively transferred T cells specific for a model antigen [ovalbumin (OVA)] was attenuated in *Fpr1*^{-/-} mice harboring OVA-expressing MCA205 tumors, as compared with WT mice (fig. S21A). WT DCs purified from OVA-expressing tumors after chemotherapy stimulated OTI responses upon their adoptive transfer into naïve mice, whereas *Fpr1*^{-/-} DCs failed to do so (fig. S21, B and C). Moreover, the frequency of tumor-infiltrating CD3⁺ T cells was increased by anthracycline-based chemotherapy in WT mice but less so in *Fpr1*^{-/-} hosts (Fig. 4, C and D).

The aforementioned results suggest that the initial defect of the *Fpr1*^{-/-} immune system consists in the failure of DCs to migrate toward dying cancer cells. We attempted to explore this hypothesis in vitro. When mouse splenocytes or human peripheral blood mononuclear cells (PBMCs) expressing functional *FPR1* (WT for mice, *FPR1*^{CC} for humans) were confronted with anthracycline-treated WT cancer cells in a microfluidic device (29), they migrated toward dying or dead cells treated with doxorubicin (but not to live untreated cells), and the fraction of leukocytes containing DCs exhibited a prolonged (>60 min) juxtaposition with the corpses (Fig. 4, E and F, and fig. S22A). Conversely, *FPR1*-deficient cells (*Fpr1*^{-/-} for mice, *FPR1*^{CA} or *FPR1*^{4A} for humans) were largely unable to engage in such long-term interactions. Moreover, no stable conjugates were

formed between DCs and dying or dead *Anxa1*^{-/-} cancer cells (Fig. 4, E to J; fig. S22, A and B; fig. S23, A to C; and movies S1 to S24). Prolonged interactions of dying cancer cells with human blood-borne DCs were observed, but only if such DCs expressed functional FPR1 (fig. S22, C and D).

Altogether, our findings underscore the obligate contribution of the interaction between ANXA1 and FPR1 to the immune response against cancer cells succumbing to chemotherapy. Although it does not influence the recruitment of inflammatory DCs (with a CD11c⁺CD86⁺Ly6C^{high} phenotype) to the tumor bed (which depends on other factors, including ATP and chemokines) (26, 28), FPR1 is required for DCs to come into close proximity of dying cancer cells, to establish stable contacts with corpses, to take up tumor-associated antigens, and to cross-present them to T cells. Hence, deficient FPR1 signaling results in defective intratumoral DC maturation and insufficient T cell-mediated anticancer immune responses, ultimately abolishing the efficacy of chemotherapy. Given the high allelic frequency of the loss-of-function *FPR1* SNP rs867228 (17), it will be important to identify means for restoring or bypassing defective FPR1 signaling.

REFERENCES AND NOTES

1. L. Zitvogel, L. Galluzzi, M. J. Smyth, G. Kroemer, *Immunity* **39**, 74–88 (2013).
2. A. Sklan, *Lancet Oncol.* **15**, e422 (2014).
3. C. Denkert et al., *J. Clin. Oncol.* **28**, 105–113 (2010).
4. M. L. Broz et al., *Cancer Cell* **26**, 638–652 (2014).
5. L. Senovilla et al., *Oncol Immunology* **1**, 1323–1343 (2012).
6. L. Senovilla et al., *Science* **337**, 1678–1684 (2012).
7. L. Apetoh et al., *Nat. Med.* **13**, 1050–1059 (2007).
8. G. Kroemer, L. Senovilla, L. Galluzzi, F. André, L. Zitvogel, *Nat. Med.* **21**, 1128–1138 (2015).
9. A. Sistigu et al., *Nat. Med.* **20**, 1301–1309 (2014).
10. G. Kroemer, L. Galluzzi, O. Kepp, L. Zitvogel, *Annu. Rev. Immunol.* **31**, 51–72 (2013).
11. L. Zitvogel, O. Kepp, G. Kroemer, *Cell* **140**, 798–804 (2010).
12. P. E. Marques et al., *Hepatology* **56**, 1971–1982 (2012).
13. B. McDonald et al., *Science* **330**, 362–366 (2010).
14. R. Seifert, K. Wenzel-Seifert, *Life Sci.* **73**, 2263–2280 (2003).
15. K. Wenzel-Seifert, R. Seifert, *Naunyn-Schmiedeberg Arch. Pharmacol.* **367**, 509–515 (2003).
16. H. M. Miettinen, *PLOS ONE* **6**, e28712 (2011).
17. A. Sahagun-Ruiz et al., *Genes Immun.* **2**, 335–342 (2001).
18. F. Ghiringhelli et al., *Nat. Med.* **15**, 1170–1178 (2009).
19. N. Prevete et al., *Oncogene* **34**, 3826–3838 (2015).
20. R. Sun et al., *J. Immunol.* **173**, 428–436 (2004).
21. W. Wang et al., *Cell. Mol. Immunol.* **12**, 615–624 (2015).
22. E. J. Tucker et al., *Cell Metab.* **14**, 428–434 (2011).
23. Y. Li, D. Ye, *J. Mol. Med.* **91**, 781–789 (2013).
24. J. Huang et al., *Br. J. Cancer* **102**, 1052–1060 (2010).
25. A. L. Stenfeldt et al., *Inflammation* **30**, 224–229 (2007).
26. Y. Ma et al., *Immunity* **38**, 729–741 (2013).
27. A. Boissonnas, L. Fetter, I. S. Zeelenberg, S. Hugues, S. Amigorena, *J. Exp. Med.* **204**, 345–356 (2007).
28. Y. Ma et al., *Cancer Res.* **74**, 436–445 (2014).
29. L. Businaro et al., *Lab Chip* **13**, 229–239 (2013).

ACKNOWLEDGMENTS

The data presented in this manuscript are tabulated in the main paper and in the supplementary materials. L.Z. filed a patent (WO2011131472 A1) that relates to the predictive role of SNPs in cancer therapy. G.K. and L.Z. are supported by the Ligue Nationale Contre le Cancer (Équipes Labellisées), Sites de Recherche Intégrées sur le Cancer (SIRIC) Socrates and CarpeM, the Swiss Institute for Experimental Cancer Research (ISREC) Foundation, Agence Nationale pour la Recherche (AUTOPH, Emergence), Cancéropole Ile-de-France, European Commission (ArtForce), European Research Council Advanced Investigator Grant (to G.K.), Fondation pour la Recherche Médicale, Fondation de France, the

LabEx Immuno-Oncology, Institut National du Cancer (INCa), and the Paris Alliance of Cancer Research Institutes. Y.M. is supported by the LabEx Immuno-Oncologie and the Chinese National Thousand Talents Program; H.Y. by the Chinese National Thousand Talents Program; J.L.S. by the Deutsche Forschungsgemeinschaft (SFB704 and SFB645) and the Excellence Cluster ImmunoSensation; F.M. by the Italian Ministry of Health (RF-2011-02347120); G.S. by Associazione Italiana per la Ricerca

sul Cancro (AIRC) (IG 14297); I.V. by AIRC (MFAG 14641), Italian Ministry of Health (RF_GR 2011-2012), and Programma per i Giovani Ricercatori "Rita Levi Montalcini" 2011; and A.S. and G.M. by AIRC.

SUPPLEMENTARY MATERIALS

www.sciencemag.org/content/350/6263/972/suppl/DC1
Materials and Methods

Figs. S1 to S23
Tables S1 to S11
Movies S1 to S24
References (30–40)

26 July 2015; accepted 8 October 2015
Published online 29 October 2015
10.1126/science.1250779

GENE REGULATION

Transcription factor trapping by RNA in gene regulatory elements

Alla A. Sigova,¹ Brian J. Abraham,¹ Xiong Ji,¹ Benoit Molinie,² Nancy M. Hannett,¹ Yang Eric Guo,¹ Mohini Jangi,^{3,4*} Cosmas C. Giallourakis,² Phillip A. Sharp,^{3,4} Richard A. Young^{1,3†}

Transcription factors (TFs) bind specific sequences in promoter-proximal and -distal DNA elements to regulate gene transcription. RNA is transcribed from both of these DNA elements, and some DNA binding TFs bind RNA. Hence, RNA transcribed from regulatory elements may contribute to stable TF occupancy at these sites. We show that the ubiquitously expressed TF Yin-Yang 1 (YY1) binds to both gene regulatory elements and their associated RNA species across the entire genome. Reduced transcription of regulatory elements diminishes YY1 occupancy, whereas artificial tethering of RNA enhances YY1 occupancy at these elements. We propose that RNA makes a modest but important contribution to the maintenance of certain TFs at gene regulatory elements and suggest that transcription of regulatory elements produces a positive-feedback loop that contributes to the stability of gene expression programs.

Active promoter and enhancer elements are transcribed bidirectionally (Fig. 1A) (1–3). Although various models have been proposed for the roles of RNA species produced from these regulatory elements, their functions are not fully understood (4–13). Evidence that some DNA binding transcription factors (TFs) also bind RNA (14, 15) led us to consider the possibility that there might be a direct and general role for promoter-proximal and -distal enhancer RNA in the binding and maintenance of TFs at regulatory elements.

We used global run-on sequencing (GRO-seq) to sequence nascent transcripts in murine embryonic stem cells (ESCs) at great depth, which confirmed that active promoter and enhancer elements are generally transcribed bidirectionally (Fig. 1B, fig. S1A, and table S1) (see also supplementary materials and methods). We then focused our studies on the TF Yin-Yang 1 (YY1), because it is ubiquitously expressed in mammalian cells, plays key roles in normal development, and can bind RNA species *in vitro* (15, 16). Chromatin immunoprecipitation sequencing (ChIP-seq) analysis in ESCs revealed that YY1

binds to both active enhancers and promoters, with some preference for promoters (Fig. 1, C and D, fig. S1, and table S2). In contrast, the pluripotency TF OCT4 preferentially occupies enhancers (fig. S1B). Consistent with this, YY1 sequence motifs were enriched at promoters, whereas OCT4 motifs were enriched at enhancers (fig. S1B). Neither YY1 nor OCT4 occupied the promoter-proximal sequences of inactive genes (fig. S2). These results establish that YY1 generally occupies active enhancer and promoter-proximal elements in ESCs.

We next used cross-linking immunoprecipitation sequencing (CLIP-seq) in ESCs to investigate YY1 binding to RNA *in vivo* (figs. S3 and S4 and table S3). Our results showed that YY1 binds RNA species at the active enhancer and promoter regions where it is bound to DNA (Fig. 1, C and D, and fig. S1C). At promoters, YY1 preferentially occupied RNA downstream rather than upstream of transcription start sites (fig. S1B), consistent with YY1 motif distribution and evidence that upstream noncoding RNA is unstable (3, 17, 18). In similar experiments with OCT4, substantial levels of RNA binding were not observed (fig. S5). These results suggest that YY1 generally binds to RNA species transcribed from enhancers and promoters *in vivo*.

The DNA and RNA binding properties of YY1 were further investigated *in vitro* (Fig. 2 and figs. S6 to S8). The recombinant YY1 protein bound both DNA and RNA probes in electrophoretic mobility shift assays (EMSA), showing greater

affinity for DNA than for RNA. The affinity of YY1 varied for different RNA sequences (fig. S8). The four YY1 zinc fingers can bind DNA (19), but the portion of YY1 that interacts with RNA is unknown. The zinc finger-containing C-terminal region and the N-terminal region of YY1 were purified, and their DNA and RNA binding properties were further investigated (fig. S9). The zinc finger region of YY1 bound to DNA but not to RNA, whereas the N-terminal region of YY1 bound to RNA (fig. S9). Furthermore, the DNA probe did not compete efficiently with the RNA probe for YY1 binding (figs. S7C and S8C). These results suggest that different regions of YY1 are responsible for binding to DNA and RNA.

The observation that YY1 binds to enhancer and promoter-proximal elements and to RNA transcribed from those regions led us to postulate that nascent RNA contributes to stable TF occupancy at these regulatory elements (Fig. 3A). If this model is correct, then reduced levels of nascent RNA at promoters and enhancers might lead to reduced YY1 occupancy at these sites. We briefly inhibited transcription elongation with the reversible inhibitor *N*-rybofuranosylbenzimidazole (DRB) to reduce RNA levels at promoters and enhancers without causing changes in the steady-state levels of YY1 (figs. S10 and S11). DRB treatment reduced transcription at promoters and enhancers, which caused a small but significant decrease in the levels of YY1 at these regions (fig. S10). Super-enhancers are clusters of enhancers that are highly transcribed (20), and DRB treatment had a profound effect on transcription at these sites (fig. S10). Similar results were observed with additional inhibitors (fig. S10). When transcription was allowed to resume after DRB removal, the levels of YY1 increased at promoters and enhancers (Fig. 3B and fig. S10A). These results suggest that nascent RNA produced at promoters and enhancers contributes to YY1 binding to these elements.

The exosome reduces the levels of enhancer RNAs once they are released from RNA polymerase II (degradation is 3' to 5') (21), so knockdown of an exosome component will cause an increase in untethered enhancer RNA, which might titrate some YY1 away from enhancers. Indeed, exosome knockdown led to increased steady-state levels of enhancer RNAs and a decrease in the levels of YY1 bound to enhancers (Fig. 3C and fig. S12). These results are consistent with the model that YY1 binding to DNA is stabilized by binding to nascent RNA.

If YY1 binding to DNA is stabilized by its binding to RNA, then ribonuclease (RNase) treatment of chromatin should reduce YY1 occupancy. Chromatin was extracted from ESC nuclei, and

¹Whitehead Institute for Biomedical Research, Cambridge, MA 02142, USA. ²Massachusetts General Hospital, Harvard Medical School, Boston, MA 02114, USA. ³Department of Biology, Massachusetts Institute of Technology, Cambridge, MA 02142, USA. ⁴David H. Koch Institute for Integrative Cancer Research, Cambridge, MA 02140, USA.
*Present address: Biogen, Cambridge, MA 02142, USA.
†Corresponding author. E-mail: young@wi.mit.edu

the levels of YY1 in the chromatin preparation were compared with and without RNase A treatment (Fig. 3D). The results show that the levels of YY1 bound to chromatin were significantly decreased when the chromatin preparation was treated with RNase, consistent with the idea that RNA contributes to the stability of YY1 in chromatin.

To test the idea that RNA near regulatory elements can contribute to stable TF occupancy *in vivo*, we tethered RNA in the vicinity of YY1 binding sites at six different enhancers in ESCs using the CRISPR/Cas9 (clustered regularly interspaced short palindromic repeats/CRISPR-associated protein 9) system and determined whether the tethered RNA increases the occupancy of YY1 at these enhancers (Fig. 4). We generated stable murine ESC lines expressing both the catalytically inactive form of bacterial endonuclease Cas9 (dCas9) and a fusion RNA composed of single guide RNA (sgRNA), trans-activating CRISPR RNA (tracrRNA), and a 60-nucleotide (nt) RNA derived from the promoter sequence of *Arid1a*, compatible with YY1 binding *in vitro* (fig. S8). For controls, stable cell lines were created that express dCas9 and sgRNA fused to tracrRNA for the six enhancers. Tethering the *Arid1a* RNA at each enhancer led to increased binding of YY1 to the targeted enhancer, as measured by ChIP-quantitative polymerase chain reaction (qPCR) (Fig. 4B). This elevation in YY1 binding was specific to the targeted locus and the sequence of tethered RNA, as there was no observable increase in YY1 binding at the enhancers not targeted in the same cells (Fig. 4B) or targeted with tethered RNA not compatible with YY1 binding *in vitro* (fig. S13). These results show that RNA tethered near regulatory elements *in vivo* can enhance the level of YY1 occupancy at these elements.

To corroborate the *in vivo* RNA tethering results, we used a competition EMSA to test whether tethered RNA increases the apparent binding affinity of YY1 to its motif in DNA (fig. S14 and S15). A 30-base pair (bp) labeled DNA probe containing a consensus YY1 binding motif was incubated with recombinant YY1 protein in the presence of increasing concentrations of cold competitor DNA with tethered or untethered RNA, and the amount of radiolabeled DNA that remained bound was quantified (fig. S15). This analysis revealed that DNA containing tethered RNA outcompetes the DNA with untethered RNA for YY1 binding. These results indicate that tethering RNA near the YY1 binding motif in DNA leads to increased binding of YY1 to DNA *in vitro*.

In summary, our results are consistent with the proposal that RNA enhances the level of YY1 occupancy at active enhancer and promoter-proximal regulatory elements (Fig. 3A). We suggest that nascent RNA produced in the vicinity of enhancer and promoter elements captures dissociating YY1 via relatively weak interactions, which allows this TF to rebind to nearby DNA sequences, thus creating a kinetic sink that increases YY1 occupancy on the regulatory element. The observation that YY1 occupies active enhancers and promoters throughout the ESC genome where RNA is produced, coupled with evidence that

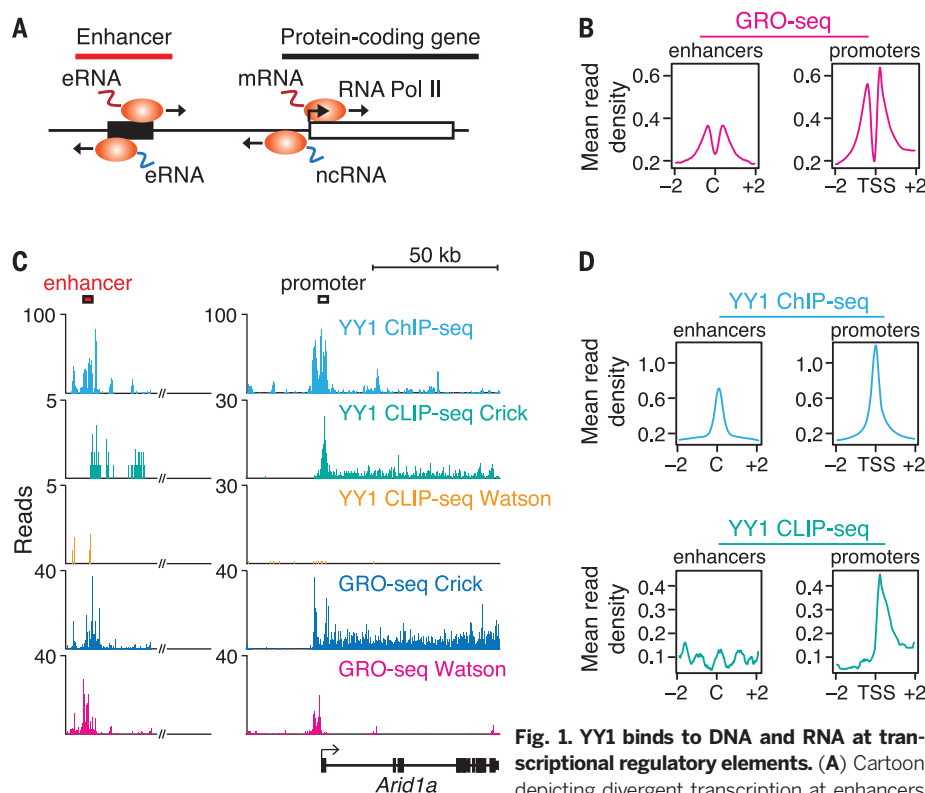


Fig. 1. YY1 binds to DNA and RNA at transcriptional regulatory elements. (A) Cartoon depicting divergent transcription at enhancers and promoters in mammalian cells. eRNA, enhancer RNA; ncRNA, noncoding RNA; RNA Pol II, RNA polymerase II. (B) Alignment of GRO-seq reads at all enhancers and promoters in ESCs. Enhancers were defined as in (23). The x axis indicates distance from either the enhancer center (C) or the transcription start site (TSS) in kilobases. The y axis indicates average density of uniquely mapped GRO-seq reads per genomic bin. (C) Gene tracks for the *Arid1a* gene and enhancer, showing ChIP-seq and CLIP-seq data, as well as GRO-seq reads for murine ESCs. kb, kilobases. (D) Mean read density of YY1 ChIP-seq and CLIP-seq reads at enhancers and promoters of all National Center for Biotechnology Information RefSeq genes in ESCs.

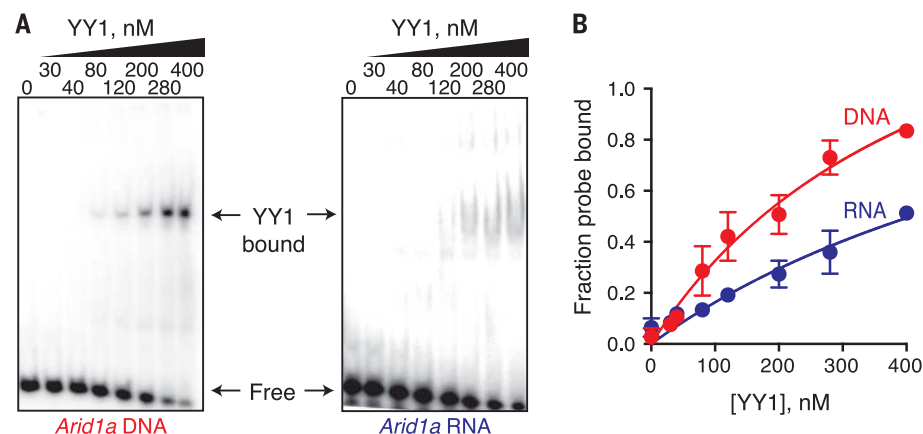


Fig. 2. YY1 binds to DNA and RNA *in vitro*. (A) (Left) EMSA of YY1-DNA complexes at different concentrations of recombinant YY1. A radioactively labeled 30-bp DNA probe (5 nM), derived from the promoter region of the *Arid1a* gene containing a consensus YY1 binding motif (CTCTTCTCTCTTAAATGCGCTGCTGCTG), was incubated with increasing concentrations of recombinant YY1 protein. (Right) EMSA of YY1-RNA complexes at different concentrations of recombinant YY1. A radioactively labeled 30-nt RNA probe (5 nM) derived from the same region of the *Arid1a* gene was incubated with increasing concentrations of recombinant YY1 protein. (B) Graph depicting the relation between the fraction of bound radioactively labeled DNA or RNA probe and the concentration of recombinant YY1 in the binding reaction. Error bars indicate SDs from the mean values.

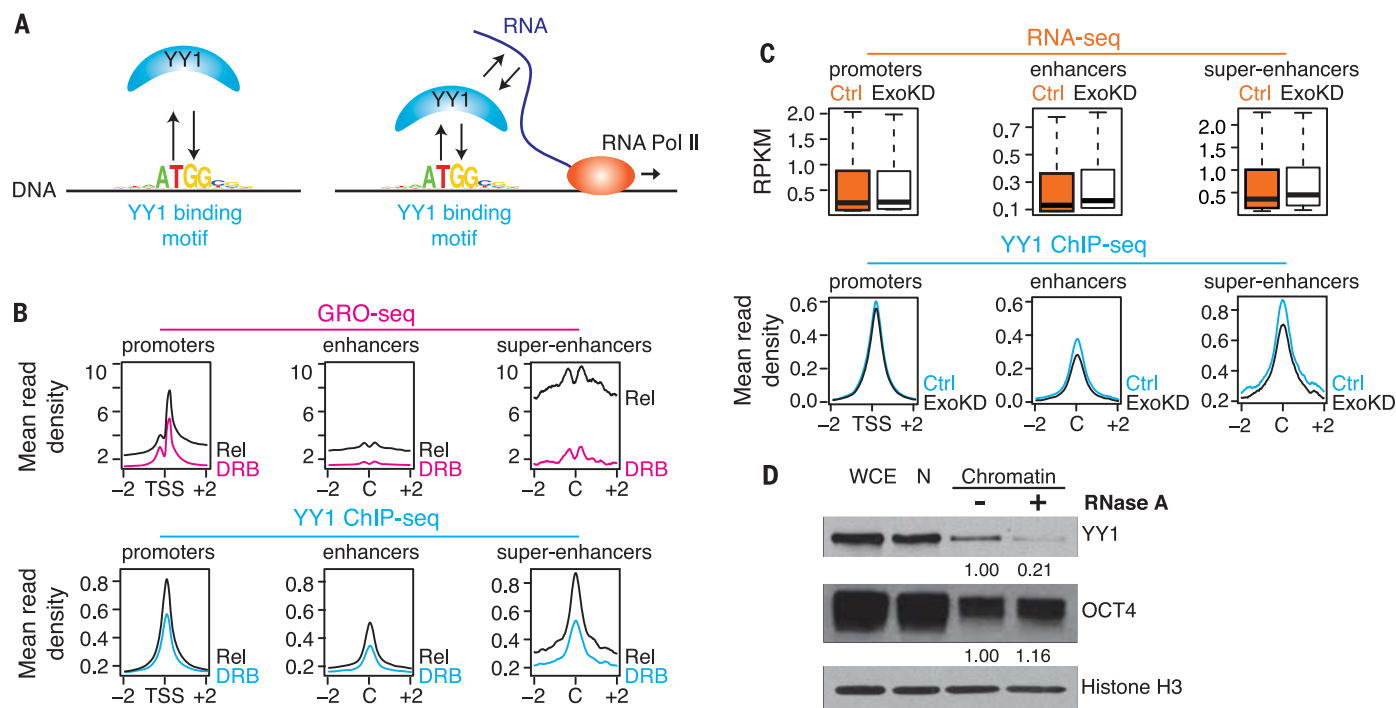


Fig. 3. Perturbation of RNA levels affects YY1 binding to DNA. (A) Cartoon depicting the hypothesis that RNA transcribed from regulatory elements enhances occupancy of these elements by TFs capable of binding both DNA and RNA. (B) (Top) GRO-seq reads (24) at promoters, enhancers, and super-enhancer constituents in cells before (DRB) and after release (Rel) from transcriptional inhibition by DRB. (Bottom) YY1 ChIP-seq reads at promoters, enhancers, and super-enhancer constituents in cells before and after release from transcriptional inhibition by DRB. The increase in YY1 binding after release from DRB inhibition is significant: $P < 3.6 \times 10^{-207}$ for promoters, $P < 1.6 \times 10^{-214}$ for enhancers, and $P < 9.8 \times 10^{-37}$ for super-enhancer constituents. (C) (Top) Box plots depicting RNA-seq data for ribo-depleted total RNA at

promoters, enhancers, and super-enhancer constituents in ESCs after targeting with control (Ctrl) or *Exosc3* (ExoKD) short hairpin RNA (shRNA). RPKM, reads per kilobase per million mapped reads. (Bottom) Alignment of YY1 ChIP-seq reads at promoters, enhancers, and super-enhancer constituents in ESCs after targeting with control or *Exosc3* shRNA. The decrease in YY1 binding in ExoKD ESCs is significant: $P < 8.1 \times 10^{-9}$ for promoters, $P < 1.8 \times 10^{-27}$ for enhancers, and $P < 3.3 \times 10^{-5}$ for super-enhancer constituents. (D) Western blot analysis of YY1, OCT4, and histone H3 levels in whole-cell extracts (WCE), nuclei (N), and a nuclear chromatin preparation before and after treatment with RNase A. Histone H3 serves as a loading control, and OCT4 serves as a negative control. Relative levels of YY1 and OCT4 are noted.

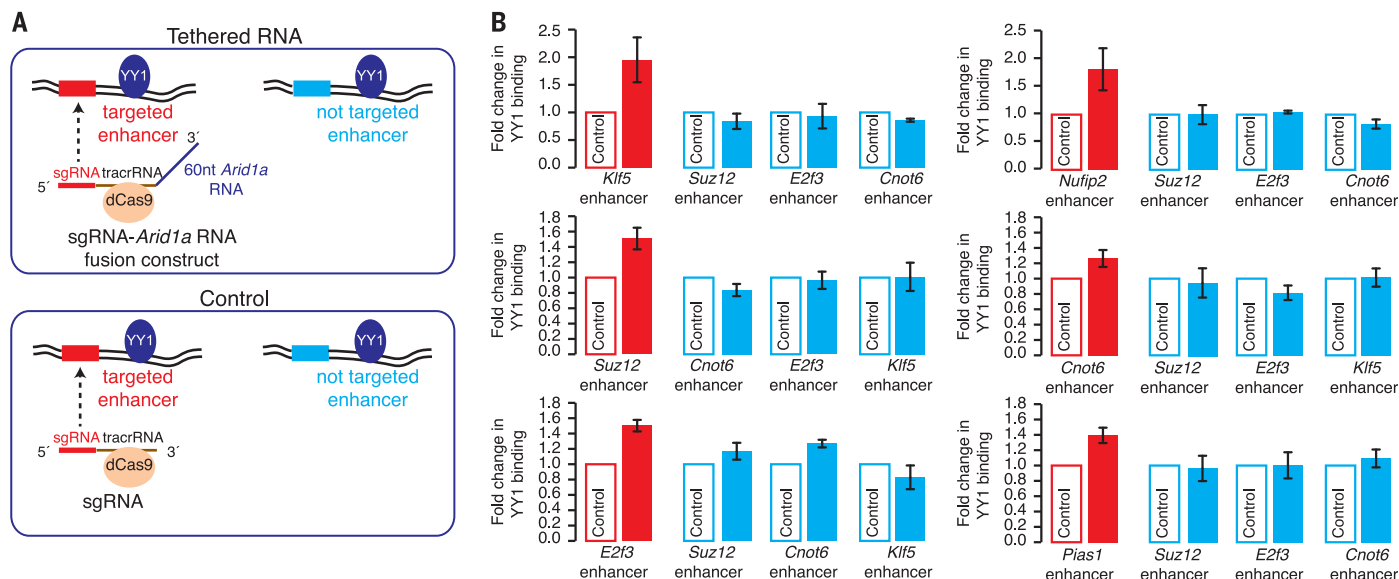


Fig. 4. Tethering of RNA adjacent to a YY1 DNA binding site enhances binding of YY1 to the genome in vivo. (A) Strategy for tethering of RNA in the vicinity of a YY1 binding site at enhancers in vivo. (B) ChIP-qPCR analysis of YY1 binding at six targeted (red) and three nontargeted (blue) enhancers in three independent experiments. The y axis indicates fold change in YY1 binding in ESCs expressing the sgRNA-*Arid1a* RNA fusion construct relative to cells expressing the control sgRNA targeted to the same locus. The difference in YY1 binding was significant for the targeted enhancers [*Klf5* ($P = 0.03$), *Suz12* ($P = 0.01$), *E2f3* ($P = 0.01$), *Nufip2* ($P = 0.03$), *Cnot6* ($P = 0.03$), and *Pias1* ($P = 0.01$)] but not for the nontargeted enhancers. Error bars indicate SDs from the mean values.

YY1 is expressed in all mammalian cells, suggests that this model is general. There are additional DNA binding TFs that can bind RNA (fig. S16) (14), so transcriptional control may generally involve a positive-feedback loop, where YY1 and other TFs stimulate local transcription, and newly transcribed nascent RNA reinforces local TF occupancy. This model helps explain why TFs occupy only the small fraction of their consensus motifs in the mammalian genome where transcription is detected, and it suggests that bidirectional transcription of active enhancers and promoters evolved, in part, to facilitate trapping of TFs at specific regulatory elements. The model also suggests that transcription of regulatory elements produces a positive-feedback loop that may contribute to the stability of gene expression programs in cells. The contribution of this TF trapping mechanism to cellular regulation has yet to be established but will be important to elucidate in future studies because much disease-associated sequence variation occurs in enhancers (20, 22) and may thus affect both DNA and RNA sequences that interact with gene regulators.

REFERENCES AND NOTES

1. L. J. Core, J. J. Waterfall, J. T. Lis, *Science* **322**, 1845–1848 (2008).
2. A. C. Seila et al., *Science* **322**, 1849–1851 (2008).
3. A. A. Sigova et al., *Proc. Natl. Acad. Sci. U.S.A.* **110**, 2876–2881 (2013).
4. T. K. Kim et al., *Nature* **465**, 182–187 (2010).
5. D. Wang et al., *Nature* **474**, 390–394 (2011).
6. C. A. Melo et al., *Mol. Cell* **49**, 524–535 (2013).
7. F. Lai et al., *Nature* **494**, 497–501 (2013).
8. M. T. Lam et al., *Nature* **498**, 511–515 (2013).
9. W. Li et al., *Nature* **498**, 516–520 (2013).
10. M. U. Kaikkonen et al., *Mol. Cell* **51**, 310–325 (2013).
11. K. Mousavi et al., *Mol. Cell* **51**, 606–617 (2013).
12. A. Di Ruscio et al., *Nature* **503**, 371–376 (2013).
13. K. Schaukowitch et al., *Mol. Cell* **56**, 29–42 (2014).
14. L. A. Cassidy, L. J. Maher III, *Nucleic Acids Res.* **30**, 4118–4126 (2002).
15. Y. Jeon, J. T. Lee, *Cell* **146**, 119–133 (2011).
16. S. Gordon, G. Akopyan, H. Garban, B. Bonavida, *Oncogene* **25**, 1125–1142 (2006).
17. R. A. Flynn, A. E. Almada, J. R. Zamudio, P. A. Sharp, *Proc. Natl. Acad. Sci. U.S.A.* **108**, 10460–10465 (2011).
18. P. Preker et al., *Science* **322**, 1851–1854 (2008).
19. H. B. Houbaviy, A. Usheva, T. Shenk, S. K. Burley, *Proc. Natl. Acad. Sci. U.S.A.* **93**, 13577–13582 (1996).
20. D. Hnisz et al., *Cell* **155**, 934–947 (2013).
21. M. Lubas et al., *Cell Reports* **10**, 178–192 (2015).
22. M. T. Maurano et al., *Science* **337**, 1190–1195 (2012).
23. W. A. Whyte et al., *Cell* **153**, 307–319 (2013).
24. L. Wang et al., *Nature* **523**, 621–625 (2015).

ACKNOWLEDGMENTS

We thank D. Orlando, C. Lin, V. Saint-André, Z. P. Fan, L. Zhang, and A. Chiu for help with computational analysis and advice. The lentiviral dCas9 and sgRNA expression plasmids are available from Addgene under the Uniform Biological Material Transfer Agreement. This work was supported by NIH grant HG002668 (R.A.Y.), the Hope Funds for Cancer Research (B.J.A.), the Cancer Research Institute (Y.E.G.), and Biogen (R.A.Y.). The Whitehead Institute intends to file a patent application that relates to transcription factor trapping by RNA. R.A.Y. is a founder of Syros Pharmaceuticals.

SUPPLEMENTARY MATERIALS

www.sciencemag.org/content/350/6263/978/suppl/DC1
Materials and Methods
Figs. S1 to S16
Tables S1 to S3
References (25–50)

29 August 2015; accepted 14 October 2015
Published online 29 October 2015
10.1126/science.123346

IMMUNOLOGY

Tissue residency of innate lymphoid cells in lymphoid and nonlymphoid organs

Georg Gasteiger,^{1,2,*} Xiying Fan,¹ Stanislav Dikiy,¹
Sue Y. Lee,¹ Alexander Y. Rudensky^{1*}

Innate lymphoid cells (ILCs) contribute to barrier immunity, tissue homeostasis, and immune regulation at various anatomical sites throughout the body. How ILCs maintain their presence in lymphoid and peripheral tissues thus far has been unclear. We found that in the lymphoid and nonlymphoid organs of adult mice, ILCs are tissue-resident cells that were maintained and expanded locally under physiologic conditions, upon systemic perturbation of immune homeostasis and during acute helminth infection. However, at later time points after infection, cells from hematogenous sources helped to partially replenish the pool of resident ILCs. Thus, ILCs are maintained by self-renewal in broadly different microenvironments and physiological settings. Such an extreme “sedentary” lifestyle is consistent with the proposed roles of ILCs as sentinels and local keepers of tissue function.

Tissue-resident leukocytes can be categorized by their cellular origin and means of maintenance as either self-renewing cells that seed nonlymphoid organs during ontogeny or cells that are replenished hematogenously from precursors in the bone marrow (BM) or secondary lymphoid organs (SLOs), such as the spleen and lymph nodes (LNs). Innate lymphoid cells (ILCs) have been identified in embryonic tissues, BM, SLOs, peripheral blood, and many nonlymphoid tissues, including mucosal sites such as the lung and small intestine, where they contribute to tissue immunosurveillance, immunoregulation, repair, and homeostasis (1, 2). How ILC populations in lymphoid and nonlymphoid organs are maintained, and whether ILCs recirculate from lymphoid to nonlymphoid tissues, have been controversial questions. Based on the identification of fetal ILC progenitors that seed the mouse intestine (3) and the proposed development of ILCs in human tonsils (4), it is reasonable to expect that ILCs may self-renew locally or be generated from immature precursors in these tissues. However, recent studies have identified progenitors to all currently known ILC subsets in adult BM, raising the possibility that ILCs in lymphoid and nonlymphoid organs are continuously replenished through medullary lymphopoiesis and subsequent recruitment to peripheral tissues (5, 6).

To directly test whether hematogenous precursors continuously replenish the pool of pe-

ripheral tissue ILCs in adult mice, we generated parabiotic mice, which establish blood chimerism through joint circulation (7, 8). Congenically marked CD45.1⁺ and CD45.2⁺ mice were surgically connected for 30 to 40 days until complete chimerism (~50:50 ratio of CD45.1⁺ to CD45.2⁺) of major lymphocyte populations was established in the peripheral blood and spleens of the parabionts (fig. S1). We analyzed the percentages of cells that derived from the donor or host parabiont for currently known populations of “helper-like” ILCs, including Lin[−]RORγt⁺Eomes[−]NK1.1⁺ ILC1, Lin[−]RORγt⁺GATA-3⁺ ILC2, Lin[−]RORγt⁺CD4[−] ILC3, and Lin[−]RORγt⁺CD4⁺ lymphoid tissue inducer (LTi) cells (fig. S2). We found that >95% of ILC1, ILC2, ILC3, and LTi cells residing in the small intestine lamina propria, salivary gland, lung, and liver (9) were of host origin, indicating that these ILC types are bona fide tissue-resident cells (Fig. 1, A to C, and fig. S3). One exception to the overwhelming tissue residency of ILCs were Eomes[−]NK1.1⁺ ILC1s in the lung and peripheral blood, which originated from both parabionts (fig. S3). Because cells isolated from enzymatically dissociated lung tissue include cells from both the vasculature and the parenchyma (10), we injected parabiotic mice intravenously with fluorescently labeled antibody to CD45 5 min before mice were euthanized, in order to identify intravascular leukocytes. This revealed that virtually all ILC2s, but only ~20% of Eomes[−]NK1.1⁺ ILC1s, localized to the lung parenchyma (Fig. 1, D and E, and fig. S3). In contrast to intravascular ILC1s, which derived evenly from both parabionts (Fig. 1E and fig. S3), extravascular ILC1s were >90% host-derived. This observation suggests that these cells are lung parenchymal ILC1s that do not continuously exchange with and are distinguishable from their intravascular counterparts, in agreement with the observation that Eomes[−]NK1.1⁺ ILC1s in the

¹Howard Hughes Medical Institute, Immunology Program, and Ludwig Center, Memorial Sloan Kettering Cancer Center, New York, NY 10065, USA. ²Institute of Medical Microbiology and Hygiene, University of Mainz Medical Centre, Mainz 55131, Germany.

*Corresponding author. E-mail: gasteiger@uni-mainz.de (G.G.); rudenska@mskcc.org (A.Y.R.) †These authors contributed equally to this work.

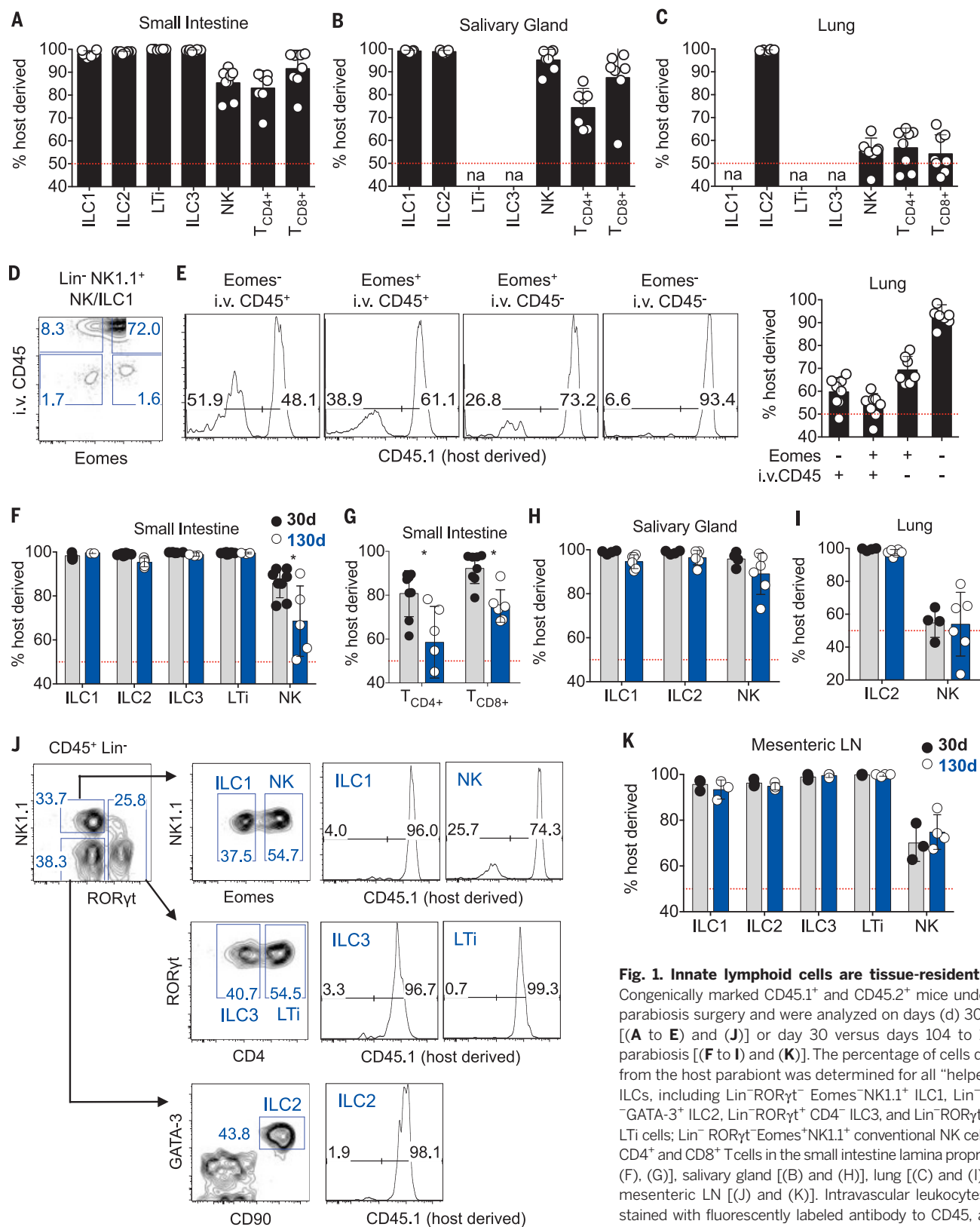


Fig. 1. Innate lymphoid cells are tissue-resident cells.

Congenically marked CD45.1⁺ and CD45.2⁺ mice underwent parabiosis surgery and were analyzed on days (d) 30 to 40 [(A to E) and (J)] or day 30 versus days 104 to 130 of parabiosis [(F to I) and (K)]. The percentage of cells derived from the host parabiont was determined for all “helper-like” ILCs, including Lin⁻RORγt⁻Eomes⁻NK1.1⁺ ILC1, Lin⁻RORγt⁻GATA-3⁺ ILC2, Lin⁻RORγt⁺CD4⁻ ILC3, and Lin⁻RORγt⁺CD4⁺ LTi cells; Lin⁻RORγt⁻Eomes⁺NK1.1⁺ conventional NK cells; and CD4⁺ and CD8⁺ T cells in the small intestine lamina propria [(A), (F), (G)], salivary gland [(B) and (H)], lung [(C) and (I)], and mesenteric LN [(J) and (K)]. Intravascular leukocytes were stained with fluorescently labeled antibody to CD45, administered intravenously 5 min before the isolation and analysis of

lung leukocytes on day 40 of parabiosis [(D) and (E)]. In the bar graphs, each circle represents an individual parabiont. The red dotted line at 50% marks complete chimerism (equal contribution from host and donor parabionts). The data are shown as mean ± SD and represent two or three independent experiments (*n* = 4 to 8 parabionts; na, not analyzed; **P* < 0.05). In (D), (E), and (J), numbers in the plot indicate the percentage of cells in the respective gates.

small intestine, salivary gland, and liver were also overwhelmingly of host origin. Together, these experiments identified all analyzed ILC types as tissue-resident cells in all examined non-lymphoid organs.

Next, we explored whether the long-term maintenance of tissue-resident ILCs was accomplished through self-renewal or through progressive replacement by hematogenous precursors. We analyzed mice that had been in parabiosis for >3 months and found that all analyzed ILC subsets remained >95% host-derived in all non-lymphoid organs tested (Fig. 1, F to I, and fig. S4). In contrast, conventional natural killer (NK) and T lymphocytes, which appeared relatively tissue-resident in the small intestine in our analysis at day 30 to 40 of parabiosis, had equilibrated with donor-derived cells at 3 months (Fig. 1, F and G). However, over time, we did detect a minor increase from <2 to ~5% donor-derived cells for ILC2s in the small intestine and ILC1s in the salivary gland, which we did not observe

for the other ILC subsets (fig. S4). Therefore, although our data are consistent with a minor contribution of hematogenous precursors (5, 6) or circulating mature ILCs (17) to the physiologic renewal of ILC subsets, the majority of ILCs appear to be tissue-resident cells that are locally maintained in peripheral organs. This is in contrast to, for example, the progressive replacement of tissue-resident embryonic macrophages in some adult tissues, such as the intestine, which experience constant immune stimulation and tissue renewal (12).

Our observation of tissue-resident ILCs in non-lymphoid tissues raised the question of whether ILCs in SLOs are replenished from hematogenous sources or whether they also are locally renewing cells. Unexpectedly, our analysis of mesenteric LNs and spleens of parabiotic mice showed that all ILC subsets tested were >95% host-derived at both 1 and 3 months (Fig. 1, J and K, and fig. S5), demonstrating that ILCs establish tissue residency in both lymphoid and nonlymphoid organs.

Although ILCs that leave peripheral tissues via afferent lymphatics can contribute to ILC populations in draining LNs (13), the identification of tissue-resident ILCs in the spleen, which does not recruit cells via afferent lymphatics, further supports the idea of ILC residency in SLOs. The regional maintenance of ILCs in SLOs thus distinguishes helper-like ILCs from developmentally related NK cells (“killer” ILCs), which, like $\alpha\beta$ T cells, are continuously replaced by BM-derived precursors and recirculate systemically and through SLOs. Nevertheless, Eomes⁺ conventional NK cells can also establish tissue residency in some organs—e.g., the salivary gland and small intestine (Fig. 1) (9, 14).

To test whether the tissue residency of ILCs is maintained under inflammatory conditions, we generated parabiotic *Foxp3^{DTR}* mice. In these mice, *Foxp3*⁺ regulatory T (T_{reg}) cells express the human diphtheria toxin receptor (DTR) under the control of the endogenous *Foxp3* locus (15). Upon administration of diphtheria toxin (DTX),

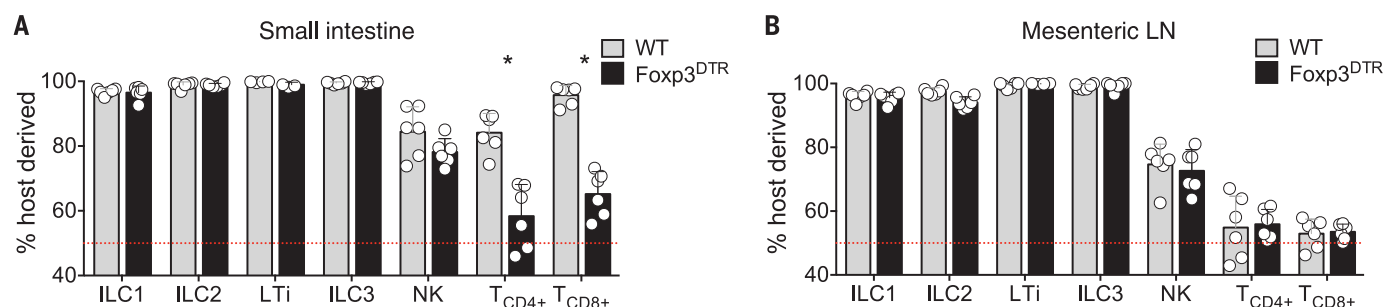


Fig. 2. Tissue residency of ILCs is maintained upon systemic immune activation. Congenically marked pairs of *Foxp3^{DTR}* or wild-type (WT) control mice underwent parabiosis surgery. After 40 days, both mice within *Foxp3^{DTR}* or WT pairs were subjected to diphtheria toxin (DTX) treatment. For the indicated populations of lymphocytes, the percentage of host-derived cells was analyzed in the small intestine lamina propria (A) and mesenteric LN (B) on day 9 of DTX. Each circle represents an individual parabiont. The data are shown as mean \pm SD and were pooled from two independent experiments ($n = 6$ parabionts).

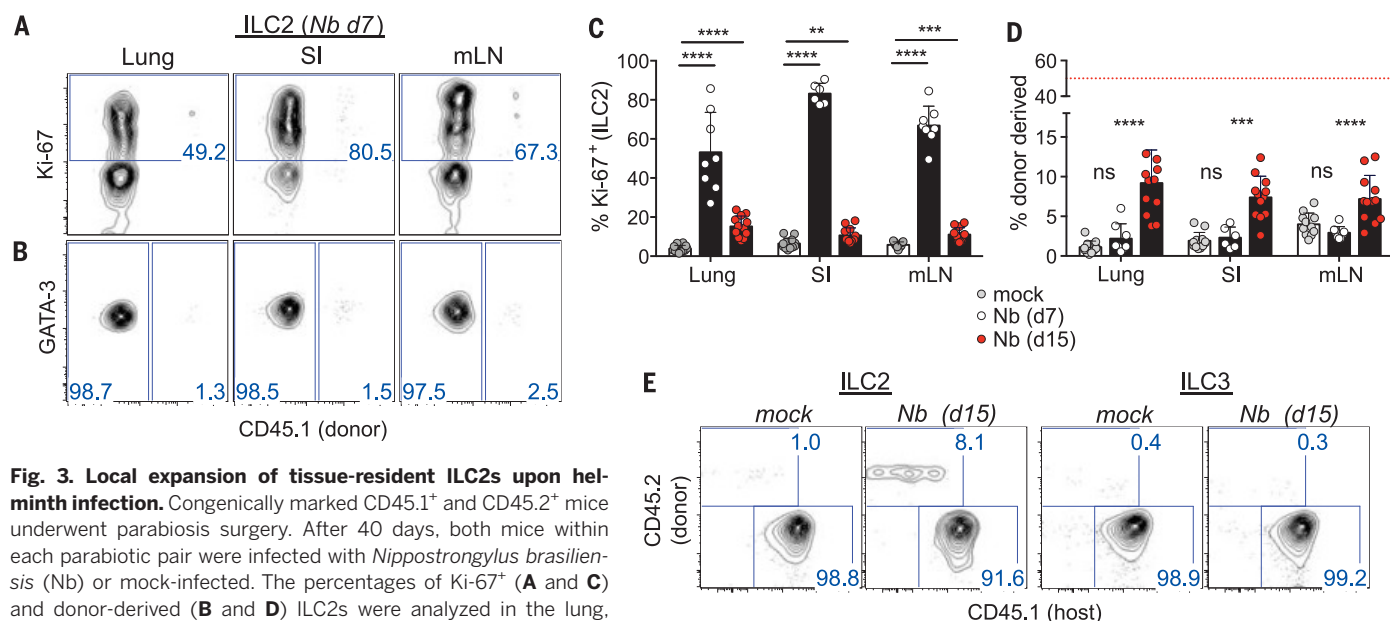


Fig. 3. Local expansion of tissue-resident ILC2s upon helminth infection. Congenically marked CD45.1⁺ and CD45.2⁺ mice underwent parabiosis surgery. After 40 days, both mice within each parabiotic pair were infected with *Nippostrongylus brasiliensis* (Nb) or mock-infected. The percentages of Ki-67⁺ (A and C) and donor-derived (B and D) ILC2s were analyzed in the lung, small intestine lamina propria, and mesenteric LN on days 7 and 15 after infection. (E) Analysis of ILC2s and ILC3s in the small intestine lamina propria on day 15 after infection. In the bar graphs, each symbol represents an individual parabiont. The data are shown as mean \pm SD and represent two or three independent experiments ($n = 6$ to 12 parabionts; ** $P < 0.01$; *** $P < 0.001$; **** $P < 0.0001$; ns, not significant).

the depletion of T_{reg} cells initiates a systemic lymphoproliferative syndrome and fatal autoimmunity (15, 16). Unexpectedly, we failed to detect an increased contribution of hematogenous cells to the expanded ILC populations in the analyzed organs of parabiotic mice depleted of T_{reg} cells (Fig. 2 and fig. S6). This suggests that the mobilization of ILCs or ILC precursors into peripheral tissues is negligible even during systemic autoimmunity, and that the associated increase in ILC populations in lymphoid and non-lymphoid organs probably results from local expansion, despite the influx of hematogenously derived myeloid cells and adaptive lymphocytes (15, 16).

Next, we examined whether local ILC expansion is observed during infection with a helminth, *Nippostrongylus brasiliensis* (Nb) (17), that induces strong proliferation and activation of ILC2s in the lung and small intestine. Recent work suggests that Nb infection triggers the appearance of “inflammatory” ILC2s that differentiate further to “natural” ILC2s to sustain the expansion of ILC2s necessary for worm expulsion (18). To determine whether the ILC response in this setting is due to the mobilization of inflammatory ILCs from the BM or elsewhere, or to local differentiation and expansion, we infected parabiotic mice with Nb and analyzed ILC2s during the acute phase of helminth infection (day 7 after infection). At this time point, ILC2s in the lung, small intestine, and mesenteric LN remained host-derived, despite their robust proliferation and expansion (Fig. 3, A to

D). In contrast, we observed a small but statistically significant increase in donor-derived ILC2s during the chronic inflammation phase on day 15 after infection (Fig. 3, C and D) (19, 20). At this time point, ILC2s continued to exhibit increased proliferation (Fig. 3C) and have been shown to serve critical functions in tissue repair (21). Thus, the local expansion of resident ILCs during the acute phase of Nb infection is followed by moderately increased hematogenous recruitment or redistribution of ILCs during the chronic inflammation and repair phase. The increase in donor-derived cells was specific to ILC2s among innate immune cell types; we could not detect any increase in donor-derived ILC3s or tissue-resident alveolar macrophages (Fig. 3E and fig. S7). However, even at this later stage, >90% of ILC2s originated from the host parabiont.

The local proliferation of tissue-resident ILCs led us to ask whether these cells can access the cytokine interleukin (IL)-2, whose availability in lymphoid organs is controlled by T_{reg} cells (22) but whose physiological relevance to ILC responses in nonlymphoid tissues has been controversial. For this purpose, we generated mixed bone marrow chimeras harboring both wild-type ILCs and ILCs deficient in CD25, the high-affinity α -chain of the IL-2 receptor (Fig. 4A), as previously described (23). We found that CD25-sufficient (wild-type) and CD25-deficient ILC2s proliferated to a similar extent and were found at equal ratios in Nb-infected and mock-infected chimeric mice, indicating that IL-2 did not directly influence the proliferation of ILC2s in re-

sponse to Nb infection (Fig. 4, B and C). However, we observed that CD25-sufficient ILC2s produced more IL-13 (Fig. 4D), which is required for worm expulsion. These results demonstrate that ILC2s can indeed access physiological levels of IL-2 in nonlymphoid organs, supporting the notion that one function of locally produced IL-2 may be to modulate ILC effector function (22, 24, 25). We previously suggested competition for IL-2 as one mechanism by which $Foxp3^+$ T_{reg} cells could restrain the homeostasis of splenic ILC1s (23). It remained unclear in that study whether T_{reg} cells are able to restrain IL-2-dependent ILC activation in nonlymphoid tissues, where they form co-clusters with ILC2s (26). We found that transient depletion of T_{reg} cells induced the IL-2- and CD25-dependent proliferation of ILC2s (Fig. 4, E to G), suggesting that ILC2s can directly access IL-2 in the lung and the small intestine and that T_{reg} cells restrain the IL-2-dependent expansion of these tissue-resident ILCs.

Our experiments identified ILCs in both lymphoid and nonlymphoid organs as tissue-resident cells that are locally renewed and expanded in response to acute environmental challenges. These findings also suggest that the plasticity of ILCs—exemplified by the differentiation of “inflammatory” to “natural” ILC2s (18), the differentiation of ILC3s to ROR γ t Eomes $^{NK1.1+}$ “ex-ILC3” cells (27), the polarization of ILC1s toward ILC3s (28), and the differentiation of CD4 $^{+}$ LT1 cells (29)—comprises local processes occurring within peripheral organs. Our study further demonstrates that the local pool of resident

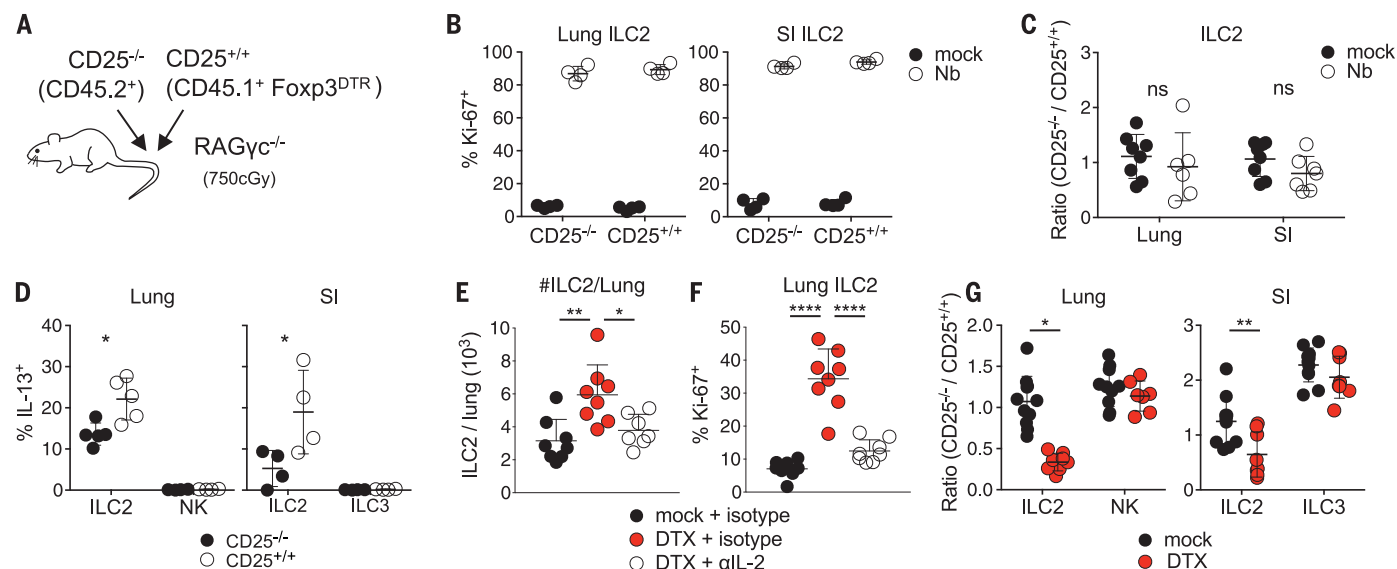


Fig. 4. IL-2 acts directly on tissue-resident ILC2s to promote cytokine production. (A to D) Mixed chimeras were generated by cotransfer of BM from CD45.2 $^{+}$ *Il2ra* $^{-/-}$ mice (CD25 $^{-/-}$) and CD25-sufficient CD45.1 $^{+}$ *Foxp3* DTR mice (CD25 $^{+/+}$) into irradiated RAG- γ c KO mice. In (B) to (D), mixed chimeras were infected with Nb, and lung and small intestine (SI) lamina propria were analyzed on day 7 post-infection. (B) shows the percentage of Ki-67 $^{+}$ ILC2 cells among CD25 $^{+/+}$ and CD25 $^{-/-}$ cells; (C) shows ratios of CD25 $^{-/-}$ to CD25 $^{+/+}$ ILC2s; and (D) shows the percentage of cells stimulated with phorbol 12-myristate 13-acetate and ionomycin that exhibited intracellular IL-13 staining.

(E to F) *Foxp3* DTR mice were subjected to DTX or mock treatment and additionally received IL-2-neutralizing antibodies JES6-1A and S4B6-1 or isotype control immunoglobulin G, as indicated. On day 9 of treatment, the absolute numbers of ILC2s per lung (E) and the percentages of Ki-67 $^{+}$ lung ILC2s (F) were analyzed. (G) Mixed chimeras were generated as in (A). Ratios of CD25 $^{-/-}$ to CD25 $^{+/+}$ lung and small intestine lamina propria lymphocytes were analyzed on day 9 of DTX or mock treatment. The data are shown as mean \pm SD and represent two to three independent experiments ($n = 4$ to 8 mice).

ILCs can be replenished and complemented, albeit only in part, through contributions of hematogenously derived precursors or mature cells in situations of extended inflammation and tissue repair. Consistent with our findings, it has been reported that ILC subsets are elevated in the peripheral blood of patients suffering from psoriasis (30, 31). Furthermore, peripheral blood ILC2s have been shown to dynamically modulate the expression of molecules that regulate tissue homing in mice and humans (20, 32). In addition, we have detected donor-derived lymphoid and ILC progenitors in parabiotic BM (fig. S8), raising the possibility that ILC progenitors can physiologically seed tissues not only during embryonic development (3) but also in adult mice. It remains to be determined whether this observation reflects the physiologic migration of ILC progenitors or the engraftment of donor-derived hematopoietic stem cells (33, 34) giving rise to ILCs. Independent of these considerations, our data support a model in which ILCs are locally maintained and expanded as tissue-resident cells during homeostasis and acute infection. This “sedentary” lifestyle of ILCs in broadly differing microenvironments is consistent with the proposed roles of ILCs as sentinels and local keepers of tissue function.

REFERENCES AND NOTES

1. D. Artis, H. Spits, *Nature* **517**, 293–301 (2015).
2. G. Eberl, M. Colonna, J. P. Di Santo, A. N. McKenzie, *Science* **348**, aaa6566 (2015).
3. J. K. Bando, H. E. Liang, R. M. Locksley, *Nat. Immunol.* **16**, 153–160 (2015).
4. E. Montaldo et al., *Immunity* **41**, 988–1000 (2014).
5. M. G. Constantinides, B. D. McDonald, P. A. Verhoef, A. Bendelac, *Nature* **508**, 397–401 (2014).
6. C. S. Klose et al., *Cell* **157**, 340–356 (2014).
7. R. A. Franklin et al., *Science* **344**, 921–925 (2014).
8. P. Kamran et al., *J. Vis. Exp.* **2013**, e50556 (2013).
9. H. Peng et al., *J. Clin. Invest.* **123**, 1444–1456 (2013).
10. K. G. Anderson et al., *Nat. Protoc.* **9**, 209–222 (2014).
11. M. H. Kim, E. J. Taparowsky, C. H. Kim, *Immunity* **43**, 107–119 (2015).
12. C. C. Bain et al., *Nat. Immunol.* **15**, 929–937 (2014).
13. E. C. Mackley et al., *Nat. Commun.* **6**, 5862 (2015).
14. D. K. Sojka et al., *eLife* **3**, e01659 (2014).
15. J. M. Kim, J. P. Rasmussen, A. Y. Rudensky, *Nat. Immunol.* **8**, 191–197 (2007).
16. K. Liu et al., *Science* **324**, 392–397 (2009).
17. M. Camberis, G. Le Gros, J. Urban Jr., *Curr. Protoc. Immunol.* (2003).
18. Y. Huang et al., *Nat. Immunol.* **16**, 161–169 (2015).
19. B. J. Marsland, M. Kurrer, R. Reissmann, N. L. Harris, M. Kopf, *Eur. J. Immunol.* **38**, 479–488 (2008).
20. E. D. Tait Wojno et al., *Mucosal Immunol.* (2015).
21. J. E. Turner et al., *J. Exp. Med.* **210**, 2951–2965 (2013).
22. G. Gasteiger, A. Y. Rudensky, *Nat. Rev. Immunol.* **14**, 631–639 (2014).
23. G. Gasteiger, S. Hemmers, P. D. Bos, J. C. Sun, A. Y. Rudensky, *J. Exp. Med.* **210**, 1179–1187 (2013).
24. B. Roediger et al., *J. Allergy Clin. Immunol.* (2015).
25. C. Wilhelm et al., *Nat. Immunol.* **12**, 1071–1077 (2011).
26. A. B. Molofsky et al., *Immunity* **43**, 161–174 (2015).
27. C. Vonnarbourg et al., *Immunity* **33**, 736–751 (2010).
28. J. H. Bernink et al., *Immunity* **43**, 146–160 (2015).
29. S. A. van de Pavert et al., *Nature* **508**, 123–127 (2014).
30. M. B. Teunissen et al., *J. Invest. Dermatol.* **134**, 2351–2360 (2014).
31. F. Villanova et al., *J. Invest. Dermatol.* **134**, 984–991 (2014).
32. J. M. Mjösberg et al., *Nat. Immunol.* **12**, 1055–1062 (2011).
33. D. E. Wright, A. J. Wagers, A. P. Gulati, F. L. Johnson, I. L. Weissman, *Science* **294**, 1933–1936 (2001).
34. J. L. Abkowitz, A. E. Robinson, S. Kale, M. W. Long, J. Chen, *Blood* **102**, 1249–1253 (2003).

ACKNOWLEDGMENTS

We thank R. Franklin, S. Dadi, M. Li, and A. Chaudhry for help with parabiosis or cell isolations; D. Artis, L. Monticelli, and B. Hoyos for providing and maintaining worms; K. Wu and A. Bravo for general laboratory support; and T. O’Sullivan, J. Sun, A. Diefenbach, W. Kastenmüller, and members of the Rudensky and Gasteiger laboratories for critical discussions. Data from this study are tabulated in the main paper or in the supplementary materials. This work was supported by an Irvington Fellowship from the Cancer Research Institute (G.G.), NIH Medical Scientist Training Program grant T32GM07739 to the Weill Cornell/Rockefeller/Sloan-Kettering Tri-Institutional MD-PhD Program (X.F.), Cancer Center Support Grant P30CA008748 from the NIH National Cancer Institute, NIH grant R37AI034206 (A.Y.R.), the Ludwig Center at Memorial Sloan Kettering

Cancer Center, and the Hilton-Ludwig Cancer Prevention Initiative (Conrad N. Hilton Foundation and Ludwig Cancer Research) (A.Y.R.). G.G. is an investigator with the Deutsche Forschungsgemeinschaft Emmy Noether Programme, and A.Y.R. is an investigator with the Howard Hughes Medical Institute.

SUPPLEMENTARY MATERIALS

www.sciencemag.org/content/350/6263/981/suppl/DC1
Materials and Methods
Figs. S1 to S8

5 July 2015; accepted 2 October 2015
Published online 15 October 2015
10.1126/science.aac9593

CANCER IMMUNOLOGY

Patrolling monocytes control tumor metastasis to the lung

Richard N. Hanna,^{1*} Caglar Cekic,² Duygu Sag,³ Robert Tacke,¹ Graham D. Thomas,¹ Heba Nowyhed,¹ Erica Herrley,¹ Nicole Rasquinha,¹ Sara McArdle,⁴ Runpei Wu,¹ Esther Peluso,¹ Daniel Metzger,⁵ Hiroshi Ichinose,⁶ Iftach Shaked,¹ Grzegorz Chodaczek,⁴ Subhra K. Biswas,⁷ Catherine C. Hedrick^{1*}

The immune system plays an important role in regulating tumor growth and metastasis. Classical monocytes promote tumorigenesis and cancer metastasis, but how nonclassical “patrolling” monocytes (PMo) interact with tumors is unknown. Here we show that PMo are enriched in the microvasculature of the lung and reduce tumor metastasis to lung in multiple mouse metastatic tumor models. Nr4a1-deficient mice, which specifically lack PMo, showed increased lung metastasis in vivo. Transfer of Nr4a1-proficient PMo into Nr4a1-deficient mice prevented tumor invasion in the lung. PMo established early interactions with metastasizing tumor cells, scavenged tumor material from the lung vasculature, and promoted natural killer cell recruitment and activation. Thus, PMo contribute to cancer immunosurveillance and may be targets for cancer immunotherapy.

Monocytes and monocyte-derived macrophages play key roles in tumor progression (1–4). Classical “inflammatory” monocytes (CCR2^{high}Ly6C⁺ in mice; CCR2^{high}CD14⁺CD16⁺ in humans) are recruited to tumor sites where they contribute to macrophage content and promote growth and metastasis (5, 6). In contrast, very little is known about the role of nonclassical “patrolling” monocytes (PMo) (CX3CR1^{high}Ly6C⁺ in mice; CX3CR1^{high}CD14^{dim}CD16⁺ in humans) in the early growth and metastasis of tumors. PMo are involved in the resolution of inflammation; they actively survey the endothelium of the vas-

culature, where they scavenge microparticles and remove cellular debris (7–9). The orphan nuclear receptor Nr4a1 (also known as Nur77/TR3/NGIFB) is highly expressed in PMo compared with other immune cells and functions as a master regulator for the development of PMo in mice (10).

To investigate the actions of PMo during early tumor metastasis, we used mice expressing green fluorescent protein (GFP) under the control of the Nr4a1 promoter (Nr4a1-GFP mice). In these mice, PMo (but not Ly6C⁺ classical monocytes) express high levels of GFP (GFP^{high}) (10, 11). We focused our studies on the lung, which is a common site of tumor metastasis and an important locus of PMo activity (12–14). We used flow cytometry to confirm that Nr4a1-GFP^{high} cells in the lung were PMo (fig. S1, A to C). Tracking of Nr4a1-GFP^{high} cells by confocal imaging in the lungs allowed us to identify a large number of Nr4a1-GFP^{high} PMo patrolling the microvasculature (movie S1 and Fig. 1A). Consistent with an important role for PMo in the lung vasculature, we found a three- to fourfold enrichment of Nr4a1-GFP^{high} PMo in the lung compared with other tissues (fig. S1D).

To examine the interactions of PMo with tumors in vivo, we imaged Nr4a1-GFP^{high} PMo in the lung after intravenous (IV) injection of Lewis

¹Division of Inflammation Biology, La Jolla Institute for Allergy and Immunology, La Jolla, CA 92037, USA.

²Department of Molecular Biology and Genetics, Bilkent University, Ankara, Turkey. ³Izmir Biomedicine and Genome Center, Dokuz Eylül University, Izmir, Turkey. ⁴Microscopy Core, La Jolla Institute for Allergy and Immunology, La Jolla, CA 92037, USA. ⁵Department of Functional Genomics and Cancer, Institut de Génétique et de Biologie Moléculaire et Cellulaire (IGBMC), INSERM U964, CNRS UMR 7104, Université de Strasbourg, Illkirch, France. ⁶Graduate School of Bioscience and Biotechnology, Tokyo Institute of Technology, Yokohama, Japan. ⁷Singapore Immunology Network (SigN), Agency for Science, Technology and Research (A*STAR), Singapore.

*Corresponding author. E-mail: rhanna@lji.org (R.N.H.); hedrick@lji.org (C.C.H.)

lung carcinoma cells expressing red fluorescent protein (LLC-RFP). The number of Nr4a1-GFP^{high} monocytes in the lung increased significantly 24 hours after injection, which implies that PMo are actively recruited to the lung tumor environment (Fig. 1A). Within 4 hours after tumor injection, most Nr4a1-GFP^{high} monocytes exhibited decreased patrolling speed in the vasculature, and by 24 hours they had arrested near lung tumor sites (Fig. 1B). The majority of Nr4a1-GFP^{high} monocytes isolated from the lung after LLC tumor transfer maintained their PMo phenotype, which we further confirmed in vitro (Fig. 1C and fig. S1).

Nr4a1-GFP^{high} PMo were recruited to tumor cell clusters within 30 min after IV tumor injection, and recruitment continued for at least 7 days (Fig. 1, D and E, and movies S2 to S5). Nr4a1-GFP^{high} cells that were recruited to lung tumor sites were not positive for Ly6C/G (GR-1) in vivo, further confirming that these Nr4a1-GFP^{high} cells are not Ly6C⁺ granulocytes or Ly6C⁺ classical monocytes (movie S4). The kinetics of PMo recruitment to the lung differed from that of Ly6C⁺ monocytes (fig. S2A). At 7 days, there were significantly higher numbers of Nr4a1-GFP^{high}

PMo (~24/100 μm^3) associated with tumor areas compared with tumor-free areas, confirming active recruitment of PMo to the tumor (Fig. 1, D and E; movie S5; and fig. S1B).

Nr4a1-GFP^{high} monocytes patrolling the vasculature 4 hours after tumor injection appeared to move toward and inhibit the attachment of tumor cells to the lung microvasculature (movie S3). We examined whether Nr4a1-GFP^{high} PMo could extravasate outside the vasculature. We found that by 4 hours after tumor injection, 10 to 20% of Nr4a1-GFP^{high} PMo had extravasated at tumor sites (fig. S2, B and C), and this increased to 40 to 50% PMo extravasation by 7 days. Together, these findings confirm that PMo establish early immune interactions with tumor cells and can extravasate and accumulate at tumor sites.

To determine whether PMo have a major role in regulating tumor invasion, metastasis, and growth in the lungs in vivo, we used Nr4a1 knock-out (*Nr4a1*^{-/-}) mice, which exhibit selective loss of PMo (10) (fig. S3). *Nr4a1*^{-/-} mice were IV injected with either syngeneic B16F10 melanoma cells expressing a luciferase reporter or LLC-RFP cells (Fig. 2, A and B, and figs. S4 and S5). As early as 24 hours and up to 21 days after IV injection of

B16F10 melanoma, we observed increased tumor invasion in the lungs of *Nr4a1*^{-/-} mice compared with control mice (Fig. 2, A and B, and fig. S4, A and B). We observed no differences in either Ly6C⁺ monocyte or Ly6G⁺ granulocyte populations in the lungs of these mice 7 days after tumor injection (fig. S4C). B16F10 tumor invasion appeared to be specific for the lung, as increased tumor metastasis was not observed in the liver (fig. S4B). Additionally, increased spontaneous metastases to the lung were observed in *Nr4a1*^{-/-} mice after subcutaneous injection of B16F10 melanoma, which suggests that Nr4a1 expression is important for suppressing primary tumor metastasis to the lung (Fig. 2C). A similar early and sustained increase in lung metastasis in *Nr4a1*^{-/-} mice was also observed after intravenous LLC tumor transfer (fig. S5). We did not detect differences in lung vascular permeability between *Nr4a1*^{-/-} and control mice (fig. S6).

We next investigated the mouse mammary tumor virus–polyoma middle T (MMTV-PyMT) model, in which female mice spontaneously develop mammary tumors that metastasize to the lung (15). To focus on Nr4a1 function exclusively in hematopoietic cells, we performed bone marrow

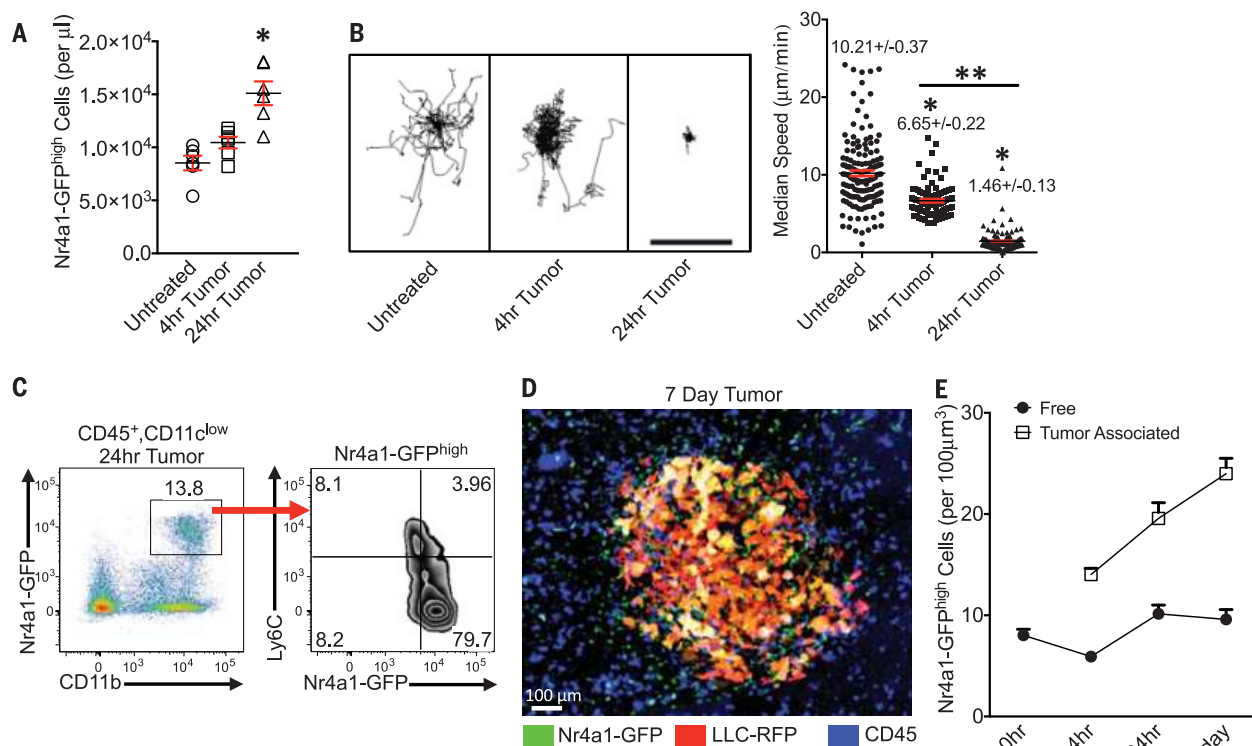


Fig. 1. Nr4a1-GFP^{high} monocytes patrol the vasculature and interact with tumor cells in the lung. (A) Quantification of Nr4a1-GFP^{high} PMo per microliter of blood volume in lung for control tissue (Untreated) or 4 or 24 hours after IV LLC-RFP transfer ($n = 5$ mice per group). (B) Quantification of Nr4a1-GFP^{high} monocyte movement in the lung before (Untreated), 4 hours after, or 24 hours after LLC-RFP tumor injection. (Left) Monocyte tracks transposed to a common origin from a representative 20-min movie (scale bar, 100 μm). (Right) Quantification of median speed of monocytes (combined speed data from analysis of three separate mice; $*P < 0.001$ lower than untreated; $**P < 0.001$ lower than 4-hour tumor). (C) Representative gating

of Nr4a1-GFP^{high}CD11b⁺ cells from all live CD45⁺CD11b^{low} cells 24 hours after IV LLC-RFP transfer. (D) Representative confocal image of Nr4a1-GFP^{high} monocytes (green) interacting with LLC-RFP cells (red) in the lung 7 days after IV LLC-RFP transfer. Immune cells in the vasculature were labeled with IV-injected antibody to CD45 (blue). (E) Quantification of free (>100 μm from tumor site) and tumor-associated (<50 μm from tumor site) Nr4a1-GFP^{high} monocytes in the lung at various time points after tumor injection (combined analysis of five mice per group; $P < 0.01$ for each tumor-associated area compared with tumor-free areas for each time point). Error bars indicate SEM.

transplants using either wild-type (WT) or *Nr4a1*^{-/-} bone marrow transferred into female recipient MMTV-PyMT mice. MMTV-PyMT mice receiving *Nr4a1*^{-/-} bone marrow developed significantly higher numbers of spontaneous metastases to the lung but no differences in primary mammary tumor growth compared to mice receiving WT bone marrow (Fig. 2, D and E).

We further tested hematopoietic *Nr4a1* function using B16F10 melanoma. Only mice receiving *Nr4a1*^{-/-} bone marrow had increased B16F10 tumor metastases, confirming that *Nr4a1* expression in hematopoietic cells regulated tumor cell metastasis to the lung (fig. S7, A and B). Analysis of immune cells isolated from lung tumors verified a selective loss of PMo in *Nr4a1*^{-/-} bone marrow-transplanted mice (fig. S7C). In the 1:1 chimera mice, we observed equal reconstitution of immune cells from each donor (fig. S7D). However, PMo were derived almost exclusively from WT bone marrow, suggesting that the restoration of the Ly6C⁺ monocyte population prevented tumor metastasis.

To confirm that *Nr4a1* expressed in myeloid cells was regulating tumor metastasis to the lung, we examined two different myeloid-specific *Nr4a1* conditional knockout models (CSF1R-Cre⁺*Nr4a1*^{fl/fl} and LysM-Cre⁺*Nr4a1*^{fl/fl}). Deletion

of *Nr4a1* using CSF1R-Cre⁺*Nr4a1*^{fl/fl} and LysM-Cre⁺*Nr4a1*^{fl/fl} mice significantly reduced the number of PMo in circulation (fig. S8) and increased tumor lung metastasis (Fig. 3, A and B, and fig. S9). *Nr4a1* deletion using CSF1R-Cre or LysM-Cre also targets *Nr4a1* in macrophages and Ly6C⁺ monocytes, so we cannot completely rule out effects of *Nr4a1* in these cells. However, *Nr4a1* expression in macrophages and Ly6C⁺ monocytes is relatively low, which suggests limited *Nr4a1* function (10, 16, 17). No differences in tumor metastasis were observed with T lymphocyte-specific *Nr4a1* deletion (fig. S10). Collectively, our studies illustrate increased lung metastasis burden in the absence of *Nr4a1* in myeloid cells in multiple cancer models.

To confirm a direct role for PMo in regulating tumor metastasis, WT Ly6C⁺ or Ly6C⁺ monocytes were adoptively transferred into recipient *Nr4a1*^{-/-} mice before tumor injection. A substantial number of the transferred monocytes could be found in the lungs (fig. S11, A and B). Reconstitution of PMo into *Nr4a1*^{-/-} mice prevented lung tumor metastasis (Fig. 3, C and D). In contrast, transfer of Ly6C⁺ monocytes into *Nr4a1*^{-/-} mice actually promoted tumor metastasis, consistent with known protumoral properties of this subset of monocytes (5, 18). The majority (80 to 90%) of transferred Ly6C⁺ monocytes in circulation did not

lose Ly6C expression (fig. S11C). Transfer of PMo 24 hours after tumor injection into *Nr4a1*^{-/-} mice did not suppress tumor metastasis (fig. S11D), suggesting that PMo must already be present and active in the vasculature to prevent early tumor metastasis. These data directly show that non-classical PMo inhibit tumor metastasis to the lung.

Patrolling monocytes can act as “intravascular housekeepers” that scavenge microparticles and remove cellular debris from the microvasculature (7). Extracellular vesicles from tumors are important mediators of tumor metastasis, progression, and immune suppression, and targeting their removal is an emerging focus for cancer therapy (19, 20). We used high-resolution confocal imaging to determine whether PMo could engulf and remove tumor material from the lung vasculature. A sizable number of *Nr4a1*-GFP^{high} PMo containing large amounts of LLC-RFP tumor material were observed at tumor sites in the lung 24 hours after IV tumor transfer (Fig. 3E). Co-culture assays of mouse PMo with fluorescently labeled tumor cells confirmed engulfment of large amounts of tumor material (Fig. 3F). Analysis of monocyte populations isolated from the lung at 24 hours after IV LLC-RFP injection indicated that PMo preferentially took up ~fivefold more tumor material than did Ly6C⁺ classical

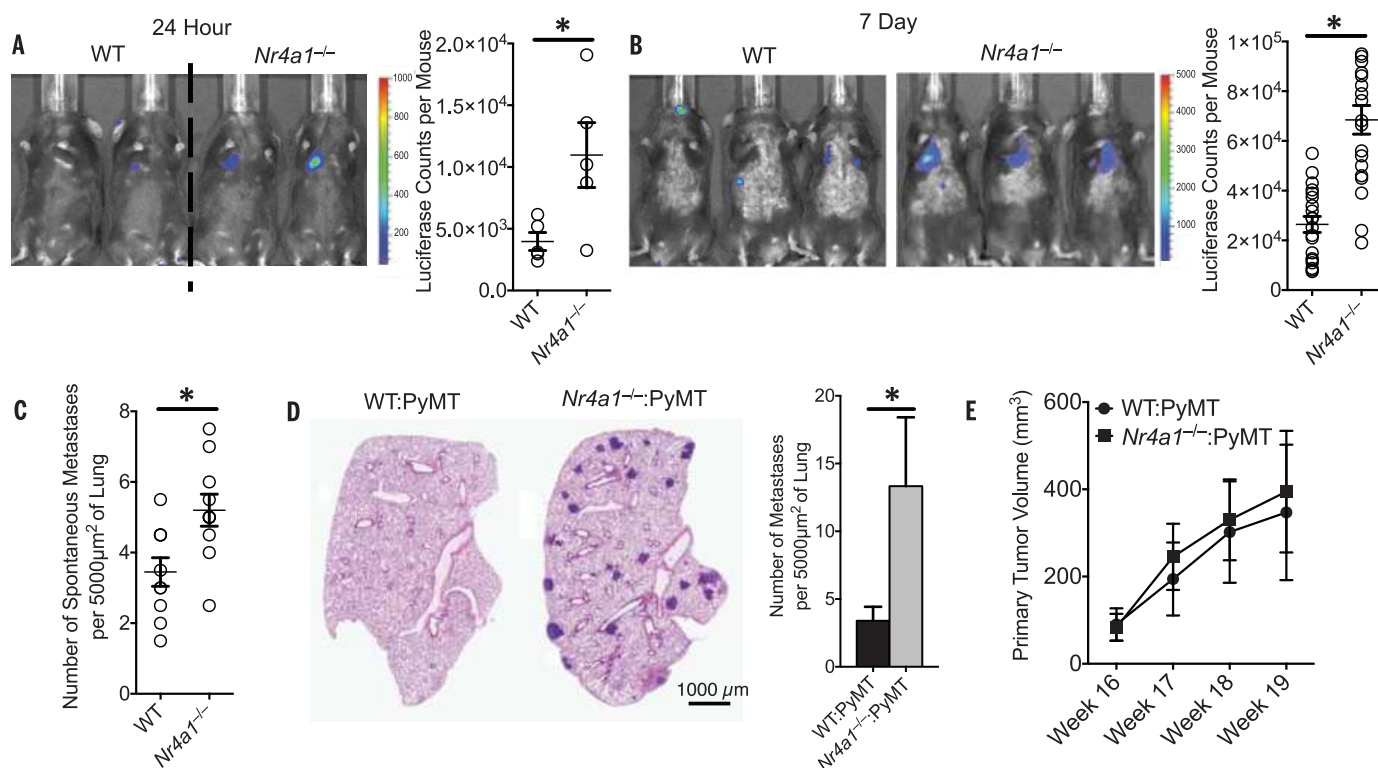


Fig. 2. Increased lung metastasis of tumors in *Nr4a1*^{-/-} mice. (A) (Left) In vivo luciferase detection in WT control and *Nr4a1*^{-/-} mice 24 hours after IV injection of 5×10^5 B16F10 melanoma cells expressing luciferase. (Right) Luciferase quantification (**P* < 0.03, representative experiment with five mice per group). (B) In vivo luciferase detection (left) and quantification (right) in WT and *Nr4a1*^{-/-} mice 7 days after IV injection with 3×10^5 B16F10-luciferase cells (**P* < 0.001, *n* = 18 mice per group combined from three separate experiments). (C) Number of spontaneous tumor metastases per 5000 μm² of lung surface

28 days after subcutaneous injection of 1×10^5 B16F10-YFP cells (**P* < 0.01, *n* = 7 mice per group). (D and E) Lung tumor metastasis in MMTV-PyMT mice reconstituted with WT (WT:PyMT) or *Nr4a1*^{-/-} (*Nr4a1*^{-/-}:PyMT) bone marrow. (D) (Left) Representative MMTV-PyMT mouse lung histology, stained with hematoxylin and eosin. (Right) Quantification of the number of spontaneous lung metastases per 5000 μm² of lung surface (**P* < 0.05, *n* = 12 for WT and 15 for *Nr4a1*^{-/-}). (E) Quantification of primary breast tumor growth in MMTV-PyMT mice (*n* = 12 for WT and 15 for *Nr4a1*^{-/-}). Error bars indicate SEM.

monocytes (Fig. 3G). PMo also preferentially took up substantially more B16F10–yellow fluorescent protein (YFP) tumor material, with an average tumor material size of $1.39 \mu\text{m}^2$ and an average total amount of tumor material per monocyte of $1.92 \mu\text{m}^2$ (fig. S12, A and B). The homologous human $\text{CD14}^{\text{dim}}\text{CD16}^+$ population of PMo, which similarly has high *Nr4a1* expression (8, 27), also engulfed a large quantity of tumor material in vitro, suggesting analogous tumor engulfment function (fig. S12C). Moreover, PMo actively engulfed tumor material within classic endocytic compartments (22) (Fig. 4A). Collectively, these results demonstrate that *Nr4a1*-dependent PMo rapidly and preferentially endocytose tumor material.

We then asked how PMo recognized tumor cells to prevent metastasis in the lung. The chemokine receptor CX3CR1 is highly expressed on PMo

and is important for their arrest at inflammatory sites (fig. S13A) (23–25). CX3CR1-deficient (*Cx3cr1*^{−/−}) mice, which also have a significant reduction in PMo, exhibit a similar phenotype to *Nr4a1*^{−/−} mice (i.e., increased tumor burden and metastasis to the lung) (26, 27). Although PMo numbers were reduced in the lung vasculature of *Cx3cr1*^{−/−} mice [~30 to 50% reduction (fig. S13B), confirming previous reports] (27), a major proportion of the remaining CX3CR1-deficient PMo was observed patrolling the vasculature, as previously observed (7). Unlike *Cx3cr1*^{−/−} or WT PMo, *Cx3cr1*^{−/−} PMo did not arrest near LLC tumor cells and instead remained patrolling within the lung vasculature (Fig. 4, B and C, and movie S6). *Cx3cr1*^{−/−} PMo were not recruited to the lung 24 hours after LLC tumor challenge, whereas *Ly6C*⁺ recruitment was unaffected by the loss of CX3CR1 expression (fig. S13B). *Cx3cr1*^{−/−} PMo present in the lung showed

defective engulfment of tumor material, indicating that CX3CR1 expression on PMo is critical for mediating the sensing and uptake of tumor material (Fig. 4D).

CX3CL1, a ligand for CX3CR1, has been reported to be present in high levels in human and mouse lungs (28). Using a CX3CL1-mCherry reporter mouse (29), we found that CX3CL1 was specifically expressed on CD31^+ endothelial cells (ECs) at low levels in the lung microvasculature (Fig. 4, E and F, and fig. S13C). CX3CL1 expression was most prevalent in lung ECs compared with ECs in other tissues (fig. S13D), which may partially explain the enrichment and preferential function of PMo in the lung. CX3CL1 expression on lung ECs increased in response to tumor challenge (Fig. 4E) and at sites of tumor metastasis (Fig. 4F), consistent with reports of increased CX3CL1 during lung inflammation (30).

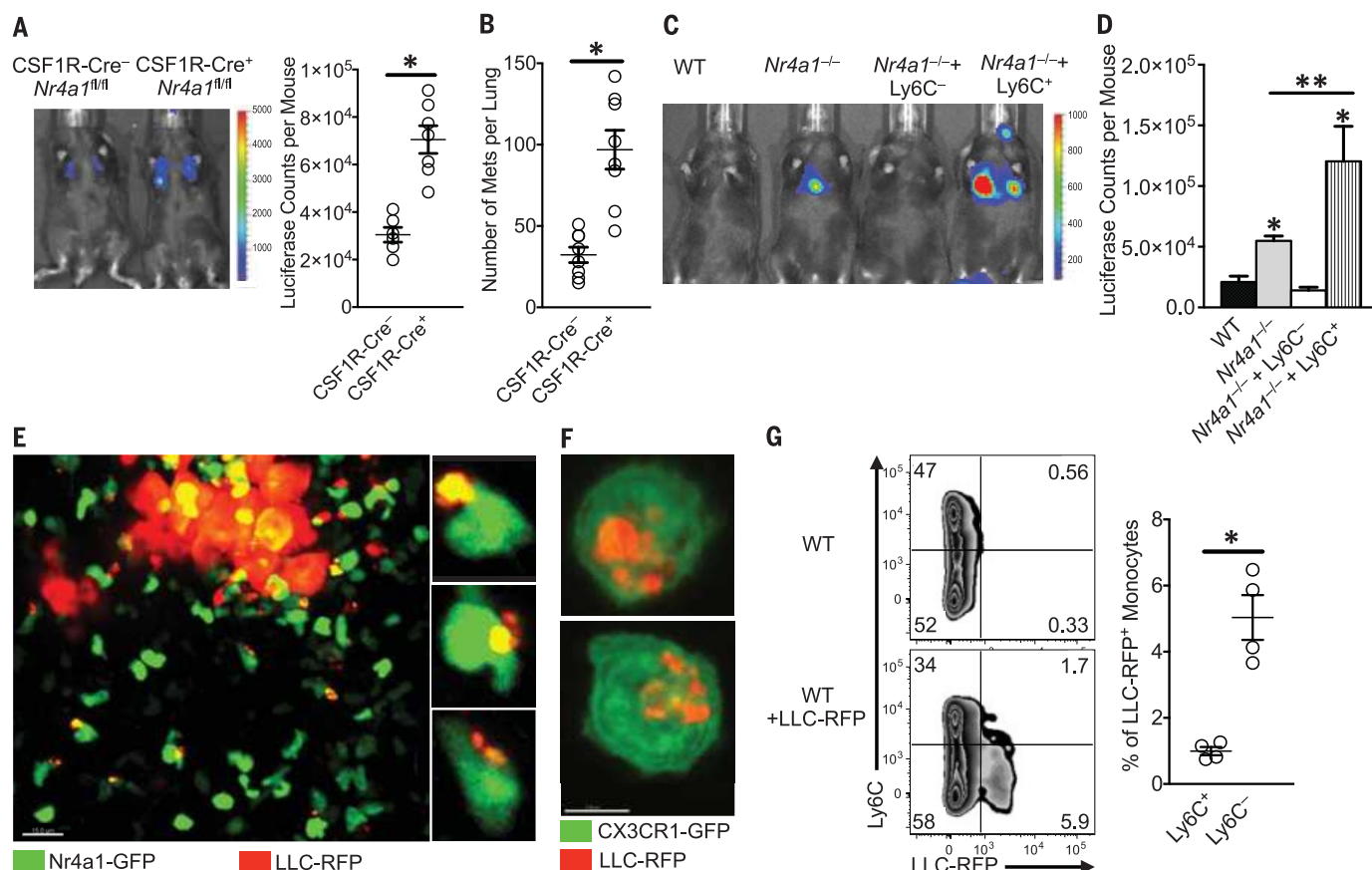


Fig. 3. *Nr4a1*-expressing PMo reduce tumor metastasis and engulf tumor material in the lung. (A) In vivo imaging (left) and quantification (right) of lung tumors in CSF1R-Cre[−] *Nr4a1*^{fl/fl} (CSF1R-Cre[−]) or CSF1R-Cre⁺ *Nr4a1*^{fl/fl} (CSF1R-Cre⁺) mice 7 days after IV injection of 3×10^5 B16F10-luciferase tumor cells ($n = 6$ mice per group; $*P < 0.01$; experiment replicated twice). (B) Quantification of the number of tumor metastases per lung of CSF1R-Cre[−] *Nr4a1*^{fl/fl} (CSF1R-Cre[−]) and CSF1R-Cre⁺ *Nr4a1*^{fl/fl} (CSF1R-Cre⁺) mice 7 days after IV injection of 3×10^5 B16F10-YFP tumor cells ($n = 8$ mice per group; $*P < 0.01$). (C and D) *Nr4a1*^{−/−} mice were injected intravenously with 5×10^5 WT *Ly6C*[−] PMo, *Ly6C*⁺ inflammatory monocytes, or PBS at day 0. On day 1, 3×10^5 B16F10-luciferase tumor cells were injected intravenously, and tumor metastasis and growth were measured by in vivo imaging on day 8. Shown are representative in vivo images (C) and quantification (D) of B16F10-luciferase

metastasis 8 days after monocyte transfer and 7 days after tumor transfer in WT or *Nr4a1*^{−/−} mice (combined data from five separate experiments with $n = 2$ mice per group; $*P < 0.01$ statistically different from WT; $**P < 0.05$ statistically different from *Nr4a1*^{−/−}). (E) Imaging of tumor material uptake in lung by *Nr4a1*-GFP^{high} monocytes 24 hours after IV injection of LLC-RFP tumor cells. Representative higher-magnification images are shown at right. Note that *Nr4a1*-GFP expression is primarily nuclear, so monocyte cell membranes are not visible in these images. (F) Uptake of LLC-RFP tumor material by CX3CR1-GFP^{high} *Ly6C*[−] PMo after 24 hours of coculture. (G) Representative flow plot (left) and quantification (right) of tumor material uptake by all monocytes in the lung 24 hours after IV tumor injection of 3×10^5 LLC-RFP cells ($n = 4$ mice per group; $*P < 0.01$; experiment replicated three times). Error bars indicate SEM.

Toll-like receptor 7 (TLR7) has been linked to recruitment of PMo in response to kidney damage in mice (7). However, we found that TLR7 did not play a major role in either recruitment of PMo to the lung after tumor injection (fig. S13B) or uptake of tumor material by PMo (Fig. 4D). We conclude that both CX3CR1 expression on monocytes and CX3CL1 expression by ECs are critical for recruitment of PMo to sites of tumor extravasation to mediate the removal of tumor material from the lung. CX3CL1 expression by tumor cells (37) may also drive monocyte recruitment. In agreement with our findings, many studies have reported that CX3CL1 expression by either tumor cells or tumor-associated cells is anti-

tumoral and correlated with good prognosis (32–34). However, the function of the CX3CL1/CX3CR1 axis, particularly during later stages of tumor growth, is complex (35, 36).

Finally, we examined whether PMo can directly kill tumor cells. After multiple attempts using various experimental conditions, direct killing of tumor cells by PMo was not observed (fig. S14). However, PMo may be important for antibody-dependent cell-mediated cytotoxicity of either tumor cells or suppressive immune cells within the tumor environment (37, 38). In response to IV-injected B16F10 tumor, PMo isolated from lungs produced significantly higher levels of natural killer (NK) cell activation and recruitment-related

chemokines CCL3, CCL4, and CCL5, as compared with classical Ly6C⁺ monocytes (Fig. 4G) (39, 40). In accord with this finding, myeloid-specific Nr4a1 knockout mice (CSF1R-Cre⁺Nr4a1^{fl/fl}) showed reduced NK cell recruitment to the lung in response to tumor (Fig. 4H), suggesting that PMo controlled the recruitment of NK cells to tumor sites. A similar reduction in NK cell recruitment and CD44 activation (fig. S15, A and B) was also observed in the lungs of PyMT mice that received Nr4a1-deficient bone marrow. However, Nr4a1 does not regulate NK cell development (fig. S15C). Uptake of tumor material by PMo does not require the presence of NK cells (fig. S16, A and B). NK cell depletion reduced the differences in

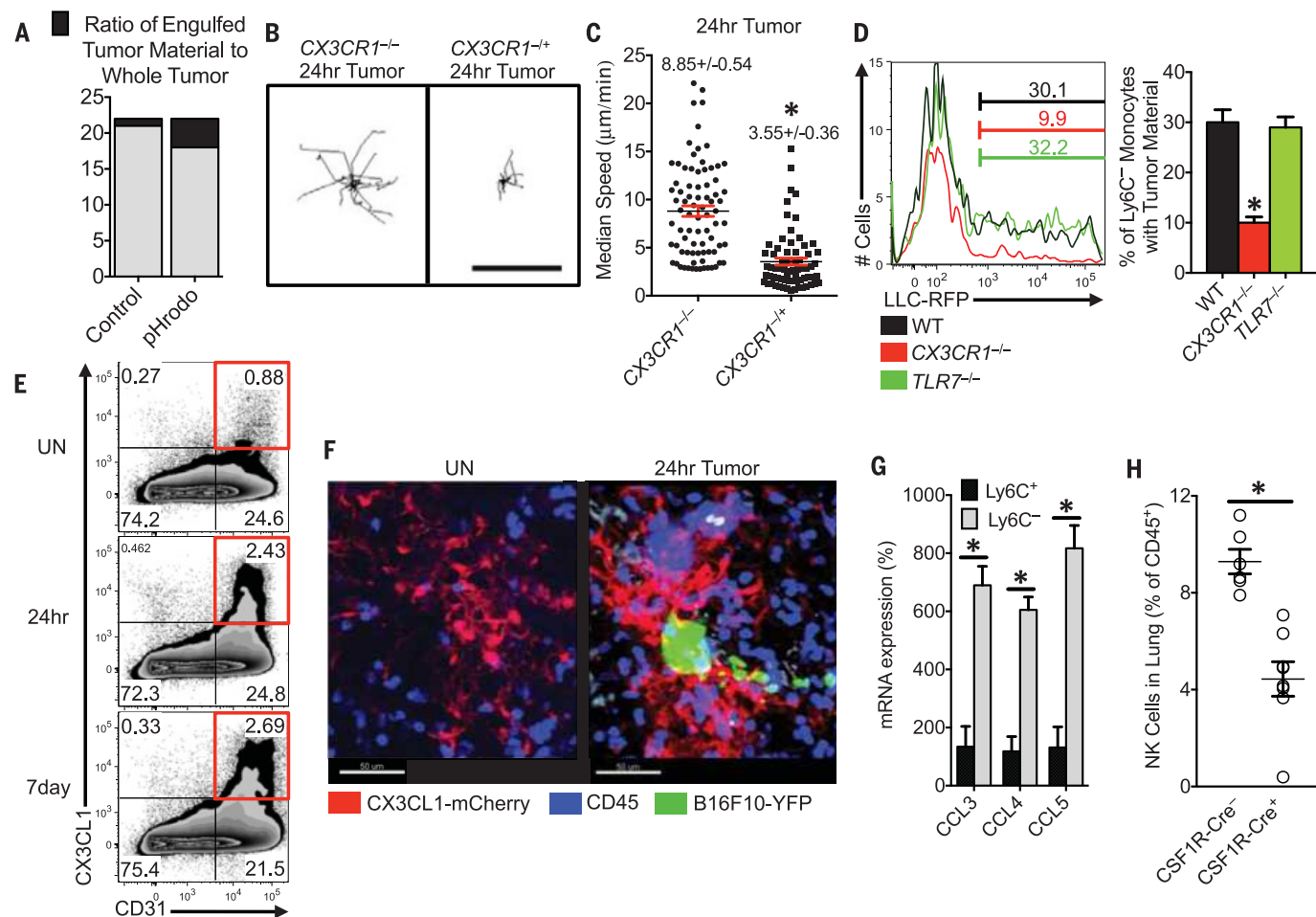


Fig. 4. Patrolling monocytes detect tumor material in a CX3CR1-dependent manner and recruit NK cells to the lung tumor environment. (A) Ratio of fluorescent intensity of tumor material engulfed by PMo (black) to fluorescent intensity of whole tumor (black and gray) 3 hours after IV LLC tumor injection. LLC tumors were labeled with either CellTrace Violet control dye (Control) or a pH-sensitive pHrodo Red dye (pHrodo) and then intravenously injected in a 1:1 ratio into a WT mouse ($n = 3$ mice per group, experiment replicated three times). Representative tracking (B) and median speed (C) of $Cx3cr1^{-/-}$ or $Cx3cr1^{+/+}$ monocyte movement 24 hours after IV tumor injection in the lung. Monocyte tracks transposed to a common origin from representative 20-min movies (scale bar, 100 μm; representative tracks are shown from one mouse, median speed was calculated from tumor areas analyzed in three separate mice per group, $*P < 0.001$). (D) (Left) Percentage of Ly6C⁻ PMo containing LLC-RFP tumor material in the lung 3 hours after IV injection of tumor into

representative WT, $Cx3cr1^{-/-}$, or $Tlr7^{-/-}$ mice. (Right) Quantification of tumor material uptake ($n = 3$ per group, $*P < 0.001$ versus WT). (E) Percentage of CD31⁺ CX3CL1⁺ lung ECs isolated from untreated (UN) mice or from CX3CL1-mCherry mice, 24 hours or 7 days after IV injection of B16F10-YFP tumor cells. (F) Representative imaging of CX3CL1-mCherry (red) expression in lung 24 hours after IV injection of B16F10-YFP tumor cells (green) in CX3CL1-mCherry mice. CD45⁺ immune cells are labeled in blue. (G) Relative chemokine mRNA expression in Ly6C⁺ or Ly6C⁻ monocytes isolated from lungs by fluorescence-activated cell sorting 24 hours after IV B16F10 tumor injection (monocyte populations isolated from three separate mice; $*P < 0.01$; experiment repeated three times). (H) Percentage of NK cells in the lungs of CSF1R-Cre⁻Nr4a1^{fl/fl} (CSF1R-Cre⁻) or CSF1R-Cre⁺Nr4a1^{fl/fl} (CSF1R-Cre⁺) mice 7 days after IV injection of 3×10^5 B16F10-luciferase tumor cells ($n = 6$ mice per group, $*P < 0.01$). Error bars indicate SEM.

metastasis between WT and CSF1R-Cre⁺Nr4a1^{fl/fl} mice (fig. S16C). Thus, PMo inhibit metastasis, at least in part, through the regulation of NK cell recruitment and activity.

In summary, we demonstrate that PMo participate in cancer surveillance by preventing tumor metastasis to lung. PMo are actively recruited to lung metastasis sites in a CX3CR1-dependent manner, where they function to scavenge tumor material, as well as to recruit and activate NK cells, leading to the prevention of tumor cell metastasis (fig. S17). Selective targeting by increasing PMo activity and/or their regulation by Nr4a1 may represent a novel therapy for the prevention of cancer metastasis to the lung.

REFERENCES AND NOTES

1. S. K. Biswas, A. Mantovani, *Nat. Immunol.* **11**, 889–896 (2010).
2. P. J. Murray, T. A. Wynn, *Nat. Rev. Immunol.* **11**, 723–737 (2011).
3. T. A. Wynn, A. Chawla, J. W. Pollard, *Nature* **496**, 445–455 (2013).
4. R. A. Franklin *et al.*, *Science* **344**, 921–925 (2014).
5. B. Z. Qian *et al.*, *Nature* **475**, 222–225 (2011).
6. K. Movahedi *et al.*, *Cancer Res.* **70**, 5728–5739 (2010).
7. L. M. Carlin *et al.*, *Cell* **153**, 362–375 (2013).
8. J. Cros *et al.*, *Immunity* **33**, 375–386 (2010).
9. C. Auffray *et al.*, *Science* **317**, 666–670 (2007).
10. R. N. Hanna *et al.*, *Nat. Immunol.* **12**, 778–785 (2011).
11. A. E. Moran *et al.*, *J. Exp. Med.* **208**, 1279–1289 (2011).
12. L. Landsman, S. Jung, *J. Immunol.* **179**, 3488–3494 (2007).
13. L. Landsman, C. Varol, S. Jung, *J. Immunol.* **178**, 2000–2007 (2007).
14. C. Jakubzick *et al.*, *J. Immunol.* **180**, 3019–3027 (2008).
15. C. T. Guy, R. D. Cardiff, W. J. Muller, *Mol. Cell. Biol.* **12**, 954–961 (1992).
16. S. Saeed *et al.*, *Science* **345**, 1251086 (2014).
17. V. Jovic *et al.*, *Nat. Immunol.* **14**, 633–643 (2013).
18. D. E. Sanford *et al.*, *Clin. Cancer Res.* **19**, 3404–3415 (2013).
19. P. Vader, X. O. Breakefield, M. J. Wood, *Trends Mol. Med.* **20**, 385–393 (2014).
20. F. Pucci, M. J. Pittet, *Clin. Cancer Res.* **19**, 2598–2604 (2013).
21. R. N. Hanna *et al.*, *Circ. Res.* **110**, 416–427 (2012).
22. Detailed methods are available as supplementary materials on Science Online.
23. G. Thomas, R. Tacke, C. C. Hedrick, R. N. Hanna, *Arterioscler. Thromb. Vasc. Biol.* **35**, 1306–1316 (2015).
24. S. Jung *et al.*, *Mol. Cell. Biol.* **20**, 4106–4114 (2000).
25. F. Geissmann, S. Jung, D. R. Littman, *Immunity* **19**, 71–82 (2003).
26. Y. R. Yu *et al.*, *Int. J. Cancer* **121**, 316–322 (2007).
27. L. Landsman *et al.*, *Blood* **113**, 963–972 (2009).
28. A. I. Su *et al.*, *Proc. Natl. Acad. Sci. U.S.A.* **101**, 6062–6067 (2004).
29. K. W. Kim *et al.*, *Blood* **118**, e156–e167 (2011).
30. J. Zhang, J. M. Patel, *Int. J. Clin. Exp. Med.* **3**, 233–244 (2010).
31. E. Ferretti, V. Pistoia, A. Corcione, *Mediators Inflamm.* **2014**, 480941 (2014).
32. M. Hyakudomi *et al.*, *Ann. Surg. Oncol.* **15**, 1775–1782 (2008).
33. J. Y. Kee *et al.*, *Mol. Clin. Oncol.* **1**, 35–40 (2013).
34. M. H. Park, J. S. Lee, J. H. Yoon, *J. Surg. Oncol.* **106**, 386–392 (2012).
35. A. Schmall *et al.*, *Am. J. Respir. Crit. Care Med.* **191**, 437–447 (2015).
36. M. Tardaguila, S. Manes, “The complex role of chemokines in cancer: The case of the CX3CL1-CX3CR1 axis,” in *Oncology: Theory and Practice* (iConcept Press, 2014).
37. E. Romano *et al.*, *Proc. Natl. Acad. Sci. U.S.A.* **112**, 6140–6145 (2015).
38. A. Szaflarska *et al.*, *Exp. Hematol.* **32**, 748–755 (2004).
39. A. A. Maghazachi, *Curr. Top. Microbiol. Immunol.* **341**, 37–58 (2010).
40. M. J. Robertson, *J. Leukoc. Biol.* **71**, 173–183 (2002).

ACKNOWLEDGMENTS

We thank K. Ley and H. Shaked for critically reviewing and editing this manuscript, K. Hogquist for Nr4a1-GFP reporter mice, M. Kronenberg for B16F10 melanoma cells, A. Blatchley and D. Yoakum for assistance with mouse colony management, A. Strasner for help with establishing tumor models, and Z. Mikulski for assistance with imaging. The data presented here are tabulated in the main paper and in the supplementary materials. Nr4a1-floxed conditional mice are available from IGBMC under a material transfer agreement with D.M. and H.I. C.C.H., R.N.H., and the La Jolla Institute for Allergy and Immunology have filed a U.S. patent application (U.S. 13/646,183) that relates to specific topic “Methods and uses of Nur77 and Nur77 agonists to modulate macrophages and monocytes, and treat inflammation, inflammatory disease and cardiovascular disease” and an invention disclosure that relates to the specific topic “Patrolling monocytes control tumor metastasis to the lung.” This work was supported by NIH grants R01 HL118765 and R01 CA202987 (both to C.C.H.), American Heart Association Postdoctoral Award 3POST16990029 (to R.T.), NIH F32 postdoctoral fellowship NIH F32 HL117533-02 (to H.N.), American Heart Association Scientist Development Grant 125SDG12070005 (to R.N.H.), the La Jolla Institute for Allergy and Immunology Board of Directors Fellowship (to R.N.H.), CNRS and INSERM (to D.M.), and core funding from SigN (A*STAR) (to S.K.B.).

SUPPLEMENTARY MATERIALS

www.sciencemag.org/content/350/6263/985/suppl/DC1
Materials and Methods
Figs. S1 to S18
References (41–48)
Movies S1 to S6

1 July 2015; accepted 2 October 2015
Published online 22 October 2015
10.1126/science.aac9407

We make research data intelligible



Photo: SciLifeLab/Wikae Wallerstedt

Teamwork. The strong bioinformatics environment at SciLifeLab enables co-workers to benefit from each other's expertise and together offer high quality support to the scientific community.

Today, in-depth knowledge about bioinformatics is essential to most life science research. The huge amount of data that researchers gather needs to be interpreted to become meaningful. At SciLifeLab, a Swedish center for molecular biosciences, we have created a research environment where bioinformatics is one of our key investments.

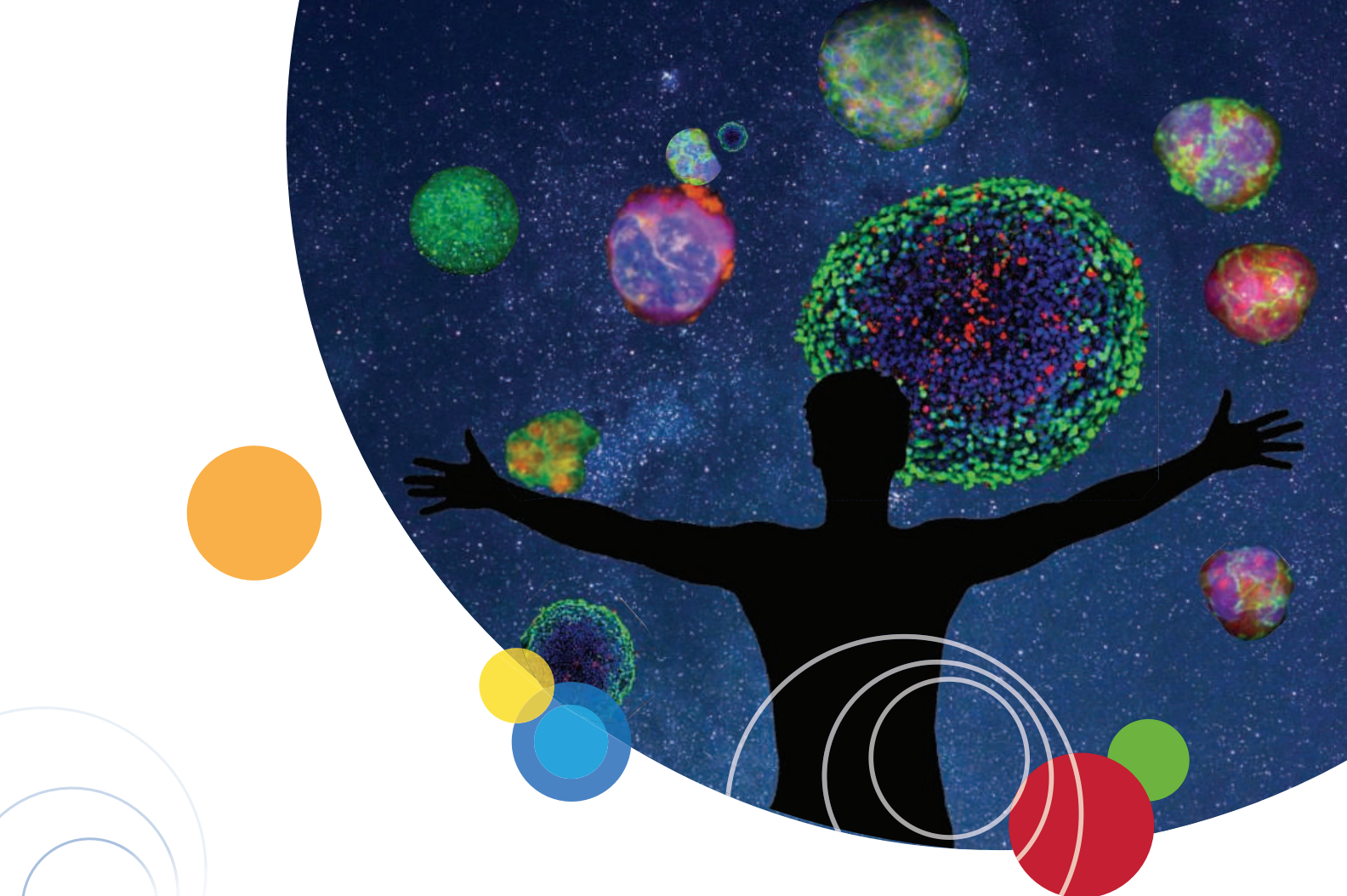
The SciLifeLab center combines frontline technical expertise with advanced knowledge of translational medicine and molecular bioscience. Researchers from all of Sweden can use both the technology and the know-how that is available at the center. In order to advance the bioinformatics expertise in the whole research community, SciLifeLab also organizes courses on advanced level.

Åsa Björklund is a single-cell transcriptomics expert at the SciLifeLab Bioinformatics platform. Her group makes their expertise available to the research community by placing senior bioinformaticians in different research groups for a specified time.

“The best part about working as a bioinformatician at SciLifeLab is the opportunity to be involved in a variety of high profile projects with novel technologies and interesting biological questions,” said Åsa Björklund.

Alongside our Bioinformatics platform, many of our other platforms employ bioinformaticians. Among them is the National Genomics Infrastructure (NGI), which is responsible for the majority of SciLifeLab's sequencing services.

“The NGI bioinformaticians are essential to us in many aspects,” said Professor Ann-Christine Syvänen at the National Genomics Infrastructure. “They advice our users when we start a new project, analyze the data, and plan strategically for future needs in terms of storage and computational capacity. In order to ensure high quality services our bioinformaticians also develop software, many of which are open source.”



Explore the new dimension

The confocal system for your complex biology

Explore the complexities of biology faster, easier and with better results. With our new ImageXpress® Micro Confocal High-Content Imaging System, you can run 3D cellular assays with confocal results—at a speed you'd only expect from widefield screening. Freely select an optical geometry from crisp confocal and whole-well widefield options to get easily quantified images and statistically relevant data. Built on the reliable, field-proven ImageXpress Micro platform, the ImageXpress Micro Confocal system is our most versatile yet.

Discover more.

moleculardevices.com/complexbiology



ImageXpress® Micro Confocal system



Unleash your brilliance™

For Research Use Only. Not for use in diagnostic procedures.
© 2015 Molecular Devices, LLC. All Rights Reserved. The trademarks mentioned herein are the property of Molecular Devices, LLC or their respective owners.

myIDP: A career plan customized for you, by you.



For your career in science, there's only one **Science**



**Recommended by
leading professional
societies and the NIH**

Features in myIDP include:

- Exercises to help you examine your skills, interests, and values.
- A list of 20 scientific career paths with a prediction of which ones best fit your skills and interests.
- A tool for setting strategic goals for the coming year, with optional reminders to keep you on track.
- Articles and resources to guide you through the process.
- Options to save materials online and print them for further review and discussion.
- Ability to select which portion of your IDP you wish to share with advisors, mentors, or others.
- A certificate of completion for users that finish myIDP.

Visit the website and start planning today!
myIDP.sciencecareers.org

ScienceCareers In partnership with:



AAAS Marion Milligan Mason Award for Women in the Chemical Sciences

Marion Milligan Mason was a chemist and a proud AAAS member. Her will provided for the creation of a fund with a \$2.2 million bequest to support research by early-career women in the chemical sciences. AAAS is grateful for philanthropic gifts like Dr. Mason's bequest, which make it possible for us to support promising scientists early in their careers.

The online application site will open
November 16, 2015

Proposals are due on or before
March 1, 2016

Awards will be announced on or before
January 2017

Apply today!

www.aaas.org/masonaward

Congratulations to the 2015 Recipients



ALISON FOUT

*Assistant Professor of Chemistry
University of Illinois at
Urbana-Champaign*

*Nitrite Reduction in a Non-Heme System:
Evidence for an Alternative Mechanism*



KATHERINE MACKEY

*Assistant Professor, Department of
Earth System Science
University of California Irvine*

*Aerosol Trace Metal Chemistry
in a Changing Ocean*



KRISTIN PARENT

*Assistant Professor of Biochemistry
and Molecular Biology
Michigan State University*

*Cryo-electron tomography of large
and challenging biological specimens*



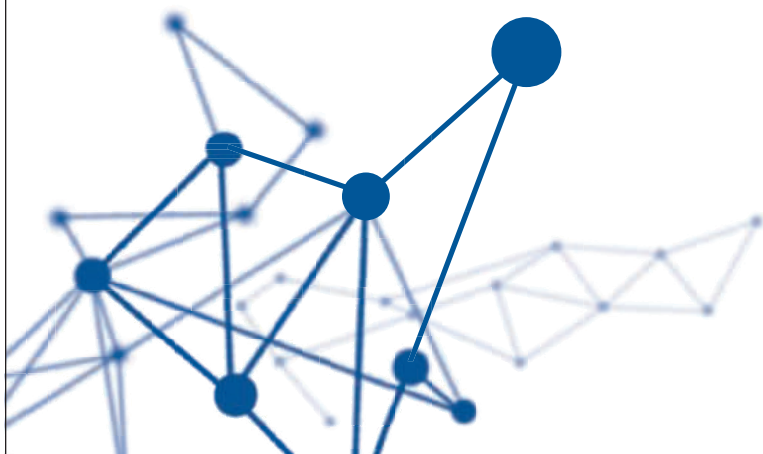
LUISA WHITTAKER-BROOKS

*Assistant Professor of Chemistry
The University of Utah*

*Exploration of scalable polymer-metal
for thermoelectric applications*



ADVANCING SCIENCE. SERVING SOCIETY





Linear Motor Microscope Stages

The HLD117 series of linear stages for inverted research microscopes sets new standards for convenience and top performance. The HLD117 linear stages operate on a different principle from conventional stepper motor, ball-screw based motorized stages. The HLD117 linear stage motor floats over a magnetic track, driving the x- and y- stage plates over precision bearing guides, providing near frictionless, ultrasmooth movement. This method of movement allows a wide range of scanning speeds (1 $\mu\text{m}/\text{sec}$ up to 300 mm/sec) to be achieved, making these stages suitable for a vast range of applications from rapid screening to detailed imaging. Superb repeatability ($\pm 1.15 \mu\text{m}$), high resolution ($\pm 0.05 \mu\text{m}$), and exceptional accuracy (0.045 $\mu\text{m}/\text{mm}$ of travel) along with 50 nm encoders as standard, make the HLD117 an excellent choice for advanced imaging techniques. Built for performance with unmatched acceleration rates and speeds, the HLD117 provides constant speeds with extremely low velocity ripple.

Prior Scientific

For info: +44-1223-881711
www.prior.com

TERS Instrumentation

Tip-enhanced Raman scattering (TERS) is a technique that provides molecular information on the nanometer scale through the combination of a Raman spectrometer and a scanning probe microscope. TERS has been hampered by extremely long acquisition times (measured in hours) required for collection of reasonable pixel density, and is seen by the research community as a difficult tool. Horiba Scientific and AIST-NT now offer a solution that addresses all the instrumentation concerns and bring TERS as an analytical method to a completely new level. The XploRA Nano platform in the upright and side configuration, in combination with AIST-NT's SmartSPM and Horiba's XploRA spectrometer, offers a very compact (complete setup stands on a 900 × 760 × 55 mm optical table), fully integrated, and automated solution. The Horiba Scientific TERS instrumentation is robust, compact, and easy to use. It is currently available for chemical imaging at the nanoscale level for real-world applications.

Horiba Scientific

For info: 732-494-8660
www.horiba.com/raman-afm



cellFRAP Imaging Platform

Enabling the easy addition of photomanipulation techniques to imaging platforms, Olympus has launched a new cellFRAP deck system for the popular "open source concept" IX83 and IX73 microscopes. The Olympus cellFRAP provides highly accurate and flexible live-cell photomanipulation with various evaluation options for data presentation needs. Unlike conventional widefield-based fluorescence recovery after photobleaching (FRAP) systems, the Olympus cellFRAP employs a diffraction-limited laser spot for high-intensity and precise positioning of the bleaching region across the full field of view (FOV). This ensures that photomanipulation reaches every point in the FOV without needing to move the sample. The system's excellent spot quality allows full flexibility in position and shape of the bleaching region, and enables control of the bleaching area with extreme accuracy. Driven by the Olympus real-time controller, the cellFRAP system achieves an unrivaled short switchover time of only 200 μs between bleach and postbleach acquisition, ensuring detection of the most valuable initial sample response after stimulation.

Olympus

For info: +49-(0)-40-23773-5913
www.olympus-lifescience.com

Scanning Electron Microscope

A new variant of the world's fastest scanning electron microscope is now available: The Zeiss MultiSEM 506 features 91 beams working in parallel and increases the throughput of the Zeiss sMultiSEM 505 by a factor of three. The unrivaled net acquisition speed of more than 2 terapixels per hour enables large-scale experiments such as the imaging of cubic millimeters of brain tissue at nanometer resolution for the analysis of neural circuits. For research work conducted as part of numerous brain initiatives, this will speed up the ability to map whole areas of the brain to help understand the neuronal network. The MultiSEM 506 also demonstrates that the Zeiss multibeam technology is scalable and will satisfy future throughput needs in other fields as well, for example in semiconductor applications. The Zeiss MultiSEM 505 and 506 are designed for continual operation and fitted with the intuitive Zeiss Efficient Navigation (ZEN) software.

Zeiss

For info: +49-3641-64-3949
www.zeiss.com

Atomic Force Microscope

The Keysight 9500 atomic force microscope (AFM) system seamlessly integrates new software, a new high-bandwidth digital controller, and a state-of-the-art mechanical design to provide unrivaled scan rates of up to 2 sec/frame (256 × 256 pixels). The ultrafast scan rates of the 9500 are made possible by Keysight's new Quick Scan technology. Available as a system option, Quick Scan is controlled through NanoNavigator, a powerful new imaging and analysis software package from Keysight. In addition to supporting Quick Scan functionality, NanoNavigator software lets researchers save time by using the new Auto Drive feature, which automatically and optimally

sets all parameters for the 9500. AFM novices and experts alike can appreciate NanoNavigator's efficient, workflow-based graphical user interface, as it guides users step-by-step through system setup and operation via intuitive, eye-catching visuals. For ultimate convenience, the NanoNavigator mobile app for smartphones and tablets allows remote monitoring of AFM experiments while they are being performed by the 9500.

Keysight Technologies

For info: 800-829-4444
www.keysight.com

Electronically submit your new product description or product literature information! Go to www.sciencemag.org/products/newproducts.dtl for more information.

Newly offered instrumentation, apparatus, and laboratory materials of interest to researchers in all disciplines in academic, industrial, and governmental organizations are featured in this space. Emphasis is given to purpose, chief characteristics, and availability of products and materials. Endorsement by *Science* or AAAS of any products or materials mentioned is not implied. Additional information may be obtained from the manufacturer or supplier.



Join AAAS. Get instant access to *Science*. Support all of the sciences.

When you subscribe to *Science*, you become part of the American Association for the Advancement of Science (AAAS), a nonprofit community of more than 100,000 members worldwide who believe in the power of science to make the world a better place. AAAS is hard at work promoting science in government, schools, and in the public commons around the globe.

AAAS's award-winning journal *Science* offers the top peer-reviewed research across multiple disciplines. With your subscription, you'll get:

- 51 weeks of home delivery of *Science*
- Instant online retrieval of every *Science* article ever published, dating back to 1880
- Full access to the *Science* mobile site and apps
- Career advice, webinars, blogs and fascinating features exclusively for AAAS members
- Members-only newsletters, and much more

With increasing public skepticism about science—and public funding for research more uncertain than ever—our work has never been more important. Join hands with us today!

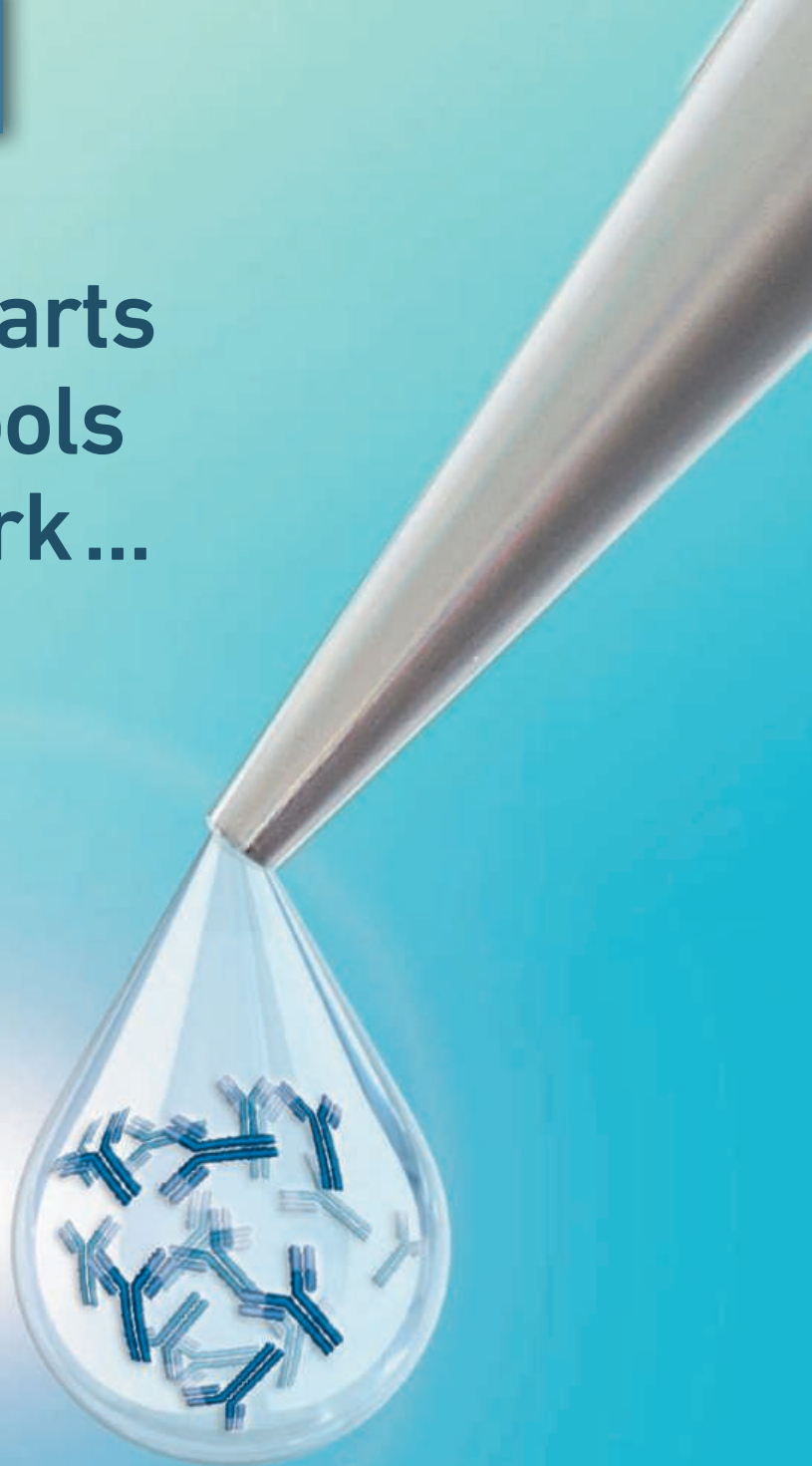
Visit promo.aaas.org/joinaaas. Together, we can make a difference.

Science
AAAS

Finding cures starts with research tools that actually work...

- Proteomic products and services
- Focused product portfolio
- Products tested for specificity and sensitivity
- Antibodies rigorously tested across a wide range of research applications
- Custom formulations
- GMP-grade recombinant rabbit monoclonal antibodies*
- Bulk orders and lot reservations

* Custom formulations of certain monoclonal antibodies can be produced by CST in compliance with FDA regulations governing ASRs. Such products would be classified as Analyte Specific Reagents. Analytical and performance characteristics are not established. All other products are for Research Use Only. Not For Use In Diagnostic Procedures.



Learn more at: www.cellsignal.com/drugdiscovery





There's only one **Science**

Science Careers Advertising

For full advertising details, go to ScienceCareers.org and click For Employers, or call one of our representatives.

Tracy Holmes

Worldwide Associate Director
Science Careers
Phone: +44 (0) 1223 326525

THE AMERICAS

E-mail: advertise@sciencecareers.org

Fax: +1 (202) 289 6742

Tina Burks

Phone: +1 (202) 326 6577

Nancy Toema

Phone: +1 (202) 326 6578

Online Job Posting Questions

Phone: +1 (202) 312 6375

EUROPE / INDIA / AUSTRALIA / NEW ZEALAND / REST OF WORLD

E-mail: ads@science-int.co.uk

Fax: +44 (0) 1223 326532

Sarah Lelarge

Phone: +44 (0) 1223 326527

Kelly Grace

Phone: +44 (0) 1223 326528

Online Job Posting Questions

Phone: +44 (0) 1223 326528

JAPAN

Katsuyoshi Fukamizu (Tokyo)

E-mail: kfukamizu@aaaas.org

Phone: +81 3 3219 5777

Hiroyuki Mashiki (Kyoto)

E-mail: hmashiki@aaaas.org

Phone: +81 75 823 1109

CHINA / KOREA / SINGAPORE / TAIWAN / THAILAND

Ruolei Wu

Phone: +86 186 0082 9345

E-mail: rwu@aaaas.org

All ads submitted for publication must comply with applicable U.S. and non-U.S. laws. *Science* reserves the right to refuse any advertisement at its sole discretion for any reason, including without limitation for offensive language or inappropriate content, and all advertising is subject to publisher approval. *Science* encourages our readers to alert us to any ads that they feel may be discriminatory or offensive.

ScienceCareers

FROM THE JOURNAL SCIENCE AAAS

ScienceCareers.org

POSITIONS OPEN



SENIOR SCIENTIST IN FISHERIES ECOLOGY AND ENHANCEMENT

Mote Marine Laboratory is seeking a fisheries scientist to join our Fisheries and Aquaculture Research Directorate in Sarasota, FL. The position is with a multi-disciplinary team that is refining a science-based approach to responsible marine fisheries enhancement, modeling enhancement potential, developing common snook aquaculture technology, and using release-recapture experiments to probe fundamental questions in marine fisheries enhancement and fisheries ecology. Applicants should hold a Ph.D. with specialization in fisheries ecology and fisheries enhancement; experience in aquatic ecology, marine aquaculture research and fisheries modeling is also desired. A strong extramural funding record, research publications in fisheries ecology and aquaculture, and exemplary partnership skills are required. The position is fully supported for 4 years with excellent benefits and salary. Subsequent funding is contingent upon research grants, publication record and funding availability. Position will remain open until filled. Send Curriculum Vitae, brief statement of research interests, and contact information for 3 references to Ken Leber (e-mail: KLeber@mote.org). Title your Email 'Senior Scientist + your name'. Mote Marine Laboratory is an Equal Opportunity/Americans with Disabilities Act/Electronic Employment Verification Employer.

ASSISTANT PROFESSOR in Comparative Invertebrate Zoology

The University of Arkansas Department of Biological Sciences seeks applicants for a tenure-track Assistant Professor position in Comparative Invertebrate Zoology. Minimum Requirements: Ph.D./strong research record. Candidates using a comparative organismal approach with broad training in invertebrate biology that complement existing departmental strengths in ecology and evolutionary biology are preferred but other focal areas will be considered. Expectations: establish externally funded research program/teach an undergraduate Principles of Zoology course and graduate courses within research area/professional service. Submit a cover letter, Curriculum Vitae, teaching statement, and research statement to website: <http://jobs.uark.edu/postings/10388>. The names, titles, email addresses, and contact numbers of five professional references willing to provide letters of reference will be requested during the application process. For information about the department see website: <http://biology.uark.edu>. Completed applications received by **December 12, 2015** will be assured full consideration. Late applications will be reviewed as necessary to fill the position. Search committee chair is Dr. Michelle Evans-White (e-mail: mevanswh@uark.edu). The University of Arkansas is Affirmative Action/Equal Opportunity Employer/Veterans/Disabled.

FACULTY POSITION University of North Carolina at Greensboro Department of Biology

The Department of Biology invites applications for a tenure-track Assistant Professor position in the field of Developmental Biology. We seek individuals whose biological research addresses environmental impacts upon development, with use of any model organism. Successful applicants will be expected to develop a strong, externally funded research program and train a diverse group of undergraduate and graduate students. Candidates must hold or anticipate a Ph.D. in Biology or a related discipline by August 1, 2016, postdoctoral experience is preferred. The position will start August 2016. University of North Carolina Greensboro is especially proud of the diversity of its student body and is an Equal Employment Opportunity/Affirmative Action Employer with a strong commitment to increasing faculty diversity. Equal Opportunity Employer Affirmative Action/Military/Female/Disabled/Veteran. To apply, visit website <https://jobsearch.uncg.edu> and click on "Faculty" (position 999417).

POSITIONS OPEN

POSTDOCTORAL FELLOW in PLANT ECOLOGY and EVOLUTION

The Department of Ecology and Evolutionary Biology (EEB) at Tulane University seeks to fill the Koch-Richardson Postdoctoral Fellowship in PLANT ECOLOGY AND EVOLUTION. The position is a two-year appointment with a start date of July 1, 2016. The department aims to recruit an outstanding PhD scientist who will merge excellence in teaching, research, and service. Applicants are encouraged to identify a potential faculty collaborator in EEB, although those interested in botanical subjects not represented among EEB faculty will be given full consideration. Information about the department may be found at website: <http://tulane.edu/sse/eebio/>

Applicants must submit a letter of application, curriculum vitae, a statement of research interests, a statement of teaching philosophy and interests, and the descriptions of at least two botanical courses they would be able to teach, one at an undergraduate level, and the other at a graduate/advanced undergraduate level. All application documents must be sent to Interfolio at website: <http://apply.interfolio.com/32819>. In addition, the applicant must supply, through the Interfolio site, the names and contact information of three individuals from whom confidential letters of recommendation will be solicited. Those letters should focus on excellence in teaching as well as research. The Interfolio site will begin accepting applications on November 16, 2015.

Review of applications will begin January 11, 2016, and the search will remain open until the position is filled. *Tulane is an Equal Opportunity Employer/Minorities/Female/Veteran/Disabled.*

Please contact the chair of the search committee if you have any questions. **Dr. Steven P. Darwin (e-mail: darwin@tulane.edu, committee chair)**

MULTIPLE TENURE TRACK POSITIONS

The University of Nevada, Reno (UNR), a national Tier 1 rank research university, is currently undergoing rapid expansion. As integral components of University of Nevada Reno, the College of Agriculture, Biotechnology and Natural Resources and the Nevada Agricultural Experiment Station seek to fill 5 tenure-track, 9-month positions: (1) Remote Sensing Science and Geospatial Analysis in the Department of Natural Resources and Environmental Science; (2) Plant Signal Transduction in the Department of Biochemistry and Molecular Biology; (3) Beef Cattle Production in the Department of Agriculture, Nutrition and Veterinary Sciences; (4) Veterinary Physiology and Animal Reproduction in the Department of Agriculture, Nutrition and Veterinary Sciences; and (5) Professor and Chair in the Department of Biochemistry and Molecular Biology. Successful candidates will teach courses within their department and establish a rigorous, innovative, and nationally recognized research program in their area of expertise. For more information and to apply, please visit website: <https://www.unrsearch.com>.

Download the
ScienceCareers
Job App



SEARCH
JOBS ON
THE GO!

apps.sciencemag.org

Faculty Position in Epidemiology

Wayne State University School of Medicine

Wayne State University located in Detroit, Michigan is seeking to strengthen its Epidemiology Unit, which deals with the incidence, distribution, and possible control of diseases and other factors relating to health.

The Epidemiology Unit collaborates with Departments within the School of Medicine, and also with the Perinatology Research Branch of the Division of Intramural Research, NICHD, NIH, DHHS, which is housed at the Wayne State University campus.

As a key staff member in support of the PRB, this individual would help to accomplish the Branch's mission by 1) developing statistical analysis, programming strategies and methodologies in support of research projects, 2) evaluating and analyzing data using accepted statistical and biostatistical techniques, 3) working closely with the scientific team and collaborators to provide operational parameters to ongoing research, 4) training the next generation of researchers, 5) translating the results of the research through publications and technology transfer.

The individual chosen for this position will become part of a highly successful, fast-paced research group that focuses on clinical and basic research in perinatal medicine and related disciplines. The goal of this internationally recognized research is to develop novel diagnostic, therapeutic and preventative strategies to reduce adverse pregnancy outcome, infant mortality and handicap. The research agenda involves novel discovery technologies in functional genomics, proteomics, metabolomics and DNA analysis.

To be considered for this position, it is recommended that candidates demonstrate the following:

1. Thorough knowledge of biostatistical methodologies, procedures and testing
2. Expertise in issues pertaining to the conduction and analysis of longitudinal studies
3. Competence in the area of mathematical modeling
4. Knowledge of data coordination, collection and statistical analysis methods and research coordination principles
5. Knowledge of medical and research protocols
6. Knowledge of computer software design and multiple programming languages
7. Demonstrated broad knowledge of the understanding of scientific principles, theories and technologies applicable to biological sciences, in general, and perinatology in particular
8. A sound understanding of academic research and related issues together with extensive experience in complex, multi-disciplinary programs (administrative and scientific)
9. Ability to foster intellectual productivity
10. Strong oral and written communication skills
11. Ability to work independently and collaboratively
12. Basic knowledge of perinatology is desirable

Academic and professional requirements:

1. Ph.D. in Epidemiology, Biostatistics, Statistics or related field
2. Minimum of five years of experience

Interested individuals should send:

a curriculum vitae,

a separate statement summarizing their experience and professional contributions,

and three references to: Jennifer Turpin, Wayne State University School of Medicine

jturpin@med.wayne.edu



Director

Biomufacturing Research Institute and Technology Enterprise

North Carolina Central University (NCCU) invites applications for the position of Director for the Biomufacturing Research Institute and Technology Enterprise (BRITE) to provide overall leadership and supervision of the unit. The Director reports directly to the Vice Chancellor for Research and Economic Development. BRITE is one of NCCU's major research institutes and houses the College of Arts and Science's Department of Pharmaceutical Sciences. BRITE is located in a \$20.1 million state-of-the-art facility and features 21,000 sq. ft. of classroom and office space, and 31,000 sq. ft. of laboratory space for faculty and students to conduct applied research in areas related to drug discovery, biomufacturing and biotechnology.

Purpose of Position: The BRITE Director will lead and manage teams of scientists conducting translational research encompassing biomufacturing and drug discovery activities in various therapeutic areas that include diabetes, cancer, neurodegenerative diseases and other metabolic disorders. The Institute owns a 460,000 compound library which is the largest academic collection in the USA. BRITE serves approximately 200 students annually who are majoring in Pharmaceutical Sciences at the undergraduate or graduate level. The newest graduate program within the unit is the Ph.D. in Integrated Biosciences/Pharmaceutical Sciences Track. The unit has approximately 38 research, faculty and staff members. The Director, in collaboration with the Chair of Pharmaceutical Sciences, will manage the recruitment of new students, BRITE scholarships, student mentoring and career development, internships, student leadership development and outreach activities for K-12. The Director will participate as a leader representing BRITE at NCBioImpact, a state initiative for workforce development. The Director is also expected to establish and manage internal and external collaborations; contribute to the assessment of external business alliances; and, out-licensing opportunities for technologies developed in BRITE.

Qualifications: The Director is expected to have an earned Ph.D. (or M.D. or PharmD) in Biochemistry, Chemistry, Biology or a related field and an in-depth understanding of the pharmaceutical industry. It is expected the Director will qualify for full professor and tenure. A minimum of 5 years of managerial experience working in the pharmaceutical/ biotechnology industry is required. The Director will have a demonstrated record of leading translational research in drug discovery to advance leads and candidate drugs; a record of effective project leadership and an in-depth understanding of drug discovery and development from target to clinical trials; demonstrated track record of innovation and development; strong interpersonal, leadership and collaboration skills to work in a team-oriented, matrix environment. Academic experience and a successful track-record of obtaining external funding are encouraged.

The Division anticipates filling the Position of Director, BRITE by July 1, 2016; however, review of applications will commence immediately and continue until the position is filled.

Applicants should apply at the following web address <https://jobs.nccu.edu/>.

Director

Julius L. Chambers Biomedical/Biotechnology Research Institute

North Carolina Central University (NCCU) invites applications for the position of Director, Julius L. Chambers Biomedical/Biotechnology Research Institute (JLC-BBRI). The Director of the JLC-BBRI reports directly to the Vice Chancellor for Research and Economic Development; and, provides leadership for a broadly based research portfolio which includes cancer, cardio-metabolic disorders, neuroscience and nutrition. Established in 1999, the JLC-BBRI facility provides 40,000 sq. ft. of basic research space. The JLC-BBRI is an innovative research and training institute dedicated to the advancement of fundamental knowledge of human diseases, particularly those that disproportionately affect underrepresented minority groups.

Purpose of Position: The Director serves as the scientific leader of NCCU's JLC-BBRI research facilities in Durham and Kannapolis, NC (North Carolina Research Campus-NCRC) and holds a tenured faculty position as Professor. The Director's responsibilities include the following: assure the quality and competitiveness of research conducted in the Institute; evaluate, plan, direct and implement activities related to the mission and function of the JLC-BBRI as a constituent body of the University; manage the Institute's budget and provide overall administrative leadership; supervises and mentors faculty and non-tenure track scientists in securing external research funding; facilitate student research experiences within the JLC-BBRI and with the Institute's internal and external partners; forge long-term successful partnerships among various academic and research units at NCCU as well as with agencies, corporations and academic research institutions within Research Triangle Park, throughout the state and beyond.

Qualifications: The Director will have an earned doctorate degree (Ph.D.) or equivalent doctoral degree in the biomedical sciences; or (M.D.) degree with relevant research experience from an accredited institution. The Director will have a distinguished record of leadership, research, grantsmanship, publications, and other scholarly activities. Sustained contribution to the sciences will be evidenced by productivity in funded research and publications. Continuous experience as a principal investigator on externally funded biomedically-related research projects is also required. A record of administration in higher education is highly preferred.

The Division anticipates filling the Position of Director, JLC-BBRI by July 1, 2016; however, review of applications will commence immediately and continue until the position is filled. Applicants should apply at the following web address, <https://jobs.nccu.edu/>.

Advance your career
with expert advice from
Science Careers.



**Download Free Career
Advice Booklets!**

ScienceCareers.org/booklets

Featured Topics:

- Networking
- Industry or Academia
- Job Searching
- Non-Bench Careers
- And More



ScienceCareers

FROM THE JOURNAL SCIENCE 



Multiple Faculty Positions on Microbiomes at Arizona State University (JOB # 11403)

The School of Life Sciences (SOLS) at Arizona State University (ASU) invites applications for up to two tenure-eligible faculty positions in the area of microbiome research. Rank and tenure status will be commensurate with experience. Anticipated start date is August 2016.

We seek to establish a strong group of scientists focused on understanding the functional and structural basis of complex systems of microbes, and their relevance for human, animal and plant biology, the environment, and man-made systems. We envision these individuals working to advance the discipline by developing and using novel technologies to provide an integrated systems understanding of microbiomes, so as to establish general functional principles that are not only explanatory, but also predictive of the behavior of communities of microorganisms.

Successful candidates will be expected to develop or maintain an innovative, independent, extramurally funded research program, provide excellent classroom instruction as assigned, contribute to curriculum development, mentor students and postdoctoral fellows and interact with a very multidisciplinary group of faculty in the Life Sciences at ASU. Competitive start-up packages will be provided. All candidates must have a doctoral degree by the time of appointment in microbiology or a related field, a proven track record of novel research in microbiome biology, and relevant postdoctoral experience. Desired qualifications include a record of publication in refereed journals, demonstrated excellence in teaching and/or mentoring, and experience working in a multi-disciplinary environment. Candidates for Associate or Full Professor rank must have a demonstrated record of significant extramural funding.

To apply, please send a cover letter that identifies the rank for which you seek consideration. Additional application materials include: curriculum vitae, three representative publications, statement of research vision and plans, teaching statement, and contact information (name, email, and phone number) for three references. References will only be contacted for finalists at a later stage of the search.

Application materials should be addressed to Rajeev Misra, Search Committee Chair, and sent electronically as pdf files to solsfacultysearch1@asu.edu. Only electronic applications will be considered. The initial closing date for receipt of applications is **December 31, 2015**; if not filled, review will continue every week thereafter until the search is closed. A background check is required for employment.

Arizona State University is a VEVRAA Federal Contractor and an Equal Opportunity/Affirmative Action Employer. All qualified applicants will be considered without regard to race, color, sex, religion, national origin, disability, protected veteran status, or any other basis protected by law. <https://www.asu.edu/aad/manuals/acd/acd401.html> <https://www.asu.edu/titleIX/>



University of
New Hampshire

Environmental Microbiology

The University of New Hampshire College of Life Science and Agriculture seeks outstanding applicants for three tenure-track faculty positions in ENVIRONMENTAL MICROBIOLOGY at the Assistant Professor level to begin Fall 2016. The CRITICAL ZONE MICROBIAL ECOLOGY position will address areas including global change, nutrient cycling, and carbon transformations in soil and groundwater. The MICROBIAL ECOLOGY position will address areas including environmental microbiology, population genetics, evolution, ecology, host-microbe interactions and symbiosis, and microbiomes. The PLANT-MICROBE INTERACTIONS / PLANT PATHOLOGY position will address the biology, ecology, or epidemiology of agricultural plant diseases to inform management strategies including host resistance in sustainable cropping systems.

All applicants must have an earned doctorate by the time of appointment and demonstrate outstanding potential in both teaching and research. Postdoctoral experience is desired. Information, including detailed position descriptions and complete application information is available at colsa.unh.edu/employment. Applicants should apply online by 12/31/2015 at <http://jobs.usnh.edu> for full consideration.

The University seeks excellence through diversity among its administrators, faculty, staff, and students. The University prohibits discrimination on the basis of race, color, religion, sex, age, national origin, sexual orientation, gender identity or expression, disability, veteran status, or marital status. Application by members of all underrepresented groups is encouraged.



SCHOOL OF
MEDICINE &
DENTISTRY
UNIVERSITY OF ROCHESTER
MEDICAL CENTER

Tenure-Track/Tenured Faculty Position

The Center for Oral Biology in the Eastman Institute for Oral Health invites applications for a faculty position at the Assistant, Associate or Full Professor level. Successful applicants should have a PhD, MD, DDS, or combined degrees, and demonstrated ability to conduct a state-of-the-art research program to investigate an area of science relevant to human disease/ oral biology. We are interested in all areas of contemporary biomedical science, including but not limited to: Developmental and Cell Biology, Genetics and Epigenetics, Stem Cell Biology, Regenerative and Reparative Medicine, Pain, and Cancer Biology. Preference will be given to applications that complement ongoing programs or bring novel expertise and research perspectives. Individuals seeking an appointment must have a demonstrated record of extramural funding. The Center of Oral Biology is located in the state-of-the-art Arthur Kornberg Medical Research Building at the University of Rochester School of Medicine and Dentistry. Faculty members in the Center carry joint appointments in appropriate academic departments and participate in graduate student training in several graduate programs in the University of Rochester.

More information about the Center and available positions can be found on the internet (<http://www.urmc.rochester.edu/center-oral-biology/>). For further details and to apply online, please go to: <http://www.rochester.edu/working/hr/jobs/> (Job ID #187991). Please provide your curriculum vitae, statement of current and future research interests, and names and addresses of at least three references.

The University of Rochester is an Equal Opportunity Employer. Women and minorities are encouraged to apply.

By Elisabeth Pain

A doctor's dilemma

Deniz Kirik was drawn to medicine by his desire to better understand the human brain, but he found that doctors in his native Turkey have little opportunity for research. Nonetheless, he has turned what first felt like a failed career choice into an advantage. Now a neuroscience professor at Lund University in Sweden and co-founder of a spinoff company, Kirik uses his medical background to develop novel gene-based therapies for Parkinson's disease and bring them to the clinic. In October, Kirik secured a partnership with his regional government in southern Sweden to build a hospital specialized for testing and implementing gene therapies. This interview was edited for brevity and clarity.

Q: How did you get into science?

A: My frustration at realizing that my purpose for entering medical school clashed with what was expected of me as a medical doctor in Turkey led me to try my hand at research in my spare time. Several people on campus opened their laboratories to me. I was to start my final-year clinical residency when one of their colleagues at Lund University invited me for a short stay in his laboratory. So I took a break from medical school and, once in Sweden, stayed on for a Ph.D.

Q: Was it hard to change course?

A: My decisions were not well understood back home. My relatives called my parents lamenting that I had lost purpose in life. Even my professional colleagues seemed to think that research was the wrong path to follow. The medical faculty board threatened to dismiss me if I didn't return. After a 4-year-long uphill battle and a lot of back-and-forth between the two countries, I eventually managed to finish my medical studies. I earned my degree to state that even though my path was different, it wasn't any less good than medical practice.

Q: Is your medical background helpful today?

A: Even though venturing through medical school initially felt like a failed attempt at fulfilling my career ambition, that decision eventually brought me to where I am today: doing science in a basic and translational research environment, still within a medical faculty. I am using viral vectors to deliver genes to the brain to treat Parkinson's disease, and I am looking into the possibility of controlling the activity of therapeutic proteins to personalize treatment.

I've also had to convince hospital directors to invest



"My purpose for entering medical school clashed with what was expected of me."

space, time, and competent people into a translational project like this. Had I had no engagement with the clinical world as a trainee years ago, I would have had a less clear view on how to get clinicians' commitment. In turn, our ability to understand clinical challenges is improved when some of us on the research team have a medical background in that area.

Q: How do you juggle your work activities and personal life?

A: As scientists, we are immersed in the questions we work on, and they become part of our personal identity. But that presents a challenge, in that I am married with two small kids. My wife is as prominent as I am in her research career, and she is also an active clinician. We have established a

routine whereby we prioritize and share taking care of the children after daycare. I wouldn't say it's been easy, but we buffer each other's difficult times at work by slowing down when the other has to really push the limits.

Q: What's your advice for young scientists?

A: Defining the purpose of their life and their ambitions is very important. Then they need to determine what path will lead them to their goals, revising it and iterating continuously. They will need a lot of strength and persistence. Also, it's ironic, but the things that taught me the most are the things that I failed at. I've always investigated the reasons for my failures much more intensely than my successes, and failing drives me to try harder the next time. ■

Elisabeth Pain is Science Careers contributing editor for Europe. Send your story to SciCareerEditor@aaas.org.

ILLUSTRATION: ROBERT NEUBECKER